PHYS

VOLUME

THE PHYSICAL REVIEW

A journal of ... and theoretical physics established by E. L. Nichols in 1893

Published by the American ... for the

AMERICAN PHYSICAL ...

Officers

President

C. C. LAURITSEN
California Institute of ...
Pasadena, California

Vice-President

J. H. VAN VLECK
Harvard University
Cambridge, Massachusetts

Secretary

K. K. DARROW
Bell Telephone Laboratories
Office:
Columbia University
New York 27, New York

Treasurer

G. B. PEGRAM
Columbia University
New York 27, New York

Local Secretary for the Pacific Coast

J. KAPLAN
University of California at ...
Angeles
Los Angeles, California

Managing Editor

S. A. GOUDSMIT
Brookhaven National ...
Upton, Long Island
New York

The Physical ...

Entered as second-class ...

Acceptance for mailing at special ...

BOARD OF EDITORS

Editor

S. A. Goudsmit

Associate Editors

F. Bitter	Harvey Brooks	M. Goldhaber
T. Bonner	R. F. Christy	E. Hart[illegible]
W. G. Hess	C. L. Critchfield	A. W. Lawson
E. Lauer, Jr.	M. Deutsch	A. Sachs
J. F. Shrader	T. H. Johnson	R. Smoluchowski
J. E. Swanson	Bruno Rossi	C. H. Townes

Manuscripts for publication should be submitted to S. A. Goudsmit, Brookhaven National Laboratory, Upton, Long Island, New York. ... authors' institutions are requested to pay a publication charge of $6 ... page which, if honored, entitles them to 100 free reprints. Instructions ... be sent with galley proofs.

Proof and all correspondence concerning papers in the process of publication should be addressed to the Publication Manager, American Institute ... Physics, 57 East 55 Street, New York 22, New York.

Subscription Price

United States and Canada $35.00
Elsewhere $37.00

Back Numbers[1]

Yearly back number rate when complete year is available:
Prior to 1949: $30.00
Thereafter: $37.00

Single numbers: $3.00 each, prior to July, 1929;
$1.00 each, July, 1929–December, 1941;
$2.00 each, January, 1942–December, 1946;
$3.00 each, January, 1947–December, 1948;
$1.25 each, thereafter.

General Index, 1893–1932: $4.00.

Subscriptions, renewals, and orders for back numbers should be addressed to the American Institute of Physics, 57 East 55 Street, New York 22, New York.

Changes of address in the case of members of the American Physical Society should be addressed to the Treasurer; in the case of other subscribers to the American Institute of Physics.

[1] Address Section 1 Library of Physics Department, Cornell University, Ithaca, New York.

... semi-monthly on Prince and Lemon Streets, Lancaster, Pennsylvania.

... at the Post Office at Lancaster, Pennsylvania, under the Act of March 3, 1879 ... provided for in paragraph (d-2), section 34.40, P. L. & R. of 1948, authorized January ...

THE
PHYSICAL REVIEW

A journal of experimental and theoretical physics established by E. L. Nichols in 1893

SECOND SERIES, VOL. 84, NO. 5 DECEMBER 1, 1951

Resonance-Region Neutron Spectrometer Measurements on Silver and Tungsten

W. SELOVE*
Argonne National Laboratory and Physics Department, University of Chicago, Chicago, Illinois
(Received June 11, 1951)

A high speed rotating-shutter spectrometer has been built for making slow neutron measurements in the resonance region, using a neutron "pile" as a source. One of the principal advantages of the new apparatus is that comparatively small samples are required—typically less than one gram. Thus measurements can be made on many comparatively rare materials, such as certain separated isotopes.

Measurements are reported here on silver and tungsten. These measurements were made with an effective resolution in reciprocal velocity somewhat better than 1.0 microsecond/meter at high energies. In silver, the measurements show clearly resolved resonances at 5, 16, 30, 41, and 53 ev, and numerous unresolved resonances at higher energies. The constants of the 5-ev resonance are $E_r=5.17\pm0.08$ ev, $\sigma_0=12{,}000\pm1500$ barns (10,000 barns for metallic silver at room temperature), $\Gamma=0.17\pm0.02$ ev, $\Gamma_n\approx0.011$ ev. The tungsten work includes measurements on separated-isotope samples of the four major isotopes. The resonance-level spacings observed in these isotopes are: 10 to 30 ev in 182, about 20 ev in 183, perhaps 100 ev in 184, and several hundred ev in 186.

1. INTRODUCTION

IN the past few years, measurements in the slow neutron resonance region have been made principally by the time-of-flight method, with a pulsed cyclotron as a source.[1] Recently, a resonance region time-of-flight spectrometer for use with a neutron "pile" has been built and put into operation. One of the principal advantages of this instrument is that comparatively small samples are required, so that measurements can be made on many comparatively rare materials, such as certain separated isotopes. The first measurements made with this apparatus are reported here.

2. APPARATUS

The rotating-shutter spectrometer is described in detail elsewhere; only a brief description will be given here.

In the time-of-flight method, a short burst of neutrons of various energies is released at a "source" point at a known time. A detector at a known distance then delivers signals representing neutrons of various energies according to the time elapsed since the burst. In the modulated-cyclotron method the burst is obtained by pulsing the particle source of the cyclotron; for time-of-flight work with a pile, the continuous neutron beam from the pile is pulsed mechanically by a shutter. This shutter, in the present instrument, consists of a steel cylinder (Fig. 1), rotated at high speed, and containing six slits like the one shown. The fixed collimating system contains similar slits, and as the rotor turns the beam passes through in a short burst at the instant that the slits are in line with each other. The slits are about 2 cm high and 0.025 cm wide, the width being chosen to give the desired resolution. The shutter is long enough to make the background counting rate small; in the measurements reported here, the background due to leakage through the shutter was generally less than 2 percent of the timed-neutron rate. (Additional background from the pile gave a total background rate of about 5 percent.)

The electronic circuitry used with the shutter consists essentially of a number of "channels," each recording a separate energy interval. The detector is a BF_3 pulse ion chamber, 30 cm long, operated at a pressure of two atmospheres, and located 10 meters from the shutter. Neutron counts from the detector, which operates continuously, are "sorted" into the appropriate

* Now at Harvard University, Cambridge, Massachusetts.

[1] C. P. Baker and R. F. Bacher, Phys. Rev. **59**, 332 (1941) and further references there; L. J. Rainwater and W. W. Havens, Phys. Rev. **70**, 136 (1946); W. W. Havens and L. J. Rainwater, Phys. Rev. **70**, 154 (1946); Rainwater, Havens, Wu, and Dunning, Phys. Rev. **71**, 65 (1947); Havens, Wu, Rainwater, and Meaker, Phys. Rev. **71**, 165 (1947); Wu, Rainwater, and Havens, Phys. Rev. **71**, 174 (1947).

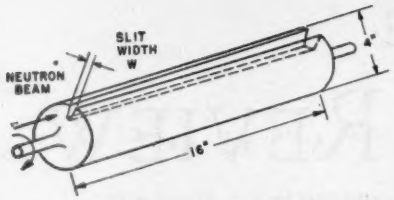

FIG. 1. Basic features of the rotating shutter.

channels at the proper time by means of a coincidence circuit in each channel. After each burst from the shutter, and after a further delay if desired, the channels are made sensitive consecutively, one at a time, for equal time intervals (a few microseconds in the present work). The entire timing operation is synchronized with the burst time by a photocell system. The measurements described here were made using 56 channels.

3. RESOLUTION

The resolution function is determined by the time shape of the burst, by the effect of detector length, and by the channel on-time. The burst was closely triangular in shape, with a base width which for most of the measurements reported here was 8 μsec. The detector was 30 cm long and thus contributed a 3 percent uncertainty to the 10 meter flight path. At "high" energies (short time-of-flight) this 3 percent is small compared to the resolution width of the burst time and channel on-time. At low energies, the detector effect becomes appreciable, and in fact makes the resolution function slightly asymmetric because the detection efficiency is high enough to make the intensity decrease along the length of the detector.

Figure 2 shows the calculated resolution function at high energies for the timing used in most of these measurements. This function is compounded from a triangular burst 8 μsec wide at the base and a channel on-time of 4 μsec. Although the curve extends 12 μsec, 90 percent of the area is included in the central 6.6 μsec, 95 percent in the central 7.8 μsec. Thus one could reasonably call the resolution width 7 or 8 μsec. However, in modulated-cyclotron systems, where both the burst and channel on-times are rectangular and the resulting resolution function triangular, it has been customary in the past to give the resolution width as the base width of the triangle. A triangular pattern, having about the same "90 percent-width" and "95 percent-width" as Fig. 2, would have a base width very nearly 10 μsec. Hence, for comparison with modulated-cyclotron work, the "resolution width" may be taken as 10 μsec, or 1.0 μsec/meter.

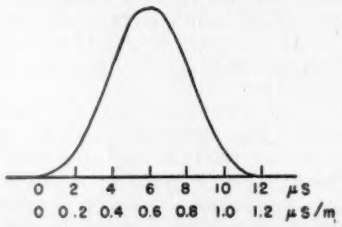

FIG. 2. Resolution function, not including detector-length effect, for 4 μsec channel time and 8 μsec triangular burst.

At low energies the detector effect on the resolution becomes appreciable, and the 1.0 μsec/m value is no longer an overestimate of the true "effective" width. For example, the detector effect amounts to 0.3 μsec/m at 50 ev. At still lower energies the detector effect is even larger and even makes the total resolution function slightly asymmetric, as noted above. No attempt has been made to correct the experimental transmission data for resolution, although in the analysis of the 5-ev resonance data for Ag the resolution was taken into account in a simple way. This is discussed further, below.

There is negligible resolution broadening introduced by detector pulse width. The amplified signals from the ion chamber have a rise time less than one microsecond; the rising edge of these signals is used to generate a very short pulse, which is then sorted into the various channels. The length of this short pulse (a few tenths of a microsecond) is set so that each signal from the detector is recorded in only one channel. Thus the only resolution broadening introduced by detector pulse width is due to the finite rise time of the ion-chamber signals. This time is short compared to the shortest channel time and burst time used.

4. ABSOLUTE ENERGY CALIBRATION

The midpoint of the 30-cm-long detector is set 1000 cm from the point where the beam enters the rotor. At low energies most of the beam is detected in the "front" part of the detector; accordingly, a correction to the flight path is made. This correction is only about 1 cm at 4 ev.

The timing pulses which switch the channels on and off in a "chain" sequence are obtained from a 1-*MC* oscillator and a series of dividers. The oscillator is quite stable, and its frequency is checked occasionally. Each time the shutter opens, a synchronized photocell pulse turns on the oscillator and, after an adjustable delay, starts the chain of channels. (The oscillator is adjusted to shut off shortly before each burst, to be resynchronized.) The photocell pulse is purposely set to occur shortly before the shutter opens so that a check can be kept on the delay between the two events. This delay is a function of the rotor speed and can be determined absolutely by changing the rotor speed and observing the resultant change in delay of "zero" time-of-flight neutrons, or of a resonance of low time-of-flight. Thus the time-of-flight scale is established on an absolute basis, when corrected for the small and measurable effect of all time lags in the electronic circuits.

5. MATERIAL MEASURED

Silver and tungsten were chosen for the first extensive measurements with this apparatus, for the following reasons: (1) They had been measured before,[1] with lower resolution than could now be used. (2) Separated-isotope samples of both elements were available at Argonne, and these could be used to investigate the isotopic distribution of the resonances. (3) Silver has a strong resonance at 5 ev, whose peak cross section σ_0 and width Γ were known only approximately. Measurements at 5 ev could now be made with sufficient resolution to determine σ_0 and Γ to within about 10 percent.

6. MEASUREMENTS ON SILVER

Measurements with Thick Sample

The measurements on normal silver were made with one thick sample and four thin ones. From the pure silver samples available at Argonne, one was chosen of approximately the same thickness as the thick sample

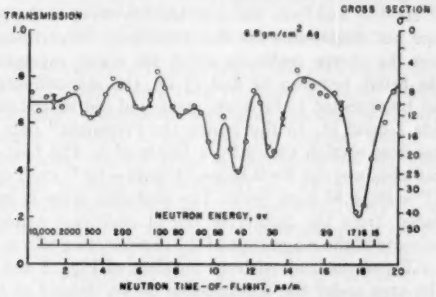

FIG. 3. Transmission of silver. Resolution ~1.0 μsec/m.

measured by Rainwater *et al.*[1] Thus it would be possible to get a fairly close comparison with their work, which will be referred to as "the earlier work."

The sample was first measured in the high energy region with a resolution (Fig. 2) about twice that used in the earlier work. The results are shown in Fig. 3. The statistical accuracy of the points is indicated for a few representative points. With 4 μsec channel time, the 56 channels used gave the transmission simultaneously in the region from very high energies (zero time-of-flight) to about 12 ev.

When compared with Fig. 7 of the earlier work, Fig. 3 shows the resolution of the broad 45-ev dip into three resonances, at 30, 41, and 53 ev. It appeared that with broader resolution the latter two might merge, but the 30-ev resonance seemed more sharply resolved than was expected from the earlier work. It was decided to run the sample again, this time with about the same resolution as in the earlier work. The results are shown in Fig. 4; the 30-ev resonance is still clearly resolved, and the two higher ones are no longer resolved. (The

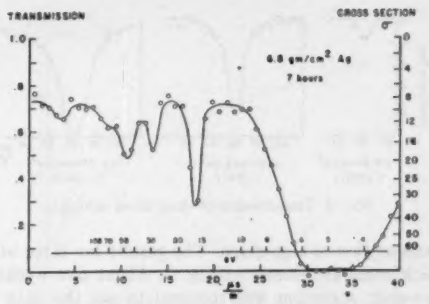

FIG. 4. Transmission of silver. Resolution ~1.6 μsec/m.

resolution used in a measurement is usually two to three times the interval between adjacent points.) The discrepancy with the earlier work has since been explained:[2] the effective resolution in that work was less than the nominal figure given, because of a "tail" on the cyclotron arc-current pulse.

Measurements with Separated Isotopes

Less than 100 mg of each separated silver isotope was available. This meant that only one slit could be used (four were used for the measurements with the thick sample) and that even then the sample would not be very thick. Hence, measurements with these samples took a very long time. Unfortunately, after many tens of hours of measurement, the samples appeared to be indistinguishable. Since they had been at the laboratory for several years and may have become mixed and since the quantities available were so small, the isotopic identification of silver's resonances has been put aside until better samples are available.

Measurements with Thin Samples

Four thin samples of normal silver were measured in the vicinity of the 5-ev resonance with high resolution (same timing as in Fig. 2). The results for a 0.0005-in. sample are shown in Fig. 5, on which a scale of apparent

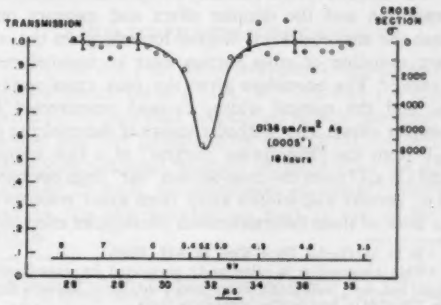

FIG. 5. Transmission of thin silver. Resolution ~1.0 μsec/m.

[2] W. W. Havens, private communication.

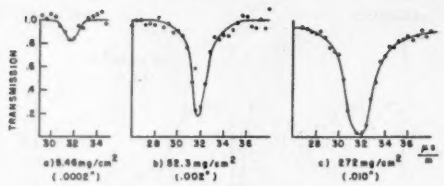

FIG. 6. Transmission of three silver samples.

cross section is also given. The results for three other thicknesses are shown in Fig. 6. About two weeks of two-shift operation was required to get the data for these four curves. (The running time given is only the "sample-in" time. Additional time is required, in the course of a measurement, to take open-beam runs in alternation with the sample-in runs, and to check the equipment occasionally.)

7. ANALYSIS OF THE 5-EV RESONANCE DATA

Since the measured cross section values, in Figs. 5 and 6, vary rapidly within a resolution width, it is clear that some correction must be made to obtain the true cross-section values. One method of analysis, which has been used in the past,[3] consists of a trial-and-error procedure. Various values of Breit-Wigner resonance parameters are assumed, and the corresponding "true" cross section curves and true transmission curves are calculated, corrected for doppler effect. The (calculated) resolution function is then numerically integrated over the true transmission curve. The final "calculated transmission" curves are compared with the experimental data, and the resonance parameters adjusted for best fit. This procedure can be expected to yield fairly accurate values only when the resolution width is smaller than the true width; in the present case this did not appear to be true. Moreover, the trial-and-error procedure involves an assumed resolution function; and, finally, the procedure is rather tedious. Consequently, a different method of analysis was used.

The method used is basically independent of both the resolution and the doppler effect and assumes only that the one-level Breit-Wigner formula gives the correct variation of cross section near an isolated resonance.[4,5] The procedure gives the peak cross section, σ_0, and the natural width, Γ, both uncorrected for doppler effect. The method consists of determining (1) $\sigma_0\Gamma$ from the "absorption integral" of a thin sample, and (2) $\sigma_0\Gamma^2$ from the cross section "far" from resonance (i.e., several half-widths away from exact resonance). In both of these determinations the doppler effect does not enter.[6] The resolution has no effect on (1); the resolution also has no effect on (2) if (a) the determination is made where the transmission varies approximately linearly with time-of-flight, and (b) the resolution is symmetrical on a time-of-flight scale. Even if (a) and (b) are not true, the resolution still has a negligible effect on (2) if the measured cross section does not vary rapidly within a resolution width. In any event, if the same value of $\sigma_0\Gamma^2$ fits a large energy region, reasonable confidence can be felt in this value.

The data of Fig. 4, in the vicinity of the 5 ev resonance, were fitted to an expression of the form $\sigma=b+(E_r/E)^{\frac{1}{2}}\sigma_0\Gamma^2/4(E-E_r)^2$ and the values of b and $\sigma_0\Gamma^2$ adjusted to give the best fit. The resonance energy E_r was determined, from the thin-sample data, as 5.17 $\pm$0.08 ev. The quantity b represents the "constant" part of the cross section in the vicinity of 5 ev. Strictly, b is not really constant; it includes effects from interference terms due to other resonances of the same J (spin of the compound nucleus) and from the asymmetric interference term involving the "potential scattering." It also includes effects from resonances of different J, and from the cross-section curve of the isotope not responsible for this resonance. Nevertheless, over the energy region in which the above expression was fitted, between $6\frac{1}{2}$ and $7\frac{1}{2}$ ev, the approximation can be expected to be fairly good, and did indeed provide a good fit. In this region the "resonant" part of the cross section varies by a factor of 3. The best fit was obtained for $b\approx 9$ barns (1 barn$=10^{-24}$ cm^2) and $\sigma_0\Gamma^2=365\pm30$ barn (ev)^2. The probable error is estimated, from the quality of the fit and from a rough estimate of the magnitude of the complicating effects.

$\sigma_0\Gamma$ was determined from the data of Figs. 5 and 6. The area under the transmission curve, defined as the "absorption integral," A, can easily be shown to be related to $\sigma_0\Gamma$, in the case of a thin sample, by $A\equiv\int(1-T)dt\approx\pi n\sigma_0\Gamma t_r/4E_r$ where T is the transmission, t is time-of-flight, t_r and E_r are the values of t and the energy at exact resonance, and n is the number of atoms/cm^2 in the sample. This result is not affected by resolution or doppler effect. For thicker samples, A no longer increases as fast as n. In Fig. 7, A is plotted against n. From the slope at the origin, $\sigma_0\Gamma$ is calculated as 2100$\pm$200 barn ev. The probable error given is again an estimated one.

From the values given for $\sigma_0\Gamma^2$ and $\sigma_0\Gamma$, one obtains $\sigma_0=12{,}000\pm2500$ barns, and $\Gamma=0.17\pm0.02$ ev. The principal contribution to the uncertainty in σ_0 comes from the probable error in $\sigma_0\Gamma$. It can be noted that σ_0 has approximately twice the relative error of $\sigma_0\Gamma$; this results from the dependence of σ_0 on the square of $\sigma_0\Gamma$, in the analysis used.

The probable error in σ_0 can be narrowed down by making an approximate calculation of the effect of the resolution, a calculation similar to that described at the

[3] B. D. McDaniel, Phys. Rev. **70**, 832 (1946).

[4] This assumption is adequately supported by experimental data. See, e.g., Goldsmith, Ibser, and Feld, Revs. Modern Phys. **19**, 259 (1947), and further references there.

[5] There is much literature on the resonance formula. See, e.g., E. P. Wigner, Phys. Rev. **70**, 15, 606 (1946), and further references there.

[6] H. Bethe, Revs. Modern Phys. 9, 140 (1937).

start of this section. First, the doppler effect must be calculated. The doppler width for this resonance is calculated to be 0.074 ev.[7] (The effective temperature of the silver atoms is taken as 12 percent higher than the room temperature of 300°K. This is on the basis of calculations by Lamb.[7]) As a result of the Doppler effect, the peak cross section is lowered to 80 percent of its "natural" value.

Using the calculated resolution, a rough calculation was then made of the apparent peak cross section which would be measured for a thin sample. This gave about 8000 barns, which is in excellent agreement with the experimentally measured 8000±1000 barns (Fig. 5). Therefore, it seems reasonable to place limits of about 1500 barns on the probable error of σ_0, instead of the 2500 barns given above.

The constants for the 5-ev resonance, as measured in the normal element, may now be summarized as follows:

$$E_r = 5.17 \pm 0.08 \text{ ev}$$
$$\Gamma = 0.17 \pm 0.02 \text{ ev}$$
$$\sigma_0 = \begin{cases} 12{,}000 \pm 1500 \text{ barns} \\ 10{,}000 \pm 1300 \text{ barns} \end{cases} \begin{matrix} \text{uncorrected for doppler effect} \\ \text{doppler-corrected.} \end{matrix}$$

With values of this accuracy and with rough values of Γ_n/Γ which have been obtained by other workers, it is easily possible to determine the spin of the compound nucleus, J, and thus the neutron width, Γ_n. The peak isotopic cross section given by the Breit-Wigner formula is $\sigma_0 = 4\pi\lambda_r^2 g\Gamma_n/\Gamma$ where λ_r is $1/(2\pi)$ times the neutron wavelength at resonance, and g is a spin factor, $\frac{1}{2}(2J+1)/(2I+1)$. The isotope having the 5-ev resonance, Ag^{109}, has an abundance of 49 percent, so that one calculates from σ_0 that $g\Gamma_n/\Gamma = 0.048$. The nuclear spin I is $\frac{1}{2}$, so that g is $\frac{1}{4}$ or $\frac{3}{4}$ according to whether J is 0 or 1. From measurements on the resonance integral (essentially $\int \sigma dE/E$) for scattering and for activation (capture) the value of Γ_n/Γ for this resonance has been found[8] to be ~0.04 for Ag^{109}. This establishes J as 1. It follows that $\Gamma_n \approx 0.011$ ev.

In conclusion, we compare our results with other measurements on this resonance. In very early measurements, Amaldi and Fermi[9] found an absorption coefficient for self-absorption of 20 cm²/g. This is equivalent to a cross section for self-absorption of 3600 barns. According to whether one assumed the doppler width to be small or not compared to the natural width, this value would then give a peak cross section of 7200 barns or higher. Attempts to determine the natural width Γ from the early data gave badly inaccurate values.[10] This is explained by the fact that the resonance energy was measured by the boron method and gave 3 ev instead of the correct value of 5; consequently, even though the relative effective total width Γ_{eff}/E_r was measured fairly accurately, the calculated value for Γ_{eff} was not larger than that expected from doppler effect alone, and hence the natural width was thought to be very small.

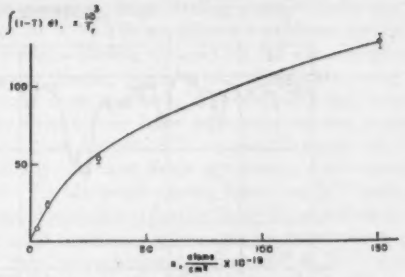

FIG. 7. "Absorption integral" of silver as a function of sample thickness.

Lowry and Goldhaber[11] have recently given values for the width and resonance integral of the 5-ev resonance. They find $\int \sigma_{capture} dE/E = 1080$ barns for all the resonances of Ag^{109} taken together and find[12] that about 75 percent of this is due to the 5-ev resonance. This gives $\sigma_0\Gamma \approx 1350$ barn ev for 5-ev capture in the normal element, which is about 30 percent less than the results of the present measurements. Their measurement of σ_0, by self-indication, is about 12,000 barns,[13] the same as that given here for the value without doppler effect, so that they obtain a value of 0.12 ev for Γ, about 30 percent less than that reported here. The differences between their figures and those given here are not very far outside the combined probable errors.

De Vries and his co-workers have obtained, for the width of the 5-ev resonance, a value in good agreement with that of the present work: their result, 0.18 ev, is an "effective" value which includes a contribution from doppler effect.[13]

8. MEASUREMENTS ON TUNGSTEN

Tungsten has four major isotopes of approximately equal abundance and a fifth (W^{180}) of very low abundance (0.14 percent). Separated-isotope samples of several hundred milligrams of each of the major isotopes were available, recently obtained from the AEC Isotopes Division. Measurements on normal tungsten and on the separated-isotope samples are shown in Fig. 8.

[7] W. E. Lamb, Phys. Rev. **55**, 190 (1939).

[8] Harris, Muehlhause, and Thomas, Phys. Rev. **79**, 11 (1950). The measurements reported there give $\Sigma_i(\sigma_0\Gamma_n/E_r)_i$ and $\Sigma_i(\sigma_0\Gamma/E_r)_i$, where Γ_n and Γ are scattering and total widths, and the summations extend over all resonances. Since the 5-ev resonance is very much stronger than the other resonances in silver (see Fig. 4), the ratio of these measurements gives approximately the value of Γ_n/Γ for the 5-ev resonance alone.

[9] E. Amaldi and E. Fermi, Phys. Rev. **50**, 899 (1936).

[10] H. Bethe, Revs. Modern Phys. **9**, 69 (1937), Sec. 61B.

[11] L. L. Lowry and M. Goldhaber, Phys. Rev. **76**, 189(A) (1949).

[12] Private communication.

[13] Hl. de Vries, Helv. Phys. Acta **23**, 169 (1950); Coster, Groendijk, and de Vries, Physica **14**, 1 (1948), and further references there.

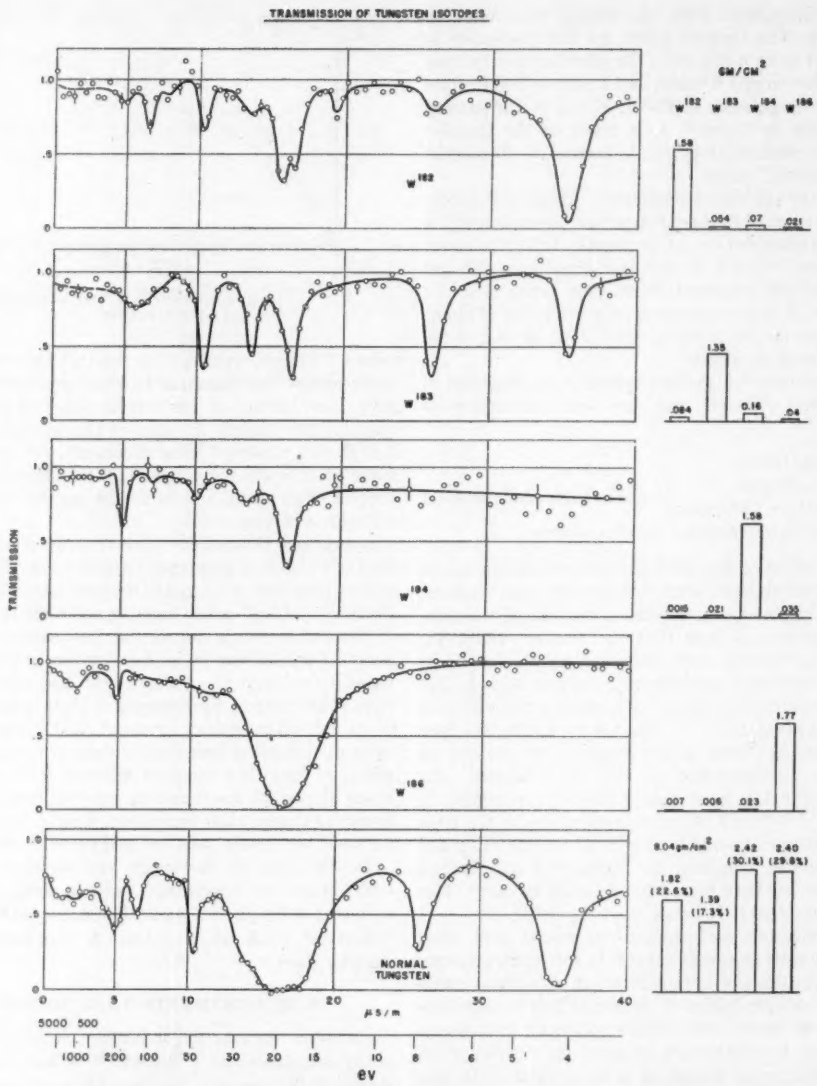

FIG. 8. Transmission of tungsten, in separated-isotope form and in normal isotopic distribution. The composition of each sample is shown at the right.

Samples

The sample thicknesses were chosen, after preliminary measurements, primarily on the basis of investigating the isotopic resonance distribution. Each separated-isotope sample contained approximately the same thickness of one isotope as was in the "normal tungsten" sample.

No cross-section values are shown on Fig. 8. Such values could be calculated from the sample thicknesses given, but they would be rather meaningless for most of the data. The samples were generally too thin to give accurate values for the cross section where σ is low, and too thick where σ is high. To obtain accurate values of σ would require the measurement of samples of various thicknesses.

As it happens, a small amount of data for various

thicknesses is included in the data of Fig. 8, because each separated-isotope sample is not absolutely pure. Thus, e.g., the W^{183} sample incidentally contains a "thin sample" of W^{182}, so that an approximate value of $\sigma_0\Gamma$ can be obtained for the 4-ev resonance.

The separated-isotope samples were in the form of WO_3. The curves shown have been corrected for the oxygen (transmission about 94 percent) and for the sample-holders used. The latter had a transmission of about 91 percent, with a possible systematic error of a few percent in this value.

Resolution

Each of the five curves shown in Fig. 8 was taken in two sections: the data from 0 to 20 microseconds/meter were taken at one time, with the same resolution pattern shown in Fig. 2. The data from 20 to 40 μsec/m were taken with slightly larger values for the burst time (10 μsec instead of 8) and channel on-time (6 μsec instead of 4).

Level Spacing

From the data of Fig. 8, one can obtain rough values for the level spacing for the various isotopes. W^{182} has definite levels at 4.15 ev and 21½ ev, possibly faint levels at 14 ev and near 90 ev, a strong level or group at 125 ev, and many more above 200 ev. W^{183} has definite levels at 7.8 ev, 28 ev, and 49 ev, and many more at 100 ev and higher. W^{184} has a level at 100 ev, a stronger one at 205 ev, and probably more levels near 300 ev and above. W^{186} has a very strong level at 19¼ ev, another at 225 ev, and many more at 1000 ev and higher. Thus the average spacing is seen to be of the order of 10 to 30 ev in W^{182}, about 20 ev in W^{183}, perhaps 100 ev in W^{184}, and hundreds of ev in W^{186}.

The general trend of these spacings with the atomic weight of the isotopes is in agreement with what one would expect from theory. Namely, level densities should increase rapidly with binding energy,[14] and binding energy should be greater for an odd-N nucleus (i.e., for a nucleus with an odd number of neutrons, which forms an even-N compound nucleus) than for an even-N nucleus. Consequently, the level spacing for W^{183} should be smaller than for the even-N isotopes. Moreover, among the even-N isotopes, one would expect the binding energy, and hence the level density, to decrease with increasing atomic weight; the heavier isotopes, richer in neutrons, should bind an additional neutron less tightly than do the lighter isotopes.

Although these expectations are qualitatively confirmed by the data, however, the level spacing for W^{182} is surprisingly small: 10 to 30 times smaller than for W^{186}, which is an even-N nucleus like W^{182}, and about the same as for W^{183}, which is an odd-N nucleus. What is the possibility that this small spacing for W^{182} is due to an unusually large binding energy[15] for a neutron added to W^{182}? The experimental evidence concerning the neutron binding energies for the various isotopes, although meager, indicates that the binding energy for this case is not unusually large—in particular, it seems to be close to the value expected from the semi-empirical mass formula.[16] If we therefore rule out this possibility, the most likely explanation which has been offered for the small spacing found for W^{182} seems to be that of a statistical fluctuation in the level density.[17,18] One other possibility which may be mentioned is that W^{182} may have a higher spin than W^{184} or W^{186}; according to Bethe's theory of level densities,[14] this would result in a greater level density. This possibility is rather small since all three of these nuclei are even Z—even N; all even Z—even N nuclei measured thus far have zero spin.

All of the above discussion is based on the somewhat rough estimates of level spacing which can be obtained from the rather limited data of Fig. 8. It is, therefore, worth remarking that these estimates of the level spacings are supported by additional evidence from the neutron widths Γ_n of some of the resonances. According to theory,[19] $\Gamma_n = cD(E_r)^{\frac{1}{2}}$, where D is the level spacing, E_r is resonance energy, and c is a universal constant. The value of c should be about 0.00013;[19] for a considerable number of slow neutron resonances in different nuclei, c has been found to have this value on the average, varying within a factor of about 3 in either direc-

[14] See, e.g., H. A. Bethe, Revs. Modern Phys. 9, 79 ff. (1937); and V. Weisskopf, Phys. Rev. 52, 295 (1937).

[15] To discuss this possibility we consider how much binding energy difference is required to explain the difference in level spacings—i.e., how rapidly is the level spacing to be expected to change with binding energy—and how much binding energy difference may be expected from the semi-empirical mass formula, allowing for possible effects of nuclear shell structure. The answer to the first of these questions is that the level spacing in the tungsten isotopes should change by a factor of 3 to 6 for a one-Mev change in binding energy [H. Bethe, *Elementary Nuclear Theory* (John Wiley and Sons, Inc., New York, 1947), p. 117]. As for the second question, from the mass formula one would expect the binding energy for a neutron added to W^{182} to be about ½ Mev greater than for W^{184} and about 1½ Mev less than for W^{186}.

The experimental information as to the binding energies in question consists of measurements made by J. Halpern (private communication) on the (γ, n) thresholds in unseparated isotopes of tungsten. The smallest threshold observed is 6.0±0.3 Mev, and the next is 7.5±0.3 Mev. These figures correspond within a few tenths of a Mev to values predicted by the mass formula. In particular, the 6.0 figure almost undoubtedly corresponds to the (γ, n) threshold of W^{183}—i.e., to the binding energy of a slow neutron added to W^{182}. If this interpretation is correct, then the binding energy for $W^{182}+n$ is not unusually large by any amount sufficient to explain the high level density found.

[16] H. Bethe, Revs. Modern Phys. 8, 165–168 (1936); E. Fermi, *Nuclear Physics* (University of Chicago Press, Chicago, 1950), p. 6.

[17] I wish to thank R. J. Sachs for this suggestion.

[18] This possibility might be checked if the level density could be measured over a wider energy range than is possible with present time-of-flight spectrometers. One possible method might be to make measurements of the (n, γ) cross section with broad resolution, in the Mev region; such measurements give the average level spacing—more accurately, the average Γ_γ/D, where D is the level spacing and Γ_γ is the radiation width. See, e.g., Hughes *et al.*, Phys. Rev. 75, 781 (1949).

[19] See, e.g., Feshbach, Peaslee, and Weisskopf, Phys. Rev. 71, 145 (1947), in particular Eq. (26). The value of 0.00013 for c is obtained by taking a value of K corresponding to an energy of ~25 Mev, and by taking $D^* \approx D$.

tion.[20] In the present case, one sees qualitatively that W^{182} has comparatively weak resonances, indicating small Γ_n and thus small D, whereas W^{186} has comparatively strong resonances, indicating large Γ_n and thus large D. Approximate values of Γ_n for the first resonances in W^{182} and W^{186} (estimated by a method given below) indicate level spacings of the order of magnitude of 4 ev and 400 ev, respectively.

Resonance Constants in W^{182} and W^{186}

Approximate values for the resonance parameters σ_0, Γ, and Γ_n can be obtained for the 4-ev resonance in W^{182} and the 19-ev resonance in W^{186}. For the 4-ev resonance, $\sigma_0\Gamma$ is estimated as $\sim$600 barn ev, from the absorption integral for the "thin-sample" data in the W^{182} curve. (See Sec. 7.) $\sigma_0\Gamma^2$ is estimated from the absorption integral for the "thick-sample" data in the W^{182} curve. (For a thick sample the absorption integral, $\int(1-T)dt$, is simply related to $\sigma_0\Gamma^2$. The method used to evaluate $\sigma_0\Gamma^2$ for the 5-ev resonance in silver is not satisfactory for the particular resolution and sample thickness used here.) The result obtained is $\sigma_0\Gamma^2 \sim 45$. Thus $\sigma_0 = 8500 \pm 3000$ barns, $\Gamma = 0.07 \pm 0.02$ ev. Γ_n is obtained by using the Breit-Wigner relation $\sigma_0 = 4\pi\lambda^2 g\Gamma_n/\Gamma$, with the above values of σ_0 and Γ and with a value of 1 for g. This value of g corresponds to the assumption that the spin of the even-even W^{182} nucleus is zero. The result is $\Gamma_n \approx 0.001$ ev.

The 19-ev resonance in W^{186} was analyzed by examining the detailed values of the cross section between 4 and 7 ev away from resonance on both sides, as obtained from Fig. 8. This type of analysis is fruitful here because there are no other resonances nearby. It is necessary to investigate both sides of the resonance because of the strong asymmetry introduced by the interference term due to potential scattering. This term is especially prominent here because this resonance is predominantly a scattering resonance.[21] The interference effects are clearly visible in Fig. 8, which shows that the cross section on the low energy side is very low, only a few barns, whereas on the high energy side it remains rather high for 50 to 100 ev and then goes through a minimum—very likely near zero—near the 225-ev resonance. (Note that the energy scale becomes rapidly compressed at high energies.)

The analysis of the 19-ev resonance gives approximate values for $\sigma_0\Gamma^2$: $14{,}000 \pm 3000$ barn ev^2, and Γ_n/Γ: 0.6 ± 0.3. From these, and, as for the 4-ev resonance, using $\sigma_0 = 4\pi\lambda^2 g\Gamma_n/\Gamma$ and assuming $g=1$, one finds $\Gamma = 0.4 \pm 0.1$ ev, $\Gamma_n = 0.25 \pm 0.1$ ev.

I wish to express my appreciation for the interest that Professor E. Teller has taken in this work. The construction of the equipment was initiated because of suggestions made by him concerning certain interesting problems in slow neutron resonance work. The construction was made possible only by the encouragement and cooperation of D. J. Hughes. Many people contributed greatly to the construction of the equipment, chiefly, N. Hochstetler and A. Denst in the engineering and precision machining of the rotating-shutter unit, C. Zaander in the development of the electronic circuits, and A. Hill in their construction. W. Woolf gave very valuable assistance in putting the equipment into operation and in taking data.

[20] E. P. Wigner, Am. J. Phys. **17**, 99 (1949).

[21] Harris, Muehlhause, and Thomas, Phys. Rev. **79**, 11 (1950).

Field-Dependent Secondary Emission

HAROLD JACOBS
Signal Corps Engineering Laboratories, Fort Monmouth, New Jersey
(Received July 16, 1951)

Experiments have been conducted with magnesium oxide surfaces in which high dc fields were applied to the surface, while at the same time secondary emission measurements were being made. Very high secondary emission ratios were obtained reproducibly (100 to 1 and greater). Under static conditions it was found that the ratios would increase exponentially with increasing fields. In addition, for constant fields, the ratio of liberated electrons to bombarding electrons was constant, over a wide range of bombardment energy. Measurements were made of secondary emission with a square wave field applied to the surface and time lag effects were noted. Decay time in the order of 30 microseconds were measured. The rise time was found to be dependent upon field and bombarding currents. The mechanism of field dependent secondary emission was shown to be related to an avalanche effect, triggered by the bombarding electrons.

I. INTRODUCTION

THE concept of using an electric field to enhance secondary emission from composite surfaces has been of considerable interest in recent years.[1-4] Several experiments[5] dealing with field enhanced liberation of secondary electrons have revealed possibilities of obtaining ratios which are higher than ordinary secondary yields by a factor of 10 to 100.

Unfortunately, in most experiments of this type, the stability of the surfaces was poor, making accurate measurements difficult. In addition, pulse measurements were generally not made, nor were the potentials at the surfaces of the emitter measured, making quantitative analyses of the mechanism difficult.[6] As a result, there are several mechanisms suggested for field enhanced secondary emission, but little agreement exists amongst the various theories proposed.

In the following work to be described, a method was found whereby field enhanced secondary emission surfaces of MgO could be constructed reproducibly and which were stable over considerable periods of time. Currents as high as 10 milliampere/cm^2 could be drawn without immediate deterioration, and tests were extended over a period of weeks on the same samples. In addition, the potential at the surface of the sample could be estimated while, at the same time, the potentials of the base metal could be measured. Finally, measurements were made under pulse conditions and build up and decay times could be recorded and used for computations.

Before describing the experiments further, it might be best to first review the work of others in similar types of experiments. Malter[2] studied secondary emission surfaces prepared by electrolytically oxidizing aluminum and subsequently treating the surfaces with caesium and oxygen during the exhaust process. The maximum beam currents he used were 3 to 4 microamperes, under which conditions he sometimes observed a blue fluorescence of his target upon electron bombardment.

Malter found experimentally that the yield from his target increased as a power of his collector voltage:

$$I_c = B(V_c)^m, \tag{1}$$

where I_c = collected current, V_c = collector voltage, and B,m = constants.

His collector current was also found to rise as a power of the beam current. In addition he found that the surface exhibited long time lag characteristics. That is, after the primary beam was cut off, the secondary emission first decayed rapidly and then more slowly, persisting for many hours in some cases.

The theory that Malter and later Koller,[7] developed was that the high secondary emission ratios observed (i.e., 1000 to 1) were due to positive ions formed at the surface of the secondary emission material by electron bombardment. These positive charges were thought to reside on the surface for long lengths of time, due to the high resistivity of the film. During this surface ionization period, high fields could exist in the material and electrons could be liberated in greater quantities due to the field.

Pensak[5] did some work too, which may be pertinent, although he studied conductivity rather than secondary emission. In his experiments, steady bombarding currents, penetrating a thickness of amorphous silica film, induced a conductivity producing a current of one hundred times the bombarding beam. He used a double-beam technique, to measure the potential at the surface.

The beam used for inducing conductivity was kept at about 10,000 volts and 0.02 μa. He concluded that the induced currents were proportional to the energy absorbed by the beam, and that the beam in question must have sufficient energy to penetrate the film for induced conductivity. It was found too, that an increase in induced currents could be obtained with an increase in field across the insulator. No time lag measurements were specifically referred to in this article.

[1] A. Guntherschulze Z. Physik 86, 778 (1933).
[2] L. Malter, Phys. Rev. 50, 48-58 (1936).
[3] E. R. Piore, Phys. Rev. 51, 1111 (1937).
[4] H. Nelson, Phys. Rev. 57, 560 (1940).
[5] L. Pensak, Phys. Rev. 75, 472-478 (1949).
[6] K. G. McKay, *Advances in Electronics* (Academic Press Inc., New York, 1948), Vol. I., p. 108.
[7] L. R. Koller and R. P. Johnson, Phys. Rev. 52, 519-523 (1937).

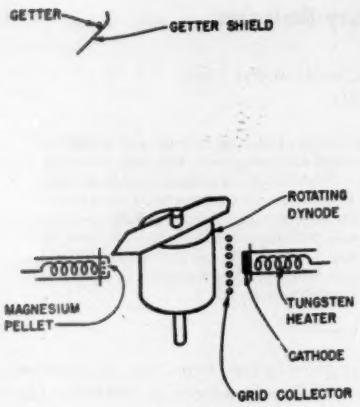

FIG. 1. Arrangement of parts in experimental tube.

The work described in the magnesium oxide experiments reported in this paper differs from that of Malter and Pensak in the following respects.

The chemistry and preparations of the surfaces are not similar.

In the work of Malter, collector current varied as a power of bombarding current and collector voltage. In the experiments to be described, collector current varied linearly with bombarding current and increased exponentially with field.

In Pensak's experiments high energy electrons were used (10,000 volts) such that the beam could penetrate through the material. In addition he measured conduction current rather than secondary current. In the work to be described with magnesium oxide, the bombarding electrons were low in energy (100–300 volts). This indicated that electron penetration of the surface was not required. In addition relatively high current densities could be used. As will be shown, high currents make possible the use of shorter time lag effects.

Finally, by means of these experiments, a piece of evidence was obtained concerning the mechanism of these field enhanced secondary emission effects. An avalanche-type theory is proposed whereby electrons, being accelerated by high fields, produce additional electrons within the volume of the material, which in turn leads to an avalanche similar to the gas discharge type of build up of presparking current.

II. EXPERIMENTAL PROCEDURES

The arrangement of parts used in experimental tubes for the study of field dependent secondary emission, is shown in Fig. 1.

The tube consisted of a cylindrical cathode coated on one end; a grid, to be used as accelerator and collector, and a dynode which could be rotated by a magnet external to the tube. On the side of the dynode, opposite the cathode, was another cylinder containing a magnesium pellet which could be evaporated upon heating by applying current to a filament contained by the cylindrical sleeve.

The purpose of this arrangement was as follows. At exhaust, the cathode (BaO–SrO) could be activated, the grid bombarded and parts heated by an induction furnace without contaminating the opposite side of the dynode, which was kept facing the magnesium pellet. After this initial tube processing and activation of the cathode, oxygen was admitted to the system (about 80 microns) and the magnesium was slowly evaporated to the dynode to a thickness of 10^{-5} to 10^{-4} cm. The oxygen was then pumped out of the vacuum system and the cathode reactivated. The cathode temperature was lowered to about 300°C to 400°C, and the MgO deposited on the anode, was then rotated in front of the cathode for test. (The oxidation process sometimes involved induction heating of the evaporated Mg on the dynode in the presence of oxygen. This technique worked equally as well.)

The use of the rotating dynode greatly reduced the possibility of contaminating the secondary emission surface, since during cathode activation the surface was shielded. When the surface was rotated back in front of the cathode for test, the cathode temperature was reduced to where only 1 to 10 μa could be drawn as temperature limited emission. Under these conditions the barium evaporation was negligible and previous experiments indicate that the barium evaporation would not interfere with results.[8,9]

At static test, the circuit used was as indicated in Fig. 2 and is somewhat standard set up for measuring dc secondary emission yields.

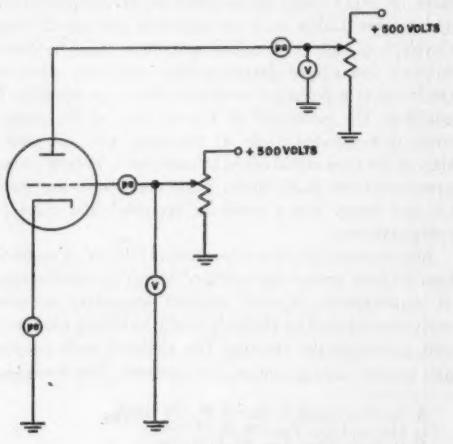

FIG. 2. Static test circuit.

[8] H. Jacobs, J. Appl. Phys. 17, 596 (1946).
[9] J. B. Johnson, Phys. Rev. 73 1058–1073 (1948).

III. STATIC TEST DATA AND INTERPRETATION

In testing the tube under dc conditions, the dynode was set at about 100 volts, the grid was then raised to about 225 volts, and the cathode was near ground potential (see Fig. 2). Secondary emission ratios of 100 to 1 were readily attained (Fig. 3, tube No. 2). In addition, it was found that the secondary emission ratio changed roughly exponentially with the change of the difference of potential between the collector grid and the dynode plate (Fig. 4, tube No. 3 and Fig. 5, tube No. 4). Thus, if one would use an equation the following relation would hold over a limited region.

$$\sigma = Ae^{+\alpha(E_g - E_p)}, \qquad (2)$$

where σ=secondary emission ratio, A, α=constants over a limited region, E_g=grid potential (collector), and E_p=plate potential (dynode).

In all, seven tubes were constructed with MgO on the dynode and all showed similar behavior. The collector voltage increment would appear to bring about an exponential increase in collector current for a given bombarding current, with a slight bending of the curve downward as the higher ratios are approached. This differs from Malter's work in which he found that for constant bombarding current, the yield varied as a power of the collector potential.

In Fig. 4, we see the results of bombarding the surface under different bombarding energies. The data indicates

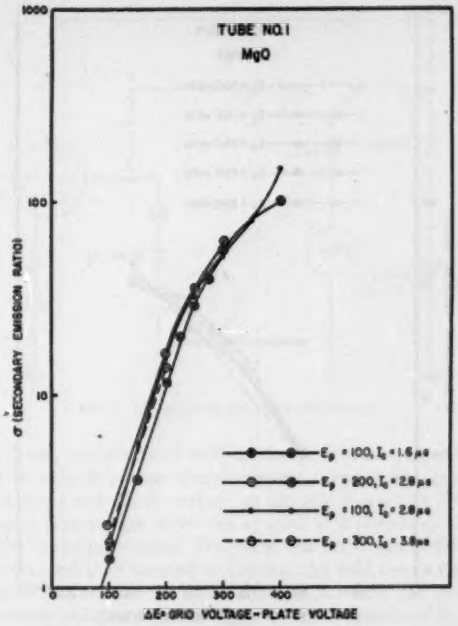

FIG. 4. Secondary emission ratios as a function of field, with various bombarding energies.

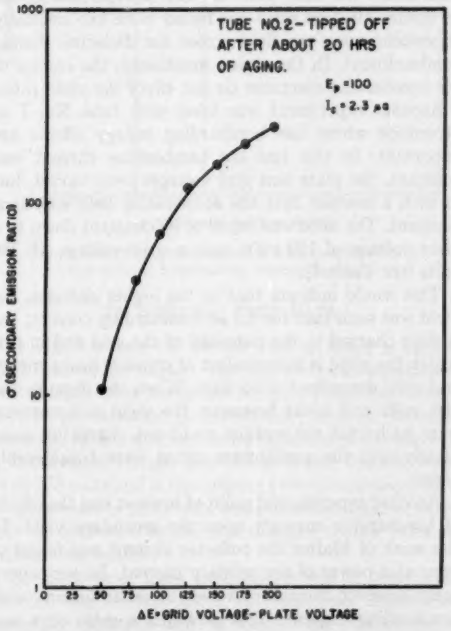

FIG. 3. Secondary emission ratio as a function of field.

that for a given field (collector voltage minus the dynode voltage), the secondary emission yield is independent of the potentials on the collector and dynode. In the first run, indicated by points marked ⊗, the dynode set at 100 volts yielded a ratio of about 60 to 1 with 400 volts on the collector. In the second run, indicated by ⊙, the dynode was set at 200 volts and collector at 500 volts. The secondary ratio was still near 60 to 1. The results indicate that the electric field effects the secondary emission ratio in such a way, that the yield is independent of bombarding energies, in the region studied. The bombarding currents in these tests, were kept in the same order of magnitude.

In Fig. 5, there is further evidence that the ratio of collected current to bombarding current is a function of field (the difference of potential between the collector grid and the dynode plate).

In some cases at high bombarding currents (100 μa or greater) a blue fluorescence appeared on the surface bombarded. This afforded a fair approximation of the area being bombarded. The area changed very little with dynode plate voltage. Several tubes were constructed too, with "willemite" phosphor coated over the dynode. These tests confirmed the conclusion that bombarded spot size did not change appreciably in the voltage ranges studied.

In previous, unpublished experiments it had been found that MgO surfaces, prepared similarly, except

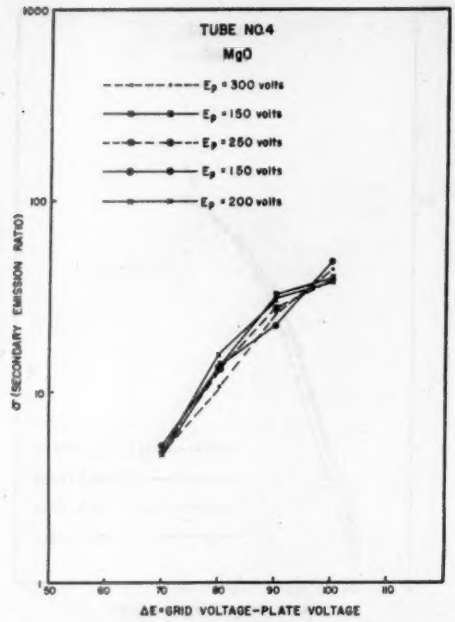

FIG. 5. Secondary emission ratios as a function of field, with various bombarding energies. Conclusion: σ is dependent only upon field and not upon bombarding voltage.

made more conductive, and not showing field dependence, yielded ratios in the order of 4 to 1 or 5 to 1. This can be interpreted as the true secondary emission yield of the surface, especially inasmuch as the accelerating fields have practically no effects on the ratios.

The large secondary emission yields would have to be due to a high accelerating electric field, active on the surface simultaneously with the bombardment. This high field would be due to positive charges built up on the outer surface of the MgO. If charges did not exist, the field would be the difference in potential between the grid and plate divided by the distance, or a ratio of roughly 100 volts/0.2 cm, giving a field of 500 volts/cm. Such a low field could hardly provide the acceleration for such high electron ratios. Suppose however the MgO surface charged due to the liberation of secondary electrons and the high resistance of the material preventing a rapid decay of charging. In this case it would be possible for the surface to charge to the same potential as the collector and if the thickness were 10^{-4} cm, the field would be 100 volts/10^{-4} cm = 10^6 volts/cm. At 10^6 volts/cm one could expect field enhanced secondary emission. Another piece of evidence supporting the premise that about 10^6 volts/cm is really across the surface material is the fact that under the test conditions the material is very close to arcing. When the high ratios are attained a tendency for arcing increases. The data represented in Figs. 3–5 was taken in the region just prior to arcing.

TABLE I. Secondary emission ratio (σ) as a function of difference in potential (ΔE) across the dielectric at different bombarding energies.

E grid	E plate	ΔE	σ	Filament potential 2.3 volts
450	350	100	10.5	
400	300	100	12.0	
350	250	100	11.6	
300	200	100	11.0	Bombarding current
250	150	100	11.1	1.5 μa
200	100	100	5.7	
150	50	100	3.15	
125	25	100	1.9	

The surface charging theory makes more intelligible the uniformity of the effects of field on secondary ratios. For a given tube, such as No. 4 (Fig. 5), the thickness of the film would be relatively constant. If we assume that the dynode surface charges to the potential of the grid collector, then the difference in potential from grid to plate would be the difference in potential across the surface film. This difference in potential would then be a measure of the field across the dielectric. By measuring the difference in potential from grid to plate we would then be measuring effectively the field accelerating secondary electrons generated in the volume of the material. The pulse measurements made in the latter part of this report confirmed this statement. To summarize the first part of this interpretation, the secondary electron ratio was found to be exponentially dependent upon the field across the dielectric during bombardment. In the region mentioned, the energy of the bombarding electrons do not effect the yield ratio.

Another experiment was tried with tube No. 7 to determine where the bombarding energy effects are important. In this test the bombarding current was constant, the plate and grid voltages were varied, but in such a manner that the accelerating field was kept constant. The ratio was found to be constant down to a plate voltage of 150 volts and a grid voltage of 250 volts (see Table I).

This would indicate that at the higher energies, the yield was such that for 1.5 μa bombarding current, the surface charged to the potential of the grid and in this region the yield is independent of primary beam energy and only dependent upon field. When the dynode was 100 volts and lower however, the yield and currents were such that the surface could not charge up completely and the equilibrium ratios were considerably lower.

Another experimental point of interest was the effects of bombarding currents upon the secondary yield. In the work of Malter the collector current was found to vary as a power of the primary current. In our experiment however, the collector current varied linearly with bombarding current. This provided a ratio that was constant as the primary current varied.

In Fig. 6 tube No. 7, we see the results of an experiment in which the field across the dielectric (*E* grid-*E* plate) was kept constant for two different settings. In each run the only factor varied was the primary beam current density. In both cases the plate was set at 150 volts. In the first case the grid was kept constant at 260 volts, and in the second case the grid was kept constant at 270 volts. The results show that the bombarding current densities do not cause a change in the secondary emission ratios. In another tube (No. 5) the primary beam was varied by a factor of 70 without appreciable change in the ratio.

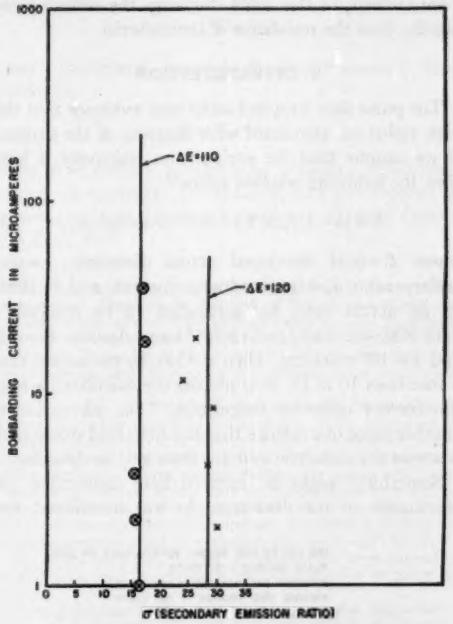

FIG. 6. Secondary emission ratios with constant fields and varying bombarding current densities.

IV. DYNAMIC TEST DATA

In Fig. 7 we see the circuit used to apply a square wave field on the surface. The cathode was temperature limited such that variations in grid potential caused little or no variation in bombarding current. A small resistor of 6000Ω was used as an indicator of the current in the dynode circuit, and the grid and dynode were set at 275 volts and in the order of 190 volts respectively. a square wave of ±20 volts was placed on the grid, such that the grid rose to 295 and dropped to 255 volts at various frequencies.

The purpose of these experiments was to determine the rise and decay times for the field dependent secondary emission and to isolate the factors most concerned, such as bombarding currents and fields.

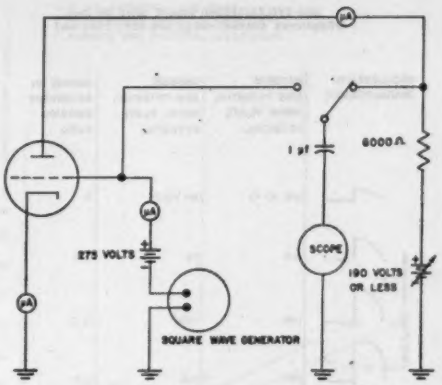

FIG. 7. Dynamic square wave test circuit.

First, the effects of field on rise time was analyzed. The cathode current (bombardment current) was kept constant and the dc voltage on the grid was set at 275 volts. The square wave was applied at a frequency of 200 cycles per second. The plate was set at about 190 volts, and then lowered to increase the field across the dielectric and at the same time, to increase the secondary emission yield. In Fig. 8 we see the results of the increasing field upon the time necessary for saturation. At the low level of fields, saturation was not found to be completed in the time allowed. However, as the field was increased the shape of the curve changed and saturation started to become apparent. Saturation would indicate a completion of positive charging of the

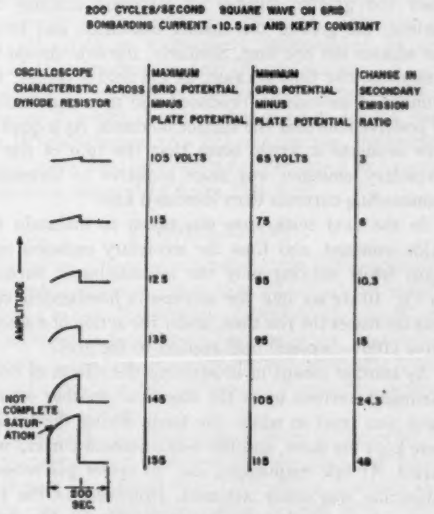

FIG. 8. The change in rise time with increasing difference in grid potential and plate potential.

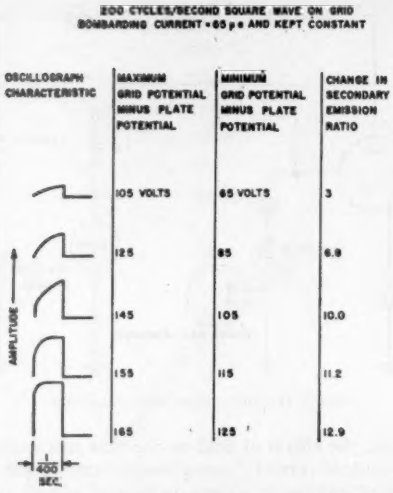

FIG. 9. The change in rise time with increasing difference in grid potential and plate potential.

surface in order for the surface to attain the potential of the grid. We might conclude from Fig. 8 that a higher dc field causes a higher rate of surface ionization and hence a shorter rise time for the secondary electron yield. In Fig. 9 we see a similar run for a higher bombarding current. Again we see that the increased field decreases the rise time. In addition, it was found that higher bombarding currents decreased the rise time. This is consistent with the concept of surface charging, since the greater number of electrons striking the surface, the greater the surface ionization and hence the shorter the rise time. Similarly, the field should increase the rise time because, as the field is higher, the number of secondaries produced and thus the number of positive ions near the surface increases. As a qualitative estimate it would seem that the rate of rise of secondary emission was more sensitive to increasing bombarding currents than increased field.

In the next tests, care was taken to maintain the fields constant, and thus the secondary emission constant while varying only the bombardment current. In Fig. 10 we see that the increase in bombarding current decreases the rise time, under the action of a square wave (100~/second) field applied to the grid.

As another means of illustrating the effects of bombardment current upon the rise time another experiment was tried in which the fields during the testing were kept the same, and the bombardment current was varied. At low frequencies, i.e., 20 cycles per second, saturation was easily attained. However, as the frequency was raised, at constant amplitude, the "saw tooth-like" appearance of dynode current started to appear. On further increasing the frequency, the dynode current no longer reached the saturation values and the amplitude of the top of the "saw tooth" started to decrease. Measurements were made of the frequency of the square wave required to decrease the maximum response to one half its saturation value. In Fig. 11, we see that as the bombardment current increases the rate of rising increases, in that higher square wave frequencies are required to halve the output.

Measurements were also made on decay times and these were found to be in the region of 15 to 40 microseconds. The decay time may be related to bombardment current, as this could discharge the surface more rapidly than the resistance of the material.

V. INTERPRETATION

The pulse data supplied additional evidence that the high yields are associated with charging of the surface. If we assume that the surface film resistivity is high then the following relation exists.[10]

$$E=(\sigma-1)j_p t\times 1.13\cdot 10^{11}/K \text{ volts/cm}, \quad (3)$$

where E=field developed across dielectric, σ=secondary ratio, j_p=bombardment current, and t=time. In an actual case, for saturation to be reached, $t=(1/800)$ sec, and $j_p=65\times 10^{-6}$ amp. Assume $K=3.5$, and $E=10^6$ volts/cm. Then $\sigma=5.6$. In the actual case σ rose from 10 to 15, thus placing the calculated σ near the correct order of magnitude. This calculation is another piece of evidence that the high field developed, is across the dielectric and not from grid to dynode.

Something might be inferred here concerning the mechanism of the discharge. As was mentioned, the

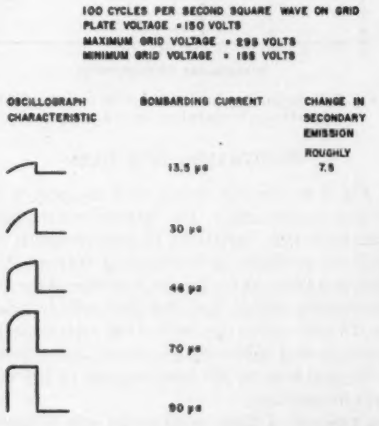

FIG. 10. Change in rise time with increasing bombarding current.

[10] See reference 6, p. 109.

films were operated in the region just prior to arcing. There have been two major schools of thought concerning this pre-arcing region. One group believes that pre-arcing currents are due to tunnel penetration of electron from the cathode into the material. Using the Fowler-Nordheim equation, the currents over a small change in field should be an exponential function of field. The alternative theory, which also yields an exponential form, is that a free electron, accelerated by a high field, will free other electrons with an avalanche resulting.

The Fowler-Nordheim relation is given in Eq. (4) and the avalanche expression in Eq. (5).

$$J = CF^2 e^{-D/F}, \tag{4}$$

where J=current density, F=field,[11] and C, D= constants.

$$N = N_0 e^{\alpha X}, \tag{5}$$

where N=Number of electrons released, N_0=initial number of electrons, X=distance, and α=Number of electron formed/cm of path/incident electron (varies with field, F).[12]

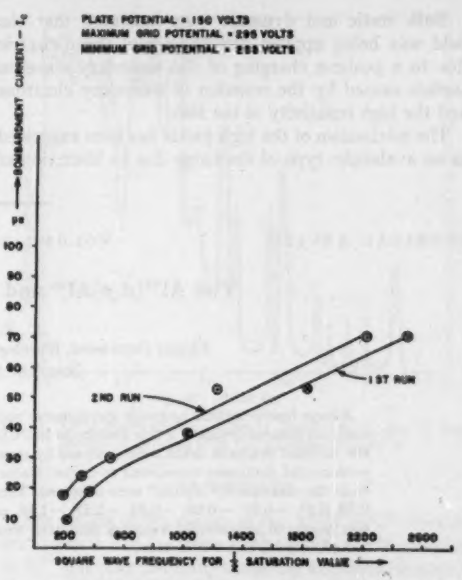

FIG. 11. Bombardment current *versus* frequency required for one-half saturation value of secondary emission.

The experiments tell us that essentially Eq. (5) is the correct expression and that the avalanche theory is more plausible. If field emission were correct, the collector current would have been independent of bombardment current, provided enough current were present to establish a high field across the dielectric. In practice, it was found that for a given field, the ratio of secondaries to primaries was constant. Referring to Eq. (5), N/N_0= a constant, independent of the size of N_0, providing the field (F) and distance (X) are constants. If we assume that an electron penetrates a distance X, which does not change much for the case of a 150-volt electron to a 250-volt electron, the experiments verify Eq. (5). The ratio was found to be constant for a constant field (see Figs. 3–6).

VI. CONCLUSIONS

Under conditions of intense electric fields, specially prepared magnesium oxide films show high secondary emission ratios. Under static condition, the secondary emission ratios have been found to be an exponential function of the field. Ratios of 100 to 1, with 100μ a/cm^2 of bombarding current and 10 ma/cm^2 collecting current was readily attained.

Under pulse conditions decay times in the order of 30 microseconds were found. The rise time was found to change depending upon bombarding currents and fields, shorter rise times being noticed with higher fields or higher bombarding currents.

[11] The field could vary if the resistance should change under bombardment. However, in the work of Pensak and others, the resistance is constant until the primary beam actually penetrates the thickness of the dielectric. This would require far greater than 10,000 volts. It can therefore be assumed that the film resistance does not change markedly and that F is constant under equilibrium conditions.

[12] In using Eq. (5), it might be well to discuss the meaning of the symbols and derivation of the equation. In the early days of gas discharge studies, J. S. Townsend used the equation in the following manner. He regarded n as the initial number of electrons (or negative particles) per second crossing one square centimeter of surface. A number of new ions dn, proportional to n and to length dx, would be produced by electron collisions. The rate of increase, or the proportionality constant, was called α. If diffusion and recombination could be neglected, $dn=\alpha n dx$, and $N=N_0 e^{\alpha X}$. N_0 represents the initial number of electrons per second crossing the unit area, and N represents the total number of electrons obtained.

Towsend did some further work on the nature of α, the probable number of ionizing collisions, per centimeter of path, per electron. He attempted to interpret in terms of field, mean free path of the electron, and ionization potential. However, the theoretical aspects of this interpretation have not proved to be correct in later years. Today, it is admitted that an empirical relationship does exist for α in terms of field, pressure and ionization potential, but the exact theory is by no means clear. It has been found experimentally, for low regions of field/pressure, that α/p varies nearly linearly with F/p, where p=pressure, over small ranges of field.

In the experiments described above, the magnesium oxide film was regarded as a high pressure gas, with the bombarding electron releasing additional electrons within the material. The released electrons, accelerated towards the surface, could then release additional electrons in a manner similar to the "Townsend Avalanche". The resulting electrons could then be accelerated into the vacuum by the positive charges on the surface of the magnesium oxide. Since α/p was found to be a linear function of F/p in gas ionization, at low F/p values, we might expect α to vary linearly with F in a solid, where p could be considered constant. Thus, over a limited range one might find N to vary as an exponential function of field, F.

For further details of the gas discharge concepts the reader can find a summary in J. D. Cobine, *Gaseous Conductors* (McGraw-Hill Book Company, Inc., New York, 1941), 147–154.

Both static and dynamic tests indicated that the field was being applied directly across the dielectric due to a positive charging of the secondary emission surface caused by the emission of secondary electrons and the high resistivity of the film.

The mechanism of the high yields has been suggested as an avalanche type of discharge due to liberation of electrons by high velocity electrons in the volume of the material near the surface.

Acknowledgment is made to Mr. Jack Martin, Mr. G. Hooker, and Mrs. Margaret I. Holmes for their help in the testing and construction of experimental tubes; and to Dr. J. E. Gorham and Dr. L. Pensak for their advice during the course of this work.

PHYSICAL REVIEW VOLUME 84, NUMBER 5 DECEMBER 1, 1951

The $Al^{27}(d,p)Al^{28}$ and $Al^{27}(d,d')Al^{27}$ Reactions*

K. K. KELLER†
Physics Department, Washington University, St. Louis, Missouri
(Received August 20, 1951)

A large heavy-particle magnetic spectrometer was used to study the proton and deuteron groups from the deuteron bombardment of a thin aluminum foil. Charged particles emitted at 90 degrees with respect to the the incident deuteron beam were analyzed by momentum in an annular-shaped magnetic field. Groups of protons and deuterons correspond to excited states in Al^{28} and Al^{27}, respectively. Fifteen groups of protons from the reaction $Al^{27}(d,p)Al^{28}$ were observed. Their Q values were 5.53, 4.49, 3.95, 3.36, 3.01, 2.06, 1.55, 0.70, 0.37, −0.27, −0.60, −0.84, −1.37, −1.86, and −2.98 Mev. The elastically scattered deuterons and five groups of inelastically scattered deuterons were also observed. Their Q values were 0, −0.97, −2.39, −3.17, −4.74, and −5.76 Mev.

I. INTRODUCTION

McMILLAN and Lawrence[1] first discovered that the protons from the deuteron bombardment of aluminum consisted of several groups. Since then this reaction has been studied by several observers[2–4] In this experiment 10-Mev deuterons bombarded an aluminum target in a magnetic spectrometer capable of focusing 15-Mev protons on a nuclear research emulsion, which was used as a particle detector. A search was made for proton groups corresponding to excited states in Al^{28} up to 9 Mev above the ground state.

The inelastic scattering of deuterons was first reported by Greenless, Kempton, and Rhoderick[5] in 1949. They observed two groups of deuterons inelastically scattered by aluminum. Holt and Young[6] subsequently observed these two deuteron groups and gave Q values (Q values and energy levels have the same magnitude for inelastic scattering but opposite signs) of -0.99 ± 0.05 and -2.17 ± 0.05 Mev. In the present experiment, the scattered deuterons were recorded simultaneously with the protons in the nuclear emulsions.

II. APPARATUS

A large charged-particle spectrometer, having 180° magnetic focusing, was made, using an annular magnet similar to one described by Cockroft.[7] The mean radius of the annulus is 42 cm, the width of the annulus is 8 cm, and the width of the gap between the pole faces is 0.658 cm. A collimated beam of deuterons from the Washington University cyclotron passes through a small hole in the magnet pole face and strikes a 0.2-mil aluminum target in the gap between the pole faces. The particles from a nuclear reaction which leave the target at 90° with respect to the incident beam travel in the evacuated gap between the pole faces of the annular magnet. The magnetic field in the gap can be adjusted from nearly zero to about 16,000 gauss. With a given magnetic field, all of the particles in a certain momentum interval will stay in the annulus through 180° and strike a nuclear photographic plate inclined in the magnet gap. The angle of inclination of the nuclear plate is 12° with respect to the pole faces. The plate is attached to a holder equipped with a long rod which is used to insert the plate between the pole faces of the magnet. This rod enables the plate holder to be placed in an air lock, which is then evacuated. The valve to the main vacuum system is opened and the plate is pushed into position between the pole faces.

The magnetic field of the annular magnet is produced by a current of up to two amperes in a water-cooled coil situated between the magnet core and the pole faces. The constant magnet current is supplied by a grid-controlled thyratron rectifier.

The magnetic field was measured with a Leeds and Northrup ballistic galvanometer in series with a flip coil which is located in the half of the annulus through

* Assisted by the joint program of the ONR and AEC.
† Now at the University of Alaska, College, Alaska.
[1] E. M. McMillan and E. O. Lawrence, Phys. Rev. **47**, 343 (1935).
[2] Pollard, Sailor, and Wyly, Phys. Rev. **75**, 725 (1949).
[3] W. D. Whitehead and N. P. Heydenburg, Phys. Rev. **79**, 99 (1950).
[4] H. A. Enge, Phys. Rev. **83**, 212 (1951).
[5] Greenlees, Kempton, and Rhoderick, Nature **164**, 663 (1949).
[6] J. R. Holt and C. T. Young, Nature **164**, 1000 (1949).
[7] J. D. Cockroft, J. Sci. Instr. **10**, 71 (1933).

which particles do not pass. Polonium alpha-particles, which have a $B\rho$ of[8] 3.3159×10^5 gauss-cm, were used to calibrate the galvanometer deflection against the magnetic field.

In order to regulate the bombardment time, an insulated faraday cup behind the target collects the deuteron beam and allows this charge to produce a potential across a condenser. This potential is measured by an electrometer so that the desired bombardment can be obtained.

III. EXPERIMENTAL PROCEDURE

A series of Ilford C2 nuclear research plates, having an emulsion thickness of 50 microns, was exposed in the spectrometer such that the momentum, or $B\rho$, values of adjacent plates were overlapped by about one-third. In this way, each particle group was found on more than one plate. After the plates were developed, they were scanned with a microscope by counting the tracks within transverse swaths one mm apart along the plate. Protons can easily be distinguished from deuterons because if they have the same momentum and come to focus near each other on the photographic plate, the protons will have approximately twice the energy of the deuterons and hence much longer ranges in the emulsion.

Before a number-of-tracks-*versus*-$B\rho$ curve can be made, the data from the microscope must be corrected to account for the facts that different parts of the nuclear plate subtend different solid angles with respect to the target, and that the $B\rho$ intervals of the microscope swaths of different plates are not the same. After these corrections were applied, the data were overlapped so that fairly smooth curves could be drawn through the points. It was estimated that, due to the energy loss in the aluminum target, the true or ideal peak position corresponded very closely in $B\rho$ with a point one-third of the height of the high $B\rho$ side of the actual peaks, as suggested by Buechner.[9] The momentum of the charged-particle groups was determined from the measurements of their radii of curvature in the magnetic field and the magnetic field strength. The groups' energies were calculated from their momenta. Knowing the kind of particles in a group and their energy enabled the Q values of the reaction to be computed using the well known formula derived from the laws of conservation of energy and momentum in nuclear reactions. Finally, the energy levels of a nucleus were obtained by subtracting the Q-values of the various particle groups produced in the nuclear reaction with the nucleus from the Q-value of the highest energy or ground-state particle group.

[8] Van Patter, Sperduto, Huang, Strait, and Buechner, Phys. Rev. 81, 233 (1951).

[9] Buechner, Strait, Sperduto, and Malm, Phys. Rev. 76, 1543 (1949).

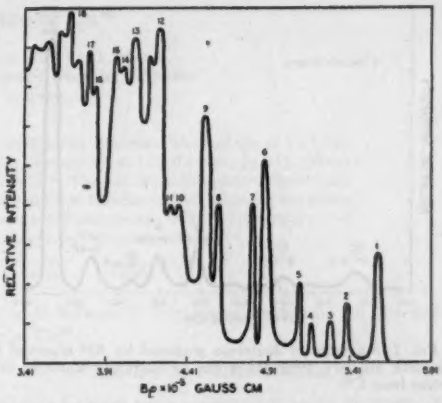

FIG. 1. $Al^{27}(d,p)Al^{28}$ proton spectrum. Peaks 14, 16, and 17 may be due to protons from the reaction $C^{12}(d,p)C^{13}$.

IV. RESULTS

The results of the survey of the $Al^{27}(d,p)Al^{28}$ reaction are shown in Fig. 1. Fifteen proton peaks can be assigned to Al^{27} (the only naturally occurring aluminum isotope). It is not possible from this experiment to say if peaks 14, 16, and 17 are due to aluminum or not. It is possible that these peaks may correspond to excited states of C^{13} formed in the $C^{12}(d,p)C^{13}$ reaction, since they occur where such peaks are to be expected. Although clean aluminum targets were used, a carbon deposit may build up on the aluminum foil during the combardment. The carbon may come from the oil used in the diffusion pump, or it may come from organic molecules given off by the hot magnet coil which was impregnated with Glyptal. Separate experiments show that peaks due to such a carbon deposit do occur. The ground-state proton group from the $C^{12}(d,p)C^{13}$ reaction is sufficiently close to the seventh group that their errors slightly overlap. It seems safe to assign the seventh proton group to aluminum, as it has been reported by several ob-

TABLE I. Proton groups observed from a thin aluminum target bombarded with 10.4-Mev deuterons.

Proton group	$B\rho\times10^{-3}$ gauss cm	Group energy in Mev	Q-value in Mev	Energy level in Mev
1	5.57	14.68	5.53	0
2	5.37	13.68	4.49	1.04
3	5.27	13.16	3.95	1.58
4	5.16	12.59	3.36	2.17
5	5.08	12.25	3.01	2.52
6	4.89	11.33	2.06	3.47
7	4.79	10.84	1.55	3.98
8	4.60	10.02	0.70	4.83
9	4.52	9.70	0.37	5.16
10	4.37	9.08	−0.27	5.80
11	4.29	8.76	−0.60	6.10
12	4.23	8.53	−0.84	6.40
13	4.10	8.02	−1.37	6.90
15	3.98	7.55	−1.86	7.40
16	3.68	6.46	−2.98	8.50

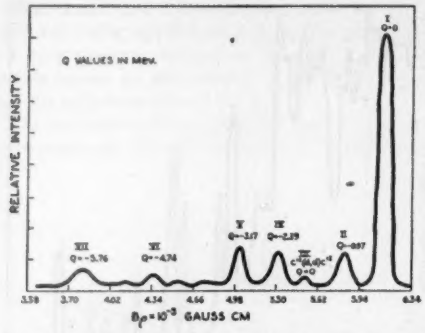

FIG. 2. Spectrum of deuterons scattered by Al^{27} observed by magnetic analysis. Peak III is due to elastically scattered deuterons from C^{12}.

servers. However, since the energy level in Al^{28} corresponding to this proton group has only been observed through the (d,p) reaction, it is not absolutely certain that the seventh proton group is from aluminum. There are indications of proton peaks near peak 18 on each side, and a peak between 12 and 13, but the statistics of the track counts make it impossible to be sure that they are real.

The resolution obtained for these proton groups is about one percent. The width of the peaks is due to several causes: (1) the deuteron beam is not monoenergetic but has a half-width of about 75 kev. (2) The target area is about 3 mm wide. (3) The particles lose energy in the aluminum target, the amount of loss depending on the depth in the target foil at which the (d,p) reaction occurs. (4) The focusing properties of the magnet contribute about one mm to the width of the peaks.

Table I gives the data concerning the proton groups and the energy levels in Al^{28}. The last two proton groups correspond to higher excited states than previously studied by the (d,p) reaction. The last proton group is from a virtual level in Al^{28} such that the residual nucleus may go to the ground state by the emission of a neutron.

The scattered deuteron groups are shown in Fig. 2. Peak I is elastically scattered deuterons, while peaks II, IV, V, VI, and VII are inelastically scattered deuterons from Al^{27}. The small peak III is just where elastically scattered deuterons from C^{12} are expected to be. The origin of the carbon on the aluminum has been previously mentioned. Table II gives the pertinent data concerning the groups of scattered deuterons. The errors

TABLE II. Groups of deuterons scattered by Al^{27}. All but the first group are inelastically scattered deuterons corresponding to excited states in Al^{27}.

Peak	$B\rho$ in gauss cm	Group energy in Mev	Energy level in Mev
I	6.14×10^5	8.98	0
II	5.81×10^5	8.08	0.97
IV	5.32×10^5	6.76	2.39
V	5.02×10^5	6.02	3.17
VI	4.38×10^5	4.57	4.74
VII	3.89×10^5	3.62	5.76

here are estimated to be the same as for the proton peaks, 0.2 Mev.

The energy of the cyclotron deuteron beam was computed from the elastically scattered deuteron peak. The deuteron beam energy was found to be 10.42 ± 0.2 Mev.

It is interesting to compare these levels in Al^{27} obtained by inelastic scattering of deuterons with levels observed by other reactions. Rhoderick[10] scattered 4.5-Mev protons from the Cambridge cyclotron with aluminum and used a proportional counter in conjunction with absorbing foils to detect the scattered protons. He found two levels, one at 0.97 ± 0.02 Mev and another at 2.15 ± 0.05 Mev, which are near the first two found in this experiment. Brolley, Sampson, and Mitchell[11] used much higher energy protons and a scattering chamber similar to Rhoderick's to study the inelastically scattered protons. They found levels at 0.95, 2.15, and 2.93 Mev in Al^{27}. These values correspond fairly well with the first three levels reported here. The level of this experiment at 4.74 Mev does not seem to correspond with a previously observed level. The highest energy level in Al^{27} found by studying the scattered deuterons correspond very well with one reported by Swann, Mandeville, and Whitehead.[12] They studied the $Mg^{26}(d,n)Al^{27}$ reaction and found an energy level at 5.81 ± 0.07 Mev above the ground state. In general the nuclear energy levels in Al^{27} that were determined by inelastically scattered deuterons are within experimental errors of the values of levels determined by other reactions, which is as it should be, since the energy levels of a given nucleus should be independent of the method of excitation.

The author wishes to thank Dr. F. B. Shull for several helpful suggestions. He is indebted to Dr. J. C. Grosskreutz and Dr. J. Townsend for their part in constructing the equipment.

[10] E. H. Rhoderick, Proc. Roy. Soc. (London) **A201**, 343 (1950).
[11] Brolley, Sampson, and Mitchell, Phys. Rev. **76**, 624 (1949).
[12] Swann, Mandeville, and Whitehead, Phys. Rev. **79**, 598 (1950).

The Decay Scheme of Cu^{66}

H. Roderick, W. E. Meyerhof, and L. G. Mann
Department of Physics, Stanford University, Stanford, California
(Received August 20, 1951)

The decay scheme of Cu^{66} has been investigated using scintillation detectors. The half-life of Cu^{66} was found to be 5.17±0.07 min. The main beta-ray spectrum has an end point of 2.7±0.1 Mev. 5½±1½ percent of the beta-rays lead to an excited state of 1.05±0.03 Mev in Zn^{66}. The half-life of this excited state is less than 5×10^{-9} sec. These results agree with the recent investigations of Friedlander and Alburger, but imply the necessity for further study of the decay scheme of Ga^{66}, which also decays to Zn^{66}. Spin, parity and shell model assignments of the pertinent states of Cu^{66}, Zn^{66}, and Ga^{66} are proposed.

I. INTRODUCTION

PRIOR to the recent work of Friedlander and Alburger[1] on Cu^{66}, which was undertaken independently and approximately concurrently with the present study, the decay scheme of Cu^{66} had not been investigated very thoroughly. We refer to Friedlander and Alburger's paper for references and since our results essentially agree with theirs we wish to report them only briefly.

II. METHOD

Sodium iodide (TlI-activated) and anthracene scintillation detectors were used exclusively to study the decay scheme of Cu^{66}. The crystals, approximately ½-in. cubes, were placed on RCA 5819 phototubes according to Hofstadter's method[2] and the phototube pulses were fed through linear amplifiers[3] to coincidence and counting circuits and to a Tektronix type 511 scope to be photographed.[3]

Cu^{66} samples were prepared by 3- to 6-min irradiations of electrolytic copper with slow neutrons produced by the Stanford cyclotron. For gamma-ray measurements sources up to a thickness of 0.6 cm were used and for beta-ray measurements the sources were approximately 0.01 cm thick.

III. HALF-LIFE DETERMINATION

The activity of the beta-rays, detected with an anthracene crystal, was followed for 1½ hours. After subtraction of a long-lived background (mostly Cu^{64}) which represented about one percent of the initial activity, a half-life of 5.17±0.07 min was obtained. The gamma-rays, detected with a sodium iodide crystal shielded by 0.6 cm Al from the source, yielded a half-life of 5.17±0.10 min.[4] These values are in good agreement with the figures 5.18±0.10 min[5] and 5.2±0.2 min[1] reported recently, although they disagree with a value of 4.34±0.03 min found by Silver[6] for the half-life of Cu^{66}.

IV. GAMMA-RAY MEASUREMENTS

Figure 1 shows some consecutive 5-min photographs of the pulse-height distribution from a single source of Cu^{66} placed over a sodium iodide scintillation detector. 0.6 cm Al was placed between the source and the detector. Photoelectron and Compton electron peaks of a 1.0-Mev gamma-ray of decreasing intensity and a 0.5-Mev gamma-ray of approximately constant intensity can be seen. Using a calibrated film, the successive intensities of the 1.0-Mev gamma-ray were found to be in the ratios of approximately 1:½:¼ showing the gamma-ray to be associated with the 5-min Cu^{66}. The 0.5-Mev gamma-ray pulses are undoubtedly due to annihilation radiation from Cu^{64}.

Figure 2 shows a photometer trace of a photograph taken for a more accurate measurement of the energy of the 1.0-Mev gamma-ray by "bracketing" its photoelectron line with the photoelectron lines of annihilation radiation and of the 1.33-Mev gamma-ray of Co^{60}. The resultant energy is 1.05±0.03 Mev. The error quoted takes into account the accuracy with which the linearity of the electronic equipment and the photometering technique could be determined. The value given by Friedlander and Alburger[1] is 1.044±0.010 Mev.

FIG. 1. Consecutive 5-min exposures of the gamma-ray pulses from slow neutron activated copper. Photoelectron and Compton electron distributions of a 1.0-Mev gamma-ray (from 5-min Cu^{66}) and of annihilation radiation (from 13-hr Cu^{64}) can be seen.

[1] G. Friedlander and D. E. Alburger, Phys. Rev. (to be published). The authors are very grateful to Dr. Friedlander for sending them a copy of the manuscript prior to publication.
[2] R. Hofstadter and J. A. McIntyre, Phys. Rev. **80**, 631 (1950).
[3] W. H. Jordan and P. R. Bell, Rev. Sci. Instr. **18**, 703 (1947).
[4] For this measurement a one-channel differential discriminator was set on the photoelectron peak of the 1.05-Mev gamma-ray. See Sec. IV.
[5] A. G. W. Cameron and L. Katz, Phys. Rev. **80**, 904 (1950).
[6] L. M. Silver, Phys. Rev. **76**, 589 (1949).

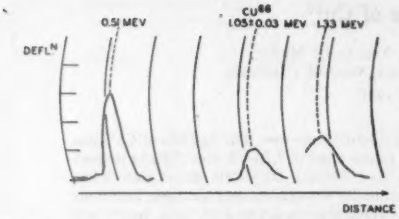

FIG. 2. Photometer trace of a single photograph for the measurement of the 1.0-Mev gamma-ray energy. Photoelectron peaks of 0.51- and 1.33-Mev calibration gamma-rays and of the Cu^{66} gamma-ray are shown.

Superposing the exposures of several 5-min irradiated sources of Cu^{66} on the same photograph and photometering the pulse-height distributions it was established that no other gamma-ray between 0.07 and 1.0 Mev could be present to more than 10 percent and between 1.0 and 4.0 Mev to more than 2 percent of the intensity of the 1.05-Mev gamma-ray in Cu^{66}.

V. BETA-RAY MEASUREMENTS

The beta-ray spectrum of Cu^{66} was obtained by photographing and photometering the pulse-height distribution from an anthracene scintillation detector. The intensity distribution was obtained by comparison with an artificial light wedge exposed on the same photograph to give film density *vs* exposure. The energy calibration was provided by the 0.97-Mev beta-spectrum of Au^{198}. Figure 3(A) shows the resulting Fermi-Kurie plot giving an end point of 2.7±0.1 Mev. The error quoted includes the uncertainty of the energy calibration. The deviation of the plot from a straight line at approximately 1.5 Mev indicates the presence of a low energy beta-spectrum (see below). The unevenness of the plot is due to statistical effects. The present endpoint is consistent with the value 2.63±0.02 Mev given in reference 1.

The beta-spectrum in coincidence with the 1.05-Mev gamma-ray was photographed by the technique of triggering the Tektronix scope with beta-gamma coincidences. For this purpose the gamma-rays were detected as described in Sec. IV, but pulses below 0.6 Mev were eliminated with an integral pulse-height discriminator. Figure 4 shows a comparison photograph of the complete beta-spectrum (A) and the coincident beta-spectrum (B). The beta-spectrum of Au^{198}, taken under identical conditions is shown also in (C). The same total number of pulses appears on all distributions. The pulses were shaped to be flat[7] to facilitate photometering. Although the statistics in Fig. 4 are poor and give rise to the intensity fluctuations, it can be seen that the coincident beta-spectrum has an end point approximately 1 Mev lower than the complete beta-spectrum. Indeed the Fermi-Kurie plot of the coincident beta-rays, shown in Fig. 3(B), yields an end point of 1.65±0.1 Mev. The deviation of the plot from a straight line below 0.8 Mev must be caused in part by source thickness (approximately 90 mg/cm²) and in part by inelastic back-scattering of electrons[8] by the anthracene crystal. The coincident beta-ray end point agrees with the expected value if the beta-ray is followed by the 1.05-Mev gamma-ray, going to the ground state of Zn^{66}.

VI. X-RAY MEASUREMENTS

An unsuccessful search was made for beta- (conversion) electron coincidences using anthracene crystal detectors. Most of the coincidences found were caused by scattered electrons which expended part of their energy in both crystals.

Also a search was made with sodium iodide crystals for the 8.6-kev K x-rays of Zn[9], but these were masked by the 7.5-kev x-rays of Ni produced in the decay of Cu^{64}. The results allowed only the setting of an upper limit of less than 0.05-Zn K x-rays per 1.05-Mev gamma-

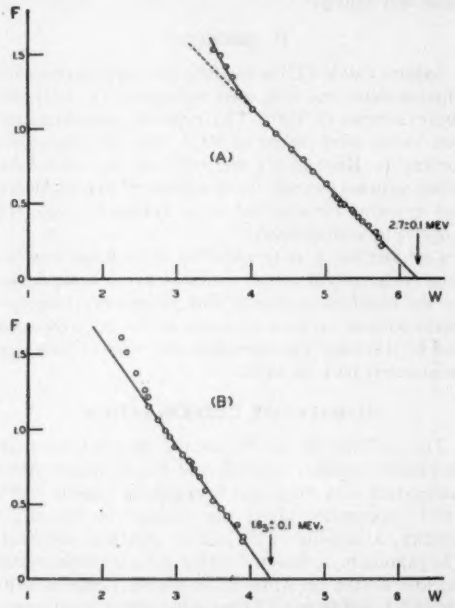

FIG. 3. (A) Fermi-Kurie plot of the complete beta-spectrum of Cu^{66}. W is the total energy of the electrons in units of their rest mass and F is the allowed Fermi-Kurie function. The deviation from the straight line at approximately 1.5 Mev is due to a lower energy beta-spectrum. (B) Fermi-Kurie plot of the coincident beta-rays. The deviation from the straight line at approximately 0.8 Mev is due to source thickness and inelastic backscattering from the anthracene crystal.

[7] The authors are indebted to Mr. H. I. West for the design and construction of the pulse shaper.

[8] W. Bothe, Z. Naturforsch. 4a, 542 (1949).

[9] For the technique see West, Meyerhof, and Hofstadter, Phys. Rev. 81, 141 (1951). For these measurements the sources were approximately 20 mg/cm² thick.

ray from Cu^{64}. This figure is not useful for the determination of a meaningful conversion coefficient, but does assure the absence of any highly converted gamma-rays which might not have been detected otherwise.

VII. COINCIDENCE MEASUREMENTS

In order to determine the branching ratio of the 1.6$_\beta$- and 2.7-Mev beta-rays the beta-ray pulses from anthracene and the gamma-ray pulses from sodium iodide crystals were passed through amplifiers and integral discriminators into a coincidence circuit of 0.25 μsec resolving time. The gamma-ray channel was biased against pulses below 0.6 Mev and the beta-ray channel against pulses below 0.2 Mev. Using both Au^{198} beta-gamma coincidences and Co^{60} gamma-gamma coincidences to calibrate the detector efficiencies, calculations of the branching ratio of the 1.6-Mev beta-rays yielded $5\frac{1}{2}\pm1\frac{1}{2}$ percent. These values were obtained consistently both from the Cu^{64} beta-gamma coincidence rates, and from the single counting rates in a manner analogous to that described by Friedlander and Alburger.[1] The effect of the bias and of self-absorption on the beta- and gamma-counting rates was taken into account in the calculations. Nevertheless the above value is slightly lower than the figure 9.2±1 percent given in reference 1.*

Using anthracene crystal detectors and wide-band amplifiers in both channels of a coincidence circuit[10] of 0.03-μsec resolving time, an attempt was made to measure the half-life of the 1.05-Mev excited state of Zn^{64}, since Langer and Moffat[11] had postulated a half-life around 10^{-6} sec for this state. For these measurements 0.6-cm Al was placed between the source and one of the anthracene crystals. Figure 5 shows delayed coincidence curves for gamma-gamma coincidences in Co^{60} (o) and for beta-gamma coincidences in Cu^{64} (×). Accidental coincidences are subtracted. The curves are not of identical shape because the pulses in both cases are not produced by identical radiations and the coincidence circuit was sensitive to pulse heights. Since there is only one coincidence branch in Cu^{64}, the steep cutoff of the delay curve allows the setting of a conservative upper limit of 5×10^{-9} sec for the half-life of the 1.05-Mev excited state of Zn^{64}. (The dotted line in Fig. 5 shows the expected cutoff of the Cu^{64} curve for a metastable state of 5×10^{-8} sec half-life.)

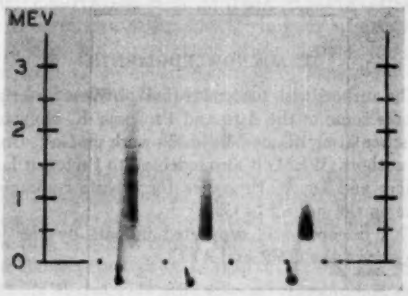

FIG. 4. Beta-ray pulse-height distributions. (A) Complete beta-spectrum of Cu^{64}. (B) Beta-spectrum coincident with gamma-ray pulses above 0.6 Mev. (C) Beta-spectrum of Au^{198} used for energy calibration.

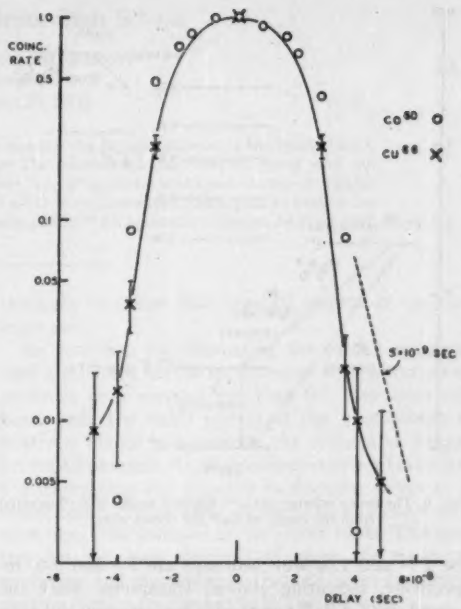

FIG. 5. Beta-gamma coincidence rate in Cu^{64} (×—×) *vs* delay of the beta-counter. The dotted line indicates the expected cutoff of the curve for a 5×10^{-9} sec metastable state. Gamma-gamma coincidences in Co^{60} (o o) are shown for comparison. The coincidence rates at zero delay are normalized to unity. Accidental coincidences are subtracted.

VIII. CONCLUSIONS

The present experimental results lead to the decay scheme of Cu^{64} shown in Fig. 6. The log *ft* values[12] for

* *Note added in proof:* Dr. Friedlander has kindly brought up the question as to a possible underestimation of the self-absorption of the beta-rays in our experiment. We have used the formula $f(1-e^{-\mu x})/\mu x$ to calculate the fraction of beta-rays issuing from a source of thickness x. With the values $\mu_{1.65}=4.6$ cm^2/g, $\mu_{2.7}=2.6$ cm^2/g, and $x=0.090$ g/cm^2 this formula yields $f_{1.65}=0.82$ and $f_{2.7}=0.89$. In the calculation using coincidence rates the final result for the branching ratio is proportional to $f_{2.7}/f_{1.65}$, where as using single rates the branching ratio is proportional to $1/f_{2.7}$. Increasing the effective μ by 40 percent would increase the branching ratio only by approximately 4 percent with either method of calculation.

[10] The authors are very much indebted to Dr. W. C. Barber for putting this coincidence circuit at their disposal. See W. C. Barber, Phys. Rev. **80**, 332 (1950).

[11] L. M. Langer and R. D. Moffat, Phys. Rev. **80**, 651 (1950).

[12] E. Feenberg and G. Trigg, Revs. Modern Phys. **22**, 399 (1950). One of the authors (WEM) is very much indebted to Dr. Trigg for sending him a set of log *ft* curves prior to publication.

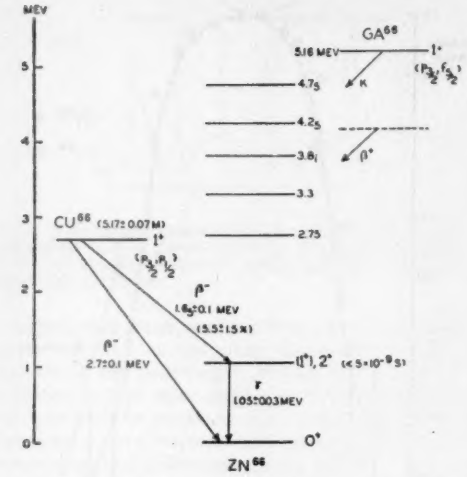

FIG. 6. The decay scheme of Cu^{66}. Excited states of Zn^{66} inferred from the decay of Ga^{66} are shown also.

the 2.7- and 1.6$_8$-Mev beta-rays are 5.3 and 5.6, respectively, indicating allowed transitions. Since the ground state of Zn^{66} presumably has zero spin and even parity and $0\rightarrow 0$ transitions are forbidden by Gamow-Teller selection rules, the spin of the ground state of Cu^{66} is probably 1 (even). This is consistent with the proton, neutron configurations $(p_{3/2}, p_{1/2})$ or $(p_{3/2}, f_{5/2})$ expected from the shell model[13] applied to beta-decay.[14] The 1.05-Mev excited state of Zn^{66} would then have a spin of 1 or 2 (even), consistent with the upper limit found for the half-life of the 1.05-Mev gamma-ray.[15] A spin 2 (even) would agree with Goldhaber and Sunyar's findings[15] that the first excited state of most (of the investigated) even-even nuclei has spin 2 (even).

As already pointed out by Friedlander and Alburger[1] these results contradict the decay scheme of Ga^{66} as proposed by Langer and Moffat[11] which can now be considered incorrect because of the recently determined value of 6.05 Mev for the $Zn^{66}(p, n)$ threshold.[16] But, furthermore, Mukerji and Preiswerk[17] propose a more nearly correct decay scheme of Ga^{66} in which a 1.06-Mev gamma-ray would be followed by a 2.75-Mev gamma-ray going to the ground state of Zn^{66}. (These gamma-rays would come from the 3.81- and 2.75-Mev levels of Zn^{66} shown in Fig. 6.) If this decay scheme is correct then the present investigation leads one to expect additional transitions to the 1.05-Mev excited state of Zn^{66} in the decay of Ga^{66}.[18]

The presently available information on Ga^{66}[2,11,17,18] would then lead to the excited states of Zn^{66} shown in Fig. 6. One may assume that a 3.1-Mev positron spectrum of the order of one percent intensity[19] was missed by previous investigators. The log ft value of this positron spectrum would be approximately 8. The 4.16-Mev positron spectrum of allowed shape[11] leading to the ground state of Zn^{66} has a log ft value of 7.9. Although these log ft values are rather high for allowed beta-spectra they are compatible with Nordheim's beta-decay rules.[14] In fact on the shell model essentially the same proton, neutron configurations are available for Ga^{66}, as for Cu^{66}. One may then assume a $(p_{3/2}, p_{1/2})$ configuration for Cu^{66} and a $(p_{3/2}, f_{5/2})$ configuration for Ga^{66} both having spin 1 (even). The beta-transitions to the ground state of Zn^{66} would be of the allowed types $\Delta I=-1$, $\Delta l=0$ and $\Delta I=-1$, $\Delta l=2$, respectively, the latter with an exceptionally high ft value as found by Nordheim[14] for odd A nuclei of this type.† The transitions to the 1.05-Mev excited state of Zn^{66} similarly could be $\Delta I=+1$, $\Delta l=0$ for Cu^{66} and $\Delta I=+1$, $\Delta l=2$ for Ga^{66}.

IX. ACKNOWLEDGMENTS

The authors wish to thank Mr. H. I. West for helping to take some of the data and Professor R. Hofstadter for stimulating discussions of his work on Ga^{66}. One of the authors (WEM) is also indebted to Professor L. M. Langer and Dr. P. Preiswerk for private communications on the subject of Ga^{66}.

This research was supported in part by the joint program of the ONR and AEC.

[13] M. G. Mayer, Phys. Rev. **78**, 16 (1950). The other plausible configurations for 29 protons and 37 neutrons do not yield the expected spin values and/or parities.

[14] L. W. Nordheim, Phys. Rev. **78**, 294 (1950).

[15] For electric quadrupole radiation the expected half-life is approximately 10^{-10} sec [M. Goldhaber and A. W. Sunyar, Phys. Rev. **83**, 906 (1951)]. The authors are very grateful to Professor Goldhaber for sending them a copy of this paper prior to publication.

[16] Blaser, Boehm, Marmier, and Peaslee, Helv. Phys. Acta **24**, 2 (1951).

[17] A. Mukerji and P. Preiswerk, Helv. Phys. Acta **23**, 516 (1950).

[18] P. Preiswerk (private communication) has found weak gamma-rays from Ga^{66} which would support this interpretation. But this point bears further study since all the gamma-ray intensities cannot be matched as yet.

[19] This assumption is consistent with a rough analysis of the $(\beta^+\text{-}\gamma)/\beta^+$ coincidence curve (Fig. 6) in reference 11.

† *Note added in proof:* Data for even A nuclei have been published recently by L. Nordheim, Argonne National Laboratory Report No. 4626 (1951), to be published in Revs. Modern Phys. The present assignment of $p_{\frac{1}{2}}$ to a 37 nucleon configuration is not quite in accord with the strict shell model application to odd-odd nuclei, but might alleviate some of the difficulties mentioned in the report.

Internal Pair Spectrum from $B^{10}+d$

S. J. Bame, Jr.,* and L. M. Baggett*
Rice Institute, Houston, Texas†

(Received August 20, 1951)

A magnetic lens pair spectrometer has been used to measure the energy spectrum of the internal pairs formed from the bombardment of B^{10} with deuterons. The spectrometer has been calibrated with the nuclear pair from $F^{19}+p$ with an energy of 6.05±0.03 Mev. The B^{10} spectrum shows gamma-rays of energies 4.43±0.07, 6.51±0.13, 6.75±0.13, 7.34±0.20, and 8.93±0.13 Mev. Unresolved lines appear to exist in the region 4.5 to 5.5 Mev. The 6.51 Mev line is tentatively assigned to C^{11*} while the other lines can be attributed to B^{11*}.

INTRODUCTION

THE detection of the internal pairs arising from a nuclear reaction is a means of determining the gamma-ray spectrum above about 3 Mev. The high energy spectrum from the deuteron bombardment of 96 percent separated B^{10} has been investigated by this method. The spectrum from the reaction has been shown by earlier cloud-chamber measurements of the pairs to contain three strong lines at approximately 4.5, 6.5, and 9.0 Mev.[1,2] Recent results with magnetic 180° pair spectrometers have confirmed the cloud-chamber determinations. Terrell and Phillips[3] found three lines at 4.52, 6.71, and 9.04 Mev, with an indication that the two lower energy lines are complex. Rutherglen[4] reports gamma-ray lines at 4.5, 6.5, 6.7, and 8.94 Mev. Recent measurements of the proton[5,6] and neutron[7,8] groups from the reaction have clarified the energy level schemes of the mirror nuclei B^{11} and C^{11} to such an extent to justify a careful investigation of the gamma-ray spectrum from $B^{10}+d$ and assignment of gamma-ray energies to the corresponding levels.

Apparatus

The spectrometer used in these experiments, shown in Fig. 1, is basically a double magnetic lens beta spectrometer. The two focusing coils contain about 150 turns each of $\frac{3}{8}$-inch copper tubing, and are cooled by water flowing through the conducting turns. The separation of the coils is completely adjustable in order to provide for changing the acceptance solid angle of the spectrometer. The current for the coils is supplied by a 24 kw 400 ampere generator which is stabilized electronically to better than one-half percent at the currents used.

No provision for eliminating the earth's magnetic field is provided for the spectrometer since electrons or positrons with energies less than 0.6 Mev have not been used. The baffle system of the spectrometer is relatively simple compared to the systems of normal beta-spectrometers. An aluminum-covered lead cylinder, 13½ inches long and 4 inches in diameter serves as a center baffle. A disk baffle of Lucite slides along a thin aluminum tube fastened to the center baffle. This system has not been designed to given the optimum resolution and transmission characteristics for single electron spectra for reasons to be treated later.

The source end plate of the spectrometer is constructed to allow the spectrometer to be attached to the accelerating tube of the Rice Van de Graaff generator. In order to avoid the fringing field, the magnetic analyzer of the Van de Graaff was not used. Since only thick targets have been used and it is not necessary to know the bombarding energy to great accuracy, the electrostatic voltmeter gives a satisfactory determination of the accelerator potential. A small magnet about two meters from the spectrometer was used to analyze the beam into its mass components. A quartz plate with a $\frac{1}{16}$-inch round aperture was mounted in a fixed position 1 inch from the target. This arrangement allowed the beam of the accelerator to be positioned accurately, by viewing the fluorescence produced by the beam on the quartz. The beam current to the target was measured with a current integrator.

The counting arrangement consists of two Victoreen "Thyrode" 30 mg/cm² thin wall aluminum Geiger

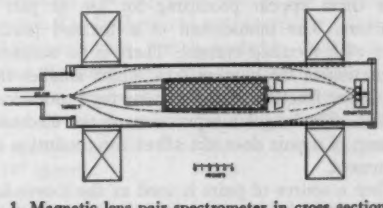

FIG. 1. Magnetic lens pair spectrometer in cross section. The accelerator beam passes through a quartz aperture to the target. Pairs produced in the source are focused and counted in coincidence in the counter assembly.

* Now at the Los Alamos Scientific Laboratory, Los Alamos, New Mexico.

† This paper is based in part on a Ph.D. thesis submitted by the first named author to the faculty of the Rice Institute in May, 1951. This work was supported by the joint program of the ONR and AEC, and by the Research Corporation.

[1] Gaerttner, Fowler, and Lauritsen, Phys. Rev. **55**, 27 (1939).
[2] J. Halpern and H. R. Crane, Phys. Rev. **55**, 415 (1939).
[3] J. Terrell and G. C. Phillips, Phys. Rev. **83**, 703 (1951).
[4] Report at the Harwell Conference, 1950.
[5] Van Patter, Buechner, and Sperduto, Phys. Rev. **82**, 248 (1951).
[6] W. O. Bateson, Phys. Rev. **80**, 982 (1950).
[7] V. R. Johnson, Phys. Rev. **81**, 316 (A) (1951) and a private communication.
[8] C. P. Swann and E. L. Hudspeth, Phys. Rev. **76**, 168 (1949).

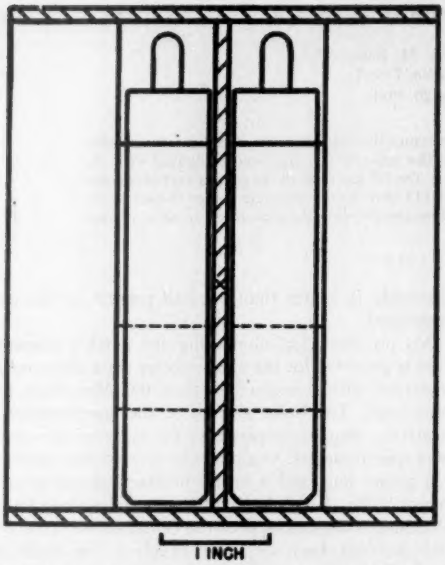

FIG. 2. Counter assembly consisting of two thin-wall Geiger tubes mounted on Lucite blocks. The assembly may be used fully open for high counting efficiency or with lead plates covering the counters with apertures located by the dotted lines.

counters, mounted on Lucite blocks. The counters are separated with ½-inch lead strip to prevent spurious coincidences from single particles passing through both counters. Figure 2 shows a front view of the counter holder as seen when looking along the axis of the spectrometer from the source end. The counters may be covered with sheet lead containing apertures in the proper positions, or they may be used in the fully exposed condition shown in the figure. The cross locates the optical axis of the spectrometer, and the dotted lines locate the apertures which were used for some of the experiments. The counter leads are brought through Kovar seals in the endplate to a conventional coincidence circuit which had a resolution of about 0.5 microsecond.

COUNTING PAIRS

Several properties of magnetic lens spectrometers make them appear promising for use as pair spectrometers. The momentum of a focused particle is linear with focusing current. There is no necessity for collimation of the gamma-rays, which enables the use of a larger fraction of the gamma-rays produced in a reaction. The angular separation of the electron and positron of a pair does not affect the resolution of the instrument.

When a source of pairs is used as the source for the spectrometer, the electrons and positrons are both focused through the instrument in similar helical orbits, with opposite directions of rotation. When the electron and positron of a pair have equal energies, both members can be focused through the spectrometer at one value of the magnetic field strength. If the energies are not the same, both members cannot be focused. Thus, for a pair of given total energy, there is a unique value of focusing current at which both members of the pair can be focused. (More accurately, there is a range of currents for which both members can get through, since the spectrometer has a finite resolving power.) Therefore, if some method of knowing when a pair is focused through the spectrometer is available, then the spectrometer can be used for measuring high energy gamma-ray spectra.

Two methods for counting pairs in coincidence have been used. The first of these methods may be described as off axis separation, and has been reported by Siegbahn.[9] If the source of pairs is placed off the optical axis of the spectrometer, the electrons and positrons have separated focal points. By placing counters at the two focal points, the pair members can be counted in coincidence. The positions of the focal points for a given source position were located by the exposure of dental x-ray film placed in the region of the focal points, using the internal conversion line from an intense Cs^{137} source. This source served as a source of electrons and positrons by reversing the direction of the focusing current for the location of the positron focus.

The second method used can be described as statistical separation.[10] The envelopes of the trajectories drawn in Fig. 1 illustrate how statistical separation takes place. The source of pairs is placed on the optical axis of the spectrometer. One of the properties of a magnetic lens spectrometer is that a ring focus exists for monoenergetic particles leaving the source in a small angular range. As shown in the figure, all trajectories pass through a ring focus, but the position at which a particle strikes the counting area depends upon the angle at which it is ejected from the source. Since a great many pairs are ejected with a small but appreciable angular separation, it is to be expected that many of them will be separated when arriving at the detector. Pair members with slightly different energies may also be focused at different regions of the detector. Therefore, coincidences may be counted between two counters placed at the focal point as shown in Fig. 1.

Both the statistical and off-axis methods have been used for counting pairs. The two methods are complementary for the following reasons. For a focusing coil separation of 8 inches, (inside to inside edges of the coils) the electron and positron focal points are separated by one inch if the source is off axis by one inch. For larger coil separations, the separation of the two foci becomes smaller. In order to increase the transmission of the spectrometer it is necessary to increase the coil separation, but this results in a very small

[9] K. Siegbahn and S. Johansson, Rev. Sci. Instr. **21**, 442 (1950).
[10] S. J. Bame, Jr., and L. M. Baggett, Phys. Rev. **79**, 415 (A) (1950).

separation or an overlapping of the positron and electron foci, so that two counters cannot be placed in position to count coincidences. For this reason the statistical method of separation becomes useful when large transmission is desired.

The single counting rates for a pair spectrometer of this type are quite high, because of several factors. Many pairs originating at the source have an energy or angular distribution such that only one member is focused to the counters. Lower energy gamma-rays produce photo- and Compton electrons which add to the single counting rate. In addition, many reactions of interest produce beta-emitters. This high single counting rate has been a limiting factor in the experiments described here, since Geiger counters are not suitable for extremely high counting rates, and small resolving times for coincidences.

Since the ratio of pairs counted to single counts is very small, it is important to reduce to a minimum spurious coincidences arising from single particles. A single electron or positron can cause a coincidence by counting in one counter and then suffering a double scattering in such a way as to set off the second counter. The number of these improbable events is of the same order of magnitude as true pair counts unless precautions are taken. Scattering from behind the counters is reduced by using a low Z material to back up the counters. In this case Lucite was used. All parts of the baffle system should be as far as possible from the counters and should be made of a material with a low Z. Thus, the baffle system of the spectrometer has been kept relatively simple, and the optimum system of baffles from the point of view of beta-ray spectroscopy has not been used. The disk baffle shown in Fig. 1 is made of Lucite, and aluminum rings are spaced on the inside of the tube to reduce scattering from the brass wall.

Three types of pair formation can be utilized by the spectrometer. These are the external, internal, and nuclear pair processes. External pairs[11] are formed by gamma-rays passing through a radiator. The spectrum of these pairs can be measured by placing a suitable converter in front of the target in the source position of the spectrometer. Internal pairs,[12–14] which are formed in the nuclear fields of the same nuclei which emit the quanta can be used with the spectrometer by placing the target in the source position without a radiator. In the same manner, the nuclear pair[15,16] from $F^{19}(p,\alpha)O^{16}$ can be detected.

The energy and angular distributions of external and internal pairs are similar, so that the spectrometer has nearly the same efficiency for counting either type of pair. The nuclear pair has a greater probability of being ejected with both members having the same energy, but the angular separation of the members is more likely to be large.[16–18] Experimentally, this spectrometer has proved to be roughly $\frac{1}{3}$ as efficient for nuclear pairs as for internal pairs.

For the measurement of gamma-ray spectra, internal pairs prove to have advantages over external pairs. In order to obtain as many external pairs from a radiator as are produced internally in the target, a lead radiator having an approximate thickness of 0.002 inch is required. While the target need be only as thick as necessary to stop the beam of charged particles, a radiator must be relatively thick. The consequent scattering and energy degradation of pairs reduce the efficiency and impair the resolution of the spectrometer. These considerations have prompted the use of the internally formed pairs whenever possible.

EXPERIMENTAL RESULTS

A. External Pairs from a Po-Be Source

The gamma-ray spectrum of a Po-Be source was determined, using statistical separation, in order to determine whether a spectrometer of this type might be adaptable for measuring weak intensity gamma-rays. The spectrum of this source contains a single line of energy 4.45 Mev from $Be^9(\alpha,n)C^{12}$, as determined and discussed by Terrell.[19] The Po-Be source has a diameter of about $\frac{1}{8}$ inch which makes it a poor source for a lens spectrometer, since small sources are necessary in order to obtain good resolution. The radiator for this run was 0.005 inch thorium, $1\frac{1}{2}$ inches by $1\frac{1}{2}$ inches square. The source was placed on the axis of the spectrometer with the radiator directly in front. The counting system was used with no apertures over the counters, and with the sensitive counting region centered on the optical axis. The coil separation for this case was 25 inches, inside to inside of the coils, and the radiator and counters were spaced 32 inches apart, symmetrically located within the coils. The disk baffle was kept against the center baffle for maximum transmission.

The spectrum in Fig. 3 consists of the completely uncorrected coincidence counting rate. The accidental coincidence rate was negligible, due to the weakness of the source. The background approximately follows the single counting rate, and is probably due to doubly scattered electrons, since the counting system is wide open. Knowing the original intensity of the source[19] and the half-life, it was calculated that the transmission of the spectrometer for this run was one pair count per 7.5×10^5 quanta.

[11] H. Bethe, Proc. Cambridge Phil. Soc. **30**, 524 (1934).
[12] J. R. Oppenheimer and L. Nedelsky, Phys. Rev. **44**, 948 (1933).
[13] J. C. Jaeger and H. R. Hulme, Proc. Roy. Soc. (London) **148**, 708 (1935).
[14] M. E. Rose and G. E. Uhlenbeck, Phys. Rev. **48**, 211 (1935).
[15] W. A. Fowler and C. C. Lauritsen, Phys. Rev. **56**, 840 (1939); E. P. Tomlinson, Phys. Rev. **60**, 159 (A) (1941).
[16] J. R. Oppenheimer and J. S. Schwinger, Phys. Rev. **56**, 1066 (1939); J. R. Oppenheimer, Phys. Rev. **60**, 164 (A) (1941).
[17] S. Devons and G. R. Lindsey, Nature **164**, 539 (1949).
[18] Rasmussen, Hornyak, Lauritsen, and Lauritsen, Phys. Rev. **77**, 617 (1950).
[19] J. Terrell, Phys. Rev. **80**, 1076 (1950).

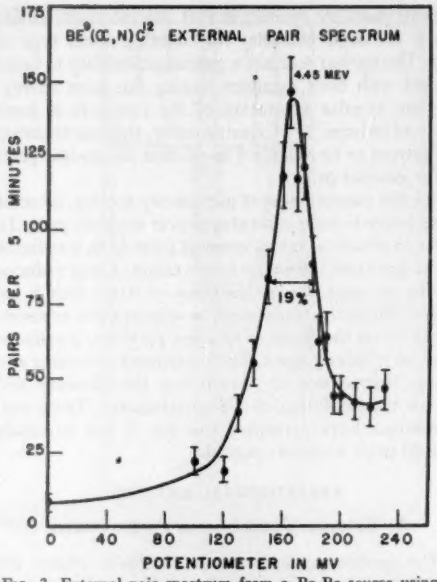

FIG. 3. External pair spectrum from a Po-Be source using a 0.005-inch thorium radiator with the spectrometer arranged for high efficiency detection. The counting rate at the peak corresponds to one pair count per 7.5×10^5 quanta.

B. Nuclear Pairs

The nuclear pairs from $F^{19}(p,\alpha)O^{16}$ offer a strong source of pairs for testing and calibrating a magnetic lens pair spectrometer. As a calibration for the run on $B^{10}+d$, the nuclear pair spectrum was taken using the off-axis method for pair separation. The coil separation for this arrangement was 10 inches. The source and counting system were symmetrically located with respect to the coils, in the same positions as shown in Fig. 1. The source was located $\frac{1}{4}$ inch below the optical axis, and the source diameter, as limited by the quartz aperture was $\frac{5}{16}$ inch. The counters were covered with $\frac{1}{8}$ inch lead plates with $\frac{3}{4}$ inch square apertures in the positions shown by the dotted lines in Fig. 2. The center of the apertures was $\frac{3}{4}$ inch below the optical axis.

This arrangement was tested with the internal conversion line from a Cs^{137} source. The results of this test, shown in Fig. 4, were obtained by taking the spectrum in both counters, for both directions of focusing current. The electron and "positron" lines have resolutions of 8 and 9 percent. To indicate the resolution attainable with the off axis separation method, Fig. 5 shows the internal conversion line taken with smaller apertures, the disk baffle in position to restrict the electron trajectories, and with a 14-inch coil separation. Of course, very strong gamma-sources would be necessary to make use of resolutions of this order.

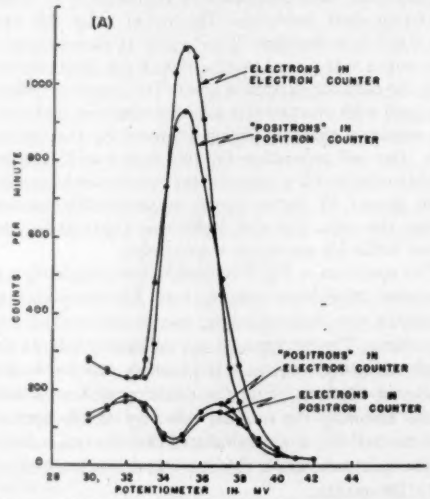

FIG. 4. Cs^{137} internal conversion line. This spectrum was a test of the off axis separation of pairs technique. The "positron" source was obtained by reversing the focusing current. Coil separation 10 in.; $\frac{1}{4}$ in. source $\frac{1}{4}$ in. off axis; exit apertures $\frac{3}{4}$ in. square, baffle system set for maximum transmission.

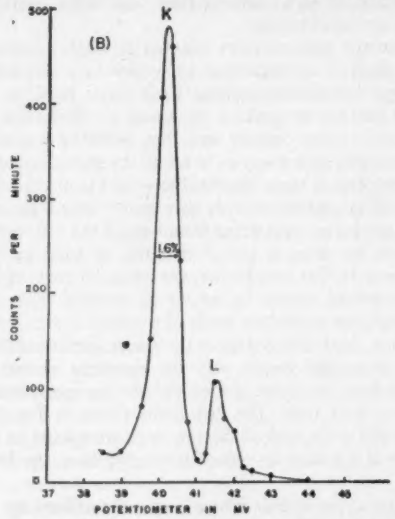

FIG. 5. Cs^{137} internal conversion line obtained with the source $\frac{1}{4}$ inch off axis. The spectrum was a test of the resolution attainable with this pair separation method. Coil separation 14 in.; $\frac{1}{4}$ in. source $\frac{1}{4}$ in. off axis; exit aperture $\frac{3}{4}$ in. diameter; baffle system set for good resolution.

The nuclear pair spectrum was taken with this arrangement, using a 9-mg/cm² calcium fluoride target evaporated on a 2-mg/cm² aluminum foil. The target was bombarded with 1.4-Mev protons, and pair counts were taken against a standard number of counts of a gamma-ray monitor and the current integrator. Figure 6

shows the nuclear pair spectrum obtained, with a resolution of 5.1 percent in contrast with the Cs^{137} calibration resolutions of 8 and 9 percent, illustrating the property of improved resolution for pairs to be expected with a spectrometer of this type. This spectrum has been corrected for a zero focusing current pair background and the accidental coincidence rate. This correction amounted to 80 counts per point, contrasted with 1600 counts at the peak. The nuclear pair total energy has been given by Chao, *et al.*[20] as 6.05±0.03 Mev, so this value has been used as a pair calibration for the spectrometer.

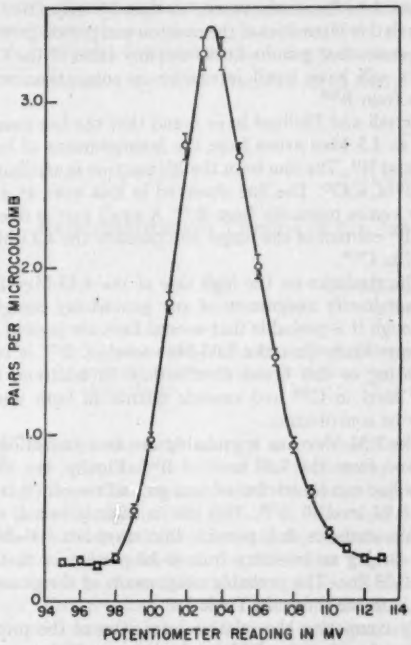

FIG. 6. Nuclear pair calibration line of total energy 6.05 Mev. The off axis separation technique was used with 1.4-Mev deuterons and a 9 mg/cm² calcium fluoride target.

C. Internal Pairs from $B^{10}+d$

The gamma-ray spectrum from $B^{10}+d$ was investigated with the off axis arrangement described in the previous section. A 20-mg/cm² target of 96 percent separated metallic B^{10} on a 1-mg/cm² aluminum foil was bombarded with 1.4-Mev deuterons. With a source of this thickness, approximately 95 percent of the pairs formed will be internal pairs. The resulting spectrum is shown in Fig. 7 plotted on an energy scale. The spectrum has been corrected by subtracting a zero magnetic field background and the accidental coincidence rate. The total correction was about 30 percent of the counting rate. There appears to be a background remaining after the corrections have been made. This background can be due to unresolved, low intensity gamma-ray lines, to inaccuracies in making the corrections, and to coincidences due to annihilation radiation and doubly scattered electrons.

[20] Chao, Tollestrup, Fowler, and Lauritsen, Phys. Rev. **79**, 108 (1950).

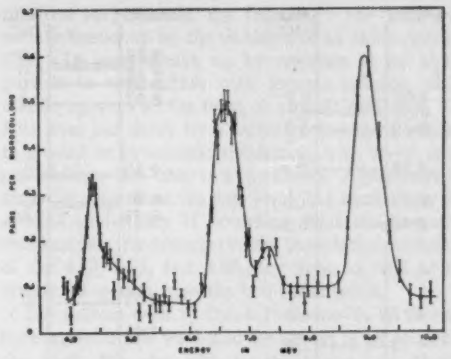

FIG. 7. Internal pair spectrum from $B^{10}+d$ with $E_d=1.4$ Mev, using a 20 mg/cm² metallic boron target. The energy scale is obtained using the 6.05-Mev nuclear pair calibration.

The gamma-ray lines found from this reaction are shown in Table I. The energies were determined on the basis of the nuclear pair calibration, taking the loss of energy in the calcium fluoride target to be 20 kev per particle and 33 kev in the B^{10} target. The probable errors assigned to the energy values were determined by inspection of the nuclear pair and internal pair spectra with regard to how the peaks may be shifted within the statistics.

From the high energy tail on the 4.43-Mev line, it is evident that one or more low intensity lines are present between 4.5 and 5.5 Mev. The resolution of the wide line is 8.8 percent, and enough data were taken to show that this line is essentially flat on top, in opposition to the sharp peak of the nuclear pair. The two energies given for the broad central peak are found by assuming this peak to be due to two nearly equal intensity lines

TABLE I. Gamma-ray energies determined from the internal pair spectrum of $B^{10}+d$, shown in Fig. 7. The yields, taken from Terrell and Phillips,* are used to calculate the spectrometer efficiency, which is defined as the number of pair counts per quantum.

Line	Gamma-ray energy	Resolution (%)	Assignment	Yield,* quanta per microcoulomb	Spectrometer efficiency
1	4.43±0.07	6.8	B^{11*}	34×10^6	0.77×10^{-6}
2	6.51±0.13	8.8	C^{12*}		
3	6.75±0.13		B^{11*}		
4	7.34±0.20		B^{11*}		
5	8.93±0.13	5.8	B^{11*}	12×10^6	4.3×10^{-6}

* See reference 3.

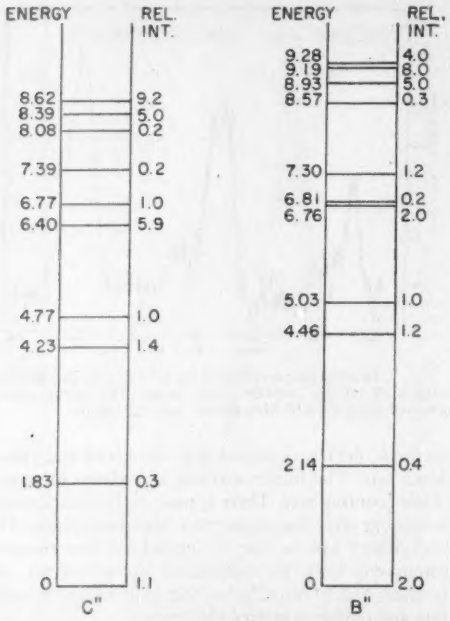

FIG. 8. $C^{11}-B^{11}$ energy levels from the neutron (see reference 7) and proton (see reference 5) groups. The neutron groups were taken at 0° to the beam at $E_d=3.64$ Mev. The proton groups were taken at 90° with $E_d=1.51$ Mev.

having line shapes similar to the nuclear pair line. That this line is actually two lines has been reported by Rutherglen,[4] who obtained energy values of 6.5 and 6.7 Mev in good agreement with the values obtained with this spectrometer. The statistics on the weak 7.34-Mev line are too poor to justify calculation of the resolution. This line has been observed in the spectra obtained from three independent runs with the spectrometer.

The yields for lines 1 and 5 shown in Table I were determined by Terrell and Phillips.[3] The efficiencies for this spectrometer were determined using these yields and the values for integrated beam current which were taken along with the gamma-ray monitor counts.

DISCUSSION

Several reactions which may account for the gamma-rays from $B^{10}+d$ are: (1) $B^{10}(d,\alpha)Be^8$, $Q=17.81$ Mev; (2) $B^{10}(d,p)B^{11}$, $Q=9.24$ Mev; and (3) $B^{10}(d,n)C^{11}$, $Q=6.53$ Mev. Reaction (1) yields Be^8 which has excited levels at 4.8, 7.0, and 9.8 Mev in addition to other levels. However, a lack of gamma-alpha coincidences from $B^{10}(d,\alpha)$ suggests that this reaction is not involved.[21] The reactions (2) and (3) have recently been studied by means of the proton[5,6] and neutron groups.[7,8]

[21] J. Thirion, Compt. rend. **229**, 1007 (1949).

The energy level schemes of the mirror nuclei B^{11} and C^{11} obtained by measurement of these groups are shown in Fig. 8, along with the observed relative intensities. The neutron groups giving the levels shown for C^{11} were measured at 0° by Johnson using 3.64-Mev deuterons. The proton groups, measured at 90° to the beam, were measured by Van Patter, *et al.*, using 1.51-Mev deuterons. In the work reported here, the levels in C^{11} above 7.93 Mev were not excited, since 1.4-Mev deuterons were used.

The broad, flat-topped line shown in Fig. 7 is attributed to the 6.76-Mev level of B^{11*} and the 6.40-Mev level of C^{11*}. The intensities of the two lines are assumed to be nearly equal, so that by inspection of the relative intensities of the neutron and proton groups, it appears that gamma-lines from any other of the C^{11*} levels will have small intensities in comparison with lines from B^{11*}.

Terrell and Phillips[3] have found that the low energy line at 4.5 Mev arises from the bombardment of both B^{10} and B^{11}. The line from the B^{11} reaction is attributed to $B^{11}(d,n)C^{12}$. The line observed in this work at 4.43 Mev comes primarily from B^{11*}. A small part is due to the B^{11} content of the target and possibly the 4.23-Mev level in C^{11*}.

The statistics on the high side of the 4.43-Mev line do not justify assignment of any gamma-ray energies, although it is probable that several lines are present. It appears likely that the 5.03-Mev level of B^{11*} is contributing to this broad distribution. In addition, the 4.77 level in C^{11*} and cascade quanta in both nuclei may be contributing.

The 7.34-Mev line is probably due to a transition to ground from the 7.30 level of B^{11*}. Finally, the 8.93-Mev line can be attributed to a ground transition from the 8.93 level of B^{11*}. This line is slightly broad, and within statistics, it is possible that there is a 9.19-Mev line having an intensity from 0–10 percent of that of the 8.93 line. The probable assignments of the gamma-ray lines are shown in Table I.

By comparing the relative intensities of the proton groups forming the B^{11*} levels, it appears that some explanation is needed for the absence of an appreciable amount of radiation from the upper two levels as well as for the relative intensities of the gamma-ray lines. From the yields given in Table I, the 4.43 line has 2.8 times the intensity of the 8.93 line. Assuming a twofold increase of the spectrometer efficiency between 6.75 and 8.93 Mev, the 6.75 line has approximately the same intensity as the 8.93-Mev line. These relative intensities do not agree with those for the proton groups.

A possible explanation for the absence of the high energy lines is that these levels usually break up with the emission of alpha-particles. The excitation energy necessary for a breakup of the B^{11*} into Li^7+He^4 is about 8.64 Mev, so the upper three levels possess enough energy to break up in this manner. The pair spectrum shows that the 8.93-Mev level emits ground

transition gamma-rays, while no significant number seem to be contributed by the higher two levels. This could be explained by the higher energy available for alpha decay for the two upper levels, and the consequent reduction in the lifetime for the breakup. Bennett, Roys, and Toppel[22] have found from the reaction $Li^7(\alpha, \gamma)B^{11}$ that the 9.28 level has a width of 6 kev, which would indicate that this level should break up by particle emission. The 8.93 and 9.19 levels were shown to be appreciably narrower than the 9.28 level, within instrumental fluctuations. The results of Bennett, *et al.*, suggest that the radiation from these three levels consists of about 15 percent emission straight to ground, the remaining radiation being due to cascade transitions.

A consistent interpretation of the gamma-ray intensities may include the following: The 9.28 level mainly breaks up by the emission of an alpha-particle. The 9.19 level breaks up by emission of an alpha-particle in competition with gamma-emission which mainly appears in the form of cascade radiation. The 8.93 level can decay by a radiative transition straight to ground or by cascade transitions, with about equal probabilities for the two processes. Alpha-emission may also arise from the 8.93 level, but most likely has a small probability of occurring. This interpretation could explain the discrepancies of the relative intensities of the 4.43, 6.75, and 8.93-Mev lines, as well as the absence of quanta from the two upper levels.

The authors wish to thank Professor T. W. Bonner for suggesting this work and for his aid in all phases of the work. We also wish to thank the Los Alamos Scientific Laboratory for the loan of the Po-Be source.

[22] Bennett, Roys, and Toppel, Phys. Rev. **82**, 20 (1951).

PHYSICAL REVIEW VOLUME 84, NUMBER 5 DECEMBER 1, 1951

Renormalization Theory of the Interactions of Nucleons, Mesons, and Photons

J. C. WARD*
Clarendon Laboratory, Oxford, England
(Received March 5, 1951)

A general program for the removal of divergencies from the theory of the interactions of nucleons, mesons, and photons is formulated. It is shown that the procedure is equivalent to renormalization of the constants of the theory.

THE success of the concept of renormalization in giving a theory of spinor electrodynamics that is both finite[1] and in good agreement with experiment[2] has made the extension of the method to other field theory problems most desirable, particularly the extension to the problem of nuclear forces. The first step in this direction is to show that the renormalized S-matrix is finite. This problem has not been satisfactorily dealt with until recently because of certain mathematical difficulties. The main source of trouble has been the overlapping divergencies. A process will be outlined below that in principle enables the renormalized S-matrix to be calculated to any degree of approximation. Bound-state phenomena remain outside the scope of the present treatment, and a suitable approach to the bound state remains to be discovered.

We select for study the interaction of pseudoscalar charged mesons, nucleons, and photons, with pseudoscalar coupling between meson and nucleon. A few remarks on the possible inclusion of neutral mesons will be made later. The Feynman rules for the construction of the S-matrix have been given by several authors,[3] and may be derived from the interaction hamiltonian

$$H=\frac{ie}{\hbar c}\left(\varphi^*\frac{\partial\varphi}{\partial x_\mu}-\frac{\partial\varphi^*}{\partial x_\mu}\varphi\right)A_\mu-\left(\frac{ie}{\hbar c}\right)^2\varphi^*\varphi A_\mu A_\mu$$
$$+ie(\bar\psi\gamma_\mu\gamma_\nu\psi)+if\bar\psi\gamma_5(\tau_-\varphi^*+\tau_+\varphi)\psi+\delta\lambda(\varphi^*\varphi)^2,$$

where mass renormalization and surface-dependent terms have been neglected. The functions $\varphi(x)$, $\psi(x)$, and $A_\mu(x)$, denote the meson, nucleon, and electromagnetic fields, respectively. We briefly state the rules again:[4]

1. Each photon line gives a factor
$$(2\pi)^{-3}\hbar c\delta_{\mu\nu}\int D_F(p)d^4p.$$
2. Each meson line gives a factor $(2\pi)^{-3}\int\Delta_F(p)d^4p$.
3. Each nucleon line gives a factor $(2\pi)^{-3}\int S_F(p)d^4p$.
4. Each meson-photon 3-vertex gives a factor
$$ie(\hbar c)^{-3}(2\pi)^4(p_1+p_2)_\mu\delta(p_1-p_2+p_3).$$
5. Each meson-photon 4-vertex gives a factor
$$-ie^2(\hbar c)^{-3}(2\pi)^4\delta_{\mu\nu}\delta(p_1-p_2+p_3+p_4).$$

* Now at the Institute for Advanced Study, Princeton, New Jersey.

[1] F. J. Dyson, Phys. Rev. **75**, 1736 (1949); J. C. Ward, Proc. Phys. Soc. (London) **A64**, 54 (1951).

[2] P. Kusch and H. M. Foley, Phys. Rev. **74**, 250 (1948). W. E. Lamb, Jr., and R. C. Retherford, Phys. Rev. **72**, 241 (1947).

[3] R. P. Feynman, Phys. Rev. **76**, 769 (1949); P. T. Matthews, Phys. Rev. **80**, 292 (1950); F. Rohrlich, Phys. Rev. **80**, 666 (1950).

[4] The similar rules for external lines have been omitted.

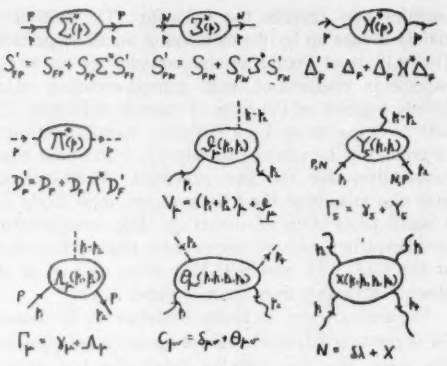

FIG. 1. The family of primitive divergent graphs, with their associated functions.

6. Each proton-photon vertex gives a factor

$$-ie\gamma_\mu\tau_\beta(2\pi)^4\delta(p_1-p_2+p_3).$$

7. Each nucleon-meson vertex gives a factor

$$-if\gamma_5(2\pi)^4\delta(p_1-p_2+p_3).$$

Charge conservation is applied in drawing the possible graphs, and each graph has a weight which may be determined by inspection of the number of ways that it can appear in the S-matrix.

The condition for primitive divergence is $\frac{3}{2}E_n+E_m+E_{p\lambda}<5$.[5] This gives rise to the family of graphs shown in Fig. 1. Because of the charge symmetry, Furry's theorem excludes $E_{p\lambda}=1$ or 3, $E_N=E_m=0$. $E_m=1$ or 3, $E_{p\lambda}=E_n=0$ is excluded by charge conservation. The neutron-photon interaction gives a finite graph,[6] as does the scattering of light by light,[7] when the effects of all graphs of the same order are considered. The scattering of mesons by mesons, however, is a true primitive divergent, which must be canceled by the introduction of the term $\delta\lambda(\varphi^*\varphi)^2$ into the hamiltonian. The effects of these divergent graphs are represented in the usual way by the insertion of functions at lines and vertices of the reduced graphs or skeletons. A list of these functions is given in Fig. 1.

The construction of the renormalized S-matrix is performed by successive approximation. We avoid dealing with self-energy parts explicitly by the introduction of the following method. Consider the function $\Sigma^*(p)$ which represents the effect of insertion of all possible proper self-energy parts into proton lines according to the equation $S_{F'}=S_F+S_F\Sigma^*S_{F'}$. This function obeys the relation[6]

$$-(1/2\pi)\partial\Sigma^*(p)/\partial p_\mu=\Lambda_\mu(p,p),$$

where $\Lambda_\mu(p_1,p_2)$ is the corresponding vertex function (see Fig. 1). We may rewrite this result in the form

$$\Sigma^*(p)-\Sigma^*(p')=-2\pi\int_0^1 d\lambda(p_\mu-p_\mu')\Lambda_\mu(p^\lambda,p^\lambda),$$

where $p^\lambda=p\lambda+p'(1-\lambda)$. The second term $\Sigma^*(p')$ can be made to play the part of the mass renormalization term if we agree to replace p'^2 and $p_\mu'\gamma_\mu$ by $-M^2$ and iM after the integration on λ, where M is the nucleon mass. (No distinction will be made between proton and neutron mass, although this could be done if desired.) This is sufficient, since p' can only appear in these invariant combinations. The function $\mathfrak{K}^*(p)$, which represents the effect of insertion of all possible proper meson self-energy parts into meson lines according to the equation $\Delta_F'=\Delta_F+\Delta_F\mathfrak{K}^*\Delta_F'$, may be treated in the same fashion. It obeys the equation relating it to the meson-photon 3-vertex function[6] $\vartheta_\mu(p_1,p_2)$

$$-(1/2\pi i)\partial\mathfrak{K}^*(p)/\partial p_\mu=\vartheta_\mu(p,p),$$

which may be written as

$$\mathfrak{K}^*(p)-\mathfrak{K}^*(p'')=-2\pi i\int_0^1 d\lambda(p_\mu-p_\mu'')\vartheta_\mu(p^\lambda,p^\lambda).$$

With the convention that we write $p''^2=-m^2$, where m is the meson mass, after the integration on λ, the second term $\mathfrak{K}^*(p'')$ can again be made to play the part of the mass renormalization. An identical procedure will be followed for the remaining self-energy parts, although it is now necessary to define functions $\Gamma_\mu(p)$ and $T_\mu(p)$ by the equations

$$-(1/2\pi)\partial\mathfrak{Z}^*(p)/\partial p_\mu=\Gamma_\mu(p),$$
$$-(1/2\pi i)\partial\Pi^*(p)/\partial p_\mu=T_\mu(p).$$

$\Pi^*(p)$and $\mathfrak{Z}^*(p)$ are the photon and neutron self-energy functions defined in Fig. 1. It is important to observe that the above definitions by differentiation are really implicit definitions, when the functions $\Gamma_\mu(p)$ and $T_\mu(p)$ are considered as calculated by the use of irreducible graphs, with appropriate insertions in lines and vertices. In fact, it is necessary to define now the functions

$$W_\mu=2p_\mu+T_\mu;\quad U_\mu=\gamma_\mu+\Gamma_\mu,$$

which may occur in the integral equations. Using these definitions, we have the results:

$$\Pi^*(p)-\Pi^*(0)=-2\pi i\int_0^1 d\lambda T_\mu(p\lambda)p_\mu,$$

$$\mathfrak{Z}^*(p)-\mathfrak{Z}^*(p')=-2\pi\int_0^1 d\lambda(p_\mu-p_\mu')\Gamma_\mu(p^\lambda).$$

[5] It should be observed that the direct application of the concept of primitive divergence may not suffice where a change in the usual perturbation method is desirable.

[6] A. Salam, Phys. Rev. **79**, 910 (1950).

[7] J. C. Ward, Phys. Rev. **77**, 293 (1950). The generalization of this kind of argument to all gauge-invariant interactions is immediate.

$\Pi^*(0)$ vanishes if calculated sufficiently carefully, paying attention to the gauge invariance. $\mathfrak{Z}^*(p')$ becomes a mass renormalization term with the above conventions for p'.

This treatment of self-energy parts is designed to avoid the trouble of overlapping divergencies, which occurs most frequently in self-energy terms. It is also a useful means of including the mutual dependence of the divergent parts of self-energy and vertex terms in the renormalization. There are no overlaps in Λ_μ or $\mathfrak{T}_\mu$; but T_μ, ϑ_μ, $\theta_{\mu\nu}$, and X still have an ambiguous construction from lower order parts. This may be dealt with in the following manner, which is the simplest way of dealing with overlapping or "b" divergencies. Let $M=\mu m$, and regard μ and m as independent variables. Then the functions T_μ, ϑ_μ, $\theta_{\mu\nu}$, and X will be considered as defined by the equations

$$T_\mu=-\int_m^\infty T_{\mu,m'}dm', \quad \vartheta_\mu=-\int_m^\infty \vartheta_{\mu,m'}dm',$$

$$\theta_{\mu\nu}=-\int_m^\infty \theta_{\mu\nu,m'}dm', \quad X=-\int_m^\infty X_{,m'}dm'.$$

Here we use the notation $\partial A/\partial m=A_{,m}$, and the functions to be inserted in the integral equations may now possibly be the original functions differentiated with respect to m as well. The reader may find it worth while to see for himself how differentiation with respect to the mass reduces the degree of divergence of integrals and sorts out the overlapping divergencies. The essential idea behind this is that "b" divergencies present a multiplicative effect and that differentiation can transform a multiplicative effect into an additive one. Illustrations of the effect of this process on simple graphs containing overlaps are given in Fig. 2. It should be noticed in passing that in the case of the calculation of T_μ it is also necesssary to substitute $\partial\vartheta_\mu/\partial p_\nu$ for the effects of corresponding insertions in the graphs defining $T_\mu(p)$.

CONSTRUCTION OF THE FINITE FUNCTIONS

It is now possible to define the scheme for construction, by repeated approximation, of the finite functions which replace the infinite functions in the calculation of the renormalized S-matrix. We use the notation $\langle F\rangle$ to imply that the finite functions to some order of approximation have been inserted in the irreducible graphs used in calculating F. The following equations define the finite functions:

$$N_c=\delta\lambda_1-\int_m^\infty[\langle X_{,m'}\rangle-\langle X_{,m'}(p'',p'',p'',p'')\rangle]dm', \quad (1)$$

where the finite function N_c is indeterminate by a finite constant $\delta\lambda_1$, which must be regarded as an empirical

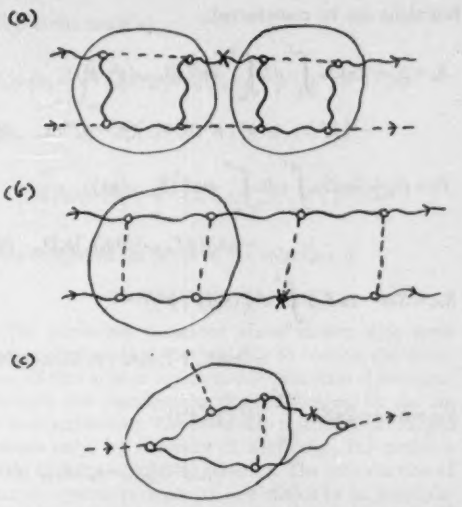

FIG. 2. Simple examples of the method of substitution into irreducible graphs. (a) A typical C-part graph. X represents the action of $\partial/\partial m$. All possible C-parts have to be inserted in the enclosures, giving factors $Z_1^{-1}C_{\mu\nu c}$. (b) A typical M-part graph. All possible M-parts have to be inserted in the enclosure, giving a factor $Z_1^{-2}N_c$. (c) Example of a term which appears in the calculation of T_μ. $Z_1^{-1}\partial V_{\mu\nu}/\partial p_\mu$ is the effect of all possible parts in the enclosure.

constant;

$$C_{\mu\nu c}=\delta_{\mu\nu}$$
$$-\int_m^\infty[\langle\theta_{\mu\nu,m'}\rangle-\tfrac{1}{4}\delta_{\mu\nu}\langle\theta_{\lambda\lambda,m'}(p'',p'',0,0)\rangle]dm'. \quad (2)$$

The integral $\int_m^\infty\langle\theta_{\mu\nu,m'}\rangle dm'$ is divergent only for $\mu=\nu$, and only the diagonal parts need a subtraction;

$$V_{\mu\nu}=(p_1+p_2)_\mu-\int_m^\infty[\langle\vartheta_{\mu,m'}\rangle$$
$$-\tfrac{1}{4}(p_1+p_2)_\mu\langle\theta_{\lambda\lambda,m'}(p'',p'',0,0)\rangle]dm', \quad (3)$$

where we have used the identity[8] $\frac{1}{2}(\partial\vartheta_\mu/\partial p_\nu)(p,p)=\theta_{\mu\nu}(p,p,0,0)$;

$$\Gamma_{\mu c}=\gamma_\mu+\langle\Lambda_\mu(p_1,p_2)\rangle-\langle\Lambda_\mu(p',p')\rangle; \quad (4)$$

$$U_{\mu c}=\gamma_\mu+\langle\mathfrak{T}_\mu(p)\rangle-\langle\mathfrak{T}_\mu(p')\rangle; \quad (5)$$

$$\Gamma_{5c}=\gamma_5+\langle Y_5(p_1,p_2)\rangle-\langle Y_5(p',p')\rangle; \quad (6)$$

$$W_{\mu c}=2p_\mu-\int_m^\infty[\langle T_{\mu,m'}\rangle-p_\nu(\langle\partial T_{\mu,m'}\rangle/\partial p_\nu)_0]dm'. \quad (7)$$

With the aid of these definitions the finite self-energy

[8] See reference 6. Strictly speaking, this identity should not be used until we discuss the renormalization proof. The reader will verify that the use then is legitimate.

functions can be constructed:

$$\Delta_c=\Delta_F+2\pi i\Delta_F\int_0^1 d\lambda\int_m^\infty dm'[\langle\vartheta_{\mu,m'}(p^\lambda,p^\lambda)\rangle$$
$$-\tfrac{1}{2}p_\mu{}^\lambda\langle\theta_{\lambda\lambda,m'}(p'',p'',0,0)\rangle](p_\mu-p_\mu'')\Delta_c, \quad (8)$$

$$D_c=D_F+2\pi iD_F\int_0^1 d\lambda\int_m^\infty dm'[\langle T_{\mu,m'}(p\lambda)\rangle$$
$$-\lambda p_\nu(\langle\partial T_{\mu,m'}\rangle/\partial p_\nu)_0]p_\mu D_c, \quad (9)$$

$$S_{Fc}=S_{FF}-2\pi S_{FF}\int_0^1 d\lambda[\langle\Lambda_\mu(p^\lambda,p^\lambda)\rangle$$
$$-\langle\Lambda_\mu(p',p')\rangle](p_\mu-p_\mu')S_{Fc}, \quad (10)$$

$$S_{Nc}=S_{NF}-2\pi S_{NF}\int_0^1 d\lambda[\langle\Gamma_\mu(p^\lambda)\rangle$$
$$-\langle\Gamma_\mu(p')\rangle](p_\mu-p_\mu')S_{Nc}, \quad (11)$$

The above equations, taken together, constitute a system of integral equations that define the finite functions.

JUSTIFICATION OF THE SUBTRACTION PROCEDURE IN TERMS OF RENORMALIZATION

It will now be proved that the following relations hold between the infinite and finite functions:

$$\left.\begin{array}{ll} C_{\mu\nu}=Z_1^{-1}C_{\mu\nu c}(e_1,f_1); & S_F'=Z_2S_{Fc}(e_1,f_1); \\ V_\mu=Z_1^{-1}V_{\mu c}(e_1,f_1); & \Gamma_\mu=Z_4^{-1}\Gamma_{\mu c}(e_1,f_1); \\ \Delta'=Z_1\Delta_c(e_1,f_1); & S_N'=Z_7S_{Nc}(e_1,f_1); \\ N=Z_1^{-2}N_c(e_1,f_1); & U_\mu=Z_7^{-1}U_{\mu c}(e_1,f_1); \\ W_\mu=Z_3^{-1}W_{\mu c}(e_1,f_1); & \Gamma_5=Z_5^{-1}\Gamma_{5c}(e_1,f_1); \\ D'=Z_3D_c(e_1,f_1); & \end{array}\right\} \text{A}$$

with $e_1=Z_3^{\frac{1}{2}}e$, $f_1=(Z_1Z_6Z_7)^{\frac{1}{2}}Z_5^{-1}f$, where Z_1, Z_3, Z_5, Z_6, and Z_7 are suitably chosen infinite constants. It is easy to see that these equations are sufficient to enable the divergent constants to disappear from the S-matrix expressed in terms of the renormalized coupling constants e_1 and f_1.[9,10]

"Z_1" Functions

The result of inserting expressions A into the integral equations defining V_μ is to give

$$Z_1V_{\mu c}=(p_1+p_2)_\mu-Z_1^{-1}\int_m^\infty\langle\vartheta_{\mu,m'}(p_1,p_2,e_1,f_1)\rangle dm',$$

which is the equation defining $V_{\mu c}$ as long as

$$Z_1=1+\tfrac{1}{4}\int_m^\infty dm'\langle\theta_{\lambda\lambda,m'}\rangle.$$

Substitution into Compton part irreducible graphs gives

$$Z_1^{-1}C_{\mu\nu c}=\delta_{\mu\nu}-Z_1^{-1}\int_m^\infty\langle\theta_{\mu\nu,m'}\rangle dm'.$$

This is the equation defining $C_{\mu\nu c}$ if

$$Z_1=1+\tfrac{1}{4}\int_m^\infty dm'\langle\theta_{\lambda\lambda,m'}\rangle,$$

which agrees with the value of Z_1 found above. Finally, substitution into the definition of Δ' gives

$$Z_1\Delta_c=\Delta_F+2\pi i\Delta_F\int_0^1 d\lambda\int_m^\infty dm'(p_\mu-p_\mu'')$$
$$\times\langle\vartheta_{\mu,m'}(p^\lambda,p^\lambda)\rangle\Delta_c,$$

which again agrees with the definition of Δ_c, with the same value of Z_1 as before.

"Z_3" Functions

Insertion of the expressions A into the graphs defining W_μ gives

$$Z_3^{-1}W_{\mu c}=2p_\mu-\int_m^\infty dm'Z_3^{-1}\langle T_{\mu,m'}\rangle.$$

This is the defining equation for $W_{\mu c}$ if $Z_3-1=\frac{1}{4}C$, where

$$C\delta_{\mu\nu}=\int_m^\infty(\langle\partial T_{\mu,m'}\rangle/\partial p_\nu)_0dm'.$$

The photon self-energy equation then becomes

$$Z_3D_c=D_F+2\pi iD_F\int_m^\infty dm'\int_0^1 d\lambda p_\mu\langle T_{\mu,m'}(\lambda p)\rangle D_c,$$

which is the correct equation for D_c with the same value of Z_3.

"Z_5, Z_6, and Z_7" Functions

Insertion of A into the definition of Γ_5 gives

$$Z_5^{-1}\Gamma_{5c}=\gamma_5+Z_5^{-1}\langle Y_5\rangle.$$

Comparison with the equation for Γ_{5c} gives for Z_5

$$\gamma_5(Z_5-1)=-\langle Y_5(p',p')\rangle.$$

The effect of substitution into the proton-photon vertex function is to give the equation

$$Z_6^{-1}\Gamma_{\mu c}=\gamma_\mu+Z_6^{-1}\langle\Lambda_\mu\rangle,$$

[9] The treatment of the external lines and the associated wave function renormalization will not be given here. The plausible argument given by Dyson (reference 1) can be justified by an approach which goes outside the S-matrix framework.

[10] It is an essential step in the following argument that the infinite constants are independent of m. Strangely enough, this is a consequence of the absence of a fundamental length.

which is the same as

$$\Gamma_{\mu c}=\gamma_\mu+\langle\Lambda_\mu\rangle-\langle\Lambda_\mu(p',p')\rangle$$

if

$$\gamma_\mu(Z_6-1)=-\langle\Lambda_\mu(p',p')\rangle.$$

From this, the self-energy treatment follows as usual:

$$Z_6S_{Pc}=S_{PF}-2\pi S_{PF}\int_0^1 d\lambda\langle\Lambda_\mu(p^\lambda,p^\lambda)\rangle(p_\mu-p_\mu')S_{Pc}$$

is the same equation as

$$S_{Pc}=S_{PF}-2\pi S_{PF}\int_0^1 d\lambda[\langle\Lambda_\mu(p^\lambda,p^\lambda)\rangle - \langle\Lambda_\mu(p',p')\rangle](p_\mu-p_\mu')S_{Pc}$$

with the above value of Z_6. Finally, from the definition U_μ, we derive the equation

$$Z_7^{-1}U_{\mu c}=\gamma_\mu+Z_7^{-1}\langle\Gamma_\mu\rangle$$

and this is identical with $U_{\mu c}=\gamma_\mu+\langle\Gamma_\mu\rangle-\langle\Gamma_\mu(p')\rangle$ if

$$(Z_1-1)\gamma_\mu=-\langle\Gamma_\mu(p')\rangle.$$

The self-energy treatment is, as before:

$$Z_7S_{Nc}=S_{NF}-2\pi S_{NF}\int_0^1 d\lambda\langle\Gamma_\mu(p^\lambda)\rangle(p_\mu-p_\mu')S_{Nc}$$

is the same as

$$S_{Nc}=S_{NF}-2\pi S_{NF}\int_0^1 d\lambda[\langle\Gamma_\mu(p^\lambda)\rangle - \langle\Gamma_\mu(p')\rangle](p_\mu-p_\mu')S_{Nc}$$

with the above value of Z_1.

Möller Parts

Insertion of A into graphs defining N gives

$$Z_1^{-2}N_c=\delta\lambda-Z_1^{-2}\int_m^\infty\langle X_{,m'}\rangle dm'.$$

This is the same as

$$N_c=\delta\lambda_1-\int_m^\infty[\langle X_{,m'}\rangle-\langle X_{,m'}(p'',p'',p'',p'')\rangle]dm'$$

with

$$Z_1^2\delta\lambda=\delta\lambda_1+\int_m^\infty\langle X_{,m'}(p'',p'',p'',p'')\rangle dm'.$$

This completes the proof of the relations A.

CONCLUDING REMARKS

The formalism presented above shows, with some degree of rigor, that it is possible to remove the divergencies that arise in the mutual interactions of nucleons, photons, and pseudoscalar charged mesons, by the use of renormalization. The proof was restricted to charged mesons only, for the sake of simplicity, the problem being already sufficiently complex. The introduction of neutral mesons presents no new difficulty in principle, since certain selection rules facilitate the introduction of neutral pseudoscalar mesons.[11] In fact, the combined effect of charge symmetry, charge conservation, and parity is to exclude all possible primitive divergent graphs not considered above, with the exception of neutral meson self-energy graphs, Möller interactions including neutral mesons, and neutral meson-nucleon vertices. Compton parts for neutral mesons, and the decay of a neutral meson into two photons, are convergent. Hence, the only effect of neutral mesons on the theory is to require the introduction of four new renormalized coupling constants. Whether such a theory can be made to fit the observed facts concerning nuclear forces is a question that can only be settled by much more detailed calculations.

The author wishes to thank Mr. A. Salam for stimulating discussions and for reviving the author's interest in this subject.

[11] These remarks have since been made in greater detail by P. T. Matthews, Phys. Rev. 81, 936 (1951).

Total Neutron Cross Sections of Cobalt, Manganese, and Molybdenum

WARREN FENTON STUBBINS*
Argonne National Laboratory, Chicago, Illinois
(Received August 13, 1951)

The total neutron cross sections of cobalt, manganese, and molybdenum were measured with a neutron energy resolution of ±6 kev using neutrons from the Li(p, n)Be reaction with an electrostatic accelerator. Cobalt and manganese were examined from 80 to 1000 kev. Both their cross sections fluctuate rapidly at low energies and level off and decrease slowly to about 3 barns at 750 kev. Molybdenum was measured from 10 to 1230 kev, and its cross section is about 9 barns to 250 kev and decreases uniformly to 6 barns at 1230 kev.

I. INTRODUCTION

THE measurement of the total neutron cross sections of many elements has been undertaken in the past few years in the range of neutron energies from 10 to 1000 kev and higher.[1] The elements which are single isotopes are particularly interesting since they may serve to confirm theoretical predictions when the energy resolution is good. Both cobalt and manganese were measured because they are single isotopes[2] and of low enough mass so that a resonance structure might be resolved, at least at the lower energies. The presence of these elements in the materials used in the construction of nuclear reactors makes their neutron cross sections at high energies of interest. The cross section of molybdenum was measured to obtain values which were not available. The several isotopes of molybdenum preclude any resolution of structure.

The energy spread of less than 10 kev in the neutron energy is sufficient to resolve much structure in cobalt and manganese below 500 kev, but the density of resonances in this region and at higher energies prevents the complete resolution and results in an averaging of cross section. For closely spaced resonances at any energy there will be a corresponding inability to resolve resonances. These measurements show this difficulty; for example, see the curve for manganese at 350 to 420 kev.

Preliminary measurements of the total neutron cross sections of cobalt and manganese were made using a 10-kev target and widely spaced points in the range of

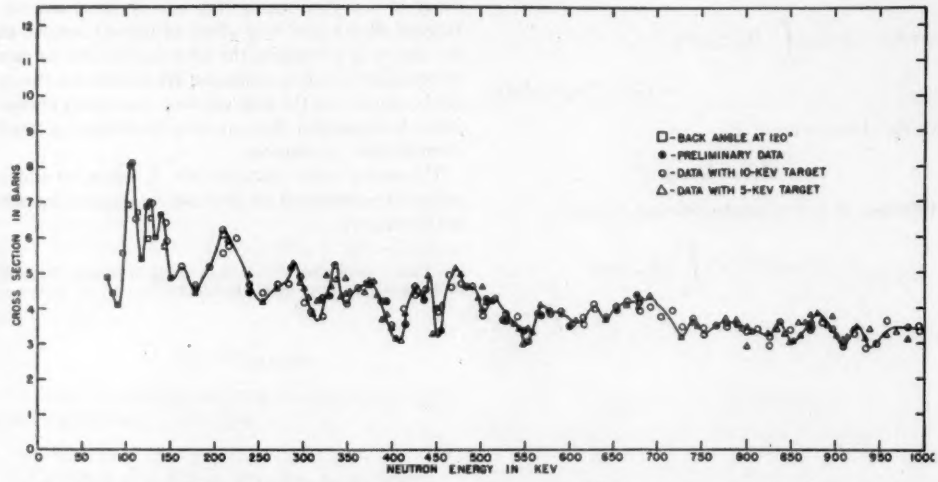

FIG. 1. Total neutron cross section of cobalt. Preliminary data are from a 10-kev-thick lithium target. The back angle measurements were taken at 120 degrees in the laboratory system with a 5-kev target. The maximum neutron energy variation is ±6 kev with the 5-kev targets.

* Present address: Radiation Laboratory, University of California, Berkeley 4, California. This paper was prepared at the Department of Physics, University of Cincinnati, Cincinnati 21, Ohio, and the work was done under the participating institutions program of the Argonne National Laboratory.

[1] J. M. Blair and J. R. Wallace, Phys. Rev. **79**, 28 (1950).

[2] G. T. Seaborg and I. Perlman, Revs. Modern Phys. **20**, 585 (1948).

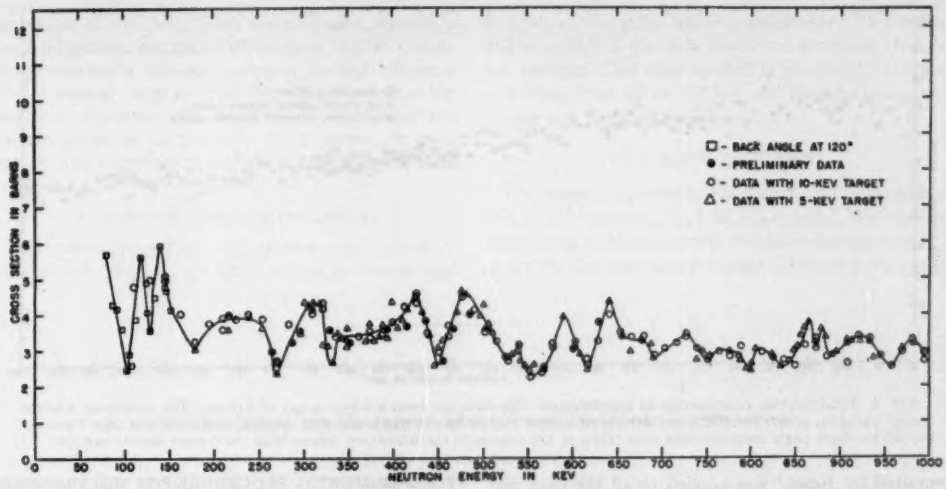
□ - BACK ANGLE AT 120°
● - PRELIMINARY DATA
○ - DATA WITH 10-KEV TARGET
△ - DATA WITH 5-KEV TARGET
CROSS SECTION IN BARNS
NEUTRON ENERGY IN KEV

FIG. 2. Total neutron cross section of manganese. Preliminary data are from a 10-kev-thick lithium target. The back angle measurements were taken at 120 degrees in the laboratory system with a 5-kev target. The maximum neutron energy variation is ±6 kev with the 5-kev targets.

120 to 750 kev. At this time vanadium,[1] cerium,[3] and columbium[3] were also examined. Later the vanadium cross section measurement was completed with a neutron energy resolution of ±6 kev from 10 to 1000 kev by Blair and Wallace.[1]

II. EXPERIMENTAL PROCEDURE FOR COBALT AND MANGANESE

The neutrons were obtained from the Li(p, n)Be reaction[4] using a thin lithium film evaporated on a tantalum disk and protons from the Argonne electrostatic generator. The technique in these measurements is similar to that described by Barschall, *et al.*[5] The proportional counter which was made for these measurements is described in detail by Blair and Wallace.[1] The target thickness was determined by the rise in neutron flux in the forward direction just above threshold. The scatterers were supported by a triangle of steel wire in a reproducible manner. The background measurements were made by interposing a paraffin cone which filled the solid angle subtended by the counter between it and the spot source of neutrons. For the average-energy neutron, the path through the cone was about 15 mean-free paths and stopped the direct beam very efficiently. The base of the cone was covered with ½-inch cadmium to stop thermal neutrons. The background was from 3 to 10 percent of the direct beam. The counter was placed in the zero-degree position from the line of protons for neutron energies above 130 kev and in the 120-degree position in the laboratory system for energies below 130 kev.

The cobalt and manganese samples are both 3.00 inches in diameter. The cobalt sample is 0.462 inch thick and weighs 470.17 grams and thus has 0.1053×10^{24} atoms per square centimeter. The manganese was pressed solidly to a thickness of 0.628 inch, and weighs 530.15 grams and has 0.1275×10^{24} atoms per square centimeter. The purity of the scatterers is known to be high, with the total impurities being less than one percent. A spectrochemical analysis of the manganese made by the Chemistry Division of the Argonne National Laboratory shows no impurities of more than 0.1 percent.

The large diameter of the scatterers as compared to the counter, whose diameter is 1 inch with ½ inch of paraffin all around, made the correction for scattering-in very important. In the forward direction the counter was 12 inches from the neutron source with the scatterer midway between. In the back-angle work, the distance from source to counter was 25 inches, and the scatterer also midway between. The scattering-in correction, as

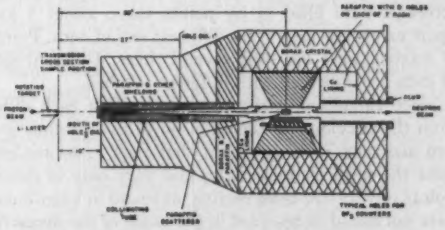

FIG. 3. Shielded neutron detector. The collimated neutrons are scattered into seven rings of nine BF_3 counters each. Excellent shielding reduces the background counts to a very low value.

[3] Argonne National Laboratory Report No. 4350 (1949).
[4] R. Taschek and A. Hemmindinger, Phys. Rev. **74**, 373 (1948).
[5] L. Seagondollar and H. Barschall, Phys. Rev. **72**, 439 (1947).

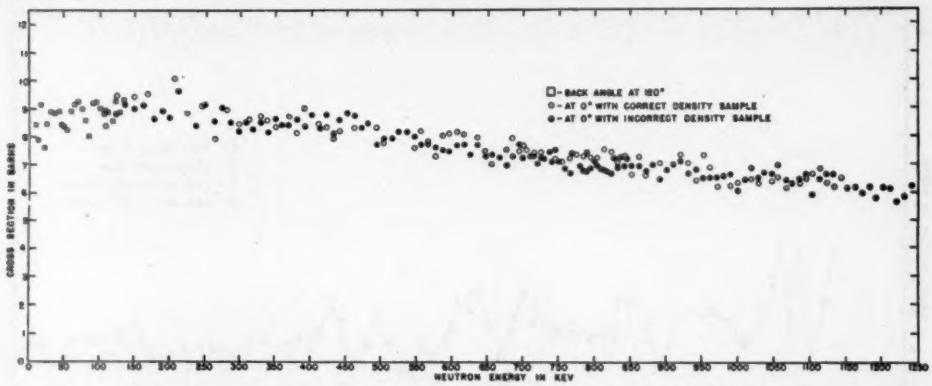
□- BACK ANGLE AT 120°
○- AT 0° WITH CORRECT DENSITY SAMPLE
●- AT 0° WITH INCORRECT DENSITY SAMPLE
CROSS SECTION IN BARNS
NEUTRON ENERGY IN KEV

FIG. 4. Total neutron cross section of molybdenum. The data are from a 6-kev target of lithium. The maximum neutron energy variation is ±6 kev. Incorrect density of sample caused by cavities in the slug. Both samples had less than 1 percent impurities. Back angle measurements were taken at 120 degrees in the laboratory system with the correct density sample.

computed by Jones,[6] was applied to all the data and amounts to a change in the transmission when corrected of 2 to 5 percent. The transmission in both samples ranged from 0.50 to 0.75 over most of the energy range of the data.

At least 10,000 counts were taken in each measurement, except the background, in order to keep the statistical errors small. It is believed that the data are accurate to 3 percent in cross section. A current integrator which measured the protons hitting the target was used as a monitor for the data.

The energy control of the electrostatic generator is accomplished by the mass-2 beam in an electrostatic analyzer and believed to be within 3 to 4 kev as estimated by the rise in the neutron production at threshold. The over-all neutron energy variation for the 5-kev target is 10 to 12 kev in the forward direction and smaller in the back-angle measurements.

III. RESULTS FOR COBALT AND MANGANESE

The high resolution measurements of cobalt, Fig. 1, and manganese, Fig. 2, were taken some time after the preliminary survey. The earlier results fit the later data over their entire range. The measurements with the 5-kev target were made in 25-kev steps, and the intervals were filled in by points taken about 5 kev apart using new targets for different sets of data. Points of interest were run over several times. Different sets of data are indicated with different symbols.

Since vanadium, manganese, and cobalt each differ from the previous by the addition of two protons and two neutrons, it is significant that their cross sections have the same characteristics and vary only in detail. Points of very low cross section, as found in vanadium,[1] were not found or resolved in the range of the measurements on manganese and cobalt.

[6] W. B. Jones, Jr., Phys. Rev. **74**, 364 (1948).

IV. EXPERIMENTAL PROCEDURE FOR MOLYBDENUM

The measurements of the cross section of molybdenum were made using neutrons from the Van de Graaff as above but with a shielded detector.[7] The detector, Fig. 3, consists of nine BF_3 counters on each of seven circles which are embedded in paraffin and shielded very completely. The neutrons, after passing through the scattering sample, were collimated by a tapered hole on the axis of the counter assembly and were scattered into the counters by a cylinder of paraffin accurately placed at the geometrical center of the counters. The background measurements were made by removing the paraffin cylinder and allowing the collimated neutrons to pass through the entire assembly. The background was 1 percent throughout the data in the forward direction and rose to a maximum of 2 percent for the back-angle measurements, which were taken at 120 degrees in the laboratory system from the proton beam. The molybdenum sample was placed against the front of the shield and symmetrically with the collimating opening. This arrangement, together with the excellent shielding, prevented any scattering-in; thus no correction was applied to the data. Since the presence of the scatterer did not modify the neutron flux appreciably outside the detector, the data were monitored by a BF_3 counter surrounded by several inches of paraffin placed at 30 degrees to the direct beam.

Two molybdenum samples were used in obtaining the data, one of which was less dense than the solid metal owing to the presence of cavities in the slug. Both were shown by spectrochemical analysis to be of high purity with not more than 1 percent impurities and not more than 0.1 percent of any one element. The sample of correct density had 0.065×10^{24} atoms per square centimeter. Different data are shown by different symbols. The transmission ranged from 0.45 to 0.70

[7] A. Langsdorf, Jr., Phys. Rev. **80**, 132 (1950).

over most of the data. Each measurement, excepting the background, consisted of at least 10,000 counts, which were easily obtained owing to the high efficiency of the several rings of counters. The statistical accuracy of 3 percent was modified by systematic and random errors to an accuracy of 10 percent in cross section. The variations in neutron energy were the same as above.

V. RESULTS FOR MOLYBDENUM

The variations in the total neutron cross section of molybdenum, Fig. 4, are small owing to the several isotopes of the same relative abundance.[2] The nature and accuracy of the data reveal no structure, even at low energies. The cross section is practically constant at 9 barns from 10 to 250 kev and then decreases uniformly to 6 barns at 1230 kev.

VI. ACKNOWLEDGMENT

The author appreciates the advice and assistance of Drs. A. S. Langsdorf, Jr., J. M. Blair, and A. Wattenberg, and Messrs. J. Wallace and R. Nobles and other members of the Physics Division, Argonne National Laboratory.

PHYSICAL REVIEW VOLUME 84, NUMBER 5 DECEMBER 1, 1951

The Stopping Power of Metals and Semiconductors*

Z. H. Heller and D. J. Tendam
Purdue University, Lafayette, Indiana
(Received August 24, 1951)

Stopping power measurements have been made on Si, Ni, Cu, Ge, Zr, Rh, Ag, Sn, and Au. The reduction in range of the cyclotron deuteron beam produced by samples of these materials was determined by measurement of the ionization in air at the end of the beam path. To evaluate the ionization curves a semi-empirical curve, given here, which relates extrapolated ranges with mean number ranges was computed for large straggling parameters. A range-energy curve for deuterons in Ge is given as well as approximate air and Al equivalents for Si and Ge. Range-energy curves were measured for the metals.

The semiconductor results were compared with those for the metals to determine whether the difference in electrical properties produces a difference in energy loss. No difference was detected within the limits of precision of this experiment.

Combining data from this experiment with those of other investigations a study of the dependence of stopping power on velocity and atomic number has been made. An empirical formula derived from these data expresses the electronic stopping power relative to Al as a function of energy and atomic number over a wide range. A formula is provided for using this relation to calculate range-energy curves in any element with $Z>10$, and its validity is discussed.

I. INTRODUCTION

IN the course of the investigations at this laboratory on the nuclear bombardment of semiconductors[1] it became necessary to know the stopping powers of Si and Ge in bulk and, since no experimental values were available, equipment to make these measurements was assembled. Since the electrical properties of a material are known to affect the rate of energy loss, it was decided to measure range-energy curves for several metals at the same time in order to compare their stopping powers with those of the semiconductors. The use of 9-Mev deuterons in this investigation also affords an opportunity to close a gap in the experimental studies of the velocity dependence of stopping power. As described below, an empirical relation which enables one to calculate approximate range-energy curves has been established from these data and those of other investigators.

II. APPARATUS

An apparatus similar to that described by Wilson[2] was used to measure the residual range of the deuteron beam of the Purdue cyclotron after transmission through sample specimens (Fig. 1). The monitor chamber was needed to follow fluctuations in beam current, and the end of the range in air was indicated by the current in the shallow chamber; both chamber voltages were adjusted to their current plateaus. The range was reduced stepwise by 0.001-inch Al foils and only the last few centimeters of the range were measured in air since the outward spreading of the beam prevented measuring the entire distance in air. An energy analyzer, employing three slits and the fringing flux of the cyclotron magnet to provide energy definition, also permitted convenient placing of the apparatus at some distance from the field. The two galvanometer arrangement employed by Wilson to record the chamber currents was replaced by the simple dual-triode bridge circuit shown in Fig. 2. The ratio of the grid resistances necessary to give zero

* Supported by the ONR.
[1] Lark-Horovitz, Bleuler, Davis, and Tendam, Phys. Rev. 73, 1256 (1948).
[2] R. R. Wilson, Phys. Rev. 60, 749 (1941).

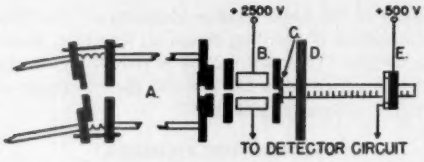

FIG. 1. Schematic of range apparatus. (A) magnetic analyzer. (B) monitor chamber. (C) sample mount. (D) aluminum foils. (E) collector chamber.

galvanometer current is proportional to the ordinate of the range ionization curve at a given point and very large fluctuations in beam current may occur without altering a balance setting. Heater fluctuations and positive ion grid current effects are canceled by having the two triodes in one envelope and by using equal grid resistors, but the plate potentiometer and the galvanometer zero rheostat are necessary to balance the tube characteristic differences. The balance readings were taken at 5–10 μa monitor current for which the sensitivity was more than adequate.

Foils of the metals Al, Ni, Cu, Zr, Rh, Ag, Sn, and Au were readily available. Their thicknesses were determined by weighing on a sensitive balance; the uniformity of the foils was checked by comparing the mass per unit area of the small strips cut for use with that of the parent foils. The samples of Si and Ge were ground by hand between parallel glass plates uniformly separated by tungsten spacers. Because these materials fractured easily and irregularly in the grinding process, their areas were found by projecting images of the samples at known magnification and tracing the enlarged outlines with a planimeter.

III. EVALUATION OF IONIZATION CURVES

The use of ionization chambers gave the well-known Bragg-type curve from which the extrapolated range was found. Because the range-energy curves for air which were used[3] are given in terms of mean number range and because the large range straggling in this

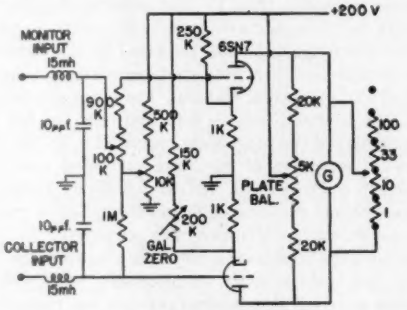

FIG. 2. Current detector circuit.

[3] M. S. Livingston and H. A. Bethe, Revs. Modern Phys. **9**, 261 (1937).

experiment (due to energy spread, foil inhomogeneities, and the natural collision statistics) made standardization necessary, all ranges were converted to mean number ranges. The straggling was assumed to be gaussian and the method which Livingston and Holloway[4] applied to the range of natural alpha-particles was extended to the case of large straggling. These authors characterized the end of the ionization curve by the numbers α, the straggling parameter, y, the distance between the extrapolated range point and the intercept of the extrapolation line with the ordinate of maximum ionization, and x, the distance from the mean range point to the extrapolated range point. The observed ionization curve is given by

$$I(\xi)=\int_{\xi}^{\infty} F(\xi')S(\xi'-\xi)d\xi', \qquad (1)$$

where ξ is the distance from the mean range point, $F(\xi)$ is the range distribution function and $S(\xi'-\xi)$ is the ionization of a single particle at distance $\xi'-\xi$ from its endpoint. For a given $F(\xi)$, the integration may be performed numerically for several points ξ, and the

TABLE I. Conversion from extrapolated range to mean range for various straggling parameters.

α, cm	x, cm	y, cm
0.000	0.00	0.06
0.354	0.30	0.63
0.707	0.69	1.19
1.414	1.47	2.14
2.121	2.17	3.02
2.828	2.98	4.16

ionization curve drawn. Using their single particle curve, they found that for small α the relation between x and y was linear, $x=0.43y-0.081$ cm. We used the single particle curve given for deuterons by Livingston and Bethe[3] extrapolated to zero energy, and folded it as indicated with the gaussian function for several values of α. The resulting curves yielded the values of x and y given in Table I. The plot of x *vs* y is linear for small values of α and then curves upward. The numerical integration was performed very carefully so that these values are as accurate as the single particle ionization curve. Errors in this would produce a second order effect in the experimental results. The ranges found in air were corrected to 15°C, and 760 mm Hg (the correction for water vapor was negligible), and converted to ranges in Al using the data of Smith.[5]

The major recognized source of error in the measurements was the unavoidable shifting of the energy of the particles used. Such shifts occurred because the analyzer employed the fringing flux of the cyclotron magnetic field which had to be adjusted for any changes in oper-

[4] M. G. Holloway and M. S. Livingston, Phys. Rev. **54**, 18 (1938).

[5] J. H. Smith, Phys. Rev. **71**, 32 (1947).

ating conditions. Small energy changes caused appreciable current changes at the end of the range where the Bragg curve descends steeply and where the extrapolation line must be drawn. These shifts were most significant for small residual ranges where the resulting uncertainties in range were of the order of 5 percent. However, the errors in the calculated quantities (Al equivalents, relative electronic stopping powers, etc.) are not that large. Reproducibility of the curves was satisfactory. Analysis of all the known sources of error yields a value of about 2 percent.

IV. RESULTS

The Range-Energy Curves for Metals

Curves of absorber thickness *vs* residual range in Al were measured for the seven metals, covering the beam range, 77.2 mg/cm² Al, in three steps with the Ni, Zr, Ag and Au foils, in four steps with Cu and Rh, and in five steps with the Sn foils. Several residual range curves were repeated to check reproducibility. Using the data of Smith[5] these could be converted to range-energy curves. Figure 3 is the range-energy curve for Rh. This was needed for use in stacked foil excitation experiments with Rh. The results of the metal measurements were reorganized as discussed subsequently.

Range-Energy Relations for Si and Ge

Two samples of Ge of 64.4 mg/cm² and 84.6 mg/cm², and one of Si of 34.0 mg/cm² thickness all having high resistivity were studied. Two residual range curves were run for each sample with different portions in front of the defining hole to average the effects of the slight sample inhomogeneities. Then Al foils were placed before the thinner Ge sample and different portions of the range in Ge were measured. The latter data were converted to the range-energy curve for Ge shown in Fig. 4. The following figures were measured for approximate range calculations: 1.44 mg/cm² Ge=1 mg/cm² Al; 2.18 mg/cm² Ge=1 cm air; 0.985 mg/cm³ Si=1 mg/cm² Al, and 1.50 mg/cm² Si=1 cm air.

The Stopping Power of Semiconductors

The well-known energy loss equations of Bohr,[6] Bethe,[7] and Bloch[8] were developed for isolated stopping atoms, rather than for atoms in the solid state. Von Weizsäcker,[9] dealing with the effects of the electrical properties, arrived at an energy loss which depended on the resistivity. However, Gerritsen[10] showed experimentally that the stopping power of Al was unchanged as it was made superconducting. Kramers[11] explained this negative result by showing theoretically that the

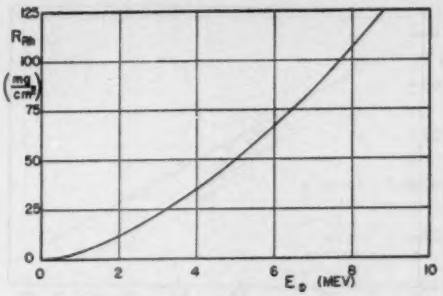

FIG. 3. Range-energy curve for deuterons in Rh.

major part of the stopping was due to the inner electron shells and is affected only slightly by the electrical properties of the medium. Subsequently, Madsen and Venkateswarlu[12] measured the stopping power of Be, for which the conduction electrons form a more significant portion of the total number, and found a difference between stopping in the solid state and that calculated for separate atoms. The theory of Bohr,[13] accounting for the free electron effects, was in excellent agreement with their results.

Despite their relatively high number of inner electrons, Si and Ge were compared with the metals to observe whether any stopping differences due to the electrical properties exist. The stopping power of a semiconductor can be compared with that which a metal of the same Z would have by using a "Bloch plot" for a guide.

The energy loss formula developed by Bethe and by Bloch is

$$-dE/dx=(4\pi z^2e^4/mv^2)NZ\ln(2mv^2/I), \qquad (2)$$

where e and m are the electronic charge and mass, v and z the velocity and charge number of the incident particle, and Z, I, and N are the atomic number, mean ionization potential, and the number per cm³ of the

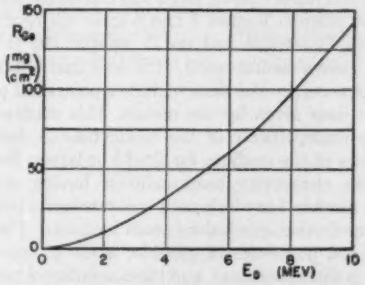

FIG. 4. Range-energy curve for deuterons in Ge.

[6] N. Bohr, Phil. Mag. **25**, 10 (1913).
[7] H. A. Bethe, Ann. Physik **5**, 325 (1930).
[8] F. Bloch, Ann. Physik **16**, 285 (1933).
[9] C. F. von Weizsäcker, Ann. Physik **17**, 869 (1933).
[10] A. N. Gerritsen, thesis, University of Leiden, 1948.
[11] H. A. Kramers, Physica **13**, 401 (1947).
[12] C. B. Madsen and P. Venkateswarlu, Phys. Rev. **74**, 648 (1948).
[13] A. Bohr, Kgl. Danske Videnskab. Selskabs Mat.-fys. Medd. **XXIV**, 19.

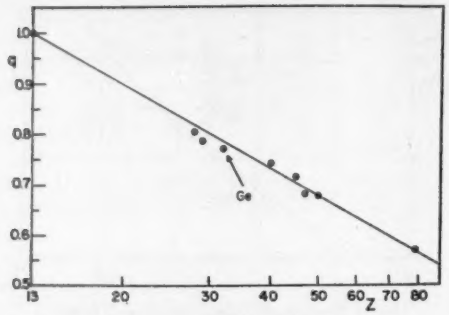

FIG. 5. Stopping power per electron relative to Al *vs* ln$Z$ for absorber thicknesses equivalent to 84.6 mg/cm² Ge.

stopping atoms. Bloch,[14] using a statistical atomic model, showed that I/Z is approximately a constant. Thus a graph of q, the stopping power per electron relative to Al, *vs* ln$Z$ for equal particle velocities (called here Bloch plots) should give a straight line according to the relation,

$$q=\frac{-1}{NZ}\left(\frac{dE}{dx}\right)_Z\Big/\left[\frac{-1}{N_{\mathrm{Al}}13}\left(\frac{dE}{dx}\right)_{\mathrm{Al}}\right]$$
$$=C-[\ln Z/(\ln 2mv^2-\ln I_{\mathrm{Al}})], \quad (3)$$

where C is a constant.

The linearity of this type of plot has been verified by Mano,[15] Wilson,[2] Kelly,[16] and Teasdale[17] even at lower velocities than the statistical model requires (see below). The position of the point for a semiconductor relative to such a line drawn for thicknesses of metals equivalent in stopping to the given semiconductor sample (to insure that the average velocities in the samples were equal) should indicate any systematic differences which may exist.

The metal thicknesses equivalent in energy reduction to the various semiconductor samples were taken from the residual range curves, and q was calculated for each case and plotted. Figures 5 and 6 show the results for the thick Ge sample and the Si sample; the thin Ge sample gave a similar result. It is seen that within the limits of accuracy the semiconductor points fall on the straight lines given by the metals. This confirms the relative unimportance of the conduction or dielectric properties of the medium for $Z\simeq 13$ or larger. Because Si is the elementary semiconductor having smallest atomic number for which such measurements could be made, no further conclusions could be drawn. The poor mechanical properties of graphite made it unsuitable for use in this experiment, and the possibility of preparation of thin diamond samples is being considered.

[14] F. Bloch, Z. Phys. **81**, 363 (1933).
[15] G. Mano, Ann. physique **1**, 407 (1934).
[16] E. L. Kelly, Phys. Rev. **75**, 1006 (1949).
[17] J. G. Teasdale, Tech. Report 3, U.C.L.A., December, 1949.

An Empirical Stopping Power Formula

Combining data from this experiment with those of other authors,[2,15–18] an empirical formula for computing range-energy relations which is valid for a very large range of Z and v values has been developed. We compared the data taken at various velocities by plotting the reciprocals of the slopes of the Bloch plots *vs* ln$\beta^2(\beta=v/c)$ which should again give a straight line according to (4).

$$-(d\ln Z/dq)=\ln(2mc^2/I_{\mathrm{Al}})+\ln\beta^2. \quad (4)$$

Values for $-(d\ln Z/dq)$ at $v=1.5$, 2.0, and 2.5×10^9 cm/sec were taken from our experiment. The resulting graph, Fig. 7, shows linearity over a very large range with small deviations at low velocities where the measurements of Mano and the present authors are subject to larger errors. The measurements of Wilson are seen to be inconsistent with the others. The value of β^2 at which Wilson's point is plotted is the mean taken for all of his samples. The agreement of the remaining points with the straight line may be deceptive since there were several steps admissive of error in the determination of $d\ln Z/dq$, and the mean velocities in the various experiments were difficult to fix. The encircled point of Bakker and Segrè[18] is plotted against lnβ^2 and that in the square against $\ln 2[(1-\beta^2)^{-\frac{1}{2}}-1]$ which is proportional to the kinetic energy in the relativistic limit. The proper relativistic correction to apply, that of Bethe[19] and Møller[20] which here gives $\ln[\beta^2\exp(-\beta^2)/(1-\beta^2)]$ as the abscissa to be used, gives the point indicated by the triangle. No correction is needed for the lower points. While the point in the square fits the curve joining the low velocity points better, the other is also to be considered as fitting the curve within the limits of precision.

From the velocity dependence found in Fig. 7 the relative electronic stopping power can be expressed as

$$q=1.00-1.18(\log Z-1.114)/(\log E_p+1.63), \quad (5)$$

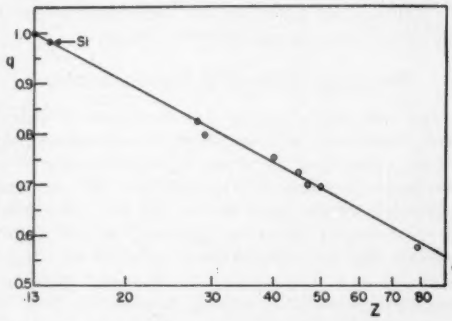

FIG. 6. Stopping power per electron relative to Al *vs* ln$Z$ for absorber thicknesses equivalent to 34.0 mg/cm² Si.

[18] C. J. Bakker and E. Segrè, Phys. Rev. **81**, 489 (1951).
[19] H. A. Bethe, Z. Physik **76**, 293 (1932).
[20] C. Møller, Ann. Physik **14**, 531 (1932).

where E_p is the energy (in Mev) of a proton having the same velocity as the particle considered. The range of validity of (5) in terms of Z and E_p is rather extensive. At the low energy end the straggling is probably due to errors, since the mechanism of stopping seems to vary smoothly down to $\beta^2 \sim 0.0005$ (200-kev protons) when the capture of electrons starts. The formula is here valid for $Z>10$ since all the investigators found linear Bloch plots down to Al (Kelly observed slight deviations for Th and U). Pending further measurements, the upper limit of validity seems to be fixed only by the threshold for radiation loss which varies with the optical properties of the medium, and requires analysis for the particular case studied. Bakker and Segrè working with protons of high enough energy (340 Mev) for all electrons to be effective found that, for $Z>26$, I/Z is a constant, but that below $Z=26$ it increases. The slope for Fig. 7 was taken from their data for $Z>26$; hence the formula becomes less reliable for $Z<26$ as the velocity increases. Evidently more information is needed in this region. Since Mano found no systematic differences in stopping between gases and metals, and since we found none for semiconductors, the formula may be applied to all physical phases and to compounds whenever the above conditions apply. In the lighter elements the formula can only be used as a very rough guide. The errors involved are difficult to evaluate but from the agreement of the measurements Eq. (5) should be correct to within 5 percent.

From (4) and Smith's data approximate range-energy curves can be calculated using the relation,

$$R(E,Z)=\frac{13A}{27.0Z}\left\{\frac{R_{Al}(E)}{q(E,Z)}-\int_0^E R_{Al}(E')\frac{d(1/q)}{dE'}dE'\right\}, \quad (6)$$

where $R(E,Z)$ is the range of protons of energy E in mg/cm² of the element of atomic number Z and atomic weight A, and $R_{Al}(E)$ is the range of protons in Al. The first term is the larger and can be considered a useful approximation; the second term is a correction to this and can be evaluated using

$$\frac{d(1/q)}{dE}=\frac{0.573-0.512\log Z}{E(\log E-1.18\log Z+2.95)^2}, \quad (7)$$

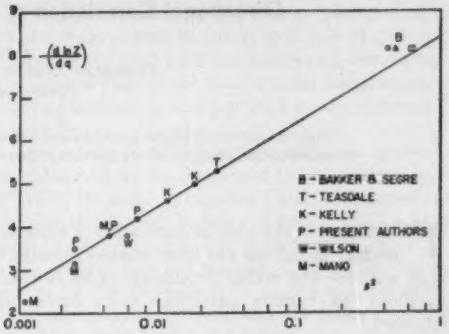

FIG. 7. Graph of $-(d\ln Z/dq)$ vs $\ln\beta^2$, using data from various experiments.

and integrating graphically. Equation (7) diverges for $E\sim 0$ but the integrand function should be cut off at about $E\sim 100$ kev and extrapolated to zero; the error involved is negligible. Range-energy relations for deuterons, alpha-particles, and mesons can be obtained from those for protons in the usual manner.

The equation of the line in Fig. 7 is

$$-(d\ln Z/dq)=8.41+0.848\ln\beta^2. \quad (8)$$

The slope is not unity as required by (4) and the value of I/Z found from the intercept is 17.4 ev, in disagreement with the best experimental value,[18] 9.4 ev. The disagreement is due in part to the fact that the mean ionization potential is a function of v in that the number of electrons effective in stopping depends on v. Moreover, the statistical model fails for $Z<26$. In the experiments at low velocities, however, the linear Bloch plots were obtained using the uncorrected Z values, and were linear for elements whose effective Z values were less than 26 (i.e., all the lines pass through $q=1$ at $Z=13$).

The authors extend their appreciation for the help of K. Lark-Horovitz who proposed the problem, and of E. Bleuler who suggested many of the methods of carrying out the measurements and analyzing the data.

Directional Correlation of Successive Nuclear Radiations

GIULIO RACAH*
Institute for Advanced Study, Princeton, New Jersey
(Received August 6, 1951)

Using the algebra of tensor operators a closed expression is obtained for the most general case of angular correlation. The structure of the correlation function is explained by means of semiclassical considerations.

THE theory of the angular correlation of successive nuclear radiations has been treated recently by many authors, and rather formidable tables of results pertaining to various particular cases have been published.[1–5]

It is the purpose of this paper to show that the problem is much simpler than it seems, both from the algebraical and from the geometrical point of view. The most general case is here treated in a very natural and straightforward manner by the general methods of the algebra of tensor operators;[6] using an appropriate expansion of the correlation function the final results are expressed in a simple closed form, and lead to a semiclassical geometrical interpretation.

The interaction hamiltonian for the emission of a particle along the direction of the z-axis may be expanded in the form,

$$H=\sum_{LM}\alpha_{LM}(\mathbf{A}_i)T_M{}^{(L)}(\mathbf{X}_i), \tag{1}$$

where the $T_M{}^{(L)}(\mathbf{X}_i)$ are the components of irreducible tensor operators of degree L which operate on the nucleus, and the $\alpha_{LM}(\mathbf{A}_i)$ are functions of the variables associated with the description of the emitted particles.[7] If the emitted particle carries off a definite angular momentum (in particular if the emission corresponds to a definite multipole order), all $T_M{}^{(L)}$ vanish except for a given L; when mixtures of multipoles are considered, $T_M{}^{(L)}$ with different values of L will be different from zero.

The M-dependence of the α_{LM} is characteristic of the polarization properties of the emitted particles. Thus for α-particles only α_{L0} is different from zero, for γ-rays only $\alpha_{L,\pm1}$ (and then the ratio $\alpha_{L1}/\alpha_{L,-1}$ depends on the polarization), for β-particles the α_{LM} depend on the energy of the electron, the direction of emission of the neutrino, etc.

For a particle emitted in a direction other than the z-axis we shall introduce a new system of axes $\xi\eta\zeta$, with the ζ-axis along the direction of emission, and come back to the old axes using the fundamental group-theoretical property of the $T_M{}^{(L)}$ of transforming according to the $(2L+1)$-dimensional irreducible representation $D^{(L)}$ of the three-dimensional rotation group:

$$\bar{H}=\sum_{LM\mu}\alpha_{LM}T_\mu{}^{(L)}D^{(L)}(\alpha\beta\gamma)_{\mu M}. \tag{2}$$

The probability for the transition from a nuclear state of spin j_1 to a state of spin j with the emission of a particle in the direction of the z-axis and for a successive transition to a state of spin j_2 with the emission of a particle in the direction of the ζ-axis is given by[8]

$$W=\sum_{m_1mm'm_2}(j_1m_1|H_1|jm)^*(j_1m_1|H_1|jm')\times(jm|\bar{H}_2|j_2m_2)^*(jm'|\bar{H}_2|j_2m_2); \tag{3}$$

introducing (1) and (2) into (3) we obtain

$$W=\sum_{LM\mu}\alpha_{L_1M_1}{}^*\alpha_{L_1'M_1'}\alpha_{L_2M_2}{}^*\alpha_{L_2'M_2'}\times(j_1m_1|T_{M_1}{}^{(L_1)}|jm)^*(j_1m_1|T_{M_1'}{}^{(L_1')}|jm')\times(jm|T_\mu{}^{(L_2)}|j_2m_2)^*(jm'|T_\mu{}^{(L_2')}|j_2m_2)\times D^{(L_2)}(\alpha\beta\gamma)_{\mu M_2}{}^*D^{(L_2')}(\alpha\beta\gamma)_{\mu'M_2'}. \tag{4}$$

The relation[9]

$$D^{(L_2)}(\alpha\beta\gamma)_{\mu M_2}{}^*=(-)^{M_2-\mu}D^{(L_2)}(\alpha\beta\gamma)_{-\mu,-M_2} \tag{5}$$

and the fundamental formula[10] for the reduction of the product of the two representations $D^{(L_2)}$ and $D^{(L_2')}$ yield

$$D^{(L_2)}(\alpha\beta\gamma)_{\mu M_2}{}^*\,D^{(L_2')}(\alpha\beta\gamma)_{\mu'M_2'}=\sum_{k\rho\sigma}(-)^{M_2-\mu}(L_2-\mu L_2'\mu'|L_2L_2'k\rho)\times D^{(k)}(\alpha\beta\gamma)_{\rho\sigma}(L_2L_2'k\sigma|L_2-M_2L_2'M_2'); \tag{6}$$

introducing it in (4) and using the expression II(29) for the matrix elements of $T_M{}^{(L)}$ and the expression II(16′) for $(L_2-\mu L_2'\mu'|L_2L_2'k\rho)$, we get

$$W=\sum_{LMm\mu k\sigma}\alpha_{L_1M_1}{}^*\alpha_{L_1'M_1'}\alpha_{L_2M_2}{}^*\alpha_{L_2'M_2'}\times(j_1\|T^{(L_1)}\|j)^*(j_1\|T^{(L_1')}\|j)(j\|T^{(L_2)}\|j_2)^*\times(j\|T^{(L_2')}\|j_2)(-)^{m'-m+M_2-\mu+k+\rho}(2k+1)^{\frac{1}{2}}\times V(j_1jL_1;-m_1mM_1)V(j_1jL_1';-m_1m'M_1')\times V(jj_2L_2;-mm_2\mu)V(jj_2L_2';-m'm_2\mu')\times V(L_2L_2'k;-\mu\mu'-\rho)D^{(k)}(\alpha\beta\gamma)_{\rho\sigma}\times(L_2L_2'k\sigma|L_2-M_2L_2'M_2'). \tag{7}$$

---

* On sabbatical leave from the Hebrew University, Jerusalem, Israel.

[1] D. R. Hamilton, Phys. Rev. **58**, 122 (1940); and **74**, 782 (1948).

[2] J. W. Gardner, Proc. Phys. Soc. (London) **A62**, 763 (1949); and **A64**, 238 (1951).

[3] D. S. Ling and D. L. Falkoff, Phys. Rev. **76**, 1639 (1949).

[4] D. L. Falkoff and G. E. Uhlenbeck, Phys. Rev. **79**, 323 (1950).

[5] I. Zinnes, Phys. Rev. **80**, 386 (1950).

[6] G. Racah, Phys. Rev. **62**, 438 (1942) §3; this paper will be referred to as II.

[7] As the z-axis has been chosen along the direction of emission the α_{LM} are no more tensors as in reference 4, Eq. (8).

[8] Reference 1, Eq. (10); reference 5, Eq. (1).

[9] This relation follows from E. Wigner, *Gruppentheorie* (Friedrich Vieweg and Sohn, Braunschweig, 1931), introducing in Eq. (27) of p. 180 a new summation index $k'=k+\mu-\nu$.

[10] Reference 9, p. 203, Eq. (16a).

The summation over the m's and μ's may be performed[11] by using the symmetry properties II(19) of the V's and applying twice II(41); we obtain, finally,

$$W(\alpha\beta\gamma)=\sum_{L_1L_1'L_2L_2'k\rho\sigma}(j_1\|T^{(L_1)}\|j)^*(j_1\|T^{(L_1')}\|j)\times(j\|T^{(L_2)}\|j_2)^*(j\|T^{(L_2')}\|j_2)(-)^{j_1+L_1-j_2-L_2+k}\times c_{k\rho}(L_1'L_1)^*c_{k\sigma}(L_2L_2')W(jL_1jL_1';j_1k)\times W(jL_2jL_2';j_2k)D^{(k)}(\alpha\beta\gamma)_{\rho\sigma}, \quad (8)$$

where the W's are defined by II(36') and

$$c_{k\tau}(LL')=\sum_{MM'}(-)^{L-M}\alpha_{LM}^*(\mathbf{A}_i)\alpha_{L'M'}(\mathbf{A}_i)\times(L-ML'M'|LL'k\tau). \quad (9)$$

If some of the characteristics of the emitted radiations (as polarization, direction of the neutrino, etc.) are not observed, the expressions of the $c_{k\tau}$ contain also an averaging over those $\mathbf{A}_i$ which are not observed.

Equation (8) seems to be still complicated, as there is a summation over seven variables; but this complication is only apparent, and is due to the fact that the equation is very general and holds for any kind of radiations with any kind of polarization and multipole mixture. If there is no multipole mixture, the summation over the L's reduces to one term; if a radiation is nonpolarized or circularly polarized, the corresponding $c_{k\tau}$ vanish for $\tau\neq 0$; if both radiations are nonpolarized or circularly polarized, only

$$D^{(k)}(\alpha\beta\gamma)_{00}=P_k(\cos\beta) \quad (9)$$

will appear in the expansion of $W(\beta)$. If one of the radiations is nonpolarized or linearly polarized, the coefficients of $D^{(k)}{}_{\rho\sigma}$ vanish for odd k; but if both the outgoing radiations are circularly or elliptically polarized, also the $D^{(k)}{}_{\rho\sigma}$ with odd k will appear in the correlation function.[12]

Equation (8) shows that the natural expansion of the correlation function is not in powers of the cosines of the angles, but in terms of $D^{(k)}{}_{\rho\sigma}$ (or legendre polynomials for nonpolarized particles), as the coefficients of this expansion break up in many independent factors. In order to understand the physical and geometrical meaning of these different factors, we shall consider the angular correlation of two γ-rays of given multipole order from a semiclassical point of view.[13]

If we assume as z-axis the direction of emission of the first quantum, and as xz-plane its polarization plane, the probability that the angular momentum $\mathbf{L}_1$ carried off by the quantum has a direction $(\beta_1\alpha_1)$ will be a certain function $f_{L_1}(\beta_1\alpha_1)$; if the quantum is nonpolarized or circularly polarized, f_{L_1} will be independent of α_1. To this emission corresponds a transition of the nucleus from a state of spin j_1 to a state of spin j; the directions of $\mathbf{j}_1$ and $\mathbf{j}$ are not determined, but, owing to the conservation of the total angular momentum, the angle β_2 between $\mathbf{L}_1$ and $\mathbf{j}$ is fixed by the values of L_1, j_1 and j.

Also for the second quantum, which we assume to be emitted along the ζ-axis and to be polarized in the $\xi\zeta$-plane, the angle β_3 between $\mathbf{j}$ and $\mathbf{L}_2$ is known, and the probability that $\mathbf{L}_2$ has a direction $(\beta_4\gamma_4)$ with respect to the $\xi\eta\zeta$-system will be given by $f_{L_2}(\beta_4\gamma_4)$.

We perform now the rotation $R(\alpha\beta\gamma)$ from the xyz-system to the $\xi\eta\zeta$-system in four steps, considering three intermediate systems with the polar axes along the directions of $\mathbf{L}_1$, $\mathbf{j}$ and $\mathbf{L}_2$; then

$$R(\alpha\beta\gamma)=R(\alpha_1\beta_1 0)R(\alpha_2\beta_2 0)R(\alpha_3\beta_3 0)R(\alpha_4-\beta_4-\gamma_4), \quad (10)$$

and

$$D^{(k)}(\alpha\beta\gamma)_{\rho\sigma}=\sum_{\lambda\mu\nu}D^{(k)}(\alpha_1\beta_1 0)_{\rho\lambda}D^{(k)}(\alpha_2\beta_2 0)_{\lambda\mu}\times D^{(k)}(\alpha_3\beta_3 0)_{\mu\nu}D^{(k)}(\alpha_4-\beta_4-\gamma_4)_{\nu\sigma}. \quad (11)$$

We are interested in the coefficients of the expansion

$$W(\alpha\beta\gamma)=\sum_{k\rho\sigma}w_{k\rho\sigma}D^{(k)}(\alpha\beta\gamma)_{\rho\sigma}: \quad (12)$$

as $w_{k\rho\sigma}$ is proportional to the mean value of $W(\alpha\beta\gamma)\times D^{(k)}(\alpha\beta\gamma)_{\rho\sigma}{}^*$, and $W(\alpha\beta\gamma)$ is proportional to $f_{L_1}(\beta_1\alpha_1)\times f_{L_2}(\beta_4\gamma_4)$, we get from (11) that

$$w_{k\rho\sigma}\sim\sum_{\lambda\mu\nu}[f_{L_1}(\beta_1\alpha_1)D^{(k)}(\alpha_1\beta_1 0)_{\rho\lambda}{}^*]_{\text{av}}\times[D^{(k)}(\alpha_2\beta_2 0)_{\lambda\mu}{}^*]_{\text{av}}[D^{(k)}(\alpha_3\beta_3 0)_{\mu\nu}{}^*]_{\text{av}}\times[D^{(k)}(\alpha_4-\beta_4-\gamma_4)_{\nu\sigma}{}^*f_{L_2}(\beta_4\gamma_4)]_{\text{av}}. \quad (13)$$

As α_2, α_3, and α_4 are undetermined, the averaging over these angles will give nonvanishing results only for $\lambda=\mu=\nu=0$, and owing to (9), and to the relations,

$$D^{(k)}(\alpha\beta\gamma)_{\rho 0}=[4\pi/(2k+1)]^{\frac{1}{2}}Y_k{}^\rho(\beta\alpha)^*$$
$$D^{(k)}(\alpha-\beta-\gamma)_{0\sigma}=[4\pi/(2k+1)]^{\frac{1}{2}}Y_k{}^\sigma(\beta\gamma), \quad (14)$$

we get

$$w_{k\rho\sigma}\sim[f_{L_1}(\beta_1\alpha_1)Y_k{}^\rho(\beta_1\alpha_1)]_{\text{av}}P_k(\cos\beta_2)P_k(\cos\beta_3)\times[f_{L_2}(\beta_4\gamma_4)Y_k{}^\sigma(\beta_4\gamma_4)^*]_{\text{av}}. \quad (15)$$

Comparing (15) with (8) we see that, apart from normalization and phase factors, $W(jL_ijL_i;j_ik)$ is the quantum-mechanical expression for $P_k(\cos\mathbf{jL}_i)$, and the $c_{k\tau}$ are the quantum-mechanical expressions for the coefficients of the expansion in a series of spherical harmonics of the correlation function between the directions of the outgoing particle and the angular momentum carried off by it.

In conclusion, we wish to point out that our calculations do not "involve an unnecessary duplication of effort,"[14] even for the cases which were already calculated. First of all a closed formula allows a deeper insight into the geometrical and physical reasons for the

[11] For a particular case see reference 2.

[12] Actually, for the essentially equivalent problem of the resonance radiation, D. R. Hamilton, Astrophys. J. **106**, 457 (1947), obtained terms involving the first power of $\cos\theta$ in the expression of the correlation of the parameters measuring the circular polarization.

[13] The author is indebted to Dr. U. Fano for many discussions on this point.

[14] D. L. Falkoff, Phys. Rev. **82**, 99 (1951).

angular correlations and the structure of the correlation function. Secondly, the use of Eq. (8) is simpler than the use of the formulas and tables previously published, as the expansion in powers of the cosines of the angles is not the natural one, and makes formulas and tables much more complicated than necessary. For the use of Eq. (8) it is sufficient to tabulate separately the values of $c_{k,r}(LL')$ for the different kinds of radiations, and the values of $W(jLjL';j_rk)$, which are independent of the kind of radiations, and to combine them according to necessity.[15] Tables of this kind are being prepared for publication.[16]

The author wishes to express his gratitude to Professor J. R. Oppenheimer for the generous hospitality in the stimulating atmosphere of the Institute for Advanced Study, and to Professor M. Fierz who suggested that he deal with this problem.

[15] Similar results have been obtained independently by S. P. Lloyd, Thesis, University of Illinois (1951); Phys. Rev. **80**, 118 (1950).

[16] J. M. Blatt and L. C. Biedenharn, Phys. Rev. **82**, 123 (1951).

PHYSICAL REVIEW VOLUME 84, NUMBER 5 DECEMBER 1, 1951

Neutron Scattering and Polarization by Ferromagnetic Materials

C. G. SHULL, E. O. WOLLAN, AND W. C. KOEHLER
Oak Ridge National Laboratory, Oak Ridge, Tennessee
(Received August 20, 1951)

Neutron diffraction studies are reported on a series of magnetized and unmagnetized ferromagnetic materials. The diffraction patterns for unmagnetized, polycrystalline samples of Fe and Co are found to possess both nuclear and magnetic components with the latter in agreement with the magnetic scattering theory with respect both to intensity of scattering and form factor angular variation. Studies on the magnetic structure of Fe_3O_4 are shown to strongly support Néel's proposed ferrimagnetic structure. Predictions of the theory regarding intensity effects upon sample magnetization are fully confirmed and the Schwinger-Halpern-Johnson formulation of the interaction function between the neutron's magnetic moment and the internal fields in a ferromagnet is substantiated. A pronounced variation of intensity around the Debye ring in the diffraction pattern for a magnetized sample is found. Neutron polarization effects in the Bragg scattered beams from magnetized crystals of Fe and Fe_3O_4 have been studied and it is shown that very highly polarized beams are obtained for certain reflections. This method of monochromatic beam polarization is found to compare very favorably with other methods with respect to polarization value, beam intensity, and ease of obtainment.

INTRODUCTION

THE theory of the scattering and polarization of neutrons by ferromagnetic substances has been given a very general treatment by Halpern and coworkers.[1] Up to the present time, experimentation in this field has centered upon studies of the single and double transmission effect[2] and more recently upon studies of critical reflection from magnetized mirrors.[3]

The present report deals with studies of the intensity distribution and the polarization of the scattered neutron radiation from both unmagnetized and magnetized ferromagnetic substances. These studies give information on the form factor dependence of magnetic scattering, on the basic nature of the neutron's magnetic interaction and on the magnetic structure existing in certain ferromagnetics, *viz.*, the spatial distribution of the various magnetic ions within the ferromagnetic lattice. A previous report[4] has discussed neutron scattering by paramagnetic and antiferromagnetic lattices and brief reports of some aspects of the present work concerning the neutron's magnetic interaction and the polarization phenomena have been given in the literature.[5]

The general expression for the differential scattering cross section of a magnetic ion has been given by Halpern and Johnson[1] (H-J) as

$$F^2=C^2+2CD\mathbf{q}\cdot\boldsymbol{\lambda}+D^2q^2 \tag{1}$$

where C is the nuclear scattering amplitude, D the magnetic scattering amplitude, $\boldsymbol{\lambda}$ a unit vector describing the polarization state of the neutron being scattered,

$$\mathbf{q}=\mathbf{e}(\mathbf{e}\cdot\boldsymbol{\kappa})-\boldsymbol{\kappa} \quad \text{and} \quad q^2=1-(\mathbf{e}\cdot\boldsymbol{\kappa})^2 \tag{2}$$

where $\mathbf{e}$ is the unit scattering vector and $\boldsymbol{\kappa}$ a unit vector parallel to the magnetic moment vector of the magnetic ion. The magnetic scattering amplitude D is given by

$$D=(e^2/mc^2)\gamma Sf=0.539\times10^{-12}Sf \text{ cm} \tag{3}$$

[1] O. Halpern and M. H. Johnson, Phys. Rev. **55**, 898 (1939). O. Halpern and T. Holstein, Phys. Rev. **59**, 960 (1941). Halpern, Hamermesh, and Johnson, Phys. Rev. **59**, 981 (1941).

[2] Hughes, Wallace, and Holtzman, Phys. Rev. **73**, 1277 (1948). Fleeman, Nicodemus, and Staub, Phys. Rev. **76**, 1774 (1949). Burgy, Hughes, Wallace, Heller, and Woolf, Phys. Rev. **80**, 953 (1950).

[3] D. J. Hughes and M. T. Burgy, Phys. Rev. **81**, 498 (1951).

[4] Shull, Strauser, and Wollan, Phys. Rev. **83**, 333 (1951).

[5] Shull, Wollan, and Strauser, Phys. Rev. **81**, 483 (1951). C. G. Shull, Phys. Rev. **81**, 626 (1951).

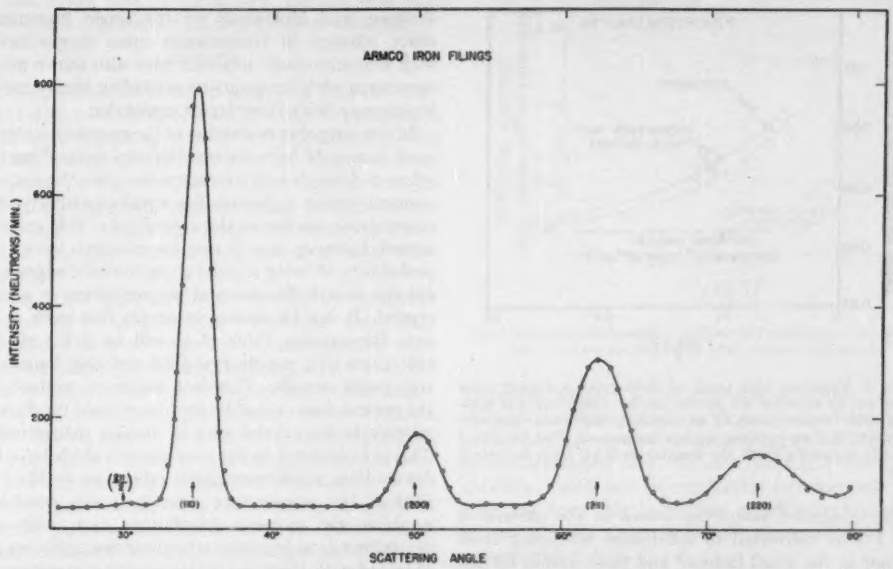

FIG. 1. Neutron diffraction pattern for polycrystalline Fe.

where γ is the neutron magnetic moment expressed in nuclear Bohr magnetons, S the spin quantum number of the magnetic atom, and f the magnetic form factor characteristic of the electrons responsible for the atomic magnetic moment.

For unpolarized incident neutron radiation, $\mathbf{q}\cdot\boldsymbol{\lambda}$ averages to zero and the differential cross section is the sum of the nuclear and magnetic contributions

$$F^2=C^2+D^2q^2. \tag{4}$$

The numerical value for q^2 will depend according to Eq. (2) upon the relative directions of the scattering vector and the magnetization vector. A further discussion of the form of this dependence will be given in a later section of this paper.

DIFFRACTION BY UNMAGNETIZED FERROMAGNETIC MATERIALS

We consider first the scattering by the ferromagnetic elements Fe and Co with no applied magnetic field. At temperatures below the Curie point, the magnetic moments of the atoms are in parallel alignment within a single domain but, without an applied field, the magnetic orientation from one domain to the next will, on the average, be random. Each domain constitutes a magnetic crystallite and since the magnetic moments are aligned within the domains, the magnetic scattering will appear in the Bragg peaks together with the nuclear scattering, the intensity of the two contributions being additive according to Eq. (4). The magnetic and nuclear contributions can be separately determined since the magnetic scattering will exhibit a form factor fall off with scattering angle due to the spatial distribution of the magnetic electrons within the atom while the nuclear scattering cross section is spherically symmetric. Following a discussion on the diffraction results for these ferromagnetic elements, data and their interpretation for a more complicated ferromagnetic substance, Fe_3O_4 (magnetite), will be given.

Iron

Figure 1 shows the powder diffraction pattern taken for a sample of polycrystalline Fe with neutrons of wavelength 1.204A. Rather high intensities are obtained for this material primarily because of the large coherent nuclear scattering amplitude for Fe. A number of samples were studied, with most emphasis on samples of filings taken from pure Armco iron blocks. The filings were given a heat treatment and hydrogen reduction to remove any oxide layer and some of the cold-working effects. The samples were contained in flat cells of thickness about $\frac{1}{2}$ in. between thin quartz windows. Corrections for second-order wavelength contribution were made to the patterns and aside from these low intensity second-order parasitic reflections, all of the observed reflections could be indexed on the basis of the usual body-centered cubic reflections for the normal cubic cell. The observed integrated intensities were placed on an absolute scale by comparison with a standard sample of nickel powder for which we have measured the coherent scattering cross section as 13.4 barns.

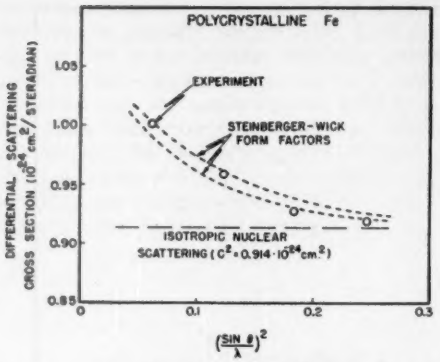

FIG. 2. Variation with angle of differential scattering cross section per Fe atom for the powder pattern reflections. The scattering cross section contains an angularly-dependent magnetic component and an isotropic nuclear component. The calculated magnetic scattering (with the Steinberger-Wick form factors) is shown.

The integrated intensities shown in the pattern of Fig. 1 were converted to differential scattering cross sections in the usual fashion[6] and these values for the four observed reflections are shown in Fig. 2. It is to be seen that this cross section shows a significant, although not pronounced, angular variation and this is because of the large isotropic nuclear scattering relative to the magnetic scattering. Using the magnetic moment per Fe atom of 2.22 Bohr magnetons as determined from saturation magnetization studies on iron, and hence a value of 1.11 for S_{eff} since the gyromagnetic ratio for Fe is very close to 2, one evaluates with Eq. (3) the expected magnetic scattering amplitude.

$$D(\text{Fe}) = 0.598 f \times 10^{-12} \text{ cm}. \quad (5)$$

Steinberger and Wick[7] have given the results of a recent calculation of the magnetic form factor f for iron and on the basis of these values, the best fit between the data and Eqs. (4) and (5) is shown on the graph of Fig. 2. Also shown on the figure are extremes in the Steinberger-Wick calculation for different assumptions about the asymptotic behavior of the 3d-wave functions. The experimental data are not considered accurate enough to distinguish between one selection or another. Previous studies by Hughes, Wallace, and Holtzman[2] on the single transmission effect (change in transmission upon magnetization) with monochromatic neutrons have also shown general agreement with the magnetic scattering theory and the Steinberger-Wick form factor evaluation.

TABLE I. The coherent nuclear scattering cross sections of iron and its isotopes.

Isotope	Coherent scattering amplitude (10^{-12} cm)	Coherent scattering cross section (barns)
Fe^{54}	+0.42	2.2±0.1
Fe^{56}	+1.00	12.6±0.2
Fe^{57}	+0.23	0.64±0.05
Fe	+0.96	11.5±0.2

In the foregoing evaluation of the magnetic scattering cross section D^2 from the experimental data, q^2 has been taken as $\frac{2}{3}$ which is its average value when the magnetic moment within a domain has equal probability of all orientations relative to the crystal axes. It is generally agreed, however, that in iron the moments have a high probability of being aligned along the cube edges which are the easiest directions of magnetization in a single crystal. It can be shown, however, that even in this case the average value of q^2 will be $\frac{2}{3}$ for all (hkl) reflections with a polycrystalline and polydomain ferromagnetic sample. This fact makes it evident that the present data cannot be used to indicate the direction relative to the crystal axes of domain magnetization. This is in contrast to the conclusions[4] which have been drawn from antiferromagnetic reflections in MnO and FeO at low temperature wherein it was possible to establish the moment orientations even with polycrystalline data because incomplete multiplicities were obtained with these particular magnetic structures.

In addition to the studies of polycrystalline iron described above, a series of samples of isotopically enriched iron was also studied. Preliminary studies to determine the nuclear scattering phase of Fe^{54}, Fe^{56}, and Fe^{57} were carried out with the enriched iron in the form of Fe_2O_3, after which the metals in a finely divided state were studied in greater detail. For each of the isotopic iron samples, as for normal iron, the differential scattering cross section exhibited an angular variation. In the case of Fe^{56} the residual magnetic scattering after subtraction of the nuclear contributions was identical, within experimental error, with that obtained from normal iron, as indeed, is to be expected. A direct determination of the magnetic scattering from Fe^{54} and Fe^{57}, for which the nuclear scattering amplitudes are more favorable, did not prove feasible because of the very small amounts of sample at our disposal. In these two latter instances, the magnetic contribution was assumed known and equal to that for normal iron and Fe^{56}, and the nuclear scattering amplitude was obtained by subtraction. In Table I are shown the nuclear scattering properties of the isotopes of iron obtained in this way. The total scattering cross section of iron, using these isotopic cross sections, may be calculated and is found to be 11.6 barns. Comparison of this value with the coherent scattering cross section of 11.5 barns indicates that the isotopic diffuse scattering in normal iron is very small. This result supports the conclusions drawn by Hughes and Burgy[8] from their investigations of the single transmission effect in a single crystal of iron with neutron energies below that corresponding to

[6] C. G. Shull and E. O. Wollan, Phys. Rev. **81**, 527 (1951).
[7] J. Steinberger and G. C. Wick, Phys. Rev. **76**, 994 (1949).
[8] D. J. Hughes and M. T. Burgy, Phys. Rev. **80**, 481 (1950).

the first Bragg peak in which they find less than 0.25 barn of spin dependent or isotopic diffuse scattering.

COBALT

Diffraction patterns for a sample of face-centered-cubic cobalt in the form of metallic filings were obtained in the same fashion as in the above study on iron. The resulting scattering cross sections per magnetic atom are shown in Fig. 3 with the data resolved into its nuclear and magnetic contributions. Because of the much smaller nuclear scattering here than was found for iron, the magnetic scattering effects show up more strikingly.

Using the experimentally determined magnetic moment for Co of 1.74 Bohr magnetons[9] from magnetization studies on cubic cobalt, the magnetic scattering amplitude is evaluated as $0.468f \times 10^{-12}$ cm. The value of the cross section corresponding to this amplitude at zero scattering angle (unit form factor) is shown on the ordinate axis of Fig. 4. The form factor describing the magnetic scattering is that suggested by the data and it is seen that this extrapolates satisfactorily to the calculated forward-direction cross section. It would be expected that this form factor would be closely similar to that calculated for iron by Steinberger and Wick and indeed this is substantiated in a quantitative comparison of the two. The slightly larger nuclear charge for Co would compress the 3d magnetic shell somewhat and the form factor would be slightly less angularly dependent than would be the case for iron. There is a suggestion of this in the Co experimental data.

As seen from the graph the coherent nuclear scattering cross section for Co amounts to only 1.0 barn and this is a consequence of the pronounced nuclear spin incoherent scattering for this nucleus. This has been discussed in an earlier report.[6] The magnetic scattering is comparable to or exceeds the nuclear scattering in the forward direction and this fact leads to interesting polarization phenomena in the neutron scattering by magnetized samples as will be discussed in a later section.

Fe_3O_4 (MAGNETITE)

This oxide possesses a spinel-type structure and is ferromagnetic on a macroscopic scale to about the same extent as nickel. There are both divalent and trivalent Fe ions present in the structure and the molecular formulation can be considered as containing one Fe^{++} ion and two Fe^{+++} ions. Verwey and Heilmann[10] consider the structure to be that of an inverted spinel in which the octahedral Fe sites are occupied at random by equal numbers of divalent and trivalent ions where as the tetrahedral sites are occupied only by trivalent ions. Further considerations by Néel[11] on the magnetic

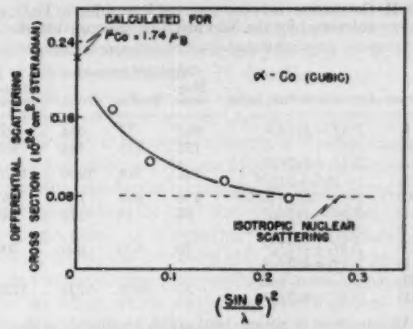

FIG. 3. Variation with angle of differential scattering cross section per Co atom for the Co powder pattern reflections.

properties suggest a ferrimagnetic structure for this material in which the magnetic moments of the tetrahedral ions are coupled antiferromagnetically to those of the octahedral ions. Because the latter are in the majority, Fe_3O_4 will be resultantly ferromagnetic and Néel has been able to explain quantitatively the observed magnetic moment per Fe atom obtained from magnetization data.

Since neutron scattering by such a magnetic lattice will be sensitive to the strength, position, and relative orientation of the magnetic ions, the neutron diffraction pattern should offer direct evidence as to the validity of these magnetic structure suppositions. Several powder samples have been examined, the principal quantitative measurements being made on a very pure sample kindly supplied by Professor A. von Hippel. A typical diffraction pattern taken at room temperature is shown in Fig. 3. As in the case of the simple ferromagnetic ele-

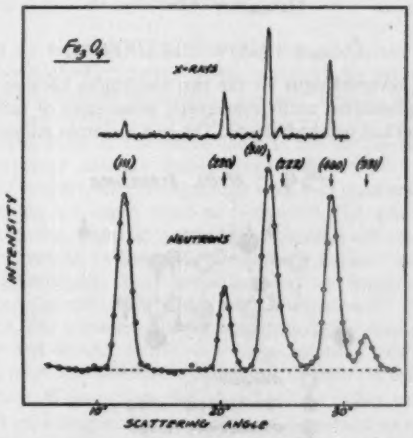

FIG. 4. Comparison between x-ray and neutron diffraction patterns for Fe_3O_4 (magnetite) at room temperature. Pronounced magnetic scattering contribution in the neutron pattern is found.

[9] A. J. P. Meyer and P. Taglang, Compt. rend. **231**, 612 (1950).
[10] E. J. W. Verwey and E. L. Heilmann, J. Chem. Phys. **15**, 174 (1947). Verwey, Haayman, and Romeijn, J. Chem. Phys. **15**, 181 (1947).
[11] L. Néel, Ann. phys. **3**, 137 (1948).

TABLE II. Comparison between observed intensities for Fe_3O_4 and those calculated for the Néel magnetic structure model.

Reflection	Crystal structure factor	Calculated intensities: Magnetic	Nuclear	Total	Observed intensity
(111)	$2(4f_1-4\sqrt{2}f_2)^2$	902	32	934	860
(220)	$(8f_1)^2$	125	218	343	360
(311)	$2(4f_1+4\sqrt{2}f_2)^2$	112	948	1060	1070
(222)	$(-16f_2+32f_0)^2$				
(400)	$(8f_1-16f_2-32f_0)^2$	116	649	765	780
(331)	$2(4f_1-4\sqrt{2}f_2)^2$	94	16	110	135
(422)	$(8f_1)^2$	20	670	690	700
(333)	$2(4f_1+4\sqrt{2}f_2)^2$				
(511)	$2(4f_1+4\sqrt{2}f_2)^2$				
(440)	$(8f_1+16f_2+32f_0)^2$	32	1692	1724	1730
(531)	$2(4f_1-4\sqrt{2}f_2)^2$				

All intensities (neutrons/min) are on an absolute scale.

ments already discussed, there will be no coherence between the nuclear and magnetic portions of the pattern. Since the nuclear scattering amplitudes for iron and oxygen are known accurately and the crystallographic structure has been well established from x-ray studies, the nuclear scattering contribution in the neutron pattern can be reliably accounted for. The remaining portion can be attributed to magnetic scattering and consequently can be compared to that predicted by any suggested magnetic structure.

The comparison between the observed and the calculated intensities for the Néel structural model is given in Table II along with the crystal structure factors which characterize the various reflections. In this tabulation, f_1, f_2, and f_0 represent the scattering amplitudes of a tetrahedral iron ion, an octahedral iron ion, and an oxygen ion respectively. For the nuclear scattering amplitudes, that for iron is taken as $0.956\cdot10^{-12}$ cm and for oxygen $0.575\cdot10^{-12}$ cm. On the Néel magnetic model,

$$(f_1)_{\text{mag}}=-D(\text{Fe}^{+++})$$

and

$$(f_2)_{\text{mag}}=+\tfrac{1}{2}D(Fe^{+++})+\tfrac{1}{2}D(\text{Fe}^{++}), \qquad (6)$$

with reversed signs for the two amplitudes because of the postulated antiferromagnetic orientation of tetrahedral and octahedral ions. The spin quantum numbers

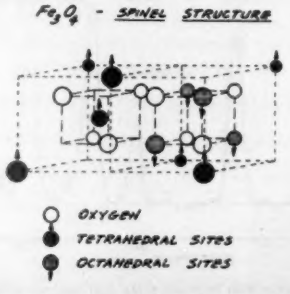

FIG. 5. Portion of the magnetic unit cell for Fe_3O_4. The octahedral and tetrahedral Fe ions are coupled antiferromagnetically.

for Fe^{+++} and Fe^{++} ions are, respectively, 5/2 and 2 and hence the appropriate magnetic scattering amplitudes are calculable from Eq. (3) as

$$\begin{aligned} D(\text{Fe}^{++})&=1.088f\times10^{-12}\text{ cm},\\ D(\text{Fe}^{+++})&=1.360f\times10^{-12}\text{ cm}. \end{aligned} \qquad (7)$$

Finally, the total intensity in an (hkl) reflection, say the (111) reflection, is taken as

$$I_{111}=I_{\text{nuclear}}+I_{\text{magnetic}}=k\{2[4f_{\text{Fe}}-4\sqrt{2}f_{\text{Fe}}]^2\}_{\text{nucl}}+\tfrac{2}{3}k\{2[4f_1-4\sqrt{2}f_2]^2\}_{\text{mag}} \qquad (8)$$

in which k is an instrumental parameter determinable from the powder diffraction formula. In the numerical evaluation, the magnetic form factor for Mn^{++} (reference 4) has been used for the Fe ions since the latter have not been established accurately at the present time. This should be a good approximation since the Mn ion and Fe ion would not be expected to differ much in their 3d-shell characteristics.

The intensities shown in Table II are all on an absolute scale and the agreement between calculated and observed total intensity values appears satisfactory. Magnetized sample studies to be discussed in the next section permit a direct resolution of the total intensity into the magnetic and nuclear components and these also support the validity of the Néel structural model. Other magnetic models have been investigated and it is found that the calculated intensity is rather sensitive to the selected model. For instance, an alternative structure would be for the Fe^{++} ions to exist wholly at tetrahedral sites and the Fe^{+++} only at octahedral sites (a normal spinel structure). The observed magnetization could be obtained for this model by having the Fe^{++} ions coupled ferromagnetically but with no orientation coupling between the Fe^{+++} ions themselves or between Fe^{+++} and Fe^{++}. Thus the trivalent ions would be in a paramagnetic state. Intensity calculations for this model are in violent disagreement with the data, with the (111) intensity for instance, being eight times lower than observed. Thus the Néel model of antiferromagnetic coupling between the tetrahedral ions and the octahedral ions in the inverted spinel structure appears fully substantiated. Figure 5 shows a portion of the magnetic unit cell of Fe_3O_4 with this antiferromagnetic arrangement of the ions.

Some diffraction data were also obtained for Fe_3O_4 at low temperatures (80°K) to see if any structural changes developed upon cooling. Fe_3O_4 exhibits interesting changes in magnetic properties and electrical conductivity at temperatures of the order 120–150°K and Verwey, Haayman, and Romeijn[10] have suggested that the pronounced increase in resistivity in lowering the temperature through 120°K is to be accounted for by an ordering of the Fe^{++} and Fe^{+++} ions at the octahedral sites. On this picture the relatively low resistivity at room temperature is caused by ionic migration (electron exchange) among the randomly

arranged ions at the octahedral sites. The neutron diffraction patterns at high and low temperatures were found to possess no significant difference (within about 1 percent) and a detailed examination of the crystal structure factors and the expected intensities for the Verwey model showed that this was not inconsistent with the model. The redistribution of the Fe^{++} and Fe^{+++} ions, which do not differ too much in magnetic scattering power (see Eq. (7)) does not appear to affect the powder intensities appreciably. If studies were to be made on single crystal, single domain samples where one does not have the superposition of various (*hkl*) reflections, then indeed the ordering effect should be noticeable but this has not been performed experimentally. The powder data do show, however, that the basic antiferromagnetic structure is maintained at low temperatures since any departure from ferromagnetic coupling between various octahedral ions, with consequent change of sign in the scattering amplitude, affects the calculated intensity pronouncedly.

SCATTERING BY MAGNETIZED SAMPLES

The magnetic contribution to the observed intensity of scattering in the diffraction pattern will depend according to Eq. (2) upon the relative orientation of the scattering vector and the ionic magnetic moment vector. Since the latter can be controlled in a ferromagnetic sample by application of a suitably high external magnetic field, there should be intensity changes when the field is altered either in strength or direction of application. By comparing the observed change with that calculated from the theory, it is possible to determine directly the magnetic component of the observed intensity and this would serve as an independent test on the magnetic scattering aside from the form-factor analysis discussed in the last section.

The diagrams shown in Fig. 6 illustrate the experimental arrangements of interest here. A monochromatic beam of neutrons is incident upon the polycrystalline ferromagnetic sample which is located within the pole gap of an electromagnet. The intensity of scattering in a portion of one of the Debye rings produced by the sample is studied (1) for the unmagnetized sample, (2) with the sample magnetized in a direction parallel to the scattering vector (arrangement (a) in the figure), and (3) with the sample magnetization perpendicular to the scattering vector [arrangement (*b*)]. According to Eqs. (2) and (4) the magnetic cross sections and hence intensities should have relative values for these three cases, $\frac{2}{3}$, 0, and 1, respectively.

For this purpose an electromagnet capable of producing a magnetic field of about 8000 oersteds in a 1-in. gap was mounted on the axis of the conventional powder diffraction spectrometer. The orientation of this field relative to the plane of scattering could be selected by suitable arrangement of the magnet. The state of magnetization of the sample was followed by search coil measurements of the magnetic field intensity at the surface of the sample. Normal sample size was about 1 in.$\times 1\frac{1}{2}$ in. in area and thickness $\frac{1}{4}$ in. or $\frac{3}{8}$ in. with the field application along the 1 in. direction.

The first measurements of this type were made with small blocks of pure Armco iron with studies of the (110) and (200) intensity as a function of magnetization strength and direction. It was found that the intensity of scattering was decreased relative to the unmagnetized sample value when the field was applied parallel to the scattering vector, as is expected from the theory. On the other hand, the intensity also decreased when the sample was magnetized perpendicular to the scattering vector, an effect which was not at first expected. The decrease in this case arises from the fact that in the scattering process for the case of field perpendicular to the scattering vector the neutrons are partially polarized and these will experience a different transmission cross section in their passage through the polycrystalline iron block. When the attenuation effects characteristic of the partially polarized beam produced upon scattering are properly taken into account, one calculates for the

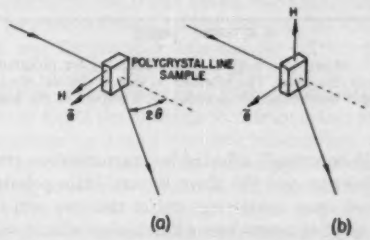

FIG. 6. Diagram of experimental arrangement used in the study of neutron scattering by magnetized, ferromagnetic substances. In (a) the applied magnetic field is in the plane of scattering and parallel to the scattering vector. In (b) the field is perpendicular to both.

(110) Fe reflection a decrease upon magnetization of 4.8 percent which agrees quite well with the experimentally observed value of 5.1 percent. Thus in spite of the larger cross section for scattering when $q^2=1$, the scattered beam is attenuated more in the sample and the expected intensity change is reversed.

The intensity effects which arise with iron upon magnetization are quite small as illustrated and this is because the magnetic scattering amplitudes are small in comparison to the unfavorably large nuclear scattering amplitude. More favorable cases are suggested for certain reflections of Co and Fe_3O_4 already discussed. The nuclear scattering amplitude for Co is quite small and should permit very large intensity effects upon magnetization but it is difficult to saturate magnetically. Magnetite on the other hand is rather easy to saturate magnetically and some of its reflections are very favorable for the present purpose. The (111) Fe_3O_4 reflection is almost completely magnetic in origin (see Table II) and this offers two advantages: (a) the inten-

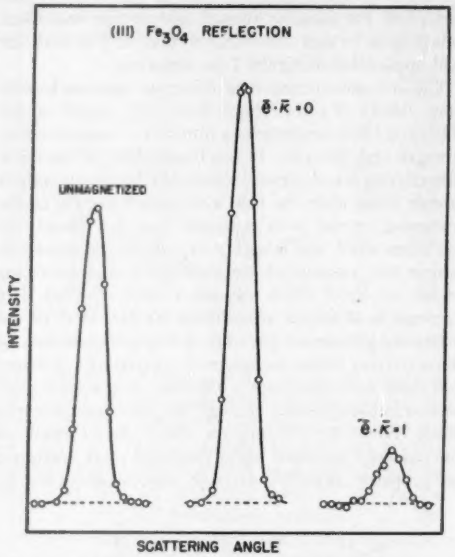

FIG. 7. Study of the (111) Fe_3O_4 reflected for different magnetization directions. The intensity is seen to depend strongly on the sample magnetization direction with respect to the scattering vector.

sity will be strongly affected by magnetization strength and direction and (b) there is very little polarization produced upon scattering, unlike the iron and cobalt cases, so that anomalous transmission effects will not be encountered. Because of these interesting and favorable properties, magnetite was studied in some detail.

Compressed powder samples of Fe_3O_4 were held between the pole pieces of the electromagnet and again field strength measurements were made with a search coil at the surface of the sample. Figure 7 shows typical traversals taken over the (111) Fe_3O_4 powder reflection with the sample block unmagnetized and when magnetized at high field strength in the two directions shown schematically in Fig. 6. It is seen that the scattered intensity varies pronouncedly with field direction. Figure 8 summarizes the data taken with varying field strength for the two field orientations and shows the saturation effects characteristic of increasing domain alignment with increasing field strength.

On Fig. 8 are shown the cross sections, $(C^2+\frac{2}{3}D^2)$, C^2, and (C^2+D^2) which correspond to the unmagnetized and two magnetized states. The nuclear cross section term C^2 is very much smaller than D^2 for this particular Fe_3O_4 reflection, in good agreement with the structure factor calculations outlined in an earlier section. Actually the nuclear scattering contribution to this reflection is even smaller than is shown in Fig. 8 because there is some second-order wavelength contamination from other reflections which accidentally contribute intensity to the position of measurement. In contrast to this distribution of intensity in the (111) reflection, Fig. 9 shows the intensity variation with field in the (220) reflection. For this reflection, the nuclear and magnetic contributions are about equal so that the intensity splitting is not as pronounced as for the (111) reflection. This close equality of nuclear and magnetic scattering in the (220) reflection allows for very interesting neutron polarization phenomena which will be discussed in a following section.

In all of the foregoing considerations, the agreement between experiment and theory was based upon the Schwinger[12] (H−J) formulation of the interaction vector $\mathbf{q}$. The numerical value of this vector squared follows from Eq. (2) as

$$q^2=\sin^2\alpha, \tag{9}$$

where α is the angle between the scattering and magnetization vectors, $\mathbf{e}$ and $\boldsymbol{\kappa}$. Prior to the Schwinger and (H−J) treatments, Bloch[13] had developed the interaction vector into the form

$$\mathbf{q}_0=\mathbf{e}(\mathbf{e}\cdot\boldsymbol{\kappa}) \tag{10}$$

with $q_0^2=\cos^2\alpha$. The difference between these two expressions for the angular dependence of magnetic scattering is related to the question as to whether the neutron in its passage through a ferromagnetic medium is affected by the magnetic field strength H or by the magnetic induction B. Ekstein has discussed this relationship recently[14] with particular reference to the interpretation of magnetized mirror experiments. The present experiments on the effect of magnetization direction upon the scattered intensity serves as a direct confirmation of the form of the magnetic interaction. After correcting the (111) Fe_3O_4 reflection for residual

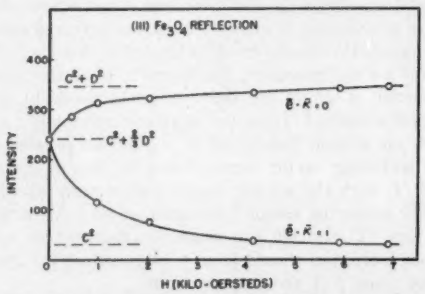

FIG. 8. Magnetic saturation for the (111) Fe_3O_4 reflection for different field directions. The variation with field strength illustrates the realignment of magnetization within the various domains into a direction parallel to the field. The nuclear scattering C^2 is seen to be very much smaller than the magnetic scattering for this reflection.

[12] J. S. Schwinger, Phys. Rev. **51**, 544 (1937).
[13] F. Bloch, Phys. Rev. **50**, 259 (1936); **51**, 994 (1937).
[14] H. Ekstein, Phys. Rev. **76**, 1328 (1949).

nuclear and second-order wavelength scattering, the remaining magnetic scattering cross section has been interpreted in terms of q^2 for four different experimentally-used values of the angle α: 0°, 23°, 54° (effective value for unmagnetized sample), and 90°. These values for q^2, normalized to the unmagnetized value of $\frac{2}{3}$, are shown in Fig. 10 along with the two theoretical curves. Within the experimental uncertainty of perhaps 2 percent the agreement with the Schwinger-Halpern-Johnson treatment is very satisfactory. Hughes and Burgy[3] in a recent study of critical reflection from magnetized mirrors have arrived at a similar conclusion although perhaps not within as close limits as in the present work.

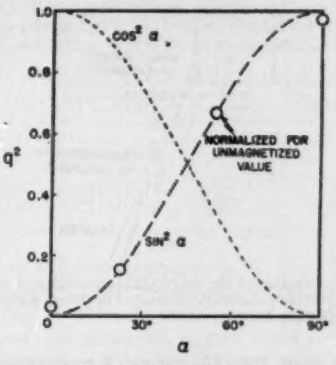

FIG. 10. Variation of q^2 with the angle α between the and scattering vectors.

POLARIZATION EFFECTS IN THE NEUTRONS SCATTERED BY MAGNETIZED SAMPLES

The commonly used method of producing a polarized neutron beam has been by transmission through highly magnetized samples of a ferromagnetic substance, usually pure iron, which possesses a different transmission cross section for the two characteristic spin states of the neutron. Supplementing this technique, Hughes and Burgy[3] have reported on the polarization effects associated with highly collimated neutron beams reflected from magnetized mirror surfaces. The present experiments are concerned with polarization of the neutrons diffracted by a crystal and are thus complimentary to the usual transmission experiments.

In the case of polarization by transmission, neutrons of one spin state are scattered out of the direct beam preferentially to those of the opposite spin state and a high degree of polarization is reached only asymptotically as larger and larger thicknesses are traversed. When one observes directly the neutrons diffracted by a small crystal it is theoretically possible to obtain complete polarization in a single scattering process. This follows from Eq. (1) in which, for the case of magnetization perpendicular to the scattering vector, $q^2=1$ and the differential cross section for unpolarized incident neutrons reduces to $(C\pm D)^2$. This is evident from the fact that an unpolarized beam can be resolved into two

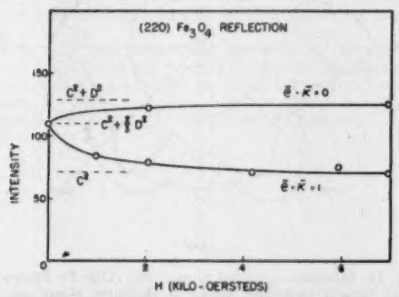

FIG. 9. Magnetic saturation for the (220) Fe_3O_4 reflection for different field directions. For this reflection the nuclear and magnetic scattering components are about equal.

equal and independent components of opposite spin state which can be arbitrarily taken parallel and antiparallel to the direction of the applied field. If the magnetic amplitude D and the nuclear amplitude C are equal for some reflection (hkl) of a crystal, the scattering will be zero for one spin state and the diffracted beam will be completely polarized. Lack of equality in the amplitudes will result in only partial polarization. As seen from Fig. 3 the first reflection from cobalt satisfies the condition for nearly complete polarization.

For those cases then where the nuclear and magnetic scattering amplitudes are known, it is possible to predict for a polycrystalline sample the degree of polarization for any given reflection and for any direction of observation relative to the direction of magnetization. The intensity of the diffracted beam from a powdered crystal is very low and hence it was considered of practical interest to see what degree of polarization could be achieved in the much more intense reflections from single crystals. The relation between the diffracted intensity and the atomic scattering amplitudes for a real single crystal depends strongly on the mosaic structure of the crystal and hence it is necessary to actually measure the polarization which can be obtained in a given case.

The polarization in the reflected radiation has been studied in two cases: the (110) reflection for Fe and the (220) reflection in Fe_3O_4. By calculation the maximum polarization to be expected in the former case is about 60 percent whereas it should be 100 percent in the latter case because of the close equivalence of the amplitudes as is evident in Fig. 9. The iron single crystal was prepared by the Bridgeman method from the melt by Mr. Frank Sherrill of this laboratory and contained 5 weight percent of silicon for phase stabilization. A thin slice of metal about $\frac{1}{2}$-in. round and $\frac{1}{4}$-in. thick was cut from the single crystal ingot with the Fe (110) plane in the surface of the slice. A natural crystal of magnetite, Fe_3O_4 of unknown purity, was used in the second examination again with a thin slice about $\frac{1}{16}$-in. thick

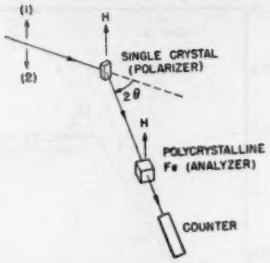

FIG. 11. Diagram of the experimental arrangement used in the study of neutron polarization produced by Bragg scattering from a magnetized crystal.

cut out along the (220) plane. Magnetization of the polarizing crystals was accomplished with an Alnico permanent magnet with H at the crystal surface about 4500 oersteds. The magnetization direction was within the plane of the crystal slices and along the [100] direction in both cases. Neutrons were reflected from internal planes within the crystal slice, the crystal being set in transmission orientation. A schematic diagram of the experimental arrangement is shown in Fig. 11.

The degree of polarization in the Bragg reflected neutron beam was studied by passing it through magnetized analyzing blocks of pure iron. Since the transmission cross section of the magnetized, analyzing block will depend upon the polarization, the latter can be evaluated if the properties of the analyzer are known. The analyzing block thickness was normally 1 in., although measurements were made with other thickness, and it was magnetized with an electromagnet to a field strength of about 8000 oersteds. The experimental procedure consisted of measuring the intensity of the polarized beam after passage through the analyzer when the latter was magnetized parallel to the polarizing fields and when unmagnetized. A magnetic field survey was conducted of the stray field between the polarizing and analyzing magnets and it was established that there was always a residual field of at least one hundred oersteds parallel to these two source fields. This situation sufficed then to insure that the neutron polarization was not altered in passing from polarizing region to analyzing region. Reversing the analyzing field with consequent depolarization effect on the beam was found to seriously effect the transmitted intensity as was to be expected.

Halpern and Holstein[1] have given general formulas describing the passage of a neutron beam through magnetized media, including the beam depolarization effects which arise when the medium is not magnetically saturated. Since the analyzing magnet in the present study was not of sufficient strength to saturate the analyzing block, it was necessary to take into consideration these depolarization effects. Their equations show that the depolarization can be allowed for in the polarization evaluation if measurements of the single transmission effect in the analyzing block are obtained with both the polarized beam and with an unpolarized beam. The latter was obtained by substituting a Cu single crystal in (111) reflecting orientation for the polarizing, ferromagnetic crystal.

In this method of polarization analysis, the nuclear and magnetic scattering amplitudes for Fe as determined in the earlier studies were used. Also in the theory application it was assumed that there existed no preferred orientation of crystallites in the polycrystalline analyzer and that the grain size was sufficiently small that the Debye-Scherrer diffraction rings were uniformly populated. This assumption, which has been implicitly accepted in all transmission studies to date, was found to be rather difficult to meet and is worthy of discussion. In studying the polarization produced in the (110) reflection from the magnetized Fe crystal, discordant results were obtained for various analyzing blocks cut from cold-rolled steel and Armco iron and further study showed that this was due to strong preferred orientation in the former and to large grain size (250μ) in the latter. As typical of these effects, there is shown in Fig. 12 the intensity distribution around the (110) Debye rings produced by two of the analyzing blocks with monochromatic incident neutron radiation. In all of the theoretical formulas developed for the polarization cross section it is assumed that this intensity distribution is uniform so that it is not surprising that the theory application would be poor for such an analyzer. Hughes and co-workers[4] have already pointed out that single transmission measurements are affected by orientation in the block although they do not appear

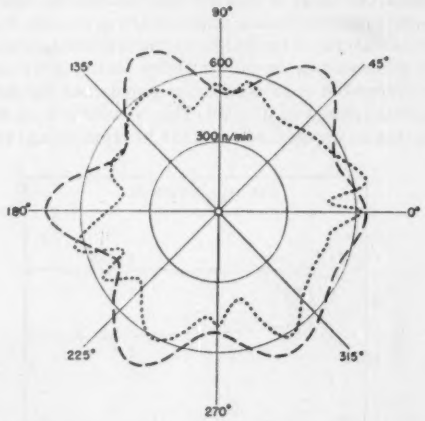

FIG. 12. Intensity variation around the (110) Fe Debye ring for two typical analyzing blocks of thickness about one centimeter. The dashed line is for a sample of cold-rolled steel (grain size about 25μ) and the dotted line is for an Armco block (grain size about 250μ).

to have taken it into account in their evaluation* of the polarization cross section for a thermal neutron distribution. It was found possible to obtain essentially complete randomness in grain orientation with a suitably small grain size (about 10μ) by solidification from the melt followed by repeated quenching of hot Armco blocks (900°C) in a dry ice-acetone mixture. This material was then cut into suitable analyzing blocks and these were used for studying the polarization in the Bragg beam from a polarizing crystal.

Table III summarizes measurements taken of the single transmission effect in a 1-in. thick analyzing block for the three different Bragg reflected beams. The unpolarized beam from a Cu crystal showed a +4.6 percent single transmission effect in the analyzing block and this served to establish the depolarization parameter in the analyzing block arising from incomplete magnetic saturation. Using the observed −3.0 percent effect with the polarized Fe beam, the polarization is calculated to be about 41 percent. This is somewhat smaller than the theoretical value for Fe (110) of 63 percent and may be caused by crystal extinction effects, silicon impurity in the crystal or lack of magnetic saturation in the polarizing crystal. All of these effects would tend to reduce the polarization from that predicted by the simple theory. The observed single transmission effect for the Fe_3O_4 (220) polarized beam is very much larger than for the other reflections, amounting to +24 percent and the evaluated polarization turns out to be 104 percent, which of course is impossibly high. It is felt that the measurements are accurate enough to say that the polarization is complete within about 5 percent which means that the relative neutron population in the two spin states is in ratio at least 40 to 1.

A very interesting further observation is to be noted in the data of Table III and this is the fact that the signs of the single transmission effect in the analyzing block for the Fe (110) and Fe_3O_4 (220) reflections are reversed. This indicates that the directions of polarization in the two polarized beams are opposite and hence that the atomic magnetic moments which are responsible for the polarization are directed oppositely with reference to the applied magnetic field on the two crystals. This is just the conclusion to be drawn from an analysis of the two magnetic structures. In the iron crystal all of the magnetic moments are aligned parallel to the applied field direction. In the magnetite crystal, on the other hand, the octahedral magnetic ions are aligned parallel to the field since they are more abundant than the antiferromagnetically coupled tetrahedral ions so that the latter are aligned antiparallel to the field. According to the crystal structure factors for magnetite given in Table II, only the tetrahedral ions contribute to the (220) reflection and hence the reversed polarization in this reflection is to be expected. The polarization observation for Fe_3O_4 can be considered a very direct proof of the antiferromagnetic nature of the magnetite structure. Interestingly there are other Fe_3O_4 reflections such as the (400) which should produce the conventional polarization sense as characterized by all of the metallic iron reflections.

TABLE III. Comparison between experimental and theoretical neutron polarization in Fe (110) and Fe_3O_4 (220) reflections.

	Single transmission effect in analyzing block (1 in. thick)	Polarization calculated from data	Theoretical polarization for an ideally mosaic crystal
Unpolarized			
Cu (111)	+0.046±0.002	—	—
Polarized			
Fe (110)	−0.030±0.005	41%	63%
Fe_3O_4 (220)	+0.24±0.010	104%	100%

It is possible to obtain approximately 10^5 monoenergetic neutrons per second in the (220) Fe_3O_4 reflection using neutron radiation from a pile with a central flux of 10^{12} neutrons/cm^2 sec. This compares very favorably in intensity with other methods of polarized beam production mentioned briefly at the beginning of this section. With regard to the three methods of polarization, *viz.*, (1) transmission through polycrystalline iron, (2) critical reflection from magnetized mirrors, and (3) Bragg scattering from ferromagnetic crystals, there appear to be unique characteristics for each and the selection of the optimum method should be decided by the requirements of the use to which the polarized beam is to be put.

ACKNOWLEDGMENTS

We wish to express our indebtedness to Dr. L. C. Biedenharn and Dr. S. Bernstein for helpful discussions and to Dr. M. K. Wilkinson and Mr. L. A. Rayburn for assistance during the polarization measurements.

* This may have contributed somewhat to the differences between the Stanford and Argonne Laboratory determinations of the polarization cross section for a thermal neutron beam (see reference 2). A large part of the difference appears to have arisen because of differences in the thermal neutron spectrum.

On Shock-Wave Phenomena; Refraction of Shock Waves at a Gaseous Interface*

H. POLACHEK AND R. J. SEEGER
Naval Ordnance Laboratory, Silver Spring, Maryland
(Received April 9, 1951)

This paper treats the problem of the refraction of a shock wave at a gaseous interface. The governing equations are formulated and analyzed. Continuous families of solutions are obtained numerically for a number of gas combinations at varying angles of incidence on a plane interface between ideal gases (characterized by a certain range of parameters). It is believed that these solutions, which represent a three-wave configuration at the interface with a reflected shock wave or with a reflected rarefaction wave, are physically real inasmuch as they tie in with the two known limiting solutions of an infinitesimal shock at any angle of incidence and of any finite shock at normal incidence. Two of the significant features of the present solutions are: (1) regular refraction (three-wave configuration at the interface) does not occur at glancing incidence and (2) in the region of regular refraction there is no "total reflection" of finite shock waves.

I. INTRODUCTION

THE relations governing the refraction of a plane shock wave at a free plane surface can be easily formulated.[1,2] An exhaustive analysis, however, based on these equations is rather difficult owing to their algebraic complexity. For instance, there are a total of five independent parameters entering into the problem. Furthermore, for a fixed set of these parameters it is usually possible to obtain more than one mathematical solution. Hence it is necessary to determine which of the solutions are physically plausible. Moreover, in general, two types of refraction paterns exist; the one with a reflected shock wave, the other with a reflected rarefaction wave. It is desirable to be able to predict which of these two types of configurations will occur for a given set of parameters.

In this paper an attempt is made to resolve the above questions for the refraction of a shock wave at a gaseous interface. Use is made of mathematical analysis, of physical intuition, and of extensive numerical calculations, without which so complex a survey would not be feasible.[3] (Unfortunately only a few exploratory experimental observations have been made to date.[4]) It is heuristically postulated that the physically plausible solutions are those which tie in continuously with the solutions for the limiting strength of an acoustic wave, and with those[5] for the limiting angle of normal incidence of a shock wave of finite strength.

II. GOVERNING RELATIONS

We shall employ a simple model of a constant shock wave in the form of a plane step-shock.[1,6] Consider such a step-shock traveling in a uniform gaseous medium and impinging at an arbitrary angle ω upon a second medium with different physical characteristics. By analogy with the case of normal incidence[7] it may be expected that a shock wave will be transmitted into the second medium, and that either a second shock wave or a rarefaction wave will be reflected back into the original medium. In the first instance, the resulting pattern will be a triple-shock configuration; in the second case, a refraction configuration will be formed consisting of two confluent shocks and an angular rarefaction wave.

We shall limit our discussion to ideal gases, and shall specify their physical states by γ_0, γ_1, the ratios of specific heats; c_0, c_1, the acoustic speeds; and p_0, p_1, the pressures in the two regions, respectively (it is noted that for equilibrium $p_0=p_1$). We postulate also the absence of thermal conductivity and viscosity, and uniformity of pressure in the regions bounded by shock waves and/or rarefaction waves. Let the strength ξ of the shock wave I (see Fig. 1) incident at the interface D of the undisturbed media be measured by the ratio of the pressure in front of the shock wave to that behind it. Then we can immediately obtain the other physical quantities pertaining to the shock I in terms of the variables ξ and ω by use of the well-known Rankine-Hugoniot relations.[1,6] We now formulate the problem from the stationary point of view of an observer traveling with the triple point 0 (representing the contact of the incident shock I and the surface D), for which the following relations hold:

$$\eta=\frac{(\gamma_0+1)\xi+(\gamma_0-1)}{(\gamma_0-1)\xi+(\gamma_0+1)},\quad \sigma=\left[\frac{(\gamma_0+1)\xi+(\gamma_0-1)}{2\gamma_0}\right]^{\frac{1}{2}},\quad \tau=\frac{(\gamma_0-1)\sigma^2+2}{(\gamma_0+1)\sigma}, \tag{1}$$

* Sponsored by the ONR. Presented in preliminary form at the Seventh International Congress on Theoretical and Applied Mechanics (London, 1948).

[1] H. Polachek and R. J. Seeger, *Proceedings of Symposia in Applied Mathematics* 1 (American Mathematical Society, New York, 1949), pp. 119–144.

[2] A. H. Taub, Phys. Rev. 72, 51 (1947).

[3] The authors acknowledge the helpful interest of the IBM World Headquarters Staff in carrying out the final computations on the IBM Selective Sequence Electronic Calculator.

[4] D. Bitondo, University of Toronto Institute of Aerophysics Report No. 7 (June, 1950). D. H. Henshaw, University of Toronto Institute of Aerophysics Report No. 11 (October, 1950).

[5] R. Courant and K. Friedrichs, Office of Scientific Research and Development Report 1567 (1943); *Supresonic Flow and Shock Waves* (Interscience Publishers, Inc., New York, 1948).

[6] H. Polachek and R. J. Seeger, BuOrd Explosives Research Report No. 13 (1944).

[7] G. I. Taylor and J. W. Maccoll, "The mechanics of compressible fluids," *Aerodynamic Theory* (W. F. Durand, Stanford University, California, 1934) Vol. 3, pp. 243–246.

where $\eta \equiv$ density ratio across shock I (normalized with respect to the region behind I), $\sigma \equiv$ material speed (normalized with respect to the acoustic speed behind I) behind I and normal to it, and $\tau \equiv$ material speed (normalized with respect to the acoustic speed behind I) in front of I and normal to it.

The tangential material speed t along the shock front I, is unchanged across the shock and is given by

$$t = \tau \cot\omega. \tag{2}$$

Thus the velocity of the gas flow in the region between the shocks I and R (reflected shock) is determined by the media characteristics (γ_0, γ_1, c_0, c_1, ρ_0) and the shock-wave characteristics (ξ, ω). Suppose β, the angle between the two shocks, is also known. Resolving the material velocity in that region into components σ' normal to the shock R and t' tangential to it, we obtain

$$\begin{aligned} \sigma' &= t\sin\beta + \sigma\cos\beta, \\ t' &= t\cos\beta - \sigma\sin\beta, \end{aligned} \tag{3}$$

where a positive value of t' signifies the direction along R toward 0.

We now apply the Rankine-Hugoniot relations to the reflected shock R to obtain ξ' and τ' for the reflected shock wave (analogous to ξ and τ for the incident shock). We normalize with respect to the same region as that above, i.e., the region ahead of shock R. We thus obtain

$$\begin{aligned} \xi' &= [2\gamma_0\sigma'^2 - (\gamma_0 - 1)]/(\gamma_0 + 1), \\ \tau' &= [(\gamma_0 - 1)\sigma'^2 + 2]/(\gamma_0 + 1)\sigma'. \end{aligned} \tag{4}$$

In this case τ' is the material speed behind the shock front R. The angle between the shock front R and the direction of flow behind it is given by

$$\delta_R = \tan^{-1}(\tau'/-t'). \tag{5}$$

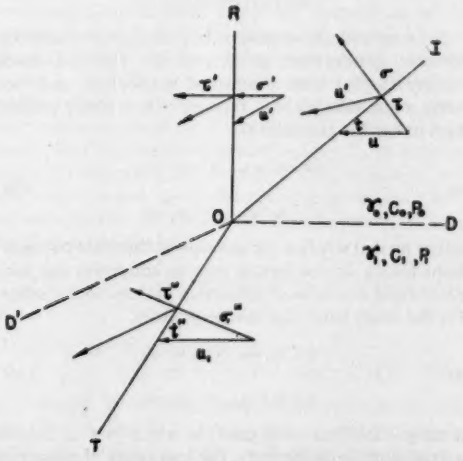

FIG. 1. Triple-shock configuration.

In the case where a rarefaction wave rather than a shock is reflected, we must replace the Rankine-Hugoniot relations with the equivalent equations governing a Prandtl-Meyer angular rarefaction wave. We include first the expression for the material speed behind the incident shock I (normalized with respect to the acoustic speed in the same region). Thus

$$u' = (\sigma^2 + \beta^2)^{\frac{1}{2}}. \tag{3'}$$

We denote by $\bar{u}$ the material speed behind the Prandtl-Meyer wave (normalized with respect to the acoustic speed in that region) and calculate the difference behind the directions of material flow ahead and behind this wave, which we denote by $(\bar{\nu} - \nu')$. This is given by the expression[7]

$$\begin{aligned} \bar{\nu} - \nu' = \left(\frac{\gamma_0+1}{\gamma_0-1}\right)^{\frac{1}{2}} &\left\{ \tan^{-1}\left[\frac{(\gamma_0-1)(\bar{u}^2-1)}{\gamma_0+1}\right]^{\frac{1}{2}} \right. \\ &\left. - \tan^{-1}\left[\frac{(\gamma_0-1)(u'^2-1)}{\gamma_0+1}\right]^{\frac{1}{2}} \right\} \\ &+ \left[\cos^{-1}\frac{1}{u'} - \cos^{-1}\frac{1}{\bar{u}}\right]. \end{aligned} \tag{4'}$$

Next we replace Eq. (5) by an analogous Eq. (5') for the angle subtended by the incident shock I and the material velocity behind the Prandtl-Meyer wave,

$$\lambda_R = 2\pi - \tan^{-1}(\sigma/t) + (\bar{\nu} - \nu'). \tag{5'}$$

For the purpose of considering the gas flow across the transmitted shock T it is convenient to normalize with respect to the region ahead of T instead of that behind I, i.e., γ_1, c_1, ρ_1. Accordingly, let ξ'' represent the ratio of the pressure behind shock T to that ahead of it. It follows by virtue of the equality of pressures on both sides of the interface D' that

$$\xi'' = \xi'/\xi \tag{6}$$

for the case of a reflected shock wave, whereas

$$\xi'' = \frac{\xi'}{\xi} = \frac{1}{\xi}\left(\frac{\bar{p}}{p'}\right) = \frac{1}{\xi}\left[\frac{(\gamma_0-1)u'^2+2}{(\gamma_0-1)\bar{u}^2+2}\right]^{\gamma_0/(\gamma_0-1)} \tag{6'}$$

for a reflected rarefaction wave (where p' and $\bar{p}$ are the pressures before and after the Prandtl-Meyer wave, respectively).

We apply again the Rankine-Hugoniot relations across the transmitted shock T, and obtain

$$\begin{aligned} \sigma'' &= [\{(\gamma_1+1)\xi'' + (\gamma_1-1)\}/2\gamma_1]^{\frac{1}{2}}, \\ \tau'' &= [(\gamma_1-1)\sigma''^2 + 2]/(\gamma_1+1)\sigma''. \end{aligned} \tag{7}$$

The material speed in the region ahead of shock T (normalized with respect to the acoustic speed in that region) is given by

$$u_1 = (\tau/\sin\omega)(\eta/\xi)^{\frac{1}{2}}(c_0/c_1). \tag{8}$$

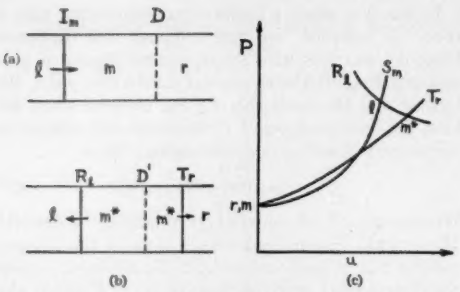

FIG. 2(a) Normal incidence of shock wave-initial state. (b) Normal incidence of shock wave-final state. (c) Material-speed-pressure diagram at normal incidence.

Also, the angle ϕ between shocks I and T, and t'' the material speed tangential to T are given by

$$\phi-\omega=\sin^{-1}(\sigma''/u_1), \quad t''=\sigma''\cot(\phi-\omega), \tag{9}$$

respectively, where a positive value of t'' signifies the direction along t toward 0.

Finally, for the case of a reflected shock wave the angle subtended by the reflected shock wave R and the direction of material velocity behind T is given by

$$\delta_T=2\pi-[\phi+\beta+\tan^{-1}(\tau''/-t'')]. \tag{10}$$

Thus the condition that the flow on both sides of the slipstream D' be parallel requires the equality

$$\delta_R=\delta_T. \tag{11}$$

For the case of a reflected rarefaction wave, on the other hand, the two analogous equations are

$$\lambda_T=2\pi-\phi-\tan^{-1}(\tau''/-t''), \tag{10'}$$

and

$$\lambda_R=\lambda_T. \tag{11'}$$

III. LIMITING SOLUTIONS

The equations derived in the previous section constitute a complete mathematical solution of the refraction of a shock wave at a gas-gas interface. As previously pointed out, however, a number of physically extraneous solutions may exist, and considerable care must be exercised in order to ascertain the physically likely roots. For instance, if the branch which is the counterpart of that used in the simple three-shock theory[1,6] be continued to $\omega=0$ (normal incidence) a reflected wave of infinite strength is obtained. Accordingly, we shall choose, as physically likely, those solutions which can be continuously connected with the known solutions for infinitesimal (acoustic) waves at any incidence angle and for finite waves at normal incidence.

For the case $\xi=1$ (acoustic limit) Snell's law of refraction, *viz.*,

$$\sin\omega/\sin(\phi-\omega)=c_0/c_1, \tag{12}$$

is known to be physically satisfactory.

The law for the interaction of a shock wave with a free surface at normal incidence may be obtained simply from the equality of material velocities on both sides of the interface (both before and after the interaction). For the case of a reflected shock wave it may be given in the form[1,5]

$$(\tau'-\sigma')+(\tau-\sigma)+(\xi/\eta)^{\frac{1}{2}}(c_1/c_0)(\tau''-\sigma'')=0; \tag{13}$$

and for a reflected rarefaction wave as

$$\frac{2}{\gamma_0-1}\left[1-\left(\frac{\bar{p}}{p'}\right)^{(\gamma_0-1)/2\gamma_0}\right]+(\tau-\sigma)+\left(\frac{\xi}{\eta}\right)^{\frac{1}{2}}\left(\frac{c_1}{c_0}\right)(\tau''-\sigma'')=0. \tag{13'}$$

IV. TRANSITION BETWEEN REFRACTION PATTERNS

Another interesting special solution of the refraction problem of particular significance in the investigation of the type of refraction pattern that takes place under given conditions is the transition solution. If we stipulate that no reflected wave (i.e., $\xi'=1$) be produced at all, we obtain the following quadratic expression in terms of $S=\sin^2\omega_t$, where ω_t is the transition angle at which such a configuration occurs:

$$4\gamma_1(1-\xi^2)\left[\frac{\gamma_0\alpha_1}{\gamma_1\alpha_0 a}-1\right]S^2+\left[\alpha_0\alpha_1\left(a-\frac{1}{a}\right)+4(\gamma_1-\gamma_0)(1-\xi^2)\right]S+\alpha_0[\alpha_0-\alpha_1 a]=0; \tag{14}$$

where the quantities α_0, α_1 and a are defined as follows,

$$\alpha_0\equiv(\gamma_0+1)+(\gamma_0-1)\xi, \quad \alpha_1\equiv(\gamma_1+1)+(\gamma_1-1)\xi, \quad a\equiv(c_0/c_1)^2(\gamma_1/\gamma_0). \tag{15}$$

Since no reflection wave exists at ω_t, any transition between a refraction pattern of the reflected shock variety to that with a reflected rarefaction, and vice versa, must take place at this angle. It is easily verified that under the conditions

$$\begin{aligned} &a<\alpha_0/\alpha_1, \quad a>\alpha_1/\alpha_0; \\ \text{or} \quad &a>\alpha_0/\alpha_1, \quad a<\alpha_1/\alpha_0; \end{aligned} \tag{16}$$

either no real solution for ω_t exists or there are two solutions for ω_t. In the former case no transition can take place from one type of refraction pattern to the other. On the other hand, for the inequalities

$$\begin{aligned} &a<\alpha_0/\alpha_1, \quad a<\alpha_1/\alpha_0 \\ \text{or} \quad &a>\alpha_0/\alpha_1, \quad a>\alpha_1/\alpha_0 \end{aligned} \tag{16'}$$

a unique solution must exist, in which case ω_t acts as a transition value between the two types of refraction configurations.

For the case of normal incidence it is actually possible to determine the type of refraction pattern that may be expected to occur by a method introduced by Courant and Friedrichs.[5] In this case it can be shown that the problem has a unique solution, and that the reflected wave must be either a shock wave or a rarefaction wave depending upon the relative magnitudes of a generalized acoustic impedance in the two media under consideration. The method consists of an analysis of a material-speed-pressure $(u-p)$ plot of the various physical states before and after the interaction. We will sketch here only the general procedure. In Fig. 2(a), I_m represents the incident shock wave, traveling from the disturbed left l to an undisturbed middle m of the initial medium, while D is the interface front of the second medium on the right r. In Fig. 2(b), R_l and T_r represent the two waves (shock or rarefaction) traveling to the left and right, respectively, after the collision of I_m with D has taken place. The states l and r remain the same, but a new middle state m^* has been produced by the interaction. In general, there exists in this region a new interface D' across which there is no variation in pressure or velocity.

In Fig. 2(c) the pressure in each state is plotted against the material speed. Thus r and m are represented by the same point, while l is to the right (since $u_l > u_m$) and above m (or r). We draw S_m, which is the curve of all possible states which can be connected to m by means of a shock wave (traveling toward the right). Naturally this curve must pass through l. We next draw T_r and R_l which represent the totality of states which can be connected to r and l, respectively, either by means of a shock or rarefaction wave. These are monotonically increasing or decreasing functions and can intersect only at one point m^*. It is apparent that this intersection occurs on the upper part of T_r, which must represent a state that can be connected to r only by means of a shock wave (since the pressure at m^* is greater than that at r). Hence a shock wave is always transmitted. The reflected wave, however, may be either a shock wave or a rarefaction wave depending on whether l is below or above T_r. For the case $\gamma_0=\gamma_1$ (the only one considered by Courant and Friedrichs) it is shown that S_m lies either entirely above T_r or entirely below it, depending on whether $\rho_r<\rho_m$ or $\rho_r>\rho_m$, respectively (ρ_r and ρ_m are the densities in regions r and m, respectively). In the general case, however, T_r and S_m intersect at the point

$$\tau(\xi)-\sigma(\xi)=(\xi/\eta)^{\frac{1}{2}}(c_1/c_0)[\tau''(1/\xi)-\sigma''(1/\xi)] \quad (17)$$

or

$$(1/c_0)[\gamma_0((\gamma_0+1)+(\gamma_0-1)\xi)]^{\frac{1}{2}} = (1/c_1)[\gamma_1((\gamma_1+1)+(\gamma_1-1))\xi]^{\frac{1}{2}}. \quad (17')$$

Accordingly, if we designate the expressions on the left and right of Eq. (17′) by A_0 and A_1, respectively, a shock or rarefaction wave will occur according as $A_0<A_1$ or $A_0>A_1$, respectively. For an acoustic wave

TABLE I. List of problems for which numerical solutions have been carried out on the Selective Sequences Electronic Calculator.

Problem	γ_0	γ_1	$(c_0/c_1)^2$	Gases
1	5/3	1.4	0.835	Argon-Nitrogen
2	1.4	5/3	0.120	Air-helium
3	1.4	1.4	0.875	Oxygen-nitrogen
4	1.4	4/3	0.600	Air-methane
5	4/3	1.4	0.600	Carbon dioxide-air
6	1.1	1.4	0.190	Freon-air
7	1.1	5/3	0.020	Freon-helium
8	5/3	1.1	0.800	Krypton-propane
9	5/3	5/3	0.240	Krypton-neon
10	1.1	5/3	0.460	Freon-krypton
11	1.1	5/3	0.600	Propane-argon
12	1.1	1.4	0.013	Freon-hydrogen
13	1.4	5/3	1/0.835	Nitrogen-argon
14	5/3	1.4	1/0.120	Helium-air
15	1.4	1.4	1/0.875	Nitrogen-oxygen
16	4/3	1.4	1/0.600	Methane-air
17	1.4	4/3	1/0.600	Air-carbon dioxide
18	1.4	1.1	1/0.190	Air-freon
19	5/3	1.1	1/0.020	Helium-freon
20	1.1	5/3	1/0.800	Propane-krypton
21	5/3	5/3	1/0.240	Neon-krypton
22	5/3	1.1	1/0.460	Krypton-freon
23	5/3	1.1	1/0.600	Argon-propane
24	1.4	1.1	1/0.013	Hydrogen-freon

$(\xi=1)$ the equality of these two quantities implies the equality of the acoustic impedances of the two media. Hence these quantities may be regarded as generalized expressions for the acoustic impedance. Thus we have found a definite criterion to determine the type of refraction pattern at $\omega=0$. The type of refraction pattern cannot change for larger angles of ω until ω_l is reached. Therefore, we can continue the solution of the problem from $\omega=0$ to the angle of incidence ω_l with the same reflection pattern. Beyond ω_l a change will, in general, occur from one type of refraction pattern to the other. As will be seen later, this may occur on the nonphysical portion of the curve.

There are two a priori limitations on the magnitude of ω for which physical solutions of the refraction equations can exist: (a) For the reflected shock-wave type the inequality $\omega \leqslant \omega_L$, where

$$\sin^2\omega_L = a\alpha_0/\alpha_1, \quad (18)$$

must be satisfied in order that the angle $(\phi-\omega)$ be real; and (b) for both types of patterns $\omega \leqslant \omega_1$, where

$$\tan\omega_1 = \tau(1-\sigma^2)^{-\frac{1}{2}} \quad (19)$$

must hold in order that supersonic flow normal to the reflected wave exist, i.e., $\sigma' \geqslant 1$. These bounds have been used in determining the range of ω for which the numerical calculations have been carried out. Actually there are more stringent limitations on the range of ω for which solutions exist. These will be discussed subsequently in connection with the analysis of the computational results.

V. SCOPE OF NUMERICAL CALCULATIONS

There are a total of five independent parameters in this problem γ_0, γ_1, c_0/c_1, ω and ξ; hence a complete

TABLE II. Limiting angles of incidence.

Problem	ξ	ω_t (deg)	ω_1 (deg)	ω_L (deg)
1	1.0	55.257	90.000	66.034
	0.9	55.378	74.526	65.663
	0.7	55.800	65.566	64.899
	0.5	56.534	61.439	64.108
	0.3	57.698	60.007	63.284
	0.1	59.397	61.297	62.425
	0.0	60.382	63.435	61.982
2	1.0	18.594	90.000	20.268
	0.9	18.819	74.146	20.330
	0.7	19.285	65.457	20.460
	0.5	19.766	61.945	20.602
	0.3	20.242	61.439	20.755
	0.1	20.686	64.272	20.922
	0.0	20.884	67.792	21.012
3	1.0	43.089	90.000	69.295
	0.9	44.090	74.146	69.295
	0.7	46.442	65.457	69.295
	0.5	49.429	61.945	69.295
	0.3	53.392	61.439	69.295
	0.1	59.009	64.272	69.295
	0.0	62.833	67.792	69.295
4	1.0	39.594	90.000	50.769
	0.9	40.260	74.146	50.705
	0.7	41.785	65.457	50.572
	0.5	43.618	61.945	50.433
	0.3	45.803	61.439	50.286
	0.1	48.211	64.272	50.131
	0.0	49.268	67.792	50.051
5	1.0	35.459	90.000	50.769
	0.9	36.392	74.031	50.832
	0.7	38.526	65.433	50.965
	0.5	41.110	62.115	51.108
	0.3	44.268	61.905	51.259
	0.1	48.011	65.259	51.421
	0.0	49.887	69.303	51.505
6	1.0	21.947	90.000	25.842
	0.9	22.476	73.554	25.981
	0.7	23.577	65.378	26.269
	0.5	24.714	62.929	26.569
	0.3	25.830	64.065	26.884
	0.1	26.824	70.061	27.215
	0.0	27.230	77.690	27.386
7	1.0	7.9037	90.000	8.1301
	0.9	8.0308	73.554	8.1953
	0.7	8.2094	65.378	8.3317
	0.5	8.3936	62.929	8.4770
	0.3	8.5831	64.065	8.6322
	0.1	8.7770	70.061	8.7987
	0.0	8.8754	77.690	8.8866
8	1.0	58.227	90.000	63.435
	0.9	57.693	74.526	62.555
	0.7	56.815	65.566	60.826
	0.5	56.192	61.439	59.129
	0.3	55.781	60.007	57.454
	0.1	55.355	61.297	55.792
	0.0	54.910	63.435	54.964
9	1.0	26.100	90.000	29.334
	0.9	26.369	74.526	29.334
	0.7	26.944	65.566	29.334
	0.5	27.561	61.439	29.334
	0.3	28.193	60.007	29.334
	0.1	28.784	61.297	29.334
	0.0	29.029	63.435	29.334
10	1.0	unreal	90.000	42.706
	0.9	unreal	73.554	43.123
	0.7	unreal	65.378	44.009
	0.5	11.820	62.929	44.972
	0.3	20.739	64.065	46.025
	0.1	31.192	70.061	47.183
	0.0	37.558	77.690	47.807
11	1.0	unreal	90.000	50.769
	0.9	unreal	73.554	51.323
	0.7	unreal	65.378	52.512
	0.5	unreal	62.929	53.821
	0.3	unreal	64.065	55.275
	0.1	unreal	70.061	56.903
	0.0	unreal	77.690	57.795
12	1.0	6.4783	90.000	6.5470
	0.9	6.5203	73.554	6.5794
	0.7	6.6053	65.378	6.6466
	0.5	6.6914	62.929	6.7172
	0.3	6.7783	64.065	6.7916
	0.1	6.8652	70.061	6.8699
	0.0	6.9088	77.690	6.9107
13	1.0	64.059	90.000	unreal
	0.9	64.563	74.146	unreal
	0.7	65.925	65.457	unreal
	0.5	67.952	61.945	unreal
	0.3	71.056	61.439	unreal
	0.1	76.122	64.272	unreal
	0.0	79.984	67.792	unreal
14	1.0	66.991	90.000	unreal
	0.9	68.195	74.526	unreal
	0.7	70.868	65.566	unreal
	0.5	73.947	61.439	unreal
	0.3	77.498	60.007	unreal
	0.1	81.574	61.297	unreal
	0.0	83.817	63.435	unreal
15	1.0	46.911	90.000	unreal
	0.9	48.059	74.146	unreal
	0.7	50.779	65.457	unreal
	0.5	54.295	61.945	unreal
	0.3	59.110	61.439	unreal
	0.1	66.410	64.272	unreal
	0.0	72.009	67.792	unreal
16	1.0	55.366	90.000	unreal
	0.9	56.623	74.031	unreal
	0.7	59.615	65.433	unreal
	0.5	63.493	62.115	unreal
	0.3	68.750	61.905	unreal
	0.1	76.277	65.259	unreal
	0.0	81.291	69.303	unreal
17	1.0	48.498	90.000	unreal
	0.9	49.930	74.146	unreal
	0.7	53.309	65.457	unreal
	0.5	57.647	61.945	unreal
	0.3	63.498	61.439	unreal
	0.1	71.949	64.272	unreal
	0.0	77.726	67.792	unreal
18	1.0	59.032	90.000	unreal
	0.9	60.792	74.146	unreal
	0.7	64.724	65.457	unreal
	0.5	69.308	61.945	unreal
	0.3	74.648	61.439	unreal
	0.1	80.784	64.272	unreal
	0.0	84.122	67.792	unreal
19	1.0	77.748	90.000	unreal
	0.9	78.552	74.526	unreal
	0.7	80.241	65.566	unreal
	0.5	82.049	61.439	unreal
	0.3	83.983	60.007	unreal
	0.1	86.050	61.297	unreal
	0.0	87.137	63.435	unreal
20	1.0	71.894	90.000	unreal
	0.9	72.247	73.554	unreal
	0.7	73.436	65.378	unreal
	0.5	75.478	62.929	unreal
	0.3	78.800	64.065	unreal
	0.1	84.147	70.061	unreal
	0.0	87.915	77.690	unreal
21	1.0	63.900	90.000	unreal
	0.9	65.043	74.526	unreal
	0.7	67.658	65.566	unreal
	0.5	70.814	61.439	unreal
	0.3	74.661	60.007	unreal
	0.1	79.373	61.297	unreal
	0.0	82.098	63.435	unreal
22	1.0	unreal	90.000	unreal
	0.9	unreal	74.526	unreal
	0.7	unreal	65.566	unreal
	0.5	16.848	61.439	unreal
	0.3	29.476	60.007	unreal
	0.1	44.916	61.297	unreal
	0.0	55.360	63.435	unreal
23	1.0	unreal	90.000	unreal
	0.9	unreal	74.526	unreal
	0.7	unreal	65.566	unreal
	0.5	unreal	61.439	unreal
	0.3	unreal	60.007	unreal
	0.1	unreal	61.297	unreal
	0.0	unreal	63.435	unreal
24	1.0	81.710	90.000	unreal
	0.9	82.338	74.146	unreal
	0.7	83.628	65.457	unreal
	0.5	84.985	61.945	unreal
	0.3	86.410	61.439	unreal
	0.1	87.902	64.272	unreal
	0.0	88.674	67.792	unreal

survey is not feasible. Instead, a number of typical gas combinations[8] (twenty-four) have been selected for which the values of ξ and ω are allowed to vary over the entire range. These are given in Table I. It will be noted that problems 1–12 are related to problems 13–24. In the latter the gases are inverted, so that the incident shock wave is located in the medium in which the transmitted shock is propagated in the initial setup. The

[8] The first 7 cases were investigated also by A. H. Taub (see reference 2) using the Aberdeen Electronic Numerical Integrator and Computer. Unfortunately the great majority of the solutions obtained by him were apparently of the kind believed by the present authors to be physically unlikely.

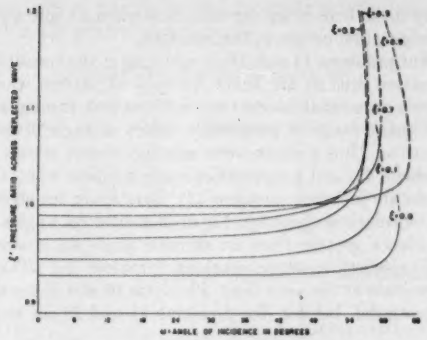

FIG. 3. Plot of strength of reflected wave *versus* angle of incidence—problem 3.

values of ξ used are $\xi=0$, 0.1, 0.3, 0.5, 0.7, 0.9, and 1.0; the values of ω have been varied from problem to problem in order to allow for the different limits in each case.

VI. ANALYSIS OF RESULTS

We shall confine our present discussion to several typical problems (the complete results are given in detail in a U. S. Naval Ordnance Laboratory report). In particular, we shall focus our attention on problems 3, 10, 11, and the corresponding problems 15, 22, and 23, in which the gas combinations are inverted. These problems represent a cross-section of the types of solutions which may generally be expected. They yield solutions which begin at $\omega=0$ with reflected shock waves as well as with rarefaction waves. Furthermore, some of the resulting curves pass through the transition stage at ω_t; in other cases, however, there is no solution of the transition Eq. (14) so that the same refraction pattern is maintained throughout the range of ω.

For both problems 3 and 15, as may be seen from Table II, the transition angle ω_t exists for all strengths ξ of the incident shock. In problem 15, however, the

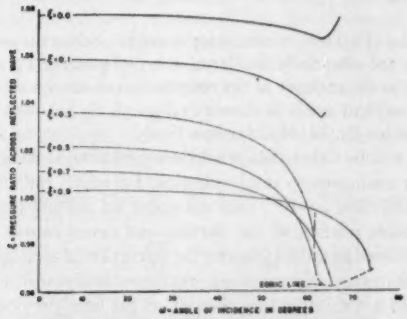

FIG. 4. Plot of strength of reflected wave *versus* angle of incidence—problem 15.

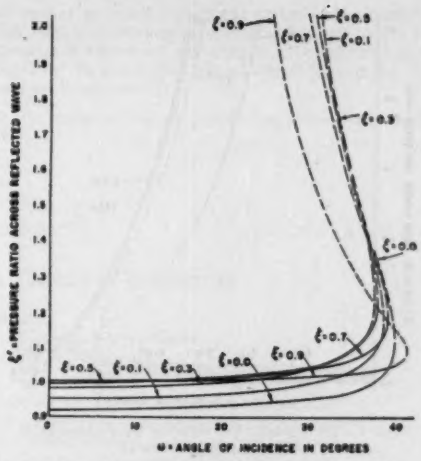

FIG. 5. Plot of strength of reflected wave *versus* angle of incidence—problem 10.

limiting angle ω_1, for which the material speed behind the incident shock becomes sonic, precedes the transition angle, ω_t (i.e., $\omega_1<\omega_t$ for strong shocks, *viz.*, $\xi=0.1$ and 0.0), so that no transition can take place for these strengths. In problem 3 a (reflected) rarefaction-wave solution exists for all values of ξ at normal incidence ($\omega=0$); whereas for the gases inverted (problem 15) there is always a (reflected) shock wave for normal incidence. The dependence of the strength ξ' of the reflected wave on the angle of incidence ω for incident shock strengths $\xi=0.9$, 0.7, 0.5, 0.3, 0.1, 0.0 is plotted in Figs. 3 and 4 for problems 3 and 15, respectively. In the case of problem 3 all curves pass through the transition angle ω_t. For an incident shock at infinite strength ($\xi=0.0$), however, the curves reach an extreme angle ω_e (beyond which no real solutions exist) in the (reflected) rarefaction phase of the problem and then pass through the transition angle ω_t at points where the apparent physical solutions no longer hold.

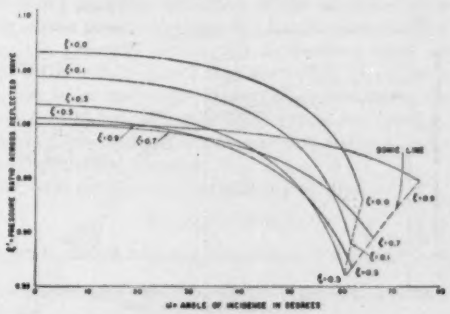

FIG. 6. Plot of strength of reflected wave *versus* angle of incidence—problem 22.

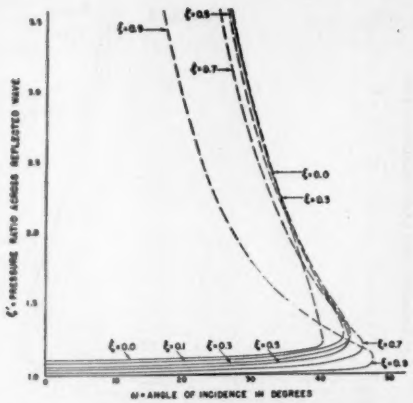

FIG. 7. Plot of strength of reflected wave *versus* angle of incidence—problem 11.

For all other incident shock strengths the curves pass through the transition stage at points on the physically plausible branch so that transition to the shock-wave pattern may actually be expected in these cases. In problem 15, on the contrary, for strong incident shocks ($\xi=0.1$ and 0.0), which undergo no transition from the original shock-wave pattern at normal incidence ($\omega=0$), the curves also do not extend beyond an extreme angle ω_e. For weaker shocks ($\xi=1.0$, 0.9, 0.7, 0.5, and 0.3), however, transition to a rarefaction pattern does occur, and the curves now terminate at an angle of incidence ω_1, beyond which the material speed behind the incident shock is no longer sonic. (The sonic limit has been indicated on the graph.) In the cases where an extreme angle exists, the situation is analogous to that which occurs in the theory[1, 6] of regular reflection of a shock at a rigid wall, where it has been observed that beyond a theoretically predictable extreme angle a more complex configuration known as a Mach configuration replaces the regular reflection pattern. In a similar fashion one may speak here of regular refraction when a triple-wave configuration occurs at the interface.

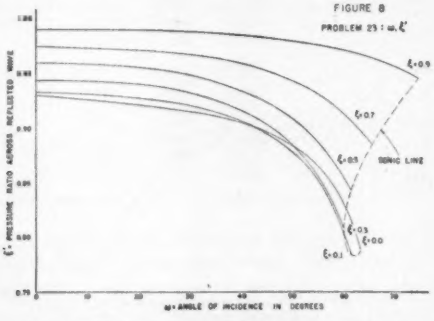

FIG. 8. Plot of strength of reflected wave *versus* angle of incidence—problem 23.

For problems 11 and 23 no solutions of the transition equation exist at all; hence the type of pattern which occurs at normal incidence ($\omega=0$) persists throughout the entire range of permissible values of angle of incidence ω. Thus a shock-wave solution always occurs in problem 11, and a rarefaction-wave solution when the gases are inverted (problem 23). Here again the shock-wave solutions (problem 11) do not exist for angles of incidence greater than an extreme angle ω_e, whereas the rarefaction-wave solutions (problem 23) always terminate at the sonic limit. Problems 10 and 22, on the other hand, behave like problems 11 and 23 for weak

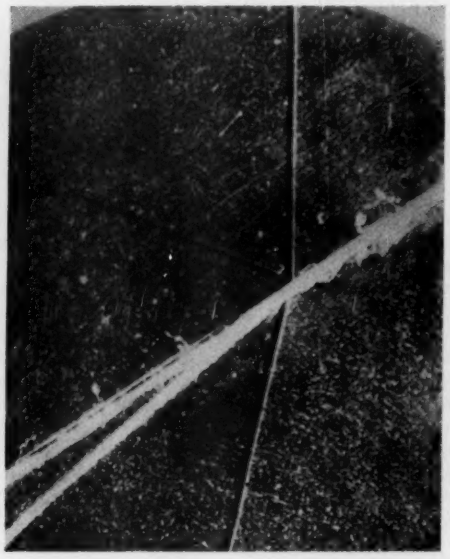

FIG. 9. Refraction of shock wave at carbon dioxide air interface. Shadowgram taken by R. G. Stoner, Pennsylvania State College.

shocks ($\xi>0.66$); whereas for stronger shocks the solutions are essentially similar to those of problems 3 and 15. The dependence of the reflected wave strength ξ' on the incident angle is shown in Figs. 5, 6, 7, and 8 for problems 10, 22, 11, 23, respectively.

It will be noted that in all these problems a phenomenon analogous to total reflection, for which the angle of refraction $\omega=90°$, does not occur on the physically plausible portion of the curves, and hence cannot be considered as a limitation on the refraction of such finite shock waves. Nevertheless, mathematically real solutions for total reflection do exist, as has been previously demonstrated[1] for the case of infinitesimal shock waves ($\xi\sim1$). For acoustic waves ($\xi=1$) Snell's law of refrac-

tion holds, as may be verified by direct substitution of $\xi=1$ in the general equations.

ADDENDUM (Received 28 March 1951)

The authors have recently received from R. E. Stoner of the Pennsylvania State College a shadowgram of the refraction of a shock wave at an interface separating air and carbon dioxide in a shock tube. With the kind permission of Professor Stoner, this shadowgram is reproduced here (Fig. 9). The measured angles produced by the interaction agree qualitatively with the theoretically predicted values.[9]

[9] R. G. Stoner and M. H. Glauberman, Phys. Rev. **76**, 882 (1949).

PHYSICAL REVIEW VOLUME 84, NUMBER 5 DECEMBER 1, 1951

Approximation Methods in the Theory of Scattering

MARVIN L. GOLDBERGER
Institute for Nuclear Studies, University of Chicago, Chicago, Illinois
(Received July 9, 1951)

The quantum theory of scattering is discussed from the point of view of a time independent formulation. A detailed discussion of the replacement of the ordinary integral equation of scattering by two others is given together with a discussion of the desirability of this procedure both from a physical and mathematical point of view. Variational formulations of these equations are given and their accuracy is indicated by comparison with examples for which exact solutions are known.

An exactly soluble problem given by Blatt is treated from the standpoint of the present paper. A formal solution of the general scattering problem is developed and illustrated with Blatt's example.

I. INTRDOUCTION

ONE of the most important problems in physics is the determination of the various matrix elements of the so-called Heisenberg S-matrix.[1] A variety of approximation methods have been used in practical calculations of these matrix elements. The types of problems studied range from nonrelativistic nucleon-nucleon scattering with static potentials to very complex field theoretical problems which are beset by divergence difficulties. The general approach to all of these problems has been a perturbation theoretic one based on a succession of Born approximations. (The nonrelativistic scattering of nucleons by a static potential is the lone exception for which an exact solution is feasible.) Actually the Heitler theory of radiation damping,[2] which will be discussed in detail later, is not a perturbation method in that it does not yield a power series in an interaction parameter. Recently, variational methods have been introduced for the treatment of scattering problems[3] but as yet only a few simple problems have been studied with this method. Their chief importance is that they provide at least in principle a method for obtaining solutions which are not power series expansions of the variety obtained by direct iteration (successive Born approximations).

The purpose of the present work is to discuss in greater detail the results of a previous paper,[4] to give examples of the use of the variational methods developed there, and finally to discuss the importance of treating separately, in so far as it is possible, the inductive and resistive parts of the field reactions. This work was begun in connection with a study of the paper by Pais and Jost[5] on the failure of the second Born approximation as applied to non-relativistic nucleon-nucleon scattering. The methods discussed below have been applied to this problem and the results already obtained are encouraging. This work is being continued by Messrs. A. Kaufman and F. Solmitz and will be reported soon. The problems to be treated in the present paper are all concerned with applications to field theories.

II. DERIVATION OF THE FORMULAS

A fairly complete derivation of the formulas to be used in this paper was given in I but for ease of reference the principal results will be restated here. In addition it will be shown that the results given there are true under much more general conditions than were previously stated. We shall again follow the development of Lippmann and Schwinger[6] with the previously noted[4] changes in notation.

We wish to solve the Schroedinger equation,

$$(E-H_0)\Psi=H_1\Psi, \tag{2.1}$$

subject to certain boundary conditions. These are taken

[1] J. A. Wheeler, Phys. Rev. **52**, 1107 (1937); W. Heisenberg, Z. Physik **120**, 513, 673 (1943).

[2] W. Heitler, Proc. Cambridge Phil. Soc. **37**, 291 (1941); A. H. Wilson, Proc. Cambridge Phil. Soc. **37**, 301 (1941); S. T. Ma and C. F. Hsuek, Proc. Cambridge Phil. Soc. **40**, 167 (1944).

[3] J. Schwinger, *Lectures on Nuclear Physics* (Harvard University, Cambridge, 1947); W. Kohn, Phys. Rev. **74**, 1763 (1948); L. Hulthen, see Mott and Massey, *The Theory of Atomic Collisions* (Oxford University Press, London, 1949), second edition, p. 128.

[4] M. L. Goldberger, Phys. Rev. **82**, 757 (1951), referred to hereafter as *I*.

[5] R. Jost and A. Pais, Phys. Rev. **83**, 840 (1951).

[6] B. Lippmann and J. Schwinger, Phys. Rev. **79**, 469 (1950).

to be an incident "plane wave" (i.e., solution of the problem with $H_1=0$) plus either incoming or outgoing scattered waves. We replace (2.1) by an integral equation which incorporates these boundary conditions:

$$\Psi_a^{(\pm)}=\Phi_a+\frac{1}{E_a\pm i\epsilon-H_0}H_1\Psi_a^{(\pm)}, \tag{2.2}$$

where Φ_a is an eigenfunction of H_0 corresponding to the energy E_a and represents the initial state of the system. The transition probability per unit time from the state characterized by Φ_a to an initially unoccupied state Φ_b is given by

$$w_{ba}=(2\pi/\hbar)|\mathbf{R}_{ba}|^2\delta(E_b-E_a), \tag{2.3}$$

where the matrix $\mathbf{R}$ is defined only for states of equal energy. Its definition is

$$\mathbf{R}_{ba}=-(\Phi_b, H_1\Psi_a^{(+)})=-(\Psi_b^{(-)}, H_1\Phi_a), \tag{2.4}$$

with $E_a=E_b$. We shall later have use for the total rate of transition from the state Φ_a which may be written as

$$\textstyle\sum_b w_{ba}=(2/\hbar)\mathrm{Im}\mathbf{R}_{aa}. \tag{2.5}$$

This is based on the unitarity of the S-matrix which is related to $\mathbf{R}$ via

$$S_{ba}=\delta_{ba}+2\pi i\mathbf{R}_{ba}\delta(E_b-E_a). \tag{2.6}$$

A variational formulation of (2.2) together with applications is given in reference 6. We now pass on to discuss in detail the considerations given in *I*.

Instead of solving (2.1) in terms of scattered waves as in (2.2) it is convenient to introduce a "standing wave" solution which contains equal amounts of incoming and outgoing scattered waves. This is achieved by noting that

$$\frac{1}{2}\left[\frac{1}{E_a+i\epsilon-H_0}+\frac{1}{E_a-i\epsilon-H_0}\right]=\frac{P}{E_a-H_0},$$

where P stands for the Cauchy principal value. In terms of this Green's function, an integral equation incorporating (2.1) and the desired boundary conditions may be written as

$$\Psi_a^{(1)}=\Phi_a+\frac{P}{E_a-H_0}H_1\Psi_a^{(1)}. \tag{2.7}$$

We now adopt the notational convention that subscripts a, b, c will be used to designate states of the same energy $E_a=E_b=E_c=E$, and subscripts α, β denote states for which $E_\alpha, E_\beta\neq E$. Forming the "radiation field" $\Psi_a^{(+)}-\Psi_a^{(1)}$ we have

$$\Psi_a^{(+)}-\Psi_a^{(1)}=\frac{P}{E_a-H_0}H_1(\Psi_a^{(+)}-\Psi_a^{(1)})+i\pi\sum_c\Phi_c\delta(E_a-E_c)\mathbf{R}_{ca}, \tag{2.8}$$

which, using (2.7) to eliminate Φ_c may be written as

$$\Psi_a^{(+)}-\Psi_a^{(1)}-i\pi\sum_c\Psi_c^{(1)}\delta(E_a-E_c)\mathbf{R}_{ca}=P\frac{1}{E_a-H_0}H_1\{\Psi_a^{(+)}-\Psi_a^{(1)}-i\pi\sum_c\Psi_c^{(1)}\delta(E_a-E_c)\mathbf{R}_{ca}\} \tag{2.9}$$

From (2.9) it follows that

$$\Psi_a^{(+)}=\Psi_a^{(1)}+i\pi\textstyle\sum_c\Psi_c^{(1)}\delta(E-E_c)\mathbf{R}_{ca} \tag{2.10}$$

provided we assume that the operator

$$\frac{P}{E_a-H_0}H_1$$

has no eigenfunction corresponding to the eigenvalue unity. Equation (2.10) is thus a sufficient condition for the pair of Eqs. (2.7) and (2.10) to be equivalent to (2.2). Our final step is the introduction of the reaction matrix, G, according to the definition

$$G_{\beta a}=-(\Phi_\beta, H_1\Psi_a^{(1)}). \tag{2.11}$$

We shall prove that $G_{\beta a}$ is not an hermitian matrix provided, as implied by our notation, $E_\beta\neq E_a=E$. This may be done by using (2.7) to eliminate Φ_β

$$\begin{aligned}-G_{\beta a}&=(\Psi_\beta^{(1)}, H_1\Psi_a^{(1)})-\left(\frac{P}{E_\beta-H_0}H_1\Psi_\beta^{(1)}, H_1\Psi_a^{(1)}\right)\\&=\left(H_1\Psi_\beta^{(1)}, \left\{\Psi_a^{(1)}-\frac{P}{E_a-H_0}H_1\Psi_a^{(1)}\right\}\right)\\&\quad+\left(H_1\Psi_\beta^{(1)}, \left\{\frac{P}{E_a-H_0}-\frac{P}{E_\beta-H_0}\right\}H_1\Psi_a^{(1)}\right)\\&=-G_{\beta a}^\dagger+(E_\beta-E_a)\\&\quad\times\left(\Psi_\beta^{(1)}, H_1\frac{P}{(E_a-H_0)(E_\beta-H_0)}H_1\Psi_a^{(1)}\right).\end{aligned} \tag{2.12}$$

Dividing by $E_\beta-E_a$ and allowing E_β to approach E_a, we derive

$$\left.\frac{\partial G_{\beta a}}{\partial E_\beta}\right|_{E_\beta=E_a}=-P\sum_\alpha\left.\frac{G_{\beta\alpha}^\dagger G_{\alpha a}}{(E_a-E_\alpha)^2}\right|_{E_\beta=E_a}. \tag{2.13}$$

This equation may be used for approximate evaluations of $G_{\beta a}$ in the neighborhood of the energy $E_\beta=E_a$ by using for G on the right hand side the Born approximation value, $G_{\beta a}\simeq B_{\beta a}\equiv-(\Phi_\beta, H'\Phi_a)$.

Our fundamental equations are now obtained by substituting (2.7) and (2.10) into (2.11) and (2.4) re-

spectively. We find

$$G_{\beta\alpha}=B_{\beta\alpha}-P\sum_a \frac{B_{\beta a}G_{a\alpha}}{E_a-E_\alpha},\quad [B_{\beta\alpha}=-(\Phi_\beta, H_1\Phi_\alpha)] \quad (2.14)$$

$$\mathbf{R}_{b\alpha}=\mathbf{G}_{b\alpha}+i\pi\sum_c \mathbf{G}_{bc}\delta(E-E_c)\mathbf{R}_{c\alpha}. \quad (2.15)$$

Before discussing these equations, we give the analogue of (2.10) that deals with $\Psi_b^{(-)}$, namely,

$$\Psi_b^{(-)}=\Psi_b^{(1)}-i\pi\sum_c \Psi_c^{(1)}\delta(E-E_c)\mathbf{R}_{bc}^*. \quad (2.16)$$

When this expression is substituted into (2.4) we obtain an alternate version of (2.15):

$$\mathbf{R}_{b\alpha}=\mathbf{G}_{b\alpha}+i\pi\sum_c \mathbf{R}_{bc}\delta(E-E_c)\mathbf{G}_{c\alpha}. \quad (2.15')$$

This shows that $\mathbf{R}$ and $\mathbf{G}$ commute. This is a well known result which is usually[6] given in the form of remarking that if $\mathbf{G}_{b\alpha}$ be written in the diagonal form

$$\mathbf{G}_{b\alpha}=\sum_A f_{bA}G_A f_{\alpha A}^*,$$

with

$$\sum_a f_{aA}^*\delta(E-E_a)f_{aA'}=\delta_{AA'},$$

$\mathbf{R}_{b\alpha}$ may be written as

$$\mathbf{R}_{b\alpha}=\sum_A f_{bA}R_A f_{\alpha A}^*$$

with

$$R_A=G_A/(1-i\pi G_A)$$

In other words, the eigenvectors of $\mathbf{G}$ are simultaneously eigenvectors of $\mathbf{R}$ and consequently $\mathbf{R}$ and $\mathbf{G}$ commute.

III. DISCUSSION OF THE FORMULATION

The above derivation of (2.14) and (2.15) is essentially the same as that given in a lecture by Schwinger,[3] and is also partly contained in reference 6. It has been given in some detail because the emphasis is somewhat different and to enable us to bring out a few important points, notably the non-hermitian nature of G and the concomitant relation (2.13). Furthermore it is important to understand clearly that the values of G off the energy shell are needed for its computation on the energy shell; this is evident from (2.14). The derivation of (2.15) given by Pauli[7] also makes this point clear; Pauli's development suffers from the fact that G is defined only by the iterated solution of (2.14). The resulting series rarely converges whereas the solution may very well exist, or at worst may exist after the now conventional renormalization processes are carried out.

Equation (2.15) is generally known as the Heitler integral equation[2] although the term is frequently applied to the equation which results from replacing G by B (or the first nonvanishing iteration approximation to G, in general). With this approximation, it has been studied in detail by Heitler and his collaborators and forms the basis of the Heitler theory of radiation damping. This theory has both defects and virtues which will be discussed later.

One may well question the advisability of replacing the single integral Eq. (2.2) by the pair of Eqs. (2.14) and (2.15). There are several arguments in favor of the procedure. First, the form of the equations enables one to see quite clearly the difficulties associated with the problem of the determination of interaction from scattering experiments. For suppose $\mathbf{R}_{b\alpha}$ were known from experiment for all states a, b for which $E_a=E_b=E$; then, in principle, (2.15) could be solved for $\mathbf{G}_{b\alpha}$. The matrix $\mathbf{G}$ then determined is not however the matrix G which is the one needed to enable one to solve (2.14) for B in terms of G. $\mathbf{G}$ as determined from scattering experiments has matrix elements only between states of equal energies which leaves undetermined the "off energy shell diagonal" matrix elements needed in (2.14). Without some additional rules for the computation of the off diagonal elements of G it would seem in general impossible to determine B uniquely from scattering experiments. Second, a clean separation is made into quantities on and off the energy shell. This is more than an esthetic advantage; the types of process involved are of an essentially different nature. Basically, the Heitler equation gives an expression of the true radiation damping processes in the classical sense of reactions due to real processes (e.g., the reaction of an emitted photon on an accelerated electron). Equation (2.14) on the other hand, since it is not restricted to the energy shell, describes the virtual processes and is closely connected with self energy problems. Generally speaking, the divergence difficulties are isolated in the equation for G; if G is finite, so is the resulting $\mathbf{R}$. Furthermore, if $\mathbf{R}$ be computed from (2.15) with any $\mathbf{G}$, the unitarity of S is maintained, which is certainly very desirable. This is an argument in favor of even the rather radical Heitler damping theory: One does not obtain obviously nonsensical cross sections which increase indefinitely with energy, etc. What appears to be even more important is that even with the crudest G, namely B, an $\mathbf{R}$ derived from solution of (2.15) does contain some correct higher order effects.

There are of course many, perhaps equally significant, higher order corrections which are omitted by the neglect of higher order terms in G and we are not advocating such a procedure; on the other hand, the damping effects are real and would appear in an exact solution of the problem. It would seem reasonable to take them into account in so far as one is able by a solution of (2.15).

There are cases where the neglect of higher order terms in G is simply incorrect. The most prominent case is in the problem of electron scattering taking into account radiative corrections, which was treated by Bethe and Oppenheimer.[8] It has been shown by Sebe[9] that the inclusion of virtual photons in G removes the

[7] W. Pauli, *Meson Theory of Nuclear Forces* (Interscience Publishers, New York, 1946), Chapter IV.

[8] H. A. Bethe and J. R. Oppenheimer, Phys. Rev. **70**, 451 (1946).

[9] T. Sebe, Prog. Theor. Phys. **3**, 304 (1948).

discrepancy found in reference 9. Blatt[10] has shown that for a few simple problems the neglect of the higher order terms would appear to be numerically unjustified in that the neglected terms are larger than those retained. The general situation in field theories is, of course, greatly complicated by the appearance of divergences and it is difficult to draw definite conclusions from formal manipulations. Setting the divergence troubles aside for a moment, however, it would seem that an approximation procedure based on approximate solution of (2.14) together with an exact solution of (2.15), if possible, might yield quite good answers. For example, in problems involving the emission of high energy quanta (photons, mesons, etc.) the real damping effects may be expected to be large; a direct iteration of (2.2), say, might easily diverge. On the other hand the iteration procedure as applied to G, because of the energy denominators might even be convergent. The separation of the problem, which we propose, would then be very advantageous. With regard to divergences, we are certainly no worse off than we usually are. Presumably the renormalization program would be applied to G in much the same way as it has been used for the S-matrix. It has been pointed out to the author by S. T. Ma that a similar proposal has been put forth by Fukuda and Miyazima.[11]

The problem of obtaining exact solutions to (2.15) is not a trivial one although it is a considerably simpler integral equation than (2.2) or (2.14) in that all quantities are restricted to the energy shell. It will be shown below that an iteration procedure is very likely to be only slowly convergent, if at all, and consequently different methods must be devised. What might be termed a semi-variational procedure has been proposed by Ma and Hsueh;[12] this will be discussed below. Only a few applications were made by those authors and the agreement with exact calculations was not too satisfactory. For this reason, and because of the importance of obtaining accurate solutions, we have investigated this problem and have found a more satisfactory variational formulation. In addition, a variational formulation of (2.14) has been found. In the next two sections the variational principles, briefly reported in I, will be discussed and examples of their utility given.

IV. VARIATIONAL FORMULATION

We shall take up first the variational formulation of (2.15). It is convenient to introduce a notation for matrix multiplication for operators defined only on the energy shell, namely,

$$(\mathbf{MN})_{ba}\equiv\sum_c \mathbf{M}_{bc}\delta(E-E_c)\mathbf{N}_{ca}, \quad E_a=E_b=E. \tag{4.1}$$

We then assert that the matrix (on the energy shell), $\mathfrak{J}$, with

$$\mathfrak{J}=\mathbf{RG}+\mathbf{GR}+i\pi\mathbf{RGR}-\mathbf{RR} \tag{4.2}$$

is stationary under arbitrary variations of $\mathbf{R}$. Performing such a variation, we obtain

$$\delta\mathfrak{J}=\delta\mathbf{R}\{\mathbf{G}+i\pi\mathbf{RG}-\mathbf{R}\}+\{\mathbf{G}+i\pi\mathbf{GR}-\mathbf{R}\}\delta\mathbf{R}. \tag{4.3}$$

Reference to (2.15) and (2.15′) shows that $\delta\mathfrak{J}$ is indeed zero for the correct $\mathbf{R}$. Conversely if $\mathfrak{J}$ is stationary, the quantities within the brackets must vanish, which yields (2.15) and (2.15′). The stationary value obtained for the correct $\mathbf{R}$ is

$$\mathfrak{J}=\mathbf{GR}=\mathbf{RG}=(\mathbf{R}-\mathbf{G})/i\pi. \tag{4.4}$$

The above formulation suffers from the defect that simply a change in normalization of the trial function will yield different approximate values of $\mathbf{R}$. A stationary formulation that meets this objection is provided by the expression

$$\mathfrak{J}_{ba}'=(\mathbf{GR})_{ba}(\mathbf{RG})_{ba}[(\mathbf{RR})_{ba}-i\pi(\mathbf{RGR})_{ba}]^{-1} \tag{4.5}$$

The verification of the stationary nature of (4.5) is straightforward and will not be given. The stationary value of $\mathfrak{J}'$ is again $(\mathbf{R}-\mathbf{G})/i\pi$.

It is worthwhile to point out the difference between these variational expressions and that given by Ma and Hsueh.[12] Their procedure is based on the observation that

$$M=\sum_a\delta(E-E_a)[\mathbf{R}^\dagger(\mathbf{R}-\mathbf{G}-i\pi\mathbf{GR})]_{aa} \tag{4.6}$$

is stationary under arbitrary variations of $\mathbf{R}^\dagger$ (but not of $\mathbf{R}$!). This is a sort of one sided variational principle. The stationary value of M is evidently zero. The method cannot be used for a direct computation of $\mathbf{R}$; one must put in a trial $\mathbf{R}$ with some independent parameters and vary the parameters appearing in $\mathbf{R}^\dagger$. We shall comment later on the accuracy of their method in connection with some examples.

It was stated in I that (4.2) and (4.5) were correct only if $\mathbf{G}$ were real and symmetric; our present derivation shows that this assumption is unnecessary. The fact that $\mathbf{R}$ and $\mathbf{G}$ commute had been overlooked. We mention in passing that the quantity

$$\mathbf{N}=\mathbf{R}^\dagger\mathbf{G}+\mathbf{GR}+i\pi\mathbf{R}^\dagger\mathbf{G}^2-i\pi\mathbf{G}^2\mathbf{R}-\pi^2\mathbf{R}^\dagger\mathbf{G}^2\mathbf{R}-\mathbf{RR},$$

is stationary under arbitrary, independent variations of $\mathbf{R}$ and $\mathbf{R}^\dagger$ about the correct values. However, the demand of vanishing variation yields the equation for R and $R^\dagger$ in iterated form, e.g.,

$$\mathbf{R}=\mathbf{G}+i\pi\mathbf{G}(\mathbf{R}+i\pi\mathbf{GR}).$$

A normalization independent form of this variational principle is easily derived. The stationary value obtained is $\mathbf{G}^2$, consequently this principle must be used much as that of Ma and Hsueh. We shall make no further use of this result.

A few remarks on the relative accuracy of (4.2) and (4.5) are in order. For example, if one puts for a trial function in (4.2) simply $\mathbf{G}$, the approximate value of $\mathbf{R}$

[10] J. M. Blatt, Phys. Rev. **72**, 466 (1947).
[11] N. Fukuda and T. Miyazima, Prog. Theor. Phys. **5**, 849 (1950).
[12] S. T. Ma and C. F. Hsueh, Phys. Rev. **67**, 303 (1945).

thus obtained is just equivalent to two iterations of (2.15). This has the effect that approximate S-matrix computed from this approximate $\mathbf{R}$ is not necessarily unitary. The same procedure as applied to (4.5) does not suffer from this difficulty. The solution thus obtained is not an expansion in $\mathbf{G}$, and in general should give a more accurate answer. We shall in fact see a case where (4.5) gives the exact solution whereas (4.2) gives, as it must, simply two iterations.

A similar development may be carried through for Eq. (2.14) which defines G in terms of B. We assert that the energy shell matrix $\mathbf{J}_{ba}$ (i.e., $E_a=E_b=E$) given by

$$\mathbf{J}_{ba}=P\sum_a\frac{G_{ba}{}^\dagger G_{aa}}{E-E_a}+P\sum_{\alpha,\beta}\frac{G_{b\alpha}{}^\dagger B_{\alpha\beta}G_{\beta a}}{(E-E_\alpha)(E-E_\beta)}$$
$$-P\sum_\alpha(G_{b\alpha}{}^\dagger B_{\alpha a}+B_{b\alpha}G_{\alpha a})/(E-E_\alpha) \quad (4.7)$$

is stationary under arbitrary independent variations of G and $G^\dagger$ about the correct values. We have

$$\delta\mathbf{J}_{ba}=P\sum_\alpha\frac{\delta G_{b\alpha}{}^\dagger}{E-E_\alpha}\left\{G_{\alpha a}+P\sum_\beta\frac{B_{\alpha\beta}G_{\beta a}}{E-E_\beta}-B_{\alpha a}\right\}$$
$$+P\sum_\alpha\left\{G_{b\alpha}{}^\dagger+P\sum_\beta\frac{G_{b\beta}{}^\dagger B_{\beta\alpha}}{E-E_\beta}-B_{b\alpha}\right\}\frac{\delta G_{\alpha a}}{E-E_\alpha}, \quad (4.8)$$

from which the stationary character of J is evident. The stationary value obtained is

$$\mathbf{J}_{ba}=-\sum_\alpha B_{b\alpha}G_{\alpha a}/(E-E_\alpha)=\mathbf{G}_{ba}-\mathbf{B}_{ba}. \quad (4.9)$$

It should be noted that if $E_a=E_b=E$,

$$P\sum_\alpha G^\dagger{}_{b\alpha}B_{\alpha a}/(E-E_\alpha)=P\sum_\alpha B_{b\alpha}G_{\alpha a}/(E-E_\alpha). \quad (4.10)$$

The normalization independent form is easily found and is given by

$$\mathbf{J}_{ba}{}'=-(G^\dagger B)_{ba}(BG)_{ba}[(G^\dagger G)_{ba}+(G^\dagger BG)_{ba}]^{-1}, \quad (4.11)$$

with matrix multiplication defined by

$$(G^\dagger G)_{ba}=P\sum_\alpha G^\dagger{}_{b\alpha}G_{\alpha a}/(E-E_\alpha), \quad \text{etc.} \quad (4.12)$$

The stationary value of $\mathbf{J}_{ba}{}'$ is again given by (4.9). It should be noted that (4.7) and (4.11) are stationary expressions for $\mathbf{G}$, i.e., on the energy shell, and cannot be used for computation of G. This is, of course, no difficulty because it is $\mathbf{G}$ that is needed for insertion into (2.15).

With the simplest trial function, $G=B$, (4.8) yields the equivalent of two iterations of (2.14) or stated otherwise the third Born approximation. The form (4.11), however, does not yield a power series expansion in B and may be expected to give a more reliable result, in general.

In applications, the above variational principles appear to have some advantage over the related ones given by Lippmann and Schwinger[4] in that instead of having to guess wave functions as trial functions one instead must guess essentially scattering amplitudes. In the case of nucleon-nucleon scattering, say, it seems much simpler to guess a reasonable scattering amplitude than a three dimensional wave function which must be especially accurate in the neighborhood of the potential. (Actually the necessary trial functions are not true scattering amplitudes in that behavior of the energy shell must be assumed.)

Our variational formulations for G and $\mathbf{R}$ have some features in common. They generally are neigher maxima nor minima and, second, they both correspond, in their nonhomogeneous form, to the same degree of approximation in an iteration solution. The homogeneous forms take into account what amounts essentially to the renormalization of the wave function familiar from perturbation theory. The necessary renormalization may be easily understood in the case of scattering by a potential. The iteration procedure adds up the contributions from single scattering scatterings, all with the same initial amplitude, then the subsequent scatterings of these scattered waves. The error made is essentially in the single scattering contributions: Those regions of potential farthest from the incident beam do not feel the full strength of the beam for their first scattering, it having been weakened by earlier scatterings.

V. APPLICATIONS

We shall now discuss a number of applications of our variational principles to specific examples. Most of our attention will be confined to (2.15) and the associated variational expressions (4.2) and (4.5), because only in rather pathological cases is it possible to solve (2.14) exactly and thus have reliable comparisons with approximate solutions. There are, on the other hand, a number of exact solutions of (2.15) available, at least for the case where the first nonvanishing approximation for $\mathbf{G}$ is used. In connection with the approximate solutions to be discussed, it is useful to bear in mind the easily derived result that the condition for the convergence of an iteration solution of (2.15) is

$$\pi^2G_{Am}{}^2<1 \quad (5.1)$$

where G_{Am} is the largest eigenvalue of $\mathbf{G}$ (see discussion following (2.15′); this result is evident from the eigenfunction expansion given there).

1. Nonrelativistic Compton Effect[13]

We limit ourselves to a discussion of (2.15) with the first nonvanishing approximation for $\mathbf{G}$. A more complete investigation is in progress. With this limitation the matrix elements of $\mathbf{G}$ between states of a single photon of momentum $\mathbf{k}$, polarization $\boldsymbol{\varepsilon}_\lambda$, electron at rest (neglecting the frequency shift) are given by

$$\langle\mathbf{k}\lambda|\,\mathbf{G}\,|\mathbf{k}'\lambda'\rangle=-(2\pi e^2/mk)\boldsymbol{\varepsilon}_\lambda\cdot\boldsymbol{\varepsilon}_{\lambda'} \quad (5.2)$$

[13] See W. Heitler, reference 2.

(here and from now on we use natural units $\hbar=c=1$). With our normalization, the density of states per unit energy interval is given by

$$\rho=k^2d\Omega/(2\pi)^3,$$

and the Heitler equation becomes

$$\langle \mathbf{k}\lambda|\mathbf{R}|\mathbf{k}_0\lambda_0\rangle=-(2\pi e^2/mk)\boldsymbol{\varepsilon}_\lambda\cdot\boldsymbol{\varepsilon}_{\lambda_0}$$
$$-i\pi\sum_{\lambda'}\int d\Omega'(2\pi e^2/mk)\boldsymbol{\varepsilon}_\lambda\cdot\boldsymbol{\varepsilon}_{\lambda'}\frac{k^2}{(2\pi)^3}$$
$$\times\langle \mathbf{k}'\lambda'|\mathbf{R}|\mathbf{k}_0\lambda_0\rangle. \quad (5.3)$$

This equation is readily solved with the "ansatz"

$$\langle \mathbf{k}\lambda|\mathbf{R}|\mathbf{k}'\lambda'\rangle=U(k)\boldsymbol{\varepsilon}_\lambda\cdot\boldsymbol{\varepsilon}_{\lambda'} \quad (5.4)$$

with the result

$$\langle \mathbf{k}\lambda|\mathbf{R}|\mathbf{k}_0\lambda_0\rangle$$
$$=-(2\pi e^2/mk)(1+i(2e^2k/3m))^{-1}\boldsymbol{\varepsilon}_\lambda\cdot\boldsymbol{\varepsilon}_{\lambda_0}. \quad (5.5)$$

We now apply (4.5), taking as trial function simply

$$\langle \mathbf{k}\lambda|\mathbf{R}_T|\mathbf{k}_0\lambda_0\rangle=\boldsymbol{\varepsilon}_\lambda\cdot\boldsymbol{\varepsilon}_{\lambda_0}. \quad (5.6)$$

The stationary value of $\mathbf{R}$ is, with this trial function precisely the value given by (5.5), the exact answer. The variational method of Ma and Hsueh also gives the exact result for this case. The condition for the validity of the iteration solution is evidently $e^2k/m<1$ which is certainly true if our neglect of recoil and frequency change are to be justified.

2a. Meson-Nucleon Scattering, $\pi^++N\rightarrow\pi^{+\prime}+N'$ (Positive Mesons by Neutrons)[14]

We again take the first nonvanishing approximation to G. With this simplification, the Heitler equation may be solved exactly for all charged meson theories. We take the pseudoscalar theory for purposes of illustration and also to point out an algebraic error in the results of Fukuda and Miyazima, and Ma and Hsueh. The relevant matrix elements of $\mathbf{G}$ may be written in the barycentric frame as

$$\langle \boldsymbol{p}k|\mathbf{G}|\boldsymbol{p}_0k_0\rangle=\bar{u}(a_1+a_2\gamma_4)u_0/2\epsilon_0(W_0^2-M^2), \quad (5.7)$$

where $\bar{u}$ and u_0 are the usual Dirac plane wave spinor amplitudes corresponding to four-momenta $\boldsymbol{p}$ and $\boldsymbol{p}_0$ respectively ($\bar{u}=u^*\gamma_4$, $u^*u=1$), $\boldsymbol{k}$ and $\boldsymbol{k}_0$ are the final and initial meson four-momenta, respectively, and in our coordinate system, $\mathbf{p}_0=-\mathbf{k}_0$, $\mathbf{p}=-\mathbf{k}$, $\epsilon_0=+(\mu^2+\mathbf{q}^2)^{\frac{1}{2}}$ with q the magnitude of the momentum of either particle and μ the meson mass. W_0 is the total energy of nucleon plus meson.

$$a_1=f^2M, \quad g^2M(M^2+3W_0^2)/\mu^2$$
$$a_2=f^2W_0, \quad g^2W_0(W_0^2+3M^2)/\mu^2, \quad (5.8)$$

where the terms in f refer to pseudoscalar coupling and those in g to pseudovector coupling. a_2 is given incorrectly in both references[14] but our results agree with those of Ashkin *et al.*[15] The Heitler equation is easily solved for this case because aside from the factors $\bar{u}$ and u_0, $\mathbf{G}$ does not depend on angles. In terms of

$$\langle \boldsymbol{p}k|\mathbf{R}|\boldsymbol{p}_0k_0\rangle=(1/2\epsilon_0)\bar{u}\mathfrak{R}u_0,$$
$$\langle \boldsymbol{p}k|\mathbf{G}|\boldsymbol{p}_0k_0\rangle=(1/2\epsilon_0)\bar{u}\mathfrak{G}u_0, \quad (5.9)$$

it becomes

$$\mathfrak{R}(\boldsymbol{p}k;\boldsymbol{p}_0k_0)=\mathfrak{G}(\boldsymbol{p}k;\boldsymbol{p}_0k_0)$$
$$+(iq/32\pi^2W_0)\int d\Omega'\mathfrak{G}(\boldsymbol{p}k;\boldsymbol{p}'k')(-i\boldsymbol{\gamma}\cdot\boldsymbol{p}'+M)$$
$$\times\mathfrak{R}(\boldsymbol{p}'k';\boldsymbol{p}_0k_0). \quad (5.10)$$

Since $\mathfrak{G}$ does not depend on angles, $\mathfrak{R}$ is proportional to $\mathfrak{G}$ and the solution is simply

$$\mathfrak{R}=(1-\lambda)^{-1}\mathfrak{G} \quad (5.11)$$

where

$$\lambda=(q/8\pi W_0)\mathfrak{G}(E_0\gamma_4+M) \quad (5.12)$$

with E_0 the nucleon energy and M its mass. This may be rewritten as

$$\mathfrak{R}=\frac{1+i\kappa_1+i\kappa_2\gamma_4}{(1+i\kappa_1)^2+\kappa_2^2}\frac{a_1-a_2\gamma_4}{W_0^2-M^2}, \quad (5.13)$$

where

$$\kappa_1=\frac{q}{8\pi W_0}\frac{E_0a_2-Ma_1}{W_0^2-M^2}, \quad \kappa_2=\frac{q}{8\pi W_0}\frac{E_0a_1-Ma_2}{W_0^2-M^2}. \quad (5.14)$$

The differential cross section may be computed from (5.13) but since we are not interested at this time in the result we shall merely give the total cross section which is most easily obtained from (2.5). This relation becomes, for our problem

$$\sigma=(1/qW_0)\tfrac{1}{4}\,\text{Im. trace}\mathfrak{R}(-i\boldsymbol{\gamma}\cdot\boldsymbol{p}_0+M) \quad (5.15)$$

which is easily evaluated to yield

$$\sigma=\frac{8\pi}{q^2}\left[\frac{\kappa_1^2+\kappa_2^2+(\kappa_2^2-\kappa_1^2)^2}{1+2(\kappa_1^2+\kappa_2^2)+(\kappa_2^2-\kappa_1^2)^2}\right]. \quad (5.16)$$

The criterion for the convergence of an iteration solution may be expressed in terms of the largest eigenvalue of the operator λ in (5.12), i.e., $\lambda^2<1$. These eigenvalues are easily found and yield the result that for pseudoscalar coupling we must have

$$\frac{1}{4}\left(\frac{f^2}{4\pi}\right)^2\frac{q^2}{W_0^2}\left(\frac{E_0+M}{W_0+M}\right)^2<1. \quad (5.17)$$

In this case the damping effect is dominated by the size of the coupling constant as may be seen by considering the extreme relativistic limit, in which case the requirement is

$$\tfrac{1}{4}(f^2/4\pi)^2<1. \quad (5.18)$$

[14] S. T. Ma and C. F. Hsueh, Proc. Cambridge Phil. Soc. **40**, 167 (1944) and also reference 12.

[15] Ashkin, Simon, and Marshak, Prog. Theor. Phys. **V**, 634 (1950).

The entire damping effect is much more important in the pseudovector coupling case. We find the convergence requirement

$$\frac{1}{4}\left(\frac{g^2}{4\pi}\right)^2\frac{q^2}{W_0^2}\left(\frac{E_0+M}{W_0+M}\right)^2\left(\frac{W_0-M}{\mu}\right)^4 \tag{5.19}$$

from which we see that for very high energies the iteration procedure will certainly fail.

We turn now to the variational treatment. Equation (4.5) may of course be used as it stands, but it is more convenient to write a stationary expression for $\mathfrak{R}$. This is

$$\frac{\mathfrak{R}-\mathfrak{G}}{i\pi}=\left(\frac{q}{32\pi^3W_0}\right)\frac{\left(\int d\Omega'\mathfrak{G}(-i\gamma\cdot p'+M)\mathfrak{R}\right)\left(\int d\Omega'\mathfrak{R}(-i\gamma\cdot p'+M)\mathfrak{G}\right)}{\int d\Omega'\mathfrak{R}(-i\gamma\cdot p'+M)\mathfrak{R}-\dfrac{iq}{32\pi^2W_0}\int d\Omega'\int d\Omega''\mathfrak{R}(-i'\gamma\cdot p'+M)\mathfrak{G}(-i\gamma\cdot p''+M)\mathfrak{R}}. \tag{5.20}$$

If we take as a trial function $\mathfrak{R}=\mathfrak{G}$ we find

$$\begin{aligned}\mathfrak{R}&\simeq\mathfrak{G}+\frac{(iq/q\pi W_0)\mathfrak{G}(E_0\gamma_4+M)\mathfrak{G}}{1-(iq/8\pi W_0)\mathfrak{G}(E_0\gamma_4+M)}\\&=\frac{1}{1-i(q/8\pi W_0)\mathfrak{G}(E_0\gamma_4+M)}\mathfrak{G},\end{aligned} \tag{5.21}$$

which is the exact answer. The same result may be obtained using the inhomogeneous form (4.2) written in terms of $\mathfrak{R}$ and $\mathfrak{G}$ with a trial function $\mathfrak{R}=a+b\gamma_4$ where $[a,\gamma_4]=[b,\gamma_4]=0$ in order that $[\mathfrak{R},\mathfrak{G}]=0$, and a and b independent of angles. It is essential to have adjustable quantities available when using (4.2) in order that the correct normalization be obtained. Ma and Hsueh have also applied their method to this problem and obtained poor results.

2b. Meson-Nucleon Scattering, $\pi^-+N\rightarrow\pi^{-\prime}+N'$ (Negative Mesons by Neutrons)

Even with the Heitler approximation for $\mathfrak{G}$, the integral Eq. (2.15) cannot be solved exactly in the relativistic case, as has been pointed out in reference 15. (Actually one may obtain the exact solution provided only that the product of v/c for meson and nucleon is small compared with unity.) We shall for simplicity deal only with the non-relativistic case where in addition we neglect the nucleon recoil. We take pseudoscalar mesons with pseudovector coupling. The matrix elements of $\mathbf{G}$ may be regarded as operators on the spin variables of the neutron and are given by

$$\langle\mathbf{k}|\,\mathbf{G}\,|\mathbf{k}_0\rangle=(g^2/2\mu^2\epsilon_0)\boldsymbol{\sigma}\cdot\mathbf{k}_0\boldsymbol{\sigma}\cdot\mathbf{k}. \tag{5.22}$$

The Heitler equation becomes

$$\begin{aligned}\langle\mathbf{k}|\,\mathbf{R}\,|\mathbf{k}_0\rangle&=(g^2/2\mu^2\epsilon_0)\boldsymbol{\sigma}\cdot\mathbf{k}_0\boldsymbol{\sigma}\cdot\mathbf{k}+i(g^2k_0/16\pi^2\mu^2\epsilon_0)\\&\quad\times\int d\Omega'\boldsymbol{\sigma}\cdot\mathbf{k}'\boldsymbol{\sigma}\cdot\mathbf{k}\langle\mathbf{k}'|\,R\,|\mathbf{k}_0\rangle.\end{aligned} \tag{5.23}$$

The solution is easily found by noting that the only scalars that can be constructed from $\mathbf{k}_0$, $\mathbf{k}$ and $\boldsymbol{\sigma}$ are $\mathbf{k}_0\cdot\mathbf{k}$ and $\boldsymbol{\sigma}\cdot(\mathbf{k}_0\times\mathbf{k})$. The solution must consequently be a linear combination of these. One finds

$$\langle\mathbf{k}|\,\mathbf{R}\,|\mathbf{k}_0\rangle=(g^2/2\mu^2\epsilon_0)\frac{(1+2ix)\mathbf{k}_0\cdot\mathbf{k}+i\boldsymbol{\sigma}\cdot\mathbf{k}_0\times\mathbf{k}}{1-ix+2x^2} \tag{5.24}$$

where

$$x=(g^2/4\pi)(k_0^3/3\mu^2\epsilon_0).$$

The cross section is easily found to be

$$\begin{aligned}d\sigma&=(g^2/4\pi)(1/\mu^2)(k_0^4/\mu^2\epsilon_0^2)\\&\quad\times[1+4x^2\cos^2\vartheta]/[(1+2x^2)^2+x^2].\end{aligned} \tag{5.25}$$

If the damping is neglected ($x=0$) one finds the well known result. It is interesting to note that for very large x, the cross section is simply

$$d\sigma=(36/k_0^2)\cos^2\vartheta d\Omega \tag{5.26}$$

independent of g and showing the characteristic p wave angular distribution of scattered mesons.

If one now attempts to solve (5.23) approximately using the trial function $\mathbf{R}=\mathbf{G}$ in (4.5), for example, one obtains a rather complicated result which does however yield the exact cross section plus correction terms of order x^3. The expression (4.2) with the same trial function would yield only x^2 terms reliably, indicating the superiority of (4.5) over (4.2). The trial function

$$\langle\mathbf{k}|\,\mathbf{R}_T/\mathbf{k}_0\rangle=\alpha\mathbf{k}_0\cdot\mathbf{k}+\beta\boldsymbol{\sigma}\cdot\mathbf{k}_0\times\mathbf{k}$$

with parameters α and β determined using the stationary character of (4.2) yields the exact solution, (5.24).

The purpose of these examples has been to show the general reliability of the variational principles. No definite statement as to their accuracy can be made. This is of course frequently the case and is the biggest objection to variational techniques. It might be noted that this uncertainty may work in one's favor as is seen by the last example; statements about the errors in the results of variationally computed quantities in terms of alleged errors in trial functions are generally meaningless.

3. Blatt's Example[10]

It is instructive to study an example given by Blatt in his discussion of the Heitler damping theory. The problem is that of the scattering of a scalar meson by a fixed, extended, source. The hamiltonian is

$$H=\frac{1}{2}\int d\mathbf{x}[\pi^2(\mathbf{x})+\varphi(\mathbf{x})(\mu^2-\nabla^2)\varphi(\mathbf{x})]+\tfrac{1}{2}\lambda\bar{\varphi}^2$$
$$\bar{\varphi}=\int d\mathbf{x}\varphi(\mathbf{x})U(\boldsymbol{\sigma}). \tag{5.27}$$

This problem has also been treated by Wentzel[10] in another connection. These authors show that an exact solution may be given in terms of normal coordinates and in particular that the problem of meson scattering reduces to a study of the equation

$$[k_0^2-(-\nabla^2)]\Psi(\mathbf{x})=\lambda\bar{\Psi}U(\mathbf{x}). \tag{5.28}$$

Our general equations may be written in terms of these quantities identifying E_a, H_0, $H_1\Psi$ with k_0^2, $-\nabla^2$, $\lambda\bar{\Psi}U(\mathbf{x})$ respectively. The wave number of the scattered meson will be called $\mathbf{k}$, its magnitude being equal to that of the incident meson, $\mathbf{k}_0$. The solution for the scattering problem as given by Blatt (slightly rewritten to correspond to quantization in a box of unit volume) is

$$\Psi_{\mathbf{k}_0}{}^{(+)}=\Phi_{\mathbf{k}_0}-\lambda\bar{\Psi}_{\mathbf{k}_0}{}^{(+)}V(k_0,\mathbf{x})$$
$$\Phi_{\mathbf{k}_0}=(2E)^{-\frac{1}{2}}e^{i\mathbf{k}_0\cdot\mathbf{x}}$$
$$V(k_0,\mathbf{x})=\frac{1}{4\pi}\int d\mathbf{x}'\frac{e^{ik_0|\mathbf{x}-\mathbf{x}'|}}{|\mathbf{x}-\mathbf{x}'|}U(\mathbf{x}')$$
$$\overline{\Psi_{\mathbf{k}_0}{}^{(+)}}=\int d\mathbf{x}\Psi_{\mathbf{k}_0}{}^{(+)}U(\mathbf{x})$$
$$=v(-k_0)[1+\lambda\bar{V}(k_0)]^{-1}(2E)^{-\frac{1}{2}} \tag{5.29}$$
$$\bar{V}(k_0)=\int d\mathbf{x}V(k_0,\mathbf{x})U(\mathbf{x})$$
$$v(k_0)=\int d\mathbf{x}e^{-i\mathbf{k}_0\cdot\mathbf{x}}U(\mathbf{x})$$
$$E=+(\mu^2+k_0^2)^{\frac{1}{2}}.$$

The scattering amplitude may be obtained from the asymptotic form of $\Psi_{\mathbf{k}_0}{}^{(+)}$ which is

$$\Psi_{\mathbf{k}_0}{}^{(+)}(\mathbf{x})\xrightarrow{\cdot}(2E)^{-\frac{1}{2}}\left[e^{i\mathbf{k}_0\cdot\mathbf{x}}-\frac{e^{ik_0|\mathbf{x}|}}{|\mathbf{x}|}\frac{\lambda}{4\pi}\frac{\gamma(k_0)}{1+\lambda\bar{V}(k_0)}\right] \tag{5.30}$$
$$\gamma(k_0)=v(-k_0)v(k_0).$$

We shall now solve this problem in two steps according to our general procedure. It is convenient to introduce in place of the matrix $\mathbf{R}$ the usual scattering amplitude $f(\mathbf{k},\mathbf{k}_0)$; the two are related by

$$f(\mathbf{k},\mathbf{k}_0)=[E(k_0)/2\pi]\langle\mathbf{k}|\mathbf{R}|\mathbf{k}_0\rangle. \tag{5.31}$$

Similarly we introduce

$$g(\mathbf{p},\mathbf{q})=[\{E(p)E(q)\}^{\frac{1}{2}}/2\pi]\langle\mathbf{p}|G|\mathbf{q}\rangle,$$
$$b(\mathbf{p},\mathbf{q})=[\{E(p)E(q)\}^{\frac{1}{2}}/2\pi]\langle\mathbf{p}|B|\mathbf{q}\rangle, \tag{5.32}$$

in terms of which (2.14) and (2.15) become, respectively,

$$g(\mathbf{p},\mathbf{k}_0)=b(\mathbf{p},\mathbf{k}_0)+\frac{P}{2\pi^2}\int d\mathbf{p}\frac{b(\mathbf{p},\mathbf{p}')g(\mathbf{p}',\mathbf{k}_0)}{p'^2-k_0^2}, \tag{5.33}$$

$$f(\mathbf{k},\mathbf{k}_0)=g(\mathbf{k},\mathbf{k}_0)+\frac{ik_0}{4\pi}\int d\Omega' g(\mathbf{k},\mathbf{k}')f(\mathbf{k}',\mathbf{k}_0). \tag{5.34}$$

For our particular problem,

$$b(\mathbf{p},\mathbf{q})$$
$$=-(\lambda/4\pi)\int d\mathbf{x}\int d\mathbf{x}'e^{-i\mathbf{p}\cdot\mathbf{x}}U(\mathbf{x})U(\mathbf{x}')e^{i\mathbf{q}\cdot\mathbf{x}'} \tag{5.35}$$
$$=-(\lambda/4\pi)v(p)v(-p).$$

The solution of these equations is trivial by virtue of the separability of b. We find for g,

$$g(\mathbf{p},\mathbf{k}_0)=g(p,k_0)=-(\lambda/4\pi)\frac{v(p)v(-k_0)}{1+\lambda\bar{W}(k_0)}$$
$$\bar{W}(k_0)=\frac{P}{(2\pi)^3}\int d\mathbf{p}\frac{\gamma(p)}{p^2-k_0^2}$$
$$=\frac{1}{4\pi}\int d\mathbf{x}\int d\mathbf{x}'U(\mathbf{x})\frac{\cos k_0|\mathbf{x}-\mathbf{x}'|}{|\mathbf{x}-\mathbf{x}'|}U(\mathbf{x}'). \tag{5.36}$$

With this value for g we have immediately

$$f(\mathbf{k},\mathbf{k}_0)=-\frac{\lambda}{4\pi}\frac{\gamma(k_0)}{1+\lambda(\bar{W}(k_0)+ik_0\gamma(k_0)/4\pi)}. \tag{5.37}$$

That this is the same as Blatt's solution follows from the fact that

$$\bar{V}(k_0)=\frac{1}{(2\pi)^3}\int d\mathbf{p}\frac{\gamma(p)}{p^2-k_0^2-i\epsilon}=\bar{W}(k_0)+\frac{ik_0\gamma(k_0)}{4\pi}. \tag{5.38}$$

The usual damping theory prescription of taking the first nonvanishing term in the iteration solution corresponds to putting $\bar{W}$ equal to zero. Blatt's failure to recognize the source function $\gamma(k_0)$ in the damping term, $ik_0\gamma(k_0)/4\pi$, of the exact solution was a result of his configuration space expansion of $\bar{V}(k_0)$; the only error in the usual Heitler method is the setting of $\bar{W}$ equal to zero. As pointed out by Blatt, the seriousness

[10] G. Wentzel, Helv. Phys. Acta XV, 111 (1942).

of this error depends essentially on numerical values. For small values of k_0, $\bar{W}(k_0)$ is related to the source radius, a, according to

$$\bar{W}(k_0)\simeq\tfrac{1}{2}\pi a, \tag{5.39}$$

so that the ratio of the damping to the inertial term in (5.38) is approximately k_0a which is by hypothesis very small. Evidently then the neglect of $\bar{W}(k_0)$ is unjustified. On the other hand this dominant term in $\bar{W}(k_0)$ is definitely a nucleon self-energy term which should be incorporated into the nucleon mass in the spirit of modern renormalization. For this simple problem it may also be regarded as a renormalization of the coupling parameter λ. To show this explicitly we write

$$\bar{W}(k_0)=\frac{1}{4\pi a}+\frac{1}{4\pi}\int d\mathbf{x}\int d\mathbf{x}'U(\mathbf{x}) \times\frac{\cos k_0|\mathbf{x}-\mathbf{x}'|-1}{|\mathbf{x}-\mathbf{x}'|}U(\mathbf{x}'). \tag{5.40}$$

Calling the second term in (5.40) $w(k_0)$ we may rewrite (5.36) as

$$g(p,k_0)=-\frac{\lambda}{4\pi}(1+\lambda/4\pi a)^{-1} \times\frac{v(p)v(-k_0)}{1+\lambda(1+\lambda/4\pi a)^{-1}w(k_0)}. \tag{5.36'}$$

Making the obvious replacement $\lambda(1+\lambda/4\pi a)^{-1}\rightarrow\lambda'$, we have

$$g(p,k_0)=-(\lambda'/4\pi)v(p)v(-k_0)/(1+\lambda'w(k_0)) \tag{5.36''}$$

$$f(\mathbf{k},\mathbf{k}_0)=-(\lambda'/4\pi)\frac{\gamma(k_0)}{1+\lambda'[w(k_0)+ik_0\gamma(k_0)/4\pi]}. \tag{5.37'}$$

The question of the legitimacy of neglecting $w(k_0)$ depends still on numerical values. If for example one now passes to the limit of a point interaction $[v(k_0)\rightarrow 1]w(k_0)$ is identically zero, and the Heitler prescription would be exact. If the source is very small, but still finite, an iteration solution for g would be feasible in an energy range for which iteration for f would fail. For example if we take a gaussian shape for $U(\mathbf{x})$ and $k_0a\ll 1$, we find

$$|4\pi w(k_0)/k_0\gamma(k_0)|\simeq 2k_0a/\pi\ll 1,$$

and the iteration solution for f fails if $k_0\lambda\gg 1$. For $k_0a\gg 1$, on the other hand,

$$|4\pi w(k_0)/k_0\gamma|\simeq e^{k_0^2a^2/\pi}/k_0a\gg 1,$$

in which case the iteration for g would not be permissible (unless $\lambda/a\gg 1$) whereas that for f would be convergent. The general situation in a theory of point particles is probably that damping terms are dominant, after renormalization of the inductive terms, but this question has not been thoroughly investigated as yet.

Almost identical discussions may be given for the other examples treated by Blatt so there is little point in presenting them.

VI. ADDITIONAL FORMAL CONSIDERATIONS

It was mentioned briefly in Sec. II that one may formally solve the Heitler Eq. (2.15) in terms of the eigenfunctions of the operator $\mathbf{G}$. It is useful also to obtain a formal solution to (2.14) which we shall refer to as the reaction equation. We begin by studying the eigenvalue problem defined by

$$\sum_\alpha B_{\beta\alpha}u_\Gamma(\alpha)/(E_\alpha-E_\alpha)=B_\Gamma(E_\alpha)u_\Gamma(\beta) \tag{6.1}$$

with the normalization condition

$$\sum_\alpha u_\Gamma^*(\alpha)u_{\Gamma'}(\alpha)/[E_\alpha-E_\alpha]=\epsilon\delta_{\Gamma\Gamma'}. \tag{6.2}$$

(Principle values are implied in the above integrals and in the subsequent ones.) The desired eigenfunction u_Γ must be normalized in the unconventional manner shown in (6.2) in order that (6.1) be an hermitian eigenvalue problem. The quantity E_α is a base energy which is conveniently chosen as the same energy appearing in (2.14) which we rewrite for ease of reference:

$$G_{\beta\alpha}=B_{\beta\alpha}-\sum_\alpha B_{\beta\alpha}G_{\alpha\alpha}/(E_\alpha-E_\alpha). \tag{6.3}$$

The quantity ϵ, which is the value of the normalization integral may be chosen as ± 1 if desired; the particular sign is not *a priori* known. It follows from (6.1) and (6.2) that

$$B_{\beta\alpha}=\epsilon^{-1}\sum_\Gamma u_\Gamma(\beta)B_\Gamma u_\Gamma^*(\alpha), \tag{6.4}$$

as may be verified by noting that multiplication of (6.4) by $u_{\Gamma'}(\alpha)/E_\alpha-E_\alpha$ and summation over α, together with (6.2) yields (6.1). The analogous operation performed on (6.1) shows the reality of the $B_\Gamma(E_\alpha)$.

In terms of the eigenfunctions $u_\Gamma(\alpha)$ the solution of the reaction equation is very simply obtained. Substituting (6.4) into (6.3) we have

$$G_{\beta\alpha}=-\frac{1}{\epsilon}\sum_{\Gamma'}u_{\Gamma'}(\beta)B_{\Gamma'}u_{\Gamma'}^*(a) -\frac{1}{\epsilon}\sum_\alpha\sum_{\Gamma'}\frac{u_{\Gamma'}(\beta)B_{\Gamma'}u_{\Gamma'}^*(\alpha)G_{\alpha\alpha}}{E_\alpha-E_\alpha}. \tag{6.5}$$

Multiplication by $u_\Gamma^*(\beta)/(E_\alpha-E_\beta)$ and summation over β yields, using (6.2),

$$\sum_\beta\frac{u_\Gamma^*(\beta)G_{\beta\alpha}}{E_\alpha-E_\beta}=B_\Gamma u_\Gamma^*(a)-B_\Gamma\sum_\beta\frac{u_\Gamma^*(\beta)G_{\beta\alpha}}{E_\alpha-E_\beta}, \tag{6.6}$$

or

$$\sum_\beta\frac{u_\Gamma^*(\beta)G_{\beta\alpha}}{E_\alpha-E_\beta}=\frac{B_\Gamma u_\Gamma^*(a)}{1+B_\Gamma}. \tag{6.7}$$

Substituting (6.7) into (6.5) yields immediately

$$G_{\beta\alpha}=\epsilon^{-1}\sum_\Gamma u_\Gamma(\beta)G_\Gamma(E_\alpha)u_\Gamma^*(a), \tag{6.8}$$

with

$$G_\Gamma(E_\alpha)=B_\Gamma(E_\alpha)/[1+B_\Gamma(E_\alpha)]. \tag{6.9}$$

The dependence of G_Γ on E_a shows again the fact that G is not an hermitian matrix [see (2.12)]. An iteration solution of the reaction equation evidently corresponds to an expansion of the denominator of (6.9) from which we obtain the convergence requirement

$$|B_\Gamma(E_a)|<1. \tag{6.10}$$

It is worth while noting that the expression

$$B_\Gamma=\left[\sum_{\alpha,\beta}\frac{u_\Gamma^*(\beta)B_{\beta\alpha}u_\Gamma(\alpha)}{(E_\alpha-E_\beta)(E_\alpha-E_a)}\right]\left[\sum_\alpha\frac{u_\Gamma^*(\alpha)u_\Gamma(\alpha)}{E_\alpha-E_a}\right]^{-1}, \tag{6.11}$$

is stationary under arbitrary variations of u_Γ and u_Γ^+.

There is a close connection between the eigenvalue G_Γ and the G_A mentioned in Sec. II in that on the energy shell the eigenfunctions $u_\Gamma(a)$ (or more properly, their energy shell projection) and the f_{aA} both provide a diagonalization of $\mathbf{G}$. The formal connection may be written as follows. In terms of the f_{aA}, the eigenvalue problem of Sec. II is

$$\begin{aligned}\textstyle\sum_c \mathbf{G}_{bc}\delta(E-E_c)f_{cA}&=G_Af_{bA},\\ \textstyle\sum_c f_{cA}^*\delta(E-E_c)f_{cA'}&=\delta_{AA'}.\end{aligned} \tag{6.12}$$

In terms of the transformation coefficient

$$\langle\Gamma/A\rangle=\textstyle\sum_c u_\Gamma^*(c)\delta(E-E_c)f_{cA}, \tag{6.13}$$

we find, introducing (6.8) for G_{bc}, that

$$f_{bA}=(\epsilon G_A)^{-1}\textstyle\sum_\Gamma u_\Gamma(b)G_\Gamma\langle\Gamma/A\rangle, \tag{6.14}$$

where $\langle\Gamma/A\rangle$ is found from the solution of the set of equations

$$\begin{aligned}\epsilon^{-1}\textstyle\sum_{\Gamma'}\langle\Gamma/\Gamma'\rangle G_{\Gamma'}\langle\Gamma'/A\rangle&=G_A\langle\Gamma/A\rangle\\ \langle\Gamma/\Gamma'\rangle&=\textstyle\sum_c u_\Gamma^*(c)\delta(E-E_c)u_{\Gamma'}(c).\end{aligned} \tag{6.15}$$

The solution of (6.15) then yields also the eigenvalues G_A in terms of the G_Γ. The normalization condition of (6.12) may be expressed in terms of the $\langle\Gamma/A\rangle$ as

$$\epsilon^{-1}\textstyle\sum_\Gamma\langle A'/\Gamma\rangle G_\Gamma\langle\Gamma/A\rangle=G_{A'}\delta_{A'A}. \tag{6.16}$$

A very simple illustration of the formal procedure is furnished by a treatment of Blatt's example. In terms of the notation used in the earlier discussion of the problem, (6.1) becomes

$$-(1/2\pi^2)\int d\mathbf{q}[b(\mathbf{p},\mathbf{q})u_\Gamma(\mathbf{q})]/[q^2-k_0^2]$$
$$=B_\Gamma(k_0^2)u_\Gamma(\mathbf{p}). \tag{6.17}$$

Inserting the explicit value of $b(\mathbf{p},\mathbf{q})$, (5.35),

$$\frac{\lambda v(p)}{(2\pi)^3}\int d\mathbf{q}\frac{v(-q)u_\Gamma(\mathbf{q})}{q^2-k_0^2}=B_\Gamma(k_0^2)u_\Gamma(\mathbf{p}). \tag{6.18}$$

The structure of this equation shows that there is only one eigenvalue and one eigenfunction which is simply proportional to $v(p)$. The proportionality factor is obtained from the normalization condition (6.2) which becomes simply

$$\frac{4\pi}{(2\pi)^3}\int d\mathbf{q}\frac{u^*(\mathbf{q})u(\mathbf{q})}{q^2-k_0^2}=\epsilon. \tag{6.19}$$

In terms of the quantity $\overline{W}(k_0)$ defined in (5.36) we have

$$\begin{aligned}B(k_0^2)&=\lambda\overline{W}(k_0)\\ u(\mathbf{q})&=(\epsilon/-4\pi\overline{W}(k_0))^{\frac{1}{2}}v(q)\end{aligned} \tag{6.20}$$

and from (6.8) and (6.9) we obtain our previous answer for $G(p,k_0)$, namely, (5.36). The energy shell eigenfunction of $\mathbf{G}(k,k_0)$ is simply $(4\pi/k_0)^{\frac{1}{2}}$. The transformation coefficient $\langle\Gamma/A\rangle$ is $(4\pi k_0)^{\frac{1}{2}}u^*(k_0)$, and G_A is given in terms of G_Γ as follows

$$\begin{aligned}G_\Gamma(k_0^2)&=\lambda\overline{W}(k_0)/[1+\lambda\overline{W}(k_0)]\\ G_A&=(k_0/\epsilon)u(k_0)G_\Gamma u^*(k_0)\\ &=-(\lambda/4\pi)k_0\gamma(k_0)/[1+\lambda\overline{W}(k_0)].\end{aligned} \tag{6.21}$$

Eigenfunction expansions of the above variety, while useful theoretically, are useful in practice only if a few eigenfunctions are needed. In many cases it is preferable to have an approximate closed expression in place of an exact solution in series form. A familiar example is high energy nucleon nucleon scattering and the clumsiness of a phase shift expansion. It is hoped that the variational methods discussed earlier may provide a practical solution in some cases.

Note added in proof.—An alternative variational formulation of the problem of finding $\mathbf{R}$ may be given as follows. Introduce

$$\begin{aligned}R_{\beta a}^{(+)}&=-(\Phi_\beta, H_1\Psi_a^{(+)})\\ R_{\beta a}^{(-)}&=-(\Psi_\beta^{(-)}, H_1\Phi_a)\end{aligned} \tag{A-1}$$

which are equal if $E_\beta=E_a$. These quantities satisfy the equations

$$\begin{aligned}R_{\beta a}^{(+)}&=B_{\beta a}-\sum_\gamma B_{\beta\gamma}\frac{1}{E_a-E_\gamma+i\epsilon}R_{\gamma a}^{(+)}\\ R_{\beta a}^{(-)}&=B_{\beta a}-\sum_\gamma R_{\beta\gamma}^{(-)}\frac{1}{E_\beta-E_\gamma+i\epsilon}B_{\gamma a}.\end{aligned} \tag{A-2}$$

It can be verified by direct computation that the energy shell matrix $\mathbf{F}_{ba}$ (i.e., $E_a=E_b=E$) defined by

$$\begin{aligned}\mathbf{F}_{ba}=&\sum_\alpha\frac{B_{b\alpha}R_{\alpha a}^{(+)}}{E-E_\alpha+i\epsilon}+\sum_\alpha\frac{R_{b\alpha}^{(-)}B_{\alpha a}}{E-E_\alpha+i\epsilon}\\ &-\sum_{\alpha,\beta}\frac{R_{b\beta}^{(-)}B_{\beta\alpha}R_{\alpha a}^{(+)}}{(E-E_\beta+i\epsilon)(E-E_\alpha+i\epsilon)}-\sum_\alpha\frac{R_{b\alpha}^{(-)}R_{\alpha a}^{(+)}}{E-E_\alpha+i\epsilon}\end{aligned} \tag{A-3}$$

is stationary under arbitrary independent variations of $R^{(+)}$ and $R^{(-)}$ about the correct values given by (A-2). The stationary value is

$$R_{ba}^{(+)}-B_{ba}=R_{ba}^{(-)}-B_{ba}. \tag{A-4}$$

A normalization independent formulation is easily given. Furthermore, the operator F of which (A-3) is the energy shell matrix element, $(\Phi_b F\Phi_a)$ may be explicitly constructed. This result will be discussed in a subsequent publication.

The Second Transition in the Decay of Sn^{119m}

J. C. Bowe* and P. Axel
Physics Department, University of Illinois,† Urbana, Illinois
(Received August 6, 1951)

The photons from the second transition in Sn^{119m} were detected by using two proportional counters in coincidence. These photons have an energy of 23.8±0.6 kev and could be differentiated from In x-rays only by coincidence measurements. The fraction of the second transitions which emits photons is 0.13±0.03, corresponding to a total conversion of 7.3±1.7. The slow neutron activation cross section of Sn^{118} was found to be 0.01 barn.

INTRODUCTION

A 250-DAY isomer in Sn^{119} was first reported and correctly assigned by Mihelich and Hill.[1] Their original report established the presence of conversion electrons from a gamma-ray of about 69 kev and they postulated a second unobserved transition. Nelson, Ketelle, and Boyd[2] confirmed the existence of this isomer, reporting a half-life of 279 days and an energy of 64 kev. The postulated presence of the second transition was confirmed by Scharff-Goldhaber, *et al.*[3] They determined a total transition energy (for the two cascade radiations) of 85±4 kev, indicating that the gamma-ray energy of the second transition is 19±5 kev.

A more precise and direct determination of the energy of this second transition was carried on independently by Hill and ourselves. Using a beta-ray spectrograph Hill[4] observed the *L* and *M* conversion electrons from a 24.2-kev transition. The identification of the lower energy conversion electrons was made even though they were strongly absorbed in the source and were partially obscured by the presence of Auger electrons of the same energy. Hill's intensity measurements, which included large corrections, indicated about equal numbers of conversion electrons from both transitions. Hill also redetermined the energy of the isomeric transition as 65.3 kev.

Our measurements were carried out before any direct evidence for the second transition was available. We observed the unconverted gamma-rays from the second transition and quantitatively distinguished them from both the In and Sn x-rays which were present. The unconverted gamma-rays were observed in coincidence with x-rays from the first transition; quantitative analysis of these coincidence data gave the conversion coefficient.

SOURCE

The Sn^{119m} source was made available to us by R. D. Hill of the University of Illinois. It had been produced by a five-month slow neutron bombardment of enriched Sn^{118}.[5] Although the sample contained only about 0.2 percent Sn^{122} and 91 percent Sn^{118}, the x-ray activity due to Sn^{122} was larger than that of Sn^{119m}. The actual ratio of the Sn^{122} to Sn^{119m} x-rays in this source after five months of bombardment was 1.7. This implies that the slow neutron activation cross section of Sn^{118} is less than 1 percent of Sn^{122}; the calculation of this cross section is given below.

EQUIPMENT

Two identical proportional counters were used, each made from 6-inch diameter brass tubing. A 175 mg/cm² circular Be window 1 inch in diameter permitted the photons to enter with a minimum of attenuation. The counters were 20 inches long and contained 9.2 liters of a mixture of 90 percent argon and 10 percent methane at atmospheric pressure. They were operated with a battery voltage of about 2500 volts corresponding to a gas multiplication of about 10^3.

The voltage pulses were amplified using a non-overloading linear amplifier with a rise time of 0.8 microsecond and a clipping time of 4 microseconds. The gain of the amplifier was 7000.

The pulses from each counter were sorted by a single channel pulse-height selector. These selectors use vacuum diodes as discriminators and a 6AS6 for an anticoincidence tube. The output of each selector was a blocking oscillator pulse which was applied to the coincidence circuit.

The coincidence circuit had four independent channels each of which had a different adjustable delay and an adjustable resolving time.[6] The multichannel delay feature was used to constantly verify that the resolving time was sufficiently large to insure 100 percent detection efficiency of true coincidences. With a resolving time of 1.85 microseconds the first three channels

* Now at Argonne National Laboratory, Chicago, Illinois. The material in this paper was submitted to the University of Illinois in partial fulfillment of the requirements for the Doctor of Philosophy degree.

† This research was supported in part by the joint program of the ONR and AEC.

[1] J. W. Mihelich and R. D. Hill, Phys. Rev. **79**, 781 (1950).

[2] Nelson, Ketelle, and Boyd, Oak Ridge National Laboratory Report ORNL 685, 1950.

[3] Scharff-Goldhaber, der Mateosian, Goldhaber, Johnson, and McKeown, Phys. Rev. **83**, 480 (L) (1951).

[4] R. D. Hill, Phys. Rev. **83**, 865 (1951).

[5] The enriched isotope was obtained from the Y-12 Plant, Oak Ridge, Tennessee. It was irradiated by special arrangement with the Isotopes Division of the AEC, Oak Ridge, Tennessee.

[6] We wish to thank Dr. Sherman Frankel, of the University of Pennsylvania, who designed and tested the pulse-height selector and the multichannel coincidence circuit.

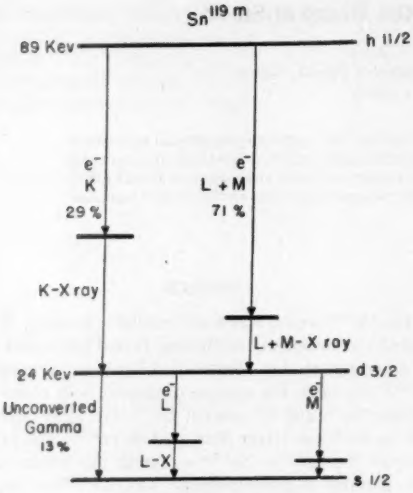

FIG. 1. Decay scheme of 280-day Sn^{119m}.

(0, 0.25, 0.60 microsecond delays) always counted the same number of coincidence pulses; the fourth channel was delayed by 1.70 microseconds and it counted fewer coincidence pulses.

A scintillation spectrometer with a 16-mm-thick NaI crystal and a RCA 5819 phototube was used. The pulses from the phototube were amplified and analyzed by a pulse height selector using the same type of equipment discussed above.

OUTLINE OF EXPERIMENTAL PROCEDURE

Several different measurements and analyses were necessary in order to obtain quantitative data on the second transition in Sn^{119m}. Since these measurements are interdependent, an outline of the entire investigation will be given before the individual measurements are described.

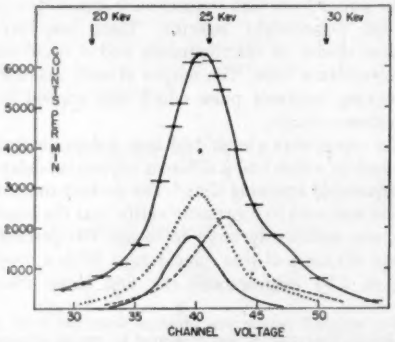

FIG. 2. Proportional counter photon spectrum of mixed Sn^{113} Sn^{119m} source. The breakdown into three components is shown: dotted curve = In x-ray; dashed curve = Sn x-ray; solid curve = 24 kev gamma-ray.

The decay scheme of Sn^{119m} is shown in Fig. 1. One major complication in the experimental determination of this scheme is the proximity in energy of the 24-kev gamma-ray to the Sn x-ray (25.2 kev). Another more limiting condition is the presence of In x-rays (24.2 kev) originating from Sn^{113}. These In x-rays completely mask the gamma-ray.

The pulse height distribution due to the photons shows a broadened peak but no detailed structure in the region of the In and Sn x-rays. The existence of the gamma-ray was shown qualitatively by the detection of coincidences between the photons contributing to the low energy part of this peak and those in the high energy part.

Quantitative data on the structure of the broadened peak were derived from three different experiments:

1. The contribution of the Sn x-ray was found by using a palladium absorber and a proportional counter detector. (Palladium absorbs the Sn x-ray more strongly than it absorbs either the Sn γ-ray or the In x-ray.)

2. To determine the contribution of the In x-rays we made use of the fact that these x-rays come from the decay of Sn^{113}. Since there is also a 390-kev gamma-ray emitted by Sn^{113} (from the In^{113m} daughter), this gamma-ray was used to indicate how much Sn^{113} was present. For this purpose, both the Sn^{119m} source and a "pure" Sn^{113} source[7] were investigated with a NaI crystal scintillation spectrometer.

3. The most accurate data on the breakdown of the composite peak into In x-ray, 24-kev Sn gamma-ray, and Sn x-ray, were obtained from coincidence experiments. Coincidences were recorded between pulses of different amplitude from two proportional counters. These coincidence data were used to quantitatively analyze and readjust the breakdown of the composite peak. Coincidence data were also taken with a palladium absorber; these data also confirmed the validity of the final breakdown.

PHOTON SPECTRUM

The photon spectrum of the mixed Sn^{113}–Sn^{119m} source is shown in Fig. 2. The final analysis of this peak into its three components is also shown.

The amount of the In x-ray was determined from the intensity of the In^{113} gamma-ray in the mixed source, using the crystal data described subsequently. The exact shape and position of the In x-ray peak was obtained by observing an In^{114m} source with a proportional counter. This source was stronger than and provided more precise data than the Sn^{113} source. However, the Sn^{113} source was also investigated and showed a similar peak due to a pure In x-ray.

To estimate the amount of Sn x-ray, a pulse-height

[7] We are indebted to Professor R. B. Duffield for the loan of this source. Although it was a neutron-bombarded Sn sample which had been enriched in Sn^{112}, the only photons present were due to Sn^{113}.

distribution curve was taken with a palladium absorber between the mixed source and the proportional counter. This curve is shown in Fig. 3 together with the original distribution. In addition, Fig. 3 shows the contribution of the Pd x-rays from the absorber. To help with the analysis of this curve, a pulse height distribution was taken with a palladium absorber and a source of pure In x-rays.

A pulse-height distribution curve was also taken with a rhodium absorber. These data showed that all the radiations in the composite peak were absorbed in the K shell of rhodium; this places a lower limit on the gamma-ray energy of 23.2 kev (the K binding energy in rhodium).

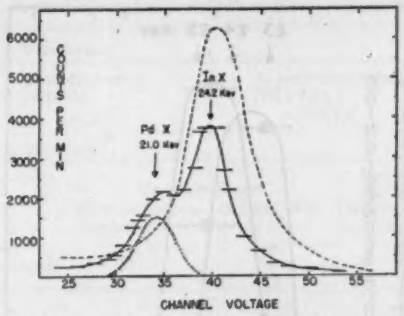

FIG. 3. Proportional counter spectrum with palladium absorber. The curve without absorber is shown dashed. The analyzed contribution of Pd x-rays is given by dotted curve.

SCINTILLATION SPECTROMETER RESULTS

A NaI crystal scintillation spectrometer was used to determine the amount of Sn^{113} in the mixed Sn^{119m}—Sn^{113} source. The scintillation spectrometer pulse height distribution curve for the mixed source is shown by the solid line in Fig. 4. In the same figure, the data for a pure Sn^{113} source are shown normalized (i.e., multiplied by a factor of 2.7) so that the two gamma-ray intensities are equal. The dashed curve in the low energy region indicates the amount of In x-rays which accompanies the 390-kev gamma-rays.

The Sn^{119m} source shows no evidence for any photons other than those in the x-ray peak and at 390 kev. The region of 85 kev was investigated with particular care and an upper limit of 0.5 percent can be placed on any gamma-ray branch of that energy in Sn^{113}. This gamma-ray had been reported by early investigators but had not been seen in the recent study of Thomas, *et al.*[8]

COINCIDENCE EXPERIMENTS

A preliminary qualitative study established the existence of coincidences in a Sn^{119m}—Sn^{113} source and showed no coincidences in the pure Sn^{113} source. For quantitative results, three separate sets of coincidence data were taken. For each of these three sets of data, the pulses from one proportional counter (counter 1) were selected in six different three volt channels covering the pulse height range from 30 to 48 volts. The pulse distribution from counter 1 had its peak at 40 volts and had a full width at half-maximum of 6.6 volts (a 6.0 volt full width would be expected for a monoenergetic radiation). The differences between the three sets of data involved the second proportional counter.

Set I: The pulse height selector of counter 2 was adjusted to select the lower ½ of the pulses in the peak. The resultant coincidence rate was plotted as a function of the channel level selected in counter 1; these data are shown by the circled points in Fig. 5. There is a peak coincidence rate at a voltage close to that of a Sn x-ray. Thus, the fixed channel can be interpreted as emphasizing the gamma-ray.

Set II: The pulse height selector of counter 2 was moved to include only the upper ½ of the pulses in the peak. The resultant coincidence rate is shown by the points enclosed in squares in Fig. 5. In this case the fixed channel emphasizes the Sn x-ray and therefore the peak in the coincidence distribution comes at the energy of the gamma-ray, 24 kev.

Set III: The pulse height selector of counter 2 was kept so that it included the upper ½ of the pulses and a palladium absorber was included between the source and counter 2. Since the palladium strongly absorbs the Sn x-ray, this fixed channel, although at a relatively high voltage, emphasized the gamma-ray. The peak of the coincidence distribution shifted back to the position of the Sn x-ray. Since the fraction of the coincidences absorbed varied from 0.6 to 0.8, the statistics obtained on the individual points were relatively poor. Thus, although these data were checked semiquantitatively, the lack of precision made it impossible to use them to determine the amount of 24-kev gamma-ray.

The quantitative analysis of the first two sets of data was based on the equations given below. The following symbols will be used:

N ≡ number of Sn^{119m} nuclei decaying per unit time.
E ≡ probability of detecting a radiation (including solid angle and efficiency).

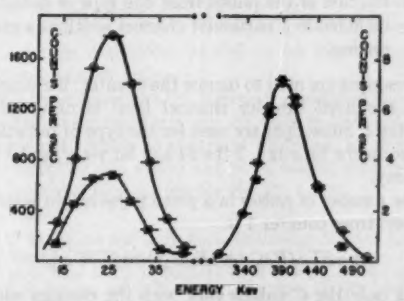

FIG. 4. NaI crystal spectrum of Sn^{113} and mixed Sn^{113}—Sn^{119m} sources. Mixed source data given by circled points. Normalized Sn^{113} data shown by points enclosed in squares.

[8] Thomas, Haynes, Broyles, and Thomas, Phys. Rev. 82, 961 (L) (1951).

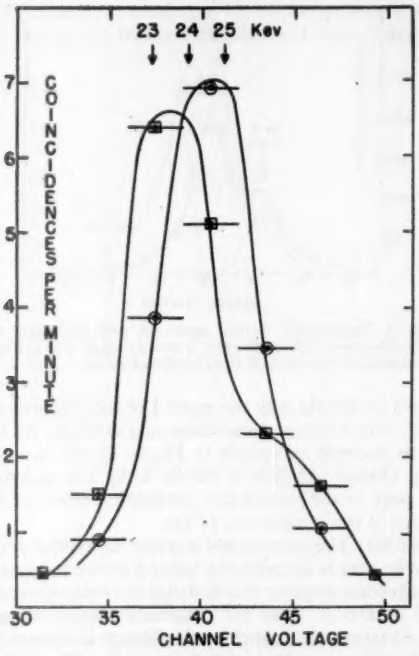

FIG. 5. Proportional counter coincidence spectrum of Sn^{113m}. The two curves represent two different channel levels in the counter with fixed bias. The circled points correspond to coincidences with lower $\frac{1}{2}$ of photon peak; the points enclosed in squares show coincidences with the upper $\frac{1}{2}$.

$r \equiv$ ratio of the number of In x-rays to Sn x-rays detected by proportional counter. r was determined as 1.5 at the time of the coincidence measurements.

$f \equiv$ fluorescence yield of Sn x-ray ($f=0.8$).[9]

$a \equiv$ fractional occurrence of K conversion in 65-kev transition ($a=0.29$).[4]

$b \equiv$ fractional occurrence of unconverted 24-kev gamma-ray.

$C \equiv$ fraction of the pulses from one type of radiation included in a particular channel width at a given setting.

Superscripts are used to denote the counter; the counter with the fixed broader channel level is designed as counter 2. Subscripts are used for the type of radiation; 1 denotes the Sn x-ray, 2 the 24-kev Sn γ-ray, and 3 the In x-ray.

The number of pulses in a given pulse height selector channel from counter 1 is

$$n^1 = N[afE_1{}^1C_1{}^1 + bE_2{}^1C_2{}^1 + rafE_1{}^1C_3{}^1],$$

where only the C values vary with the channel width and channel level. Similarly, the number of coincidences are

$$n^{12} = Nafb[E_1{}^1C_1{}^1E_2{}^2C_2{}^2 + E_1{}^2C_1{}^2E_2{}^1C_2{}^1].$$

If these two equations are combined and the values for a, f, r and E_2/E_1 are substituted, one finds

$$n^{12}/n^1 = bE_1{}^2[C_1{}^1C_2{}^2 + C_1{}^2C_2{}^1]/ [0.88(C_1{}^1 + 1.5C_3{}^1) + 4.35bC_2{}^1].$$

Experimental data from eleven different coincidence points were used to determine b. The probability of counter 2 detecting a Sn x-ray emitted by the source was known from an independent set of measurements to be (1.9±0.2) percent. The values for the constants, C, were determined by using the breakdown shown in Fig. 2. In the course of estimating the experimental error several extreme breakdowns were used. In addition, estimates were made of the possible variation of channel level and channel width during the coincidence runs.

The resultant value of b is found as $b=0.13\pm0.03$. The statistical accuracy and the internal consistency are well within this assigned error which includes a reasonable allowance for possible systematic errors. The best value of the total conversion coefficient is 6.7, with a possible range from 5.6 to 9. However, in view of the size of the possible error, the value of the conversion coefficient can be most conveniently expressed as 7.3 ± 1.7.

DISCUSSION OF RESULTS

The experimental measurements give only the total conversion coefficient, including electron contributions from the L, M and N shells. However, the theoretical calculations available are only for the L shell.

The only experimental data on the electron contributions from different shells are those of Hill.[4] He reports that (72±8) percent of the electrons originate in the L_{I} subshell while the others originate in the M_{I} shell.

The only two sets of conversion calculations applicable to this problem are those of Gellman, Griffith, and Stanley[10] and those of Hebb and Nelson.[11] The calculations of Gellman, *et al.* are more accurate; they use relativistic expressions but neglect screening. However these have been made only for the L_{I} shell. The calculations of Hebb and Nelson are valid only for the internal conversion of electric multipoles. These calculations are made on the basis of poorer, nonrelativistic formulas and the contributions of the individual L subshells are not given.

The comparison of the experimental and theoretical values are shown in Table I.

A comparison of the theoretical results of Gellman, *et al.* with the combined experimental results of Hill and ourselves favors an assignment of magnetic dipole to the 24-kev transition. However, this assignment

[9] H. Tellez-Plasencia, J. phys. et radium **10**, 14 (1949); Steffen, Huber, and Humbel, Helv. Phys. Acta **22**, 167 (1949).

[10] Gellman, Griffith, and Stanley, Phys. Rev. **80**, 866 (1951).

[11] M. H. Hebb and E. Nelson, Phys. Rev. **58**, 486 (1940).

cannot be based solely on the conversion data now available. Experimentally, it is possible that some L_{II} or L_{III} conversion electrons are obscured in the Auger electron background.

Theoretically, the conversion contribution from the L_{II} and L_{III} shells is not known for magnetic radiation. Also, the effects of screening on the L_I conversion are not known. For electric radiation, a comparison of the calculations of Gellman, *et al.*, with those of Hebb and Nelson indicate that the predominant conversion contribution comes from the L_{II} and L_{III} shell. Although Hebb and Nelson's calculations are approximate, the approximation is expected to be accurate at low energy. Furthermore, Goodrich[12] has separated the formulas of Hebb and Nelson to show the L_I contribution explicitly. Goodrich finds that for electric quadrupole radiation, the approximate calculation gives values which are within a factor of two of those of Gellman, *et al.* below 75 kev in energy. If these calculations prove to be correct when the more complete L conversion tables of Rose and his collaborators become available, the experimental data presented in this paper will give an unambiguous assignment of magnetic dipole to the 24-kev transition.‡

The assignment of the spins and parities to the levels in Sn^{119} can also be based on more indirect evidence from both the shell model of Mayer[13] and the analogous two step transitions in Sn^{117m},[1] Te^{121m},[14] Te^{123m} [14] and Te^{125m}.[15] These assignments have already been suggested[1,3] without knowledge of the conversion coefficient.

Thus, the present experimental report quantitatively establishes the existence of the 24-kev gamma-ray. Furthermore it strongly supports the level assignments. The conversion data will provide a check of conversion theory when more adequate calculations become available. They now seem to indicate that in Sn^{119} the 24-kev magnetic dipole conversion is predominantly in the L_I shell.

CALCULATION OF Sn^{118} CROSS SECTION

To calculate the neutron absorption cross section of Sn^{118} relative to Sn^{112} the following data were used:

1. The relative number of x-rays due to Sn^{113} (and its daughter In^{113m}) compared to those of Sn^{119m}, after five months of slow neutron bombardment, was experimentally determined as 1.7.

2. The fraction of Sn^{112} in the bombarded sample was about 0.2 percent, while Sn^{118} was 91 percent.

TABLE I. Conversion coefficients of 24-kev gamma-ray.

A. Experimental

Total conversion all shells	L_I conversion using Hill's data
7.3±1.7	5.3±1.4

B. Theoretical

	Electric multipole		Magnetic multipole
	Hebb and Nelson complete L shell	Gellman, *et al.* L_I shell	Gellman, *et al.* L_I shell
Dipole	1.16	0.92	4.7
Quadrupole	200	3.5	

3. The half-life of Sn^{113} was taken as 112 days;[16] that of Sn^{119m} as 279 days.

4. The electron capture disintegration of Sn^{113} results in a K shell hole 71 percent of the time. This figure is based on the experimental L to K electron capture ratio of 0.42 determined by Thomas, *et al.*;[3] this experimental figure is used although the theoretical L to K ratio[17] is 0.11.

5. The Sn^{113} daughter, 1.7-hour In^{113m} has a K to L ratio[18] of 5.4 and a theoretical K conversion coefficient[19] of 0.5.

6. K conversion electrons are emitted by Sn^{119m} in 29 percent of the isomeric transitions.[4]

Using these data, the cross section for the activation of Sn^{119m} is 1/110 that for Sn^{113}. This large difference in activation cross section does not necessarily imply a comparable difference in the total capture cross section. When Sn^{118} captures a slow neutron, the compound nuclear state formed probably has a low spin. The radiations from this state probably lead predominantly to the ground state of Sn^{119} (spin 1/2) rather than the isomeric level, Sn^{119m} (probable spin 11/2).

Using the value of 1.1 barns[20] for the activation cross section of Sn^{112}, the absolute cross section of Sn^{118} for the activation of Sn^{119m} is 0.01 barn.

ACKNOWLEDGMENTS

We wish to thank Mr. Robert Baer who proficiently helped in taking and analyzing the data.

We are also grateful to Professor R. D. Hill for many enlightening discussions as well as for his cooperation in loaning us the source.

We are indebted to Dr. Sherman Frankel of the University of Pennsylvania for discussions and aid pertaining particularly to electronic problems. Dr. Frankel also designed and tested the pulse height selector and the multichannel coincidence circuit.

[12] R. F. Goodrich, University of Illinois, private communication.

‡ *Note added in proof.*—Additional evidence for the predominance of L_I conversion in magnetic dipole transitions has been given by Mihelich and Church, Bull. Am. Phys. Soc., Chicago, Illinois, October 24–27, 1951, p. 37. They also point out that electric quadrupole transitions give rise to mainly L_{II} and L_{III} conversion.

[13] M. G. Mayer, Phys. Rev. **78**, 16 (1950).

[14] Katz, Hill, and Goldhaber, Phys. Rev. **78**, 9 (1950).

[15] J. C. Bowe and P. Axel (to be published).

[16] C. M. Nelson and G. E. Boyd, Oak Ridge National Laboratory Report ORNL 499, 1949.

[17] M. E. Rose and J. L. Jackson, Phys. Rev. **76**, 540 (L) (1949).

[18] J. L. Lawson and J. M. Cork, Phys. Rev. **57**, 982 (1940).

[19] Rose, Goertzel, Spinrad, Harr, and Strong, Phys. Rev. **83**, 79 (1951).

[20] Seren, Friedlander, and Turkel, Phys. Rev. **72**, 888 (1947).

Spectroscopy of the Solid State: Potassium and Calcium*

R. H. KINGSTON
Research Laboratory of Electronics, Massachusetts Institute of Technology, Cambridge, Massachusetts

(Received August 27, 1951)

Utilizing the techniques developed by O'Bryan and Skinner for the study of the emission bands of metals, it has been possible to determine the structure of the conduction bands of the metals, potassium and calcium. The spectrograph used utilizes a photomultiplier in place of a photograph plate, thus enabling higher sensitivity and ease of operation. The particular radiation studied is produced by transitions of the conduction electrons into the ionized $3p$ state of the atom. The limiting factor in the accuracy of the emission band obtained in this way is the purity of the sample studied. The contamination of the surface of an evaporated sample affects the resultant curve mainly as a result of insufficient penetration of the electrons, since the photon absorption is negligible at depths required to produce radiation representative of the pure bulk metal. The results for potassium and calcium at temperatures between 25°C and 100°C are not in good agreement with previous theoretical calculations. The experimental values of band width are 1.9 and 3.0 ev, respectively, compared with the theoretical calculations of 3.6 and 5.0 ev.

I. INTRODUCTION

BY means of spectrographic techniques originally developed by O'Bryan and Skinner[1] it has been possible to determine the energy distribution of the valence electrons in metallic potassium and calcium. If a sample of the metal is bombarded with electrons of several hundred volts energy it is possible to observe an emission band whose intensity distribution is directly related to the density of occupied states in the conduction band. The transition studied in this work is the valence band to $3p$ level, having a short wavelength limit of 500 and 670A for calcium and potassium, respectively. This wavelength radiation lies in the extreme ultraviolet and requires a spectrograph evacuated to pressures of 10^{-5} mm Hg or better, utilizing a grazing incidence concave grating. The instrument used, described elsewhere in the literature,[2] consists of two separate vacuum systems; one containing the spectrograph proper and the other containing a copper target, electron gun, and evaporating furnace for preparation of the sample. The two systems are separated by a sliding-type vacuum valve and the specimen chamber is maintained at a vacuum of 10^{-6} mm Hg to assure minimum contamination of the specimen. The spectrograph is of the same type as that used by O'Bryan and Skinner except that the photographic plate has been replaced by a Be-Cu photomultiplier which may be driven by an external coupling along the focusing trajectory of the spectrograph. This modification greatly enhances the sensitivity and flexibility of the apparatus.

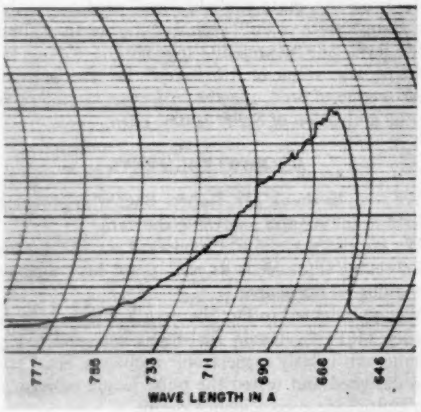

FIG. 1. Band emission curve of potassium. $E_b = 300$ volts. $I_b = 3$ ma. Counting rate = 500 counts/sec full scale.

II. EXPERIMENTAL PROCEDURE

The potassium used for this work was reagent grade metal packed in kerosene. For evaporation purposes the metal was rinsed in toluene and cut in small pieces before being placed in the evaporating cup. In this way the active surface of the material was not exposed until the toluene had evaporated during evacuation of the chamber.

After the specimen chamber, containing the evaporating furnace, target, and electron gun, had been evacuated to a pressure of 10^{-6} mm Hg, the furnace and gun were turned on and the system allowed to outgas. When a suitable vacuum had again been obtained, the valve separating the specimen chamber from the spectrograph was opened and the target adjusted to obtain maximum photon counting rate. Then, with the detection system set at a wavelength corresponding to the maximum intensity of the emission band, the power to the evaporating furnace was increased and evaporation continued until the observed radiation reached a steady maximum in intensity. At

* This work has been supported in part by the Signal Corps, the Air Materiel Command, and the ONR.

[1] H. M. O'Bryan and H. W. B. Skinner, Phys. Rev. **45**, 370 (1934).

[2] E. M. Gyorgy and R. H. Kingston, Phys. Rev. **83**, 220(A) (1951); Piore, Harvey, Gyorgy and Kingston, "A high vacuum recording spectrograph for the study of radiation from solids in the 100–800A range" (to be published, Rev. Sci. Instr.).

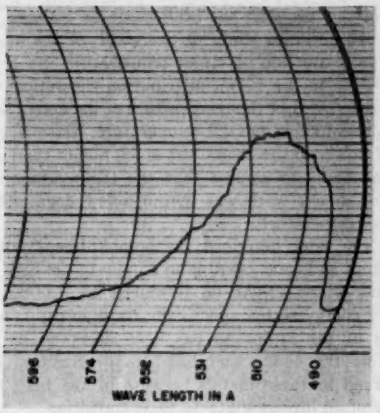

FIG. 2. Band emission curve of calcium. $E_b = 500$ volts. $I_b = 6$ ma. Counting rate = 500 counts/sec full scale.

this point the photomultiplier was moved to a wavelength slightly shorter than that of the emission edge and a curve such as shown in Fig. 1 was recorded. A total of a dozen curves were taken, with several values of bombarding voltage and varying evaporation cycles; that shown was taken several minutes after the metal had been evaporated onto the target and the furnace shut off. It is representative of all the curves taken within a few minutes of the evaporation. An interesting point is that at voltages of 300 volts and higher the curves reproduce well; however, if the voltage is decreased to 150 volts, a sharp peak no longer appears at the high energy end of the band. The same results occur if the curve is taken ten or more minutes after the evaporation is stopped. This is interpreted as meaning that the penetration of the electrons is not sufficient at 150 volts to produce radiation representative of the pure bulk metal. In all probability the loss of the high energy peak is a result of oxide forming on the surface of the specimen. The fact that this effect is observed at higher voltages if the target has had time to deteriorate would indicate a slow penetration of the contaminating atoms into the interior of the metal.

Much more difficulty was experienced in obtaining the calcium emission band as a result of the contamination of the sample. There are two reasons for this. First, calcium does not melt before it reaches a temperature sufficient to evaporate metal onto the target; this means that an oxidized layer may easily form on the surface of the solid calcium, preventing the pure metal atoms from leaving the material. Second, calcium does not form a protective coat as do metals such as potassium and aluminum; instead of a thin layer of oxide forming on the surface and protecting the metal, the oxygen atoms seem to penetrate into the bulk of the metal in a matter of seconds. Because of this the curve shown in Fig. 2, one of approximately 30 curves, had to be taken with the evaporating furnace still running. The calcium on the target was thus being replenished continually with pure metal. To assume maximum purity the metal chips were first ground by means of a mortar and pestle to expose as much fresh surface as possible before being evaporated. Even with these precautions it was not possible to take more than one accurate curve for each filling of the evaporating cup. A second plot taken with the furnace still in operation produced a curve of the same general shape, but decreases in intensity by a factor of 50 to 75 percent. The behavior of the curve at the emission edge was checked carefully by starting the record at the peak of the edge, thus starting the curve only a few seconds from the time a satisfactory coat was on the target. In this way it was definitely established that the rising intensity with increasing wavelength was an accurate observation. If the evaporating furnace is shut off before the curve is started the result is a band emission curve which looks like a decreasing exponential, since the decrease in intensity as a function of time because of contamination completely masks the true shape of the emission band. This same effect may be observed if the photomultiplier is set at the peak of the emission band and the intensity of radiation as a function of time is studied at the one particular wavelength. The time required for the intensity to drop to one-half of its maximum for potassium. On the whole this seems to indicate that the behavior of metallic surfaces is not simply related to the activity of the free atom. These effects should certainly be considered in any future work on the band emission of solids.

A curve of a contaminated sample of calcium is shown in Fig. 3. Note how the intensity has fallen to almost half its value and the maximum has shifted to longer wavelengths. This particular curve was run ten

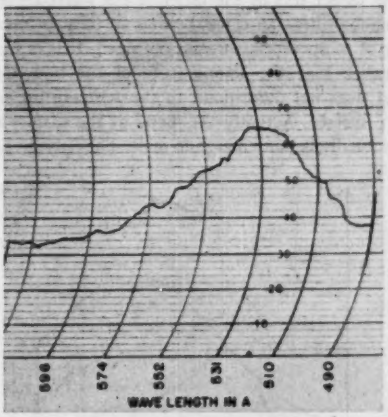

FIG. 3. Band emission curve of contaminated calcium. $E_b = 330$ volts. $I_b = 6$ ma. Counting rate = 200 counts/sec full scale.

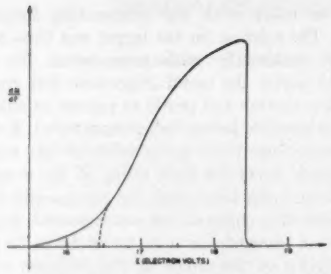

FIG. 4. S and d electron distribution in potassium.

minutes after the evaporating furnace had been turned on. Although the coat was being slowly replenished, oxidation of the metal in the cup and on the target caused a high percentage of impurities in the target. As was observed in potassium it was impossible to obtain any representative curve at all at 150 volts bombardment potential, even though the record was started at the beginning of the evaporation cycle.

During all the runs taken the object slit was set at 0.25-mm width and the image slit at 1.0 mm. This corresponds to a resolution of approximately 5A in the region studied. The calibration of the spectrograph was made at this same slit setting so that the wavelength of the emission edges should be accurate within 1 or 2A, if this value is measured at 50 percent of the maximum value of intensity at the emission edge. The calibrating edge was that of aluminum in the third and fourth order, corresponding to wavelengths of 510 and 680A.

The target temperature was somewhere between 25 and 100°C since during all the experiments the copper target was filled with tap water. Since the input power to the target was of the order of 1.5 watts there was not enough heat to cause boiling so that an accurate value of temperature was not obtained. It is important to realize that the temperature of the body of the target does not correspond to the temperature of the active surface. Actually the metal at the surface could theoretically be hot enough to melt. The only investigation of this problem has been made by Skinner,[3] who made an accurate study of the width of the emission edge as a function of target temperature. By relating this width to the Fermi distribution theoretical width he concluded that the temperature of the active surface was close to the over-all temperature. Since Skinner's input power to the target was much higher than ours it is reasonable to assume that the temperature of the sample in our work was within a few degrees of the target temperature.

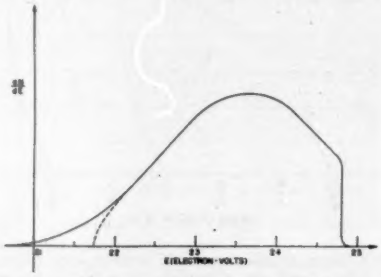

FIG. 5. S and d electron distribution in calcium.

In the work described the bombardment potential was kept as low as possible to eliminate the high background which might be produced by excitation of higher energy states, specifically those in the $2s$ and $2p$ shells of the atom. As has been observed by other workers the conduction band-to-$3s$ transition is not observed in these metals because of the high probability of an intermediate $3p$-to-$3s$ transition.

III. INTERPRETATION OF DATA

The experimental curves may be modified to represent the density, dN/dE, of the s-type and d-type electrons according to a method given by Skinner.[3] The background is first subtracted from the emission curve and then the resultant distribution replotted as a function of quantum energy; the ordinate having been divided by a factor proportional to the fourth power of the energy. The final curve then represents the density of electrons weighted according to their particular wave function. For example, if the wave function of electrons at some specific point in the band is composed of s and p functions, the resultant plot will give only the contribution of the s part of the function since the final state in the transition is a p state. For simplicity the emission edge has been sharpened to correspond to the shape of the theoretical edge obtained from the Fermi statistics at the temperature used. This is not a strictly accurate interpretation since it cannot be said definitely that the edge would be this sharp if the spectrograph were operated at its limiting resolution. The width of the edge, however, as measured on the experimental curves corresponds to the calculated resolution of the spectrograph and it is therefore assumed that the above alteration is reasonable. The energy at the emission edge was determined by a direct comparison with higher orders of the aluminum edge obtained by Skinner. The cross calibration was made at the midpoint of the experimental edge.

Since potassium is a monovalent metal, it is quite well described by the Sommerfeld free-electron approximation. Figure 4 shows the distribution of electrons as a function of energy as determined from the experimental curves. The dotted line at the low energy end of the curve shows the probable position of the bottom of the Brillouin zone. The low energy "tail" on the curve is a common characteristic of emission bands and

[3] H. W. B. Skinner, Trans. Roy. Soc. (London) **A239**, 95 (1940).

has been discussed by Skinner[3] and Seitz.[4] There are several explanations for the effect. Skinner concludes that it is a result of Auger transitions during the radiative process while Seitz attributes it to either contamination or the vestiges of excited states formed below the band. A detailed analysis applied to sodium is given by Landsberg.[5] In this curve and the curve for calcium a parabola has been fitted to the bottom of the band, since it is known that electrons in this region behave according to the free electron theory. The position of the estimated limit of the band cannot be determined accurately because of this phenomenon, but a reasonable value of the band width is 1.9 ± 0.2 electron-volts. It is of interest to note that the Sommerfeld approximation gives 2.1 volts for this value, while a Wigner-Seitz calculation of the effective mass of the electrons at the bottom of the zone gives a band width of 3.6 volts.[6] Evidently the wave functions of the electrons in the potassium band are predominantly of the *s*-type, since the over-all curve is a good representation of the parabolic distribution which would be expected in this case.

The calcium conduction band shows a shape much different than the free electron theory would predict. Figure 5 indicates that the first Brillouin zone is nearly filled, since the density of states falls off well before the high energy edge. The second zone must necessarily overlap with the first since the metal is a conductor; however there is an uncertainty as to the wave functions at the bottom of this excited band. There is certainly no definite indication of an overlapping curve such as may be seen in Fig. 6, taken from data obtained for aluminum.[3] Even though calcium has two valence electrons, compared with three for aluminum, Skinner's curves[3] for magnesium indicate that even in the divalent case an overlap should be observed. There are two possible explanations for the lack of structure in the calcium case. First, it is possible that the wave functions at the bottom of the second band are *p*-type, therefore not observable in a transition to the $3p$ state; or second, the excited band rises so slowly that it would not produce any observable inflection in the curve. Manning and Krutter's calculations[7] indicate a *d* band as the overlapping zone; however, examination of their predicted curve in Fig. 7 shows that the calculations cannot be too sound since the band widths are in very poor agreement. The observed band width is 3.0 ± 0.2 volts, Manning and Krutter's value, 5.0 volts and the free-electron determination, 4.3 volts. It is not possible to determine from the above authors' calculations whether the electrons in the bottom of the *d* band are *s*-, *p*-, or *d*-type. If the band is as sharp as their calculations would indicate then *p*-type functions would be

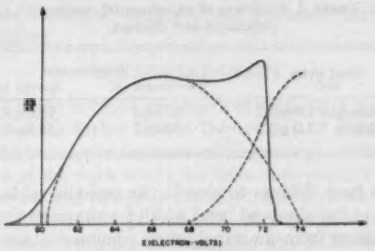

FIG. 6. *S* and *d* electron distribution in aluminum. (Dashed lines indicate probable zone structure.)

expected, since a sharp rise is not visible in the experimental curve; however, there is possibly an overlap into the $4p$-derived band rather than the $3d$, in which case it would most likely be fairly broad and would therefore not be obvious in the curves. The peak of the density curve does not necessarily correspond to the maximum number of electrons per unit energy range since there is every indication that the electron wave function changes from *s* to either *p* or *d* as the eigenvalue increases in magnitude. It may certainly be stated, however, that the degeneracy at the top of the band is as high if not higher than the observed curve indicates, contrary to the theory. A survey of the literature indicates that there are no data on the Hall coefficient for calcium. When such measurements are made, it should prove instructive to ascertain the relation of this coefficient to the filling of the first Brillouin zone. Since this zone is almost completely full it is highly probable that the coefficient would have the anomalous sign, that is, the negative mass effect in the quantum mechanical treatment would cause the current carriers to appear as positive charges.

The experimental results for potassium and calcium are summarized in Table I.

IV. GENERAL DISCUSSION OF METALLIC ENERGY BANDS

Table II is a survey of the theoretical and experimental results obtained for the electronic structure of

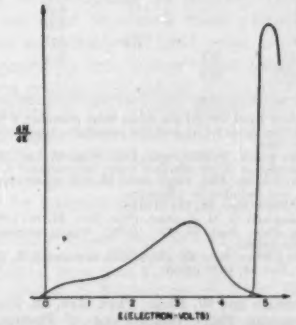

FIG. 7. Manning and Krutter's calculated distribution curve.

[4] F. Seitz, *Modern Theory of Solids* (McGraw-Hill Book Company, Inc., New York, 1940), p. 439.
[5] P. T. Landsberg, Proc. Phys. Soc. (London) **A62**, 806 (1949).
[6] See reference 4, p. 354.
[7] M. F. Manning, H. M. Krutter, Phys. Rev. **51**, 761 (1937).

TABLE I. Summary of experimental results for potassium and calcium.

	Band width (ev)	Emission edge Wavelength (A)	Energy (ev)
Potassium	1.9±0.2	675±2	18.4±0.1
Calcium	3.0±0.2	500±2	24.8±0.1

metals from lithium to zinc in the periodic table. The values of the observed band width for titanium through zinc, taken from an unpublished communication from Skinner, are not considered too reliable, since the emission edges are not at all sharp. The free-electron band widths for the transition metals have not been calculated, as the value obtained would be in complete disagreement with the actual band widths, since the *d* electrons are known to be tightly bound. The cellular calculations for the transition metals are also unreliable, since they are only qualitative values obtained by Slater by extrapolating Krutter's results for copper. The lithium value has been recalculated by Silverman[8,9] giving a value of effective mass in closer correspondence with the observed band width.

The calculations show generally good agreement for the first two periods of the table; however, the potassium and calcium band widths are closer to the free electron value than that of the Wigner-Seitz calculation, and the work on the transition metals is too sketchy to make any generalizations. It is interesting that the Fletcher and Wohlfarth calculation for nickel gives a band width just one-half the value of that obtained by Slater using the cellular method. If similar results were to be expected for potassium and calcium using the Bloch perturbation method the band widths would correspond much more closely with the experimental values. It is not immediately obvious why the Bloch calculation gives a band width corresponding to much tighter binding than the cellular method. It may be that the presence of a 3rd level with energy very close to the 4*s* energy, and yet a mean radius corresponding to that of the 3*p* level, introduces complications not taken into full account in the cellular method. This might be a result of the fact that the Bloch scheme seems to take a much more accurate account of exchange interactions. Slater[10] has proposed an intermediate method of calculating the interaction potentials and a trial calculation is now being carried out by Parmenter[11] to determine the validity of this approach. The idea is to modify the Hartree-Fock equations in such a way that the potential seen by the electron is somewhere between the extreme of the Bloch method, where neighboring cells are assumed to contain no valence electrons, and the cellular method, where the neighboring cells are treated as electrically neutral.

TABLE II.* Summary of band emission data and theoretical calculations. (All energies given in electron-volts).

Metal	No. of valence electrons	Band width Free electron	Bloch pert.	Cellular	Obs.
Li	1	4.7	···	3.1[b]	3.7±0.5
Be	2	14.3	···	11.8[c]	13.8±1.0
Na	1	3.2	···	3.2[d]	2.5±0.3
Mg	2	7.2	···	···	6.2±0.3
Al	3	11.7	13.0	···	11.8±0.5
K	1	2.1	···	3.6[b]	1.9±0.2
Ca	2	4.3	···	5.0[e]	3.0±0.2
Ti	4	···	···	1.8[f]	5.6±0.5
Va	5	···	···	2.5[f]	5.6±0.5
Cr	6	···	···	3.1[f]	6.3±0.5
Mn	7	···	···	3.7[f]	6.0±0.5
Fe	8	···	···	4.3[f]	4.4±0.5
Co	9	···	···	4.6[f]	5.8±0.5
Ni	10	···	2.4[a]	4.9[f]	4.7±0.5
Cu	1(?)	7.1	···	7.3[g]	7.0±0.5
Zn	2(?)	9.5	···	···	11.0±0.5

* Note: Observed band widths are taken from reference 3 for Li to Al; from this paper, for K and Ca; and the remainder from Skinner's data mentioned in the text.

[a] G. C. Fletcher and E. P. Wohlfarth, Phil. Mag. **42**, 106 (1951).

[b] Based on calculation of the effective mass; see reference 4, p. 354.

[c] C. Herring and A. G. Hill, Phys. Rev. **58**, 132 (1940). Not strictly a cellular method, but included for reference.

[d] J. C. Slater, Phys. Rev. **45**, 794 (1934).

[e] M. F. Manning and H. M. Krutter, Phys. Rev. **51**, 761 (1937).

[f] J. C. Slater, Phys. Rev. **49**, 537 (1936). Values extrapolated from Krutter's work on copper.

[g] H. M. Krutter, Phys. Rev. **48**, 664 (1935). See also S. R. Tibbs, Proc. Cambridge Phil. Soc. **34**, I, 89 (1938).

V. SUMMARY

The experimental work described has definitely established the fact that the emission edges of the metals potassium and calcium are sharp as has been observed in aluminum and the preceding conductors in the periodic table. On the basis of these results it seems possible that future work on the transition metals, with the more sensitive techniques described, will produce better resolution than that obtained by Skinner, above. A study of the absorption coefficients of metals for radiation of the wavelengths[12] used has shown that the important factor in determining the reliability of the observed band emission curves is the depth of penetration of the bombarding electrons. For the metals described in this paper the necessary bombarding potential has been found to be 300 volts or higher. There is of course the possibility that the metals which have *d* band structure may have higher electron absorption, in which case the voltage should be raised to take this into account. A thorough study of electron penetrations at voltages of 100 to 1000 volts would be an extremely valuable addition to the literature, as well as further studies on photon absorption in the 100 to 800A range.

[8] R. A. Silverman and W. Kohn, Phys. Rev. **80**, 912 (1950).

[9] R. A. Silverman, Ph.D. thesis, Dept. of Physics, Harvard University (1951).

[10] J. C. Slater, Phys. Rev. **81**, 385 (1951).

[11] R. H. Parmenter, Quarterly Profress Report, Solid State and Molecular Theory Group, M.I.T., Cambridge, Massachusetts (July 15, 1951), p. 15.

[12] H. W. B. Skinner and J. E. Johnston, Proc. Roy. Soc. (London) **A161**, 420 (1937); J. E. Johnston, Proc. Cambridge Phil. Soc. **35**, 108 (1939).

Another important result of the work is the observation that the chemical activity of a metal is not a decisive factory in determining its resistance to oxide contamination. Before intensive studies of the transition metals are taken up it seems advisable that the protective layer effect as observed in potassium should be investigated more thoroughly, probably by a survey of the metallurgical literature.

The use of the photomultiplier in place of photographic plates has added another variable to the experimental observations. This is the possibility of studying time-dependence of the radiation from the sample. The high sensitivity and the foregoing effect suggest possible studies of surface effects in metals and nonconductors.

ACKNOWLEDGMENT

This paper is based on results obtained in a doctoral thesis by the author for the Department of Physics at the Massachusetts Institute of Technology. The completion of the work would not have been possible without the aid and advice of Dr. E. R. Piore, of the Office of Naval Research, Professor G. G. Harvey, Professor J. C. Slater, Professor L. Tisza, and Mr. E. M. Gyorgy of M.I.T., and the able technical staff of the Research Laboratory of Electronics.

PHYSICAL REVIEW VOLUME 84, NUMBER 5 DECEMBER 1, 1951

A Phenomenological Theory of the Lamb Shift and of Anomalous Magnetic Moments

FREDERIK J. BELINFANTE
Department of Physics, Purdue University, Lafayette, Indiana

(Received August 14, 1951)

If one assumes that self-interactions don't exist and can be ignored, the explanation of the anomalous magnetic moments of proton and electron and the Lamb shift require new types of interaction between protons, photons, and electrons. A theory with such additional interactions is here developed in gauge-independent form, thus avoiding longitudinal and scalar photons throughout. The covariance of the formalism is proved. The resulting modification of Maxwell's equations for charged elementary particles in the vacuum involves only the introduction of an intrinsic polarization and magnetization of elementary particles, so that these equations for the vacuum now take the familiar form of the macroscopic Maxwell equations in matter. A further modification of the Dirac equation for electrons and protons involves the introduction of a delta-function interaction between them, opposite in sign to the Coulomb interaction. It is indicated how one can derive an energy density tensor for this theory. It is then shown how this formalism explains the anomalous moments and the Lamb shift. The three new interaction constants are adjusted to the experimental data. The dependence of the Lamb shift on the quantum numbers automatically comes out to be nearly the same and the dependence on the atomic number to be exactly the same as in the theory of Bethe, French and Weisskopf.

1. INTRODUCTION

THE Lamb shift[1,2] and the anomalous magnetic moment of the electron[3,4,4a] have been explained as consequences of self-interaction of the electron through the radiation field.[5–8a] The necessity of infinite "renormalizations" or "subtractions" or of other special devices to make divergent expressions finite makes this theory not fully satisfactory. There have also been attempts at explaining the anomalous magnetic moment of nucleons[9–11] as a consequence of their mesic ("pionic") self-interaction.[12] These theories too are not quite satisfactory.

Instead of attempting to improve these existing theories, we want to attack these problems in this paper from an entirely different point of view. It has been suggested by this author[13] that perhaps no self-interactions exist at all in nature. Although this hypothesis formulated in this oversimplified form is subject to various serious objections, which the author intends to discuss in a forthcoming paper, and which need further investigations for their complete solution, it might yet be interesting to examine already now, how

[1] W. E. Lamb and R. C. Retherford, Phys. Rev. **72**, 241 (1947).
[2] R. C. Retherford and W. E. Lamb, Phys. Rev. **75**, 1325 (1949); W. E. Lamb and R. C. Retherford, Phys. Rev. **79**, 549 (1950); and **81**, 222 (1951).
[3] P. Kusch and H. M. Foley, Phys. Rev. **72**, 1256 (1947); H. M. Foley and P. Kusch, Phys. Rev. **73**, 412 (1948).
[4] P. Kusch and H. M. Foley, Phys. Rev. **74**, 250 (1948).
[4a] S. Koenig, A. G. Prodell, and P. Kusch, Phys. Rev. **83**, 687(L) (1951).
[5] H. A. Bethe, Phys. Rev. **72**, 339 (1947).
[6] J. B. French and V. F. Weisskopf, Phys. Rev. **75**, 1240 (1949).
[7] Bethe, Brown, and Stehn, Phys. Rev. **77**, 370 (1950).
[8] Similar results were obtained by J. Schwinger and others using manifestly covariant methods, in which, however, the non-normalizability of the state vector makes the derivations somewhat more doubtful.
[8a] R. Karplus and N. Kroll, Phys. Rev. **77**, 536 (1950).
[9] H. Taub and P. Kusch, Phys. Rev. **75**, 1481 (1949).
[10] Sommer, Thomas, and Hipple, Phys. Rev. **80**, 487 (1950).
[11] C. D. Jeffries, Phys. Rev. **81**, 1040 (1951).
[12] See for example, S. Borowitz and W. Kohn, Phys. Rev. **76**, 818 (1949).
[13] F. J. Belinfante, Phys. Rev. **82**, 767 (1951); Progress of Theor. Physics **6**, 202 (1951).

in such a theory without self-interactions one can explain the Lamb shift as well as the anomalous magnetic moments,[14] even if self-interactions are (perhaps wrongly) ignored *completely*.[15]

Such explanation requires introduction of properly chosen interactions between fermions and photons. It will be our first task to fit these interactions into the framework of gauge-independent quantum electrodynamics,[16–18] and to prove their covariance. In the second place, we have to explain how the theory thus extended leads to the experimentally observed phenomena of Lamb shift and anomalous moments, and we have to determine, what values for this purpose should be given the newly introduced interaction constants. For the sake of simplicity, we shall here completely ignore nuclear forces, and we shall not discuss the neutron,[18a] although this could easily have been done by the same methods. We shall merely discuss the interaction between electrons, photons, and protons.

2. INTERACTION REPRESENTATION AND COVARIANCE

Using methods developed recently for gauge-independent quantum electrodynamics, we could simply take over without change the formulas (G-I:1) through (G-I:7) of reference 16; however, we shall find it useful here to substitute the notation $\mathbf{D}_{\text{II}}$ for the Coulomb field called $\mathbf{E}_{\text{II}}$ in reference 16, replacing (G-I:6) by

$$\mathbf{D}_{\text{II}}=-\nabla V, \quad \text{div}\mathbf{D}=-\triangle V=4\pi\rho. \tag{1a–b}$$

Similarly, we shall replace the definition (G-I:44) by

$$\mathbf{D}=\mathbf{D}_{\text{II}}+\mathfrak{E}, \text{ thence } \mathbf{D}_{\perp}=\mathfrak{E}. \tag{2a–b}$$

In Eq. (1), ρ is this time the sum of the charge distributions of electrons and protons, so that the charge density in esu and the current density in emu are given in terms of the electron and proton fields ψ_e and ψ_P by

$$\left.\begin{aligned} &j^0=\rho=\rho_P+\rho_e, \quad \mathbf{j}=\mathbf{j}_P+\mathbf{j}_e, \quad j^\mu=\textstyle\sum_n j_n{}^\mu, \\ &j_n{}^\mu=e_n\,{:}\psi_n{}^\dagger\alpha^\mu\psi_n{:}, \text{ with } e_P=-e_e=|e|, \quad \alpha^0=1, \end{aligned}\right\} \tag{3}$$

where n is P or e, and where : : stands for subtraction of vacuum values. As in Eq. (E-T:7) of reference 18, we may replace the symbol : : in Eq. (3) by the symbol $\mathfrak{R}\{\ \}$ defined by Eq. (E-T:6).

In interaction representation, the transverse electric field $\mathfrak{E}$ forms a tensor together with the magnetic field $\mathfrak{B}$ (with $\mathfrak{E}_x=\mathfrak{F}_{10}=\mathfrak{F}^{01}$, $\mathfrak{B}_x=\mathfrak{F}_{23}=\mathfrak{F}^{23}$, etc.). A solenoidal vector potential $\mathfrak{A}$ is defined in terms of $\mathfrak{B}$ by Eq. (G-I:3).

The state vector $\Psi_\sigma[\sigma]$, defined for flat space-like surfaces σ only, will again satisfy the generalized Schrödinger equation (G-I:9) for progress of time as well as for Lorentz transformations. However, we shall now replace the interaction operator (G-I:10) by a new operator showing some additional types of interaction:[19]

$$W=\mathbf{D}_{\text{II}}{}^2/8\pi+\mathbf{D}_{\text{II}}\cdot\mathfrak{E}/4\pi-\mathbf{D}_{\text{II}}\cdot\mathbf{P}-\mathfrak{E}\cdot\mathbf{P}+2\pi\mathbf{P}^2 \\ -\mathfrak{A}\cdot\mathbf{j}-\mathfrak{B}\cdot\mathbf{M}+\tfrac{1}{2}C(j^2-\rho^2). \tag{4}$$

Here, $(-\mathbf{P})$ and $\mathbf{M}$ form an antisymmetric tensor $M^{\mu\nu}$ transforming like ${}^\circ\mathfrak{E}$ and ${}^\circ\mathfrak{B}$, and they are expressed in terms of ψ_e and ψ_P by

$$\left.\begin{aligned} &M^{\mu\nu}=M_{\mathfrak{E}}{}^{\mu\nu}+M_e{}^{\mu\nu}=\textstyle\sum_n \frac{1}{2}if_n\,{:}\bar\psi_n(\gamma^\nu\gamma^\mu-\gamma^\mu\gamma^\nu)\psi_n{:}\,; \\ &M_{01}=M^{10}=P_x, \ M_{23}=M_x; \quad \bar\psi=\psi^\dagger\beta, \ \gamma^\mu=-i\beta\alpha^\mu; \\ &\mathbf{P}_n=f_n\,{:}\psi_n{}^\dagger\gamma\psi_n{:}, \quad \mathbf{M}_n=f_n\,{:}\psi_n{}^\dagger\beta\sigma\psi_n{:}. \end{aligned}\right\} \tag{5}$$

The quantities f_e and f_P are here interaction constants of the dimension of a dipole moment or magnetic moment in Gaussian units, while the interaction constant C in (4) has the dimension of an area. Again, the symbol : : in (5) is Wick's symbol for omission of vacuum terms[20] and can be replaced by the symbol $\mathfrak{R}\{\ \}$ of (E-T:6), by an argument similar to that of footnote 12 of reference 18, using Eqs. (29), (23), (23a), (2), (15), and (17) of reference 21.

We shall verify the covariance of our theory by showing for our interaction (4) the validity of Eq. (G-I:11) by the methods of Chap. 3 of reference 16. Calculating the right-hand member of (G-I:11) for the interaction (4) and for the infinitesimal Lorentz transformation (G-I:13) by means of Eqs. (G-I:14, 15, 21, 23, 26) and the result (G-I:28) for $\int\delta(\mathbf{D}_{\text{II}}{}^2/8\pi)$, using also

$$\delta\mathbf{P}=-\mathbf{b}\times\mathbf{M}, \quad \delta\mathbf{M}=\mathbf{b}\times\mathbf{P}, \tag{6a-b}$$

putting $\mathbf{r}'=\mathbf{x}'-\mathbf{x}$, and understanding tacitly all q-numbers to be taken in interaction representation, we find, with some abbreviations of reference 16,

$$\int\delta\,{}^\circ W=\int\delta(\mathbf{D}_{\text{II}}{}^2/8\pi)-\int\delta(\mathbf{D}_{\text{II}}\cdot\mathbf{P})+\int\delta(2\pi\mathbf{P}^2) \\ =-\int V\mathbf{j}_\perp\cdot\mathbf{b}+4\pi\int\int'(\mathbf{b}\cdot\mathbf{r}')\mathbf{j}'\cdot\delta^{\text{long}}(\mathbf{r}')\cdot\mathbf{P} \\ +\int\mathbf{b}\cdot\mathbf{M}\times(\mathbf{D}_{\text{II}}-4\pi\mathbf{P}), \tag{7}$$

where we treated the longitudinal delta-function[22] as a dyadic.

Because of antisymmetries in $\mathbf{x}$ and $\mathbf{x}'$ we have

$$\mathbf{x}_Q\int\int'[{}^\circ W';{}^\circ W]=0=\int\int'(\mathbf{x}'+\mathbf{x})[{}^\circ W';{}^\circ W]. \tag{8}$$

---

[14] The possibility of explaining anomalous moments by ascribing intrinsic magnetizations to fermions was already suggested by W. Pauli, *Handbuch der Physik*, vol. 24/1 (Verlag Julius Springer, Berlin, 1933), p. 233. (Compare also pages 236–239.)

[15] It would seem better to omit only "virtual" self-interactions, if this can be done in a covariant way.

[16] F. J. Belinfante and J. S. Lomont, Phys. Rev. 84, 541 (1951). In the following we refer to equations from this paper by (G-I:).

[17] F. J. Belinfante, Phys. Rev. 84, 546 (1951).

[18] F. J. Belinfante, Phys. Rev. 84, 648 (1951). In the following we refer to formulas from this paper by (E-T:).

[18a] For a discussion of electron-neutron forces see for instance L. L. Foldy, Phys. Rev. 83, 688(L) (1951).

[19] For the applications of the theory made in this paper, one might have omitted from (4) the direct electron-electron and the direct proton-proton interactions by replacing its last term by $C(\mathbf{j}_e\cdot\mathbf{j}_P-\rho_e\rho_P)$. An additional term $\frac{1}{2}K(\mathbf{M}^2-\mathbf{P}^2)$ in (4) would not disturb the covariance, but is not needed here. Note that $\mathbf{D}_{\text{II}}$ and $\mathbf{P}$ commute.

[20] G. S. Wick, Phys. Rev. 80, 268 (1950).

[21] F. J. Belinfante, Physica 6, 849 (1939).

[22] See F. J. Belinfante, Physica 12, 1 (1946), for definition of the longitudinal and transverse delta-function and for formulas for the longitudinal and transverse parts of vector fields.

Using this and Eqs. (G-I:2) and (G-I:5), and Eq. (G-I:20) for eliminating all contributions from delta-function commutators, and employing methods as used in deriving Eq. (G-I:12), we find for the left-hand member of (G-I:11), with W from Eq. (4) and with $a=(i\hbar c)^{-1}$,

$$\begin{aligned}a\int\int'\mathbf{b}\cdot(\mathbf{x}'-\mathbf{x}_Q)[{}^\circ W';{}^\circ W]&=\tfrac{1}{2}a\int\int'(\mathbf{b}\cdot\mathbf{r}')[{}^\circ W';{}^\circ W]\\&=a\int\int'(\mathbf{b}\cdot\mathbf{r}')\{-\mathbf{D}_{\mathrm{II}}'\cdot[\mathfrak{E}';\mathfrak{B}]\cdot\mathbf{j}/4\pi\\&\quad-\mathbf{D}_{\mathrm{II}}'\cdot[\mathfrak{E}';\mathfrak{B}]\cdot\mathbf{M}/4\pi+\mathbf{j}'\cdot[\mathfrak{A}';\mathfrak{E}]\cdot\mathbf{P}\\&\quad+\mathbf{P}'\cdot[\mathfrak{E}';\mathfrak{B}]\cdot\mathbf{M}\}\\&=-\int V\mathbf{j}_\perp\cdot\mathbf{b}+\int\mathbf{b}\cdot\mathbf{M}\times\mathbf{D}_{\mathrm{II}}\\&\quad-4\pi\int\int'(\mathbf{b}\cdot\mathbf{r}')\mathbf{j}'\cdot\delta^{\mathrm{tr}}(\mathbf{r}')\cdot\mathbf{P}-4\pi\int\mathbf{b}\cdot\mathbf{M}\times\mathbf{P}.\end{aligned}\tag{9}$$

The difference of (7) and (9) vanishes by[22]

$$\delta_{ij}{}^{\mathrm{long}}(\mathbf{r}')+\delta_{ij}{}^{\mathrm{tr}}(\mathbf{r}')=\delta_{ij}\delta(\mathbf{r}')\tag{10}$$

together with Eq. (G-I:20). Thus, we have shown (G-I:11) and proved the covariance of our theory with interaction (4).

3. HEISENBERG REPRESENTATION

Beside our abbreviations (1)–(2), we shall here introduce the following:[23]

$$\mathbf{H}=\mathfrak{B}-4\pi\mathbf{M},\quad \mathbf{E}=\mathbf{D}-4\pi\mathbf{P};\tag{11a-b}$$

$$\Phi=V-\int'\operatorname{div}'\mathbf{P}'/r,\tag{12a}$$

so that[22]

$$-\nabla\Phi=\mathbf{D}_{\mathrm{II}}-4\pi\mathbf{P}_{\mathrm{II}}=\mathbf{E}_{\mathrm{II}};\tag{12b}$$

$$\sigma=\rho-\operatorname{div}\mathbf{P}=\operatorname{div}\mathbf{E}/4\pi=-(1/4\pi)\triangle\Phi,\tag{13a}$$

so that

$$\Phi=\int'\sigma'/r.\tag{13b}$$

After transformation to Heisenberg representation as in chapters 5 and 6 of reference 16, we find that under the infinitesimal Lorentz transformation (G-I:13) the q-numbers in Heisenberg representation are transformed according to (G-I:41). By Eqs. (G-I:14), (4), (G-I:2, 5, 20, and 23) this yields, if in the following all q-numbers are tacitly understood to be taken in Heisenberg representation (as we shall indicate explicitly only by subscripts H to the symbols δ and $\partial/\partial t$):[22]

$$\delta_{\mathrm{H}}\mathfrak{E}=\mathbf{b}\times\mathfrak{B}-4\pi\int'(\mathbf{b}\cdot\mathbf{r}')\mathbf{j}'\cdot\delta^{\mathrm{tr}}(\mathbf{r}')-4\pi(\mathbf{b}\times\mathbf{M}),\tag{14a}$$

$$\delta_{\mathrm{H}}\mathbf{D}_{\mathrm{II}}=-4\pi\int'(\mathbf{b}\cdot\mathbf{r}')\mathbf{j}'\cdot\delta^{\mathrm{long}}(\mathbf{r}'),\tag{14b}$$

so, by (2a), (10), (G-I:20), and (11a),

$$\delta_{\mathrm{H}}\mathbf{D}=\mathbf{b}\times\mathbf{H}.\tag{14}$$

Similarly, by (G-I:41), (G-I:14), (4), (G-I:2), (G-I:20), (11a), (6), and (2a),

$$\delta_{\mathrm{H}}\mathfrak{B}=-\mathbf{b}\times\mathfrak{E}-\mathbf{b}\times\mathbf{D}_{\mathrm{II}}+4\pi\mathbf{b}\times\mathbf{P},\tag{15}$$

$$\delta_{\mathrm{H}}\mathbf{H}=-\mathbf{b}\times\mathbf{D}.\tag{16}$$

[22] The quantity $\mathbf{E}$ used here is not identical with $\mathbf{E}$ of reference 16, for which we wrote here $\mathbf{D}$.

Equations (14) and (16) show that $\mathbf{D}$ and $\mathbf{H}$ form a tensor in Heisenberg representation. Since also $-\mathbf{P}$ and $+\mathbf{M}$ do so on account of (6), (G-I:41), and (G-I:20), we conclude that similarly $\mathbf{E}$ and $\mathfrak{B}$ form a tensor in Heisenberg representation:

$$\delta_{\mathrm{H}}\mathbf{E}=\mathbf{b}\times\mathfrak{B};\quad \delta_{\mathrm{H}}\mathfrak{B}=-\mathbf{b}\times\mathbf{E}.\tag{17}$$

(In interaction representation, $\mathfrak{B}$ formed a tensor with $\mathfrak{E}=\mathbf{D}_\perp$.)

By Eqs. (G-I:41), (G-I:14), (4), (G-I:48), (G-I:20), (2a), and (11b) we get

$$\begin{aligned}\delta_{\mathrm{H}}\psi&=-\tfrac{1}{2}\mathbf{b}\cdot\boldsymbol{\alpha}\psi-(e/4\pi i\hbar c)\int'(\mathbf{b}\cdot\mathbf{r}')\mathfrak{S}\{\psi\mathbf{E}'\cdot\nabla'(1/r)\}\\&=-\tfrac{1}{2}\mathbf{b}\cdot\boldsymbol{\alpha}\psi+(e/i\hbar c)\mathbf{b}\cdot\int'\mathfrak{S}\{\psi\mathbf{E}'/4\pi r+\psi\sigma'\mathbf{r}'/r\},\end{aligned}\tag{18}$$

where all products q_1q_2 of two q-numbers between the brackets $\{\ \}$ behind $\mathfrak{S}$ are to be read as $\frac{1}{2}(q_1q_2+q_2q_1)$. By (G-I:41), (G-I:21), (4), (G-I:5), (10), (G-I:20), (2a), and (11b) also

$$\begin{aligned}\delta_{\mathrm{H}}\mathfrak{A}&=\int'(\mathbf{b}\cdot\mathbf{r}')\mathbf{E}'\cdot\delta^{\mathrm{long}}(\mathbf{r}')\\&=-\int'(\mathbf{b}\cdot\mathbf{r}')(\mathbf{E}'\cdot\nabla')\nabla'(1/4\pi r)\\&=\int'(\mathbf{b}\cdot\mathbf{E}')\nabla'(1/4\pi r)-\mathbf{b}\Phi+\int'\sigma'\nabla'(\mathbf{b}\cdot\mathbf{r}'/r).\end{aligned}\tag{19}$$

Eqs. (18)–(19) show that in Heisenberg representation ψ is no undor[21] and $\mathfrak{A}$ is not the spatial part of a four-vector.

4. FIELD EQUATIONS, MAGNETIZATION AND POLARIZATION OF ELEMENTARY PARTICLES

According to chapter 7 of reference 16, the total energy is given by Eq. (G-I:52) with (4) for interaction. This gives

$$\mathcal{H}=\mathcal{H}_{\mathrm{mat}}+\mathcal{H}_{\mathrm{el}}+\mathcal{H}_{\mathrm{magn}}(-\mathcal{H}_{\mathrm{vac}}),\tag{20}$$

$$\mathcal{H}_{\mathrm{mat}}=\mathcal{H}_{\mathrm{P}}+\mathcal{H}_{\mathrm{s}}=\textstyle\sum_{\mathrm{n}}\int\psi_{\mathrm{n}}{}^\dagger(m_{\mathrm{n}}c^2\beta-i\hbar c\boldsymbol{\alpha}\cdot\nabla)\psi_{\mathrm{n}},\tag{20a}$$

$$\begin{aligned}\mathcal{H}_{\mathrm{el}}&=\int\{(\mathfrak{E}+\mathbf{D}_{\mathrm{II}}-4\pi\mathbf{P})^2/8\pi-\tfrac{1}{2}C\rho^2\}\\&=\int\{\mathbf{E}^2/8\pi-\tfrac{1}{2}C\rho^2\},\end{aligned}\tag{20b}$$

$$\mathcal{H}_{\mathrm{magn}}=\int\{\mathfrak{B}^2/8\pi-\mathfrak{A}\cdot\mathbf{j}-\mathfrak{B}\cdot\mathbf{M}+\tfrac{1}{2}C\mathbf{j}^2\}.\tag{20c}$$

By Eqs. (2a), (11b), (G-I:48) for $[\psi;\mathbf{D}_{\mathrm{II}}']$, and Eq. (5), we find

$$[\psi_{\mathrm{n}};\mathbf{E}']=-e_{\mathrm{n}}\psi_{\mathrm{n}}\nabla'(1/r)-4\pi f_{\mathrm{n}}\delta(\mathbf{r}')\gamma\psi_{\mathrm{n}},\tag{21}$$

$$[\psi_{\mathrm{n}};\sigma']=e_{\mathrm{n}}\delta(\mathbf{r}')\psi_{\mathrm{n}}'-f_{\mathrm{n}}\nabla'\cdot\{\delta(\mathbf{r}')\gamma\psi_{\mathrm{n}}'\},\tag{22}$$

$$[\psi_{\mathrm{n}};\Phi']=e_{\mathrm{n}}\psi_{\mathrm{n}}/r+f_{\mathrm{n}}\gamma\psi_{\mathrm{n}}\cdot\nabla(1/r),\tag{23}$$

$$[\psi_{\mathrm{n}};\mathbf{M}]=f_{\mathrm{n}}\delta(\mathbf{r}')\beta\sigma\psi_{\mathrm{n}}'.\tag{24}$$

The field equations of motion in Heisenberg representation follow from (G-I:53) with (20). By Eqs. (21), (13a-b), (G-I:48), and (24), this gives

$$\begin{aligned}i\hbar\partial_{\mathrm{H}}\psi_{\mathrm{n}}/\partial t&=(m_{\mathrm{n}}c^2\beta-i\hbar c\boldsymbol{\alpha}\cdot\nabla-e_{\mathrm{n}}\mathfrak{A}\cdot\boldsymbol{\alpha}-f_{\mathrm{n}}\mathfrak{B}\cdot\beta\sigma)\psi_{\mathrm{n}}\\&\quad+\mathfrak{S}\{e_{\mathrm{n}}\Phi\psi_{\mathrm{n}}-f_{\mathrm{n}}\mathbf{E}\cdot\gamma\psi_{\mathrm{n}}-Ce_{\mathrm{n}}\rho\psi_{\mathrm{n}}+Ce_{\mathrm{n}}\mathbf{j}\cdot\boldsymbol{\alpha}\psi_{\mathrm{n}}\}.\end{aligned}\tag{25}$$

Similarly, by (G-I:53), (20), (G-I:5), and (G-I:2),

$$\partial_H \mathfrak{E}/c\partial t = \text{curl}\mathfrak{B} - 4\pi \mathbf{j}_\perp - 4\pi\, \text{curl}\mathbf{M}, \tag{26}$$

$$-\partial_H \mathfrak{A}/c\partial t = \mathbf{E}_\perp, \tag{27}$$

$$-\partial_H \mathfrak{B}/c\partial t = \text{curl}\mathbf{E}; \quad \text{and always} \quad \text{div}\mathfrak{B} = 0. \tag{28a-b}$$

Further, by (G-I:53) and (G-I:48) or by (3) with (25) we find in Heisenberg like in interaction representation

$$\partial\rho/c\partial t = -\text{div}\mathbf{j}. \tag{29}$$

Thence, by (G-I:7) and (1a),.

$$\partial V/c\partial t = -\text{div}\int \mathbf{j}'/r, \quad \partial \mathbf{D}_{II}/c\partial t = -4\pi \mathbf{j}_{II}. \tag{30a-b}$$

From (G-I:4), from (12b) and (27), from (2a), (26), (11a), and (30b), and from (1b) we find

$$\mathfrak{B} = \text{curl}\mathfrak{A}, \quad \text{div}\mathfrak{A} = 0; \tag{31a-b}$$

$$\mathbf{E} = \mathbf{E}_{II} + \mathbf{E}_\perp = -\nabla\Phi - \partial_H \mathfrak{A}/c\partial t; \tag{32}$$

$$\partial_H \mathbf{D}/c\partial t = \text{curl}\mathbf{H} - 4\pi \mathbf{j}; \quad \text{div}\mathbf{D} = 4\pi\rho. \tag{33a-b}$$

Equations (28a-b) and (33a-b) take the form of Maxwell's macroscopic (phenomenological) equations. Thence, the quantities $\mathbf{M}$ and $\mathbf{P}$ occurring in Eqs. (11a-b), and defined by Eq. (5), may be called the intrinsic magnetization and polarization of elementary particles. The expressions (3) for ρ and $\mathbf{j}$ then describe the so-called "true" charge distribution.[24] In analogy to Lorentz' derivation of the phenomenological equations for the macroscopic field, from the vacuum Maxwell equations for the microscopic field, we might also here consider σ of Eq. (13a) as the "actual" charge density[25] (=true+polarization charge density) in esu, and

$$\mathbf{i} = \mathbf{j} + \partial_H \mathbf{P}/c\partial t + \text{curl}\mathbf{M} \tag{34}$$

as the "actual" charge current density[25] (=true+polarization+magnetization current density) in emu, so that, in Heisenberg representation, we can write (33a-b) as equations for $\mathbf{E}$ and $\mathfrak{B}$, by

$$\text{div}\mathbf{E} = 4\pi\sigma, \quad \text{curl}\mathfrak{B} = \partial_H \mathbf{E}/c\partial t + 4\pi\mathbf{i}. \tag{35a-b}$$

Then, $\mathbf{i}$ and σ together form a four-vector $i^\mu = \sum_n i_n^\mu$ in Heisenberg representation given by

$$i^\mu = j^\mu + \nabla_\nu M^{\mu\nu} \tag{36}$$

and satisfying in Heisenberg representation the continuity equation

$$\nabla_\mu i^\mu = \nabla_\mu j^\mu + \nabla_\mu \nabla_\nu M^{\mu\nu} = 0. \tag{37}$$

[24] See for instance M. Abraham and R. Becker, *The Classical Theory of Electricity and Magnetism* (Hafner Publishing Company, Inc., New York, 1932), p. 74; and R. Becker, *Theorie der Elektrizität*, Band II, Elektronentheorie, 6. Auflage (B. G. Teubner, Leipzig, 1933), pp. 108–118. The name "true" for this charge is rather arbitrary and meaningless.

[25] The "actual" charge distribution σ, $\mathbf{i}$ is sometimes called the "free" charge distribution; see reference 24. It is to be distinguished from the "true" charge distribution ρ, $\mathbf{j}$.

5. THE ENERGY DENSITY TENSOR

Equations (28a-b) and (35a-b) suggest a different grouping of the terms in the energy equation (20):

$$\mathcal{H} = \mathcal{H}_{\text{Field}} + \mathcal{H}_{\text{direct}} + \mathcal{H}_{\text{Kinetic}} = \int T^{00} d^3\mathbf{x}, \tag{38}$$

where $T^{\mu\nu} = T_{\mathfrak{F}}{}^{\mu\nu} + T_{\text{dir}}{}^{\mu\nu} + T_{\text{Kin}}{}^{\mu\nu}$ with

$$4\pi T_{\mathfrak{F}}{}^{\mu\nu} = F^{\lambda\mu}F_\lambda{}^\nu - \tfrac{1}{4}g^{\mu\nu}F_{\rho\sigma}F^{\rho\sigma}, \tag{39}$$

$$T_{\text{dir}}{}^{\mu\nu} = -\tfrac{1}{2}C g^{\mu\nu} j_\lambda j^\lambda. \tag{40}$$

Here $g^{00} = -1$, $g^{11} = 1$, etc., and $F^{\mu\nu}$ is the tensor in Heisenberg representation of $\mathbf{E}$ with $\mathfrak{B}$, so that

$$T_{\mathfrak{F}}{}^{00} = (\mathbf{E}^2 + \mathfrak{B}^2)/8\pi, \quad T_{\text{dir}}{}^{00} = \tfrac{1}{2}C(\mathbf{j}^2 - \rho^2). \tag{41a-b}$$

In agreement with (20a-c) we further choose $T_{\text{Kin}}{}^{\mu\nu} = T_{\text{K(P)}}{}^{\mu\nu} + T_{\text{K(e)}}{}^{\mu\nu}$ with

$$T_{\text{K(n)}}{}^{00} = \mathfrak{R}\{\psi_n^\dagger H_n \psi_n\} - \mathfrak{A}\cdot\mathbf{j}_n - \mathfrak{B}\cdot\mathbf{M}_n, \tag{42}$$

where

$$H_n = m_n c^2\beta - i\hbar c\boldsymbol{\alpha}\cdot\nabla, \tag{43}$$

$$\mathfrak{R}\{\psi^\dagger\Omega\varphi\} = \tfrac{1}{4}\{\psi^\dagger\Omega\varphi + \varphi^\dagger\Omega^\dagger\psi - \varphi^{\mathrm{T}}\Omega^{\mathrm{T}}\psi^* - \psi^{\mathrm{T}}\Omega^*\varphi^*\} \tag{44}$$

in the notation explained in the text below Eq. (E-T:6) and in footnote 10 of reference 18. (Note that for c-number Dirac matrices $(\omega\Omega)^{\mathrm{T}} = \Omega^{\mathrm{T}}\omega^{\mathrm{T}}$, $(\omega\Omega)^* = \omega^*\Omega^*$, but that $(qQ)^{\mathrm{T}} = qQ$, $(qQ)^* = Q^*q^*$ for q-numbers without undor indices.)

The other components of $T_{\text{K(n)}}{}^{\mu\rho} = T_{\text{K(n)}}{}^{\rho\mu}$ should now be chosen in such a way that also these quantities transform in Heisenberg representation as a symmetric tensor, like in (E-T:18). After lengthy calculation of $\delta T_{\text{K(n)}}{}^{00}$, in which profuse use is made of the reasoning leading from Eq. (E-T:A.2) to (E-T:A.3), one thus finds for $G_{\text{K(n)}}{}^l \equiv T_{\text{K(n)}}{}^{0l} = (1/c)\times$kinetic energy current density $= c\times$kinetic momentum density:

$$\mathbf{G}_{\text{K(n)}} = -\mathfrak{R}\{\psi_n^\dagger i\hbar c\nabla\psi_n\} + \tfrac{1}{4}\hbar c\ \text{curl}\mathfrak{R}\{\psi_n^\dagger\boldsymbol{\sigma}\psi_n\} - \mathfrak{A}\rho_n - \mathfrak{B}\times\mathbf{P}_n. \tag{45}$$

The integral of $\mathbf{G}_{\text{Kin}}$ over space gives $c\times$the kinetic momentum $\mathcal{P}_{\text{Kin}}$ of the particles. One often calls the integral of the first one or two terms in (45) $c\times$the "total" momentum of the particles. The "potential" momentum subtracted from it at the end of Eq. (45) contains one more term than in the conventional theory. The second term in (45) does not contribute to $\mathcal{P}_{\text{Kin}}$, but when one calculates the total angular momentum $\mathcal{J} = \int(\mathbf{r}\times\mathbf{G}/c)d^3\mathbf{x}$ this second term yields the spin angular momentum.[26]

By calculating $\delta_H T_{\text{K(n)}}{}^{0l}$ one can find $T_{\text{K(n)}}{}^{kl}$, and one has a check on the result by calculating $\delta_H T_{\text{K(n)}}{}^{kl}$. We expect the resulting total energy density tensor $T_{\mathfrak{F}} + T_{\text{dir}} + T_{\text{Kin}}$ to satisfy conservation laws $\nabla_\nu T^{\mu\nu} = 0$ in Heisenberg representation.

6. ELECTRON OR PROTON IN EXTERNAL FIELD

Consider a single electron or proton in a c-number external field. The c-number one-particle wave function

[26] F. J. Belinfante, Physica **6**, 887 (1939). See also Physica **7**, 449 (1940).

of such electron or proton satisfies Eq. (25). We shall omit the subscripts $_n$. (Thus $e=+|e|$ for a proton, but $e=-|e|$ for an electron.)

We shall consider only the following cases:

(1) A slow electron or proton alone in a constant, purely magnetic field. As we ignore self-interactions, we can then put in (25)

$$0=\mathbf{j}=\rho=V=\mathbf{P}=\sigma=\Phi=\mathbf{E}_{\shortparallel}=0. \tag{46}$$

(2) A stationary state of an electron in the constant central field of a nucleus containing Z protons, with perhaps a constant magnetic field superimposed on this coulomb field. We assume the protons to be at rest in the origin, so that we put

$$\mathbf{j}=0, \quad \mathbf{P}=0, \quad \Phi=V, \tag{47a}$$

$$\mathrm{div}\mathbf{E}=\mathrm{div}\mathbf{D}=4\pi\rho=4\pi Z|e|\,\delta(\mathbf{x}). \tag{47b}$$

In both cases we further put

$$0=\partial_{\mathrm{H}}\mathfrak{B}/\partial t=\partial_{\mathrm{H}}\mathfrak{H}/\partial t=\mathbf{E}_{\perp}=\mathrm{curl}\mathbf{E}= =\mathrm{curl}\mathbf{D}=\mathbf{D}_{\perp}=\mathfrak{G}=0 \tag{48a}$$

and

$$-\nabla\Phi=\mathbf{E}_{\shortparallel}=\mathbf{E}=\mathbf{D}=\mathbf{D}_{\shortparallel}=-\nabla V. \tag{48b}$$

(In case **(1)** this vanishes.) We also put $i\hbar\partial_{\mathrm{H}}\psi/\partial t=\mathrm{E}\psi$, regarding E as an operator in case **(1)** and as a constant in case **(2)**. Since we ignore self-interactions, we further omit the symbol $\mathfrak{H}$ from Eq. (25).

We introduce the following further abbreviations:

$$\mathbf{p}=-i\hbar\nabla, \quad \boldsymbol{\pi}=\mathbf{p}-(e/c)\mathfrak{A}, \quad \Pi_{\pm}=\{\boldsymbol{\pi}\pm(if/c)\mathbf{D}\}\cdot\boldsymbol{\sigma}, \quad \mathrm{T}=\mathrm{E}-mc^2, \quad \mu_0=e\hbar/2mc. \tag{49a-e}$$

Thus, $\mu_0=1$ nuclear magneton ($\equiv\mu_{\mathrm{K}}$) for a proton; but for an electron, $\mu_0=-\mu_B$ is negative.

In a representation, in which $\beta=\rho_3$, $\boldsymbol{\alpha}=\rho_1\boldsymbol{\sigma}$, $\boldsymbol{\gamma}=\rho_2\boldsymbol{\sigma}$, Eq. (25) is resolved into the following equations for the upper two components ($\psi_{1,2}$) and the lower two components ($\psi_{3,4}$) of ψ:

$$(T-eV+Ce\rho)\psi_{1,2}+f\mathfrak{B}\cdot\boldsymbol{\sigma}\psi_{1,2}=c\Pi_{+}\psi_{3,4}, \tag{50a}$$

$$(2mc^2+\mathrm{T}-eV+Ce\rho)\psi_{3,4}-f\mathfrak{B}\cdot\boldsymbol{\sigma}\psi_{3,4}=c\Pi_{-}\psi_{1,2}. \tag{50b}$$

We divide Eq. (50b) by $2mc^2$. The equation thus obtained we solve for $\psi_{3,4}$ by multiplication by

$$\Lambda\equiv\left\{\left(1+\frac{\mathrm{T}-eV+Ce\rho}{2mc^2}\right)^2-\frac{f^2\mathfrak{B}^2}{4m^2c^4}\right\}^{-1} \times\left\{1+\frac{\mathrm{T}-eV+Ce\rho+f\mathfrak{B}\cdot\boldsymbol{\sigma}}{2mc^2}\right\}. \tag{51}$$

Substituting the result $\psi_{3,4}=(\Lambda\Pi_{-}/2mc)\psi_{1,2}$ into Eq. (50a) we get

$$\mathrm{T}\psi_{1,2}=\{eV-Ce\rho-f\mathfrak{B}\cdot\boldsymbol{\sigma}+\Omega\}\psi_{1,2}, \tag{52}$$

with

$$2m\Omega\equiv\Pi_{+}\Lambda\Pi_{-}=\Pi_{+}[\Lambda;\Pi_{-}]+\Pi_{+}\Pi_{-}\Lambda \tag{53a}$$

$$=[\Pi_{+};\Lambda]\Pi_{-}+\Lambda\Pi_{+}\Pi_{-}. \tag{53b}$$

We expand Λ in powers of $(1/c)$. As $Ce\rho$ in (51) contributes only in case **(2)** and there by (47b) only in an infinitesimal region, in which the expansion for Λ does not rapidly converge anyhow, we shall simply omit $Ce\rho$ from (51) and neglect in (52) the interaction terms from Ω completely in this infinitesimal region.[27] We further neglect here and in the following all terms with factors c^{-3} or $c^{-2}f$ or $c^{-2}\mu_0$ or $c^{-2}f^2$ or $c^{-1}f\mu_0$ or $c^{-1}\mu_0^2$. This leaves us with

$$\Lambda\approx 1-(2mc^2)^{-1}(\mathrm{T}-eV). \tag{54}$$

Thence, by (49a-e) and (48b),

$$[\Lambda;\Pi_{-}]\approx(\mu_0/ic)(\mathbf{D}\cdot\boldsymbol{\sigma})\approx-[\Pi_{+};\Lambda], \tag{55}$$

and, by (52), in our approximation in the term with Ω,

$$\Lambda\psi_{1,2}\approx\{1-(\Omega/2mc^2)\}\psi_{1,2}. \tag{56}$$

Further, by (49a-c),

$$\Pi_{+}\Pi_{-}\approx(\boldsymbol{\pi}\cdot\boldsymbol{\sigma})(\boldsymbol{\pi}\cdot\boldsymbol{\sigma})+(f/ic)\{(\boldsymbol{\pi}\cdot\boldsymbol{\sigma})(\mathbf{D}\cdot\boldsymbol{\sigma}) -(\mathbf{D}\cdot\boldsymbol{\sigma})(\boldsymbol{\pi}\cdot\boldsymbol{\sigma})\}, \tag{57a}$$

$$(\boldsymbol{\pi}\cdot\boldsymbol{\sigma})(\boldsymbol{\pi}\cdot\boldsymbol{\sigma})=\boldsymbol{\pi}^2-2m\mu_0\boldsymbol{\sigma}\cdot\mathfrak{B}. \tag{57b}$$

From (53a), (49c), (55), (57a-b), and (56) we obtain

$$2m\Omega\cong\boldsymbol{\pi}^2-2m\mu_0\boldsymbol{\sigma}\cdot\mathfrak{B}-\boldsymbol{\pi}^2\Omega/2mc^2+(\mu_0/ic)\boldsymbol{\pi}\cdot\boldsymbol{\sigma}\mathbf{D}\cdot\boldsymbol{\sigma} +(f/ic)\{\boldsymbol{\pi}\cdot\boldsymbol{\sigma}\mathbf{D}\cdot\boldsymbol{\sigma}-\mathbf{D}\cdot\boldsymbol{\sigma}\boldsymbol{\pi}\cdot\boldsymbol{\sigma}\}, \tag{58}$$

where $A\cong B$ means $A\psi_{1,2}\approx B\psi_{1,2}$ in case **(1)** and $\int\psi_{1,2}^{\dagger}A\psi_{1,2}\approx\int\psi_{1,2}^{\dagger}B\psi_{1,2}$ in case **(2)**.

In the third term of the second member of (58) we substitute the approximation $\Omega\approx\boldsymbol{\pi}^2/2m$. Using $\nabla\cdot\mathbf{D}=4\pi\rho$, $\nabla\times\mathbf{D}=0$ by (47b) and (48a), we thus find

$$\Omega\cong\frac{\boldsymbol{\pi}^2}{2m}-\frac{\boldsymbol{\pi}^4}{8m^3c^2}-\mu_0\boldsymbol{\sigma}\cdot\mathfrak{B}-\frac{\mu_0+2f}{2mc}\{h\rho+\boldsymbol{\sigma}\cdot\mathbf{D}\times\boldsymbol{\pi}\}+A, \tag{59a}$$

$$A\equiv(\mu_0/4imc)\{\boldsymbol{\pi}\cdot\boldsymbol{\sigma}\mathbf{D}\cdot\boldsymbol{\sigma}+\mathbf{D}\cdot\boldsymbol{\sigma}\boldsymbol{\pi}\cdot\boldsymbol{\sigma}\}. \tag{59b}$$

Case (1)

Inserting (59a) in (52) with (46), (48a-b), $\mathbf{D}=0$, $A=0$ in this case, we find the Schrödinger equation with a relativistic correction and with the nonrelativistic magnetic interaction term of the external field $\mathfrak{B}$ with a magnetic moment

$$\boldsymbol{\mu}=(\mu_0+f)\boldsymbol{\sigma}; \quad |\boldsymbol{\mu}|=|\mu_0+f|. \tag{60}$$

Experimental data for protons[9-11] give

$$|\boldsymbol{\mu}_{\mathrm{P}}|=(2.793\pm0.001)\mu_{\mathrm{K}},$$

thence

$$f_{\mathrm{P}}=1.793\mu_{\mathrm{K}}=(0.000\,976\pm0.000\,001)\mu_B. \tag{61}$$

[27] Thus we avoid in the final expression for $\langle\Omega\rangle_{Av}$ in the first order perturbation energy terms involving $\langle\nabla^2\rho_P\rangle_{Av}$ and $\langle(\nabla\rho_P)\cdot\boldsymbol{\sigma}\times\boldsymbol{\pi}\rangle_{Av}$, which could not be trusted anyhow as these operators differ from zero only in the region where the expansion of Λ and therefore the expression for Ω is no good. Note, however, that we leave $Ce\rho$ in the first part of Eq. (52), where it derives directly from (50a) without intervening expansion.

For electrons one found[2,4,4a]

$$|\mu_e| = (1.001\ 145 \pm 0.000\ 013)\mu_B,$$

thence

$$f_e = -(0.001\ 145 \pm 0.000\ 013)\mu_B. \quad (62)$$

Note that f_P and f_e are within 20 percent opposite equal. The conventional theory of self-interaction gives[3a] $|\mu_e| = 1.001\ 147\mu_B$, which would correspond to $f_e/\mu_B = -\alpha/2\pi + 2.973\alpha^2/\pi^2$, with $\alpha = e^2/\hbar c$.

Case (2)

From (52) with (59) we see that we can use the Schrödinger eigenfunctions for the hydrogen-like atom of atomic number Z as zero-order approximation for our stationary state.[28] The remaining terms we take into account in first-order approximation only calculating their expectation value. Doing so, we might have used (53b) with the conjugate of Eq. (56), instead of (53a) with (56). This leads to the hermitian conjugate of (59a). By taking the average of this and (59a) itself, the antihermitian term (59b) is eliminated and we find from (52)

$$\mathrm{T} \cong eV + \frac{\pi^2}{2m} - \frac{\pi^4}{8m^3c^2} - (\mu_0 + f)\boldsymbol{\sigma}\cdot\mathfrak{B} - \frac{\mu_0 + 2f}{2mc}\{h\rho + \boldsymbol{\sigma}\cdot\mathbf{D}\times\boldsymbol{\pi}\} - Ce\rho. \quad (63)$$

We take $eV + \mathbf{p}^2/2m_e = -Ze^2/r - (\hbar^2/2m_e)\nabla^2$ as the unperturbed Hamilton operator. As first-order perturbation energy we take in absence of external magnetic fields the expectation value of

$$\frac{|e|}{m_e c}(\mathfrak{A}\cdot\mathbf{p}) - \frac{p^4}{8m_e^3c^2} + \frac{\mu_B + 2|f_e|}{2m_e c}\{h\rho_P + \boldsymbol{\sigma}\cdot\mathbf{D}\times\mathbf{p}\} + C|e|\rho_P. \quad (64)$$

The first term, from $(\boldsymbol{\pi}^2 - \mathbf{p}^2)/2m$, shows the magnetic action of the moving nucleus on the electron. With[22]

$$|e|\mathfrak{A} \approx Ze^2\{(\mathbf{v}_P/2cr) + (\mathbf{v}_P\cdot\mathbf{r})\mathbf{r}/2cr^3\}, \quad (65)$$

it is essentially the Breit energy Y, which, when taken together with the kinetic energy of the proton,[29] has been shown by Breit[30] to alter the Bohr levels by a factor $\{1 - (m_e/m_P)\}$, which is approximately equivalent to replacing the electron mass by the reduced mass in the expression for the energy levels.

The other magnetic terms in (63) are negligible. For instance $-\mu_0\mathbf{v}\cdot\mathfrak{B}$ is, by $\mathfrak{B} \approx \mathbf{D}\times\mathbf{p}/m_P c$ at the position of the electron, smaller by a factor $(2m_e/m_P)$ than the small term $(\mu_B/2mc)\boldsymbol{\sigma}\cdot\mathbf{D}\times\mathbf{p}$ in (64).

The expectation value of the second term in (64) is equal to[31]

$$\langle -p^4/8m_e^3c^2\rangle_{kl} = Z^4\alpha^2 Ry\{3/4n^4 - 1/n^3(l+\tfrac{1}{2})\}, \quad (66)$$

where $Ry = \frac{1}{2}\alpha^2 m_e c^2$. The expectation value of the next terms is calculated from [28]

$$(\mu_B h/2m_e c)\langle\rho_P\rangle_{kl} = (Z|e|\mu_B h/2m_e c)|\psi(0)|^2 = \delta_{l,0}Z^4\alpha^2 Ry/n^3, \quad (67)$$

and[32]

$$\frac{\mu_B}{2m_e c}\langle\boldsymbol{\sigma}\cdot\mathbf{D}\times\mathbf{p}\rangle_{kl} = \frac{\mu_B Z|e|}{2m_e c}\left\langle\frac{\boldsymbol{\sigma}\cdot\mathbf{r}\times\mathbf{p}}{r^3}\right\rangle_{kl} = \frac{(1-\delta_{l,0})Z^4\alpha^2 Ry}{n^3(2k)(l+\frac{1}{2})}. \quad (68)$$

Thence

$$(\mu_B/2m_e c)\langle h\rho_P + \boldsymbol{\sigma}\cdot\mathbf{D}\times\mathbf{p}\rangle_{kl} = Z^4\alpha^2 Ry/n^3 k(2l+1). \quad (69)$$

Adding this to (66) we find the old fine-structure formula

$$\left\langle -\frac{p^4}{8m_e^3c^2} + \frac{\mu_B}{2m_e c}(h\rho_P + \boldsymbol{\sigma}\cdot\mathbf{D}\times\mathbf{p})\right\rangle_{kl} = Z^4\alpha^2 Ry\left\{\frac{3}{4n^4} - \frac{1}{n^3(j+\frac{1}{2})}\right\}. \quad (70)$$

According to (64), the level shift (70) is to be supplemented by the amount

$$\delta_L E_{nlj} = (|f_e|/m_e c)\langle h\rho_P + \boldsymbol{\sigma}\cdot\mathbf{D}\times\mathbf{p}\rangle_{kl} + C|e|\langle\rho_P\rangle_{kl}. \quad (71)$$

With the results from Eqs. (69) and (67), and putting

$$1/k = (-)^{l-j+\frac{1}{2}}/(j+\tfrac{1}{2}) \equiv c_{l,j} \quad (72)$$

we find

$$\delta_L E_{nlj} = \{|f_e/\mu_B|\cdot c_{l,j}/(l+\tfrac{1}{2}) + (2C/\pi)(m_e c/\hbar)^2\delta_{l,0}\}Z^4\alpha^2 Ry/n^3. \quad (73)$$

---

[28] For an s-state the part $\psi_{1,2}$ of the Dirac wave-function behaves for small r like $(r/a)^b$ with $b = (1-Z^2\alpha^2)^{\frac{1}{2}} - 1 \approx -\frac{1}{2}Z^2\alpha^2$. This starts to deviate appreciably from 1 when $\ln(a/r) \approx -1/b \approx 2/Z^2\alpha^2$ or $r \approx a\exp(-2/Z^2\alpha^2)$, which is for small Z at such tremendously small r that the slightest extension of the charge distribution approximated in (47b) by a delta-function would justify the treatment of $\psi_{1,2}$ as a Schrödinger function, so that we may put $\langle|e|\rho_P\rangle_{kl} = Ze^2|\psi_{nl}(0)|^2 = \delta_{l,0}(Z^4e^8m_e^3/\pi n^3\hbar^6)$.

[29] Discussed in the next chapter.

[30] G. Breit and G. E. Brown, Phys. Rev. **74**, 1278 (1948).

[31] See for instance, E. U. Condon and G. K. Shortley, *The Theory of Atomic Spectra* (Cambridge University Press, London, 1935), Eqs. (6)–(7) and Eq. (15) on pages 119–120.

[32] Here, $k = l+1$ for $j = l+\frac{1}{2}$, and $k = -l$ for $j = l-\frac{1}{2}$. For Eq. (68) see for instance H. A. Kramers, *Grundlagen der Quantentheorie, Quantentheorie des Elektrons und der Strahlung* (Akademische Verlagsgesellschaft, Leipzig, 1938), Eqs. (59) and (71) on pp. 247–251. The added factor $(1-\delta_{l,0})$ is due to the vanishing of $\mathbf{r}\times\mathbf{p}\psi_{1,2}$ for an s-state. The apparent divergence of $\langle r^{-3}\rangle_{kl}$ in (68) is not to be taken serious, as the terms with $\boldsymbol{\sigma}\cdot\mathbf{D}\times\mathbf{p}$ in (64) derive by (53a–b) from Ω, which we neglect in the immediate neighborhood of the origin; see the text above footnote 27. Compare also pp. 130–131 of reference 31.

This is our expression for the Lamb shift. The theory of Bethe, French and Weisskopf[5-7] gave

$$\delta_L E'_{nlj}=\{(\alpha/2\pi)c_{l,j}/(l+\tfrac{1}{2}) +(8\alpha/3\pi)[\ln(Ry/k_{nl})+10.0988\delta_{l,0}]\}Z^4\alpha^2Ry/n^3, \quad (74)$$

where $10.0988=(11/24)-(1/5)-\ln 2+\ln(m_e c^2/Ry)$, and where k_{nl} is Bethe's $k_0(n,l)$. Bethe states that k_{n0} is rather insensitive for the value of n, with $\ln|Ry/k_{2,0}| =-2.812$, while $\ln|Ry/k_{nl}|$ is very small for $l\neq 0$. Therefore, $\ln|Ry/k_{nl}|\approx -2.8\delta_{l,0}$ in Bethe's theory, and the dependence of (74) on n and l is about the same as in our Eq. (73). Also, the value $|f_e/\mu_B|=0.001\,145 \pm 0.000\,013$ in Eq. (73) agrees with the value $\alpha/2\pi =0.001\,16$ in Eq. (74).

For the Lamb shift in M(ega)c(ycles) we calculate from (73), with $Z=1$, $n=2$, $\frac{1}{8}\alpha^2Ry=21\,890\pm 15$ Mc, and $h/mc=(2.426\,07\pm 0.000\,03)\times 10^{-10}$ cm,

$$\left.\begin{aligned}\delta_L E_{2s\frac{1}{2}}&=\{(0.9347\pm 0.0007)\times 10^{24}\text{C/cm}^2 \\ &\qquad +(43\,780\pm 30)\times|f_e/\mu_B|\}\text{ Mc},\\ \delta_L E_{2p\frac{1}{2}}&=-(14\,593\pm 10)\times|f_e/\mu_B|\text{ Mc},\\ \delta_L E_{2p\frac{3}{2}}&=+(7\,297\pm 5)\times|f_e/\mu_B|\text{ Mc}.\end{aligned}\right\} \quad (75)$$

Thence, to bring $\delta_L E_{2s\frac{1}{2}}-\delta_L E_{2p\frac{1}{2}}$ into agreement with the experimental value of 1062 Mc, we must choose, with f_e from Eq. (62),

$$C=(1.0646\pm 0.0016)\times 10^{-22}\text{ cm}^2. \quad (76)$$

Then, $\delta_L E_{2p\frac{1}{2}}-\delta_L E_{2p\frac{3}{2}}=(26\pm 1)$ Mc.

The coefficient of $\psi_P^\dagger\psi_P\psi_e^\dagger\psi_e$ in the last term of Eq. (4) is now

$$Ce^2=(2.455\pm 0.004)\times 10^{-41}\text{ cm}^3\text{ erg} =(0.2856\pm 0.0005)\mu_B^2. \quad (77)$$

7. ENERGY OF INTERACTING PARTICLES

For a justification of the inclusion of the nuclear kinetic energy to give with the Breit interaction the appearance of the reduced mass in the Rydberg constant,[30] we should not have considered a single electron in an external field, but an electron and a nucleus interacting with each other. First we shall consider a number of electrons and protons in their mutual fields, omitting self-interactions and assuming absence of further external fields. A number of approximations will be made. We shall neglect $\partial_H\mathfrak{A}/c\partial t=-\mathbf{E}_\perp$, so that by $\mathbf{E}\approx\mathbf{E}_{II}=-\nabla\Phi$, by (20b), and by (13a-b) we may write

$$\mathcal{H}_{el}+\tfrac{1}{2}C\int\rho^2\approx\int\mathbf{E}_{II}^2/8\pi =-\int\Phi\triangle\Phi/8\pi=\tfrac{1}{2}\int\int'\sigma\sigma'/r. \quad (78)$$

We shall also neglect $\partial_H\mathfrak{E}/c\partial t$, so that, by (31a), (11a), and (26), and with the definition

$$\mathbf{i}=\mathbf{j}+\text{curl}\mathbf{M}\quad(=\mathbf{i}-\partial_H\mathbf{P}/c\partial t), \quad (79)$$

we find

$$-\triangle\mathfrak{A}=\text{curl}\mathfrak{B}\approx 4\pi\mathbf{i}_\perp,\quad \mathfrak{A}\approx\int'\mathbf{i}_\perp'/r. \quad (80)$$

Thence, by (20c),

$$\mathcal{H}_{magn}-\tfrac{1}{2}C\int\mathbf{j}^2=\int\mathfrak{A}\cdot(\text{curl}\mathfrak{B}/8\pi-\mathbf{i})\approx -\tfrac{1}{2}\int\mathfrak{A}\cdot\mathbf{i}=-\tfrac{1}{2}\int\mathfrak{A}\cdot\mathbf{i}_\perp=-\tfrac{1}{2}\int\int'\mathbf{i}_\perp\cdot\mathbf{i}_\perp'/r. \quad (81)$$

The total energy (20) is then the sum of (20a), (78), (81), and $\mathcal{H}_{dir}$(= the integral of (41b)).

Next, we shall pay special attention to one single particle (n) and consider the fields of the other particles at the position of particle n as "external" fields. Then,

$$\mathcal{H}\approx\mathcal{H}_{mat,n}+C\int(\mathbf{j}_n\cdot\mathbf{j}_{ext}-\rho_n\rho_{ext})+\mathcal{S}, \quad (82)$$

$$\mathcal{S}=\int\int'\sigma_n\sigma_{ext}'/r-\int\int'\mathbf{i}_{n\perp}\cdot\mathbf{i}_{ext\perp}'/r =\int\sigma_n\Phi_{ext}-\int\mathbf{i}_{n\perp}\cdot\mathfrak{A}_{ext} =\int\rho_n\Phi_{ext}-\int\mathbf{P}_n\cdot\mathbf{E}_{ext}-\int\mathbf{i}_n\cdot\mathfrak{A}_{ext}, \quad (83)$$

where we finally used (13a-b) and (12b). If the external magnetic field $\mathfrak{B}_{ext}$ is nearly homogeneous in the region of the particle (where $\mathbf{i}_n\neq 0$), then $\mathfrak{A}_{ext}\approx\frac{1}{2}\mathfrak{B}_{ext}\times\mathbf{r}$, and the last term of (83) becomes, by (79),

$$-\int\mathbf{i}_n\cdot\mathfrak{A}_{ext}=-\tfrac{1}{2}\int\mathbf{j}_{n\perp}\cdot[\mathfrak{B}_{ext}\times\mathbf{r}]-\int\mathbf{M}_n\cdot\text{curl}\mathfrak{A}_{ext} =-\mathfrak{B}_{ext}\cdot\int\{\tfrac{1}{2}[\mathbf{r}\times\mathbf{j}_{n\perp}]+\mathbf{M}_n\}=-\mathfrak{B}_{ext}\cdot\boldsymbol{\mu}_n. \quad (84)$$

We can regard

$$\boldsymbol{\mu}_n=\tfrac{1}{2}\int[\mathbf{r}\times\mathbf{j}_{n\perp}]+\int\mathbf{M}_n\equiv\boldsymbol{\mu}_n^{(s)}+\boldsymbol{\mu}_n^{(l)} \quad (85)$$

as the magnetic moment of the particle n. In a stationary state with $i\hbar\partial_H\psi_n/\partial t=\mathrm{E}\psi_n$ and thence with $\partial_H\rho_n/\partial t=0$, so that $\text{div}\mathbf{j}_n=0$ and $\mathbf{j}_{n\perp}=\mathbf{j}_n$, we find for the first term in (85) for a slow particle n (temporarily omitting subscripts n to $\boldsymbol{\mu}$, e, ψ, m, and f),

$$\begin{aligned}\boldsymbol{\mu}^{(s)}&=\tfrac{1}{2}e\int\psi^\dagger(\mathbf{r}\times\boldsymbol{\alpha})\psi\equiv\tfrac{1}{2}e\int\psi^\dagger[(\mathbf{r}\times\boldsymbol{\alpha}\beta);\beta]\psi\\ &\approx(e/4mc^2)\int\psi^\dagger[(\mathbf{r}\times\boldsymbol{\alpha}\beta);(\mathrm{E}-U-c\boldsymbol{\alpha}\cdot\mathbf{p}_{op})]\\ &=(e/2mc)\int\psi^\dagger\beta\{(\mathbf{r}\times\mathbf{p}_{op})+\hbar\boldsymbol{\sigma}\}\psi\\ &=(e/2mc)\int\psi^\dagger\beta(\mathfrak{L}_{op}+2\mathcal{S}_{op})\psi,\end{aligned} \quad (86)$$

while, by Eq. (5),

$$\boldsymbol{\mu}^{(l)}=\int\mathbf{M}=f\int\psi^\dagger\beta\boldsymbol{\sigma}\psi. \quad (87)$$

Thus, besides an orbital magnetic moment, particle n has an intrinsic magnetic moment

$$\boldsymbol{\mu}^{(s+l)}=\{(e\hbar/2mc)+f\}\int\psi^\dagger\beta\boldsymbol{\sigma}\psi, \quad (88)$$

in agreement with our result (60), since $\beta\approx 1$.

Next, we consider two interacting particles (e and P) without self-interaction and without further external fields. In this case we find, similar to (82)-(83),

$$\mathcal{H}=\mathcal{H}_{mat,e}+\mathcal{H}_{mat,P}-\int\int'\mathbf{i}_\perp\cdot\mathbf{i}_P'/r +\int\rho_e\Phi_P-\int\mathbf{P}_e\cdot\mathbf{E}_P+C\int(\mathbf{j}_e\cdot\mathbf{j}_P-\rho_e\rho_P), \quad (89)$$

where Φ_P denotes the Φ-field of P acting on e.

In (89), with $\mathbf{E}\approx\mathbf{E}_{II}$, we substitute the longitudinal part of (11b), and (12a) with $-\int\int'\rho_e(\text{div}'\mathbf{P}_P')/r =\int'\mathbf{P}_P'\cdot\nabla'\int\rho_e/r=\int\mathbf{P}_P\cdot\nabla V_e$. Also substituting (79)

we find

$$\mathcal{H}=\mathcal{H}_1+\mathcal{H}_2+\mathcal{H}_3+\mathcal{H}_4+\mathcal{H}_5+\mathcal{H}_6; \tag{90}$$

$$\mathcal{H}_1=\mathcal{H}_{\text{mat},\epsilon}+\mathcal{H}_{\text{mat},P}+\int\int' \rho_\epsilon\rho_P'/r, \tag{90a}$$

$$\mathcal{H}_2=-\int\int' \mathbf{j}_\epsilon\cdot(\mathbf{j}_P'/r)_\perp, \tag{90b}$$

$$\mathcal{H}_3=-\int\int' \mathbf{i}_\epsilon\cdot\text{curl}'\mathbf{M}_P'/r, \tag{90c}$$

$$\mathcal{H}_4=-\int\int'(\text{curl}\mathbf{M}_\epsilon)\cdot\mathbf{j}_P'/r+\int \mathbf{P}_P\cdot\nabla V_\epsilon, \tag{90d}$$

$$\mathcal{H}_5=4\pi\int \mathbf{P}_\epsilon\cdot\mathbf{P}_P+C\int \mathbf{j}_\epsilon\cdot\mathbf{j}_P, \tag{90e}$$

$$\mathcal{H}_6=\int \mathbf{P}_\epsilon\cdot\nabla V_P-C\int \rho_\epsilon\rho_P. \tag{90f}$$

We use (90) as the Hamilton operator in a two-particle Schrödinger equation. Breit[30] has shown that, if hyperfine structure (and thence $\mathcal{H}_3$) is neglected, and if the center of gravity of the atom is at rest, the occurrence of $\mathcal{H}_{\text{mat},P}$ in this Hamilton operator can be taken into account in sufficient approximation by considering $\mathcal{H}_{\text{mat},\epsilon}$ as operating on the relative coordinates of electron and proton instead of on the electron coordinates, and by adding a term $\mathbf{p}_{op}^2/2m_P$ to replace $\mathcal{H}_{\text{mat},P}$. He has also shown that this $\mathbf{p}_{op}^2/2m_P$ and the Breit interaction energy[33]

$$\mathcal{H}_2=-\tfrac{1}{2}\int\int'\{(\mathbf{j}_\epsilon\cdot\mathbf{j}_P'/r)+(\mathbf{j}_\epsilon\cdot\mathbf{r})(\mathbf{j}_P'\cdot\mathbf{r})/r^3\}\equiv V, \tag{91}$$

together yield a first-order perturbation energy $=(-m_\epsilon/m_P)\times$the unperturbed energy not including rest energies. Thus, $\mathcal{H}_1+\mathcal{H}_2$ gives the conventional expression for the energy levels featuring the "reduced mass."

Beside $\mathcal{H}_2$ we can also neglect $\mathcal{H}_4+\mathcal{H}_5$. The first term of $\mathcal{H}_4$ gives the interaction of $\mathfrak{y}_\epsilon^{(I)}$ with the magnetic field from $\mathbf{j}_P$ and is by $\mathfrak{y}_\epsilon^{(I)}\ll\mathfrak{y}_\epsilon^{(0)}$ negligible as compared with the interaction (91) of $\mathfrak{y}_\epsilon^{(0)}$ with this field. The second term of $\mathcal{H}_4$ is negligible as compared with the first term of $\mathcal{H}_6$ because of the slowness of the proton making $\mathbf{P}_P\ll\mathbf{P}_\epsilon$. The slowness of both particles makes both terms of $\mathcal{H}_5$ negligible compared with the second term of $\mathcal{H}_6$. (The first term of $\mathcal{H}_5$ is even smaller than its second term since $|4\pi f_\epsilon f_P|\ll Ce^2$ according to (61), (62), and (77).)

Finally, $\mathcal{H}_6$ gives the Lamb shift (71). The last terms of (71) and (90f) are obviously identical. The first term of (90f) is evaluated by

$$\begin{aligned}\langle\int \mathbf{P}_\epsilon\cdot\nabla V_P\rangle_{Av}&=f_\epsilon\int\Psi^\dagger\gamma\cdot\nabla V_P\Psi\\&\approx(if_\epsilon/2m_\epsilon c^2)\int\Psi^\dagger[(\alpha\cdot\nabla V_P);(E-U-c\alpha\cdot\mathbf{p}_{op})]\Psi\\&=-(f_\epsilon\hbar/m_\epsilon c)\langle\hbar^{-1}\sigma\cdot\mathbf{p}\times(\nabla V_P)-\tfrac{1}{2}(\nabla^2V_P)\rangle_{Av}\\&=(f_\epsilon/m_\epsilon c)\langle\sigma\cdot\mathbf{D}_{II}\times\mathbf{p}+h\rho_P\rangle_{Av},\end{aligned} \tag{92}$$

which by $f_\epsilon=-|f_\epsilon|$ gives the first term of (71). Thus, energy considerations lead to the same results as Pauli's approximate treatment of the spin, but at the same time yield the nuclear kinetic energy needed for application of Breit's arguments.[30]

8. DISCUSSION

The three constants occurring in the new interactions proposed in this paper were adjusted to the experimental values of $\mathfrak{y}_\epsilon$, $\mathfrak{y}_P$, and the Lamb shift $(\delta_L E_{2s\frac{1}{2}}-\delta_L E_{2p\frac{1}{2}})$ for hydrogen. The dependence of the Lamb shift on the atomic number comes out automatically in the same way as in Bethe's theory. The dependence on the quantum numbers n, l, j is found to be nearly the same as in Bethe's theory. In principle, therefore, one could decide experimentally between the theory developed here and the theory of Bethe, by measuring very accurately the Lamb shift of other atomic levels than $n=2$, and by repeating Bethe's numerical calculations for such states in order to evaluate the difference between Bethe's $k_0(n,l)$ and $k_0(2,l)$. As it is to be expected that the difference between the theoretical values thus obtained from the Bethe-French and Weisskopf theory and from the present theory will be rather small, one should then also verify whether none/any of the effects neglected in either theory has an influence on the result in the approximation needed for detecting the difference between the theories.

[33] See Eqs. (3) and (57)–(58) of reference 22 and Eq. (1.3) of reference 30.

Magnetostrictive Vibration of Prolate Spheroids. Analysis and Experimental Results*

F. J. Beck, J. S. Kouvelites, and L. W. McKeehan
Dunham Laboratory of Electrical Engineering and Sloane Physics Laboratory, Yale University, New Haven, Connecticut†

(Received August 14, 1951)

Small centrally-clamped ferromagnetic specimens are uniformly and axially magnetized by an applied static field. They are simultaneously subjected to an axial *hf* magnetic field and allowed to vibrate longitudinally in the frequency region of their fundamental mode. Through an analysis of this vibrational system, a method is developed whereby from the resonance changes of the impedance of the *hf* magnetizing coil, values may be computed for the incremental permeability, magnetostriction constant, modulus of elasticity, and dissipation constant of the ferromagnetics. Annealed specimens of nickel and of several nickel-iron alloys, as well as the nickel in the unannealed state, were thus tested. The variations of the physical parameters with composition, magnetic bias, and heat treatment, are examined qualitatively in the light of present domain theory and found to be consistent. A good quantitative check of the experimental method is provided by the calculation of the saturation magnetostriction of nickel as -36.7×10^{-6}.

INTRODUCTION

THE magnetostrictive processes are very intimately related to many other physical characteristics of ferromagnetic media. Considerable experimental work[1] has firmly established this fact. Most of the individual experiments, however, have been limited to the quasi-static measurement of a maximum of two physical properties as functions of controlled external conditions. This limitation is not serious as long as the investigators' concern is restricted to reproducible quantities such as the differences in magnetostrictive strain and Young's modulus between the unmagnetized and saturated states. When the variations of the physical parameters for intermediate states of magnetization are of interest, it becomes advisable to measure as many of the parameters as possible simultaneously. Otherwise, any correlation of results of different experiments and any subsequent theoretical deductions are subject to considerable error due to inevitable discrepancies between specimens of similar composition and heat treatment.

We have therefore resorted to measurements of the magnetostrictive vibrational response of ferromagnetic rods. A computational procedure (to be described later), when applied to the results of these measurements, yields accurate values for four physical properties of the specimens, as they concurrently exist for a given set of external conditions.

The performance of our equipment, designed for high frequency measurements of the effects induced in the exciter coil by the vibrational motion of the specimen, is described in a previous paper.[2] Also discussed there are the reasons for the particular size and shape of the specimens (prolate spheroids with major axis 20 mm and minor axes 1 mm).

Some of the basic arguments of our analysis of the magnetostrictively-excited vibrational system pertinent to a prolate spheroid, were first developed by Pierce[3] in his treatment of a magnetostrictively vibrating cylindrical rod. We have leaned more heavily, however, on the later and more refined analysis of the same problem (except for a toroidal specimen) by Butterworth and Smith.[4]

ANALYSIS

The prolate spheroid, bounded by the surface, $b^2x^2+a^2r_1^2=a^2b^2$ (where a, the semimajor axis $\gg b$), was clamped centrally so that it was free to vibrate longitudinally in its fundamental mode. It was placed coaxially in the long, cylindrical exciter coil, of n turns per cm, through which the *hf* current, j, was flowing.

Thoroughly annealed, polycrystalline metals, to which our present experimentation has been mainly restricted, are essentially isotropic elastically as well as magnetically. Hence, since the eccentricity of the spheroid is nearly unity, its equiphase surfaces of displacement, ξ, may be considered to be planes perpendicular to the X-axis. The second law of motion applied to a cross-sectional plane lamina of differential thickness, dx, of the spheroid, may be stated then as

$$(\partial F/\partial x)dx=\pi\rho(b/a)^2(a^2-x^2)(\partial^2\xi/\partial t^2)dx, \qquad (1)$$

where ρ is the mass density. F, the axial force on the lamina, is composed of three parts. The elastic force, F_E, is related to the strain through Hooke's law; thus

$$F_E=\pi E(b/a)^2(a^2-x^2)(\partial\xi/\partial x), \qquad (2)$$

where E is the modulus of elasticity. A dissipative force, F_G, related to the velocity of the strain, is defined in terms of the dissipation constant, G, as

$$F_G=\pi G(b/a)^2(a^2-x^2)(\partial/\partial t)(\partial\xi/\partial x). \qquad (3)$$

Finally, by virtue of Joule's empirical law, there is a magnetostrictive force,

$$F_M=-\lambda\Phi_x, \qquad (4)$$

* This paper is based on a dissertation submitted by J. S. Kouvelites in partial fulfillment of the requirements for the degree of Doctor of Philosophy at Yale University.

† Assisted by the ONR.

[1] Thoroughly outlined in Chapter 13 of R. M. Bozorth, *Ferromagnetism* (D. Van Nostrand Company, Inc., New York, 1950).

[2] J. S. Kouvelites and L. W. McKeehan, Rev. Sci. Instr. 22, 108 (1951).

[3] G. W. Pierce, Proc. Am. Acad. Arts Sci. 63, 1 (1928).

[4] S. Butterworth and F. D. Smith, Proc. Phys. Soc. (London) 43, 166 (1931).

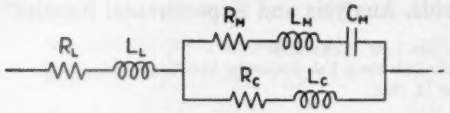

FIG. 1. The equivalent electrical circuit for the magnetostrictive vibrational system.

produced by Φ_s, the axial component of magnetic induction integrated over a cross-sectional area of the spheroid. The negative sign in (4) allows the magnetostriction constant, λ, to be positive when the magnetostrictive effect is positive. Furthermore, Φ_s consists of two parts. One is associated with the exciter coil current. The other, through the inverse magnetostrictive effect: $H=4\pi\lambda(\partial\xi/\partial x)$, is the magnetic flux produced by the mechanical strain. Hence, in terms of the two corresponding magnetic intensities at the surface of the spheroid, the total magnetic flux is

$$\Phi_s=4\pi\mu[n\beta j+\lambda(\partial\xi/\partial x)]W(x), \tag{5}$$

where μ is the magnetic permeability, β is a reducing factor due to the self-demagnetization of the spheroid, and W, an area dimensionally, is a field distribution function.

When Eqs. (2) through (5) are substituted into (1), and it is assumed that ξ and j vary harmonically with time, i.e., $\xi=X(x)e^{i\omega t}$ and $j=Je^{i\omega t}$, the equation of motion takes the form

$$[(a^2-x^2)(E+i\omega G)-U](d^2X/dx^2) -[2x(E+i\omega G)+(dU/dx)](dX/dx) +\omega^2\rho(a^2-x^2)X=(n\beta J/\lambda)(dU/dx), \tag{6}$$

where $U=4\mu W(a\lambda/b)^2$. A solution of this equation, subject to the condition that $X=0$ at $x=0$, would yield X as a linear function of J. Consequently, X could be eliminated from Eq. (5), and the procedure in establishing the relationship between the measured impedances of the exciter coil and the physical constants, would be virtually completed. Unfortunately, even at extremely low frequencies where there are essentially no eddy currents and W becomes $\pi b^2(a^2-x^2)/a^2$, the solutions of (6) are much too unwieldy to allow reasonably fast computation. In fact, for the range of resonant frequencies, permeabilities, and conductivities of the metallic specimens of the present work, the eddy current "skin depth," δ, is much smaller than r_1 over almost the entire specimen length; hence, W takes the form const. $(a^2-x^2)^{\frac{1}{2}}$, making matters even worse.

Although a solution of the equation of motion appears rather impratical, an approximate solution to the vibration problem may be obtained from energy considerations. The normal situation in most crystalline structures vibrating mechanically, is that the potential and kinetic energies far exceed the dissipative losses. It follows that for a spheroidal rod of such a substance, the displacement pattern for forced vibration would be closely that for free vibration in the same mode. It has already been found[8] that for the fundamental mode of free vibration of a prolate spheroid, the displacement varies essentially sinusoidally as a function of x, i.e., $\xi=X_a\sin(\pi x/2a)e^{i\omega t}$. With this displacement configuration, we proceed to sum up the energies of each of the cross-sectional plane lamina to obtain the energies of the entire spheroid. The total kinetic energy is found to be

$$T=\tfrac{1}{2}\int_{x=-a}^{x=a}(\partial\xi/\partial t)^2dm =-\tfrac{1}{2}\pi(b\omega X_a/a)^2\rho e^{2i\omega t}\int_{-a}^{a}(a^2-x^2)\sin^2(\pi x/2a)dx =-0.728b^2a\omega^2\rho X_a^2e^{2i\omega t}. \tag{7}$$

With the help of Eq. (2), the elastic-potential energy is determined as

$$V_E=\tfrac{1}{2}\int_{-a}^{a}F_E(\partial\xi/\partial x)dx=3.36(b^2/a)EX_a^2e^{2i\omega t}, \tag{8}$$

and the dissipative energy is computed to be

$$V_G=\tfrac{1}{2}\int_{-a}^{a}F_G(\partial\xi/\partial x)dx=3.36i(b^2/a)GX_a^2e^{2i\omega t} \tag{9}$$

by means of Eq. (3). To obtain an expression for the magnetostrictive energy, V_M, it is necessary first to determine Φ_s in terms of x. As discussed in the Appendix, the equations resulting from a rigorous analysis of the field configuration problem, are not readily solvable. However, since the field in the specimens of this study diminishes rapidly with penetration, two simplifications can be made with regard to Eq. (5). First, it is easily found that β is very nearly unity (i.e., negligible *hf* self-demagnetization). Secondly, the magnetic field distribution within the spheroid is essentially that of a semi-infinite solid, whose well-known solution integrated over a cross section gives

$$W=\int_0^{2\pi}\int_0^{r_1}\exp[-(1+i)(r_1-r)/\delta]rdrd\theta =\pi\delta\{(1+i)r_1+i\delta-i\delta\exp[-(1+i)r_1/\delta]\} \simeq\pi\delta[(1+i)r_1+i\delta]\text{ for }\delta\ll r_1. \tag{10}$$

With the help of (5) and (10), it is now possible to evaluate V_M as

$$V_M=\tfrac{1}{2}\int_{-a}^{a}F_M(\partial\xi/\partial x)dx \simeq-\mu\lambda N[36.2nJ+44.2\lambda X_a/a] \tag{11}$$

where $N=(1-i)\delta b+1.17i\delta^2$.

[8] J. S. Kouvelites, Quart. Appl. Math. 9, 105 (1951).

To satisfy the conservation of energy principle, the sum of the energies must equal zero. Hence, from (7), (8), (9), and (11), we obtain

$$[3.36(E+i\omega G)-0.728\omega^2a^2\rho]b^2X_a - \mu\lambda N(36.2anJ+44.2\lambda X_a)=0. \quad (12)$$

Moreover, the electromotive force induced in the exciter coil by the *hf* magnetic flux passing through the spheroid, may be stated as

$$e=n\int_{-a}^{a}(\partial\Phi_z/\partial t)dx \simeq i\omega n\mu N(59.2anJ+72.2\lambda X_a)e^{i\omega t}. \quad (13)$$

Combining the last two relationships to eliminate X_a and remembering that $\delta=1/[2\pi(f\sigma\mu)^{\frac{1}{2}}]$ in emu, where σ is the electrical conductivity, we arrive at the expression for an impedance,

$$Z=e/j=Z_eZ_M/(Z_e+Z_M),$$

where

$$Z_e=59.2abn^2[(1+i)(f\mu/\sigma)^{\frac{1}{2}}-0.186/\sigma b] \quad (14)$$

and

$$Z_M=4.50a(bn/\lambda)^2[\omega^2G+i\omega(\omega^2/\omega_0^2-1)E],$$

$\omega_0=(4.62E/a^2\rho)^{\frac{1}{2}}$ being the resonant angular frequency for free vibration in the fundamental mode.[5] From Eqs. (14), it appears that Z, the impedance of the exciter coil produced by the total magnetic flux of the spheroid, may be represented as the impedance of an electrical circuit consisting of a parallel combination of Z_e and Z_M. Both Z_e, the "clamped" impedance, and Z_M, the "motional" impedance, may be broken down to the series combinations of resistive, inductive, and capacitive elements, $Z_e=R_e+i\omega L_e$ and $Z_M=R_M+i(\omega L_M+1/\omega C_M)$. Because of magnetic hysteresis, the incremental permeability is a complex quantity and may be written as $\mu_\Delta e^{-i\eta}$. The components of Z_e and Z_M are then found from Eqs. (14) to be

$$\left.\begin{aligned} R_e&=59.2abn^2[(\cos\tfrac{1}{2}\eta+\sin\tfrac{1}{2}\eta)(f\mu_\Delta/\sigma)^{\frac{1}{2}}-0.186/b\sigma],\\ L_e&=9.43abn^2(\cos\tfrac{1}{2}\eta-\sin\tfrac{1}{2}\eta)(\mu_\Delta/f\sigma)^{\frac{1}{2}},\\ R_M&=4.50(\omega bn/\lambda)^2aG,\\ L_M&=4.50(\omega bn/\omega_0\lambda)^2aE\\ &\simeq 4.50(bn/\lambda)^2aE \text{ near resonance, and}\\ C_M&=1/\omega_0^2L_M. \end{aligned}\right\} \quad (15)$$

Finally, a series combination of the resistance, R_L, and the inductance, L_L, is added to the circuit to account for the electrical resistance of the coil and for the magnetic flux "leakage." The equivalent electrical circuit for the vibrational system is then complete as shown in Fig. 1.

The resonance characteristics of this circuit have been fully investigated.[4] It will suffice here to restate some of its more pertinent properties. By means of the definitions,

$$Z_e=|Z_e|e^{i\phi_e} \quad \text{and} \quad Z_e+Z_M=(R_e+R_M)e^{i\phi_{Me}}/\cos\phi_{Me},$$

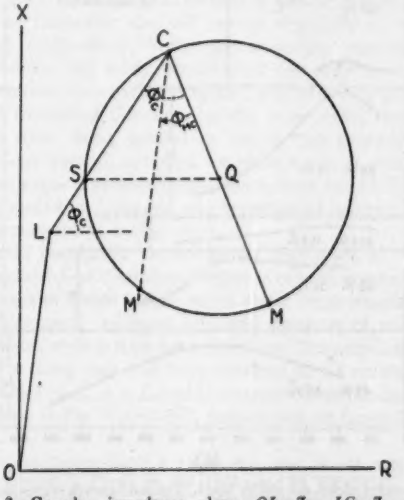

FIG. 2. Complex impedance plane, $OL=Z_L$, $LC=Z_e$, and $CM=Z_e^2/(R_e+R_M)$. Points C and S are referred to in Table I.

TABLE I. The procedure for the determination of the physical parameters from the experimental state.

Quantity	Method of determination
σ; ρ	Resistance, volume, and mass measurements of 15-cm-long wire of the same material (in the same state) as the specimen
Impedance-circle points and corresponding frequencies	Impedance-bridge measurements (with specimen)
R_L	Impedance-bridge measurements (without specimen)
Point C; S; f_1; ϕ_e	Trial-and-error selection until $\tan\phi_{Me}/(f-f_1)$ is a constant
R_e	$R_e=(R_s$ at pt. $C)-R_L$
L_e	$L_e=159R_e\tan\phi_e/f_1$
R_M	$R_M=\dfrac{[(R_s \text{ at pt. } S)-R_L]R_e}{(R_s \text{ at pt. } C)-(R_s \text{ at pt. } S)}$
L_M	$L_M=79.7(R_M+R_e)\left(\dfrac{\tan\phi_{Me}}{f-f_1}\right)-L_e$
η	$\tan\dfrac{\eta}{2}=\dfrac{1+N-\tan\phi_e}{1+N+\tan\phi_e}$, $N=11.0an^2/R_e\sigma$
μ_Δ	$\mu_\Delta=\dfrac{f_1\sigma}{89.0(1-\sin\eta)}\left(\dfrac{L_e}{abn^2}\right)^2$
E	$E=8.57(10)^6(1+L_e/L_M)f_1^2a^2\rho$
$\pm\lambda$	$\pm\lambda=0.067[aE/L_M]^{\frac{1}{2}}bn$
G	$G=0.217(10)^6a^2\rho(R_M/L_M)(1+L_e/L_M)$

Units:

ρ	gm/cm³	n	turns/cm
σ	mho/cm	μ_Δ	gauss/oersted
R	ohm	E	dyne/cm²
L	abh	λ	dyne/cm³ gauss
f	kc/sec	G	dyne sec/cm²
a, b	cm		

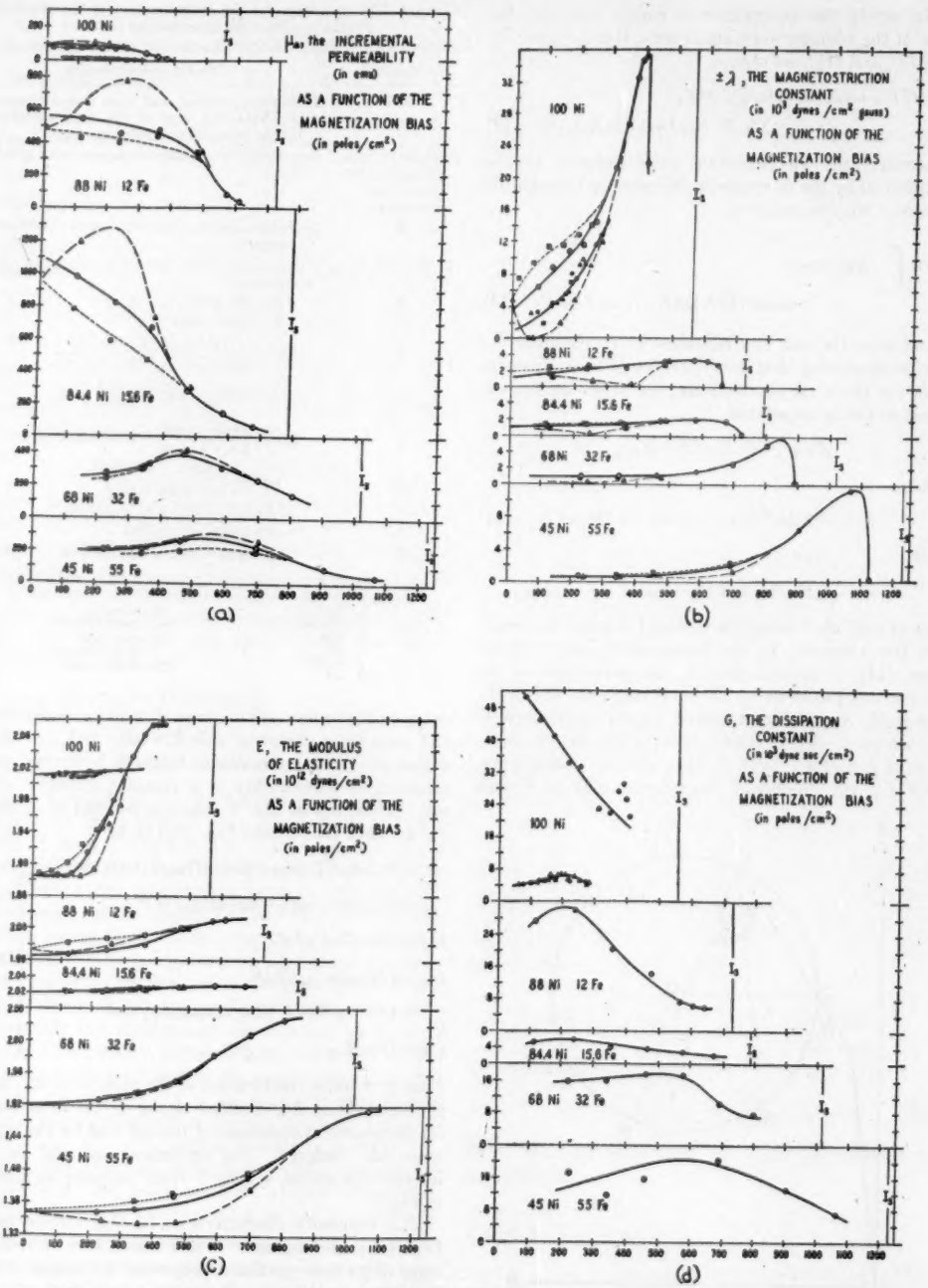
100 Ni
μ_{as}, the INCREMENTAL PERMEABILITY (in cgs) AS A FUNCTION OF THE MAGNETIZATION BIAS (in poles/cm²)
88 Ni 12 Fe
84.4 Ni 15.6 Fe
68 Ni 32 Fe
45 Ni 55 Fe
(a)
±λ, THE MAGNETOSTRICTION CONSTANT (in 10⁶ dynes/cm² gauss) AS A FUNCTION OF THE MAGNETIZATION BIAS (in poles/cm²)
(b)
E, THE MODULUS OF ELASTICITY (in 10¹² dynes/cm²) AS A FUNCTION OF THE MAGNETIZATION BIAS (in poles/cm²)
(c)
G, THE DISSIPATION CONSTANT (in 10⁹ dyne sec/cm²) AS A FUNCTION OF THE MAGNETIZATION BIAS (in poles/cm²)
(d)

FIG. 3. Experimental results. The experimental points for the unannealed nickel are solidly black. The solid curves correspond to the static magnetization curves. The long dashes represent a bias decreasing from saturation on a hysteresis loop, while a hysteresis-loop-bias increasing to saturation is represented by the short dashes.

the total impedance of the circuit may be expressed as

$$Z_X = Z_L + Z_e Z_M/(Z_e+Z_M)$$
$$= Z_L + Z_e - |Z_e|^2 \cos\phi_{Me} e^{i(2\phi_e - \phi_{Me})}/(R_e+R_M), \quad (16)$$

the last term describing a circular variation of Z_X on the impedance plane for changes of ϕ_{Me}. Near resonance, ϕ_{Me} varies sharply with frequency in the manner found to be

$$\tan\phi_{Me} \simeq 2(\omega-\omega_1)(L_e+L_M)/(R_e+R_M), \quad (17)$$

where $\omega_1^2 = 1/(L_e+L_M)C_M$. The variation of Z_X with frequency is shown on the impedance plane of Fig. 2 as the circular locus of M'.

From the resonance properties of the equivalent electrical circuit and from Eqs. (15), a systematic method was developed for facile calculation of the defined physical constants. This method is outlined in Table I, where the experimental and computational steps must be taken in the indicated sequence. The points referred to in this table are the points appropriately labeled in Fig. 2. Some of the quantities have been converted from emu to practical units in which they are more commonly measured.

EXPERIMENTAL RESULTS

To substantiate the correctness of our analysis of the vibrational system and the utility of the resulting computational scheme, we chose to study by the method outlined, the properties of the γ-phase Ni-Fe alloy series, the permalloys, at room temperature. It has long been established that the magnetostriction of the permalloy of approximately 81 percent nickel is zero, while for compositions with less or more nickel, the magnetostriction is, respectively, positive or negative.[6] Since there are theoretical reasons to believe that other physical properties also will behave singularly at this critical composition,[7,8] the polycrystalline materials selected for this study consisted of one close to this composition, two with less nickel, and two with more nickel (including the commercially pure nickel specimen). After being ground to shape, the spheroidal specimens were all annealed for three hours at 650°C in a hydrogen atmosphere and then furnace-cooled. The nickel specimen, however, was investigated before this heat-treatment as well as after.

The hf impedance measurements were made of the magnetostrictive vibrational response of each specimen while it was biased either on its static magnetization curve (as usual, achieved by many reversals of magnetization) or on a large hysteresis loop. The amplitude of the exciting field was kept constant at 1.4 oersted. The values of μ_Δ, $\pm\lambda$, E, and G computed from this data are shown in Fig. 3 (a) to (d), respectively, as functions of the magnetization bias. The estimated value for the saturation magnetization, I_s, of each material is indicated as a reference level. It should be noted that only the absolute magnitude of λ may be obtained by means of Table I. Some previous knowledge of the "sign" of the magnetostriction of the test-material is therefore always required. In Fig. 3(b), λ is positive for the 45 and 68 percent—nickel permalloys, and negative for the other three compositions.

The errors in the evaluation of the physical parameters from impedance circle-diagrams arise in the determination of the size of the circles, of the rate of frequency variation about their circumferences, and of the location of the clamped impedance point (point C in Fig. 2). They are estimated to be 0.1 percent for E, 5 percent for μ_Δ, λ, and G, and at least 10 percent for η. The calculated values of η are therefore much too inaccurate to be plotted for even qualitative study.

The magnetostriction constant, λ, as defined by Eq. (4), is equal to the slope of the static magnetostrictive stress-*versus*-magnetic flux density curve, if time lag effects are negligible. Consequently, when λ is multiplied by 4π and divided by the value of the modulus of elasticity for the corresponding bias, the area under the curve of this quantity plotted against the magnetization bias, is essentially equal to the magnetostrictive strain. From the values of λ and E for the annealed nickel [Figs. 3(b) and 3(c)] passed through this integration process, the saturation magnetostriction was calculated to be -36.7×10^{-6} which agrees quite well with previous quasistatic measurements.[9]

A qualitative comparison of the different annealed specimens based on their static magnetization curves, reveals in several ways the expected uniqueness of a composition near 81 percent nickel. From Figs. 3(a) to 3(d), it is observed that the closer the composition was to this critical value, the larger was the maximum incremental permeability, and the smaller were the saturation magnetostriction, the saturation change of Young's modulus, and the maximum dissipation factor. The dissipation factor, incidentally, is associated only with magnetomechanical hysteresis and micro eddy current losses since the losses due to *macro* eddy currents have been accounted for in the hf field distribution equations.

It is interesting enough that as the bias was taken around a hysteresis loop, μ_Δ, λ, and E for each annealed material had different magnitudes of the two hysteresis loop branches for the same magnetization. This was especially evident at small biases. However, it is perhaps more significant that the variations of these parameters about the hysteresis loop appear to be interrelated. For example, as the magnetization was decreased from saturation, the incremental permeability increased rapidly to a maximum at a magnetiza-

[6] L. W. McKeehan and P. P. Cioffi, Phys. Rev. **28**, 146 (1926).
[7] M. Kersten, Z. Physik **76**, 505 (1932); and **85**, 708 (1933).
[8] R. Becker and W. Döring, *Ferromagnetismus* (Springer, Berlin, 1939), pp. 157–167, 339–348, 365–371.

[9] See reference 8, p. 279.

tion other than zero. At this particular bias, the magnetostriction constant dropped essentially to zero. Since λ is associated with rotations of ferromagnetic domains and μ_Δ with domain reversals, it may be deduced that in this portion of the hysteresis loop, the domains were only reversing discontinuously in response to the hf field. In this bias region, the small variation of the elasticity modulus, known not to be affected significantly by domain reversals, adds support to this conclusion.

The mode of variation of the dissipation constant with bias, for the specimens biased on their static magnetization curves, was similar to that of the incremental permeability. Hence, it is strongly suggested that the losses are a direct manifestiation of irreversible domain boundary displacement. Because of the inherent inaccuracies of the measurements, it was difficult to establish any trends in the variation of the dissipation constant with hysteresis-loop-bias.

The large internal strains of the unannealed nickel undoubtedly hampered the growth and mobility of the magnetic domains. Hence, in harmony with current theory,[7] the maximum μ_Δ, maximum G, and ΔE effect were considerably lower than for its annealed state.

The quantitative agreement of the calculated saturation magnetostriction values and the qualitative correspondence of most of our other experimental results, with previous theory and experimentation, give ample support to our analysis and use of magnetostrictive vibration. Incorporating some small improvements such as the use of a smaller hf field, we are presently exploting some of the promising possibilities of this method in the determination of precise relationships between various physical properties of ferromagnetics.

APPENDIX: FIELD DSITRIBUTION PROBLEM

The Maxwellian field equations applicable within the longitudinally-vibrating prolate spheroidal conductor are

$$\nabla\times\mathbf{H}=4\pi\sigma\mathbf{E}+\epsilon(\partial\mathbf{E}/\partial t)/c^2 \tag{1a}$$

and

$$\nabla\times\mathbf{E}=-\mu(\partial\mathbf{H}/\partial t)+\mu\nabla\times(\mathbf{v}\times\mathbf{H}), \tag{1b}$$

while outside the spheroid, the equations

$$\nabla\times\mathbf{H}=\epsilon(\partial\mathbf{E}/\partial t)/c^2 \tag{2a}$$

and

$$\nabla\times\mathbf{E}=-\mu(\partial\mathbf{H}/\partial t) \tag{2b}$$

apply, the divergences of the electric and magnetic intensity vectors, $\mathbf{E}$ and $\mathbf{H}$, being everywhere zero. Moreover, the term, $\epsilon(\partial\mathbf{E}/\partial t)/c^2$, in (1a) and (2a) is negligibly small since the resonance frequencies for the 2 cm-long Ni and Ni-Fe specimens are all in the order of 150 kc/s; hence, from the above equations, are derived the expressions,

$$\nabla\cdot\nabla\mathbf{H}=4\pi\sigma\mu[(\partial\mathbf{H}/\partial t)-\nabla\times(\mathbf{v}\times\mathbf{H})] \tag{3}$$

and

$$\nabla\cdot\nabla\mathbf{H}=0, \tag{4}$$

which are valid inside and outside the spheroid, respectively. From previous discussion, the displacement, $\xi=\mathbf{X}e^{i\omega t}$, and velocity. $\mathbf{v}=i\omega\mathbf{X}e^{i\omega t}$. Thus, when $\mathbf{H}$ expanded into its Fourier series components:

$$\mathbf{H}_{(0)}+\mathbf{H}_{(1)}e^{i\omega t}+\mathbf{H}_{(2)}e^{2i\omega t}+\cdots,$$

is substituted into (3), and the sum of the coefficients of each of the frequency terms is set equal to zero, it is found that

$$\nabla\cdot\nabla\mathbf{H}_{(n)}=4\pi i\omega\sigma\mu[n\mathbf{H}_{(n)}-\nabla\times(\mathbf{X}\times\mathbf{H}_{(n-1)})], \tag{5}$$

where $n=0, 1, 2, \cdots$. Since only the fundamental component of $\mathbf{H}$ induces an electromotive force in the exciter coil that is not filtered out in the measurements, (5) is consequential only for $n=1$. Furthermore, $\mathbf{H}_{(0)}$, the static bias field, is everywhere axial and uniform within the spheroid, and $\mathbf{X}\times\mathbf{H}_{(0)}=0$. We arrive, therefore, at the expressions,

$$\nabla\cdot\nabla\mathbf{H}_{(1)}=4\pi i\omega\sigma\mu\mathbf{H}_{(1)} \tag{6}$$

and

$$\nabla\cdot\nabla\mathbf{H}_{(1)}=0, \tag{7}$$

which, subject to the boundary conditions, completely define $\mathbf{H}_{(1)}$ inside and outside the conductor.

The boundary conditions are most conveniently expressed by means of prolate spheroidal coordinates, whose orthogonal surfaces are confocal prolate spheroids $[(u^2-1)x^2+u^2r^2=d^2u^2(u^2-1)]$, confocal hyperboloids of two sheets $[(1-v^2)x^2-v^2r^2=d^2v^2(1-v^2)]$, and planes perpendicular to the YZ plane that pass through the X-axis [constant ϕ], $2d$ being the interfocal distance. $\mathbf{H}_{(1)}$ has only u and v components, and they do not vary with ϕ. Therefore, the vector potential, defined by $\nabla\times\mathbf{A}=\mathbf{H}_{(1)}$ and $\nabla\cdot\mathbf{A}=0$, has only a ϕ component, and it also is invariant with ϕ. The equations,

$$\nabla\cdot\nabla\mathbf{A}_i=4\pi i\omega\sigma\mu\mathbf{A}_i \tag{8}$$

and

$$\nabla\cdot\nabla\mathbf{A}_0=0, \tag{9}$$

for the potentials inside and outside the spheroid are derived directly from (6) and (7). Expressed in spheroidal coordinates, (8) is then separated in terms of these coordinates by the assumption of the usual product solution, $A_i=U_i(u)V_i(v)$. Both U_i and V_i are found to be described by the same equation,

$$\frac{d}{du}\left\{(1-u^2)\frac{dU_i}{du}\right\}+\left(\beta_i-\frac{1}{1-u^2}+ku^2\right)U_i=0, \tag{10}$$

where β_i is the separation constant and $k=4\pi i\omega\sigma\mu d^2$. Similarly, by letting $A_0=U_0V_0$, we find that the

equation,

$$\frac{d}{du}\left\{(1-u^2)\frac{dU_0}{du}\right\}+\left(\beta_0-\frac{1}{1-u^2}\right)U_0=0, \quad (11)$$

is appropriate for both U_0 and V_0.

Equation (10) has already been solved by Page and Adams[10] for small, real values of k. Their solution is also valid for a small, imaginary k, but unfortunately, the magnitudes of k for the specimens of this study were in the order of a few thousand. Another method,[11] however, has proved fruitful for the case of large but real values of k, and it offers possibilities which we hope to pursue soon. The fact that k may be complex due to magnetic hysteresis, is not expected to help matters.

The authors wish to thank Mr. R. V. Dyba for his capable assistance in the experimentation.

[10] L. Page and N. I. Adams, *Electrodynamics* (D. Van Nostrand Company, Inc., New York, 1940), Sec. 80.

[11] Stratton, Morse, Chu, and Hutner, *Elliptic Cylinder and Spheroidal Wave Functions* (John Wiley and Sons, Inc., New York, 1941).

PHYSICAL REVIEW VOLUME 84, NUMBER 5 DECEMBER 1, 1951

The Alpha-Particle Disintegration of Beryllium*

WILLIAM O. MCMINN, M. B. SAMPSON, AND V. K. RASMUSSEN
Physics Department, Indiana University, Bloomington, Indiana

(Received August 27, 1951)

The disintegration of Be^9 by 21.7-Mev alpha-particles has been studied with observations of the emitted particles made at various angles. Q-values of -6.92, -7.87, -8.57, and -10.74 Mev were found for the $Be^9(\alpha, p)B^{12}$ reaction giving levels in B^{12} at 0.95, 1.65, and 3.82 Mev. Two groups of deuterons from $Be^9(\alpha, d)B^{11}$ were found giving a level in B^{11} at 2.18 Mev. A third group, if assigned to this reaction would give a level in B^{11} at 0.65 Mev. The inelastic scattering $Be^9(\alpha, \alpha')Be^{9*}$ gives a level in Be^9 at 2.63 Mev.

I. INTRODUCTION

THE charged particle groups produced in the bombardment of thin beryllium films with 21.7-Mev alpha-particles have been investigated by determining their ranges in aluminum absorbers. A preliminary report has been made of some of the results of this investigation which were obtained with apparatus where the angle between the beam direction and the axis of the detecting system was 90°.[1] This report presents the results from observations of the particles emitted in various directions with respect to the direction of the incident particles. This permits the more certain assignment of a group to a definite reaction. The occurrence of the $Be^9(\alpha, d)B^{11}$ reaction is revealed, which was not suspected in our earlier work.

The results of proton scattering experiments by several investigators indicate the lowest excited state of Be^9 to be about 2.42 Mev.[2] Van Patter *et al.* assign two groups obtained by magnetic analysis of the products of the deuteron bombardment of boron to the $B^{11}(d, \alpha)Be^9$ reaction.[3] The Q-values obtained indicate an excited state of Be^9 at 2.422 ± 0.005 Mev.

No excited state below 2.1 Mev has been reported for B^{11}. This level has been obtained from the $B^{10}(d, p)B^{11}$ reaction as 2.138 ± 0.014 Mev by Van Patter *et al.*[4] Li and Whaling[5] have reported a tentative value of 2.107 ± 0.017 Mev from the $C^{13}(d, \alpha)B^{11}$ reaction.

Hudspeth and Swann[6] found a level in B^{12} at about 1 Mev from the deuteron bombardment of boron. Buechner *et al.*,[7] using the same reaction, got a value of 0.947 ± 0.005 Mev. Bockelman[8] found a resonance in the neutron cross section of boron for neutrons of 0.43 Mev which he attributed to the formation of B^{12}. This energy gives a level in B^{12} at 3.70 Mev.

II. EXPERIMENTAL METHOD

The charged particles produced in the alpha-particle bombardment of beryllium were detected with a proportional counter biased to count particles only near the end of their paths. Corrections were made for variations in the beam intensity by monitoring the current which was collected after passing through the thin target foil. A current integrator circuit was used for this purpose.[9]

The beam energy was determined by measuring the ranges of the alpha-particle groups elastically scattered

* Supported by the joint program of the ONR and AEC.

[1] McMinn, Sampson, and Bullock, Phys. Rev. **78**, 296 (1950).

[2] K. E. Davis and E. M. Hafner, Phys. Rev. **73**, 1473 (1948); E. H. Rhoderick, Proc. Roy. Soc. (London) **201**, 348 (1950); Browne, Williamson, Craig, and Donahue, Phys. Rev. **83**, 179 (1951).

[3] Van Patter, Sperduto, Huang, Strait, and Buechner, Phys. Rev. **81**, 233 (1951).

[4] Van Patter, Buechner, and Sperduto, Phys. Rev. **82**, 248 (1951).

[5] C. W. Li and W. Whaling, Phys. Rev. **82**, 122 (1951).

[6] E. L. Hudspeth and C. P. Swann, Phys. Rev. **76**, 1150 (1949).

[7] Buechner, Van Patter, Straight, and Sperduto, Phys. Rev. **79**, 262 (1950).

[8] C. K. Bockelman, Phys. Rev. **80**, 1011 (1950).

[9] H. T. Gittings, Rev. Sci. Instr. **20**, 325 (1949).

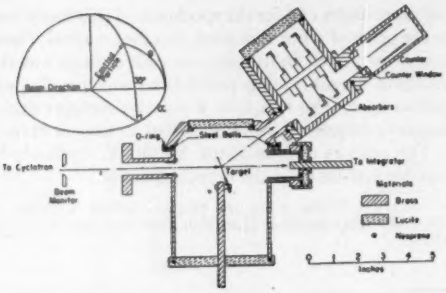

FIG. 1. Apparatus for observing reaction particles at various angles with respect to the cyclotron beam. $\cos\theta = \cos\alpha \cos 35°$.

from the beryllium and from known contaminating elements in the target.

The mean range in aluminum of a group of particles which gave a peak in the curve of number of particles detected *versus* aluminum absorption was obtained by adding a correction described below to the total aluminum absorption, including the counter window, at the peak A correction was made for the energy lost in the target.

The range-energy data of Livingston and Bethe[10,11] was used to construct mean range *versus* energy relations for protons, deuterons, and alpha-particles in aluminum, for use in this experiment. Conversion of mean ranges in aluminum to equivalent ranges in air was made with the factor 1.52 mg/cm² Al=1 cm air, and with the correction curves in Livingston and Bethe.

The correction, r, to be added to the absorption at a peak of the yield curve in order to obtain the mean range of the group responsible for the peak was regarded as a constant for all ranges, for a given type of particle as discussed by Holloway and Moore.[12]

III. APPARATUS AND PROCEDURE

Figure 1 represents the apparatus consisting of a target chamber, system of aluminum absorbers, and a proportional counter which was used to observe the reaction particles emitted at various angles θ with respect to the direction of the cyclotron alpha-particle beam. The variable angle chamber is designed to allow θ to be varied between 35° and 145°. The figure shows the counter in its most forward (35°) position. The angle θ is changed by rotating the head of the target chamber which rests upon a ring of ¼-inch steel balls and carries the absorber chamber and counter. A greased rubber O-ring around the edge of the target chamber head seals the vacuum.

The aluminum absorbers which are interposed between the target and the counter are mounted in stacks over $\frac{9}{16}$-inch holes in three wheels. Each wheel carrying the absorbers is rotated and positioned by a pawl and ratchet wheel arrangement which is actuated by an electromagnet. The unit absorbers were cut from a roll of 1.1 mg/cm² aluminum foil. Each set of absorbers was weighed to 0.1 mg/cm².

The proportional counter was constructed with a 5-mil tungsten wire inside a copper cylinder 1 inch in diameter and 1¼ inches long. Counter windows of 1 mil and 0.7-mil aluminum foil were used. The counter was filled with argon and CO_2 in the ratio 12:1 to a total pressure of 13 cm Hg. The outer cylinder of the counter limited the directions of particles entering the counter to a maximum of 3.5° from the axis of the counter.

A model 100 pulse preamplifier was used, followed by three stages of amplification. The amplified pulses were discriminated against according to pulse height by a Schmidt circuit.

It was desirable to have target foils free of heavy contaminations to prevent the scattering of more energetic alpha-particles. The foils were prepared by evaporation in vacuum in an apparatus suggested by the method of H. Smith for making beryllium foils.[13] Granulated beryllium was heated in a graphite crucible with a solid bottom by electron bombardment from a heated tungsten filament below the crucible. 800 watts was sufficient to evaporate the beryllium. The beryllium was collected on 3-mil sheet steel, from which it was separated by flexing. The films used for targets weighed approximately 1 mg/cm². Tungsten evaporated from the filament was prevented from condensing on the collector by having the collector in the shadow of the crucible. Aluminum and lead were detected in the experiment from scattered alpha-particle groups, and their presence in the metal used for evaporation was determined by spectroscopic analysis. Carbon which was deposited on the targets during bombardment, and oxygen were other contaminants revealed by scattered alpha-particle groups.

The residual range, r, of alpha-particles in the counter was determined with thorium groups of known range. The residual range for protons was determined by an auxiliary experiment in which a gas target composed of water vapor and hydrogen was bombarded with alpha-particles and the ranges of both the scattered alpha-particles and of the recoil hydrogen nuclei were observed A counter having $r=1.5$ mg/cm² Al for alpha-particles had a residual range of 1.6 mg/cm² Al for protons by this determination. A value of r for deuterons was approximated by adding 0.2 mg/cm² Al to r for protons. This is approximately the difference in the distances from the end of the range to the peaks of the specific ionization curves for the two hydrogen isotopes.

The investigation of the products of the alpha-

[10] M. S. Livingston and H. A. Bethe, Revs. Modern Phys. **9**, 261 (1937).
[11] H. A. Bethe, Revs. Modern Phys. **22**, 213 (1950).
[12] M. G. Holloway and B. L. Moore, Phys. Rev. **58**, 851 (1940).
[13] H. Smith, J. Sci. Instr. **26**, 378 (1949).

particle bombardment of beryllium was begun by making runs over the entire range of emitted particles at a given angle, and repeating this for several angles. The alpha-particle groups scattered from beryllium and from known contaminating elements in the targets were used to calculate the beam energy at each angle of observation. The mean beam energy calculated for each angle was used in the calculations of Q-values corresponding to the observed particle groups under assumptions of different reactions. Later observations were made of the positions of peaks of particular interest over as great a range of angles as was possible. During these observations frequent checks were made on the beam energy by observations of the position of the beryllium scattered alpha-particle peak.

IV. RESULTS

Figure 2 shows absorption curves which were obtained at the least angle θ (35°) obtainable with the apparatus. The shorter range curve is an absorption curve for alpha-particles. This was obtained with a counter voltage of −410 volts. The curve for longer ranges (beyond the range of the scattered alpha-particles) was obtained with the same discriminator bias setting and with the counter at −620 volts which permitted counting of protons and deuterons. Figure 2 is typical of the absorption curves obtained. Proton and deuteron peaks were not located where they occurred over a large background of alpha-particles.

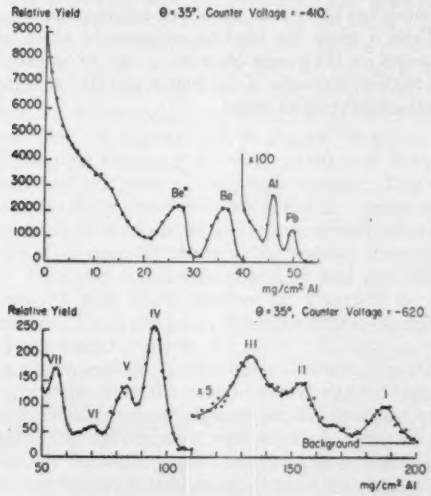

FIG. 2. Relative yield of particles *versus* aluminum absorption, obtained in the alpha-particle bombardment of a thin beryllium film. $E_\alpha = 21.84$ Mev. $\theta = 35°$. The mean range in aluminum of a group is obtained by adding to the absorption at the peak of the curve the weight of the counter window (6.2 mg/cm² Al) and r. The continuous distribution of α-particles at shorter ranges may be attributed to the breakup of C^{12*} or to $Be^9(\alpha, \alpha'n)Be^8$.

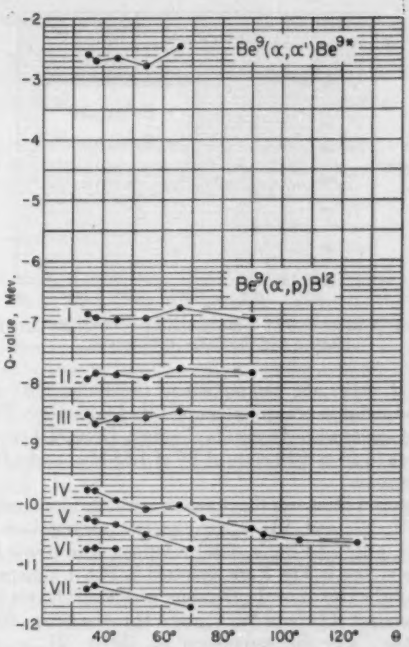

FIG. 3. Q-values for inelastic scattering of alpha-particles from beryllium, and for the reaction $Be^9(\alpha, p)B^{12}$.

The alpha-particle absorption curves for different angles, like Fig. 2 for $\theta = 35°$, represented two strong groups of alpha-particles of about equal intensity. These groups were elastically and inelastically scattered from beryllium. Peaks about 1/100th as high as the beryllium peaks rose at greater ranges than the beryllium elastic scattering peak. These small peaks were due to scattering by contaminating elements. The Q-values calculated for inelastic scattering from beryllium are plotted at the top of Fig. 3.

Seven peaks due to proton and deuteron groups appear in the absorption curve shown in Fig. 2. These seven groups, which are given roman numerals in Fig. 2, were observed at several angles. The results of the observations are presented in Fig. 3 where Q-values calculated under the assumption that the groups are proton groups from the $Be^9(\alpha, p)B^{12}$ reaction are plotted against angle. The horizontal trend of the points for Groups I, II, and III in Fig. 3 suggest that the correct reaction has been assumed. This is supported in the case of Group I by the reasonable agreement between the mean of all the experimentally determined Q-values for the group (−6.92 Mev) and the value −7.01 Mev calculated from the mass tables of Mattauch and Flammersfeld.[14] The experimental Q-values for Groups I

[14] J. Mattauch and A. Flammersfeld, *Isotopic Report, Special Issue*, Z. Naturforsch (1949).

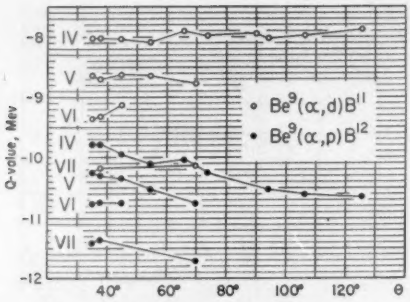

FIG. 4. Q-values under the two assumptions of the $Be^9(\alpha, p)B^{12}$ reaction and the $Be^9(\alpha, d)B^{11}$ reaction.

and II under the assumption of the $Be^9(\alpha, p)B^{12}$ reaction indicate an excitation of B^{12} of 0.95 Mev. This value agrees with the results of others. Group III corresponds to an excited state of B^{12} of 1.65 Mev under this assumption.

Figure 4 compares the Q-values calculated for Groups IV, V, VI, and VII under the two assumptions of $Be^9(\alpha, p)B^{12}$ and $Be^9(\alpha, d)B^{11}$ reactions. The points for these groups in Fig. 3 are replotted in Fig. 4. Comparison of the trends of the Q-values with angle favors the assignment of Groups IV, V, and VII to the $Be^9(\alpha, d)B^{11}$ reaction, and the assignment of Group VI to the $Be^9(\alpha, p)B^{12}$ reaction.

The assignment of Group IV to the (α, d) reaction is supported by the reasonable agreement between the mean of all our Q-values for this group (-8.01 Mev) and the value -8.07 Mev calculated from the mass table. The experimental Q-values for Groups IV and VII assuming the $Be^9(\alpha, d)B^{11}$ reaction indicate an excited state of B^{11} at 2.18 Mev. This excitation is in reasonable agreement with the results of other. The assignment of Group V to the $Be^9(\alpha, d)B^{11}$ reaction is favored by the results of this experiment which are represented in Fig. 4. The assignment is made tentatively since the indicated excited state of B^{11} at 0.65 Mev has not been found in the experiments of others.

Group VI is assigned from the incomplete data represented in Fig. 4 to the $Be^9(\alpha, p)B^{12}$ reaction. This assignment indicates an excited state of B^{12} at 3.82 Mev which may be compared with the value 3.70 Mev indicated by Bockelman's work.

The assignment of the reaction particle groups to (α, p) and (α, d) reactions involving contaminating elements in the targets was investigated and found to be much less likely than the above assignments.

Table I gives the reaction assignments which are proposed for the groups observed in this investigation, the relative intensities of the groups, and the calculated Q-values and excited states.

TABLE I. Reaction assignments, Q-values, and excited states.

Reaction	Group	Relative intensity*	Q-value Mev	Excited state Mev
$Be^9(\alpha, \alpha')Be^{9*}$	α'	1	-2.63 ± 0.15	2.63 ± 0.15
$Be^9(\alpha, d)B^{11}$	IV	20	-8.01 ± 0.05	0
	V	12	-8.66 ± 0.10	(0.65 ± 0.10)
	VII	10	-10.19 ± 0.10	2.18 ± 0.10
$Be^9(\alpha, p)B^{12}$	I	1.0	-6.92 ± 0.05	0
	II	1.2	-7.87 ± 0.05	0.95 ± 0.05
	III	2.0	-8.57 ± 0.05	1.65 ± 0.05
	VI	4.5	-10.74 ± 0.10	3.82 ± 0.10

* The intensity of the inelastically scattered alpha-particle group is compared with the intensity of the elastically scattered alpha-particle group. The intensities of the proton and deuteron groups are compared with the intensity of Group I. Averages are given because the relative intensities did not vary with angle by more than the experimental uncertainty. No determination of the angular dependence of the intensity of a given group was made.

Excited States of F^{19} from $O^{16}(\alpha, p)F^{19}$*

M. Loren Bullock and M. B. Sampson
Department of Physics, Indiana University, Bloomington, Indiana
(Received August 13, 1951)

Oxygen gas has been bombarded with 20.6-Mev alpha-particles, and the resulting proton groups have been studied using a proportional counter. The energies of the proton groups were measured by their range in aluminum. Q-values of -8.08, -9.44, -10.75, and -12.00 Mev were obtained giving levels in F^{19} at 1.36, 2.67, and 3.92 Mev.

INTRODUCTION

MANY investigators in recent years have observed excited states of the F^{19} nucleus. Several close levels have been found in the region of 10 to 15 Mev by studying the excitation function of the $O^{18}(p, n)F^{18}$ reaction, and a low level at about 1.4 Mev has been found from the beta-decay of O^{19} and also from inelastically scattered neutrons from F^{19}. These findings have been summarized by Hornyak *et al.*[1]

The present investigation was undertaken to look for additional low-lying levels in F^{19}. The 21-Mev alpha-particle beam of the Indiana University cyclotron was used to bombard oxygen gas, and the proton groups from the $O^{16}(\alpha, p)F^{19}$ reaction were studied. The excitation possible with this beam energy permitted the observation of protons from excited states of the F^{19} nucleus up to 4.3 Mev.

EXPERIMENTAL PROCEDURE

The apparatus used was essentially that described before.[2] It was modified, however, by the use of a new target chamber which permitted the angle of observation to be varied continuously from 35 degrees to 145 degrees, measured from the forward direction of the beam. In this investigation, two angles of observation were used: 36 degrees and 90 degrees. Windows of 3.28 mg/cm² aluminum foil were placed over the entrance and exit ports of the target chamber. This allowed the entire chamber to be filled with a target gas. The windows were placed on the end of stainless steel tubes which extended almost to the center of the chamber. This gave additional collimation and also minimized the path length traveled by a particle in the target gas. The target gas in this experiment was oxygen at ½-atmosphere pressure.

A proton emitted into the angle of observation initiated a pulse from the counter which was fed into a conventional pre-amplifier, amplifier, discriminator, and scaler. The discriminator was adjusted, however, to pass only the larger pulses corresponding to those protons near the end of their range. Thus for a proton which stopped in the counter after passing through a given thickness of aluminum absorber, the mean range could be found by adding the absorber thickness, the aluminum equivalent of the target gas passed through, the thickness of the target chamber window, and the counter absorption. The counter absorption for alpha-particles was found by calibration with ThC′ alpha-particles. The counter absorption for protons was then calculated by comparing the residual range curve for an alpha-particle[3] and the residual range curve for a proton.[4]

Curves such as shown in Figs. 1 and 2 were obtained by varying the absorber thickness in front of the counter. The ordinate is the number of protons counted and normalized to the integrated beam current. The ordinate is therefore proportional to the number of protons counted per alpha-particle in the beam. The main peaks, numbered I, IV, VI, and IX in Figs. 1 and 2, correspond to the proton groups from the $O^{16}(\alpha, p)F^{19}$ reaction. The energies of these proton groups were obtained from their ranges in aluminum, using the range-energy calculations of Smith.[5] The highest energy proton group was thus 10 Mev at 36 degrees and 7.8 Mev at 90 degrees.

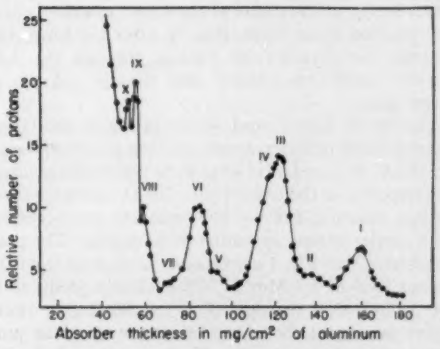

FIG. 1. Proton groups observed at 36° from the forward direction of the beam. The ordinate is proportional to the number of protons counted per alpha-particle in the beam. The target gas was cylinder oxygen with nitrogen and carbon impurities. The proton groups from oxygen are I, IV, VI, and IX.

* This work was assisted by the joint program of the ONR and AEC.

[1] Hornyak, Lauritsen, Morrison, and Fowler, Revs. Modern Phys. 22, 353 (1950).

[2] Brolle, Sampson, and Mitchell, Phys. Rev. 76, 624 (1949).

[3] M. G. Holloway and M. S. Livingston, Phys. Rev. 54, 29 (1938).

[4] M. G. Holloway and B. L. Moore, Phys. Rev. 58, 852 (1940).

[5] J. H. Smith, Phys. Rev. 71, 32 (1947).

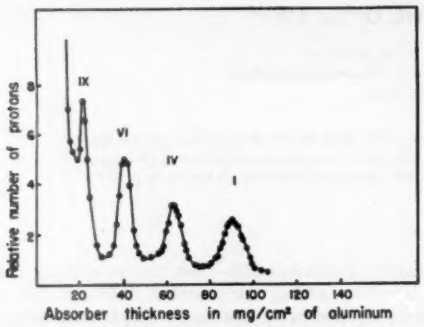

FIG. 2. Proton groups from oxygen observed at 90° from the forward direction of the beam. The ordinate is proportional to the number of protons counted per alpha-particle in the beam. The target gas was pure oxygen.

When the discriminator is set to count only those protons stopping in the counter, all of the alpha-particles passing through the counter will be counted. Hence, an alpha-particle group will give an integral curve instead of a peak. In Figs. 1 and 2 the large rise at the low energy end is the beginning of the integral curve for the elastically scattered alpha-particles from the beam. Any proton group with less range, therefore, cannot be observed, so the lower limit to the observable proton groups is determined by the range of the elastically scattered alpha-particles. Adjusting the discriminator to pass only those pulses corresponding to alpha-particles stopping in the counter, the range of these alpha-particles was obtained. Their energy was then found using Livingston and Bethe's range-energy relation for alpha-particles.[6] The beam energy thus calculated was 20.6±0.1 Mev. This is the value of the beam energy at the center of the target chamber where the reaction takes place, that is, after the beam has entered the chamber by passing through the 3.28 mg/cm² aluminum window and through 1.5 cm of target gas.

For the 36 degree curve shown in Fig. 1, the target gas was Linde cylinder oxygen, and the peaks numbered II, III, V, VII, and VIII seem to be protons from nitrogen impurity in the oxygen gas. The Q-values for these groups, assuming a $N^{15}(\alpha, p)O^{18}$ reaction, are consistent with similar groups appearing at 90 degrees. The peak numbered X in Fig. 1 corresponds to protons from the known level at 5.3 Mev in N^{15}, evidently produced in the $C^{12}(\alpha, p)N^{15}$ reaction. For the 90 degree curve shown in Fig. 2, however, the target gas was pure oxygen obtained from the Matheson Company, and these impurity peaks do not appear.

[6] M. S. Livingston and H. Bethe, Revs. Modern Phys. **9**, 263 (1937).

TABLE I. Measured Q-values of the $O^{18}(\alpha, p)F^{19}$ reaction and energy levels in F^{19}.

Group	Q-value Mev	Level in F^{19} Mev
I	−8.08±0.1	0
IV	−9.44±0.1	1.36±0.05
VI	−10.75±0.1	2.67±0.05
IX	−12.00±0.1	3.92±0.05

RESULTS

The Q-values for the proton groups were calculated using the beam energy obtained from the scattered alpha-particle range. The results for the various curves obtained at the two angles of observation were averaged together and are shown in Table I. The errors indicated are estimated from the limits of measurement on the data. The errors in the Q-values are predominantly due to the error in the beam energy determination, but since these errors tend to be canceled out when subtracting Q-values, the error in the energy level determination is smaller and is mainly due to the error in the proton energy determination.

The width of the peaks at half-maximum is about 6 percent of the proton energies and is entirely instrumental. Most of it can be attributed to the width of the peak of the Bragg ionization curve, for this allows the discriminator to pass pulses representing a spread of ranges.

The first excited level has been observed before. Bleuler and Zunti[7] and also Fulbright *et al.*,[8] in studying the beta-decay of O^{19}, found an excited state of F^{19} at 1.6 Mev. More recently, Beghian *et al.*[9] made absorption measurements on the gamma-ray accompanying the inelastically scattered neutrons from F^{19}, and they found an energy of 1.3±0.1 Mev. These values seem consistent with the 1.36±0.05 Mev value found in this experiment.

The −8.08 Mev ground state Q-value gives a calculated atomic mass of 19.0044±0.0002 for F^{19}, using the He^4 and the H^1 masses of Bainbridge.[10] This can be compared with the value of 19.00450±0.00026 in Bethe's 1947 table.[11]

The authors wish to thank Dr. V. K. Rasmussen, who designed the target chamber used in this investigation, and also Mr. William Stefanich and Mr. Byron M. Carmichael for their time and skill in the operation of the cyclotron.

[7] E. Bleuler and W. Zunti, Helv. Phys. Acta **20**, 195 (1947).
[8] Fulbright *et al.*, Plut. Proj. Report CP-1357 (February, 1944).
[9] L. E. Beghian *et al.*, Phys. Rev. **77**, 286 (1950).
[10] K. T. Bainbridge, Phys. Rev. **81**, 146 (1951).
[11] H. A. Bethe, *Elementary Nuclear Theory* (John Wiley and Sons, Inc., New York, 1947).

Neutron Refraction in O_2, N_2, He, A Gases*

A. W. McReynolds
Brookhaven National Laboratory,† Upton, Long Island, New York
(Received August 13, 1951)

The index of neutron refraction of oxygen, nitrogen, helium, and argon has been studied by reflection of a neutron beam from a liquid gas interface and observation of decreasing reflectivity with increasing gas pressure. Results verify that the index for gases is given by the same formulas which hold for liquids and solids. Comparative measurements of the different gases then give values for the coherent bound scattering cross sections: assuming oxygen = 4.2 barns as a standard, nitrogen = 11 barns, helium = 1.1 barns, argon = 0.5 barn.

INTRODUCTION

THE total thermal neutron scattering cross section is the sum of an incoherent and a coherent part, the latter determining all interference effects between neutron waves scattered from different nuclei. Diffraction in crystalline media is therefore the most general means of determining coherent cross sections, and has been applied by Shull and Wollan[1] to a large number of nuclei. Another interference phenomenon which may be used is total reflection from a plane surface, which may also be regarded as zero order diffraction, the critical angle for total reflection being determined by the density and coherent scattering cross section of nuclei, independent of atomic arrangement. This method was demonstrated by Fermi and Marshall[2] with solid mirror surfaces and later applied, by Hughes, Burgy *et al.*[3] to hydrocarbon liquid mirrors, to measure accurately σ_{coh} for hydrogen. Although crystal diffraction measurements are at neutron wavelengths $\sim$1A and total reflection measurements at 4–20A, the coherent cross section should be constant over the thermal range except for a few cases of near-by resonances.

The present paper reports measurements of the index of neutron refraction of a gas, and hence of coherent scattering cross section, by total reflection from an interface between the gas and a plane surface of liquid or solid. For these surfaces, materials were selected which have low indices of refraction either because of low density and cross section or because of cancellation of nuclei with positive and negative scattering phases to give a net small positive scattering amplitude. As gas index of refraction increases with pressure, reflected intensity from the interface decreases. Observations of reflected intensity *vs* gas pressure have a twofold purpose: (1) The usual formulas for index of neutron refraction assume interaction of the neutron with the entire medium rather than with individual nuclei and therefore use the bound atom, coherent cross section, exceeding the free cross section by the reduced-mass factor $(A+1/A)^2$. These formulas are verified for solids and liquids, but it was less certain that they could be extended to gases, where the nuclei are in independent motion, free of intermolecular binding forces. Comparison of cross sections by reflection with those derived from other methods serves as a check on applicability of the theory to gases. (2) By comparative measurements with oxygen, for which σ_{coh} was well known, coherent cross sections could be measured for other gases such as nitrogen, not previously measured accurately by crystal diffraction, and helium and argon, which of course are not amenable to crystal diffraction.

EXPERIMENTAL METHOD

Neutron beams from the Oak Ridge and Brookhaven reactors were defined by two horizontal slits between slabs of lucite and boron carbide. As shown in Fig. 1, the beam was reflected at angles of 3–5 minutes from 10-cm mirrors of liquid, placed inside a pressure tank, and was detected by a BF_3 proportional counter. A slit in front of the counter excluded the direct beam but allowed the entire reflected beam to enter. The reflected beam contains all incident neutrons from zero to a critical energy. Total reflected intensity was measured as a function of gas pressure from 0 to 150 atmospheres in the tank.

When a beam of neutrons heterogeneous in wavelength, strikes a mirror surface at small angle θ, the part totally reflected contains all neutrons of wavelength greater than a critical value[4]

$$\lambda_c = \theta/(n\sigma^{\frac{1}{2}}/2\pi^{\frac{1}{2}})^{\frac{1}{2}}$$

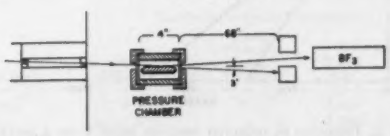

FIG. 1. Apparatus for reflection of a neutron beam from a liquid surface surrounded by gas at high pressure.

* Research carried out under contract with AEC.
† Part of work carried out at Oak Ridge National Laboratory.
[1] C. G. Shull and E. O. Wollan, Phys. Rev. **81**, 527–35 (1951).
[2] E. Fermi and L. Marshall, Phys. Rev. **71**, 666–77 (1948).
[3] Hughes, Burgy, and Ringo, Phys. Rev. **77**, 291 (1950).
[4] Reflectivity is not zero for neutrons of less than the critical wavelength, but since the shape of the reflectivity curve is the same for each critical angle, this correction does not significantly alter the reflected intensity *vs* gas pressure curve.

TABLE I. Characteristics of materials used as reference mirrors.

Material	n_0 nuclei/cc	σ_0 barns	$\lambda^2\delta\left(=\frac{n_0\sigma_0^{\frac{1}{2}}}{4\pi^{\frac{1}{2}}}\right)$
Ethylene glycol ($C_2H_6O_2$)	1.13×10^{23}	0.0055	3.9×10^{3}
Triethylene glycol ($C_6H_{14}O_4$)	1.09	0.0212	7.5
Lucite	1.07	0.111	16.0

where $\delta=n\sigma^{\frac{1}{2}}\lambda^2/4\pi^{\frac{1}{2}}=1-$index of refraction, $m=$neutron mass, $n=$nuclei/cc, and $\sigma=$coherent cross section. For a Maxwellian[5] distribution, the total reflected intensity can be computed by integrating

$$I=\int_{\lambda_c}^{\infty}N(\lambda)d\lambda$$

to get

$$I=\text{const}\times(n\sigma^{\frac{1}{2}}/2\pi^{\frac{1}{2}})^{\frac{1}{2}},$$

for long wavelengths, corresponding to $E\ll kT$.

In the case of reflection from an interface between media of indices of refraction $1-\delta_0$ and $1-\delta_1$,

$$I=\text{const}(\delta_0-\delta_1)^2=\text{const}(n_0\sigma_0^{\frac{1}{2}}-n_1\sigma_1^{\frac{1}{2}})^2.$$

Thus the introduction of gas of coherent cross section σ, above a liquid or solid surface decreases the reflected intensity in the ratio

$$\frac{I}{I_0}=\left(1-\frac{n_1\sigma_1^{\frac{1}{2}}}{n_0\sigma_0^{\frac{1}{2}}}\right)^2=\left(1-\frac{P}{P_0}\right)^2. \qquad (2)$$

It is seen that σ may be determined by plotting $(I/I_0)^{\frac{1}{2}}$, which is a linear function of P going to zero at the pressure P_0 at which the indices of refraction of the two media are equal. Then

$$\sigma_1=[n_0/n_1(P_0)]^2\sigma_0, \qquad (3)$$

where $n_0=$nuclei/cc in liquid or solid mirror; $n_1(P_0)=$nuclei/cc in gas at pressure P_0, and $\sigma_0=$average coherent cross section for nuclei in mirror$=[(\pm\sigma^{\frac{1}{2}})$ average$]^2$, taking account of negative scattering phases.

The materials used as reference mirrors are listed in Table I with values of $\sigma_0^{\frac{1}{2}}$ from best available data;[1,3] and δ computed from Eq. (1).

Several corrections must be applied to the foregoing analysis: (1) Introduction of gas into the pressure chamber decreases intensity of the reflected beam not only by change of the reflectivity of the interface but also by isotropic scattering of the beam in transmission through the gas. This attenuation increases at low energies and represents an appreciable fraction of the total change of intensity, particularly in diatomic gases like oxygen and nitrogen, where molecular effects increase the cross section for low energy neutrons to 20–25 barns. It has been corrected for, both by measurement of attenuation of a beam reflected from a mirror outside the gas chamber, and by application of the data of Melkonian.[6]

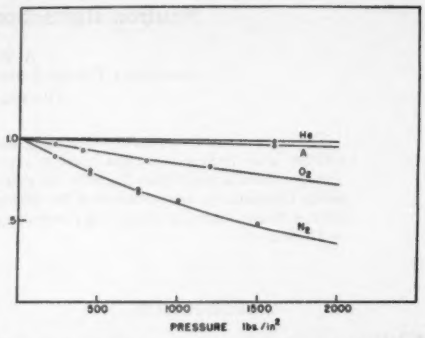

FIG. 3. Attenuation of neutron beam in transmission through the pressure tank. Curves are calculated from Melkonian's[4] data, assuming 2.5A neutron wavelength; points experimental. Correction for attenuation was made in Figs. 2, 4. Path length 10 cm. Total cross section assumed: Helium—0.7b, Argon—1.5b, Oxygen—4.5b, Nitrogen—14b.

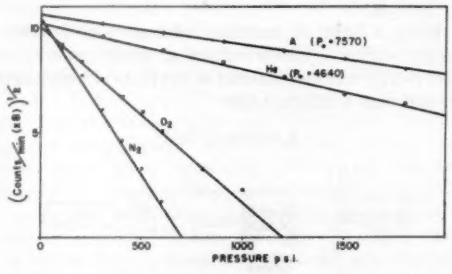

FIG. 2. Intensity of reflected neutron beam from a surface of ethylene glycol at about 3 minutes angle as a function of pressure of surrounding gas. Where $I=0$, index of neutron refraction is equal for gas and liquid.

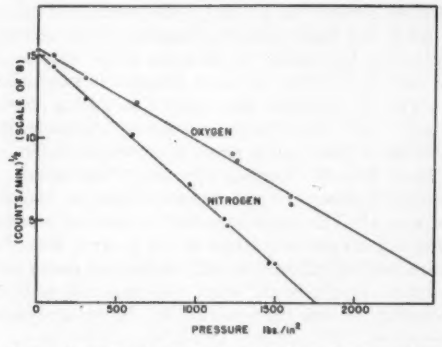

FIG. 4. Intensity of reflected neutron beam from a surface of triethylene glycol, as a function of pressure of the surround gas. Angle of incidence 3 minutes.

[5] The flux distribution deviates from Maxwellian form in the vicinity of the graphite cutoff at 6.7 angstroms, but does not alter significantly reflected intensity from the liquid mirrors used, for which critical wavelengths were in the range 2–5 angstroms.

[6] E. Melkonian, Phys. Rev. **76**, 1750–59 (1949).

(2) At high pressures an appreciable quantity of the gas dissolves in liquid mirrors. The density of dissolved gas atoms, however, is never more than a few percent of the gas density. (3) At gas pressures of 100–150 atmospheres densities could not be computed exactly from the perfect gas laws, but required empirical corrections of a few percent, for oxygen and argon. Corrections were negligible for helium and nitrogen.

RESULTS

Mirrors of ethylene glycol were 10 cm long and set at an angle of about 2.7 minutes, corresponding to a critical wavelength of 2.8A at zero gas pressure. In Fig. 2 are shown the curves of variation of reflected intensity with pressure of oxygen, nitrogen, helium and argon. All points are corrected according to Fig. 3 for attenuation of the beam in transmission through the gas. The curves of Fig. 3, calculated using cross sections as indicated from Melkonian's[6] results, assuming wavelength about 2.5A, agree with the experimental points shown.

The linear variation of $(I/I_0)^{\frac{1}{2}}$ for each gas verifies the analysis of the previous section and permits extrapolation of the curves to determine P_0 at which the gas index of refraction equals that of the liquid. A number of intensity *vs* pressure curves similar to those shown in Fig. 2 have been determined. Table II shows the average values of P_0 and corresponding values for the bound coherent scattering cross section, calculated from Eq. (1), taking $\sigma=4.2$b for oxygen as a standard. Corrections for isotropic scattering in the gas, absorption in the liquid, and deviation from perfect gas laws are included.

TABLE II. Results from total reflection on ethylene glycol mirrors.

Gas	P_0(psi)	σ_{coh}(barns)
Oxygen	1260	(4.2)
Nitrogen	770	11.0±1.5
Helium	4890	1.1±0.15
Argon	7220	0.51±0.1

Similar data were obtained for oxygen and nitrogen using the higher index liquid, triethylene glycol. The effects of helium and argon were too small for accurate measurement in this case. Results are shown in Table III.

In principle the cross section of each gas can be measured by direct comparison to the liquid mirrors, for which calculated refractive indices are shown in Table I. Since this refractive index depends on a delicate balance between positive phase scattering from carbon nuclei and negative phase scattering from hydrogen nuclei, small errors in the cross-section values of these constituents would lead to large errors in the final result. Consequently only a rough cross-section value can be measured. The values of $\lambda^2\delta$ in Table I and of P_0 in Tables II and III give for oxygen

$$\sigma_{coh}=2.7 \text{ barns}$$

measured against both ethylene glycol and triethylene glycol, as compared to the accepted value of 4.2 barns.

TABLE III. Results from total reflection on triethylene glycol mirrors.

Gas	P_0(psi)	σ_{coh}(barns)
Oxygen	1800	
Nitrogen	2770	9.7±1.1

In Table IV the present results, shown in the first column, are compared with the results of crystal diffraction by Shull and Wollan and of transmission measurements by Melkonian,[6] and by Bashkin *et al.*[7] References for the data are indicated in each case. Values for nitrogen are in fairly good agreement although slightly higher than Shull and Wollan's value, and are still somewhat lower than the total scattering cross section, as would be expected since nitrogen's spin should lead to some incoherence. The value for argon should equal the total cross section, since argon, being monoisotopic and having zero spin should exhibit no incoherent scattering. In the case of helium the difference between bound and free cross sections, resulting from the reduced mass factor $[\{(A+1)/A\}^2=1.55$ for helium] is large enough to attempt to distinguish between them. Transmission measurements give 1.22 and 0.8 barns respectively. The total reflection value of 1.1 barns lies between these two, but in better agreement with the bound value, confirming the recent theoretical analysis of gas index of refraction by Kleinman and Snow.[8]

CONCLUSIONS

Variation of reflected intensity from the mirrors with gas pressure is as expected from theory. Cross sections

TABLE IV. Comparison of present results with other determinations.

	Scattering cross section—barns			
		Crystal diffraction	Transmission	
Element	Total reflection	(bound coherent)	Total free	Total bound
Nitrogen	11.0, 9.7±1.5	9.1[a]	9.96[b]	11.5
Argon	0.51±0.1		0.68[b]	0.72
Helium	1.1±0.15		0.8[c]	1.25

[a] See reference 1.
[b] See reference 6.
[c] See reference 7.

[7] Bashkin, Petree, Mooring, and Peterson, Phys. Rev. **77**, 748 (1950).
[8] D. Kleinman and G. Snow, Phys. Rev. **82**, 952 (1951).

measured by total reflection agree sufficiently well with those from transmission and crystal diffraction methods to verify the applicability of the usual formulas for solids or liquids, involving coherent cross section, to calculating the index of neutron refraction of a gas. Cross section values were determined for He, A, and N as listed in Tables II and III.

ACKNOWLEDGMENTS

The author is indebted to G. W. Johnson for his collaboration in many of the measurements, to E. O. Wollan of Oak Ridge National Laboratory for the use of facilities and apparatus there and for many valuable suggestions, and to other members of the Oak Ridge and Brookhaven staffs for assistance in the experiments.

PHYSICAL REVIEW VOLUME 84, NUMBER 5 DECEMBER 1, 1951

The Significance of the Absence of Primary Electrons for Theories of the Origin of the Cosmic Radiation

T. M. DONAHUE*
Johns Hopkins University, Baltimore, Maryland
(Received July 11, 1951)

Electrons of energy above 5 Bev appear to constitute less than 0.4 percent of the primary cosmic radiation incident on the earth. An analysis of acceleration mechanisms reveals no distinctions can readily be made in acceleration per se on the basis of sign of charge or mass. The absence of high energy electrons must be explained on the basis of selective absorption. Bremsstrahlung collisions in the galaxy or the solar system and radiation caused by motion in galactic or local magnetic fields are inadequate to account for the large absorption of electrons compared with heavy particles. In collisions between energetic electrons and thermal photons losses approaching the total electron energy occur. An analysis of such collisions reveals that if cosmic rays are confined to the solar system these collisions are so frequent that no electrons should be present at energies higher than 5 Bev. The photon density is too low in interstellar space to cause a similar removal of electrons there. These results favor the solar or stellar origin theories of the cosmic radiation.

I. INTRODUCTION

EXPERIMENTAL evidence is by this time preponderantly against the presence of electrons at energies greater than 5 Bev in detectable numbers among the primary cosmic-ray particles incident on the earth.[1,2] An effect so gross as to exclude completely high energy electrons from the spectrum at the earth should, it would seem, be accounted for unambiguously by any successful theory for the origin of the cosmic radiation. Such an effect is to be sought in an accelerating mechanism which is capable of discriminating against particles on the basis of their mass or, perhaps, their charge, or else in a form of energy degradation which is selective for electrons and can either compete effectively with the acceleration or remove most of the electrons from the high energy spectrum before they reach the earth.

A. Acceleration Mechanisms

To require an accelerator which almost completely discriminates against the emergence of electrons comparable in number and in energy to protons and heavier nuclei seems quite objectionable. Perhaps the most likely requirement for a generator which would discriminate is a minimum injection energy which electrons would not in large numbers be capable of attaining. This, however, merely removes the difficulties to a different range of energies. The only obvious process by which nuclei or nuclear fragments can attain moderately high energies without similar electron acceleration would require already the existence of energetic bombarding particles.

For example, it can be noted that the two most recent proposals for the origin of cosmic rays[3–6] should provide equally well for electron and heavy particle acceleration. Where particles are accelerated in the galaxy by collisions with wandering regions of high magnetic field strength[3] a minimum injection energy is required, it is true, but, as will be shown, this energy is about the same for electrons and protons and, after injection, electrons and protons should be equally well accelerated. On the other hand, there is no apparent reason that electrons should not be available equally with positive ions among the initial particles in a system of local solar or stellar origin.[4,5] The mechanics of the betatron type of accelerator envisioned by Alfvén[5] apply as well to electrons as to heavier particles.

Therefore, it would appear that the explanation for the missing electronic component is most likely to be found by an analysis of the various ways in which

* Now at the University of Pittsburgh, Pittsburgh, Pennsylvania.
[1] R. Hulsizer, Phys. Rev. **76**, 164 (1949).
[2] Critchfield, Ney, and Oleska, Phys. Rev. **79**, 402 (1950).
[3] E. Fermi, Phys. Rev. **75**, 1169 (1949).
[4] R. D. Richtmeyer and E. Teller, Phys. Rev. **75**, 1729 (1949).
[5] H. Alfvén, Phys. Rev. **75**, 1732 (1949); **77**, 375 (1950).

particles can lose energy in space before they reach the earth. The purpose of the present paper is to show that the only energy losses frequent and serious enough to remove electrons above a few Bev from the spectrum incident on the earth are those caused by collisions between high energy electrons and thermal photons, and then only when cosmic-ray particles are forced to remain for a long time in bound orbits close to the sun or, at least, to the stars from which, then, they must originate. The absence of electrons thus argues strongly in favor of the theories of local origin for the cosmic radiation.

B. Types of Absorption Processes

The principal means by which particles in interstellar space or in local regions near stars can lose energy are the following: 1. Collisions with matter; 2. Radiation produced by acceleration in extended magnetic fields; 3. Compton collisions with photons.

Each of these will be considered as a possible cause of absorption selective for electrons in various parts of the universe.

II. BREMSSTRAHLUNG OF ELECTRONS IN INTERSTELLAR MATTER

If it is assumed that interstellar matter consists chiefly of protons with a density of 10^{-24} g/cm^3, then a rather generous value for the radiation length of 100 g/cm^2 will give a mean free path of electrons for radiative collisions of 10^{26} cm. This is of the same order of magnitude as the mean free path for proton-proton collisions taken by Fermi[3] to be

$$\Lambda=(\rho\sigma)^{-1}\cong 1/2\times 10^{-26}=5\times 10^{25}\text{ cm}. \qquad (1)$$

Thus this distance, 10^8 light years, is no shorter than that which must be considered the absorption free path of the other particles in the cosmic radiation.

III. RADIATION OF ELECTRONS IN GALACTIC AND LOCAL MAGNETIC FIELDS

The power radiated by electrons at cosmic ray energies in a magnetic field is most conveniently written

$$P=\tfrac{2}{3}c\left(\frac{e^2}{mc^2}\right)^2 H^2\left(\frac{U}{mc^2}\right)^2 \text{ erg/sec}$$

$$\cong 10^{-3}H^2(U/mc^2)^2 \text{ ev/sec} \qquad (2)$$

where U, the electron energy, is assumed to be much larger than mc^2, and the magnetic field, **H**, and the electron velocity, **v**, are taken to be perpendicular to each other. Thus, for a galactic magnetic field assumed as strong as 10^{-10} gauss an electron of 10^{14} ev energy radiates only at the rate of 4×10^{-7} ev sec^{-1}, or of 10^{12} ev at the rate of 4×10^{-11} ev sec^{-1}. Even if the average magnetic field through which the electrons travel in the galaxy were as high as 10^{-6} gauss the rate at which energy would be lost by a 10^{12} ev electron would be only 4×10^{-3} ev sec^{-1}, and almost 10^7 years would be required to reduce it to 10^{11} ev. Fermi[3] requires that the rate of energy gain be given by

$$dU/dt=2.5\times 10^{-14}U \qquad (3)$$

in order that it compete successfully with recognized absorption losses to yield the observed primary energy spectrum. Equation (2) may be written

$$-dU/dt\cong 4\times 10^{-15}H^2U^2$$

so that any combination of H and U such that

$$H^2U<5$$

would permit electrons to attain that value of U in the cosmic radiation. Thus if H is 10^{-10} gauss, $U<5\times 10^{20}$ ev could be attained. A magnetic field of about 5×10^{-6} gauss would be necessary to exclude the acceleration of electrons to energies greater than 2.5×10^9 ev.

During Fermi's acceleration process electrons would travel in fields presumably as strong as 10^{-5} gauss at the time of their collisions with high field strength clouds. The fractional energy gained in the collision is

$$\Delta U/U\cong(V/c)^2\cong 10^{-6} \qquad (4)$$

where V is the velocity of the cloud with respect to the earth.[3] In contrast to this must be put the energy radiated, (2),

$$-\Delta U\cong 4\times 10^{-15}H^2U^2\Delta t$$

where Δt is the collision time. If Δt is put at 0.1 light year, 3×10^6 sec,

$$-\Delta U/U\cong 1.2\times 10^{-20}U. \qquad (5)$$

It is necessary that U be less than 10^{12} ev if this loss is not to be serious.[6]

Thus radiation caused by acceleration of electrons in interstellar magnetic fields might place an upper limit of 10^{12} ev on the energy of electrons in the primary cosmic radiation, if collisions with magneto-hydrodynamic fields are the source of cosmic-ray energy. Other types of acceleration which also permit cosmic rays to travel throughout the galaxy would not have even this limitation if the permanent galactic magnetic field is any weaker than 10^{-6} gauss.

Close to the sun and the earth magnetic fields much stronger than this are eventually encountered. Travel times are ordinarily short, however, and Pomeranchuk[7] has shown, by integrating Eq. (2), that while electrons with energy initially above 10^{17} ev would be reduced to about 10^{17} ev by the time they struck the high atmosphere, electrons below 10^{17} ev would be little affected.

[6] The radiation loss is probably over-estimated because of the assumption that the electron is moving perpendicular to the field. Furthermore 10^{-6} gauss seems perhaps an order of magnitude too large for the average field during collision. The value of Δt chosen would appear to be an upper limit if the mean time between collisions is only 1.3 years.

[7] I. Pomeranchuk, J. Phys. (U.S.S.R.) **2**, 65 (1940).

TABLE I. Energy radiated per second, P, and per year, P' for electrons in troichoidal orbits of energy U. Values are listed for two different assumptions concerning the solar dipole moment a. Also tabulated is the fractional energy lost per year, P'/U, and the time, t, required for the energy of an electron to decrease from U_0 to U, where $U_0 \gg U$, because of radiation in such orbits.

Sun's dipole moment	U ev	P ev sec^{-1}	P' ev yr^{-1}	P'/U yr^{-1}	t sec
$a=1.0\times10^{34}$ gauss cm^3	10^9	3×10^{-3}	9×10^{-3}	9×10^{-11}	10^{17}
$P\cong3\times10^{-34}U^2$	10^{10}	3×10^{-4}	9×10^{8}	9×10^{-7}	10^{12}
$t\cong10^{33}U^{-4}$	10^{11}	3×10	9×10^{13}	9×10^{-3}	10^{8}
	10^{12}	3×10^{4}	9×10^{18}	9×10	10^{4}
	10^{13}	3×10^{11}	9×10^{23}	9×10^{3}	10
	10^{14}	3×10^{18}	9×10^{28}	9×10^{9}	10^{-2}
$a=4.2\times10^{33}$ gauss cm^3	10^9	7×10^{-3}	2×10^{-1}	2×10^{-10}	
$P\cong7\times10^{-34}U^2$	10^{10}	7×10^{-4}	2×10^{4}	2×10^{-6}	
	10^{11}	7×10	2×10^{9}	2×10^{-2}	
	10^{12}	7×10^{6}	2×10^{14}	2×10^{2}	
	10^{13}	7×10^{11}	2×10^{19}	2×10^{6}	
	10^{14}	7×10^{16}	2×10^{24}	2×10^{10}	

Radiation losses, on the other hand, become very important if the cosmic-ray particles and, in particular, electrons are forced to spend long times in orbits near the sun (or, for that matter, any star with no stronger dipole moment). This is particularly true for high energy electrons which in a dipole field occupy orbits in regions of high magnetic field strength. The relationship between electron energy, U, and the average radius, R, of a stable trochoid in the field of the sun is

$$R^2=300(3-2\sqrt{2})a/U \tag{6}$$

where a is the dipole moment of the sun in gauss cm^3 and U is in ev. Thus

$$H^2=a^2R^{-6}=7.3\times10^{-6}U^3/a \text{ gauss}^2 \tag{7}$$

and the power radiated by such electrons as a function of energy is, from Eq. (2)

$$P\cong2.9\times10^{-20}U^3/a \text{ ev/sec}. \tag{8}$$

If $a\cong1.0\times10^{34}$ gauss cm^3 this energy loss is enormous for the most energetic electrons possible in such orbits—that is, those of 10^{14} ev which travel just outside the sun. But below 2×10^{11} ev the radiation becomes feeble and is inadequate by about two orders of magnitude to account for the lack of electrons if the cosmic radiation originates and is accelerated in the solar system.

The power radiated by electrons in trochoidal orbits for two different assumptions about the solar dipole moment is tabulated in Table I. The fractional energy lost per year is also plotted in Fig. 2, where it may be compared with the fractional gain provided by Alfvén's mechanism for cosmic-ray acceleration. In any reasonable theory of solar or stellar origin these losses might account for a high energy cut off between 10^{11} ev and 10^{12} ev, but not any lower.

Integration of Eq. (8) to obtain the time required for an electron to decline in energy from U_0 to U gives

$$t\cong10^{33}(U^{-4}-U_0^{-4}). \tag{9}$$

If $U_0 \gg U$ the time required for an electron to reach an orbit associated with energy U is also given in Table I. Nearly 30 years are required to bring an electron out from the 10^{14} ev orbit to the 10^{11} ev orbit by radiation and 3×10^5 years to get it into the 10^{10} ev orbit. Even if there is no competing acceleration in these orbits the energy loss is too slow.

To argue that cosmic rays are accelerated near stars with considerably weaker dipole moment so that the radiation from Eq. (8) is still strong at 10^9 ev leads to two difficulties. First the flux transported by stellar beams is reduced, and the effectiveness of an Alfvén type accelerator becomes doubtful. Second, and more serious, radiation losses even from protons will grow excessive. For Eq. (2) and Eq. (8) become, for protons,

$$P\cong2.5\times10^{-28}H^2U^2 \tag{9}$$

$$P\cong1.8\times10^{-33}U^3/a. \tag{10}$$

To make the radiation from a 10^9 ev electron comparable to that from a 10^{11} ev electron which is near a dipole of moment 10^{34} gauss cm^3, it is necessary to reduce the dipole moment to 10^{24} gauss cm^3. But then the power radiated by a 10^{14} ev proton is, from Eq. (10), 1.8×10^{13} ev/sec, and, from a 10^{12} ev proton, 1.8×10^3 ev/sec. This is excessive competition if acceleration is simultaneously occurring and, if not, during the time a fast electron is being reduced to 2×10^9 ev, the protons will be drawn down to at most 2.5×10^{12} ev. This is close to two orders of magnitude too low to agree with the observed highest energy in the singly charged component of the cosmic radiation.

IV. COLLISIONS WITH THERMAL PHOTONS

Another type of energy loss can become almost catastrophic for electrons when their energy is very high, and the probability of its occurring also becomes significantly high in regions where the density of low energy photons is high. This type of loss occurs when a high energy electron collides with a photon of any energy, in particular with photons in the radiofrequency and thermal range.

A. General Theory

It was pointed out some time ago by Feenberg and Primakoff[8] that the collision between an electron whose energy is greater than a few Bev and a low energy photon in the black body radiation from the sun or some other star results in a reduction of the electron's energy in the rest frame of the observer which can be very great indeed. These authors, using Planck distribution functions at 6000°K for the photons and the appropriate approximations to the Klein-Nishina cross sections for photon-electron collision in the rest system of the electron, derived general expressions for the collision rates and energy loss, and applied these to several special cases—of an electron passing through the low density photon distribution in interstellar and

[8] E. Feenberg and H. Primakoff, Phys. Rev. **73**, 449 (1948); see also J. W. Follin, Phys. Rev. **72**, 743(A) (1947).

inter-galactic space and of an electron which comes from far in the galaxy directly to the earth against the stream of solar photons. They showed that, of these three cases, only when the electrons must traverse distances as great as those in inter-galactic space are photon encounters numerous enough to reduce seriously the high energy component of the primary electron spectrum.

Here, for the sake of completeness, the general scheme of low frequency photon-high energy electron encounters will be reviewed, and one other special case—that of an electron which remains for a comparatively long time close to the sun or any other similar star—will be considered in detail.

Consider an electron of energy U in the rest system of the earth passing through a region in which the density of photons is given as $n(\epsilon, \alpha)$, a function of ϵ, the photon energy and α, where $\alpha+\pi$ is the angle between the directions of motion of the electron and the photon. Then, denoting by $'$ quantities measured in the frame of reference in which the electron is initially at rest, the rate at which electrons are scattered is

$$\frac{dN}{dt}=\frac{1}{\gamma}\frac{dN}{dt'}=\frac{c}{\gamma}\int d\Omega'\int_0^\infty n'(\epsilon', \alpha')\sigma'(\epsilon')d\epsilon' \quad (11)$$

where $\gamma=(1-\beta^2)^{-\frac{1}{2}}$, $\sigma'(\epsilon')$ is the Klein-Nishina total cross section for the scattering of a photon of energy ϵ' by an electron at rest,

$$\epsilon'=\gamma\epsilon(1+\beta\cos\alpha), \quad (12)$$

and $n'(\epsilon, \alpha')d\epsilon'd\Omega'$ is the number of photons per cm^3 with energy between ϵ' and $\epsilon'+d\epsilon'$ travelling initially within a cone of solid angle $d\Omega'$. In virtue of the invariance of

$$[\epsilon n(\epsilon, \alpha)d\epsilon d\Omega]^{\frac{1}{2}}/\epsilon,$$

Eq. (11) may also be written

$$dN/dt=c\int d\Omega\int_0^\infty n(\epsilon, \alpha)(1+\beta\cos\alpha)\sigma'(\epsilon')d\epsilon. \quad (13)$$

If the energy lost by the electron and gained by the photon in a collision is $(\epsilon_1-\epsilon)$ where ϵ_1 is the energy of the photon after the collision, the rate of energy loss by the electron is

$$-dU/dt=c\int d\Omega\int_0^\infty n(\epsilon, \alpha)(1+\beta\cos\alpha)\times\int\sigma'(\epsilon', \theta')(\epsilon_1-\epsilon)d\Omega'd\epsilon. \quad (14)$$

Here $\sigma'(\epsilon', \theta')d\Omega'$ is the differential Klein-Nishina cross section, where θ' is the angle of scattering for the photon and Ω' the corresponding solid angle.

In the rest frame of the electron the usual Compton relation

$$\epsilon_1'=\epsilon'\Big/\left[1+\frac{\epsilon'}{mc^2}(1-\cos\theta')\right] \quad (15)$$

holds. By virtue of Eq. (12) and the fact that for $\beta\cong1$, α' is a very small angle, this leads to

$$\epsilon_1=\frac{\gamma\epsilon'(1-\beta\cos\theta')}{1+(\epsilon'/mc^2)(1-\cos\theta')}. \quad (16)$$

In those cases in which the energy of the photon in the electron's frame is very high, that is, because of (12),

$$\epsilon'=(U\epsilon/mc^2)(1+\beta\cos\alpha)\gg mc^2 \quad (17)$$

the Klein-Nishina differential cross section reduces to

$$\sigma'(\epsilon', \theta')d\Omega'\cong\tfrac{1}{2}(e^2/mc^2)^2(\epsilon_1'/\epsilon')d\Omega'. \quad (18)$$

The condition (17) can, of course, be satisfied because U is high, ϵ is high, or because α is sufficiently small. The value (18) for the cross section together with proper attention to (17) makes it possible to write for the contribution to Eq. (12) by photons and electrons satisfying the condition $\epsilon'\gg mc^2$

$$-\left[\frac{dU}{dt}\right]^*\cong c\int d\Omega\int_{\epsilon_a}^\infty n(\epsilon, \alpha)(1+\beta\cos\alpha)\times\left[2\pi r_0^2\frac{mc^2}{2\epsilon'}\ln\left(1+\frac{2\epsilon'}{mc^2}\right)\times U\left\{1-\frac{2\epsilon'/mc^2}{(1+2\epsilon'/mc^2)\ln(1+2\epsilon'/mc^2)}\right\}\right]d\epsilon \quad (19)$$

where $\epsilon_a\gg(mc^2)^2/U(1+\cos\alpha)$ and r_0 is the classical electron radius.

Likewise, for the contribution of these collisions to dN/dt, the total cross section to this approximation

$$\sigma'(\epsilon')\cong2\pi r_0^2(mc^2/2\epsilon')\ln(2\epsilon'/mc^2) \quad (20)$$

must be used. Then

$$\left[\frac{dN}{dt}\right]^*\cong c\int d\Omega\int_{\epsilon_a}^\infty n(\epsilon, \alpha)(1+\beta\cos\alpha)\times\left[2\pi r_0^2\frac{mc^2}{2\epsilon'}\ln\frac{2\epsilon'}{mc^2}\right]d\epsilon. \quad (21)$$

From (19) and (21) it is clear that the average energy lost by an electron in one collision is, in this case,

$$\Delta U\cong U\left\{1-\frac{2\epsilon'/mc^2}{(1+2\epsilon'/mc^2)\ln(1+2\epsilon'/mc^2)}\right\}. \quad (22)$$

On the other hand for such photon, electron combinations that

$$\epsilon'=U\epsilon(1+\beta\cos\alpha)/mc^2\ll mc^2, \quad (23)$$

the appropriate approximations to the Klein-Nishina cross sections are

$$\sigma'(\epsilon', \theta')d\Omega'\cong\tfrac{1}{2}r_0^2(1+\cos^2\theta')d\Omega' \quad (24)$$

and

$$\sigma'(\epsilon')\cong(8\pi/3)r_0^2. \quad (25)$$

The contributions of these low energy collisions to (13) and (14) are

$$\left[\frac{dN}{dt}\right]^{**}\cong c\int d\Omega\int_0^{\epsilon_0} n(\epsilon,\alpha)(1+\beta\cos\alpha)\left[\frac{8\pi}{3}r_0^2\right]d\epsilon \quad (26)$$

and

$$-\left[\frac{dU}{dt}\right]^{**}\cong c\int d\Omega\int_0^{\epsilon_0} n(\epsilon,\alpha)(1+\beta\cos\alpha)\times\frac{8\pi}{3}r_0^2\frac{\gamma\epsilon'}{1+\epsilon'/mc^2}d\epsilon. \quad (27)$$

The average energy lost in one collision is thus, clearly,

$$\Delta U\cong\gamma\epsilon'/[1+(\epsilon'/mc^2)]. \quad (28)$$

B. Cosmic Rays Confined to the Solar System Near the Earth

Four special cases of interest will now be considered. One is that of an electron executing a circular orbit about the sun at a distance equal to that of the earth from the sun. The energy lost by such an electron will be roughly equivalent to that lost in a stable trochoid of the same dimensions. In this case the angle between the photon and electron trajectories will be fixed at $\pi/2$. These results will then be extended to the case of electrons moving in the trochoids properly belonging to the energy U. The two other cases were treated by Feenberg and Primakoff.[8] One is that of an electron passing through a sea of isotropically moving photons of low density. This is equivalent to the state of affairs in interstellar space. The other case is that of an electron which comes into the earth from far out in the galaxy under the condition $\alpha=0$.

At a distance R_e from the sun, where R_e is the radius of the earth's orbit, the density of photons from the sun in the energy interval between ϵ and $\epsilon+d\epsilon$ is

$$n(\epsilon)d\epsilon=C\epsilon^2d\epsilon/(e^{\epsilon/kT}-1) \quad (29)$$

where

$$C=(15/\pi^4)(\eta/c(kT)^4) \quad (30)$$

and $\eta=1.94$ cal/min cm^2 is the solar constant at the earth. The total number of photons per cm^3 at R_e is, therefore,

$$n_{R_e}=\int_0^\infty n(\epsilon)d\epsilon=2\pi^3c(kT)^3/25.8=1.9\times10^7\ \text{cm}^{-3} \quad (31)$$

for $T=6000°$K, $kT\cong0.52$ ev. The energy density is

$$\rho_{R_e}=\eta/c=2.7\times10^7\ \text{ev/cm}^3 \quad (32)$$

and the average energy of these photons is

$$\bar{\epsilon}_{R_e}=\rho_{R_e}/\eta_{R_e}=1.42\ \text{ev}=2.73kT. \quad (33)$$

To compute the energy which a fast electron of energy U may be expected to lose because of collisions with sunlight when it is circling the sun in an orbit of radius R_e we set $\alpha=\pi/2$ in (11) and (13). In this case, from (12), a photon of energy ϵ will have, in the rest frame of the electron, an energy

$$\epsilon'=\gamma\epsilon=U\epsilon/mc^2. \quad (35)$$

For the purpose of being definite, the maximum photon energy to be considered in the case $\epsilon'\ll mc^2$ will be $\epsilon^*/4$ where

$$\epsilon^*=\epsilon^*(U)=(mc^2)^2/U. \quad (36)$$

Since, for an electron of $U=2.5\times10^{10}$ ev

$$\epsilon^*/4=0.1\ \text{ev}$$

practically all the photons present will be accepted for $U<2\times10^{10}$ ev.

In this case, Eq. (26) becomes

$$\left[\frac{dN}{dS}\right]^{**}\cong\frac{8\pi}{3}r_0^2\int_0^{\epsilon=(mc^2)^2/4U} n(\epsilon)d\epsilon$$

$$\cong6.67\times10^{-25}n_{R_e}\left\{1-\frac{25.8}{2\pi^3}\sum_{j=1}^{\infty}\left[\left(\frac{1.3\times10^{11}}{U}\right)^2\frac{1}{j}+\frac{2.6\times10^{11}}{U}\frac{1}{j^2}+\frac{2}{j^3}\right]\exp(-1.3\times10^{11}j/U)\right\} \quad (37)$$

where $s=ct$.

The subtractive term within the brackets remains important down to $U\cong2\times10^{10}$ ev, where it has the value 0.055. At $U=10^{11}$ ev this term is 0.8. When U is sufficiently low that the entire photon distribution may be used

$$dN/dS\cong(8\pi/3)r_0^2\int_0^\infty n(\epsilon)d\epsilon\cong6.67\times10^{-25}n_{R_e}$$

$$\cong1.3\times10^{-17}\ \text{cm}^{-1}. \quad (38)$$

Thus above 2×10^{10} ev, Eq. (37) does not give the total collision rate but only the contribution of those photons in the distribution whose energy is less than $\epsilon^*/4$. For 2×10^{10} ev electrons these are all photons less than 3.1 volts, but for 10^{11} ev electrons, only those below 0.6 volts.

In each of these collisions the average energy loss is, from (28),

$$\Delta U\cong U^2\bar{\epsilon}_{R_e}/(mc^2)^2\cong5.7\times10^{-12}U^2. \quad (39)$$

At the other extreme are those collisions in which $\epsilon'\gg mc^2$, which here will be taken as those in which the photon's energy in the earth rest frame is not less than

$$4\epsilon^*=4(mc^2)^2/U. \quad (40)$$

For electron energies higher than 4×10^{12} ev, all of the

sun's radiation except that in the extreme infrared below 5μ qualifies.

Now (21) becomes

$$\left[\frac{dN}{dS}\right]^* \cong \int_{4\epsilon^*}^{\infty} \pi r_0^2 C \frac{\epsilon\epsilon^*}{e^{\epsilon/kT}-1} \ln\frac{2\epsilon}{\epsilon^*} d\epsilon$$

$$\cong \pi r_0^2 C (kT)^2 u^* \int_{4kTu^*}^{\infty} \left(u \ln\frac{2u}{u^*}\right) \sum_{j=1}^{\infty} e^{-ju} du \quad (41)$$

where $u=\epsilon/kT$.

When $U \geqq 4\times 10^{12}$ ev the lower limit may be safely set at 0. Then

$$\frac{dN}{dS} \cong \pi r_0^2 C (kT)^2 u^* \sum_{j=1}^{\infty} \left[\frac{\Gamma'(2)}{j^2} + \frac{1}{j^2}\ln\frac{2}{u^*} - \frac{\ln j}{j^2}\right]$$

$$\cong \pi^3 r_0^3 C (kT)^2 \frac{(mc^2)^2}{U}\left[\tfrac{1}{6}\ln\frac{2UkT}{(mc^2)^2} - 0.030\right]$$

$$\cong \frac{9.43\times 10^{-6}}{U}\left[\tfrac{1}{6}\ln\frac{4U}{10^{12}} - 0.030\right]. \quad (42)$$

On the other hand, where U is so small that a significant range in ϵ does not contribute to the collision rate in the higher energy region (40), a nonvanishing lower limit of integration must be set in (41). Then

$$\left[\frac{dN}{dS}\right]^* \cong \pi r_0^2 C (kT)^2 \frac{(mc^2)^2}{U} \sum_{j=1}^{\infty} \left\{\left[\frac{1}{j}\left(\frac{4(mc^2)^2}{U}+\frac{1}{j}\right) \times \ln 8kT + \frac{1}{j^2}\right] \exp[-4j(mc^2)^2/U] - \frac{1}{j^2}\,\mathrm{Ei}[-4j(mc^2)^2/U]\right\}$$

$$\cong \frac{9.57\times 10^{-7}}{U} \sum_{j=1}^{\infty} \left\{\left[\frac{1}{j}\left(\frac{10^{12}}{U}+\frac{1}{j}\right)\ln 4.16 + \frac{1}{j^2}\right] \times \exp(-10^{12}j/U) - \frac{1}{j^2}\,\mathrm{Ei}(-10^{12}j/U)\right\} \quad (43)$$

where

$$-\mathrm{Ei}(x) = \int_x^{\infty} e^{-t} dt/t. \quad (44)$$

For large values of U (and sufficiently small values of j)

$$-\mathrm{Ei}(-10^{12}j/U) \sim 1/\ln(\delta 10^{12} j/U)$$

where

$$\ln\delta \cong 0.577$$

and (43) then reduces to

$$\left[\frac{dN}{dS}\right]^* \cong \frac{9.57\times 10^{-7}}{U} \sum_{j=1}^{\infty} \left[\frac{1}{j^2}\ln\frac{16U}{10^{12}} + \frac{1-\ln\delta}{j^2} - \frac{\ln j}{j^2}\right] \quad (45)$$

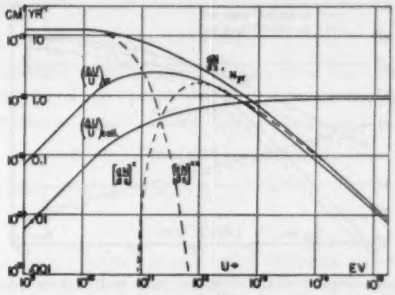

FIG. 1. Collision rate and energy loss for encounters between thermal photons from the sun and an electron of energy U constrained to a circular orbit about the sun of radius equal to that of the orbit of the earth. The solid curve for dN/ds and N_{yr} gives to a good approximation the total collision rate per cm and per year for thermal photons of any energy, calculated from Eq. (38) for $U<2\times 10^{10}$ ev and Eq. (42) for $U>4\times 10^{10}$ ev. The broken curves are for $[dN/ds]^{**}$ and $[dN/ds]^*$, Eq. (37) and Eq. (43), and give the contribution of collisions in which $\epsilon' \ll mc^2$ and $\epsilon' \gg mc^2$.

The average fractional energy loss per collision $\Delta U/U = dU/Uds$ is computed from (39) and (46) for $U<2\times 10^{10}$ ev and $U>4\times 10^{10}$ ev. A smooth connecting curve is assumed.

The average fractional loss per year $(\Delta U/U)_{yr}$ is computed by multiplying $3\times 10^7 cdN/ds = N_{yr}$ and $dU/UdN = \Delta U/U$.

which is equivalent to (42). At 10^{14} ev the collision rate calculated from (45) is 9.15×10^{-20} cm^{-1} or 2.75×10^{-9} sec^{-1}.

The average energy lost by an electron in one collision is now, from (22),

$$\Delta U \cong U\{1-[\ln 2U\epsilon_{R_e}/(mc^2)^2]^{-1}\} \cong U\{1-[\ln(U/10^{11})]^{-1}\}. \quad (46)$$

Hence, for electrons of energy no greater than 2×10^{10} ev, (38) and (39), and for electrons above 10^{13} ev, (42) and (46) represent the collision frequency and the energy loss per collision with the entire photon output of the sun to an approximation as valid as are the approximations to the Klein-Nishina cross sections. In the range $10^{13}>U>2\times 10^{10}$ ev, neither (37) nor (43), nor their sum gives the total number of collisions per cm. The range of photon energies between $(mc^2)^2/4U$ and $4(mc^2)^2/U$ which there contains a large number of photons is not covered by either one. In this region the full expression for the Klein-Nishina cross sections must be used in (13) and (14), since there ϵ' is of the order of mc^2.

Instead of carrying out such a calculation it is simpler to use the fact that the full expression for the cross sections does not lead to oscillations or discontinuities in (13) and (14) as functions of U and connect with a smooth curve the graphical representations of (38) and (42) for dN/ds as function of U, and of (39) and (46) for $\Delta U/U$ as a function of U. This is done in Fig. 1.

A third curve in Fig. 1 gives the average fractional loss of energy per year and is obtained by multiplying the number of collisions per year, $N_{yr}=3\times 10^7 cdn/ds$ and $\Delta U/U = dU/Udn$.

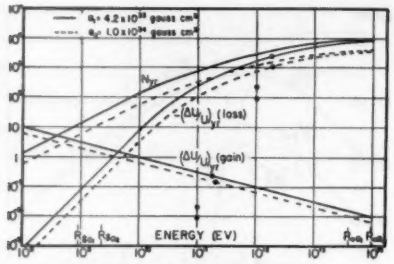

FIG. 2. Number of collisions per year with thermal photons from the sun by electrons with energy U traveling in the bound orbits belonging to that energy. Average fractional energy loss per year owing to these collisions: $-(\Delta U/U)_{yr}$ (loss) and fractional energy gain per year by the Alfvén acceleration process. The circles are points on the straight line curve giving the fractional loss because of radiation by electrons going in these orbits.

Curves are given for two assumptions concerning the dipole moment of the sun. (The lower of each pair of circles corresponds to the lower value of the dipole moment.) The energies corresponding to orbits at the earth's distance R_δ and at the sun's rim $R_\odot$ are marked.

The collision rate remains high, at 1.27×10^{-17} per cm or 11.4 pc. year up to a little above 10^{10} ev. For higher energies it drops steadily to 5 per year at 2.4×10^{11} ev, 1 per year at 4.0×10^{12} ev, and only one every 100 years at 1.26×10^{15} ev. On the other hand the average fractional energy lost in each collision rises with U and approaches unity as $U\to\infty$. Thus at 10^9 ev it is only 5.7×10^{-13}, at 10^{10} ev, 5.7×10^{-2}, at 10^{11} ev, 0.302, at 10^{12} ev, 0.793, and at 10^{15} ev, 0.893. The combination of these two sends the average fractional energy lost per year by an electron forced to rotate about the sun near the earth through a maximum of 2.5 at 1.26×10^{11} ev. It is greater than unity from 1.4×10^{10} ev to 2.4×10^{12} ev, but falls to 7.2×10^{-2} at 10^9 ev and 1.06×10^{-2} at 10^{15} ev.

The contribution of high energy collisions, $[dN/ds]^*$ and of low energy collisions $[dN/ds]^{**}$ from (43) and (37) are also plotted in Fig. 1.

C. Cosmic Rays in Stable Trochoids About the Sun

Acceleration of cosmic radiation in the solar system according to the proposal of Alfvén[5] is accomplished while the particles are trapped in trochoidal orbits in the dipole field of the sun. The radius of these orbits is inversely proportional to the square root of the particle energy according to Eq. (6). Alfvén shows that if the mechanism of acceleration is the betatron action of the magnetic flux transported by solar beams the fractional energy gain per year (neglecting losses) is

$$\Delta U/U\cong2.08\times10^{-13}R \qquad (47)$$

where $a=4.2\times10^{33}$ gauss cm^3 is taken as the dipole moment of the sun. Thus, orbits in the neighborhood of the earth, where $R=1.45\times10^{13}$ cm and $U\cong10^9$ ev, have a fractional gain of 3 per year, and at $R=4.7\times10^{12}$ cm with $U=10^{10}$ ev the gain is still 1 per year. The most energetic singly charged particles possible in this view are those which move along the solar disk with $R=R_\odot\cong7\times10^{10}$ cm and $U\cong4.5\times10^{13}$ ev. Here $\Delta U/U$ is only about 0.015 per year.

In the case of electrons this accretion of energy must be contrasted with the rate at which electrons lose energy. It has already been shown that radiation competes ineffectively below 2×10^{11} ev. But the higher the electron energy the closer it moves to the sun. The expressions above for the collision rate and energy losses of electrons encountering sunlight must be modified because the density of photons increases as R^{-2}. Thus, in (29), where R_e is replaced by R,

$$C=C(R)=(R_e/R)^2C_{R_e}=(U/U_0)C_{R_e} \qquad (48)$$

where

$$U_0=9.63\times10^8 \text{ ev}.$$

Thus the expressions for dN/ds and $(\Delta U/U)_{yr}$ must be multiplied by

$$U/U_0=1.04\times10^{-9}U$$

to give the true collision rate and fractional energy loss per year for electrons in stable trochoidal orbits. Hence (38) and (42) become

$$dN/dS \cong1.32\times10^{-26}U, \quad U<2\times10^{10} \text{ ev} \qquad (49)$$

$$\cong1.63\times10^{-15}[\ln(4U/10^{12})-0.030], \quad U>10^{13} \text{ ev} \qquad (50)$$

with similar expressions for (37), (43), and (45).

The frequency of collision rises now to a very high value as U increases toward 10^{14} ev and the electron moves closer and closer to the sun. At 10^{12} ev when $R=4.65\times10^{11}$ cm collisions occur at the rate of 1830 per year. Just outside the sun the rate is about 7750 per year.[9] Since $\Delta U/U$ per collision remains as it is given in Fig. 1, this increasing collision rate forces the fractional energy loss per year to increase steadily with energy. Both the number of collisions per year and the average yearly fractional decrease in energy are plotted in Fig. 2 as a function of the energy in these stable orbits. They are shown for two values of the dipole moment, 4.2×10^{33} gauss cm^3 the value given by Hale and others[10] and 1.0×10^{34} gauss cm^3 the value indicated from considerations of the low energy cosmic-ray cut off at the earth. The energies belonging to stable trochoids at the earth's distance R_δ and at the edge of the sun $R_\odot$ are marked on the abscissa. The rate of energy loss can be compared with the rate of gain given by the betatron mechanism which is also drawn in this figure. The loss exceeds the gain for all energies higher than 4.4 Bev in the case of the lower dipole moment and 5 Bev in the

[9] Because of the failure of the inverse square law near the sun, this is a rather poor approximation, of course.

[10] Hale, Seares, Van Maanen, and Ellerman, Astrophys. J. **47**, 206 (1918); Thiessen, Observatory **36**, 230 (1946).

case of the higher. For energies very little above these values, in fact, the loss is overwhelming so that there is an altogether negligible chance that any electron can penetrate into these energy regions.

On the basis of this simplified scheme of acceleration and degradation the critical energy, 5 Bev is in the band from 2.3 Bev to 13.6 Bev in which we can assume that only particles in bound orbits can arrive at the earth.[11,12] But, whatever is the explanation of this cut off, it should apply to electrons as well as to heavier primaries. Thus, according to this scheme of cosmic-ray production, there are very few electrons in the primary cosmic radiation. Whatever ones there are would lie in the energy interval between the general cosmic-ray cut off and the energy at which degrading collisions with the photons of the sun neutralize the slow gain in the solar betatron. This band is undoubtedly narrow, but there seems to be a definite possibility of electrons incident on the earth at very high latitudes in a very narrow band above 2.2 Bev. Such electrons would perhaps have been missed in experiments so far performed[1,2] which were sensitive only for the electrons incident above 5 Bev. However, the losses are probably underestimated in this treatment, which ignores radio-frequency radiation from the sun as well as the fact that the angle α between the electron and photon trajectories is not a constant. The rate of gain is almost certainly overestimated.[13] Any mechanism which requires electrons to spend a long time close to the sun, whether they are accelerated there or elsewhere, so long as the simultaneous acceleration is less than 0.2 U at 2.3×10^9 Bev, will lead to a complete absence of electrons at the earth.

The cross section of the earth for cosmic rays[12] is far too small to compete with a cross section which allows 11 collisions every year, each of them removing 0.02 U of the electron's energy.

High energy quanta resulting from these encounters certainly should be incident on the earth, but since they cannot be trapped in the solar system, the intensity is expected to be very low.

D. Cosmic Rays Confined Only to the Galaxy

If the cosmic radiation is considered to fill up the entire galaxy, the electrons present should collide in interstellar space with thermal photons from the stars. Feenberg and Primakoff[8] have shown in effect that despite the isotropy of radiation there the photon density is far too low to provide a serious drain even on electron energy.

In the calculation of the effects of Compton collision processes in interstellar space it is most simple to take the usual value for the energy density of radiation in the galaxy[14]

$$\rho_g=0.3 \text{ ev cm}^{-3} \tag{51}$$

and consider all of these photons to come from sources at 6000°K. Then the density of photons in the galaxy becomes

$$n_g=\rho_g/\bar{\epsilon}\cong0.3/1.42=0.21 \text{ cm}^{-3} \tag{52}$$

and, because of the isotropy,

$$n(\epsilon,\alpha)=n_g(\epsilon)/4\pi.$$

A cosmic-ray electron will suffer collisions with these photons at a rate given by (11), whence, for $\epsilon'\ll mc^2$

$$\begin{aligned} dN/ds&\cong\tfrac{1}{4}[(8\pi/3)r_0^2]n_g, \quad U<2\times10^{10} \text{ ev} \\ &\cong3.3\times10^{-26} \text{ cm}^{-1}. \end{aligned} \tag{53}$$

One collision with a loss of energy given by (39) every 3×10^7 years does not exceed the collision rate given by (1) for $p-p$ meson producing collisions in interstellar space.

When $\epsilon'\gg mc^2$ the time between collisions is, naturally, even longer. In fact

$$\left[\frac{dN}{dS}\right]^*\cong\int_0^{2\pi}d\phi\int_0^{\pi}\int_{4\epsilon^*}^{\infty}\frac{n_g(\epsilon)}{4\pi}(1+\beta\cos\alpha)\times\sin\alpha\left[2\pi r_0^2\frac{mc^2}{2\epsilon'}\ln\frac{2\epsilon'}{mc^2}\right]d\epsilon d\alpha. \tag{54}$$

When $U\geqq10^{12}$ ev this may be written

$$\begin{aligned} \frac{dN}{dS}&\cong\frac{1}{2}\frac{C}{C_{R_0}}\left(\frac{dN}{dS}\right)_{R_0,\pi/2}(1-1/\ln[2UkT/(mc^2)^2]) \\ &\cong\frac{4\times10^{-14}}{U}\left(\ln\frac{4U}{10^{12}}-1\right) \end{aligned} \tag{55}$$

where

$$C/C_{R_0}=n_g/nR_0\cong10^{-7}. \tag{56}$$

The collision rate decreases steadily with U. At $U=4\times10^{12}$ ev it is one in 6×10^7 years, at 4×10^{13} ev, one in 3×10^8 years. In the galaxy these collisions are no more serious for electrons than other types of collisions for the other constituents of the primary cosmic radiation.

E. Electron Traveling to Earth from Far Out in the Galaxy

An electron which strikes the earth after travelling from a point distant R from the sun directly counter to the sun's rays does not make enough collisions with this light to disappear from the high energy spectrum. Feenberg and Primakoff[8] also calculate the loss in this case by setting $\alpha=0$ and obtaining expressions as func-

[11] H. Alfvén, Phys. Rev. **72**, 88 (1947).
[12] E. O. Kane, T. J. B. Shanley, J. A. Wheeler, Revs. Modern Phys. **21**, 51 (1949).
[13] H. Alfvén, Phys. Rev. **77**, 379 (1950).
[14] T. Dunham, Proc. Am. Phil. Soc. **81**, 277 (1939).

tions of s, the instantaneous distance of the electron from the sun. Thus

$$n(\epsilon, s) = nR_e(\epsilon)(R_e/s)^2 \tag{57}$$

and

$$dN/ds \cong (16\pi/3) r_0^2 nR_e (R_e/s)^2, \quad U < 4\times 10^{10} \text{ ev}$$
$$N \cong 2.5\times 10^{-17}[R_e - (R_e/R)^2] \tag{58}$$

$$\cong 3.7\times 10^{-4} \qquad \text{for } R \gg R_e. \tag{59}$$

In each collision the energy lost, from (28)

$$\Delta U \cong 2U^2\bar{\epsilon}/(mc^2)^2 \cong 11U^2/10^{12}. \tag{60}$$

This is a large loss. At 10^{10} ev, it is 1.1×10^9 ev. But the probability of collision is still too low to produce a discernible effect on the electron spectrum in this energy region.

Similarly

$$\frac{dN}{dS} \cong \left(\frac{8\times 10^{-7}}{U} \ln \frac{8U}{10^{12}}\right)\left(\frac{R_e}{s}\right)^2, \quad U > 10^{13} \text{ ev} \tag{61}$$

$$N \cong (8\times 10^{-7}/U) R_e \ln(8U/10^{12}). \tag{62}$$

For $U = 10^{13}$ ev this is only 5×10^{-6} collisions.

Thus cosmic-ray electrons would suffer Compton losses sufficient to remove them from the incident primary radiation at the earth if all, or almost all, the electrons can reach it only after travelling for a long time in a succession of bound orbits inside the earth's, occupying each long enough to suffer a degrading collision. At 10^{14} ev the time between collisions is (Fig. 2) $3\times 10^7/3660 = 8\times 10^3$ sec and the period 20 $R/c = 140$ sec. So after 57 revolutions the electron would suffer a collision which reduces it to 1.5×10^{13} ev. If it should go then into the proper orbit it will suffer another collision in 1.3×10^4 sec after 360 revolutions and go out to the 3.3×10^{12} ev orbit. Finally in the 5×10^9 ev orbit the collision time is only up to 0.1 year. The time involved is quite short compared to the average life time of cosmic rays in the solar system, ~5000 years.[12]

But there are two serious objections. One is obvious: for electrons as well as heavy particles all orbits from infinity are permitted to reach the earth for energies greater than 13.6 Bev. There is no apparent reason that these orbits should not produce, as is now believed, by far the greater contribution to the observed primary intensity at the earth. Even those high energy electrons which reach the earth after passing close to the sun have a chance of less than 1/57 of meeting a photon near the sun's disk. The second objection is that if cosmic rays are forced to come to the earth only after entering bound orbits then protons as well as electrons must suffer this restriction. Protons are, of course, observed. So, therefore, should electrons, and these in large numbers even if they are crowded into the low energy end of the spectrum. The low energy cut off mechanism should not be applicable if the electrons are forced to reach the earth from far inside its orbit.

V. CONCLUSIONS

Energy losses among high energy electrons which are specific for them alone appear to be on a scale large enough to account for the absence of high energy electrons incident among cosmic ray particles on the earth only when cosmic rays have a chance to encounter large numbers of low energy photons during their life time. This restricts theories of the origin of the cosmic radiation on the one hand to the entire universe, so that large intergalactic distances will usually have been traversed by particles which come to the earth (or perhaps high photon densities encountered at the beginning of the universe) or, on the other hand, it restricts them to the immediate vicinity of the sun, or perhaps other stars where the cosmic rays must at least receive the principal part of their acceleration. In particular, the loss in energy by electrons in their encounters with sunlight is sufficient to counteract the gain in energy caused by the action of the solar betatron proposed by Alfvén as the agent of acceleration in a theory for the purely solar origin of the cosmic radiation.

Proton-Meson Analysis of the Cosmic Radiation at 3.4 Kilometers*

CHARLES E. MILLER, JOSEPH E. HENDERSON, DAVID S. POTTER, AND JAY TODD, JR.
Department of Physics, University of Washington, Seattle, Washington

(Received August 13, 1951)

A magnetic cloud chamber has been used along with an appropriate arrangement of coincidence and anti-coincidence counters to photograph tracks of those charged particles at 3.4 km altitude having ranges of 0.5 to 5, 5.5 to 15, and 15 to 25 cm in lead. An additional 2.5 cm lead was used above the chamber to remove showers. Plotting in each case the distribution in momentum of positive and negative particles there is shown a clear resolution into protons and mesons. It is found that about twice as many protons as mesons stop in lead at ranges between 2.5 and 7.5 cm lead. The meson intensity (differential range intensity) is found to be $6.1\pm0.06\times10^{-6}$ particles per (g sec sterad) of air at 60 g air range and $12.0\pm1.0\times10^{-6}$ at 125 g air range.

I. INTRODUCTION

THE many investigations of penetrating showers and star production give some information regarding the intensity, altitude, and latitude dependence of a generalized nuclear component of the cosmic radiation. These measurements usually cover a not too well-defined range as regards both the type and energy of processes involved. This qualitative character of the investigations makes it difficult either to interpret the results in terms of fundamental processes or to compare the results of various investigators. A knowledge of the intensity and spectral distribution of the various nuclear species, predominately protons and neutrons, throughout the atmosphere would give a better basis for the interpretation of the nuclear phenomena observed. Some progress has been made in this direction in the case of neutrons, because these are easily distinguished from other components of the radiation. Protons, particularly at higher energies, are difficult to distinguish from other charged particles, so that, although they are considered to constitute the major part of the primary radiation, little is known of their intensity and energy distribution at any altitude. Rossi[1] has summarized the scanty information available as of 1948. Recently several investigations relating to the proton content of the radiation at sea level have been published[2–4] while in previous work of this laboratory[5] it was shown that at 3.4 km protons have an intensity at least several percent of that of the penetrating component.

The present investigation is one of a series directed towards providing better information on the proton flux at lower altitudes. At an altitude of 3.4 km it is found that more protons than mesons stop in a 5 cm lead absorber. Thus, even at this altitude protons cannot be considered to constitute a negligible part of the total flux of charged particles. As the experimental method provides a separation of the meson and proton components better information is also obtained for the spectral distribution of mesons.

II. THE APPARATUS AND EXPERIMENT

In previously reported observations[5] at 3.4 km a momentum spectrum of all non-electronic charged particles to a momentum of 2.5 Bev/c was obtained. Here the magnetic cloud chamber was triggered by coincidence counters above and below the chamber. A 5 cm lead absorber above the chamber insured cascade multiplication of electrons penetrating it, and all photographs showing more than one time coincident track were ignored in obtaining the momentum distribution. This selection will be discussed later. Of the single tracks, some could be easily identified as due to protons from their density. In this way an attempt was made to find the ratio of protons to mesons in the momentum interval above the proton absorption cutoff of the equipment (250 Mev/c) and below 600 Mev/c. Because of apparent variations of track density for successive expansions (related at least in part to variations in time interval between expansions), selection of protons in this way seems not to be certain even at an ionization of three times minimum. In addition, this selection was made in a conservative way so that any error would be in the direction of too few protons. The estimate of ten percent protons in the momentum interval mentioned and arrived at in this way seems, in view of the present investigation, to have been too low.

In the present work the proton-meson separation has been based on simultaneous determination of range and momentum. Range intervals sufficiently broad to give a maximum stopping rate consistent with good separation in the momenta of mesons and protons have been used. The arrangements of counters and absorbers used to trigger the chamber are shown in Fig. 1. The chamber is triggered by an event of type $(C_1+C_2+C_3-A_1-A_2)$. This tends to define particles (as observed in the chamber) of minimum range equal to the absorbing material between the sensitive volume of the chamber and that of the counters C_3 and of maximum range equal to the absorbing material between the sensitive volume of the chamber and that of counter

* Assisted by the joint program of the ONR and AEC.

[1] B. Rossi, Revs. Modern Phys. **20**, 537 (1948).
[2] Merkle, Goldwasser, and Brode, Phys. Rev. **79**, 926 (1950).
[3] Goldwasser and Merkle, Phys. Rev. **83**, 43 (1951).
[4] Nonnemaker and Street, Phys. Rev. **82**, 564 (1951).
[5] Miller, Henderson, *et al.*, Phys. Rev. **79**, 459 (1950).

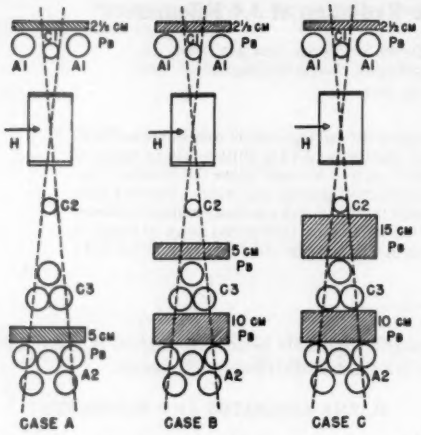

FIG. 1. Schematic of experimental arrangement for each of the three sets of observations.

group A_2. The 2½ cm lead above C_1 is provided to produce cascade multiplication of electrons which then either block expansion of the chamber by triggering one of the A_1 counters, or are recognized by the appearance of time coincident tracks in the chamber. Three series of photographs were taken with the arrangements shown as cases A, B, and C of Fig. 1. Including the absorbing material represented by the chamber and counter walls, the three experimental arrangements define particles of range, as observed in the chamber and for the idealized case of normal incidence and no scattering, of 0.5 to 5.5, 5.5 to 15.5, and 15.5 to 25.5 cm lead. Additional absorber of 3 cm lead equivalent is present above the chamber. Based on the expected ionization energy losses of protons and mesons, the momentum intervals of the protons and mesons selected will be well separated in each case. A plot giving the momentum distribution of particles photographed should then show maxima corresponding to protons and mesons for positively charged particles and a single maximum for negative particles. Effects of scattering and nuclear reactions of protons will be discussed later.

The magnet and cloud chamber used in the present investigation as well as the method of track selection, curvature measurement, etc., have been described in a previous paper.[5] The only essential change has been the substitution of the event selecting system shown in Fig. 1 for that previously used. All observations are for a field strength of 8000 gauss and at an altitude of 3.4 km (Climax, Colorado).

III. DISCUSSION OF EXPERIMENTAL METHOD

A. Event Selection

The experimental arrangements of Fig. 1 are intended to select charged particles which having passed through the chamber traverse the absorber between C_2 and C_3 and stop in the absorber between C_3 and A_2. Some cascade showers originating in the 2½ cm lead above C_1 will fail to actuate the A_1 counters and also fail to penetrate as far as the A_2 group of counters and so will be photographed. As will be discussed, the probability of obtaining a photograph of a single electron track (which could not then be distinguished from a meson or high energy proton) seems to be very small. An error of exclusion occurs for those particles so scattered, after triggering counter C_2, as to fail to traverse one of the counters C_3. Errors of inclusion occur for those particles so scattered, after traversing C_3, as to fail to reach one of the A_2 counters. Errors of inclusion have only the effect of limiting the resolution of events into protons and mesons among positive particles by including some higher energy mesons. The momentum distributions for negative particles (mesons only) show the extent to which higher energy mesons have been included through scattering. For protons nuclear energy losses will cause errors of both inclusion and exclusion as compared to the idealized treatment based on ionization loss only. Accidental coincidences and all errors due to counter inefficiencies and to counter and circuit dead times and resolution either have no effect or are small compared to statistical uncertainties of the data.

B. Elimination of Electron Component

A single electron appearing in the chamber could not be distinguished from a meson or high energy proton. The 2½ cm of lead absorber placed above counter C_1 was to insure that through cascade multiplication electrons would either actuate the A_1 counters or reveal themselves through the appearance of multiple tracks in the chamber. Even so, there is some probability that a single electron track could appear in the chamber. In previous work[5] in which the chamber was actuated by counters C_1 and C_2 only, it was shown that the large number of single tracks with momenta near 100 Mev/c photographed with no absorber above C_1 disappeared when 5 cm lead was placed above the equipment. The smaller shower absorber (2½ cm lead) used in the present case seems to have been adequate. In Case A the intensity of the first positive and negative maxima match closely the intensities of the over-all spectrum at the same momentum as determined under 5 cm lead (Fig. 3). Thus, no additional electron removal seems to take place in using more than 2½ cm lead. The proton maximum of Fig. 2 case A certainly cannot be contaminated with positrons as the total negative intensity here is small, and positrons would not be expected to behave differently.

The use of anticoincidence counters and disregard of all multiple events in the chamber would, in addition to eliminating the electron component, discriminate against protons which occurred multiply or in coincidence with other charged particles. Protons from at-

mospheric stars would be expected to be well separated from other components of the star at the point of observation and so occur singly. However, this would not be true for stars produced locally in the 2½ cm lead above C_1 and these would be discriminated against. Actually, such protons do not constitute a large fraction of the total proton flux through the chamber. In previous observations[8] in which 5 and 20 cm of lead were used above the chamber, of those tracks that could be identified as protons only a few percent were found to be accompanied by one or more other tracks. Actually, the discrimination against locally produced protons is desirable as the intention here is a determination of the atmospheric proton flux rather than local production.

C. Counter and Circuit Efficiency

Accidental coincidences of the type $(C_1+C_2+C_3-A_1-A_2)$ are expected to have so small a rate as to be completely negligible as compared to statistical uncertainties of the experiment. Any inefficiency of the counter group A_2 will lead to inclusion of some higher energy particles which have penetrated the lower absorber. Experimentally, the number of particles so included is shown to be very small. As shown in Fig. 2 case A, this rate for negative particles of momenta above 1 Bev/c is less than 0.1 particle $(\text{Bev}/c)^{-1}$ hr^{-1} ster^{-1} cm^{-2}. This compares to a total negative particle rate (Fig. 3) of about 5. Of the high momentum negative particles of Fig. 1 case A, some are due to scattering outside the coverage of the A_2 counters. Thus, the leakage due to effects other than scattering is less than two percent. The appearance of almost no particles below 250 Mev/c (the meson absorption cutoff), as shown in Fig. 2 case C, is an indication of the efficiency of the system of selection in eliminating particles of range too small to reach counter group C_3.

D. Rate Determination and Normalization

Only those single tracks of length at least 15 cm (out of a chamber diameter of 17 cm) have been measured for curvature in determining the rates as given in Fig. 2. The fractional yield among all photographs of single tracks, regardless of length, has been determined by an examination of all exposures and will be symbolized by "f." The $C-A$ counting rate (r) in counts per hour was determined during the course of each run. This is larger than the picture taking rate because of chamber recovery time. If n is the number of single trakcs with momenta lying in an interval ΔP and m the total number of single tracks of all momenta (both n and m for tracks of length greater than 15 cm) obtained during a run, then the differential momentum rate in the momentum interval ΔP is taken to be:

$$\text{Rate}=fr(n/m)(1/\Delta P).$$

For r in counts per hour and ΔP in Bec/c this gives the differential momentum rate in particles hour^{-1}

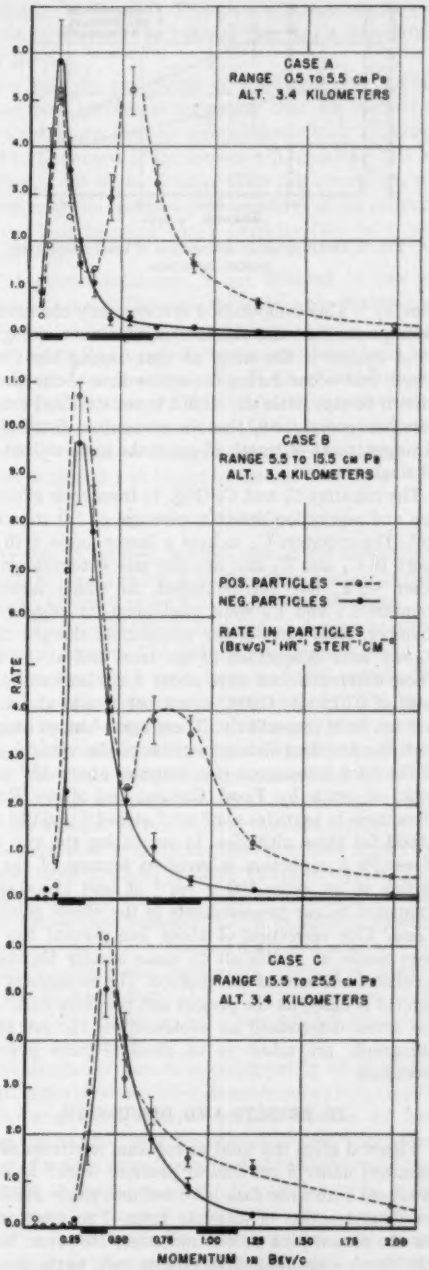

FIG. 2. Distribution in momentum of particles selected with experimental arrangements A, B, and C, as shown in Fig. 1. Rate is given in particles $(\text{Bev}/c)^{-1}$ hr^{-1} sterad^{-1} cm^{-2}.

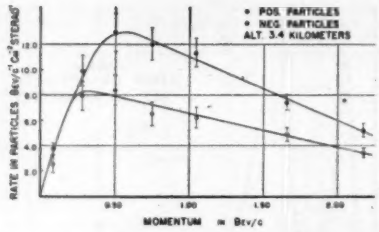

FIG. 3. Distribution in momentum of total meson plus proton radiation.

$(\text{Bev}/c)^{-1}$. This computation involves only the natural assumptions that the distribution of events among all $C-A$ counts is the same as that among the $C-A$ counts that occur during the active time of the circuit (that is to say, while the circuit is not sterilized during chamber recovery) and that the momentum distribution of single tracks of length 15 cm is the same as that for all single tracks.

The counters C_1 and C_2 (Fig. 1) from their effective size and separation define a coverage of 1.0 steradian cm². The counters C_3 include a larger angle with respect to C_1 and C_2 and are not rate determining. In other work, not yet published, in which identical counters C_1 and C_3 were used alone to trigger the chamber, total rates of the noncascade charged component were determined at sea level and at 3.4 km. These determinations were under 5 cm lead and gave rates of 0.015 and 0.0087 count per second at 3.4 km and sea level respectively. These agree almost exactly with the excellent determinations of the vertical rate of the hard component (for latitudes above 45° magnetic) as made by Rossi, Greisen, and others. Rossi[1] gives rates in particles cm^{-2} sec^{-1} sterad^{-1} of 0.016 and 0.0084 for these altitudes. In comparing the two sets of results a correction is involved because of the inclusion of an extra 100 g cm^{-2} of lead absorber as compared to our measurements in the values given by Rossi. This correction of about five percent has not been made. It is difficult to make exactly because it involves both mesons and protons. The estimate of five percent is based on the present and previous work[5] and the rates, determined as explained in the preceding paragraph, are taken to be absolute rates per cm² steradian.

IV. RESULTS AND DISCUSSION

Figure 3 gives the total momentum spectrum as determined under 5 cm lead in previous work.[5] It is reproduced here since data were not previously available for determination of absolute rates. The spectrum is for the meson plus proton radiation. However, below 250 Mev/c it should include mesons only, as the method of observation imposed a minimum proton range corresponding to this momentum. The intensities given in Fig. 3 can be compared to the particle intensities for selected range intervals as given in Fig. 2. No normalization between the two sets of data is involved.

Differential momentum distributions for cases A, B, and C are given for both positive and negative particles in Fig. 2. The method of determining the rates has been explained. The rates as plotted are average rates for each of 12 momentum intervals. These intervals (the same in all cases) are: 0.025–0.080, 0.080–0.13, 0.13–0.19, 0.19–0.24, 0.24–0.31, 0.31–0.39, 0.39–0.49, 0.49–0.61, 0.61–0.77, 0.77–1.0, 1.0–1.5, and 1.5–2.5 (Bev/c). The uncertainties indicated are for statistics only.

The distribution of positive particles for case A, Fig. 2, shows a clear resolution into protons and mesons. The data are thought to contain an insignificant number of electrons. The intensity at the second positive maximum (protons) should include few positive mesons as judged by the smallness of the negative distribution at this momentum value. Effects of scattering and nuclear energy losses of protons need to be considered. An approximate computation of multiple meson scattering shows that, while a large number of those mesons with just more than sufficient range to penetrate from the sensitive volume of the chamber to the sensitive volume of the C_3 counters will be so scattered as to miss the C_3 counters, of those mesons with sufficient range to reach the A_2 counter, very few will be lost by scattering out of the coincidence train. Thus, the meson peak value should correctly represent the meson intensity at this range (5.5 cm lead or 175 Mev/c). The leading edge of the meson peak is also affected by the magnetic cutoff of the equipment. This has no effect at the peak value (see reference 5). The trailing edge of the (negative) meson peak is reasonably accounted for as due to scattering in the 5 cm lead absorber. Variations in particle path lengths through the absorber also prevent a sharp high momentum cutoff. The total (positive plus negative) meson intensity at a range of 5 cm lead (or about 200 Mev/c) is found to be 11.0 ± 1.0 particles $(\text{Bev}/c)^{-1}$ hr^{-1} sterad^{-1} cm^{-2} (altitude 3.4 km). Converting to range, this gives the number of mesons stopping per second-steradian in one gram of air, at a total range including absorber above the chamber of 60 g cm^{-2} air, as $6.1 \pm 0.06 \times 10^{-6}$ per second. This is appreciably smaller than the figure 1.7×10^{-5} given by Rossi and Sands.[6,7]

The second positive maximum of Fig. 2, A is interpreted as due to protons. Here, because of the higher momentum, scattering is less important than is the case for the mesons, and there should be no loss in intensity at the maximum because of proton scattering out of the C train. As is seen from the magnitude of the negative (meson) distribution, there should be no contribution (within statistics) from positive mesons at the position of the proton maximum. The heavy rectangles along the abscissa of each graph of Fig. 2 show the meson and proton limits to be expected on the basis

[6] Rossi, Sands, and Sard, Phys. Rev. **72**, 120 (1947).
[7] M. Sands, Phys. Rev. **77**, 180 (1950).

of ionization loss only and no scattering. The low energy proton cutoff of Fig. 2, *A* comes at the expected value. Too many protons occur above the maximum (ionization) cut-off value to be accounted for as scattering out of the coverage of the A_2 counters. The magnitude of the coulombic (multiple) scattering can be obtained from the negative meson distribution of Fig. 2, *A* and the known total intensity (Fig. 3). A direct comparison between meson and proton scattering is now possible as the geometrical factors are the same in both cases. Thus, meson and proton scattering should be the same at equal values of $P\beta$. Assuming that the total proton intensity does not decrease, the intensity near 1 Bev/c is at least ten times that to be expected from multiple scattering. The obvious explanation is that the appearance of large numbers of protons above the ionization absorption cutoff in Fig. 2 is due rather to nuclear energy losses of protons in the 5 cm of lead absorber. On the other hand, nuclear losses in the small amount of absorber between the chamber and C_3 should be too small to affect the intensity at the proton maximum. The differential momentum intensity of protons at a range of 5 cm lead is found to be 5.0 ± 0.05 particles $(\text{Bev}/c)^{-1}$ hr^{-1} cm^{-2}. This cannot at present be converted to the differential range value because this would involve the path length for nuclear absorption and a knowledge of the complete proton spectrum. Because of the greater width of the proton maximum, Fig. 2, *A* shows that at 3.4 km more protons than mesons (positive plus negative) stop in a 5 cm lead absorber.

For the distribution of Fig. 2, *B* the effects of scattering and nuclear losses of protons are more important (as compared to distribution *A*) because of the greater thicknesses of absorber used. Here an approximate computation shows that fifteen percent of the mesons at a range of 15 cm lead will be lost by scattering out of the *C* train. The directly measured intensity at the maximum (positive plus negative) is 20.4 ± 2.0. Corrected for scattering this becomes 23.5 ± 2.0 for the differential momentum intensity at a range of 15 cm lead. Converting to range, this gives $12.0\pm1.0\times10^{-6}$ mesons stopping per second-steradian in one gram of air at the range 125 g cm^{-2} of air.

The proton maximum of Fig. 2, *B* is less clearly defined than that of distribution *A*. Here, because of the increasing difficulty of momentum measurement, it is not possible to plot more closely spaced intensity values. The difference between the positive and negative distributions is clearly evident. The scattering losses to be expected are not important compared to the statistical uncertainty. Nuclear losses in the absorber between C_2 and C_3 are important. This can be judged from the distribution of Fig. 2, *A*, where the proton intensity at 1.0 Bev/c is interpreted as due to nuclear losses in the 5 cm lead absorber between C_3 and A_2. The total intensity at 1 Bev/c can then be approximated as the sum of the intensities of *A* and *B*. This gives a proton intensity of 4 protons $(\text{Bev}/c)^{-1}$ hr^{-1} sterad^{-1} cm^{-2} at a momentum of 1 Bev/c.

For case *C*, the effects of scattering and nuclear losses have become so important that the method is not satisfactory. Here an approximate calculation shows that forty percent of the mesons will have been lost by scattering out of the *C* train. With this correction, the meson intensity (positive plus negative) at the range of 25 cm lead becomes 16 ± 1 particles $(\text{Bev}/c)^{-1}$ hr^{-1} sterad^{-1} cm^{-2}.

The proton maximum is not resolved in case *C*, although a real difference is found between the positive and negative distributions at higher momenta. Here, it would seem that most of the protons have been lost through nuclear reaction in the 15 cm of lead between C_2 and C_3. No attempt will be made to estimate proton intensities at momenta above 1 Bev/c. However, the results of cases *A* to *C* suggest that there is a sharp decrease in intensity at higher momenta.

V. CONCLUSIONS

Perhaps of greatest interest here is the demonstration of the large number of protons among those charged particles of small range at 3.4 km. The integrated intensities for the distribution of Fig. 2, *A* show as many protons as mesons. The distribution, however, includes those mesons which have been scattered outside the coverage of the *A* counters as well as those which have stopped in the 5 cm of lead. Including only those mesons of momenta below that corresponding to 5 cm of lead, about twice as many protons as mesons stop in the absorber. Those stopping include, of course, high energy protons brought to rest through nuclear collisions. At higher altitudes the preponderance of protons among the shorter range particles probably increases rapidly. This is judged in part from the work of Adams, *et al.*[8] and from further measurements (not yet published) showing a large proton ratio between 3.4 km and sea level. At 3.4 km the differential momentum intensity of protons has not decreased much at 1 Bev/c as compared to its value at lower momenta, but it seems to fall off rapidly at higher momenta.

The number of mesons stopping per (g sec sterad) in air at ranges of 60 and 125 g air are found to be $6.1\pm0.06\times10^{-6}$ and $12.0\pm1.0\times10^{-6}$ at the altitude 3.4 km. Rossi and Sands[6,7] give the value 17.0×10^{-6} per (g sec sterad) for this altitude and find the differential range intensity to be independent of range up to 80 g air. Few values for the slow meson intensity are available for altitudes above sea level. For the intensity at sea level Germain[9] has summarized the results of a large

[8] Adams, Anderson, *et al.*, Revs. Modern Phys. **20**, 334 (1948).
[9] L. Germain, Phys. Rev. **80**, 616 (1950).

number of observers who find values varying over a factor of two depending on the method of observation.

The work described here was carried out on the grounds of the Climax Molybdenum Company at Fremont Pass in Colorado. The generous cooperation of Mr. C. J. Abrams, General Manager, and other personnel of the company is recognized. Important contributions to the research have also been made by Mr. Don Eng, Electronic Technician, and Mr. Elmer Wright, Instrument Maker, of our staff.

PHYSICAL REVIEW VOLUME 84, NUMBER 5 DECEMBER 1, 1951

The Relative Intensity of Cosmic Rays at Sea Level at Geomagnetic Latitudes 56.8 and 83.0

D. C. Rose, W. Heikkila, and E. Ford
Division of Physics, National Research Council of Canada, Ottawa, Canada

(Received August 15, 1951)

During the summer of 1950 two cosmic-ray counter telescopes were exchanged between Ottawa (geomagnetic latitude 56.8°N) and Resolute (geomagnetic latitude 83.0°N) in such a way that an accurate comparison of vertical intensities could be made. The telescopes were operated under almost identical conditions for about three weeks; then they were exchanged, the Ottawa telescope being flown to Resolute and the equipment there returned to Ottawa. Corrections were made for barometer and differences in altitude by reducing all counting rates to that at 1000 mb pressure using known barometer coefficients. Corrections were made for differences in the atmospheric temperature by integrating numerically through the mean atmosphere at each station to get the probability of meson decay between production levels and the 1000-mb layer. When all corrections were made there remained a difference in intensity of 1.76 ± 0.75 percent. No difference would be expected with the absorbers used (14½ inches of lead) at latitudes so high above the "knee." Arguments are presented to show that the difference is probably due to mesons produced by a group of field sensitive primaries and scattered into the telescope. This group of primaries could come from directions with large zenith angles, which would be allowed at Resolute but excluded at Ottawa.

I. INTRODUCTION

DURING the summer of 1950 an opportunity arose to exchange counter trays in two sets of cosmic-ray measuring apparatus, one located at Ottawa (geomagnetic latitude 56.8°N) and the other at Resolute in the Canadian Arctic (geomagnetic latitude 83.0°N). This opportunity made possible a precise measurement of the relative intensity of vertical cosmic rays at the two stations. Corrections for atmospheric changes in intensity could be made fairly accurately since the barometer coefficients had been measured with similar apparatus at both stations. Upper atmosphere data were also available from weather stations of the Canadian Meteorological Service.

Since the discovery of the geomagnetic latitude effect many measurements have been made on the variation in intensity with latitude. The survey of Compton and Turner[1] shows the sea level latitude effect,—the so-called "knee" occurring at about 40° geomagnetic latitude. Variations in intensity at sea level at latitudes above the "knee" have been observed[2,3] but these are mostly considered to be due to differences in the mean atmospheric conditions at different latitudes. At all latitudes where the low energy cutoff due to absorption in the atmosphere, plus the absorbers in the instrument, is well above the low energy cutoff due to the geomagnetic field, the intensity would be expected to be constant except for small differences caused by different atmospheric conditions. Any effect due to a solar magnetic field seems unlikely since recent measurements by Pomerantz[4] and Dolbert and Elliot[5] show evidence against any appreciable influence of a solar magnetic field on cosmic rays.

With present knowledge of the structure of cosmic rays a reasonable estimate of the differences to be expected due to differences in the atmosphere can be made, at least for altitudes up to the mean levels of production of the μ-mesons which are observed at sea level. Residual differences in intensity between the two stations after all corrections have been made may then be assumed to be due to geomagnetic effects on the primary rays, or due to some phenomenon in the process of production of mesons (τ to π to μ, or π to μ).

II. APPARATUS

The apparatus was designed to study meteorological variations in intensity and to watch for phenomenal changes in intensity such as those associated with solar flares.[6] It was identical at both stations and consisted essentially of three counter trays in a vertical line with 6 inches of lead between Nos. 1 and 2 (No. 1 on top) and 8½ inches of lead between Nos. 2 and 3. Number 3 had 4 inches of lead on the sides and ends and one inch

[1] A. H. Compton and R. N. Turner, Phys. Rev. **52**, 799 (1937).
[2] Caro, Law, and Rathgeber, Australian J. Sci. **A1**, 261 (1948).
[3] P. F. Gast and D. H. Laughridge, Phys. Rev. **59**, 127 (1941).
[4] M. A. Pomerantz, Phys. Rev. **77**, 830 (1950).
[5] D. W. N. Dolbert and H. Elliot, Nature **165**, 353 (1950).
[6] D. C. Rose, Can. J. Phys. **29**, 227 (1951); and Phys. Rev. **78**, 181 (1950).

underneath. It rested on the floor near the ground. Each tray contained two brass counters in parallel one inch in diameter and about 16 inches effective length. The trays were connected in two double coincidence circuits, (1–2) and (1–3). Trays 1 and 3 were exchanged. Therefore, the results described here concern only the results from a double coincidence telescope (1–3) with 14½ inches of lead between counters and 4 inches surrounding the bottom counter. In addition there was the second counter tray made of 16-gauge aluminum between counters 1 and 3. As this was identical at both stations the effect of the center tray has been neglected.

The roof over the apparatus was roughly the same at both stations, consisting of two layers of plywood with rock wool insulation. The outer roof covering at Resolute was of sheet aluminum (about 18 gauge); at Ottawa tar paper. In addition to the roof, the counters at Resolute were housed in a wooden box with a top consisting of about one inch of wood and one inch of cork. The difference in covering of the telescope at the two stations was approximately 4 grams per sq cm of low atomic weight material. An examination of the integral range spectrum of mesons indicates that this difference (4 g/cm²) would mean about 0.35 percent change in integral intensity. The effect of the differences in the geometry of the roofs is a little uncertain. The error in this correction, however, can hardly be greater than ±0.1 percent. The thickness of covering over the telescope at Resolute was greater than at Ottawa and, therefore, in comparing the relative intensities the Resolute value has been increased by 0.3±0.1 percent relative to the Ottawa value. The temperature around the counter trays was maintained very close to 70°F at both stations since the counters are argon-alcohol filled.

The electronic equipment for amplification, pulse shaping, coincidence mixing, and recording was designed for reliability and continuous service. Its reliability has been well proved in several experiments. Therefore it will not be described here.

III. MEASUREMENTS AND CORRECTIONS

The exchange of counter trays took place in the following way. Two counter trays had been in use at Resolute for some months; another two were in use in Ottawa for about one month before the exchange. Early in July 1950 the two trays including their preamplifiers which had been in use at Ottawa were flown to Resolute and exchanged for the two trays there. The Resolute trays were put in use in Ottawa. It was found that the counter voltage at Resolute was slightly higher than that at Ottawa, but after the exchange the voltage used in Resolute was applied in Ottawa and the former Ottawa voltage applied in Resolute. Therefore, the conditions of operation were as identical as possible.

The periods covered in the analysis of results, and the mean counting rates, after correction for barometer variations only, are shown in Table I.

TABLE I. Mean counting rates, after correction for barometer variations only.

	Before exchange	Counts/min
Ottawa	June 19 to 29	4.389±0.025
Resolute	June 16 to 30	4.528±0.018
	After exchange	Counts/min
Ottawa	Aug. 29 to Sept. 11	4.370±0.020
Resolute	Aug. 7 to 31	4.541±0.017

Though the operation was continuous over these periods, all the data were not used. Selections were made of periods in which the barometer did not vary by more than two or at most three millibars in twelve hours or more. The number of such periods during the four intervals shown in Table I are, respectively, 6 and 9 before the exchange, and 9 and 8 after the exchange. The errors in Table I are standard deviations based on the total number of counts in each case. The first measurement at Ottawa is the least accurate,—the standard deviation being 0.57 percent. The others are below 0.5 percent.

The barometer coefficients for each station were known[7] and the mean counting rate over each of the above selected periods was corrected to a pressure of 1000 millibars. The mean pressure over the periods used at Resolute was 1011.0 mb and at Ottawa 1005.7 mb. The same barometer coefficient was used at both stations, namely, −2.06 percent per cm of mercury or −0.155 percent per mb. Actually the measurements[7] indicate a slightly higher coefficient at Resolute than at Ottawa but not enough to make a significant difference. Reducing all values to a pressure of 1000 mb should also correct for differences in altitude above sea level at the two stations as accurately as such a correction can be made. The actual difference in sea level was about 100 feet, the Ottawa station being higher.

The correction for temperature is much more difficult. Corrections for sea level temperature are known to be of no value; therefore a correction was made for the differences in the mean atmosphere. Unfortunately there is no radiosonde at the weather station in Ottawa. Radiosonde data for four stations surrounding Ottawa (Sault Ste. Marie, Michigan; Moosonee, Ontario; Buffalo, New York; Albany, New York) had been examined in connection with previous measurements and it seemed that the atmosphere over Sault Ste. Marie was on the average much like that over Ottawa. Sault Ste. Marie is due west of Ottawa and is usually in the same air mass. The twice daily radiosonde data for the selected periods was plotted and a mean curve drawn. This was taken as the mean atmosphere over Ottawa.

An estimate was then made of the integral intensity of μ-mesons at production by a process of numerical integration similar to that used previously.[7] The method consisted of calculating the probability of decay of the mesons during their flight from a mean production level

[7] D. C. Rose, Can. J. Phys. **29**, 97 (1951).

TABLE II. Intensity comparison between Resolute and Ottawa.

Ratio of intensity (reduced to 1000-mb pressure) at Resolute to that at Ottawa	1.031 ±0.005
Correction factors to reduce intensity at Resolute to that at Ottawa, due to differences in:	
Mean atmosphere	0.986 ±0.004
Geometry of counter supports	0.998 ±0.002
Roof covering	1.003 ±0.001
Side showers	1.000 ±0.003
Corrected ratio of intensities	1.0176±0.0075

to the 1000-mb level. This was calculated for the Ottawa atmosphere for a series of values of momenta at the lower level. By applying these results to the sea level spectrum a spectrum at production levels was obtained. The sea level spectrum chosen was that of Wilson, as described by Rossi,[8] with some modifications at higher energies suggested by analyses of barometer coefficients. These modifications are explained in reference 7. The exact spectrum chosen is of little importance as long as it represents the facts approximately, because the atmosphere corrections were compared relatively at the two stations and, as the differences were small, absolute values could be considerably in error with little effect on the comparison. The production spectrum was then integrated numerically from a point corresponding to an energy of about 500 Mev (actually a momentum of 600 Mev/c) at sea level up to a value beyond which the integral became negligible. This process was repeated for the mean atmosphere over Resolute during the periods selected for use there. Since Resolute has a radiosonde station the atmosphere there was more accuratley known. The sea level spectrum at Resolute was assumed to be the same as at Ottawa. Preliminary results from later measurements of the spectrum at both stations indicate that it is substantially the same. 500 Mev at sea level was used for the lower limit of integration because the lead absorbers and roof over the counters fix the lowest energy accepted by the telescope very close to this value. It might have been more precise to assume a production spectrum and calculate the sea level integral spectrum at each station and compare their values, but as a comparison factor between the two is all that is required, the inverse process which was followed would have negligible effect on the results.

These calculations show that if the production intensity were the same at both stations the intensity at Resolute would be expected to be 1.014 times higher than that at Ottawa, this difference being due to atmospheric differences only. To reduce the Resolute intensity to that at Ottawa, the correction factor is the reciprocal of the above figure, namely, 0.986. The accuracy of this figure is difficult to assess. Errors due to the constants used in the integration are likely to be small but the calculation is subject to the criticism that the mean atmosphere over Sault Ste. Marie is not necessarily identical with that at Ottawa. The differences would, however, be small compared to the differences between Sault Ste. Marie and Resolute. Therefore, an error of ±0.004 has been assumed.

Differences due to the different roofs over the equipment have already been considered but the results should also be corrected for slight differences in the geometry of the racks supporting the counters at the two stations and for any differences that there may be in side showers. The actual number of side showers for two counter telescopes is difficult to assess but two different arrangements of counter telescopes in triple coincidence with identical shielding around the bottom counter tray to that described here have been used at both stations. The results indicate that the side shower correction for these two counter telescopes would be approximately 1.6±0.3 percent and that the differences in the side shower correction at the two stations is not significant. Therefore, in the ratio between the intensities no correction was made for side showers but a statistical error due to this standard deviation was included. The final difference in intensity with all corrections is shown in Table II.

There remains, therefore, 1.76±0.75 percent difference between the intensity at Resolute and at Ottawa. The errors in Table II are liberally estimated. Where they are obtained from counting rates they are standard deviations. In the other cases they are considered to be the maximum possible error. However, the final error of the product is calculated as though the error in each factor were a standard deviation.

IV. DISCUSSION OF RESULTS

The final difference in intensity in Table II seemed too great to be discarded as insignificant and the consideration of possible contributing factors to this difference in intensity is interesting. The minimum energy with which primary rays can reach the earth in a vertical direction at different latitudes has been calculated by Vallarta.[9] These calculations and others have been summarized by Alpher[10] and Fig. 1 has been drawn from data obtained from Fig. 4 of reference 10. At the latitude of Ottawa the cutoff is about 0.7 Bev for protons and somewhat lower per nucleon for heavier primary particles. In the production of mesons or other secondary particles in the range of energies with which these measurements are concerned the energy per nucleon seems to be the critical factor, though the actual cut-off energy for a heavy nucleus might be much higher. The particles which were counted in the present measurements must have had sufficient energy to penetrate 418 grams per cm^2 of lead plus about 4 grams per cm of lighter material, a minimum energy of about 510 Mev. The energy loss for a meson going through the atmosphere from a mean production level to sea level is about 1900 Mev. The minimum energy which we are accepting is therefore 2410 Mev.

[8] B. Rossi, Revs. Modern Phys. **20**, 537 (1948).

[9] M. S. Vallarta, Phys. Rev. **74**, 1837 (1948).

[10] R. A. Alpher, J. Geophys. Research **55**, 437 (1950).

In order to reach the mean layer of production the primary particle, on the average, would have penetrated about 100 grams per cm² of air. Such a primary proton would have lost approximately 200 Mev of energy in reaching this level. Therefore, the primary particle must have had an energy of at least 2610 Mev when it reached the earth's atmosphere in order to produce the lowest energy particle observed. As this energy is much higher than the geomagnetic cutoff at the lower latitude (Ottawa) differences in intensity at the two stations due to geomagnetic effects would not be expected. The solid curve in Fig. 1 shows the cut-off energy based on the Stormer cone and the shadow cone. Vallarta[9] has also made some calculations on the cutoff due to the "penumbra" or the region between fully allowed and completely forbidden trajectories. His calculations indicate that the penumbra region at latitudes as high as Ottawa is mostly light. Therefore, it can be neglected. Actual calculations have not been made above about 40° latitude.

The two points marked in Fig. 1 represent the latitude of Ottawa and Resolute and are at the energy level of 2610 Mev. One sees that they are both well above the solid line for protons but if the broken line representing the limit of the penumbra were extrapolated to higher latitudes it might well be above the Ottawa point but not above that for Resolute. The difference in intensity between Resolute and Ottawa could therefore be explained simply if the penumbra at the Ottawa latitude were not entirely negligible. A calculation of its effect for this latitude is quite beyond the scope of this paper.

The effect of longitude can be ruled out. The two stations were at different geomagnetic longitudes but are not very different in geographic longitude (Ottawa 76°W and Resolute 95°W). Vallarta[9] has plotted corrections for the curves in Fig. 1 showing both the change in minimum energy and in the angle of the geomagnetic vertical due to longitude effects. His calculations extend only to 40° latitude but both corrections are much too small to affect the present results and no longitude effect would be expected where the minimum accepted energy fixed by absorbers is so much higher than that due to the geomagnetic field.

There are other contributing factors which should be discussed. The telescope was asymmetrical. The half-angle at right angles to the plane of the counters was about 5° and in that plane about 35°. The counter trays were aligned in the vertical direction with sufficient accuracy to be sure that any deviation from the vertical would make a negligible difference between the two stations. As the angular spread is large compared to the deflection of mesons in the earth's field during their path from production levels any asymmetry such as that calculated by Johnston[11] due to this deflection would be negligible.

[11] T. H. Johnston, Phys. Rev. **59**, 11 (1941).

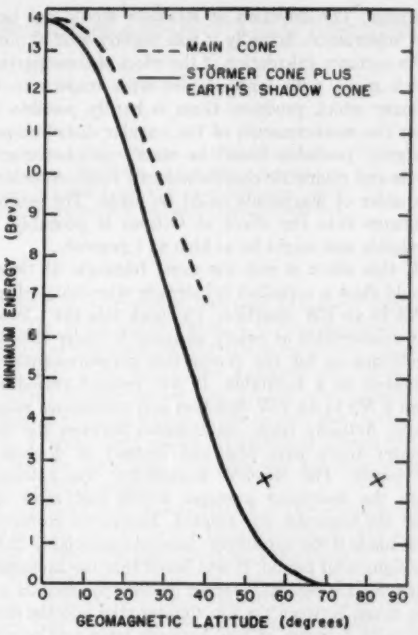

FIG. 1. Minimum allowed energy of arrival for vertical cosmic-ray protons.

An examination of the curves published by Alpher[10] shows that at high zenith angles the minimum energy allowed by the earth's field rises rapidly for particles coming into that field from an easterly direction. The minimum energy accepted after passage through the atmosphere and absorbers must vary roughly inversely as the cosine of the zenith angle. Alpher's curves show that at zenith angles above about 50° the minimum allowed energy of particles coming from easterly directions rises rapidly and at 60° it is of the order of 10 Bev, while remaining quite low from the west. At any angle included in the telescope the absorber (atmosphere plus lead) fixes a minimum energy which is well above that due to the geomagnetic cutoff but particles could enter the telescope from nuclear collisions in the upper atmosphere caused by primaries which have much larger zenith angles. For zenith angles in the neighborhood of 60° and higher there will be a group of primary rays with energies in regions from 5 to 25 Bev (depending on the angle) which if coming from the east (or north at the larger zenith angles) will be excluded at Ottawa and allowed at Resolute. Secondary mesons from these might have a zenith angle less than 35° and so be included in the telescope at Resolute and excluded at Ottawa. The direction of the widest aperture of the telescope at Ottawa happened to be NE–SW, a direction in which this exclusion would be expected to be ap-

preciable. The direction at Resolute should not be of any importance. Actually it was slightly west of north.

An accurate calculation of the effect of these particles which move with large angles with respect to the primary which produces them is hardly possible but from the measurements of the angular distribution of energetic particles found in stars[12] in photographic plates and geometric considerations a rough estimate of the order of magnitude could be made. The estimate indicates that the effect at Ottawa is probably not negligible and might be as high as 1 percent.

If this effect is real the same telescope at Ottawa should show a variation in intensity when rotated from a NS to an EW direction. To check this the telescope was reassembled as nearly as possible under the same conditions as for the comparison measurements, but mounted on a turntable. It was rotated periodically from a NS to an EW direction and continuous records taken. Actually triple coincidences between the three counter trays were observed instead of doubles as previously. The NS–EW asymmetry was calculated from the four-hour averages before and after each time the telescope was rotated. Barometer corrections were made if the barometer changed appreciably during the eight-hour period. It was found that the asymmetry was 0.8 ± 1.4 percent. Double coincidence records were also taken between the top counter tray and the center tray with 6 inches of lead between trays and no other absorber surrounding either. The half angular widths of the telescope in this case would be about 60° in the direction in the plane of the counters and about 10° at right angles to this. This asymmetry was found to be -0.4 ± 0.4 percent. A positive asymmetry is inferred when the NS direction gives a greater intensity than the EW. For very large zenith angles the maximum asymmetry should be expected to be almost in a NE–SW direction. Therefore, for the largest zenith angles, the asymmetry between NS and EW might be expected to be small and these results, though not very satisfactory, are not necessarily inconsistent. Preliminary results from another investigation in this laboratory on NS and EW asymmetry using tilted telescopes indicate that the asymmetry seems to vary from time to time perhaps being influenced by disturbances in the geomagnetic field. A portion of the above asymmetry results was taken during a magnetic disturbance.

While these asymmetry results with a vertical telescope are not entirely satisfactory they do indicate that at least a portion of the difference in intensity between Ottawa and Resolute may be attributed to the angular distribution of mesons with respect to the direction of primary particles, and the fact that for large zenith angles the geomagnetic effect extends to high latitudes. Another factor that would contribute to the observed differences in intensity, if it were appreciable, is the possibility of a meson penetrating the telescope, having been produced by a primary of energy below cutoff due to absorption but reaching the telescope without appreciable loss of energy in the atmosphere. Such a particle would have to be tertiary, the intermediate particle being neutral. The probability of this happening seems very remote as the minimum energy accepted by the telescope is about 500 Mev. The geomagnetic cutoff at Ottawa is about 700 Mev for protons at vertical incidence. The number of occasions must be very small where a primary nucleon with around 700 Mev of energy will give nearly all of its energy to a neutral particle, the neutral particle would then penetrate the complete atmosphere without decay or another collision until reaching a position just above the telescope where another collision would produce some particle like a meson with enough energy to penetrate the telescope.

[12] Brown, Camerini, Fowler, Heitler, King, and Powell, Phil. Mag. 40, 862 (1949).

V. CONCLUSIONS AND SUMMARY

Measurements with a vertical counter telescope exchanged between Ottawa (geomagnetic latitude 56.8°) and Resolute in the Canadian Arctic (geomagnetic latitude 83.0°) indicate that after meteorological and local geometrical corrections have been made the intensity at Resolute is 1.76 ± 0.75 percent higher than at Ottawa. The absorbers in each telescope were $14\frac{1}{2}$ inches of lead plus about 4 grams per cc of light material. The meteorological corrections were made first by reducing the intensity during each period of observation to that at a pressure of 1000 mb by using known barometer coefficients. Then an integration was made over the mean atmosphere to correct for differences in the probability of meson decay in flight from a mean production level to the 1000-mb level. The residual difference in intensity is considered to be greater than can be accounted for by different atmospheric conditions. The conditions were such that no difference would be expected due to geomagnetic effects at any angles included by the telescope.

Other phenomena may contribute to the difference in intensity. These are (*i*) the penumbra in the theory of the geomagnetic effect, (*ii*) the effect of mesons produced by field sensitive primaries, the primary having directions not included in the telescope, the meson however coming from a direction from which it may enter the telescope, (*iii*) the possibility of particles being observed in the telescope being from a second collision, the intermediate particle being neutral.

Vallarta considers the penumbra at Ottawa latitudes to be mostly light though whether it is completely negligible is uncertain and calculations are very difficult. Calculations and a subsidiary experiment indicates that the second contributory effect mentioned above is probably dominant in accounting for the difference in intensity. The third is almost certainly negligible.

Measurement of Electron Pairs for the Determination of a 65-Mev X-Ray Spectrum*

RICHARD H. STOKES†
Institute for Atomic Research and Department of Physics, Iowa State College, Ames, Iowa
(Received July 30, 1951)

A magnetic cloud chamber has been used to observe electron pairs produced by the beam of a synchrotron operating at 65 Mev. The cross section for pair production given by the Bethe-Heitler theory was used to obtain the x-ray energy spectrum. The observed spectrum was in agreement with that expected theoretically. Values of the quantum and energy flux are given in terms of the reading of a Victoreen thimble ionization chamber.

INTRODUCTOIN

SEVERAL recent investigations[1–3] have measured the x-radiation produced by extreme relativistic electrons that are decelerated in heavy materials. These experiments show substantial agreement with the Bethe-Heitler theory at electron energies of 19.5, 309, and 322 Mev. The present investigation was undertaken at a peak energy of 65 Mev to study the energy spectrum and the quantum flux of the Iowa State College synchrotron operated with a tungsten target 0.005 inch thick. This information is of interest for a comparison with the results of the Bethe-Heitler theory and furnishes a basis for future studies of gamma-interactions with nuclei.

The experimental method consisted of the observation of electron pairs produced by the x-ray beam in the gas of a magnetic cloud chamber. The pairs were observed under conditions which allowed good curvature measurements to be made on both the electron and positron. The information thus obtained was used, together with the theoretical values of pair production cross section, to obtain the energy spectrum of the quanta. Two experimental investigations[4,5] at high energy indicate the reliability of the theoretical cross section for pair production.

APPARATUS

A 12-inch diameter cloud chamber and magnetic coils were used in the experiment. Air was used as the noncondensible component and a mixture of 1 part water and 2 parts ethyl alcohol was introduced into the chamber to provide the condensible vapor. Accurately regulated air pressure, admitted below a rubber diaphragm whose motion was not constrained, was used to compress the chamber. Expansion of the chamber was effected by opening a large capacity valve which rapidly reduced the chamber to atmospheric pressure. Line air pressure was used and was regulated by two stages of pressure reducers. A modified Hoke reducer designed for low pressures was used to achieve accurate regulation of expansion ratio. A three-dimensional description of the tracks was obtained by use of a stereoscopic attachment on the 35-mm camera lens. To obtain curvature measurements the tracks were projected through the optical system of the camera used to record them. A translucent screen arrangement similar to the one used by Brueckner *et al.*[6] allowed the radii of curvature to be measured.

A magnetic field was produced in the chamber by a pair of coils similar to the Helmholtz type. The mean radius of the coils was 30 cm and the cross section of the windings was 14.25 cm, radially, by 15.25 cm, axially. These are approximately in the ratio of the square root of 31 over 36, a uniformity condition suggested by the field expansions of Ruark and Peters.[7] Ference, Shaw, and Stephenson[8] have shown that a separation between coils less than that given by the Helmholtz condition is useful in producing a field of great uniformity over a considerable volume. With the measurements of Ference as a guide, calculations were made using the expansions of Ruark. This procedure showed that a 5 percent reduction of the separation was best for uniformity over the useful volume of the chamber. The field used in the experiment was uniform to one-half percent and had a value of 2500 gauss.

Each magnetic coil was constructed of 550 turns of 0.25-inch diameter copper tubing with a 0.065-inch wall thickness. The tubing had glass fiber insulation bonded with silicone varnish and was wound on brass coil forms. DC 996 silicone varnish was applied between successive layers and after the winding was completed the coils were baked in an oven to cure the varnish. Cooling of the coils was accomplished by passing soft water at 500 psi through the hollow conductors in 12 parallel paths. The paths were electrically separated by rubber hose sections.

The control system of the cloud chamber is shown in block diagram form in Fig. 1. This circuit synchronized the cloud-chamber expansion with a single x-ray pulse and provided the various delays necessary

* Contribution No. 151 from the Ames Laboratory of the AEC.
† Present address: Box 1663, Los Alamos, New Mexico.
[1] H. W. Koch and R. E. Carter, Phys. Rev. **77**, 165 (1950).
[2] Powell, Hartsough, and Hill, Phys. Rev. **81**, 213 (1951).
[3] J. W. DeWire and L. A. Beach, Phys. Rev. **83**, 233 (1951).
[4] J. L. Lawson, Phys. Rev. **75**, 433 (1949).
[5] R. L. Walker, Phys. Rev. **76**, 1440 (1949 .
[6] Brueckner, Hartsough, Hayward, and Powell, Phys. Rev. **75**, 555 (1949).
[7] A. E. Ruark, and M. F. Peters, J. Opt. Soc. Am. **13**, 205 (1926).
[8] Ference, Shaw and Stephenson, Rev. Sci. Instr. **11**, 57 (1940).

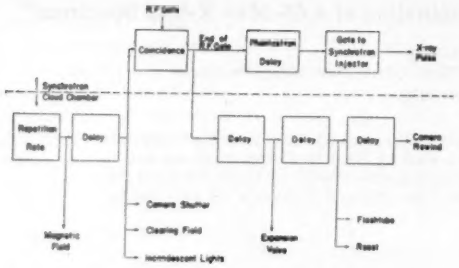

FIG. 1. Cloud-chamber control circuit—block diagram.

for cloud-chamber operation. As shown in the block diagram, after the magnetic field had been turned on, the cloud chamber interrogated the synchrotron and received an answer in the form of a pulse that was in definite phase relationship with the time of the x-radiation. This pulse, after delays in both the synchrotron and the cloud-chamber circuits, enabled the chamber to be expanded immediately prior to the x-ray pulse.

To eliminate difficulties with a high background of pair electrons, a collimated beam of radiation was allowed to enter the chamber through a beryllium window 0.005 inch thick. The collimator was a stack of lead bricks 18 inches thick with a hole five-eighths inch in diameter.

PROCEDURE

About 4000 photographs were recorded in obtaining the x-ray energy spectrum. The x-ray pulse intensity of the synchrotron was reduced by a factor of 50 to 100 from its peak value and was monitored by the ballistic deflection of an ionization chamber monitor. For monitoring that part of the data used to determine the number of quanta, a Victoreen thimble ionization chamber was used in a single-ended cylinder of lead one-eighth inch thick. Since the Victoreen chamber measures only large dosages of radiation, it was exposed with the synchrotron operating continuously and at high pulse intensity. The ionization chamber monitor was used, over a portion of its range known to be linear, to determine the ratio between the x-ray beam intensity at the high level of continuous operation and the low level beam intensity used to produce pairs in the cloud chamber.

From the reprojected tracks the radius of curvature was deduced from a measurement of the following quantities: the apparent radius of curvature, r', of a segment of the helical electron track as determined by matching a circle at each end and the midpoint, the length of the chord of this helical segment, K, and the angle, a, between the chord and a plane normal to the magnetic field. By use of the relation,

$$r/r'=\tfrac{1}{2}[1+\{1-(\tfrac{1}{2}K/r')^2\}^{\frac{1}{2}}]\cos^2 a+\tfrac{1}{2}[1-\{1-(\tfrac{1}{2}K/r')^2\}^{\frac{1}{2}}],$$

the radius of curvature, r, of the helix projected onto a plane normal to the magnetic field was computed. From the relation

$$\frac{\tan a'}{\tan a}=\frac{K\cos a/2r}{\sin^{-1}(K\cos a/2r)},$$

the pitch angle, a', of the helix was computed. The correction factor by which one multiplies the measured radius of curvature, r', to obtain the radius of curvature corresponding to the magnitude of the electron momentum, is

$$F=r/(r'\cos a').$$

For small values of $\frac{1}{2}K/r'$ this correction factor reduces to $\cos a$.

Due to the high energy of the quanta and the consequent strong forward-directed characteristic of the pairs, most of the electron tracks lay nearly in a plane normal to the magnetic field. A portion of the chamber near the window, 15.3 cm long, was used to detect pairs and all pairs that originated in this portion were measured. Under these conditions it was possible to observe sufficient length of track so that the percentage relative error of the radii of curvature would be limited. The criterion used was that all tracks have a ratio of chord length squared over radius of curvature greater than one centimeter. Of all observed pairs from 5–65 Mev, less than one percent failed to satisfy this requirement and thus no appreciable energy discrimination arose through accuracy requirements on the radius of curvature measurements. Measurements indicate that the maximum error in the radius of curvature measurement was about 15 percent and that most of the data had errors in the range 5–10 percent.

RESULTS

The number of pairs, N, and the corresponding energy interval are shown in Table I. For the mid-energy, E, of each of these intervals the relative cross section, σ, for pair production was read from the curve given by Bethe and Heitler.[9] The curve used was the

TABLE I. Energy spectrum.

Total energy of pairs in Mev	N	σ	$\frac{NE}{\sigma}$	$\Delta\%=\frac{100}{\sqrt{N}}$
5– 9.9	123	2.90	318	9
10–14.9	119	4.35	344	9
15–19.9	90	5.20	303	10
20–24.9	67	5.90	255	12
25–29.9	64	6.50	270	12
30–34.9	59	7.10	270	13
35–39.9	44	7.50	220	15
40–44.9	52	7.80	283	14
45–49.9	46	8.10	270	15
50–54.9	36	8.30	227	17
55–59.9	32	8.55	215	18
60–64.9	20	8.80	142	22
65–67.4	3	9.00	22.1	58

[9] H. Bethe and W. Heitler, Proc. Roy. Soc. (London) **A146**, 83 (1934).

one for H_2O, which is slightly different from the unscreened case at the highest energies. In each energy interval the number of pairs is multiplied by the total energy, E, and divided by σ. These relative values of the x-ray energy spectrum are shown in Fig. 2. The solid curve is the Bethe-Heitler bremsstrahlung energy spectrum for air as obtained from Rossi and Greisen.[10] An upper limit of 65 Mev was used for this curve, corresponding to the operating conditions of the synchrotron as given by a calibration chart which has as a basis the measurement of the synchrotron field strength at the time the electron beam strikes the target.

All data were taken with the cloud-chamber magnetic field at nearly the same value. This situation causes some discrimation at the lowest energies due mainly to a decreasing ability to identify pairs. When pronounced inequalities in the energy division between members of a pair occur, the low energy positron, a small circle, can be missed, either due to overlapping with other tracks or because it makes a large angle with a plane normal to the magnetic field. The lowest energy experimental point is affected appreciably in this way.

The data were observed by observing a portion of the center of the synchrotron beam having an angular width small with respect to the total beam width. Schiff[11] has shown that the x-ray beam width of electron accelerators usually is determined not entirely by the characteristics of the radiation process, but also by the multiple scattering of the electrons in the target before the radiation occurs. This latter effect produces an effective integration over the angles of quantum emission and makes it reasonable to compare the experimental data with the Bethe-Heitler curve which represents values of cross section integrated over all angles. In the present case calculations and measurements indicate that the over-all beam width is due at least as much to multiple scattering as to the inherent nature of the bremsstrahlung process in an infinitely thin target.

When a comparison of the experimental points with the curve of Fig. 2 is made, two facts should be recognized. First, it is clear that one should compare the experimental points with the average value of the curve over the 5-Mev interval. The difference between the averaged value and the value of the curve at the center of the interval is small, however, except for the interval 60–65 Mev. In this case the averaged value is about 15 percent lower then the value at the center, but still falls within the statistical accuracy of the experimental point. The second point to be considered is the distortion that arises from the finite energy resolution of the cloud chamber. The general magnitude of this resolution has been indicated, but an exact determination has not been attempted due to the variety of track lengths

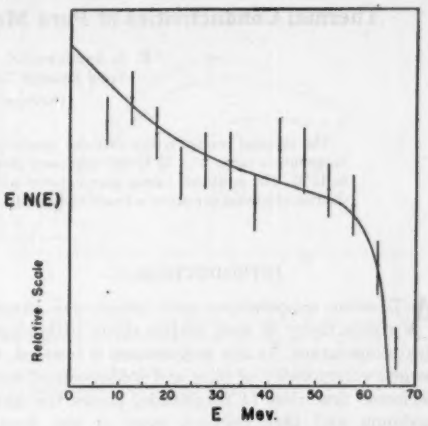

FIG. 2. Synchrotron energy spectrum.

contributing to each energy interval. The energy resolution effect causes the greatest distortion at the upper end of the spectrum and, if corrected for, would tend to raise slightly the experimental point at 62.5 Mev. The effect of both these corrections would be in the direction of making the spectrum fall off more sharply at the upper limit. This agrees with the suggestions of Heitler[12] and of Guth,[13] that if the correct wave functions were used in the theory, the upper end of the bremsstrahlung spectrum would probably tend to a finite limit.

The value for the quantum flux obtained was 6.6×10^7 quanta per square cm per r unit of the Victoreen chamber for the energy range 10–65 Mev. Corresponding to this value the energy flux is found to be 2.2×10^9 Mev per square cm per r unit for the energy range 0–65 Mev. These values have a statistical error of 20 percent. McMillan, Blocker, and Kenney[14] recently obtained results from the Berkeley synchrotron which can be used for a general comparison with the above value of the energy flux. McMillan's Victoreen chamber was in an open-ended cylinder one-eighth inch thick while our value was obtained with a single-ended cylinder of the same wall thickness. For the peak energies of 320 and 160 Mev, McMillan's values are, respectively, 3.3 and 2.2×10^9 Mev per square cm per r unit.

The author wishes to express his great appreciation to Dr. L. J. Laslett whose continued assistance and valuable suggestions greatly facilitated this work. Much credit is due Dr. James Palmer, Mr. Robert McKenzie, and Mr. I. Coleman for their part in the construction of the equipment.

[10] B. Rossi and K. Greisen, Revs. Modern Phys. **13**, 240 (1941).
[11] L. I. Schiff, Phys. Rev. **70**, 87 (1946).
[12] W. Heitler, *Quantum Theory of Radiation* (Oxford University Press, London, 1944), second edition, p. 171.
[13] E. Guth, Phys. Rev. **59**, 325 (1941).
[14] McMillan, Blocker, and Kenney, Phys. Rev. **81**, 455 (1951).

Thermal Conductivities of Pure Metals at Low Temperatures. I. Aluminum*

F. A. ANDREWS,† R. T. WEBBER, AND D. A. SPOHR
Naval Research Laboratory, Washington, D. C.

(Received August 20, 1951)

The thermal conductivities of three specimens of highly pure aluminum have been measured in the temperature range 2 to 20°K. All specimens showed maximum conductivities in the temperature range 14 to 17°K. The measured values are compared with the theory of Sondheimer. The number of effective conduction electrons per atom is found to be 0.061.

INTRODUCTION

AT room temperatures and above, the thermal conductivity of most metals shows little change with temperature. As the temperature is lowered, the thermal conductivity of pure and well-annealed metal specimens first rises in magnitude, passes through a maximum and then declines more or less linearly toward zero at 0°K. The thermal conductivity of metals in the range of temperatures from 20°K up to room temperature has been the subject of numerous investigations by Grüneisen and his co-workers.[1] The range of temperatures below 20°K spans a region of considerable interest, for in this range extremely pure and strain-free metal specimens exhibit their maximum thermal conductivity. Furthermore, at these low temperatures the free electron theory of thermal conductivity reduces to a relatively simple form which facilitates comparison with experiment. Although there have been a number of investigations of the thermal conductivities of pure metals at temperatures below 20°K,[2–12] the majority have been concerned primarily with phenomena associated with the incidence and destruction of superconductivity and have employed a relatively restricted range of temperatures.

As the first of what is planned to be a systematic series of investigations of thermal conductivities of pure metals over the 2 to 20°K temperature range, we have studied the thermal conductivities of three highly pure aluminum specimens, two of them single crystals.

EXPERIMENTAL DETAILS

The three specimens reported in this paper were rods of exceptionally pure aluminum, approximately four inches in length and 0.15 inch in diameter. Details on the purity and crystalline state of these specimens are given in Table I. To facilitate mounting of the rods and the attachment of thermometers, a thin layer of copper was plated on each end of the rod for a distance of about $\frac{3}{4}$ of an inch.

The calorimeter used in this work was similar to that previously described by de Haas and Rademakers,[9] but differed in some details. The specimen rods were soldered with one end protruding through the bottom of a brass can which could be evacuated. A sufficiently high degree of thermal insulation was found for vacuums of better than 0.05 micron. To permit a measured flow of heat through the specimen, a heater coil of manganin wire was attached to the isolated end of the specimen inside the can.

For those measurements of the thermal conductivity at temperatures above that of the refrigerant bath, an auxiliary heater of manganin was wrapped around the end of the specimen protruding through the bottom of the calorimeter can. The whole bottom of the can was then partially insulated from the bath by means of a tight-fitting thin brass cap filled with vacuum grease.

The absolute temperature and temperature gradient along the specimen were determined by two gas thermometer bulbs, approximately 6 cm^3 in volume, attached to the specimen. These bulbs were separated by about 5 cm and were connected by means of small diameter thin-wall *K*-monel tubes to an external manometer system. This system consisted of two closed-end mercury manometers, which measured the absolute temperature of each of the thermometer bulbs, and a capillary differential oil manometer used for a precision determination of the temperature difference between the two thermometer bulbs. The temperature difference between the gas thermometers ranged from about 0.03°K in the measurements at 2°K up to about 0.15°K in the measurements at 20°K. A summary of the corrections due to departures of the thermometer system from ideal behavior at liquid helium temperatures is given by Hulm.[2]

---

* A portion of this paper formed part of a thesis submitted by F. A. Andrews in partial fulfillment of the requirements for the degree of Doctor of Philosophy, Yale University.

† Now at Submarine Base, New London, Connecticut.

[1] A summary of the work of Grüneisen, together with a complete bibliography, is given in an obituary article appearing in the Ann. Physik **5**, V–XII (1949).

[2] J. K. Hulm, Proc. Roy. Soc. (London) **A204**, 98 (1950) (Sn, In, Hg, Ta).

[3] K. Mendelssohn and J. L. Olsen, Proc. Phys. Soc. (London) **A63**, 2 (1950) (Ta, Nb).

[4] K. Mendelssohn and R. B. Pontius, Phil. Mag. **24**, 777 (1937) (Pb).

[5] A. Rademakers, Physica **15**, 849 (1949) (Pb, Sn).

[6] J. de Nobel, Physica **15**, 532 (1949) (W).

[7] J. F. Allen and E. Mendoza, Proc. Cambridge Phil. Soc. **44**, 280 (1948) (Cu).

[8] S. Shalyt, J. Phys. USSR **8**, 315 (1944) (Bi).

[9] W. J. de Haas and A. Rademakers, Physica **7**, 992 (1940) (Pb).

[10] H. Bremmer and W. J. de Haas, Physica **3**, 672 (1936) (Pb, Cu).

[11] de Haas, Gerritsen, and Capel, Physica **3**, 1143 (1936) (Bi).

[12] W. J. de Haas and H. Bremmer, Commun. Phys. Lab. Univ. Leiden 214d, 220b, 220c (1931) (Pb, Sn).

At temperatures above 4.2°K the volume of that part of the manometer system at room temperature made necessary the calculation of a significant correction factor. In this case, the calculation of the temperature[13] and the temperature gradient was simplified if the thermometer system were "balanced"; that is, if the corresponding volumes on the two branches of the system were made equal. This was achieved by first carefully constructing and then etching the copper bulbs until their volumes were equal to within 0.1 percent. The *K*-monel tubes connecting these bulbs to the manometer system were made of equal lengths. Finally, the volumes of the two sides of the manometer system were made equal with the help of a small O-ring-sealed cylinder and piston whose volume could be adjusted sensitively and reproducibly by a standard micrometer head attached to the piston. The position of the piston was adjusted until large changes of temperature of the bulbs, produced by warming them from the temperature of liquid nitrogen to that of the room, caused no net difference in pressure as observed on the oil manometer.

Total error in the thermal conductivity measurements in the temperature regions 2 to 4.2°K and 14.5 to 20.5°K is estimated to be approximately 4 percent. In the temperature region 4.2 to 14.5°K, uncertainty in evaluating the magnitude of the correction factors led to somewhat larger errors (up to 10 percent at 14°K).

The electrical conductivity measurements were made after the specimens had been removed from the calorimeter. A Wenner potentiometer and standard techniques were employed. Total error in these measurements is estimated to be less than 2 percent.

RESULTS AND DISCUSSION

The thermal conductivities of the three aluminum specimens are plotted against temperature in Fig. 1. An understanding of these curves may be gained from consideration of the theory of transport phenomena in free electrons. Assuming the simplest monovalent model in which the electrons are quasi-free, it is possible to set up an integral equation for the velocity distribution of the conduction electrons.[14] This equation includes scattering both by impurities and by thermal vibrations of the lattice. A complete solution of this equation has been recently given by Sondheimer[15] in the form of the infinite series:

$$K=K_0+K_1+\cdots. \tag{1}$$

At temperatures $T/\Theta<0.05$, where Θ is the Debye characteristic temperature, K_0 in (1) is given by:

$$(1/K_0)=(\rho_r/L_0T)+(1/K_\infty)(T/\Theta)^2 \times[95.3N_a^{\frac{1}{3}}-533(T/\Theta)^2], \tag{2}$$

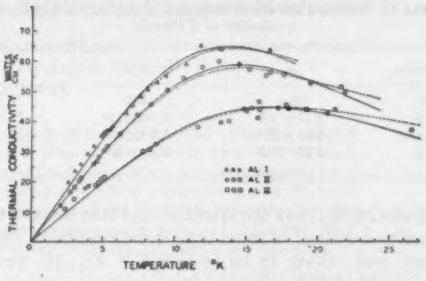

FIG. 1. Thermal conductivity of aluminum specimens as a function of temperature. The points represent experimental data. The solid curves are calculated from the theory of Makinson, Eq. (3), using A and B values of Table I, but neglecting the T^4 term. The dashed curves are calculated from the theory of Sondheimer, Eq. (1), using $N_a=0.061$ and $L_0=A\rho_r$.

where ρ_r = residual electrical resistivity, L_0 = Lorenz ratio, K_∞ = high temperature thermal conductivity, and N_a = number of effective free electrons per atom. This expression, previously derived by Makinson,[16] is of the form

$$(1/K_0)=(1/AT)+BT^3+CT^4. \tag{3}$$

Ignoring for the present the relatively small T^4 term, we may plot data for the three aluminum specimens on a graph of T/K *vs* T^3 getting nearly straight lines of slope B and intercept $1/A$. The values of A and B determined in this way are given in Table I. It is seen that A is proportional to the residual electrical conductivity whereas B is the same constant for all three specimens. From Eq. (2):

$$B=95.3(N_a)^{\frac{1}{3}}/K_\infty\Theta^2. \tag{4}$$

TABLE I. Characteristics of aluminum specimens.

		Al I	Al II	Al III
Source of metal		Aluminum Company of America	Aluminum Company of America	Johnson and Matthey
Purity of metal[a]	Al:	99.996+ percent	99.996+ percent	99.995+ percent
	Mg:	0.001	0.001	0.002
	Si:	0.001	0.001	<0.001
	Fe:	0.0006	0.0006	<0.0005
	Cu:	0.0004	0.0004	<0.0005
	Na:	0.0004	0.0004	faint trace
Crystalline form[b]		Single crystal	Single crystal	Annealed polycrystal
Residual resistivity, ρ_r in ohm-cm		3.04×10^{-9}	3.85×10^{-9}	5.51×10^{-9}
Resistance ratio, $\rho_{4.2}/\rho_{273}$		1.19×10^{-4}	1.48×10^{-4}	2.14×10^{-4}
Impurity constant, A in watts/cm(°K)^2		7.04	6.06	4.05
Lattice constant, B in cm/watt °K		2.70×10^{-5}	2.72×10^{-5}	2.72×10^{-5}

[a] The claims of purity stated here are based on spectrographic analyses performed by the suppliers of the metal.

[b] We are very much indebted to Dr. F. Rosi of the Sylvania Company for supplying us with a number of very fine single crystals of pure aluminum.

[13] The characteristics of helium gas thermometers with large dead space are given by A. H. Woodcock, Can. J. Research **A16**, 133 (1938).

[14] A. H. Wilson, Proc. Cambridge Phil. Soc. **33**, 371 (1937); *The Theory of Metals* (Cambridge University Press, London, 1936), p. 157 et seq.

[15] E. H. Sondheimer, Proc. Roy. Soc. (London) **A206**, 75 (1951).

[16] R. E. B. Makinson, Proc. Cambridge Phil. Soc. **34**, 474 (1938).

TABLE II. Values of the coefficients α, β, and γ in relationship (6) evaluated at $T/\Theta=0$.

Function	α	β	γ
a	78.4	-438	0.823
b	2.37×10^3	-4.16×10^3	11.4
c	1.64×10^5	6.83×10^3	355
d	4.25×10^2	6.20×10^3	0

TABLE III. Lorenz ratios of aluminum specimens at low temperatures.

Temperature (°K)	$(\rho K/T)\times10^8$ (watt-ohm/deg^2) Al I	Al II	Al III
4.2	2.21	2.34	2.41
14.5	1.55	1.80	1.88
20.4	...	1.40	1.57

Calculating K_∞ from the Wiedemann-Franz law and the Handbook value[17] of room temperature electrical resistivity and taking Θ to be 390°K,[18] Eq. (4) yields $N_a=0.040\pm0.001$ effective free electrons per atom. This value is in good agreement with the values of N_a found in tin, indium and mercury by Hulm.[2]

To this order of approximation, the thermal resistivity may thus be considered to be a simple addition of resistivities due to two scattering mechanisms:[19]

(1) The thermal resistivity due to impurity scattering $(1/AT)$.

(2) The thermal resistivity due to scattering by thermal vibrations of the lattice (BT^2).

The remaining terms of the series expression for the thermal conductivity (1) appear to converge and are of increasing difficulty of calculation. They include scattering by impurities and by the lattice in a manner such that they may not be separated and distinguished. The K_1 term in (1) is of the form:

$$K_1=7.60\times10^{-2}K_\infty[d^2/(a^2c-ab^2)](T/\Theta), \qquad (5)$$

where a, b, c, and d are each functions of the form:

$$\alpha N_a^{\frac{1}{3}}(T/\Theta)^3+\beta(T/\Theta)^5+\gamma\rho_r/\rho_\Theta. \qquad (6)$$

Here ρ_Θ is the electrical resistivity at $T=\Theta$, and the numerical coefficients α, β, and γ have the values given in Table II. These values are valid in the temperature range $0<T/\Theta<0.05$.

Extending the approximate solution, Eq. (1), to include K_1 and the T^4 term in K_0 and once again adjusting N_a, the number of free electrons, to fit our measurements, we obtain a value $N_a=0.061\pm0.002$. This is about 50 percent larger than the value obtained using Eq. (4). The T^4 term in Eq. (3) and K_1 contributed roughly equal amounts to this increase.

A disparity in order of magnitude is found in comparing these values of N_a with the number of free electrons calculated from measurements on aluminum of electron specific heats[20] and of soft x-ray emission[21] which yield values of N_a close to the valence number. This disparity might be resolved by modification of the transport theory to account for the role of filled and nearly filled zones occurring in multivalent metals.

Values of the Lorenz ratio, $K\rho/T$, as measured in our three specimens are given in Table III. At low temperatures, where impurity scattering predominates, the Lorenz ratio agrees moderately well with the value 2.45×10^{-8} watt-ohm/(°K)^2 predicted by the Sommerfeld theory.[22] At higher temperatures, where coherent scattering by the lattice plays a more important role, the values of the Lorenz ratio drop significantly below the theoretical value. This is in qualitative agreement with the predictions of Makinson.[16]

[17] *Metals Handbook* (Am. Soc. Metals, Cleveland, 1948), p. 810.
[18] N. F. Mott and H. Jones, *Theory of the Properties of Metals and Alloys* (Oxford University Press, London, 1936), p. 14.
[19] This is analogous to the well-known Mattheissen rule of electrical resistivity and was first established empirically for the case of thermal resistivity by Grüneisen, Z. Physik 44, 615 (1927).
[20] J. A. Kok and W. H. Keesom, Physica 4, 835 (1937).
[21] H. M. O'Bryan and H. W. B. Skinner, Phys. rev. 45, 370 (1934).
[22] A Sommerfeld, Z. Physik 47, 1 (1928).

Scattering of Radiation by Electrons in Relativistic Quantum Mechanics

OTTO HALPERN AND HARVEY HALL*
University of Southern California, Los Angeles, California
(Received July 30, 1951)

The theory of the scattering of radiation by Dirac electrons is revised and extended. Assuming negative energy states unoccupied, a formula for the cross section of coherent scattering of very hard quanta is derived. It is, furthermore, shown that the previously claimed and accepted one-to-one correspondence of the matrix elements for the cases of free or occupied negative energy states is generally untrue. It can be proved that for moderately small quanta the cross sections of coherent and incoherent scattering by bound electrons are approximately the same in the case of unoccupied negative energy states and in the pair theory proper. Characteristic differences are shown to exist for very hard radiation. The historical development of the problems here treated is also discussed.

I. INTRODUCTION

THE treatment of coherent x-ray scattering as presented in well-known textbooks[1] goes back to papers by Dirac[2] and Waller,[3] in which for the first time a relativistic theory of these phenomena was presented. Waller's paper[3] limits itself to the treatment of coherent scattering for incident frequencies whose $h\nu$ is large compared with the binding energy of the electron but small compared with mc^2.

The essential point in the relativistic theory is the treatment of the transitions to and from intermediate states of negative energy. In particular, the question arises as to whether the two assumptions: negative energy states free or occupied, lead to the same results for the scattering amplitude. Dirac,[2] in the paper quoted, gave a general proof, according to which there exists a one-to-one correspondence of the matrix elements for the two versions of the theory. The result, therefore, should be generally independent of any assumption as to whether the states of negative energy are empty or occupied. We shall, in future, refer to these two assumptions respectively as scheme I and scheme II.

In a brief communication[4] we presented a revision of these arguments customarily accepted. It was shown that no one-to-one correspondence of the various matrix elements exists in general if the exclusion principle is taken into account properly. We furthermore pointed out that the relation between schemes I and II becomes rather difficult to visualize if the interaction between the electrons is taken into account properly, and announced a more detailed treatment by us in a later publication.

The present paper contains a more complete elaboration of the ideas sketched in our first note. We here extend the treatment to the discussion of high frequency and inelastic scattering on the basis of scheme I as well as scheme II, and show how for certain cases agreement between the two schemes can be analytically obtained. We also discuss deviations between the two schemes for special scattering problems.

Since we announced our views on this question, and our forthcoming detailed treatment, the problems raised by us have attracted the attention of two authors who have presented their versions already.[5] We shall here proceed with the exposition of our theory and reserve some comparative remarks for the closing section of this paper.

The present paper divides itself up as follows. In Sec. II, the coherent scattering of hydrogen for $h\nu \gg mc^2$ is presented as based on scheme I. Section III contains a detailed criticism of the present views as presented in the literature and text books. In Sec. IV, the approximate equivalence of schemes I and II is shown for those cases in which the interaction between the electrons is neglected. In Sec. V, we show that the one-electron treatment is insufficient for both schemes I and II, and present in Sec. VI a general method based on scheme II for coherent and incoherent scattering. Section VII contains a discussion of the scattering of very large quanta according to scheme II, while finally in Sec. VIII the differences are examined between earlier theories and the results obtained in this investigation.

II. THE SCATTERING OF LARGE QUANTA ACCORDING TO SCHEME I

The differential cross section for coherent scattering by a single atomic electron may be written in the form

$$d\sigma = (e^2/mc^2)^2 d\Omega |A_1^+ + A_1^-|^2. \quad (2.1)$$

The symbols in Eq. (2.1) are self-explanatory apart from the partial amplitudes A_1^+ and A_1^-, which will be defined subsequently.

The quantity A_1^+ shall denote in scheme I as well as in scheme II the scattering amplitude due to transitions which involve positive energy states only. Defining the matrix elements M, M' through the Eqs. (2.3), we can

* Now at the ONR, Washington, D. C.

[1] G. Wentzel, *Quantentheorie d. Wellenfelder* (Vienna, 1943), p. 185; W. Heitler, *Quantum Theory of Radiation* (Oxford University Press, London, 1936), p. 189.

[2] P. A. M. Dirac, Proc. Roy. Soc. (London) **126**, 360 (1930).

[3] J. Waller, Z. Physik **61**, 837 (1930).

[4] O. Halpern and H. Hall, Phys. Rev. **75**, 910 (1949).

[5] E. Arnous, Phys. Rev. **77**, 149 (1950); W. H. Furry, Phys. Rev. **81**, 115 (1951).

write for A_1^+ the expression,

$$A_1^+=\sum_{E>0}\left(\frac{M_{E_0E}(-k_0)M'_{EE_1}(k)}{E_0+k_0-E}+\frac{M'_{E_0E}(k)M_{EE_1}(-k_0)}{E_0-k-E}\right). \quad (2.2)$$

In Eq. (2.2), E_0 represents the energy of the original bound state, E the energy in the intermediate state, while the vectors $\mathbf{k}_0$, $\mathbf{k}$ are the propagation vectors of the incident and scattered radiation; in the case of coherent scattering $k_0=k$, $E_1=E_0$.

In scheme I, the partial scattering amplitude A_1^- is the same as A_1^+ except that the summation must be extended over negative values of E. We finally give the definition of the matrix elements,

$$M_{E_0E}(-k_0)=\int\psi_{E_0}^*(\boldsymbol{\alpha}\cdot\mathbf{e}_0)\psi_E e^{-ik_0\cdot r}dV,$$
$$M'_{EE_1}(k)=\int\psi_E^*(\boldsymbol{\alpha}\cdot\mathbf{e})\psi_{E_1}e^{ik\cdot r}dV. \quad (2.3)$$

The matrix element M corresponds to the absorption of the incident quantum k_0 whose polarization vector is assumed to be parallel to the unit vector $\mathbf{e}_0$. The matrix element M' refers to the emission of the scattered quantum which is polarized parallel to $\mathbf{e}$. All quantities are expressed throughout this paper in relativistic units, i.e., mc^2 for energy, $\hbar/mc$ for length, and mc for momenta.

In the limiting case of large quanta, since $h\nu\gg mc^2$, terms of the order $1/k_0$ will always be negligible compared with unity. We, furthermore, assume that the generalized fine structure constant $\alpha=Z/137$ will be so small that terms of the order α^2 can be neglected.

An inspection of the matrix elements M and M' entering into A_1^+ and A_1^- makes it obvious that transitions from the bound state will occur only to such intermediate states ψ_E which have a momentum p which equals the momentum of the light quantum plus a correction of the order of magnitude of the average momentum in the bound state. This means that

$$\mathbf{p}=\mathbf{k}_0+\mathbf{p}_0 \quad (2.4)$$

with $p_0\cong O(\alpha)$; and since $k_0\gg p_0$ we have

$$p_0\cong k_0+(\mathbf{k}_0\cdot\mathbf{p}_0)/k_0\cong k_0+O(\alpha). \quad (2.5)$$

The energy denominator E_0+k_0-E, therefore, takes on the approximate value

$$E_0+k_0-p, \quad \text{to} \quad O(1/k_0) \quad (2.6)$$

or,

$$E_0-(\mathbf{k}_0\cdot\mathbf{p}_0)/k_0, \quad (2.7)$$

where we replace $E_0=(1-\alpha^2)^{\frac{1}{2}}$ by one, since α^2 is being neglected consistently. The term $(\mathbf{k}_0\cdot\mathbf{p}_0)/k_0$ in the sum over intermediate states can also give rise to a correction of $O(\alpha^2)$, which is also neglected. The energy denominator E_0+k_0-E may vanish at certain points of the integration range over E. This does not cause any divergencies; in fact, a more detailed study shows that these points do not contribute appreciably to the values of the scattering amplitude. The reason for this can be found in a simple argument referring to the method of variation of constants which underlies the derivation of all our expressions for $d\sigma$. A more correct formulation would show that the population of the initial state actually decreases like $\exp(-\Gamma t)$, where the quantity Γ with which we are familiar from the theory of line breadth was neglected in the derivation of $d\sigma$. Otherwise, the energy denominator would have had the form

$$E_0+k_0-E+i\Gamma/2 \quad (2.8)$$

and would never have vanished. Integration over this region containing an apparent singularity shows that it contributes to the value of A only a term which is proportional to a higher power of α^2.

The second term in Eq. (2.2) corresponds to an inverted order process, emission followed by absorption. The energy denominator, therefore, becomes of the order E_0-k_0-E, which allows us to neglect this term as compared to the first, since the matrix elements in the numerator are similar in both cases except that $-k_0$ and k are interchanged. We, therefore, arrive with these simplifications at the following expression for A_1^+, A_1^-:

$$A_1^+\cong\sum_{E>0}M_{E_0E}(-k_0)M'_{EE_0}(k),$$
$$A_1^-\cong\sum_{\epsilon<0}M'_{E_0\epsilon}(k)M_{\epsilon E_0}(-k_0). \quad (2.9)$$

Using the completeness theorem and the well-known factor

$$\tfrac{1}{2}(1+H/|E|), \quad (2.10)$$

we can extend our summation now over all values of E (negative as well as positive). The sharp dependence of the matrix elements in Eq. (2.9) on p allows us to write

$$1/|E|\cong 1/k_0, \quad (2.11)$$

so that the factor (2.10) can be written in the form

$$\tfrac{1}{2}(1+H/k_0). \quad (2.12)$$

Here, H is the Hamiltonian operator defined by the Dirac equation $H\psi=E\psi$:

$$H=-[\boldsymbol{\alpha}\cdot(1/i)\,\mathrm{grad}+\beta-V]. \quad (2.13)$$

Now, the insertion of Eq. (2.12) into Eq. (2.9) leads to

$$A_1^+\cong\sum_{E\gtrless 0}\int\psi_{E_0}^*(\boldsymbol{\alpha}\cdot\mathbf{e}_0)e^{-ik_0\cdot r}\tfrac{1}{2}(1+H/k_0)\psi_E dV \times\int\psi_E^*(\boldsymbol{\alpha}\cdot\mathbf{e})e^{ik\cdot r}\psi_{E_0}dV \quad (2.14)$$

$$\cong\int E\psi_0(\boldsymbol{\alpha}\cdot\mathbf{e}_0)e^{-ik_0\cdot r}\tfrac{1}{2}(1+H/k_0)(\boldsymbol{\alpha}\cdot\mathbf{e}) \times e^{ik\cdot r}\psi_{E_0}dV; \quad (2.15)$$

and since according to Eq. (2.13),

$$He^{i\mathbf{k}\cdot\mathbf{r}}=e^{i\mathbf{k}\cdot\mathbf{r}}(H-\boldsymbol{\alpha}\cdot\mathbf{k}), \tag{2.16}$$

we have, with the abbreviation

$$\mathbf{q}=\mathbf{k}_0-\mathbf{k} \tag{2.17}$$

$$A_1^+\cong\int\psi_{E_0}^*(\boldsymbol{\alpha}\cdot\mathbf{e}_0)e^{-i\mathbf{q}\cdot\mathbf{r}}$$

$$\times\tfrac{1}{2}(1+(H-\boldsymbol{\alpha}\cdot\mathbf{k})/k_0)(\boldsymbol{\alpha}\cdot\mathbf{e})\psi_{E_0}dV. \tag{2.18}$$

In the integrand of Eq. (2.18) we can neglect the whole term

$$(\boldsymbol{\alpha}\cdot\mathbf{e}_0)[(H-\boldsymbol{\alpha}\cdot\mathbf{k})/k_0](\boldsymbol{\alpha}\cdot\mathbf{e}). \tag{2.19}$$

The part of the numerator containing H is independent of k_0; and this part is, therefore, small of the order $1/k_0$, while the other term

$$(\boldsymbol{\alpha}\cdot\mathbf{e}_0)(\boldsymbol{\alpha}\cdot\mathbf{k})(\boldsymbol{\alpha}\cdot\mathbf{e})/k_0 \tag{2.20}$$

contains an odd number of $\boldsymbol{\alpha}$ factors, and, therefore, vanishes for bound stationary states.

Our expression for A_1^+, therefore, takes on the form

$$A_1^+\cong\frac{1}{2}\int\psi_{E_0}^*(\boldsymbol{\alpha}\cdot\mathbf{e}_0)(\boldsymbol{\alpha}\cdot\mathbf{e})e^{-i\mathbf{q}\cdot\mathbf{r}}\psi_{E_0}dV. \tag{2.21}$$

The partial scattering amplitude A_1^- can be treated in an entirely similar manner; it turns out only during the derivation that the processes of emission and absorption are interchanged, which means that in the final formula $\mathbf{e}_0$ must be replaced by $\mathbf{e}$ and vice versa. Now,

$$\tfrac{1}{2}[(\boldsymbol{\alpha}\cdot\mathbf{e}_0)(\boldsymbol{\alpha}\cdot\mathbf{e})+(\boldsymbol{\alpha}\cdot\mathbf{e})(\boldsymbol{\alpha}\cdot\mathbf{e}_0)]=(\mathbf{e}_0\cdot\mathbf{e}), \tag{2.22}$$

which, therefore, gives

$$\begin{aligned}A_1&=A_1^++A_1^-\\&\cong(\mathbf{e}_0\cdot\mathbf{e})\int\psi_{E_0}^*\psi_{E_0}e^{-i\mathbf{q}\cdot\mathbf{r}}dV.\end{aligned} \tag{2.23}$$

The integral expression for the scattering amplitude exhibits the usual form factor as originally derived by Waller for the scattering of very small quanta. No further discussion of A_1 seems indicated in this connection, except that attention should be called here to a point which acquires even greater significance in scheme II. For sufficiently large values of q, that means for scattering angles larger than α/k_0, the form factor in Eq. (2.23) becomes quite small (of the order of a high power of α). Since all terms of the order α^2 have been consistently neglected in the derivation given, we cannot be sure that our final result is correct at large angles, where terms of the order α^2 become dominant.

It is easy to see how one can extend the treatment to the case of many electrons.

III. GENERAL REMARKS ON THE RELATION BETWEEN SCHEMES I AND II

It has first been argued by Dirac[2] and since accepted by Waller[3] and in various textbooks[1] that there exists a one-to-one correspondence between the matrix elements leading to intermediate states of the two schemes. The argument for this statement runs about as follows:

If the intermediate states are of positive energy, then the contributions are obviously the same for both schemes. If, on the other hand, the intermediate state is one of negative energy according to scheme I, then it gives rise to an expression of the type,

$$A_1^-=\sum_{\epsilon<0}\frac{M_{E_0\epsilon}(-k_0)M'_{\epsilon E_1}(k)}{E_0+k_0-\epsilon}+\text{Em-Abs.} \tag{3.1}$$

Here, the electron goes first from its state of positive energy E_0 to the intermediate state of negative energy ϵ, the matrix element being $M_{E_0\epsilon}$, and then it passes from the state of negative energy ϵ to the final state E_1. The energy denominator is obviously given by $E_0+k_0-\epsilon$.

If, on the other hand, the negative energy states are filled (scheme II), then Dirac[2] studies the follqwing process.

He considers an electron passing first from the negative energy state ϵ to the final state E_1, and then another electron from its initial state E_0 to the vacated state of negative energy ϵ. The energy denominator in this case is the same as above. Obviously, these two expressions are equal; and if we sum over all intermediate states of negative energy, the total contribution to the scattering amplitude is the same in both cases, since all individual matrix elements are identical, even if changed in order. This argument of Dirac, was, for example, used for the calculation of the relativistic Compton effect and led to satisfactory agreement with experiment.

It was now pointed out by us[4] that as correct as this argument may be for the case of free electrons (Compton effect), it becomes inapplicable when we are dealing with coherent scattering or the incoherent scattering by bound electrons. It is very clear that in the case of coherent scattering the inverted order of transitions proposed by Dirac is just as forbidden by the exclusion principle as is the original arrangement of terms. The final state to which the electron of negative energy should pass is identical with the initial state, and therefore, occupied. All these matrix elements, therefore, do not exist in scheme II.

While in the case now discussed the difficulty arises primarily from the exclusion principle and only secondarily from the fact that scheme II always leads to a $Z+1$ electron problem, while scheme I is always a Z electron problem, the case is slightly different for the incoherent scattering by bound electrons. All the principal points can here, as well as in the case of coherent

scattering, be understood by an analysis of the one-electron problem (for example, H). Consider, for example, the incoherent scattering in which the electron is transferred from the ground state to the second excited state. Here, it would in principle be possible to invert the scheme I transitions as sketched by Dirac to lead to a scheme II transition. But the difficulty is now of the following nature. In scheme I, we are always dealing with a one-electron problem, while in scheme II the intermediate state would be formed in such a way that we have the hydrogen nucleus surrounded by two electrons, one in the ground state and one in the second excited state. This intermediate state exists only if, most unrealistically, the interaction between the electrons is neglected. Otherwise, essentially only intermediate states with one bound and one excited electron in the continuum can occur. There is, therefore, no identity of the individual matrix elements of scattering for the two schemes, not so much on account of the exclusion principle, but on account of the fact that certain matrix elements exist in the one- but not in the two-electron problem.

It is very clear that this difference in the number of electrons occurring in the intermediate states of positive energy constitutes a fundamental difference between the two schemes, also for all coherent scattering processes. The treatment, according to scheme II, will, therefore, have to take into account not only the exclusion principle, but also the change in the number of electrons; that is, the different effective fields and the eigenfunctions corresponding to them. The principal difficulty of the treatment which, therefore, requires various methods, lies in the fact that this effective field is not a constant; that means that it depends on the different intermediate states. It, therefore, becomes advisable to proceed in the treatment of scheme II in various steps of approximation, isolating the changes between the two schemes. We, therefore, treat first in Sec. IV the changes brought about by the Pauli principle alone, neglecting unrealistically the interaction between the electrons, while later on in the paper we include these interactions and their possible influence on the form factor. We have already pointed out in our first note[4] that any changes between the two schemes can be expected to show themselves, if at all, in the form factor of the scattering amplitude.

It is thus proved that the individual matrix elements of scheme I corresponding to electronic transitions from an occupied state of positive energy to a state of negative energy and back have no counterpart in scheme II, where all matrix elements refer to transitions from occupied states of negative energy to unoccupied states of positive energy and back. The remainder of this paper will now be devoted to an analysis of the question how far the *s u m* over the individual matrix elements, in the absence of their one-to-one correspondence, depends on the use of scheme I or scheme II.

IV. SCATTERING ACCORDING TO SCHEME II. NO ELECTRON INTERACTION

Proceeding by various steps of approximation, we treat in this paragraph the coherent scattering by a nuclear atom (for example, H) under the assumption that interaction between the electrons can be neglected. Furthermore, we drop all terms of the order α^2, k_0^2 or higher. For the electrons in the negative energy states or in the intermediate states of positive energy we now make two different assumptions.

A. The Use of Plane Waves

In this crudest approximation, we allow for interaction only between the nucleus and the bound electron, while treating the electrons in the negative energy states or in their transitions from negative energy states to intermediate states of positive energy, and back, as being perfectly free.

Following the procedure in II, we can again write the total scattering amplitude in the form

$$A_2 = A_2^+ + A_2^- . \tag{4.1}$$

Here, A_2^+ can be neglected for small frequencies ($\alpha^2 mc^2/2 \ll h\nu \ll mc^2$) and can be described by Eq. (2.21) for large frequencies, since the calculation of the positive positive transitions is not influenced, in our approximation, by the electrons in the negative energy states.

A_2^-, on the other hand is now given by the following expression:

$$A_2^- = \sum_A \sum_I \frac{\int \Psi_A^* O \Psi_I \int \Psi_I^* O' \Psi_A}{E_A + k_0 - E_I} + \text{Em-Abs.} \tag{4.2}$$

In the eigenfunctions appearing in Eq. (4.2), the exclusion principle must be taken into account. One is here, strictly, dealing with an infinite number of electrons in the negative energy states, plus one electron in the bound state. Since all electrons are equivalent, it is sufficient to calculate one term in the operator O, which more completely would have to be written as an infinite sum

$$\left.\begin{aligned} O &= O_1 + O_2 + \cdots \\ &= (\boldsymbol{\alpha}_1 \cdot \mathbf{e}_0) e^{-i\mathbf{k}_0 \cdot \mathbf{r}_1} + \cdots , \\ O' &= O_1' + O_2' + \cdots \\ &= (\boldsymbol{\alpha}_1 \cdot \mathbf{e}) e^{-i\mathbf{k} \cdot \mathbf{r}_1} + \cdots . \end{aligned}\right\} \tag{4.3}$$

A similar simplification can be carried out for the eigenfunctions $\Psi_{A,I}$. Since Ψ is antisymmetrical in all the electron coordinates, one can limit the treatment in the present case to eigenfunctions referring to two electrons only. The initial eigenfunction will then read

$$\Psi_A = \tfrac{1}{2}\sqrt{2}[\psi_{E_0}(x_1) U_\epsilon(x_2) - \psi_{E_0}(x_2) U_\epsilon(x_1)], \tag{4.4}$$

where $\epsilon < 0$. The intermediate eigenfunction will be given

by

$$\Psi_I=\tfrac{1}{2}\sqrt{2}[\psi_{E_0}(x_1)U_E(x_2)-\psi_{E_0}(x_2)U_E(x_1)], \quad (4.5)$$

where $E>0$, and the final eigenfunction will agree with the initial eigenfunction. ψ_{E_0} shall denote the eigenfunction of the bound state, while U_ϵ, U_E are plane wave eigenfunctions. A_2^- thus takes on the form

$$A_2^-=\sum_{\epsilon,E}\frac{\int\Psi_A^*O\Psi_I\int\Psi_I^*O'\Psi_A}{\epsilon+k_0-E}+\text{Em-Abs.}, \quad (4.6)$$

where O, O' now contain only two terms.

It should be pointed out that all the eigenfunctions U_ϵ and U_E are mutually orthogonal, while ψ_{E_0} is not strictly orthogonal to any of them; but, according to well-known properties of the Dirac equation,

$$\int\Psi_A^*\Psi_I dV_1dV_2=-(E_0/\epsilon)(E/E_0) \quad (4.7)$$

is always sufficiently small in relation to

$$\int\Psi_{A,I}^*\Psi_{A,I}dV_1dV_2. \quad (4.8)$$

Evaluating now exactly the expression corresponding to Eq. (4.6), we find

$$\left.\begin{aligned}M&=\int\Psi_A^*O\Psi_I dV_1dV_2\\&=(E_0|O|E_0)(\epsilon/E)+(\epsilon|O|E)\\&\quad-(E_0|O|E)(\epsilon/E_0)-(\epsilon|O|E_0)(E_0/E).\end{aligned}\right\} \quad (4.9)$$

According to the orthogonality mentioned, the term containing (ϵ/E) vanishes and the term $(E_0|O|E)(\epsilon/E_0)$ is small. So we find

$$M\cong(\epsilon|O|E)-(\epsilon|O|E_0)(E_0/E) \quad (4.10)$$

and by analogous procedure a similar expression for the second matrix element

$$M'\cong(E|O'|\epsilon)-(E/E_0)(E_0|O'|\epsilon). \quad (4.11)$$

In the product

$$\left.\begin{aligned}MM'\cong&(\epsilon|O|E)(E|O'|\epsilon)\\&+(E_0/E)(E/E_0)(E_0|O|\epsilon)(\epsilon|O|E_0)\\&-(E_0|O'|\epsilon)(\epsilon|O|E)(E/E_0)\\&-(E_0/E)(E|O'|\epsilon)(\epsilon|O|E_0)\end{aligned}\right\} \quad (4.12)$$

the first term vanishes for all angles of scattering except $\vartheta=0$. This δ-function has obviously no physical meaning; its contribution is reabsorbed in the incident beam, and it can be put equal to zero.

Summing now over the expression

$$MM'/(\epsilon+k_0-E), \quad (4.13)$$

we put the denominator $\epsilon+k_0-E\cong-2$, an approximation valid for $h\nu\ll mc^2$. The problem thus reduces to the summation of the remaining three terms of MM' over E,ϵ. Each of these two summations extends within the approximation used over a complete set of wave functions, so that we have

$$\sum_{E>0}(E_0/E)(E/E_0)\cong 1, \quad (4.14)$$

$$\sum_{\epsilon<0}(E_0|O'|\epsilon)(\epsilon|O|E_0)\cong(E_0|O'O|E_0). \quad (4.15)$$

In the sum of MM' over ϵ, E each of the three terms in question thus has the same value apart from the sign, so that we finally obtain

$$\sum_{\epsilon,E}MM'/(\epsilon+k_0-E)\cong\tfrac{1}{2}(E_0|O'O|E_0). \quad (4.16)$$

Interchanging the order of the emission and absorption process and adding the result to Eq. (4.16) gives us again, as in Eq. (2.23)

$$A\cong(e_0\cdot e)\int\psi_{E_0}^*\psi_{E_0}e^{-iq\cdot r}dV. \quad (4.17)$$

The agreement obtained in Eq. (4.17) with Waller's result is exclusively due to the antisymmetrization of the complete wave function. It cannot be called very surprising, since we have deliberately, for the purpose of analysis, neglected electron interaction.

B. Use of Coulomb Eigenfunction

While still neglecting interaction between the electrons, we describe the state of all electrons by coulombian eigenfunctions under the influence of the nuclear charge. We can again obtain expressions in analogy to Eqs. (4.4), (4.5) and proceed with the evaluation as before, leading up to the expression (4.12) for MM', except that now all wave functions in the matrix elements pertain to coulomb states and are, therefore, strictly orthogonal. A_2^- can now be evaluated with some slight difference only as compared with Eq. (4.16). We thus obtain

$$\left.\begin{aligned}A_2^-=&\sum_{\epsilon,E}[(\epsilon|O|E)(E|O'|\epsilon)/(\epsilon+k_0-E)]\\&+\sum_{\epsilon,E}\{(E_0/E)(E/E^1)(E_0|O'|\epsilon)(\epsilon|O|E_0)\\&-(E_0|O'|\epsilon)(\epsilon|O|E)(E/E_0)\\&-(E_0/E)(E|O'|\epsilon)(\epsilon|O|E_0)\}/\epsilon+k_0-E\\&+\text{Em-Abs.}\end{aligned}\right\}. \quad (4.18)$$

In Eq. (4.18), terms of the structure

$$\sum_{\epsilon,E}(\epsilon|O|E)(E|O'|\epsilon)/(\epsilon+k_0-E) \quad (4.19)$$

appear for the first time. They would be present also if we were dealing with a bare nucleus; one could even generalize them by assuming any potential field in the absence of electrons and using the eigenfunctions corresponding to that potential. For the case of a bare nucleus they represent a scattering phenomenon to which attention was first called shortly after the dis-

covery of the pair theory and which has received an approximate treatment by various authors.[6] For small quanta, the value of Eq. (4.19) has been found to be negligibly small indeed, while it must assume very large values for $h\nu \gg mc^2$ and sufficiently small angles of scattering. Estimates in the literature justify our assumption that for moderate values of $h\nu$, Eq. (4.19) can be totally neglected.

We shall, in the future, refer to terms of the structure (4.19) as nuclear terms, without distinguishing the cases of a bare nucleus with a coulomb field or any other constant potential.

The remaining terms in the sum over E in (4.18) now vanish exactly on account of the orthogonality conditions unless $E=E_0$, so one finds Eq. (4.17) for A_2^-. Apart from the nuclear terms which are vanishingly small for $h\nu \ll mc^2$, we have, therefore, again established equivalence between scheme I and scheme II. It has, on the other hand, already become clear that a strict separation in the scattering amplitude of electronic and nuclear terms will, in general, not be feasible if terms of higher order in α^2, k_0^2 are included.

V. DIFFICULTIES OF THE ONE-ELECTRON MODEL TREATMENT

The procedure followed by Waller[3] and also adopted so far in the present paper will now be shown to be not satisfactory if we consider systems with more than one electron. The difficulties appear already in calculations done according to scheme I, although in this case it is sometimes not difficult to justify the approximation used. Analogous calculations according to scheme II, on the other hand, can in general not be carried out on account of mathematical difficulties; this will require the introduction of some new method like that presented in VI.

Turning first to a two-electron problem in scheme I, we want to discuss the scattering of small quanta by, for example, the neutral helium atom; this sufficiently illustrates the essential points. If we write again, as before,

$$A_1 = A_1^+ + A_1^-, \tag{5.1}$$

one can readily verify that for the present case A_1^+ is again negligible compared with A_1^-.

The formal expression for A_1^- is again given by

$$A_1^- = \sum_I \frac{M_{AI}(-k_0)M_{IA}'(k)}{E_A + k_0 - E_I} + \text{Em-Abs.} \tag{5.2}$$

The point of importance is now the exact expression for the eigenfunctions in the intermediate state.

Since we are dealing with a two-electron problem, we have to antisymmetrize the eigenfunctions, and we can in a suitable approximation again assume that the eigenfunctions for the two-electron system are separable into products of eigenfunctions referring to one electron alone. We thus obtain for the eigenfunction of the ground state the expression

$$\Psi_A = \tfrac{1}{2}\sqrt{2}[\psi_{E_1}(x_1)\psi_{E_2}(x_2) - \psi_{E_1}(x_2)\psi_{E_2}(x_1)]. \tag{5.3}$$

Here, ψ_{E_1, E_2} stands for the coulombian eigenfunctions of opposite spin for the ground state corresponding to an effective nuclear charge $Z-s$. It is well known from the study of light elements that such an eigenfunction is a good approximation of the actual conditions if $s \leqq 0.3$.

Similarly, we write for a representative eigenfunction of an intermediate state

$$\Psi_I = \tfrac{1}{2}\sqrt{2}[\psi_{E_0}(x_1)\psi_\epsilon(x_2) - \psi_{E_0}(x_2)\psi_\epsilon(x_1)]. \tag{5.4}$$

Here, ψ_ϵ stands for the coulombian eigenfunction of a free electron of negative energy ϵ under the influence of a nuclear charge $Z-1$, while ψ_{E_0} represents the coulombian eigenfunction of a bound electron with a nuclear charge Z. Attention is now called to the fact that the integral

$$(E_{1,2}/E_0) = \int \psi^*_{E_{1,2}} \psi_{E_0} dV, \tag{5.5}$$

though close to one, is no longer equal to one. If this difference between $\psi_{E_{1,2}}$ and ψ_0 is kept in mind, then a direct transfer of the previously used methods to the two-electron problem would lead to a change in the scattering cross section by the factor $(E_1/E_0)^4$. This can immediately be verified by following through the previous calculations leading to A_1^- if we sum over all intermediate states of negative energy but let—erroneously—the second electron always occupy the ground state of the He^+ ion. Correctly, what should be done is a summation over all possible intermediate states, which include excited states of positive energy of the second electron. Written in detail, M_{AI} takes on the form

$$\begin{aligned} M_{AI} = {} & (E_2|O|\epsilon)(E_1/E_0) - (E_1|O|\epsilon)(E_2/E_c) \\ & + (E_1|O|E_0)(E_2/\epsilon) - (E_2|O|E_0)(E_1/\epsilon) \end{aligned} \tag{5.6}$$

with a similar expression for M'. Dropping now small terms of the form $(E_1|O|E_0)(E_2/\epsilon)$ and summing first over ϵ, we find

$$\left.\begin{aligned} & \sum_\epsilon MM'/D \\ & \leqq \sum_\epsilon \{(E_0/E_1)(E_1/E_0)(E_2|O|\epsilon)(\epsilon|O'|E_2) \\ & \quad + (E_0/E_2)(E_2/E_0)(E_1|O|\epsilon)(\epsilon|O'|E_1)\}/ \\ & \qquad [E_1 + E_2 + k_0 - (E_0 + \epsilon)] \end{aligned}\right\}, \tag{5.7}$$

or

$$\left.\begin{aligned} & \sum MM'/D \leqq |(E_0/E_2)(E_2/E_0)(E_1|OO'|E_1) \\ & \quad + (E_0/E_1)(E_1/E_0)(E_2|OO'|E_2)\}/ \\ & \qquad (E_1 + E_2 + k_0) \end{aligned}\right\}, \tag{5.8}$$

where, in the sum over ϵ we have set $E_0 + \epsilon \leqq 0$. Now, the

[6] M. Delbrueck, Z. Physik **84**, 144 (1933); N. Kemmer, Helv. Phys. beta **10**, 112 (1937); A. Achieser and T. Pomerantschuk, Physik Z. Sowjetunion **11**, 478 (1937); R. Gluckstern and F. Rohrlich, Phys. Rev. **83**, 218 (1951).

sum over the matrix elements

$$\sum_{E_1>0}(E_0/E_1)(E_1/E_0) = \sum_{E_2>0}(E_0/E_2)(E_2/E_0) \cong 1 \quad (5.9)$$

up to terms of the order α^2, as we have already utilized before in IV. The calculation from here on follows exactly the scheme indicated by Waller and will lead again, after putting the energy denominator $E_1+E_2+k_0 \cong 2$ and adding the emission-absorption terms, to

$$A_1 = (\mathbf{e}_0\cdot\mathbf{e})\left[\int \psi_{E_1}^*\psi_{E_1}e^{-i\mathbf{q}\cdot\mathbf{r}}dV + \int \psi_{E_2}^*\psi_{E_2}e^{-i\mathbf{q}\cdot\mathbf{r}}dV\right]. \quad (5.10)$$

This expression (5.10) constitutes a generalization of the Waller formula for the two-electron case.

It is obvious that in the case of scheme II the various excited states of positive energy have similarly to be taken into account. But a straightforward procedure on this basis does not seem to be practical. Consider, for example, the case of the Li^+ ion, where all intermediate states contain three electrons of positive energy. The various excited states do not permit any longer a description utilizing one and the same potential energy; one has to take into explicit account the interaction energy between the electrons and is, therefore, unable to give simple, complete expressions for the matrix elements which describe the transitions to the intermediate states. We have, for example, carried out calculations with an approximate potential constructed in analogy with the Heisenberg potential used in the calculation of excited He terms. We refrain from reproducing these calculations here in any detail, since they clearly show that residual differential effects depending upon the form of the potential for the excited states will be obtained. Since the method developed in VI shows that these differential effects between scheme I and scheme II are, for small values of $h\nu$, not existant, we refrain from a reproduction of these approximate calculations. The whole discussion is here only presented to illustrate the incompleteness of a method which is based on the use of a one-electron model in a constant average potential field.

The difficulties become even more obvious, and in our opinion insoluble, for the simple model-theory if one attempts to study inelastic scattering processes, e.g., the scattering accompanying the transition of a hydrogenic electron from the ground state to some excited state. There does not exist any intermediate state in which the hydrogen nucleus would be capable of binding two electrons, one of them excited, and therefore, no one-electron model procedure is feasible in scheme II. Cases of this type, which require the consideration of all possible states of a two-electron system, can only be calculated with the use of a general method of the kind presented in the following paragraph.

VI. A GENERAL METHOD FOR THE TREATMENT OF THE SCATTERING OF MODERATELY LARGE QUANTA

The case of coherent or incoherent scattering of quanta with $h\nu \ll mc^2$ will now be treated for both schemes with a general method that makes it possible to overcome the various difficulties discussed in the preceding paragraphs. We shall primarily limit the explicit discussion to the scattering by hydrogen; the method permits extension to many-electron problems, but no explicit presentation is given in this paper for reasons of economy of space and also because the generalization, carried out by us, follows well-marked lines.

Obviously, we have again

$$A_1^+ = A_2^+ \quad (6.1)$$

and so want to study first the expression for A_1^- which takes on the form

$$A_1^- = \sum_{\epsilon<0}\frac{MM'}{E_0+k_0-\epsilon} + \text{Em-Abs.} \quad (6.2)$$

Since we include inelastic scattering, the final state may now in general differ from the initial state. We expand the energy denominator

$$\frac{1}{D} = \frac{1}{E_0+k_0-\epsilon} \cong \frac{1}{2+k_0}\left(1+\frac{\epsilon+2-E_0}{2+k_0}+\cdots\right) \quad (6.3)$$

under the assumption that $|\epsilon+2-E_0| \ll 1$. The summation over $\epsilon<0$ can now be extended over a complete set of hydrogenic states by adding and subtracting the summation over $\epsilon>0$. In this way, the absorption-emission part of A_1^- takes on the form

$$\sum_{\epsilon<0}\frac{MM'}{D} \cong \sum_{\epsilon<0}\frac{MM'}{2+k_0}\left(1+\frac{\epsilon+2-E_0}{2}\right) \quad (6.4)$$

$$\cong \frac{1}{2+k_0}\int \psi_0^* O \times\left(1+\frac{H+2-E_0}{2}\right)O'\psi_1 dV - \sum_{E>0}\frac{MM'}{2+k_0}\left(1+\frac{E+2-E_0}{2}\right). \quad (6.5)$$

We have here replaced ϵ by the Hamiltonian in the second part of (6.3). It is, furthermore, clear that we had to place the operator H after the first operator O, making it act on ψ_ϵ so as to obtain the proper factor in (6.4). In (6.5) the terms which have to be summed over $E>0$ are, as shown before, small of second order due to the properties of the Dirac matrices contained in them; it is, therefore, only consistent to neglect k_0 in the denominator, and, equally, to put $E+2-E_0$ equal to 2. We now add the emission-absorption terms which

are to be treated similarly, remembering that $E_0+k_0=E_1+k$, and thus finally obtain

$$\left.\begin{aligned} A_1^- \cong & \frac{1}{2+k_0}\int\psi_0^* O\left(1+\frac{H+2-E_0}{2}\right)O'\psi_1 dV \\ & +\frac{1}{2-k_0}\int\psi_0^* O'\left(1+\frac{H+2-E_1}{2}\right)O\psi_1 dV \\ & -\sum_{E>0}\left\{\int\psi_0^* O\psi_E dV\int\psi_E^* O'\psi_1 dV\right. \\ & \left.+\int\psi_0^* O'\psi_E dV\int\psi_E^* O\psi_1 dV\right\} \end{aligned}\right\} \quad (6.6)$$

The later comparison with A_2^- makes it advisable to rewrite the first two terms in (6.6). Introducing a commutator

$$C'=HO'-O'H, \quad (6.7)$$

we obtain by elementary matrix algebra

$$O[1+\tfrac{1}{2}(H+2-E_0)]O'=2OO'-\tfrac{1}{2}CO' \quad (6.8)$$

and, similarly

$$O'[1+\tfrac{1}{2}(H+2-E_1)]O=2O'O+\tfrac{1}{2}O'C \quad (6.9)$$

so that the expression for A_1^- may now be put into the form

$$\left.\begin{aligned} A_1^- \cong & (2+k_0)^{-1}\int\psi_0^*(2OO'-\tfrac{1}{2}CO')\psi_1 dV \\ & +(2-k_0)^{-1}\int\psi_0^*(2O'O+\tfrac{1}{2}O'C)\psi_1 dV \\ & -\textstyle\sum_{E>0}\{M_{E_0E}M'_{EE_1}+M'_{E_0E}M_{EE_1}\} \end{aligned}\right\} \quad (6.10)$$

In calculating

$$A_2^-=\sum_{A,I}\frac{M_{AI}M_{IF}'}{E_A+k_0-E_I}+\text{Em-Abs.} \quad (6.11)$$

with an analogous method, we have to observe several differences from scheme I which have their origin in the fact that we now deal with a two-electron problem. The essential advantage of the method consists, of course, as will be seen, in the fact that we do not require an explicit knowledge of Ψ_I. We can again limit ourselves as far as antisymmetrization is concerned to the consideration of two electrons. We shall assume that the initial energy E_A as well as the expression E_I-2 shall both be small of the second order. This assumption is not quite as obvious as an analogous assumption made in scheme I and will be discussed below. We can then expand the energy denominator as follows

$$\frac{1}{D}=\frac{1}{E_A+k_0-E_I} \cong \frac{1}{-2+k_0}\left(1+\frac{2+E_A-E_I}{2}+\cdots\right). \quad (6.12)$$

The summation over intermediate states in (6.11) is meant to extend over all states in which two electrons occupy states of positive energy, while all other electrons occupy states of negative energy. If we now extend the summation over a complete set of Ψ_I, we have added to the allowed intermediate states those in which one electron has a positive energy and all others a negative energy, as well as all those states in which more than two electrons have positive energy. The second addition is insignificant because the matrix elements are all of smaller order of magnitude. The first addition, on the other hand, must be corrected for, because it refers apart from the energy denominator, to intermediate states which are already taken into account in $A^+_{1,2}$. We can, therefore, write the absorption-emission part of A_2^- in the following form:

$$\left.\begin{aligned} \sum_{A,I}\frac{MM'}{D} \cong & \frac{1}{-2+k_0}\sum_A\int\Psi_A^* O \\ & \times\left(1+\frac{2+E_A-H}{2}\right)O'\Psi_F dV_1 dV_2 \\ & -\sum{}'\frac{1}{-2+k_0}M_{AI}M'_{IF} \\ & \times\left(1+\frac{2+E_A-E_I}{2}\right) \end{aligned}\right\} \quad (6.13)$$

In $\sum'$ the prime indicates that the summation is to be extended over all excited states of positive energy, leaving all states of negative energy fully occupied.

In the last sum, $E_I=\epsilon+E$, so that we have $E_A-E_I=E_0-E$. This is small and may, therefore, be neglected, since, as before, the expressions for M and M' are small. We thus arrive at the following expression for

$$\left.\begin{aligned} \sum\frac{MM'}{D} \cong & \frac{1}{-2+k_0}\sum_A\int\Psi_A^* O \\ & \times\left(1+\frac{2+E_A-H}{2}\right)O'\Psi_F dV_1 dV_2 \\ & +\sum_{E>0}MM' \end{aligned}\right\} \quad (6.14)$$

Apart from the difference in sign, we observe that the sum over $E>0$ is the same as in (6.5) of scheme I.

The assumption leading to (6.12) will now be dis-

cussed more closely. It is, strictly speaking, not justified to assume that E_A and E_I-2 are both small of second order in the transitions considered. So, for example, the assumption turns out to be wrong if the electron in the negative energy states has originally an energy the absolute value of which is very large compared to mc^2. Since we have to sum over all negative energy states, we will encounter an infinity of such electrons. A similar remark could be made with respect to E_I-2.

Nevertheless, for small quanta the assumption still seems to be quite justified. Transitions in which such electrons with exceptionally large energies are involved contribute only to the modified nuclear terms which are assumed to be very small. We can, therefore, be sure that the error introduced is of no significance.

We obtain the complete expression for A_2^- by adding, as before, the similarly treated emission-absorption terms. Before doing this, however, we proceed as follows:

To compare A_1^- and A_2^-, we must evaluate the spur in (6.14). We can write

$$(E_F-H)O'=O'H-HO'. \tag{6.15}$$

Now the Hamiltonian H can be written in the form

$$H=H_1+H_2+V_{12}. \tag{6.16}$$

Here the interaction with the nuclear field is contained in H_1 and H_2, while V_{12} refers to the electronic interaction. The symmetrical part played by all the electrons clearly shows that

$$\begin{aligned} O'H-HO'&=2(O_1'H_1-H_1O_1')\\ &=-2C_1', \end{aligned} \tag{6.17}$$

where C_1' is defined similarly as in (6.7) by the relation

$$C_1'=H_1O_1'-O_1'H_1. \tag{6.18}$$

We can thus write for

$$\sum\frac{MM'}{D}\cong\frac{1}{-2+k_0}\sum_A\int\Psi_A^*O\cdot 2\left[O_1'+\frac{(2+E_0-E_1)O_1'-C_1'}{2}\right]\Psi_F+\sum_{E>0}MM'\Bigg\}, \tag{6.19}$$

and introduce the abbreviation

$$P_1'=O_1'+\tfrac{1}{2}[(2+E_0-E_1)O_1'-C_1']. \tag{6.20}$$

Recalling that

$$O_1'=(\boldsymbol{\alpha}_1\cdot\mathbf{e})e^{i\mathbf{k}\cdot\mathbf{r}_1} \tag{6.21}$$

we note that P_1' contains O', i.e., one Dirac matrix in each term.

We now introduce explicit expressions for Ψ_A and Ψ_F. It is assumed that the wave function is separable in the coordinates of the atomic electron and of the electron in the negative energy state

$$\Psi_A=\tfrac{1}{2}\sqrt{2}[\psi_0(x_1)U_\epsilon(x_2)-\psi_0(x_2)U_\epsilon(x_1)], \tag{6.22}$$

$$\Psi_F=\tfrac{1}{2}\sqrt{2}[\psi_1(x_1)U_\epsilon(x_2)-\psi_1(x_2)U_\epsilon(x_1)]. \tag{6.23}$$

Here ψ_0 and ψ_1 are hydrogenic functions for the initial and final states, respectively, while U_ϵ is an appropriately screened eigenfunction of negative energy. One then obtains

$$\begin{aligned}&\int\Psi_A^*O2P_1'\Psi_F dV_1dV_2\\ &=(E_0|OP'|E_1)+(E_0/E_1)(\epsilon|OP'|\epsilon)\\ &+(E_0|P'|E_1)(\epsilon|O|\epsilon)+(E_0|O|E_1)(\epsilon|P'|\epsilon)\\ &-(E_0|OP'|\epsilon)(\epsilon/E_1)-(E_0/\epsilon)(\epsilon|OP'|E_1)\\ &-(E_0|P'|\epsilon)(\epsilon|O|E_1)-(E_0|O|\epsilon)(\epsilon|P'|E_1)\end{aligned}\Bigg\}. \tag{6.24}$$

Of the eight terms appearing on the right side of (6.24), only three are found to be significant for the coherent case $E_1=E_0$. The second term here corresponds to the nuclear terms discussed in IV and is again neglected for moderate $h\nu$. In the incoherent case, this term vanishes on account of the orthogonality $(E_0/E_1)=0$. The third and fourth terms are exchange terms which vanish in the coherent case on account of the property of the Dirac matrices in stationary states, while in the inelastic case, one term vanishes and the other becomes small of the fourth order. The fifth and sixth terms are also small of at least fourth order due to the approximate orthogonality of U_ϵ and $\psi_{0,1}$, combined with the properties of the Dirac matrix elements connecting states of opposite sign of energy. This can perhaps be illustrated by looking at the largest term in OP' for parallel polarization, which will be of the order one. Thus the fifth term becomes of the order

$$(E_0/\epsilon)(\epsilon/E_{0,1})\lesssim\text{4th order}. \tag{6.25}$$

In this way, one eventually finds

$$\begin{aligned}&\int\Psi_A^*O2P_1'\Psi_F dV_1dV_2\cong(E_0|OP'|E_1)\\ &-(E_0|P'|\epsilon)(\epsilon|O|E_1)-(E_0|O|\epsilon)(\epsilon|P'|E_1).\end{aligned} \tag{6.26}$$

To sum (6.26) over all screened states U_ϵ, $\epsilon<0$, we extend the sum over a complete set including all $\epsilon>0$ and subtract the (small) part for $\epsilon>0$.

$$\begin{aligned}\sum_A\int\Psi_A^*O2P_1'\Psi_F dV_1dV_2\cong&-(E_0|P'O|E_1)\\ &+\sum_{E>0}\{(E_0|P'|E)(E|O|E_1)\\ &+(E_0|O|E)(E|P'|E_1)\}_S.\end{aligned} \tag{6.27}$$

In (6.27), the subscript S indicates that the wave functions U_E differ from those of energy E in (6.6) by virtue of the screening.

Now $\sum_{E>0}$ in (6.27) can be simplified. Since all terms in this sum are already small of second order on account of the properties of the Dirac matrices, we may neglect in the expression P' appearing in them the term E_0-E_1 and simply put

$$P'=2O'-C'/2 \tag{6.28}$$

instead of (6.20). Now, since

$$(E_0|C'|E_1)=(1/i)(E_0|\dot{O}'|E_1) \tag{6.29}$$

$$=(E_0-E_1)(E_0|O'|E_1), \tag{6.30}$$

it is clear that all these terms will be not larger than of fourth order and may be dropped. Furthermore, we have

$$\left.\begin{aligned}(E_0|P'|E)(E|O|E_1)&\cong 2(E_0|O'|E)(E|O|E_1)\\&\cong 2M'_{E_0E}M_{EE_1}\end{aligned}\right\}, \tag{6.31}$$

and so obtain

$$\left.\begin{aligned}\sum_A\int\Psi_A^*O2P_1'\Psi_F dV_1dV\cong&-(E_0|P'O|E_1)\\&+2\textstyle\sum_{E>0}(M_{E_0E}M'_{EE_1}+M'_{E_0E}M_{EE_1})_S\end{aligned}\right\}. \tag{6.32}$$

To complete the comparison of A_1^- and A_1^-, we now have to examine the term

$$(E_0|P'O|E_1) \tag{6.33}$$

Here, the second-order terms in P' must be retained. It is now possible to write out the complete expression for A_2^- combining (6.11), (6.19) and (6.32) and including both sequences of emission and absorption processes

$$\left.\begin{aligned}A_2^-\cong&(2+k_0)^{-1}\int\psi_0^*(2O'-\tfrac{1}{2}CO')\psi_1dV\\&+(2-k_0)^{-1}\int\psi_0^*(2O'O+\tfrac{1}{2}O'C)\psi_1dV\\&+\textstyle\sum_{E>0}(M_{E_0E}M'_{EE_1}+M'_{E_0E}M_{EE_1})\\&-2\textstyle\sum_{E>0}(M_{E_0E}M'_{EE_1}+M'_{E_0E}M_{EE_1})_S\end{aligned}\right\}. \tag{6.34}$$

The results (6.6) and (6.34) for A_1^- and A_2^- appear to differ in the terms $\sum_{E>0}$, but these terms are already small of the second order and their difference is only due to differences in the screening of the wave functions which makes it appear that A_1^- and A_2^- will differ only by terms that are smaller than α^2 or k_0^2 from each other.

VII. THE SCATTERING OF HARD QUANTA ACCORDING TO SCHEME II

The theoretical treatment according to scheme II of the scattering of quanta $h\nu\gg mc^2$ encounters various difficulties by which we were forced to limit ourselves in this paper to the discussion of some important special cases and of some qualitative differences between schemes I and II.

No scheme analogous to the procedure in VI could be devised for the scattering of very hard quanta; this is due to the fact that simplified expressions for the energy denominator like those used in (6.12) are no longer valid in the case of large quanta. One cannot, therefore, use the general methods of summing over complete sets which form the basis of the procedure in VI.

We proceed, therefore, with the treatment on the basis of a model, keeping well in mind the unsatisfactory features of such an attempt which have been discussed before. We treat here, for purposes of illustration, the scattering by a hydrogen atom. The antisymmetrization, as discussed in IV, has then again to be extended to two electrons only; there is, furthermore, no difference in the calculation of A_1^+ and A_2^+ as given in II.

The eigenfunctions for the initial and intermediate states which have to be used for the purpose of calculating A_2^- can then be written

$$\Psi_A\cong\tfrac{1}{2}\sqrt{2}[\psi_{E_0}(x_1)U_\epsilon(x_2)-\psi_{E_0}(x_2)U_\epsilon(x_1)], \tag{7.1}$$

$$\Psi_I\cong\tfrac{1}{2}\sqrt{2}[\psi_{E_0}(x_1)U_E(x_2)-\psi_{E_0}(x_2)U_E(x_1)]. \tag{7.2}$$

In (7.1, 2), the symbol ψ_{E_0} denotes the coulombian eigenfunction of the electron in its ground state. U_ϵ and U_E form together a complete orthogonal system of eigenfunctions of negative and positive energy, respectively, originating from some suitable potential which takes into account the effect of the nucleus as well as that of the electron in the ground state.

For A_2^- we then write in complete analogy to earlier discussions in II and IV.

$$A_2^-\cong\sum_A\sum_I\frac{M_{AI}M_{IA}'}{E_A+k_0-E_I}+\text{Em-Abs}, \tag{7.3}$$

where

$$E_A=E_0+\epsilon,\quad E_I=E_0+E.$$

Introducing the explicit expressions M, M' for the operators (4.3), we now find for M_{AI} the following expression

$$\begin{aligned}M_{AI}=&(E_0|O|E_0)(\epsilon/E)+(\epsilon|O|E)\\&-(E_0|O|E)(\epsilon/E_0)-(\epsilon|O|E_0)(E_0/E),\end{aligned} \tag{7.4}$$

which consists of four terms. The first of these terms is obviously zero.

Constructing a similar expression for M_{IA}' and carrying out the multiplication, we arrive at the following expression for MM'

$$\left.\begin{aligned}MM'\cong&(\epsilon|O|E)(E|O'|\epsilon)\\&+(E_0/E)^2(E_0|O'|\epsilon)(\epsilon|O|E_0)\\&-(E_0|O'|\epsilon)(\epsilon|O|E)(E/E_0)\\&-(E_0/E)(E|O'|\epsilon)(\epsilon|O|E_0)\\&+(E_0|O|E)[(E|O'|\epsilon)\\&-(E/E_0)(E_0|O'|\epsilon)](\epsilon/E_0)\\&+(E_0/\epsilon)[(\epsilon|O|E)\\&-(\epsilon|O|E_0)(E_0/E)](E|O'|E_0)\\&+(E_0/\epsilon)(\epsilon/E_0)(E_0|O|E)(E|O'|E_0)\end{aligned}\right\}. \tag{7.5}$$

MM' consists of nine terms, which will now be discussed for two special cases.

a. Scattering into Sufficiently Small Angles

The first term in (7.5) represents the well-known modified nuclear scattering. In the case of very large quanta, the differential scattering cross section due to it alone becomes rather large in the forward direction and can no longer be neglected compared with the ordinary electron scattering.

The following three terms all carry factors of the form (E_0/E). These Fourier coefficients of the eigenfunction describing the ground state, expanded into eigenfunctions which are very similar to plane waves have a sizeable value only for values of E with a momentum which is comparable to αmc. One can now show easily that for sufficiently small angles which will soon be defined more quantitatively these three terms are of the same order of magnitude and are all complete analogs of the generalized Waller terms discussed in II. We illustrate this statement by a simple discussion of the second of these three terms. The same discussion can be almost literally transposed to the other two terms mentioned.

Since (E/E_0) is of the order one only if p_E is of the order α, we have thereby a defined range for E; the same argument, therefore, leads to a range for ϵ which lies in momentum space in the range of $-\mathbf{k}+O(\alpha)$. But the remaining factor in this term, $(\epsilon|O|E)$, will be of order one also only if the range of $\mathbf{p}_E$ overlaps through action of the operator O with the range of $O(\mathbf{k}_0+\mathbf{p}_E)$. This requires, therefore, that

$$\mathbf{p}_E\sim\mathbf{k}_0+\mathbf{p}_\epsilon\sim\mathbf{k}_0-\mathbf{k}\sim O(\alpha). \tag{7.6}$$

If we study the scattering into angles satisfying the condition $|\mathbf{k}_0-\mathbf{k}|\simeq k_0\theta\lesssim\alpha$, the matrix element here discussed will have its maximum value and take on the form of the generalized Waller matrix element given in II; summation over all values of ϵ, E makes this term equal to

$$\left.\begin{aligned}\sum_{\epsilon,E}\frac{-(E_0|O'|\epsilon)(\epsilon|O|E)(E/E_0)}{\epsilon+k_0-E}\\ \simeq\sum_{\epsilon<0}\frac{-(E_0|O'|\epsilon)(\epsilon|O|E_0)}{\epsilon+k_0-1}\\ \cong(E_0|O'O|E_0)\end{aligned}\right\}. \tag{7.7}$$

As mentioned before, the same argument holds true for the other terms containing the factor (E/E_0). We have thus rederived the scattering formula presented in II.

Obviously, for this small angle scattering, the remaining five terms in (7.5) are small, since all of them carry a very small factor (E_0/ϵ). One can, therefore, summarize that for sufficiently small angles the scattering amplitude A_2^- of hard quanta is composed by a superposition of the amplitudes arising from the modified nuclear term and that given in II.

b. Scattering into Large Angles

In this second case, no quantitative discussion is attempted. We know from II that for large angles the form factor of the scattering according to scheme I becomes proportional to a high power of α/k_0. It, therefore, is no longer permissible to neglect terms which are perhaps of the order α^2 in the general formula, since the end result is obtained only by a large size cancellation of the various contributions. One can similarly see quite easily that the three terms carrying factors (E_0/E) which were the leading terms in the case of small angle scattering are no longer equal to each other. The remaining five terms in the expression (7.5) can be calculated only with difficulty, and cannot *a priori* be considered to be small compared to those terms retained in the case of small angle scattering. One must, therefore, be prepared to find as a result of a calculation left to later endeavors that the wide angle scattering of hard radiation differs considerably from the result suggested by II and may not in general be representable as a simple superposition of generalized Waller terms and modified nuclear terms.

VIII. GENERAL DISCUSSION

We may now perhaps summarize the main results of this investigation. It was proved that up to orders of α^2, k_0^2 the cross section for elastic and inelastic scattering of small quanta is the same in both schemes. The problem of the scattering of hard quanta is in a much less satisfactory state. While it was comparatively easy to extend the treatment for the case of scheme I, we had to limit ourselves to the not quite satisfactory method of a model for scheme II and were unable to transpose the general method used for small quanta. Furthermore, the appearance of modified nuclear terms affects the results appreciably and does not allow us to make, in the present state of the theory, a reliable prediction of the scattering under sufficiently large angles.

There are several points of contact between the paper[5] of Furry's and the present analysis. As to the formalism applied, Furry used recently-developed methods which guarantee the avoidance of divergence difficulties. We did not find it necessary to do so, since in the approximation used we encountered only one divergence, namely the δ function in IV, which obviously has to be put equal to zero.

In contrast to the present paper Furry has treated the transitions of the electron from the negative to the positive intermediate state and back as a one-electron problem under the influence of a constant potential somewhat analogous to the procedure in IVb. We believe to have proved that such a treatment is not satisfactory and is incomplete. The example of inelastic scattering by the H atom shows without calculation how necessary

it is to abandon the simplified concepts and use a general method as introduced by us in VI. We are not certain if Furry wants his results to apply to the scattering of very hard quanta; if this is the case then there exist basic differences with the content of VII.

We want to express the hope that later investigations of a deeper-reaching mathematical nature will lead not only to a formulation as given here, but also to a computation of the differences in the two schemes and thereby present opportunities for an experimental decision between the two forms of the theory, which in our opinion will doubtless show the validity of scheme II.

PHYSICAL REVIEW VOLUME 84, NUMBER 5 DECEMBER 1, 1951

Reversibility of Quantum Electrodynamics

SATOSI WATANABE
Wayne University, Detroit, Michigan
(Received May 23, 1951)

The aim of this paper is to re-establish the reversibility of classical electrodynamics in terms of the "expectation values" given by quantum electrodynamics. The reversibility requirement combined with the charge conjugation necessitates that charged fields should obey certain types of statistics. However, the reversibility requirement as such does not determine the statistics, showing that it is the requirement of charge-invariance that has the power to determine the statistics of charged fields. A new interpretation will be given to the old problem concerning the conflict of electromagnetic reversibility *versus* "retarded" potential. Four different kinds of tensors, four different kinds of spinors (pseudospinors), bi-spinors (eight-component spinors) and bi-tensors are introduced as useful representation vectors of the entire congruent group including spatial and temporal inversions.

I. INTRODUCTION

IN connection with the proof that phenomenological irreversibility originates essentially from the process of observation, it seemed to the present author to be of importance to ascertain the complete time-reversibility of quantum mechanics. In an earlier paper,[1] reversibility of the Dirac equation was demonstrated in its one-particle interpretation, and the behavior of the spin, electric moment and magnetic moment of the electron in the "reversed" motion was examined in detail. Then, the reversibility of quantum electrodynamics was proved in the frame-work of Dirac's many-time theory.[2] It was thereafter noticed that the same method can be applied to the theory in which the electron field also is quantized if a correct treatment of charge conjugation is introduced.[3] In all these considerations, it was observed that commutation relations of the field quantities, under certain assumptions, played important roles in the proof of reversibility.

Now that many authors are interested in the problem of necessary general forms of commutation relations, it may be of some interest to publish a summary of the results hitherto obtained by the author, clarifying the relationship between reversibility and commutation relations. In the meantime, Schwinger is reported to have used in his lectures a similar consideration to deduce the commutation relations from the requirement of reversibility.[4] However, since his method as well as his conclusion seems to be at variance with those of the present author, perhaps they may justifiably be presented here.

Against a formal requirement of reversibility objections are often raised to the effect that we can never reverse the direction of time in our actual experience. However, we can formulate the "reversibility" in such a manner that it does not involve any hypothetical inversion of time.

The reversibility of classical point mechanics can be expressed in the following way. Let us call two states of a mechanical system mutually reversed states if particles have the same positions and the opposite velocities. Then the reversibility of mechanics means that, if a mechanical system, which was in the state S_1 at the initial instant ($t=0$), finds itself in the state S_2 at the final instant ($t=t_1$), then the fundamental laws allow for another solution representing the similar system which was in the reversed state of S_2 at the initial instant ($t=0$) and which finds itself in the reversed state of S_1 at the final instant ($t=t_1$).

To extend this notion of reversibility to electrodynamics, we need only to add to the definition of reversed states the condition that the electric field has the same value and the magnetic field has the same absolute value but opposite sign. Then the above statement of reversibility holds again in the Maxwellian theory.

It is to be noted that this concept of reversibility does not invoke any fictional time-reversal. Also, as far as

[1] S. Watanabe, *Le Deuxième Théorème de la Thermodynamique et la Mécanique Ondulatoire* (Hermann et Cie, Paris, 1935).
[2] S. Watanabe, Sci. Pap. Inst. Phys. Chem. Research (Tokyo) 31, 109 (1937).
[3] Unpublished.
[4] Lectures by J. Schwinger, notes taken by M. L. Goldberger.

Newton's laws and the Maxwell equations are correct, this reversibility is guaranteed by their mathematical structure.

Now the Maxwell equations have, other than their Lorentz invariance, a trivial invariance under charge conjugation. Namely, the simultaneous change of signs of the electromagnetic field quantities and change of signs of the sources leave the equations unchanged. In virtue of this charge invariance, we can modify the definition of reversed states in the following way. In the reversed states, particles of opposite charges are performing the reversed motion, the magnetic field has the same value and the electric field has the same absolute value but opposite sign. Then the reversibility with this modified definition holds also insofar as the Maxwell equations are true. Physically, this modified standpoint corresponds to a combination of charge conjugation and reversal of motion.

Now we require that quantum electrodynamics should provide this classical reversibility in the "expectation values" of the physical quantities concerned. More precisely, two state-functions Ψ and Ψ' are said to represent mutually reversed states if the expectation values of the physical quantities in the states Ψ and Ψ' satisfy the classical definitions of reversed states. Then our requirement is that, if a physical system which was in the state Ψ_1 at the initial instant ($t=0$) develops with time according to the Schroedinger equation and becomes Ψ_2 at the final instant ($t=t_1$), then the similar system which is in the reversed state Ψ'_2 of Ψ_2 at the initial instant ($t=0$) should become the reversed state Ψ'_1 of Ψ at the final instant ($t=t_1$).

It will be shown that this condition can be restated as follows: the probability of finding the physical system which was in the state Ψ_A at the initial instant in the state Ψ_B at the final instant is equal to the probability of finding the system which was in the reversed state of Ψ_B at the initial instant in the reversed state of Ψ_A at the final instant, where Ψ_A and Ψ_B are arbitrary states.

Here again, attention is drawn to the fact that our conception of reversibility does not imply any hypothetical inversion of time.

Our analysis will show that if we use the "modified" definition of reversed states, the reversibility requirement in quantum electrodynamics can be satisfied only if the charged field quantities are assumed to obey certain types of commutation rules. But if we translate the original definition of reversed states in the quantum theory, the reversibility requirement does not determine the commutation rules. This shows, in its physical implications, that it is not reversibility but charge conjugation that has the power of determining the commutation relations of the charged field quantities.

It is interesting to notice that if we consider the reversibility from a purely formalistic point of view, i.e., if we search for the simplest transformation that keeps the mathematical expressions covariant for the time-reversal, we hit upon a transformation which corresponds to the "modified" definition of reversibility. This, of course, does not preclude the original definition of reversed states from being mathematically formulated.

One may raise an objection to the theory already sketched and contend that the classical electrodynamics is not reversible, because we have always to choose only the "retarded" solution out of the possible solutions. To answer to this question, we shall show, in Sec. IX, that the reversible quantum electrodynamics indeed gives one-half the retarded potential plus one-half the advanced potential; however, that in spite of this formal symmetry of past and future, this advanced potential refers to the mathematically constructed future and can be transformed into the retarded potential, thus leading to a full retarded potential. This expression in terms of full retarded potential is the only permissible one, if we admit as a postulate that any physical law should be formulated in the form of a prediction based on a past observation.

As a matter of fact, in classical electrodynamics, the dismissal of advanced potential cannot be logically reconciled with the basic reversibility except by resorting to a statistical assumption of some kind.[5] In contrast to this, in quantum electrodynamics, the reduction of advanced potential to the retarded potential, and therefore the elimination of the former, can be done on a very general basis, see Sec. IX.

This situation presents an instructive parallelism to the problem of entropy increase. In classical physics, decrease of entropy can happen, seldom as it may be, while, in quantum physics, increase of (microscopically defined) entropy by the act of observation is definitive.

Our understanding of these problems can then be summarized in the statement that the fundamental laws *per se* are completely reversible, while the irreversible phenomena appear as the result of the particular nature of our human cognition. In classical physics, this conflict between basic reversibility and phenomenological irreversibility cannot easily be clarified, because the physical quantities (and the state) are, in this theory, taken for "reality" rather than for "potentiality," i.e., mathematical instruments to correlate one observation to another observation. Indeed, reversibility in quantum physics pertains to this "potentiality."

Section II of this paper will give a c-number lagrangian formalism of electromagnetic interaction, which is completely covariant for any congruent transformation including time-reversal. This c-number theory will also help understand the mathematical gist of the time-reversible q-number theory, which is developed in the following sections. In the q-number theory of reversibility, a unitary operator R, introduced previously by the author under the name of reversion operator,[2] will play a central role: This paper is essentially a study of the nature of this reversion operator.

[5] See for instance, J. A. Wheeler and R. P. Feynman, Revs. Modern Phys. **17**, 157 (1945).

The customary tensor- and spinor-analysis are very inadequate for a problem like the present one. The mathematical instrumentalities introduced in this paper are believed to prove useful for many other problems involving spatial and temporal inversions. For this reason, they are explained in some detail in the Appendix. Those who want to use spinors in a 5-dimensional space will also find our definition of spinors particularly convenient.

II. COVARIANT FORMULATION OF ELECTROMAGNETIC INTERACTION

We consider the electromagnetic field a^μ interacting with the electric current generated by a spinor field ψ and a complex scalar (or pseudoscalar) field u. The ordinary lagrangian density $\mathfrak{L}$ can be written in the form:

$$\mathfrak{L}=\mathfrak{L}_1+\mathfrak{L}_2+\mathfrak{L}_3+\mathfrak{L}_{12}+\mathfrak{L}_{13}, \tag{2.1}$$

with

$$\left.\begin{aligned}
&\mathfrak{L}_1(a)=-(1/2)(\partial a_\mu/\partial x_\nu)(\partial a^\mu/\partial x^\nu),\\
&\mathfrak{L}_2(u)=-(\partial\bar u/\partial x_\nu)(\partial u/\partial x^\nu)-\kappa^2\bar u u,\\
&\mathfrak{L}_3(\psi)=(1/2i)\bar\psi[(\partial/\partial x_\mu)E_\mu\\
&\qquad\qquad -(\overleftarrow{\partial/\partial x_\mu})E_\mu+2imE_5]\psi,
\end{aligned}\right\} \tag{2.2}$$

$$\left.\begin{aligned}
&\mathfrak{L}_{12}(a,u)=ea^\mu i_\mu;\\
&\qquad i_\mu(u)=i[(\partial\bar u/\partial x^\mu)u-\bar u(\partial u/\partial x^\mu)],\\
&\mathfrak{L}_{13}(a,\psi)=ea^\mu s_\mu;\quad s_\mu(\psi)=-\bar\psi E_\mu\psi
\end{aligned}\right\} \tag{2.3}$$

The second order (in e) interaction term in $\mathfrak{L}_{12}$ is dropped, for inclusion of such term does not affect our discussion in the following.

This lagrangian has, of course, a wrong property for transformations of the classes $\mathfrak{B}$ and $\mathfrak{D}$ ($\sigma_4=-1$). (See Appendix.) For $\mathfrak{L}_1$ and $\mathfrak{L}_2$ are regular scalars whatever kind of tensors a^μ and u may be, whereas $\mathfrak{L}_3$ is a second kind pseudoscalar. $\mathfrak{L}_{12}$ and $\mathfrak{L}_{13}$ are necessarily of different kinds from each other, for s_μ is a second kind pseudovector while i_μ is a regular vector.

All the terms (2.2) (2.3) can be brought to any one "kind" of scalar by the method developed in the Appendix whatever kinds of property we may assign to a^μ and u. We shall, however, discuss only two of the various possibilities:

(I) $\mathfrak{L}$: regular scalar; a^μ: regular vector

(II) $\mathfrak{L}$: regular scalar; a^μ: 2nd kind pseudovector.

The method consists in introducing two tensors or two spinors to represent one field. These two tensors or two spinors are not only transformed according to the ordinary transformation rules but also interchanged whenever we perform a transformation with $\sigma_4=-1$. Corresponding to a^μ, u and ψ, we introduce, respectively, (a^μ, b^μ), (u, v) and (ψ, φ), which constitute two bi-tensors and a bi-spinor:

$$\left.\begin{aligned}
&A^\mu=\begin{pmatrix}a^\mu\\ b^\mu\end{pmatrix};\quad U=\begin{pmatrix}u\\ v\end{pmatrix};\quad \bar U=\begin{pmatrix}\bar u\\ \bar v\end{pmatrix};\\
&X=\begin{pmatrix}\psi\\ \varphi\end{pmatrix};\quad \bar X=\begin{pmatrix}\bar\psi\\ \bar\varphi\end{pmatrix}.
\end{aligned}\right\} \tag{2.4}$$

And to represent the current we introduce two bi-tensors by

$$I^\mu=\begin{pmatrix}i^\mu(u)\\ i^\mu(v)\end{pmatrix};\quad S^\mu=\begin{pmatrix}s^\mu(\psi)\\ s^\mu(\varphi)\end{pmatrix}. \tag{2.5}$$

In virtue of the theorem given in connection with (A.60), I^μ is a regular bi-vector whatever property u (and v) may have. S^μ is a second kind pseudo-bi-vector according to (A.61).

Case (I): We can then using (A.47), (A.53), and (A.55) easily build a regular scalar lagrangian density by replacing (2.2) and (2.3) by

$$\left.\begin{aligned}
&2\mathfrak{L}'_1=-(1/2)(\partial A_\mu/\partial x_\nu)(\partial A^\mu/\partial x^\nu)\\
&\qquad\qquad =\mathfrak{L}_1(a)+\mathfrak{L}_1(b)\\
&2\mathfrak{L}'_2=-(\partial\bar U/\partial x_\mu)(\partial U/\partial x^\mu)-\kappa^2\bar U U\\
&\qquad\qquad =\mathfrak{L}_2(u)+\mathfrak{L}_2(v)\\
&2\mathfrak{L}'_3=(1/2i)\bar X[(\partial/\partial x_\mu)\mathbf{E}_\mu\\
&\qquad -(\overleftarrow{\partial/\partial x_\mu})\mathbf{E}_\mu+2im\mathbf{E}_5]\Pi X\\
&\qquad\qquad =\mathfrak{L}_3(\psi)-\mathfrak{L}_3(\varphi)
\end{aligned}\right\} \tag{2.6}$$

$$\left.\begin{aligned}
&2\mathfrak{L}'_{12}=eA^\mu I_\mu=ea^\mu i_\mu(u)+eb^\mu i_\mu(v)\\
&2\mathfrak{L}'_{13}=eA^\mu\Pi S_\mu=ea^\mu s_\mu(\psi)-eb^\mu s_\mu(\varphi)
\end{aligned}\right\}. \tag{2.7}$$

In expressions (2.6) and (2.7) the terms in a^μ, u, $\bar u$, ψ, $\bar\psi$, and the terms in b^μ, v, $\bar v$, φ, $\bar\varphi$ should be written in such a way that corresponding factors are placed in the same order in both. This is essential for the later reinterpretation in q-number theory.

Case (II): $\mathfrak{L}'_1$, $\mathfrak{L}'_2$ and $\mathfrak{L}'_3$ in (2.6) need not be changed. (2.7) should however be changed into

$$\left.\begin{aligned}
&2\mathfrak{L}'_{12}=eA^\mu\Pi I_\mu=ea^\mu i_\mu(u)-eb^\mu i_\mu(v)\\
&2\mathfrak{L}'_{13}=eA^\mu S_\mu=ea^\mu s_\mu(\psi)+eb^\mu s_\mu(\varphi)
\end{aligned}\right\}. \tag{2.8}$$

Thus we have succeeded in writing the lagrangian in a covariant form for the entire congruent group in the c-number theory.

Although the quantum-theoretical consideration of reversibility is being developed in the later sections, the mathematical core of the results obtained there will now be given in anticipation.

In the q-number theory all the field quantities are, of course, to be regarded as matrices, and the require-

ment of reversibility is then expressed by certain relations involving these matrices and their transposes. In terms of bi-tensors and bi-spinors, these relations will imply certain connections between their first and second parts involving the operation of transposition.

The operation of transposition is of course not commutable with the ordinary unitary transformations. But, for a reason which will be explained later, we need not here specify the representation which is to be used.

It should be borne in mind that the second half of a bi-tensor or of a bi-spinor must belong to the same transformation rules as its first half, except for their interchange. Therefore, we can expect without a detailed analysis that the aforementioned connections between the first halves and the second halves will turn out to be certain combinations of the following possibilities (see (A.32)):

$$\left.\begin{aligned} &b^\mu = a^{T\mu}, \\ &v = u^T, \quad \bar{v} = \bar{u}^T \quad \text{or} \quad v = \bar{u}^T, \quad \bar{v} = u^T, \\ &\psi = \psi^T, \quad \bar{\varphi} = \bar{\psi}^T \quad \text{or} \quad \varphi = \bar{\psi}^T K, \quad \bar{\varphi} = \psi K^{-1}. \end{aligned}\right\} \tag{2.9}$$

Case (I): In this case, the conclusions drawn from the requirement of reversibility in q-number theory can be summarized in the following two items:

(a) $b^\mu = a^{T\mu}$; $v = u^T$; $\bar{v} = \bar{u}^T$; $\varphi = \psi^T$; $\bar{\varphi} = \bar{\psi}^T$, (2.10)

(b) $\mathfrak{L}' = \mathfrak{L}^{T\prime}$, (2.11)

where $\mathfrak{L}'$ is the sum of all the $\mathfrak{L}'$'s of (2.6) and (2.7). The symbol of equality in (2.11) is to be understood in the sense of "equal except for an additional c-number."

If relations (2.10) are substituted in (2.6) and (2.7), condition (2.11) lets us draw conclusions as to the commutation relations for the u-field and the ψ-field. The condition that $\mathfrak{L}'_{12} = \mathfrak{L}^{T\prime}_{12}$ and $\mathfrak{L}'_{13} = \mathfrak{L}^{T\prime}_{13}$ with (2.10) evidently requires:

$$\bar{\psi} E_\mu \psi = -\psi E^T{}_\mu \bar{\psi};$$

$$(\partial \bar{u}/\partial x^\mu) u - \bar{u}(\partial u/\partial x^\mu) = u(\partial \bar{u}/\partial x^\mu) - (\partial u/\partial x^\mu)\bar{u}, \tag{2.12}$$

which can be true only when

$$\left.\begin{aligned} &\psi\bar{\psi} + \bar{\psi}\psi = c\text{-number}, \\ &u\bar{u} - \bar{u}u = c\text{-number}. \end{aligned}\right\} \tag{2.13}$$

It can easily be seen that (2.13) guarantees the conditions $\mathfrak{L}'_2 = \mathfrak{L}^{T\prime}_2$ and $\mathfrak{L}'_3 = \mathfrak{L}^{T\prime}_3$ in (2.6).

The foregoing method applied to the electromagnetic field a^μ entails no conclusion as to its commutation rule. For (2.10) for a^μ automatically satisfies $\mathfrak{L}'_1 = \mathfrak{L}^{T\prime}_1$ with (2.6). Indeed, if a^μ obeyed the Fermi statistics, $\mathfrak{L}_1$ would become essentially a c-number, so that such an assumption can hardly become a subject of the present consideration.

Case (II): Reversibility requirement here takes the form:

(a) $b^\mu = a^{T\mu}$; $v = \bar{u}^T$; $\bar{v} = u^T$; $\varphi = \bar{\psi}^T K$; $\bar{\varphi} = \psi^T K^{-1}$, (2.14)

(b) $\mathfrak{L}' = \mathfrak{L}^{T\prime}$, (2.15)

with (2.6) and (2.8).

It can be verified that (2.14) substituted in (2.6) and (2.8) automatically satisfies (2.15), so that no conclusion as to the commutation rules can be drawn.

It is interesting to notice that we in reality do not need all of the conditions enumerated in (2.10) or (2.14) in order to obtain the foregoing results. In fact, we need only $b^\mu = a^{T\mu}$ and $\mathfrak{L}' = \mathfrak{L}^{T\prime}$, if we knew that the choice of v and φ should be made out of the possibilities indicated in (2.9).

III. REVERSIBILITY OF CLASSICAL ELECTRODYNAMICS

The reversibility of point mechanics can be stated in the following manner. Two states $Z_{(1)}$ and $Z_{(2)}$ are called "reversed" states of each other if

$$\left.\begin{aligned} &x^a{}_{(1)} = x^a{}_{(2)}, \quad p^a{}_{(1)} = -p^a{}_{(2)} \quad (a = 1, 2, 3); \\ &p^0{}_{(1)} = p^0{}_{(2)}; \quad E_{(1)} = E_{(2)}, \end{aligned}\right\} \tag{3.1}$$

where x^μ, p^μ ($\mu = 1, 2, 3, 0$) and E stand, respectively, for the positions of the particles, their momenta and the total energy of the system, and the subscripts (1) and (2) refer to the two states. This situation (3.1) will be written symbolically as

$$Z_{(1)} \overset{\text{rev}}{\sim} Z_{(2)}. \tag{3.2}$$

The statement that the mechanical law is reversible means that if $Z_{(1)}(t)$ is a solution then it allows for a second solution $Z_{(2)}(t)$ such that, if at a certain instant τ

$$Z_{(1)}(\tau) \overset{\text{rev}}{\sim} Z_{(2)}(\tau), \tag{3.3}$$

then

$$Z_{(1)}(\tau + t) \overset{\text{rev}}{\sim} Z_{(2)}(\tau - t) \tag{3.4}$$

for any value of t. In virtue of the displacement group in time that the mechanical law allows for, we can write, instead of (3.3) and (3.4),

$$Z_{(1)}(t) \overset{\text{rev}}{\sim} Z_{(2)}(-t). \tag{3.5}$$

This is true not only in the absence of external forces, but also in the cases in which the external forces for $Z_{(1)}$ at t are the same as those for $Z_{(2)}$ at $-t$. Frictional forces which change their signs in the reversed motion invalidates the reversibility.

There are now two "standpoints" by which the concept of reversibility can be adapted to electrodynamics.

According to one standpoint, the reversed states $Z_{(1)}$ and $Z_{(2)}$ are defined by

$$\left.\begin{aligned} &x^a{}_{(1)} = x^a{}_{(2)}, \quad p^a{}_{(1)} = -p^a{}_{(2)}, \quad (a = 1, 2, 3); \\ &\qquad\qquad\qquad\qquad\qquad\qquad p^0{}_{(1)} = p^0{}_{(2)} \\ &i^a{}_{(1)} = -i^a{}_{(2)}; \quad i^0{}_{(1)} = i^0{}_{(2)}; \quad a^a{}_{(1)} = -a^a{}_{(2)}; \\ &\qquad\qquad\qquad\qquad\qquad\qquad a^0{}_{(1)} = a^0{}_{(2)}; \quad E_{(1)} = E_{(2)} \end{aligned}\right\}, \tag{3.6}$$

where i^μ and a^μ are, respectively, the current and the potential vectors. This standpoint corresponds to the

"original" standpoint in our "Introduction" and will be hereafter referred to as standpoint (II).

Then it can be proved that the classical electrodynamics guarantees the reversibility which can be written as (3.5). This is because we can regard the field quantities a^μ, $f^{\mu\nu}$, the current i^μ and the four-velocity v^μ as pseudo-tensors of the second kind in the Maxwell equations:

$$\left.\begin{aligned} &\Box a^\mu(x) = -i^\mu(x) = -\sum e v^\mu(x')\delta(x-x'); \\ &\qquad\qquad \partial a^\mu/\partial x^\mu = 0 \\ &f^{\mu\nu} = \partial a^\nu/\partial x_\mu - \partial a^\mu/\partial x_\nu; \quad m\dot{v}^\mu = e f^{\mu\nu} v_\nu \end{aligned}\right\}. \tag{3.7}$$

(the proper time is a second kind pseudoscalar).

We now notice that, in these equations, we can alternatively regard a^μ, $f^{\mu\nu}$, i^μ as regular tensors. This entails, since the velocities must be second kind pseudovectors, that e should behave as a second kind pseudoscalar. This means that, in the reversed state, particles of the opposite charges are performing the reversed motion. In symbols:

$$\left.\begin{aligned} &x^\alpha{}_{(1)}(\pm) = x^\alpha{}_{(2)}(\mp); \quad p^\alpha{}_{(1)}(\pm) = -p^\alpha{}_{(2)}(\mp); \\ &\qquad\qquad p^0{}_{(1)}(\pm) = p^0{}_{(2)}(\mp) \\ &i^\alpha{}_{(1)} = i^\alpha{}_{(2)}; \quad i^0{}_{(1)} = -i^0{}_{(2)}; \quad a^\alpha{}_{(1)} = a^\alpha{}_{(2)}; \\ &\qquad\qquad a^0{}_{(1)} = -a^0{}_{(2)}; \quad E_{(1)} = E_{(2)} \end{aligned}\right\}. \tag{3.8}$$

This modified definition of the reversed state will be referred to as (I) in the following. It is obvious that this standpoint (I) is nothing but the combination of the reversal of motion in its proper sense and the reversal of charge. The latter means the change of signs of the charges and the field quantities, for which the equations (3.7) remain invariant. If the electrodynamics is reversible in standpoint (II), it is also reversible in standpoint (I), and vice versa, provided the charge invariance is guaranteed.

In both standpoints, electromagnetic waves in the reversed states propagate in opposite directions, with the same direction of linear polarization. There is however a phase difference of 180 degrees between (I) and (II). It is also clear in both standpoints that, if in $Z_{(1)}$ a light pulse is emitted at instant t, the corresponding light pulse is absorbed at instant $-t$ in $Z_{(2)}$.

IV. REVERSION OPERATOR

In the following sections, use will mainly be made of the interaction picture, in which the state function Ψ changes with time according to the Schroedinger equation with the interaction hamiltonian:

$$d\Psi/dt = -i\mathbf{H}\Psi, \tag{4.1}$$

while all the physical quantities Q changes with time according to the Heisenberg equation with the noninteracting hamiltonian:

$$dQ/dt = i(\mathbf{H}_0 Q - Q\mathbf{H}_0). \tag{4.2}$$

The values of Ψ at t_1 and at t_2 are related to each other by

$$\Psi(t_1) = U(t_1, t_2)\Psi(t_2), \tag{4.3}$$

where

$$\begin{aligned} &\partial U(t_1, t_2)/\partial t_1 = -i\mathbf{H}(t_1)U(t_1, t_2); \\ &\partial U(t_1, t_2)/\partial t_2 = +iU(t_1, t_2)\mathbf{H}(t_2) \end{aligned} \tag{4.4}$$

with

$$U(t_1, t_2) = 1 \quad \text{for} \quad t_1 = t_2. \tag{4.5}$$

The transformation function $U(t_1, t_2)$ has the properties:

$$\bar{U}(t_1, t_2) = U^{-1}(t_1, t_2) = U(t_2, t_1). \tag{4.6}$$

We now proceed to define the reversed states in the quantum-mechanical language. $\Psi_{(1)}(t_1)$ and $\Psi_{(2)}(t_2)$ are said to be reversed states of each other if the expectation values of physical quantities for $\Psi_{(1)}(t_1)$ and those for $\Psi_{(2)}(t_2)$ are related by the conditions which characterize the reversed states in classical electrodynamics, i.e., relations (3.8) in standpoint (I) and relation (3.6) in standpoint (II). These conditions will then take the general form:

$$(\Psi_{(1)}(t_1), P(t_1)\Psi_{(1)}(t_1)) = (\Psi_{(2)}(t_2), Q(t_2)\Psi_{(2)}(t_2)). \tag{4.7}$$

For instance, in standpoint (I), $P = a^0$, $Q = -a^0$; $P = N_\pm(\mathbf{k})$, $Q = N_\mp(-\mathbf{k})$; etc., where $N_+(\mathbf{k})$, for example, means the number of positively charged particles of a certain field having momentum $\mathbf{k}$.[6] There are quantities in the quantum theory which do not have direct counterparts in the classical theory. The physical meaning of such a quantity, however, always enables us to deduce its transformation property from the known transformation properties of the physically related quantities.

If relation (4.7) is satisfied for all the relevant physical quantities, we say that $\Psi_{(1)}(t_1)$ and $\Psi_{(2)}(t_2)$ are reversed states of each other and write

$$\Psi_{(1)}(t_1) \overset{\text{rev}}{\sim} \Psi_{(2)}(t_2). \tag{4.8}$$

Now the requirement of reversibility demands that, if $\Psi_{(1)}(t)$ is a solution of the Schroedinger equation, it should allow for a second solution $\Psi_{(2)}(t)$ such that for any value of t,

$$\Psi_{(1)}(t) \overset{\text{rev}}{\sim} \Psi_{(2)}(-t). \tag{4.9}$$

(4.9) is a summarized expression for

$$\begin{aligned} &d\Psi_{(1)}(t)/dt = -i\mathbf{H}(t)\Psi_{(1)}(t); \\ &d\Psi_{(2)}(t)/dt = -i\mathbf{H}(t)\Psi_{(2)}(t), \end{aligned} \tag{4.10}$$

and

$$(\Psi_{(1)}(t), P(t)\Psi_{(1)}(t)) = (\Psi_{(2)}(-t), Q(-t)\Psi_{(2)}(-t)). \tag{4.11}$$

[6] Classical electrodynamics is a mixture of particle picture (for charge fields) and wave picture (for electromagnetic field). We can reformulate all the reversibility requirements consistently in terms of wave picture. In this point of view, requirements regarding particle numbers such as the one indicated in the text can be dispensed with, if requirements are fulfilled regarding momentum density, energy density, current density, charge density, spin density, and electromagnetic moment density.

If $\Psi_{(1)}(t)$ and $\Psi_{(2)}(t)$ are normalized they can be linked by a yet to be determined unitary operator R:

$$\Psi_{(2)}(-t)=\Psi^*_{(1)}(t)R, \tag{4.12}$$

with

$$\tilde{R}=R^{-1}. \tag{4.13}$$

The star on Ψ means its complex conjugate. The "reversion operator" R is to be determined by (4.11).

Substitution of (4.12) in (4.11) gives, because of the hermiticity of P and Q,

$$(\Psi_{(1)}(t),\ P(t)\Psi_{(1)}(t)) = (\Psi_{(1)}(t),\ RQ^T(-t)R^{-1}\Psi_{(1)}(t)), \tag{4.14}$$

which must hold for any value of t. Since the choice of $\Psi_{(1)}$ is independent of (P, Q), it follows from (4.14) that

$$Q(-t)=(R^{-1}P(t)R)^T. \tag{4.15}$$

As for the Schroedinger Eqs. (4.10), they can be rewritten as

$$\begin{aligned} d\Psi^*_{(1)}(t)/dt &= i\Psi^*_{(1)}(t)\mathbf{H}(t);\\ d\Psi_{(2)}(-t)/dt &= i\Psi_{(2)}(-t)\mathbf{H}^T(-t), \end{aligned} \tag{4.16}$$

which cannot be made compatible with each other by (4.12) unless R is independent of time and

$$\mathbf{H}(-t)=(R^{-1}\mathbf{H}(t)R)^T. \tag{4.17}$$

This last relation is nothing but a special case of (4.15) for $\mathbf{H}(t)$.

Therefore, the reversibility requirement is equivalent to the requirement of existence of a time-independent unitary operator R which is defined by (4.15).

Under a time-independent unitary transformation which transforms hermitian operators (and ordinary unitary operators) Q into $T^{-1}QT$ and state functions Ψ into $T^{-1}\Psi$, the reversion operator will, according to its definition, be transformed into

$$R\rightarrow T^{-1}RT^{T-1}=T^{-1}RT^*, \tag{4.18}$$

which preserves (4.13). This particular transformation warrants invariant meanings to the operation of transposition and to the operation of taking complex conjugates of state functions, which have been involved in the foregoing formulas.

Solutions of (4.2) can be expressed in terms of a time-dependent unitary transformation:

$$Q(t)=U_0^{-1}(t)Q(0)U_0(t), \tag{4.19}$$

with

$$dU_0(t)/dt=-i\mathbf{H}_0U_0(t);\quad U_0(0)=1. \tag{4.20}$$

The defining relation for R (4.15) then takes the form:

$$Q^T(0)=(U^T{}_0^{-1}(-t)R(t)U_0^{-1}(t)) \times P(0)(U_0(t)R(t)U_0{}^T(-t)), \tag{4.21}$$

showing

$$R(t)=U_0^{-1}(t)R(0)U^T{}_0^{-1}(-t), \tag{4.22}$$

from which follows

$$dR(t)/dt=i(\mathbf{H}_0R(t)-R(t)\mathbf{H}^T{}_0), \tag{4.23}$$

because $\mathbf{H}_0$ is independent of time. The time-independence of R implies

$$\mathbf{H}_0R-R\mathbf{H}^T{}_0=0. \tag{4.24}$$

This is only a special case of (4.15) for $\mathbf{H}_0$.

Hence, if the reversion operator defined by (4.15) exists, it automatically satisfies the requirement that it should be time-independent.

(4.24) gives an interesting information: The time-independent R commutes with $\mathbf{H}_0$ in the particular representation in which $\mathbf{H}_0$ is diagonal. Since $\mathbf{H}_0$ is a degenerate operator, this does not imply that R is diagonal in this representation.

Since P and Q must be interchangeable in (4.15) and since we have not specified the sign of t, we can write

$$P(t)=(R^{-1}Q(-t)R)^T=R^TR^{-1}P(t)RR^{T-1}, \tag{4.25}$$

which implies that R^TR^{-1} commutes with P. If we were allowed to make an assumption that any arbitrary hermitian operator P should have its associated operator Q satisfying (4.7), then (4.25) would mean that R^TR^{-1} should be a c-number, i.e.,

$$R^T=cR,\quad \text{or}\quad R^T=\pm R. \tag{4.26}$$

It is interesting to note that the symmetry or antisymmetry of R is preserved under the transformation (4.18). However, such an assumption is obviously too hasty a generalization. In fact, we shall encounter in a later section a concrete example of R which without being symmetrical or antisymmetrical warrants the symmetry of relevant physical quantities with respect to t and $-t$ as expressed by the commutability relation (4.25). Physically, however, R and R^T have the same meaning.

Application of (4.3) to (4.12) yields

$$U^{T-1}(t,-t)=R^{-1}U(t,-t)R. \tag{4.27}$$

If the reversion operator exists, we can demonstrate the following statement with the help of (4.27): The probability of finding a physical system, which was in state Ω at $-t$, in state Θ at t is equal to the probability of finding a system, which was in the reversed state of Θ at $-t$, in the reversed state of Ω at t. This can be regarded as an alternative expression of the "reversibility." The first probability is given by

$$|(\Theta,\ U(t,-t)\Omega)|^2, \tag{4.28}$$

and the second by

$$|((\Omega^*R),\ U(t,-t)(\Theta^*R))|^2. \tag{4.29}$$

The latter is, in virtue of (4.6), equal to

$$|(\Omega,\ RU^{T-1}(t,-t)R^{-1}\Theta)^*|^2, \tag{4.30}$$

which coincides with (4.28) on account of (4.27).

Finally, the method of Sec. II can be linked to the consideration of this section in the following manner. The lagrangian density, on account of its relation to the hamiltonian density, must have the same sign in the reversed state:

$$\mathfrak{L}(t)=(R^{-1}\mathfrak{L}(-t)R)^{T} \tag{4.31}$$

or

$$\mathfrak{L}'(t)=\mathfrak{L}^{T'}(t)$$

with

$$\mathfrak{L}'(t)=\mathfrak{L}(t)+R^{-1}\mathfrak{L}(-t)R. \tag{4.32}$$

Relations (2.10) or (2.14) give the field quantities transformed by the reversion operator, from which the factors due to the congruent transformation (time-reversal) are dropped. In the following sections, we shall investigate the effect of the reversion operator on the field quantities, determining this operator by (4.15), in which P and Q should be taken in accordance with (3.6) or (3.8). The lagrangian (2.1) will be assumed.

V. CHARGED SCALAR FIELD

In the three sections that follow, standpoint (I) will be adopted, while Sec. VIII will be reserved for the discussion in standpoint (II).

In the case of a scalar or a pseudoscalar field, we shall have to consider the current i^{μ} and the noninteracting hamiltonian density H_0 as the physical quantities under the time-reversal:

$$\left.\begin{aligned} &i^{\mu}=i[(\partial\bar{u}/\partial x_{\mu})u-\bar{u}(\partial u/\partial x_{\mu})],\\ &H_0=(\partial\bar{u}/\partial t)(\partial u/\partial t)+(\partial\bar{u}/\partial x_a)(\partial u/\partial x^a)+\kappa^2\bar{u}u.\\ &\qquad\qquad (a=1,2,3)\end{aligned}\right\} \tag{5.1}$$

The requirement of reversibility is now expressed as the requirement of existence of R such that

$$\left.\begin{aligned} &i^{T\mu}(-t)=R^{-1}i^{\mu}(t)R;\quad i^{T0}(-t)=-R^{-1}i^{0}(t)R;\\ &H^{T}{}_{0}(-t)=R^{-1}H_0(t)R.\end{aligned}\right\} \tag{5.2}$$

We need not consider the interaction hamiltonian because the correct transformation of the current guarantees the correct transformation of the interaction hamiltonian provided the electromagnetic field satisfies the correct transformation. Regarding the particle numbers, see (5.9).

We shall first show that the assumption of Bose statistics permits the existence of R, and then show that the Fermi statistics is incompatible with the existence of R.

It is easy to prove that conditions (5.2) are satisfied by

$$\left.\begin{aligned} &R^{-1}u(x,t)R=\pm u^{T}(x,-t);\\ &R^{-1}\bar{u}(x,t)R=\pm\bar{u}^{T}(x,-t).\end{aligned}\right\} \tag{5.3}$$

For this proof we need once change the order of u and $\bar{u}$ using the Bose assumption. Hence the above statement is true "except for an additional c-number." On this point, see Sec. VIII. Since choice of the sign in (5.3), which refers to the "kind" of the u-field, does not essentially affect the argument, the positive sign will be adopted.

It should be noted that the two relations of (5.3) are just hermitian-conjugate of each other, provided the unitarity of R (4.13) and the hermitian-conjugate relation between u and $\bar{u}$. The transpose of a relation in (5.3) becomes identical with the original relation with t and $-t$ interchanged if $R^{T}=\pm R$. Hence, we can expect here a symmetrical or antisymmetrical R.

It can easily be ascertained that the transformation (5.3) leaves the commutation relation:

$$u(x,t)\bar{u}(x',t')-\bar{u}(x',t')u(x,t)=-iD_{\kappa}(x-x',t-t') \tag{5.4}$$

unchanged, because the D_{κ}-function is an odd function of $t-t'$.

We now want to pass to the particle picture by the expansion:

$$\left.\begin{aligned} u(x,t)=&\sum[1/\sqrt{(2V|k^0|)}]\{u_{+}(\mathbf{k})\\ &\times\exp(i\mathbf{kx}-i|k^0|t)+\bar{u}_{-}(\mathbf{k})\\ &\times\exp(-i\mathbf{kx}+i|k^0|t)\}\\ \bar{u}(x,t)=&\sum[1/\sqrt{(2V|k^0|)}]\{\bar{u}_{+}(\mathbf{k})\\ &\times\exp(-i\mathbf{kx}+i|k^0|t)+u_{-}(\mathbf{k})\\ &\times\exp(i\mathbf{kx}-i|k^0|t)\}\end{aligned}\right\}, \tag{5.5}$$

with

$$\mathbf{k}^2+\kappa^2=(k^0)^2. \tag{5.6}$$

Then

$$N_{+}(\mathbf{k})=\bar{u}_{+}(\mathbf{k})u_{+}(\mathbf{k});\quad N_{-}(\mathbf{k})=\bar{u}_{-}(\mathbf{k})u_{-}(\mathbf{k}), \tag{5.7}$$

bear the usual meanings. The transformation (5.3) applied to (5.5) now take the form:

$$R^{-1}u_{\pm}(\mathbf{k})R=\bar{u}^{T}{}_{\mp}(-\mathbf{k});\quad R^{-1}\bar{u}_{\pm}(\mathbf{k})R=u^{T}{}_{\mp}(-\mathbf{k}) \tag{5.8}$$

from which follows:

$$\left.\begin{aligned} &(R^{-1}N_{+}(\mathbf{k})R)^{T}=N_{-}(-\mathbf{k});\\ &(R^{-1}N_{-}(\mathbf{k})R)^{T}=N_{+}(-\mathbf{k}).\end{aligned}\right\} \tag{5.9}$$

This is exactly what was expected in the discussion given below (4.7). (5.9) shows that R commutes with $\mathbf{H}_0$ in the representation in which the particle numbers are diagonal. See (4.24). In the N-representation, (5.8) can be written as

$$R^{-1}u_{\pm}(\mathbf{k})R=u_{\mp}(-\mathbf{k}). \tag{5.10}$$

The reversion operator can now be written explicitly

as a matrix in this representation:

$$\left.\begin{aligned}&(\cdots N'_+(\mathbf{k}_i),\ N'_+(-\mathbf{k}_i)\cdots N'_-(\mathbf{k}_i),\\&N'_-(-\mathbf{k}_i)\cdots|R|\cdots N''_-(-\mathbf{k}_i),\\&N''_-(\mathbf{k}_i)\cdots N''_+(-\mathbf{k}_i)N''_+(\mathbf{k}_i)\cdots)\\&=\Pi\delta(N'_+(\mathbf{k}_i),\ N''_-(-\mathbf{k}_i))\\&\times\delta(N'_+(-\mathbf{k}_i),\ N''_-(\mathbf{k}_i))\\&\times\delta(N'_-(\mathbf{k}_i),\ N''_+(-\mathbf{k}_i))\\&\times\delta(N'_-(-\mathbf{k}_i),\ N''_+(\mathbf{k}_i)).\end{aligned}\right\}\quad(5.11)$$

Let us now proceed to examine the assumption of Fermi statistics for the u-field. In this case, we realize that there are two and only two possible ways to fulfill (5.2), *viz.*

$$\left.\begin{aligned}&R^{-1}u(x,t)R=\mp(1/c)u^T(x,-t);\\&R^{-1}\bar{u}(x,t)R=\pm c\bar{u}^T(x,-t),\end{aligned}\right\}\quad(5.12)$$

$$\left.\begin{aligned}&R^{-1}u(x,t)R=\mp(1/c)\bar{u}^T(x,-t);\\&R^{-1}\bar{u}(x,t)R=\pm cu^T(x,-t).\end{aligned}\right\}\quad(5.13)$$

(N.B. Double sign is inverted in two relations of each group.) c is arbitrary. (5.12) requires, in the process of proof, the change of order of u and $\bar{u}$ according to the Fermi-statistics, while (5.13) does not.

It can now easily be seen that either choice, (5.12) or (5.13), destroys the hermitian relationship between u and $\bar{u}$, if R is to satisfy (4.13). Therefore, there cannot exist a reversion operator in the case of Fermi statistics. This is what was to be demonstrated.

The incompatibility of the hermitian relationship between u and $\bar{u}$ and the two relations in (5.12) or (5.13) leads us to attempt a formalism in which $\bar{u}$ is not the hermitian conjugate of u. Such a formalism has recently been discussed also by Pauli.[7] To avoid confusion, $\bar{u}$ in the foregoing will be written $\bar{v}$ in the following.

The first thing to notice is that either transformation (5.12) or (5.13) leaves the following Fermi type commutation relation unchanged:

$$u(x,t)\bar{v}(x',t')+\bar{v}(x',t')u(x,t)=-iD_s(x-x',t-t').\quad(5.14)$$

Instead of (5.5), u and $\bar{v}$ will here be developed as

$$\left.\begin{aligned}u(x,t)&=\sum[1/\sqrt{(2V|k^0|)}]\\&\times\{u_+(\mathbf{k})\exp(i\mathbf{kx}-i|k^0|t)+\bar{u}_-(\mathbf{k})\\&\times\exp(-i\mathbf{kx}+i|k^0|t)\}\\\bar{v}(x,t)&=\sum[1/\sqrt{(2V|k^0|)}]\\&\times\{\bar{u}_+(\mathbf{k})\exp(-i\mathbf{kx}+i|k^0|t)-u_-(\mathbf{k})\\&\times\exp(i\mathbf{kx}-i|k^0|t)\}\end{aligned}\right\},\quad(5.15)$$

[7] W. Pauli, Prog. Theor. Phys. 5, 526 (1950).

while (5.7) retains its meaning. Of the two possibilities (5.12) and (5.13), the first one will give (adopting the upper sign and $c=1$)

$$\left.\begin{aligned}&R^{-1}u_+(\mathbf{k})R=-\bar{u}^T_-(-\mathbf{k});\\&R^{-1}u_-(\mathbf{k})R=-\bar{u}^T_+(-\mathbf{k})\\&R^{-1}\bar{u}_+(\mathbf{k})R=-u^T_-(-\mathbf{k});\\&R^{-1}\bar{u}_-(\mathbf{k})R=-u^T_+(-\mathbf{k})\end{aligned}\right\},\quad(5.16)$$

which does not contradict with the hermitian relationship between $u(k)$ and $\bar{u}(k)$, assuming (4.13). (5.16) evidently gives the desired transformation for the particle numbers:

$$(R^{-1}N_\pm(\mathbf{k})R)^T=N_\mp(-\mathbf{k}).\quad(5.17)$$

VI. CHARGED SPINOR FIELD

According to the standpoint (I), the quantities which should change their signs in the reversed state are the charge s^0, the electric moment ϵ^a and the spin σ^a, and those which should keep their signs are the current s^a, the magnetic moment μ^a and the noninteracting energy H_0:

$$s^{T0}(-t)=-R^{-1}s^0(t)R;\quad\epsilon^{Ta}(-t)=-R^{-1}\epsilon^a(t)R;$$
$$\sigma^{Ta}=-R^{-1}\sigma^a(t)R,\quad(6.1)$$

$$s^{Ta}(-t)=R^{-1}s^a(t)R;\quad\mu^{Ta}(-t)=R^{-1}\mu^a(t)R;$$
$$H^T{}_0(-t)=R^{-1}H_0(t)R,\quad(6.2)$$

where

$$\left.\begin{aligned}&s^a\approx\bar{\psi}E^a\psi;\quad\epsilon^a\approx\bar{\psi}E^bE^c\psi;\quad\mu^a\approx\bar{\psi}E^0E^a\psi;\\&\sigma^a\approx\bar{\psi}E^bE^a\psi\\&H_0\approx\bar{\psi}[E^a(\partial/\partial x^a)-E^a\overleftarrow{(\partial/\partial x^a)}+2imE^b]\psi\end{aligned}\right\}.\quad(6.3)$$

In (6.3) all the numerical factors are dropped for the sake of simplicity. In the expression of the electric moment ϵ^a, (a, b, c) must be an even permutation of a given order, say (1, 2, 3). Requirements regarding the particle numbers will be considered later.

We shall first show that the reversion operator exists if the Fermi statistics is assumed for the spinor field.

Under the Fermi assumption, it is easy to prove that all the foregoing requirements can be satisfied, except for an additional c-number (see Sec. VIII), by

$$\left.\begin{aligned}&R^{-1}\psi(t)R=cE^0\bar{\psi}^T(-t);\\&R^{-1}\bar{\psi}(t)R=(1/c)\psi^T(-t)E_0,\end{aligned}\right\}\quad(6.4)$$

where c is arbitrary. In the process of proof, we must once invert the order of ψ and $\bar{\psi}$ according to the Fermi statistics. In order that all the physical quantities be hermitian, it is necessary that ψ and $\psi^*=\bar{\psi}J$ [see (A.23)] be hermitian conjugate to each other. For this reason, the two relations in (6.4) can be compatible with each other only if $c^*c=1$ or $c=e^{i\vartheta}$, in virtue of

(4.13). To fix our further calculation, we shall adopt $\theta=\pi/2$:

$$R^{-1}\psi(t)R=iE^0\psi^T(-t);\quad R^{-1}\bar\psi(t)R=-i\bar\psi^T(-t)E_0. \tag{6.5}$$

By adopting this value for c, we can expect to obtain a symmetrical or antisymmetrical R. Indeed, the transposes of relations (6.5) are identical with the original relations (with t and $-t$ interchanged) if $R^T=\pm R$.

If we adopt $\theta=0$ or $\theta=\pi$, (6.4) coincides with (A.48). It can also be shown that transformation (6.4) transforms the usual commutation relation:

$$\psi_r(x,t)\bar\psi_s(x',t')+\bar\psi_s(x',t')\psi_r(x,t)=[E^\mu(\partial/\partial x^\mu)+imE^5]_{rs}D_m(x-x',t-t') \tag{6.6}$$

back into itself.

We shall now examine the effect of R on the particle numbers. In the interaction picture, ψ and $\bar\psi$ obey

$$[E^\mu(\partial/\partial x^\mu)+imE^5]\psi=0;\quad \bar\psi[E^\mu(\overleftarrow{\partial/\partial x^\mu})-imE^5]=0. \tag{6.7}$$

If we, according to (A.32), decompose ψ and $\bar\psi$ into charge conjugate waves by

$$\psi=\psi_+ +\bar\psi_- K;\quad \bar\psi=\bar\psi_+ +\psi_- K^{-1}, \tag{6.8}$$

then each of ψ_+ and ψ_- will again obey the first equation of (6.7), and each of $\bar\psi_+$ and $\bar\psi_-$ will obey the second equation of (6.7).

We now expand ψ and $\bar\psi$ into their fourier components by

$$\left.\begin{aligned}\psi(t)&=(1/\sqrt{V})\textstyle\sum_{\mathbf k}\sum_\rho[g_+{}^\rho(\mathbf k)\alpha^\rho(\mathbf k)\\&\quad\times\exp(i\mathbf{kx}-i|k^0|t)+g_-{}^\rho(\mathbf k)\bar\alpha^\rho(\mathbf k)K\\&\quad\times\exp(-i\mathbf{kx}+i|k^0|t)]\\ \bar\psi(t)&=(1/\sqrt{V})\textstyle\sum_{\mathbf k}\sum_\rho[\bar g_+{}^\rho(\mathbf k)\bar\alpha^\rho(\mathbf k)\\&\quad\times\exp(-i\mathbf{kx}+i|k^0|t)+g_-{}^\rho(\mathbf k)\alpha^\rho(\mathbf k)K^{-1}\\&\quad\times\exp(i\mathbf{kx}-i|k^0|t)]\end{aligned}\right\}, \tag{6.9}$$

where the index $\rho=1,2$ corresponds to the spin freedom. g and $\bar g$ are supposed to satisfy

$$\bar g_+{}^\rho(\mathbf k)g_+{}^\sigma(\mathbf k)+g_+{}^\sigma(\mathbf k)\bar g_+{}^\rho(\mathbf k)=\delta_{\rho\sigma}\text{ etc.}, \tag{6.10}$$

and the c-number spinors α and $\bar\alpha$ are solutions of

$$(k_\alpha E^\alpha-|k^0|E^0+mE^5)\alpha^\rho(\mathbf k)=0,\quad \bar\alpha^\rho(\mathbf k)(-k_\alpha E^\alpha+|k^0|E^0-mE^5)=0. \tag{6.11}$$

They should be orthogonal and normalized so that

$$\bar\alpha^\rho(\mathbf k)E^0\alpha^\sigma(\mathbf k)=-\delta_{\rho\sigma};\quad \bar\alpha^\rho(\mathbf k)\alpha^\sigma(\mathbf k)=0. \tag{6.12}$$

This normalization is certainly possible in the hermitian system (A.19). Then $N_\pm{}^\rho(\mathbf k)=\bar g_\pm{}^\rho(\mathbf k)g_\pm{}^\rho(\mathbf k)$ represents the electron numbers of the specified kind.

From (6.11), we see that $\alpha^\rho(\mathbf k)$ and $E^0K\bar\alpha^\rho(-\mathbf k)$ obey the same equation. And moreover they belong to the opposite spin if ρ has the same value. We therefore establish the correspondence between α^1 and α^2 by

$$\alpha^1(\mathbf k)=E^0K\bar\alpha^2(-\mathbf k);\quad \alpha^2(\mathbf k)=-E^0K\bar\alpha^1(-\mathbf k). \tag{6.13}$$

Theorem (A.17) proves that the two relations (6.13) are identical. The orthogonality of α^1 and α^2 is guaranteed by the fact that α^1 and α^2 can be considered as eigenfunctions belonging to different eigenvalues of a spin operator, say, σ_3:

$$E_\alpha E_3\alpha^\rho(\mathbf k)=\pm E^0\alpha^\rho(\mathbf k). \tag{6.14}$$

Now we construct, remembering (6.13), the right sides of (6.5):

$$\left.\begin{aligned}&iE^0\psi^T(-t)\\&=(1/\sqrt{V})\textstyle\sum_{\mathbf k}\sum_\rho[\{g^T{}_+{}^1(-\mathbf k)(i\bar\alpha^2(\mathbf k)K)\\&\quad+g^T{}_+{}^2(-\mathbf k)(-i\bar\alpha^1(\mathbf k)K)\}\\&\quad\times\exp(-i\mathbf{kx}+i|k^0|t)\\&\quad+\{g^T{}_-{}^1(-\mathbf k)(i\alpha^2(\mathbf k))\\&\quad+g^T{}_-{}^2(-\mathbf k)(-i\alpha^1(\mathbf k))\}\\&\qquad\times\exp(i\mathbf{kx}+i|k^0|t)]\\&-i\bar\psi^T(-t)E_0\\&=(1/\sqrt{V})\textstyle\sum_{\mathbf k}\sum_\rho[\{g^T{}_+{}^1(-\mathbf k)(-i\alpha^2(\mathbf k)K^{-1})\\&\quad+g^T{}_+{}^2(-\mathbf k)(i\alpha(\mathbf k)K^{-1})\}\exp(i\mathbf{kx}-i|k^0|t)\\&\quad+\{g^T{}_-{}^1(-\mathbf k)(-i\bar\alpha^2(\mathbf k))\\&\quad+g^T{}_-{}^2(-\mathbf k)(i\alpha^1(\mathbf k)\}\exp(-i\mathbf{kx}+i|k^0|t)]\end{aligned}\right\}, \tag{6.15}$$

which yields, by comparison with (6.9),

$$\left.\begin{aligned}R^{-1}g_\pm{}^1(\mathbf k)R&=\mp ig^T{}_\mp{}^2(-\mathbf k);\\R^{-1}g_\pm{}^2(\mathbf k)R&=\pm ig^T{}_\mp{}^1(-\mathbf k)\\R^{-1}\bar g_\pm{}^1(\mathbf k)R&=\pm i\bar g^T{}_\mp{}^2(-\mathbf k);\\R^{-1}\bar g_\pm{}^2(\mathbf k)R&=\mp i\bar g^T{}_\mp{}^1(-\mathbf k)\end{aligned}\right\}. \tag{6.16}$$

This entails the desired transformation rule for the particle numbers:

$$(R^{-1}N_\pm{}^1(\mathbf k)R)^T=N_\mp{}^2(-\mathbf k);\quad (R^{-1}N_\pm{}^2(\mathbf k)R)^T=N_\mp{}^1(-\mathbf k). \tag{6.17}$$

The matrix elements of R can now be obtained. For simplicity, we consider here only those matrix elements which affect $N_+{}^1(\mathbf k)$ and $N_-{}^2(-\mathbf k)$. Assigning to the matrices $g_+{}^1$ and $g_-{}^2$ the values:

$$g_+{}^1=\begin{pmatrix}0&1\\0&0\end{pmatrix};\quad \bar g_+{}^1=\begin{pmatrix}0&0\\1&0\end{pmatrix};\qquad g_-{}^2=\begin{pmatrix}0&i\\0&0\end{pmatrix};\quad \bar g_-{}^2=\begin{pmatrix}0&0\\-i&0\end{pmatrix}, \tag{6.18}$$

we obtain

$$(N'_+{}^1(\mathbf{k}), N'_-{}^3(-\mathbf{k})|R|N''_+{}^1(\mathbf{k}), N''_-{}^3(-\mathbf{k})) = (1-2N'_+{}^1(\mathbf{k}))(1-2N'_-{}^3(-\mathbf{k})) \times\delta(N'_+{}^1(\mathbf{k}), N''_-{}^3(-\mathbf{k})) \times\delta(N'_-{}^3(-\mathbf{k}), N''_+{}^3(\mathbf{k})), \quad (6.19)$$

which obviously satisfies (6.16). This R is symmetric.[8]

Now we want to demonstrate that the Bose statistics is incompatible with the reversibility requirement in standpoint (I). Let us first consider only two of the requirements:

$$R^{-1}s^{\mu}(t)R=-s^{T}{}_{\mu}(-t);\quad R^{-1}\mu^{\mu\nu}(t)R=-\mu^{T}{}_{\mu\nu}(-t), \quad (6.20)$$

with

$$\mu^{\mu\nu}\approx\bar{\psi}E^{\mu}E^{\nu}\psi. \quad (6.21)$$

By a simple inspection, we learn that, under the Bose assumption, there are two and only two possibilities to satisfy (6.20), *viz.*,

$$\begin{aligned} R^{-1}\psi(t)R&=V^{-1}E^{0}\psi^{T}(-t);\\ R^{-1}\bar{\psi}(t)R&=-\bar{\psi}^{T}(-t)E_{0}U, \end{aligned} \quad (6.22)$$

and

$$\begin{aligned} R^{-1}\psi(t)R&=V^{-1}E_{0}K\bar{\psi}^{T}(-t);\\ R^{-1}\bar{\psi}(t)R&=\psi^{T}(-t)K^{-1}E^{0}U, \end{aligned} \quad (6.23)$$

where, in both cases, the yet undetermined nonsingular matrices U and V must satisfy

$$UE^{\mu}V^{-1}=E^{\mu};\quad UE^{\mu}E^{\nu}V^{-1}=E^{\mu}E^{\nu}, \quad (6.24)$$

to meet the requirements (6.20). Combination of the two relations in (6.24) gives

$$UV^{-1}=U^{-1}V=1 \quad \text{or} \quad U=V. \quad (6.25)$$

Then the first relation of (6.24) becomes an expression to the effect that U commutes with all the four basic E^{μ}. Therefore, due to Theorem (4), Appendix,

$$U=V=c. \quad (6.26)$$

(6.23) satisfies the requirements without using the Bose assumption, while (6.22) satisfies them only by once inverting the order of ψ and $\bar{\psi}$ according to the Bose statistics, therefore "except for an additional c-number."

The first possibility (6.22) becomes, on account of (6.26),

$$\begin{aligned} R^{-1}\psi(t)R&=(1/c)E^{0}\psi^{T}(-t);\\ R^{-1}\bar{\psi}(t)R&=-c\bar{\psi}^{T}(-t)E_{0}. \end{aligned} \quad (6.27)$$

Incompatibility of the two relations of (6.27) is obvious. Indeed, the hermitian conjugate of one relation of (6.27) contradicts the other, assuming of course the hermitian conjugate relation between ψ and ψ^{*} and the unitarity of R (4.13).

In consideration of (6.26), the second possibility (6.23) takes the form:

$$\begin{aligned} R^{-1}\psi(t)R&=(1/c)E_{0}K\bar{\psi}^{T}(-t);\\ R^{-1}\bar{\psi}(t)R&=\psi^{T}(-t)K^{-1}E^{0}. \end{aligned} \quad (6.28)$$

This, however, gives the wrong sign for the requirement:

$$R^{-1}H_{0}(t)R=H^{T}{}_{0}(-t). \quad (6.29)$$

Thus, we conclude that, as far as we take the standpoint (I), the Fermi statistics is allowed for the charged spinor field but not the Bose statistics, in order to fulfill the reversibility requirement.

It suggests itself that we could save (6.27), and through it the Bose statistics, by abandoning the hermitian relationship between ψ and ψ^{*}.

VII. ELECTROMAGNETIC FIELD

According to standpoint (I), the requirements regarding the electromagnetic field can be written as

$$\begin{aligned} a^{Tb}(-t)&=R^{-1}a^{b}(t)R \quad (b=1,2,3);\\ a^{0}(-t)&=-R^{-1}a^{0}(t)R, \end{aligned} \quad (7.1)$$

and

$$H^{T}{}_{0}(-t)=R^{-1}H_{0}(t)R, \quad (7.2)$$

with

$$H_{0}=(\partial a_{\mu}/\partial t)(\partial a^{\mu}/\partial t)+(\partial a_{\mu}/\partial x_{\alpha})(\partial a^{\mu}/\partial x^{\alpha}). \quad (7.3)$$

It is evident that the transformation (7.1) automatically, i.e., without any specific assumption as to the statistics, satisfies (7.2). It is also obvious that (7.1) is self-consistent, in consideration of (4.13). The matrix R in this case will be symmetric or antisymmetric, for the transposes of the relations in (7.1) are identical with themselves, if $R^{T}=\pm R$.

The transformation (7.1) leaves invariant the customary commutation relation:

$$a^{\mu}(x,t)a^{\nu}(x',t')-a^{\nu}(x',t')a^{\mu}(x,t) = -ig^{\mu\nu}D_{0}(x-x',t-t'). \quad (7.4)$$

However, it leaves the Fermi type commutation relations also invariant:

$$a^{\mu}(x,t)a^{\nu}(x',t')+a^{\nu}(x',t')a^{\mu}(x,t) = g^{\mu\nu}F_{0}(x-x',t-t'), \quad (7.5)$$

where F_{0}, in order to be consistent with the left side, must remain unchanged for the interchange of all the four x^{μ} with $x^{\mu'}$ and also for the interchange of x^{α} with $x^{\alpha'}$ $(\alpha=1,2,3)$ and for the interchange of t with t' separately. $D_{0}{}^{(1)}$ is such a function.

As is well known, no self-consistent particle picture can be made on the Fermi assumption for the electromagnetic field,[9] but this is due to the difficulties which

[8] After having thus determined R, we should restore Jordan-Wigner's signum operators $\Pi(1-2N)$, which have provisorily been omitted in the g's and f's. The effect of R on them is just altering the ordering of the oscillators for the description of the reversed state.

[9] W. Pauli, Revs. Modern Phys. 13, 203 (1941).

are irrelevant to the reversibility requirements. The requirement that the photons in the reversed states should be traveling in the opposite momenta may be replaced by the requirement that the momentum density (Poynting vector) should be reversed in the reversed motion. It goes without saying that the transformation (7.1) fulfills this requirement irrespective of the statistics adopted.

Thus the reversibility requirement does not determine the commutation relations of the electromagnetic field.

Finally, the effect of R on the quantities in the particle picture will be given, assuming the Bose statistics. With the help of the expansion

$$a^\mu(x)=\sum[1/(2V|k^0|)^{\frac{1}{2}}][a^\mu(\mathbf{k})\exp(i\mathbf{kx}-i|k^0|t) +\bar{a}^\mu(\mathbf{k})\exp(-i\mathbf{kx}+i|k^0|t)]; \quad (k^0)^2=\mathbf{k}^2, \tag{7.6}$$

with

$$a^\mu(\mathbf{k})\bar{a}^\nu(\mathbf{k}')-\bar{a}^\nu(\mathbf{k}')a^\mu(\mathbf{k})=g^{\mu\nu}\delta(\mathbf{k},\mathbf{k}'), \tag{7.7}$$

the transformation (7.1) will be transcribed as

$$R^{-1}a^\mu(\mathbf{k})R=\bar{a}^T{}_\mu(-\mathbf{k}); \quad R^{-1}\bar{a}^\mu(\mathbf{k})R=a^T{}_\mu(-\mathbf{k}). \tag{7.8}$$

which naturally satisfies

$$(R^{-1}N^\mu(\mathbf{k})R)^T=N^\mu(-\mathbf{k}). \tag{7.9}$$

The matrix elements of R can readily be obtained from (7.8).

In the foregoing sections, we have not considered the interaction hamiltonian density H. This is because the requirement regarding H is automatically satisfied if the current and the electromagnetic potentials satisfy the reversibility requirements separately.

It was noticed at the end of Sec. III that emission of a photon in a state should correspond to absorption of a corresponding photon in the reversed state. We can reproduce this fact, in a probabilistic language, using R as defined above (7.8). Similar considerations apply also with regard to the emission and absorption of charged particles using (5.8) and (6.16).

VIII. CHARGE CONJUGATION AND STANDPOINT (II)

Two states $\Psi_{(1)}$ and $\Psi_{(2)}$ will be called "charge-conjugate" states of each other if the expectation values of the "electromagnetic" quantities have the same absolute values but opposite signs and those of the "mechanical" quantities have the same values; this situation will symbolically be written as

$$\Psi_{(1)}\overset{\text{cha}}{\sim}\Psi_{(2)}. \tag{8.1}$$

By electromagnetic quantities are meant: electromagnetic field, current, electromagnetic moment; and by mechanical quantities are meant: momentum, energy, spin.

Then the "charge-invariance" requires

$$\Psi_{(1)}(t)\overset{\text{cha}}{\sim}\Psi_{(2)}(t), \tag{8.2}$$

where $\Psi_{(1)}(t)$ and $\Psi_{(2)}(t)$ should obey the same Schroedinger equation. The requirement of charge-invariance can be replaced by the requirement of existence of a time-independent unitary operator C such that

$$\Psi_{(1)}(t)=C\Psi_{(2)}(t). \tag{8.3}$$

Then the argument runs parallel to our argument regarding the reversion operator, culminating in certain conditions about the commutation relations of charged field quantities. This conclusion is exactly the same as the one which we have drawn from our reversibility requirement in standpoint (I). Determination of commutation relations by the charge-invariance was previously discussed by Pauli and Belinfante.[10]

This situation raises a suspicion that the determination of statistics by the reversibility requirement was rather illusory and that the reversibility requirement may fail to determine the statistics if we take standpoint (II) of the reversed motion. That, in fact, this is the case will be shown in this section.

Before passing to the discussion of standpoint (II), a few words may be spent regarding the reservation we have always made in the preceding sections to the effect: "proven except for an additional c-number." This clause can be dropped if, after having determined R, modify the definitions of physical quantities $P(t)$ by the prescription:

$$P(t)\rightarrow\tfrac{1}{2}(P(t)+RQ^T(-t)R^{-1}), \tag{8.4}$$

where Q is associated to P in the sense of (4.7). This modification is nothing but a generalization of the well-known Heisenberg prescription which can be derived from a consideration of charge symmetry.[9]

Let us first consider the scalar field. In standpoint (II), the first two relations of (5.2) change their signs while the third relation of (5.2) remains unchanged. Before discussing our main problem, we want to show that the Bose statistics is compatible also with standpoint (II).

We see that all the requirements in standpoint (II) can be satisfied by

$$\begin{aligned} R^{-1}u(x,t)R&=\pm\bar{u}^T(x,-t);\\ R^{-1}\bar{u}(x,t)R&=\pm u^T(x,-t). \end{aligned} \tag{8.5}$$

Or in the particle picture (for the upper sign of (8.5))

$$\begin{aligned} &R^{-1}u_\pm(\mathbf{k})R=\bar{u}^T{}_\pm(-\mathbf{k}); \quad R^{-1}\bar{u}_\pm(\mathbf{k})R=u^T{}_\pm(-\mathbf{k}),\\ &(R^{-1}N_\pm(\mathbf{k})R)^T=N_\pm(-\mathbf{k}). \end{aligned} \tag{8.6}$$

This transformation stands all the tests which are imposed upon the reversion operator. In particular, it is free from the self-contradiction involved in the transformation (5.13).

Now it is essential to notice that the transformation (8.5) satisfies the reversibility requirements without any change of order of u and $\bar{u}$ based on a specific statistics. Therefore, (8.5) is valid also in the case of

[10] W. Pauli and F. J. Belinfante, Physica 7, 177 (1940).

Fermi statistics for the u-field. We can also confirm that (8.5) leaves the Fermi type commutation relation unchanged:

$$u(x,l)\bar{u}(x',l')+\bar{u}(x',l')u(x,l)=F_s(x-x',l-l'), \quad (8.7)$$

where F_s has a similar property to the F_0 of (7.5).

Because of the well-known difficulties,[9] which are irrelevant to the reversibility consideration, we cannot construct a consistent particle picture in the Fermi case. However, (8.5) gives the correct transformation to the momentum density, irrespective of the statistics.

We thus conclude that the reversibility requirement is ineffective in determining the statistics of the charged scalar (pseudoscalar) field in standpoint (II).

Let us now examine the spinor field in standpoint (II), assuming first the Fermi statistics. The requirements in standpoint (II) are

$$\begin{gathered} s^{T_s}(-l)=-R^{-1}s^s(l)R; \quad \mu^{T_s}(-l)=-R^{-1}\mu^s(l)R; \\ \sigma^{T_s}(-l)=-R^{-1}\sigma^s(l)R, \end{gathered} \quad (8.8)$$

$$\begin{gathered} s^{T_0}(-l)=R^{-1}s^0(l)R; \quad \epsilon^{T_s}(-l)=R^{-1}\epsilon^s(l)R; \\ H^{T_0}(-l)=R^{-1}H_0(l)R, \end{gathered} \quad (8.9)$$

which take the place of (6.1) and (6.2). All these requirements can be satisfied by

$$\begin{aligned} R^{-1}\psi(l)R&=E_0K\bar{\psi}^T(-l); \\ R^{-1}\bar{\psi}(l)R&=-K^{-1}E^0\psi^T(-l). \end{aligned} \quad (8.10)$$

That these two relations do not contradict each other can be shown with the help of (4.13) and (A.17). We can also verify that the transformation (8.10) leaves the commutation relations (6.6) unchanged.

Passing to the particle picture by the instrumentality of the expansion (6.9), we obtain here, instead of (6.16),

$$\left.\begin{aligned} R^{-1}g_\pm^1(\mathbf{k})R&=-g^T{}_\pm^2(-\mathbf{k}); \\ R^{-1}g_\pm^2(\mathbf{k})R&=g^T{}_\pm^1(-\mathbf{k}) \\ R^{-1}\bar{g}_\pm^1(\mathbf{k})R&=-g^T{}_\pm^2(-\mathbf{k}); \\ R^{-1}\bar{g}_\pm^2(\mathbf{k})R&=g^T{}_\pm^1(-\mathbf{k}) \end{aligned}\right\}, \quad (8.11)$$

which guarantee

$$\begin{aligned} (R^{-1}N_\pm^1(\mathbf{k})R)^T&=N_\pm^2(-\mathbf{k}); \\ (R^{-1}N_\pm^2(\mathbf{k})R)^T&=N_\pm^1(-\mathbf{k}), \end{aligned} \quad (8.12)$$

as is required in standpoint (II).

Assuming

$$g=\begin{pmatrix}0&1\\0&0\end{pmatrix}, \quad \bar{g}=\begin{pmatrix}0&0\\1&0\end{pmatrix}, \quad (8.13)$$

we can write the matrix elements of R as

$$\begin{aligned} &(N'_+{}^1(\mathbf{k}),N'_+{}^2(-\mathbf{k})|R|N''_+{}^1(\mathbf{k}),N''_+{}^2(-\mathbf{k})) \\ &\quad=i(1-2N'_+{}^1(\mathbf{k}))\delta(N'_+{}^1(\mathbf{k}),N''_+{}^2(-\mathbf{k})) \\ &\qquad\times\delta(N'_+{}^2(-\mathbf{k}),N''_+{}^1(\mathbf{k})), \end{aligned} \quad (8.14)$$

for the part of R which affects $N_+^1(\mathbf{k})$ and $N_+^2(-\mathbf{k})$.

The matrix as given in (8.14) is unitary, but neither symmetric nor antisymmetric. Nevertheless, this R warrants the complete symmetry with respect to l and $-l$. The matrix R^TR^{-1} which was in question in relation to (4.25) becomes here

$$\begin{aligned} &(N'_+{}^1(\mathbf{k}),N'_+{}^2(-\mathbf{k})|R^TR^{-1}|N''_+{}^1(\mathbf{k}),N''_+{}^2(-\mathbf{k})) \\ &\quad=(1-2N'_+{}^2(-\mathbf{k}))(1-2N'_+{}^1(\mathbf{k})) \\ &\qquad\times\delta(N'_+{}^1(\mathbf{k}),N''_+{}^1(\mathbf{k})) \\ &\qquad\qquad\times\delta(N'_+{}^2(-\mathbf{k}),N''_+{}^2(-\mathbf{k})). \end{aligned} \quad (8.15)$$

This R^TR^{-1}, without being a c-number, commutes with all the physical quantities bilinear in ψ and $\bar{\psi}$.

Now it is of importance to note that the transformation (8.10) satisfies (8.8) and (8.9) without changing the order of ψ and $\bar{\psi}$ using a statistical assumption. Therefore it applies also to the Bose statistics. It can readily be seen that (8.10) leaves the Bose type commutation relation unchanged:

$$\begin{aligned} &\psi_r(x,l)\bar{\psi}_s(x',l')-\bar{\psi}_s(x',l')\psi_r(x,l) \\ &\quad=i[E^p(\partial/\partial x^p)+imE^5]_{rs}F_m(x-x',l-l'). \end{aligned} \quad (8.16)$$

Of course, the difficulties[9] that are irrelevant to the reversibility consideration prevent us to formulate a consistent particle theory on the Bose assumption. However, in place of the requirement about particle momentum, the transformation (8.10) satisfies the requirement about the momentum density.

Thus we come to the conclusion that the reversibility requirement as such does not determine the statistics of the charged spinor field.

It is evident that, although the modification of definition (8.4) is not necessary in standpoint (II), it can equally well be used.

IX. RETARDED AND ADVANCED POTENTIALS

The notion of retarded potential is apparently an "irreversible" one. We shall show how this irreversible action can be derived from the completely reversible theoretical scheme. This was one of the main problems which motivated an earlier paper of the author.[2]

As far as we do not perform an observation, i.e., the development of the state function by the Schroedinger equation is concerned, the distinction between the retarded and advanced actions is merely verbal. For exchange of a photon between two electrons can be interpreted either as a retarded or as an advanced action, according as on which electron our attention is placed. This fact, self-evident in quantum theory, can be translated in classical language only as a specific hypothesis such as Tetrode's.[5] Moreover, in the reversed motion, emission and absorption, therefore retarded and advanced actions, exchange their roles. This complete symmetry takes an explicit form if we calculate the interaction potential between two electrons by the second-order perturbation theory.

From the interaction picture in which we have the

Schroedinger equation

$$d\Psi(t)/dt=-i\mathbf{H}(t)\Psi(t);\quad \mathbf{H}(t)=\int(dx)^3H(x,t);\qquad H=ea^\mu\bar\psi E_\mu\psi. \tag{9.1}$$

we pass, following Schwinger,[11] to the second-order perturbation picture by the unitary transformation:

$$V(t)=\exp(-iW(t));\qquad V^{-1}(t)=\bar V(t)=\exp(+iW(t)), \tag{9.2}$$

with

$$W(t)=\frac{1}{2}\int_{-\infty}^{\infty}\epsilon(t-t')\mathbf{H}(t')dt', \tag{9.3}$$

where

$$\epsilon(t)=1\quad\text{for}\quad t>0;\quad \epsilon(t)=-1\quad\text{for}\quad t<0. \tag{9.4}$$

The transformed wave function:

$$\Psi'(t)=V^{-1}(t)\Psi(t) \tag{9.5}$$

obeys, in the e^2-approximation,

$$d\Psi'(t)/dt=-i\mathbf{H}'(t)\Psi'(t), \tag{9.6}$$

where

$$\left.\begin{aligned}\mathbf{H}'(t)&=\tfrac{1}{2}i(W(t)\mathbf{H}(t)-\mathbf{H}(t)W(t))\\&=-\tfrac{1}{4}ie^2\int(dx)^3\int(dx')^3\\&\quad\times\int_{-\infty}^{\infty}dt'\epsilon(t-t')B(x,t,x',t'),\end{aligned}\right\} \tag{9.7}$$

with

$$B=(1/e^2)[H(x,t)H(x',t')-H(x',t')H(x,t)]. \tag{9.8}$$

The reversion operator is transformed by (9.2) into

$$R\to R'=\bar V(t)RV^{T-1}(-t). \tag{9.9}$$

However, on account of the supposed property of R that

$$R^{-1}\mathbf{H}(t)R=\mathbf{H}^T(-t), \tag{9.10}$$

we obtain

$$R^{-1}W(t)R=-W^T(-t),$$

therefore

$$R'=R. \tag{9.11}$$

We can ascertain that the second-order energy retains its sign by reversion:

$$R^{-1}\mathbf{H}'(t)R=\mathbf{H}'^T(-t). \tag{9.12}$$

It goes without saying that the reversibility we have discussed in the preceding sections is a "rigorous" reversibility, independent of approximation by perturbation. (9.12) is only one aspect of the general reversibility.

[11] J. Schwinger, Phys. Rev. **74**, 1439 (1948); **75**, 651 (1949); **76**, 790 (1949).

We now express B (9.8) in terms of the absorption and emission operators of positrons, negatrons and photons. Then, by Tati-Tomonaga's prescription,[12] we bring all the emission operators to the left of the corresponding absorption operators, using appropriate commutation relations. The application of the Tati-Tomonaga prescription effaces all the differences between P and its modified definition (8.4). From among the terms thus obtained, we retain only those terms which contains two $\bar\psi$'s and two ψ's and no photon operators, and then we drop those terms which involve pair-creation and pair-annihilation. We are then left with

$$\left.\begin{aligned}B=iD_0(x-x',t-t')[&\bar\psi_{+l}\bar\psi'_{+r}\psi_{+m}\psi'_{+s}E_{\mu lm}E^\mu{}_{rs}\\&+\bar\psi_{-m}\bar\psi'_{-s}\psi_{-l}\psi'_{-r}E_{\mu mi}E^\mu{}_{sr}\\&-\bar\psi_{+l}\bar\psi'_{-s}\psi_{+m}\psi'_{-r}E_{\mu lm}E^\mu{}_{sr}\\&-\bar\psi_{-m}\bar\psi'_{+r}\psi_{-l}\psi'_{+s}E_{\mu mi}E^\mu{}_{rs}],\end{aligned}\right\} \tag{9.13}$$

where the ψ's with primes refer to (x',t'). The first two terms in (9.13) represent repulsion between like electrons, while the last two represent attraction between unlike electrons. Taking the first one term as a representative, we rewrite it as follows:

$$\left.\begin{aligned}B=(iD_0/2)\{&-s_{+\mu}(x,t)s_+{}^\mu(x',t')\\&-s_{+\mu}(x',t')s_+{}^\mu(x,t)\\&+\bar\psi_+E_\mu[E_\lambda(\partial/\partial x_\lambda)+imE_6]E^\mu\psi'_+D_m{}^+\\&+\bar\psi'_+E_\mu[E_\lambda(\partial/\partial x_\lambda)-imE_6]E^\mu\psi_+D_m{}^-\}.\end{aligned}\right\} \tag{9.14}$$

The last two terms of this expression obviously has the effect of subtracting the corresponding self-energy. Taking the first two terms, we execute the integration over t' by Nambu's method.[13] The result it

$$\mathbf{H}'_{\rm pot}(t)=(\tfrac{1}{2})(U_{\rm ret}(t)+U_{\rm adv}(t)) \tag{9.15}$$

with

$$\left.\begin{aligned}U_{\rm ret}=-(e^2/16\pi)\int(dx)^3\int(dx')^3(1/r)\\\times[s_{+\mu}(x,t)s_+{}^\mu(x',t-r)\\+s_{+\mu}(x',t-r)s_+{}^\mu(x,t)]\end{aligned}\right\} \tag{9.16}$$

$$\left.\begin{aligned}U_{\rm adv}=-(e^2/16\pi)\int(dx)^3\int(dx')^3(1/r)\\\times[s_{+\mu}(x,t)s_+{}^\mu(x',t+r)\\+s_{+\mu}(x',t+r)s_+{}^\mu(x,t)]\end{aligned}\right\} \tag{9.17}$$

$U_{\rm ret}$ and $U_{\rm adv}$, respectively, represent obviously the retarded and the advanced potentials. We can check

$$R^{-1}\mathbf{H}'_{\rm pot}(t)R=\mathbf{H}'^T{}_{\rm pot}(-t). \tag{9.18}$$

[12] T. Tati and S. Tomonaga, Prog. Theor. Phys. **3**, 391 (1948).
[13] Y. Nambu, Prog. Theor. Phys. **5**, 614 (1950).

The expression (9.17) is apparently contradictory to the customary classical "dictum" which precludes the use of advanced potential.

To understand the deep-lying difference between the classical theory and the quantum theory, we must recall the meaning of "future" in both theories. In classical physics, the future state as calculated by mathematical continuation is to become "reality" at the future instant in question. In quantum physics, the actual state at a future instant may be different from the mathematical prolongation of the present, because an observation made between the present and the future instant in question may abruptly change the state.

Any physical law becomes significant for empirical cognition when it is so formulated as to give a prediction (deterministic or statistic) based on the past observation. In fact, we can bring the formula (9.15) to a form which conforms to this criterion, because the physical quantities referring to the future in (9.17) are determined by definite differential equations and are to be considered as operative on the mathematically prolonged future state. This reduction to the past is particularly easy when we can assume "absence of any real first order process between the remote past and the remote future (again mathematical future)." See also Nambu.[13] For it is an established fact that Schwinger's second-order picture, under this assumption, becomes mathematically identical with Tomonaga's second-order picture,[12] which is obtained by replacing W (9.3) by

$$W(t)=\int_{-\infty}^{t} dt'\mathbf{H}(t'). \tag{9.19}$$

Now a similar calculation in Tomanaga's picture gives a full retarded potential. Therefore, (9.15) is, under such assumption, mathematically identical to the full retarded potential.

Of course, we can also bring (9.15) to the expression of full advanced potential. This is mathematically equally correct, but physically useless because it refers to the mathematical future.

A more general reduction of Schwinger's reversible picture to Tomanaga's formally irreversible picture may be done in the following manner. We notice that Schwinger's second order energy is not "standardized," in the sense that it does not become identically zero at any instant between $-\infty$ and $+\infty$, unless the aforesaid assumption is made. If we standardize it with reference to the remote past, i.e., if we make the difference between its expectation value at t and its expectation value at $t=-\infty$, we obtain, to the e^2-approximation, exactly the same expression as the Tomonaga picture, thus leading to the full retarded potential. Naturally, if we standardize it with reference to the remote future, we obtain the pure advanced potential. This again can be of little significance to physical experience, for it refers to the mathematically concocted future.

We thus see not only that we can deduce the retarded potential from the quantum electrodynamics without interfering with its basic reversibility, but also that the expression of potential energy in terms of retarded action is the only legitimate expression conformable to the nature of human cognition.

The author is indebted to the members of the theoretical seminar of the University of Michigan for their critical discussions of the problem of reversibility and, in particular, to Dr. K. M. Case for the enlightening exposition of his own interpretation of Schwinger's contention about reversibility. The author is also happy to express appreciation for the constant interest and suggestions that Dr. K. Husimi has given to the author's investigation of reversibility since the time he took up the problem some seventeen years ago.

APPENDIX

(a) Four Kinds of Tensors

It is customary to define spinors by their transformation properties for infinitesimal rotations and then to assign to them, in a more or less *ad hoc* fashion, properties for reflections in such a way that they do not contradict the original definition. It will then be simpler and more consistent to define the spinors from the outset by their properties for reflections and then to deduce from them the properties for rotations using the fact that any rotation can be decomposed into a series of reflections.[14–16]

We consider the entire group of congruent linear transformations:

$$x^{\mu'}=a^{\mu}{}_{\nu}x^{\nu} \quad (\mu, \nu=1, 2, 3, 0), \tag{A.1}$$

which do not change the value of

$$D^2=(x^1)^2+(x^2)^2+(x^3)^2-(x^0)^2=x_\mu x^\mu = g_{\mu\nu}x^\mu x^\nu = g^{\mu\nu}x_\mu x_\nu. \tag{A.2}$$

We shall consistently adhere to the real time coordinate $x^0=-x_0=t$, $(c=1)$.

We define three signum functions σ, σ_t, and σ_s by

$$\sigma=\partial(x^{1'}, x^{2'}, x^{3'}, x^{0'})/\partial(x^1, x^2, x^3, x^0), \tag{A.3}$$

$$\sigma_t=\frac{\partial x^{0'}}{\partial x^0}\Big/\left|\frac{\partial x^{0'}}{\partial x^0}\right|, \tag{A.4}$$

$$\sigma_s=\frac{\partial(x^{1'}, x^{2'}, x^{3'})}{\partial(x^1, x^2, x^3)}\Big/\left|\frac{\partial(x^{1'}, x^{2'}, x^{3'})}{\partial(x^1, x^2, x^3)}\right|. \tag{A.5}$$

Any congruent transformation can be decomposed into a series of reflections with respect to planes passing through the origin. According as the normal n^μ to a

[14] E. Cartan, *La Théorie des Spineurs* (Hermann et Cie, Paris, 1938).

[15] S. Watanabe, Sci. Pap. Inst. Phys. Chem. Research (Tokyo) 39, 157 (1941).

[16] S. Watanabe, *Classical Mechanics of Fields* (Kawade-Shobo, Tokyo, 1948). (In Japanese.)

TABLE I. Classification of congruent transformations. For the definitions of σ, σ_t and σ_s, see (A.3), (A.4), and (A.5).

	σ	σ_t	σ_s	
$\mathfrak{A}$	+	+	+	Proper rotations
$\mathfrak{B}$	+	−	−	Improper rotations
$\mathfrak{C}$	−	+	−	Proper inversions
$\mathfrak{D}$	−	−	+	Improper inversions

plane of reflection is time-like or space-like, i.e.,

$$n_\mu n^\mu = -1 \quad \text{or} \quad +1, \tag{A.6}$$

we speak of a temporal or spatial reflection.

The total number ν of reflections of both kinds, the number ν_t of temporal reflections and the number ν_s of spatial reflections in the decomposition of a transformation are connected with the values of the signum functions by

$$\sigma=(-1)^\nu; \quad \sigma_t=(-1)^{\nu_t}; \quad \sigma_s=(-1)^{\nu_s} \tag{A.7}$$

from which follows

$$(\nu=\nu_t+\nu_s): \quad \sigma=\sigma_t\sigma_s. \tag{A.8}$$

The values of σ, σ_t and σ_s have invariant geometrical meanings independent of the coordinates used and of the way of decomposition.

The entire congruent group (A.1) can be divided into four classes: $\mathfrak{A}$, $\mathfrak{B}$, $\mathfrak{C}$, and $\mathfrak{D}$, whose definitions are given in Table I.

It can be easily seen that $\mathfrak{A}$, $\mathfrak{A}+\mathfrak{B}$, $\mathfrak{A}+\mathfrak{C}$ and $\mathfrak{A}+\mathfrak{D}$ are invariant partial groups of the whole group. σ, σ_t and σ_s are faithful representations of the factor groups engendered, respectively, by the invariant partial groups $\mathfrak{A}+\mathfrak{B}$, $\mathfrak{A}+\mathfrak{C}$ and $\mathfrak{A}+\mathfrak{D}$.

The transformation rule of a "regular" tensor which is transformed according to

$$t'^{\mu\nu\cdots}=a^\mu{}_\kappa a^\nu{}_\lambda \cdots t^{\kappa\lambda\cdots} \tag{A.9}$$

will be written for brevity

$$t'=At. \quad \text{(regular)}. \tag{A.10}$$

It is clear from the foregoing remark that, if A is a faithful representation of the entire group (A.1), then each of σA, $\sigma_t A$ and $\sigma_s A$ is also a faithful representation of the same order. Three kinds of tensors which are transformed according to

$$\begin{aligned} t'&=\sigma At, && \text{(1st kind)} \\ t'&=\sigma_t At, && \text{(2nd kind)} \\ t'&=\sigma_s At, && \text{(3rd kind)} \end{aligned} \tag{A.11}$$

were introduced by the present author under the names, respectively, of a first kind, a second kind and a third kind pseudotensors.[15]

If the improper rotations and improper inversions are disregarded, the second kind pseudotensors become identical with the regular tensors and the third kind pseudotensors with the first kind. The pseudotensors in the ordinary terminology correspond to the latter.

(b) Spinors Defined by Reflections

Four basic matrices E_1, E_2, E_3, E_0 are defined by

$$\tfrac{1}{2}(E_\mu E_\nu+E_\nu E_\mu)=g_{\mu\nu}. \tag{A.12}$$

The basic matrices with superscripts are related to those with subscripts by

$$E^\mu=g^{\mu\nu}E_\nu. \tag{A.13}$$

For convenience in later use, we define $E_5=E^5$ by

$$E_5=-iE_1E_2E_3E_0. \tag{A.14}$$

Then (A.12) can be generalized to five dimensions with $g_{55}=+1$ and $g_{5\mu}=0$ ($\mu=1, 2, 3, 0$).

For our analysis, the following theorems are essential:[17]

(1) For any set of E_μ there exists a matrix J such that

$$J^{-1}E_iJ=-\bar{E}_i; \quad J=-J. \quad (i=1, 2, 3, 0, 5), \tag{A.15}$$

where the bar on a matrix means its hermitian conjugate.

(2) For any set of E_μ there exists a matrix K such that

$$K^{-1}E_\mu K=-E^T{}_\mu; \quad K^{-1}E_5K=E^T{}_5; \quad K^T=-K, \tag{A.16}$$

and

$$\bar{K}=J^TK^{-1}J, \tag{A.17}$$

where the symbol T on a matrix means its transpose.

(3) There exist such sets of E_μ that

$$E_i=\bar{E}^i. \tag{A.18}$$

Such sets of E_μ will be called hermitian systems for E_1, E_2, E_3, (iE_0) and E_5 are hermitian. In a hermitian system

$$J=E^0; \quad \bar{K}=K^{-1}=-K^*, \tag{A.19}$$

where the star is used in the sense of complex conjugate.

(4) Any matrix that commutes with all the four basic matrices (of any set) is the unity matrix multiplied by a number.

We now define a matrix N corresponding to the reflection with respect to a normal n^μ by

$$N=n_\mu E^\mu \quad (N^2=n_\mu n^\mu). \tag{A.20}$$

And corresponding to a transformation which can be decomposed into a series of reflections $N_1, N_2, \cdots N_\nu$, we introduce a matrix S:

$$S=N_\nu N_{\nu-1}\cdots N_1; \quad S^{-1}=\sigma_t N_1 N_2 \cdots N_\nu, \tag{A.21}$$

where each N is defined by (A.20).

It can be shown that S is a two-valued faithful representation of the entire group (A.1). The two valuedness comes from the fact that a plane does not determine the sign of its normal.

[17] W. Pauli, Ann. Inst. Henri Poincaré **6**, 137 (1936).

The spinor ξ is defined as the representation vector of S:

$$\xi' = S\xi. \tag{A.22}$$

Then its spinor conjugate:

$$\bar{\xi} = \xi^* J^{-1} \tag{A.23}$$

transforms according to

$$\bar{\xi}' = \bar{\xi}\sigma_\nu S^{-1}. \tag{A.24}$$

Definition (A.21) leads to the relation:

$$E_\mu a^\mu{}_\nu = \sigma S E_\nu S^{-1}. \tag{A.25}$$

Comparison of our definition of S with the ordinary transformation rule for spinors establishes the correspondence between the E-system and the γ-system:

$$E_\mu = i\gamma_5\gamma_\mu; \quad E_5 = \gamma_5, \tag{A.26}$$

where

$$\gamma_0 = -\gamma^0 = i\gamma_4. \tag{A.27}$$

A hermitian system of E_μ (A.18) corresponds to a hermitian γ-system. The ordinary conjugate spinor $\xi^\dagger = \xi^*\gamma_4$ is connected to our conjugate spinor $\bar{\xi}$ in the hermitian system by

$$\xi^\dagger = -\bar{\xi}E_5. \tag{A.28}$$

The transformation rule (A.25) is rewritten in the γ-system in the form:

$$\gamma_\mu a^\mu{}_\nu = S\gamma_\nu S^{-1}, \tag{A.29}$$

which coincides with the ordinarily assumed rule, but here we have no ambiguity as to the sign in case of reflections.

The transformation properties of tensorial quantities built with the spinors are tabulated in Table II.

One of the convenient features of the present method consists in that, in case of reversal of a axis, the spinor is simply multiplied by the E_μ corresponding to that axis. See (A.20). For instance, for the time-inversion, we have

$$\xi \to \pm E^0\xi; \quad \bar{\xi} \to \pm \bar{\xi}E_0, \tag{A.30}$$

where the same sign should be adopted in both relations.

It is of importance to note the effect of K (A.16) on the transformation matrix (A.21):

$$KS^TK^{-1} = \sigma_\nu S^{-1}, \tag{A.31}$$

which is true as far as 4-dimensional congruent transformations are concerned. If two spinors ψ_1 and ψ_2 are connected by

$$\psi_1 = -K\bar{\psi}_2 = \bar{\psi}_2 K; \quad \bar{\psi}_1 = -K^{-1}\psi_2 = \psi_2 K^{-1}, \tag{A.32}$$

this connection, in virtue of (A.31), is kept invariant for any transformation provided that ψ_1 and ψ_2 obey the same transformation rule (A.22). Conversely, there is no other matrix than K that enjoys this property. The compatibility of the two relations (A.32) is proved by (A.17).

TABLE II. Transformation properties of tensors built with spinors of the same "kind."

$\bar{\xi}\xi$	$\xi^\dagger\gamma_5\xi$	3rd kind pseudoscalar
$\bar{\xi}E_5\xi$	$\xi^\dagger\xi$	2nd kind pseudoscalar
$\bar{\xi}E_\mu\xi$	$\xi^\dagger\gamma_\mu\xi$	2nd kind pseudovector
$\bar{\xi}E_5E_\mu\xi$	$\xi^\dagger\gamma_5\gamma_\mu\xi$	3rd kind pseudovector
$\bar{\xi}E_\mu E_\nu\xi$	$\xi^\dagger\gamma_5\gamma_\mu\gamma_\nu\xi$	3rd kind pseudotensor
$\bar{\xi}E_5E_\mu E_\nu\xi$	$\xi^\dagger\gamma_\mu\gamma_\nu\xi$	2nd kind pseudotensor

In place of (A.26), an alternative correspondence between the E-system and the γ-system can be established by

$$E_\mu = \gamma'_\mu; \quad E_5 = \gamma'_5; \quad \bar{\xi} = -i\xi^\dagger \tag{A.33}$$

which leads to

$$\gamma'_\mu a^\mu{}_\nu = \sigma S\gamma_\nu S^{-1}. \tag{A.34}$$

The use of this γ'-system instead of the γ-system only interchanges the second kind and the third kind of the resulting tensors. Other than this modification, this choice of correspondence produces nothing essentially new; we shall adhere to the previous choice (A.26) in this work.

(c) Pseudospinors, Bi-Spinors, Bi-Tensors

In view of the fact that regular tensors and first kind pseudotensors cannot be built by the foregoing method, one may be tempted to introduce "pseudospinors" by

$$\eta' = \sigma S\eta; \quad \zeta' = \sigma_\nu S\zeta; \quad \omega' = \sigma_\nu S\omega. \tag{A.35}$$

But obviously, the tensors built with these pseudospinors have the same transformation properties as those indicated in Table II. Different kinds of tensors, of course, can be obtained if one of ξ-spinor and η-spinor and one of ζ-spinor and ω-spinor are combined to build tensors. Table III gives the case of mixed products of a ξ-spinor and a ζ-spinor.

The method of pseudospinors is mathematically not elegant because S has by definition an indefinite sign. Combined use of two kinds of spinors is equivalent to employing eight components. If, from the outset, eight components are to be used, we can devise a more compact formalism, which also will prove to be useful for our problem.

We introduce signum matrices Σ, Σ_t and Σ_s by

$$\left.\begin{aligned} \Sigma &= \begin{pmatrix} 0 & 1 \\ 1 & 0 \end{pmatrix}^r; \quad \Sigma^t = \begin{pmatrix} 0 & 1 \\ 1 & 0 \end{pmatrix}^{r_t}; \\ \Sigma_s &= \begin{pmatrix} 0 & 1 \\ 1 & 0 \end{pmatrix}^{r_s} \end{aligned}\right\} \tag{A.36}$$

which form groups, respectively, isomorphic to the groups formed by σ, σ_t and σ_s. To avoid repetition, we shall discuss only Σ_t in this Appendix.

TABLE III. Transformation properties of tensors built with a ξ-spinor and a ζ-spinor.

$\bar{\zeta}\xi$	$\zeta^\dagger\gamma_5\xi$	1st kind pseudoscalar
$\bar{\zeta}E_5\xi$	$\zeta^\dagger\xi$	regular scalar
$\bar{\zeta}E_\mu\xi$	$\zeta^\dagger\gamma_\mu\xi$	regular vector
$\bar{\zeta}E_5E_\mu\xi$	$\zeta^\dagger\gamma_5\gamma_\mu\xi$	1st kind pseudovector
$\bar{\zeta}E_\mu E_\nu\xi$	$\zeta^\dagger\gamma_5\gamma_\mu\gamma_\nu\xi$	1st kind pseudotensor
$\bar{\zeta}E_5E_\mu E_\nu\xi$	$\zeta^\dagger\gamma_\mu\gamma_\nu\xi$	regular tensor

We now regard each row and each column of the matrix (A.36) as corresponding to four spinorial components. Correspondingly, the basic matrices E_μ will be replaced by eight-eight matrices $\mathbf{E}_\mu$ defined by

$$\mathbf{E}_\mu=\begin{pmatrix}E_\mu & 0\\ 0 & E_\mu\end{pmatrix}, \tag{A.37}$$

which satisfy the definition (A.12).

We next introduce a matrix Π which is defined by

$$\Pi=\Pi^{-1}=\begin{pmatrix}1 & 0\\ 0 & -1\end{pmatrix}. \tag{A.38}$$

This matrix Π as well as Σ_t commutes with $\mathbf{E}_\mu$:

$$\Pi^{-1}\mathbf{E}_\mu\Pi=\mathbf{E}_\mu;\quad \Sigma_t^{-1}\mathbf{E}_\mu\Sigma_t=\mathbf{E}_\mu;\quad (\Sigma_t^{-1}=\Sigma_t). \tag{A.39}$$

The commutation rule between Σ_t and Π has an important property

$$\Sigma_t^{-1}\Pi\Sigma_t=\sigma_t\Pi. \tag{A.40}$$

The transformation matrix S will be replaced by

$$\mathbf{S}=\mathbf{N}_\nu\mathbf{N}_{\nu-1}\cdots\mathbf{N}_1, \tag{A.41}$$

where each $\mathbf{N}$ is defined by $\mathbf{N}=n^\mu\mathbf{E}_\mu$.

Corresponding to $\sigma_t S$ we introduce

$$\Sigma_t\mathbf{S}. \tag{A.42}$$

That $\Sigma_t\mathbf{S}$ is a representation of the group is guaranteed by the commutability of Σ_t with $\mathbf{E}_\mu$, and therefore with $\mathbf{S}$.

TABLE IV. Transformation properties of tensors built with bi-spinors.

$\bar{X}X$	$X^\dagger\Gamma_5X$	3rd kind pseudoscalar
$\bar{X}\Pi X$	$X^\dagger\Gamma_5\Pi X$	1st kind pseudoscalar
$\bar{X}\mathbf{E}_5X$	$X^\dagger X$	2nd kind pseudoscalar
$\bar{X}\mathbf{E}_5\Pi X$	$X^\dagger\Pi X$	regular scalar
$\bar{X}\mathbf{E}_\mu X$	$X^\dagger\Gamma_\mu X$	2nd kind pseudovector
$\bar{X}\mathbf{E}_\mu\Pi X$	$X^\dagger\Gamma_\mu\Pi X$	regular vector
$\bar{X}\mathbf{E}_5\mathbf{E}_\mu X$	$X^\dagger\Gamma_5\Gamma_\mu X$	3rd kind pseudovector
$\bar{X}\mathbf{E}_5\mathbf{E}_\mu\Pi X$	$X^\dagger\Gamma_5\Gamma_\mu\Pi X$	1st kind pseudovector
$\bar{X}\mathbf{E}_\mu\mathbf{E}_\nu X$	$X^\dagger\Gamma_5\Gamma_\mu\Gamma_\nu X$	3rd kind pseudotensor
$\bar{X}\mathbf{E}_\mu\mathbf{E}_\nu\Pi X$	$X^\dagger\Gamma_5\Gamma_\mu\Gamma_\nu\Pi X$	1st kind pseudotensor
$\bar{X}\mathbf{E}_5\mathbf{E}_\mu\mathbf{E}_\nu X$	$X^\dagger\Gamma_\mu\Gamma_\nu X$	2nd kind pseudotensor
$\bar{X}\mathbf{E}_5\mathbf{E}_\mu\mathbf{E}_\nu\Pi X$	$X^\dagger\Gamma_\mu\Gamma_\nu\Pi X$	regular tensor

Now an eight-component spinor or bi-spinor X can be defined as the representation vector of $\Sigma_t\mathbf{S}$:

$$X'=\Sigma_t\mathbf{S}X. \tag{A.43}$$

The spinor conjugate to X will be given by

$$\bar{X}=X^*\mathbf{J}^{-1};\quad \mathbf{J}=\begin{pmatrix}J & 0\\ 0 & J\end{pmatrix}. \tag{A.44}$$

Then $\bar{X}$ is obviously transformed according to

$$\bar{X}'=\bar{X}\sigma_t\mathbf{S}^{-1}\Sigma_t, \tag{A.45}$$

Tensors formed with a Π between $\bar{X}$ and X have the transformation properties different from those of the tensors without Π by the factor σ_t due to (A.40). Table IV shows that all the four kinds of tensors can be formed with the help of a bi-spinor.

$X^\dagger$ and Γ_i in Table IV are natural extensions of $\xi^\dagger$ and γ_i to the eight-component case and will hardly require any explanation.

Corresponding to the two columns and two rows of the matrices, we shall write the eight components of X in two parts:

$$X=\begin{pmatrix}\psi\\ \varphi\end{pmatrix}, \tag{A.46}$$

where each of ψ and φ has four components. For the present, we do not assume any relation between ψ and φ.

A tensor or pseudotensor constructed without the help of Π is just the sum of the corresponding two terms constructed respectively with ψ and φ. A tensor or pseudotensor constructed with the help of Π is on the contrary the difference between the corresponding term in ψ and the corresponding term in φ. For instance:

$$\begin{aligned}\bar{X}\mathbf{E}_\mu X&=\bar{\psi}E_\mu\psi+\bar{\varphi}E_\mu\varphi,\\ \bar{X}\mathbf{E}_\mu\Pi X&=\bar{\psi}E_\mu\psi-\bar{\varphi}E_\mu\varphi.\end{aligned} \tag{A.47}$$

The transformation rule given in (A.43) means that, for the transformations of the classes $\mathfrak{A}$ and $\mathfrak{C}$, ψ and φ are separately transformed as ξ-spinors, and that, for the transformations of the classes $\mathfrak{B}$ and $\mathfrak{D}$, ψ and φ are interchanged besides their transformations as ξ-spinors. In particular, for the time reversal, ψ, φ, $\bar{\psi}$ and $\bar{\varphi}$ are transformed as

$$\begin{aligned}&\psi\rightarrow\pm E^0\varphi;\quad \bar{\psi}\rightarrow\pm\bar{\varphi}E_0,\\ &\varphi\rightarrow\pm E^0\psi;\quad \bar{\varphi}\rightarrow\pm\bar{\psi}E_0,\end{aligned} \tag{A.48}$$

where either the upper or the lower sign should be adopted throughout.

The method which has been used to define the bi-spinor can also be applied to tensors with some advantage in our discussion. If B represents any one of A, σA, $\sigma_t A$ and $\sigma_t\sigma A$, the matrix:

$$\mathbf{B}=\begin{pmatrix}B & 0\\ 0 & B\end{pmatrix}, \tag{A.49}$$

as well as $\Sigma_i \mathbf{B}$, is a faithful representation of the group. The bi-tensor (and pseudo-bi-tensor) is defined by

$$T' = \Sigma_i \mathbf{B} T, \tag{A.50}$$

with

$$T = \begin{pmatrix} t \\ u \end{pmatrix}. \tag{A.51}$$

Taking two such bi-tensors T_1 and T_2:

$$T_1 = \begin{pmatrix} t_1 \\ u_1 \end{pmatrix}; \quad T_2 = \begin{pmatrix} t_2 \\ u_2 \end{pmatrix}, \tag{A.52}$$

which can be of different ranks and different "kinds," we construct a product tensor:

$$T_1 T_2 = t_1 t_2 + u_1 u_2, \tag{A.53}$$

which is the result of a contraction with regard to the index specifying the two parts of bi-tensors. Then $T_1 T_2$ will transform by

$$(T_1 T_2)' = B_1 B_2 (T_1 T_2), \tag{A.54}$$

where B_1 operates on t_1 and u_1, while B_2 operates on t_2 and u_2.

If we construct

$$T_1 \amalg T_2 = t_1 t_2 - u_1 u_2, \tag{A.55}$$

then the transformation rule of this quantity differs from that of (A.54) by the factor σ_i:

$$(T_1 \amalg T_2)' = \sigma_i B_1 B_2 (T_1 \amalg T_2). \tag{A.56}$$

In particular, if we take as T_2 a constant regular bi-scalar ($B_2 = 1$):

$$T_1 = \begin{pmatrix} t \\ u \end{pmatrix}; \quad T_2 = \begin{pmatrix} 1 \\ 1 \end{pmatrix}, \tag{A.57}$$

then

$$T_1 T_2 = t + u; \quad (T_1 T_2)' = B(T_1 T_2), \tag{A.58}$$

and

$$T_1 \amalg T_2 = t - u; \quad (T_1 \amalg T_2)' = \sigma_i B (T_1 \amalg T_2), \tag{A.59}$$

writing B for B_1.

When two bi-tensors (A.52) are given, we can construct a third bi-tensor by

$$T_3 = \begin{pmatrix} t_1 t_2 \\ u_1 u_2 \end{pmatrix}, \tag{A.60}$$

which satisfies (A.50) with $B_3 = B_1 B_2$. The tensor products considered in (A.53) and (A.55) can be derived from this bi-tensorial product (A.60) by the processes given in (A.58) and (A.59), respectively.

A good example of a bi-tensor is given by the term in ψ and the term in φ in the tensors constructed out of bi-spinors. For instance, the first and the second terms of (A.47) form a 2nd kind pseudo-bi-tensor:

$$T_\mu = \begin{pmatrix} \bar{\psi} E_\mu \psi \\ \bar{\varphi} E_\mu \varphi \end{pmatrix}, \tag{A.61}$$

for this T_μ (A.61) obeys the transformation rule (A.50) with

$$B = \sigma_i A. \tag{A.62}$$

$\bar{X} \mathbf{E}_\mu X$ and $\bar{X} \mathbf{E}_\mu \amalg X$ correspond then, respectively, to (A.58) and (A.59).

It goes without saying that, by using Σ, Σ_i, and Σ_s instead of only Σ_i, we can obtain any kind of tensor by (A.53) and (A.55).

(d) Remark for 5-Dimensional Space

All the formulas and statements in this Appendix, except those indicated below, are applicable without modification to the 5-dimensional space whose metric is given by

$$D^2 = (x^1)^2 + (x^2)^2 + (x^3)^2 - (x^0)^2 + (x^5)^2. \tag{A.63}$$

The only exceptions are (A.29), (A.31) and (A.32). The tensors built with spinors containing E_4 will be incorporated in tensors of rank higher by one.[17] The third rank antisymmetric tensor is naturally complementary to a second rank antisymmetric tensor, and its transformation rule differs from that of this latter by the factor σ. In order to obtain all the four kinds of tensors by mixed products of spinors, we need here all the four kinds of spinors. Correspondingly, we have to use all the three Σ's to obtain all the four kinds of tensors by the method of bi-spinors.

[17] One can for instance easily see that Møller's 5-dimensional theory of mesons has a wrong transformation property whether one adopts (A.26) or (A.33). See S. Watanabe, Proc. Phys. Math. Soc. (Japan) 25, 561 (1943).

Generalized Statistical Mechanics

PETER G. BERGMANN
Department of Physics, Syracuse University, Syracuse 10, New York
(Received July 26, 1951)

In this paper, a start is made toward the development of a statistical mechanics that will be suited to the treatment of dynamic changes in thermodynamic systems and which, at the same time, will be in the appropriate form for a relativistically invariant theory. The formal device consists of making the time coordinate one of the canonical variables. As a result, stationary ensembles no longer occupy a privileged position among all conceivable Gibbs ensembles, and it becomes necessary to redefine and to reformulate most statistical and thermodynamic concepts. This has been done with the concept of a canonical ensemble, with entropy, temperature, heat flux, and performance of work. With a suitable definition of the entropy of an individual system, a new formulation of the H-theorem is provided, which in turn leads to a formulation of the Second Law.

I. INTRODUCTION

EARLIER attempts to formulate a consistent relativistic thermodynamics[1–5] have usually been concerned with giving the concepts of entropy, temperature, and heat a relativistically invariant significance. Except for the very early work by Einstein and Planck, these attempts have been largely on the so-called phenomenological level, without any reference to the underlying statistical concepts. As a result, many of these papers appear rather formal in approach, achieving their results primarily by the method of seeking Lorentz-invariant modifications of the concepts familiar in ordinary thermodynamics. Eckart[5] has pointed out that ordinary thermodynamics is fragmentary in so far as it deals only with equilibrium situations and with quasistatic processes. Essentially dynamical processes are outside its scope. On the other hand, relativistic theories become necessary in physics only if velocities are involved which by ordinary laboratory standards are very large. While it is always possible to introduce a local framework in which any one velocity is reduced to zero, a truly relativistic theory is likely to give novel and therefore interesting answers only if velocities are involved that are very large relative to each other. But if two streams of matter interact with each other whose relative velocity is comparable to that of light, then no observer can describe that interaction as a quasi-static process, and the approach of formal invariantization breaks down.

These considerations lead inescapably to the conclusion that the development of relativistic thermodynamics can be tackled successfully only as part of a more comprehensive program, to develop a theory of heat that is independent of the concept of thermal equilibrium. Such a theory we shall call a generalized theory of heat, for want of a better expression. Such a development is bound to lead to a much more complex theory than the conventional thermodynamics, for the simple reason that a stationary situation has fewer degrees of freedom than one in which time derivatives of the thermal variables also enter into the description. The conventional theory is quite trustworthy in its assertion that a violent development leading from one stationary situation to another stationary situation is bound to increase the entropy. But if there is neither a stationary initial situation nor a stationary terminal situation, then we cannot assign entropies to two states succeeding each other in the course of time without going beyond the confines of conventional thermodynamics. It is not that conventional thermodynamics gives the wrong answers; it fails to give any answer at all.

If we are to generalize the conventional theory of heat, then we must, in this writer's opinion, start out with the fundamentals, and that means not with thermodynamics, but with statistical mechanics. Hence this paper is devoted to the development of a statistical mechanics independent of the notion of the stationary ensemble. Formally, we shall proceed by depriving the time coordinate of its privileged role vis-a-vis the usual canonical coordinates. While the formal method is well known and amounts to the addition of two further dimensions to the ordinary phase space (time and its canonical conjugate, the negative Hamiltonian), the description of an ensemble in this new phase space in terms of the density of its member systems is complicated by the fact that all the systems are constrained to move on one hypersurface, and furthermore, each individual system is no longer represented by a point but by a curve, its trajectory. Thus, the ensemble must be described in terms of the density of a field of curves on a hypersurface. Fortunately, such a description in terms of geometric invariants is quite feasible and leads to the introduction of a single invariant quantity which for all practical purposes assumes the role of the usual density in phase space.

The development of this description occupies most of the following two sections. The invariant description

[1] A. Einstein, Jahrbuch d. Radioktivität und Elektronik **4**, 441 (1907).
[2] M. Planck, Preuss. Akad. Wiss. Berlin, Sitz. Ber. **29**, 542 (1907).
[3] M. Planck, Ann. Physik **26**, 1 (1908).
[4] R. C. Tolman, *Relativity, Thermodynamics, and Cosmology* (Oxford University Press, London, 1934).
[5] C. Eckart, Phys. Rev. **58**, 919 (1940).

of an ensemble of quantum-theoretical systems is also indicated. From then on, we shall reformulate the concept of the canonical ensemble, and with it that of the ensemble entropy. We shall find that in general a single temperature is not sufficient to characterize a canonical ensemble, nor can the interaction of a thermodynamic system with its surroundings be adequately described in terms of a scalar "heat transfer" and another scalar "performance of work." But there are natural generalizations of these all-important quantities, and there exists a relationship between the generalized heat transfer, multiplied by the generalized reciprocal temperature, and the increase in entropy.

In this generalized statistical mechanics, the development of a relativistic, i.e., Lorentz-invariant, theory depends solely on the availability of a relativistic Hamiltonian. Such Hamiltonians are, of course, known and of particular importance in covariant field theories (such as the theory of the electromagnetic field). Thus, relativistic thermodynamics requires no additional concepts.

II. PARAMETRIZATION

In the ordinary formulation of analytical mechanics, the time t is not a dynamic variable while the generalized coordinates q_k are. In Lorentz transformations, on the other hand, the time appears symmetrically with the spatial coordinates, and the (negative) energy with the linear momentum components. It is, therefore, desirable, to modify the usual analytical mechanics in such a manner that the privileged position of the time coordinate and its canonical conjugate, the (negative) energy, is destroyed. Similar comments apply to the analogous quantum-mechanical situation.

A. Classical Mechanics

Consider a system with f degrees of freedom whose generalized coordinates shall be designated by q_k and their canonical conjugates by p_k, k taking values from 1 to f. Let the Hamiltonian be a known function $H(q_k, p_k, t)$. It is not necessary to assume for what follows that the system be conservative, i.e., that the Hamiltonian be explicitly independent of t. In the phase space S with the coordinates q_k, p_k, the trajectory of the system is then a single curve which depends in a definite manner on the time t. In other words, if we solve the equations of motion, the resulting functions $q_k(t)$, $p_k(t)$ represent not merely a convenient parametric representation of the mechanical trajectory, but t is a physically significant variable of its own, though not a coordinate of our present phase space.

It is well known that the canonical equations of motion are the Euler-Lagrange equations of a variational principle in phase space,

$$\delta S=0, \quad S=\int[\textstyle\sum_k p_k dq_k/dt-H(q_k, p_k, t)]dt. \tag{2.1}$$

If we wish to "symmetrize" with respect to the variable t, we may interpret the variational principle as one in a $(2f+2)$ dimensional space, possessing the coordinates q_k, p_k, t, $\bar{E}$ (the latter being equal to $-H$). The variation in that higher-dimensional space, which we shall call the "expanded phase space," is, however, restricted by a subsidiary condition,

$$\bar{H}\equiv H(q_k, p_k, t)+\bar{E}=0. \tag{2.2}$$

The variational principle itself can be formulated conveniently if we introduce an arbitrary parameter $\theta(q_k, p_k, t, \bar{E})$, subject only to the inequality

$$\partial\theta/\partial t>0, \tag{2.3}$$

and takes the form

$$\begin{aligned}\delta S=0, \quad S&=\int\left(\sum_{k=1}^{f} p_k\frac{dq_k}{d\theta}+\bar{E}\frac{dt}{d\theta}\right)d\theta\\ &=\int\left(\sum_{\kappa=1}^{f+1} p_\kappa\frac{dq_\kappa}{d\theta}\right)d\theta=\int\left(\sum_{\kappa=1}^{f+1} p_\kappa dq_\kappa\right),\end{aligned} \tag{2.4}$$

where we have used the abbreviating notation

$$q_{f+1}=t, \quad p_{f+1}=\bar{E}; \quad \kappa=1, \cdots, f+1. \tag{2.5}$$

The variational principle (2.4) with the subsidiary condition (2.2) in the expanded phase space is equivalent to the principle (2.1) in the original phase space. The canonical equations of motion are obtained by the method of Lagrange's multipliers and come out as

$$dq_\kappa/d\theta-\alpha\partial\bar{H}/\partial p_\kappa=0, \quad dp_\kappa/d\theta+\alpha\partial\bar{H}/\partial q_\kappa=0. \tag{2.6}$$

The multiplier α cannot be determined uniquely. Its arbitrariness reflects the fact that the parameter θ is arbitrary, and that this new formalism is invariant with respect to arbitrary parameter transformations. Instead of keeping the multiplier in the equations of motion (2.6), we shall incorporate it in the subsidiary condition and set, from now on.

$$\begin{gathered}dq_\kappa/d\theta=\partial\mathrm{H}/\partial p_\kappa, \quad dp_\kappa/d\theta=-\partial\mathrm{H}/\partial q_\kappa,\\ \mathrm{H}=0,\end{gathered} \tag{2.7}$$

where H is an arbitrary function of $\bar{H}$ and $(2f+1)$ canonical coordinates, so that $\mathrm{H}=0$ where $\bar{H}=0$, and that for $\bar{H}=0$ the derivative $(\partial\mathrm{H}/\partial\bar{H})$ does not vanish.

The canonical transformations in the expanded phase space are all those which will not change the form of the variational integral (2.4). The form of the subsidiary condition is usually changed by the substitution of the new variables for the old ones. In the special case of an infinitesimal canonical transformation, the changes in the coordinate values at any fixed point in the expanded phase space are

$$\delta q_\kappa=\partial\Gamma/\partial p_\kappa, \quad \delta p_\kappa=-\partial\Gamma/\partial q_\kappa, \quad \Gamma=\Gamma(q_\kappa, p_\kappa). \tag{2.8}$$

$\delta\mathrm{H}$ vanishes by definition. But if we consider H as a function of its arguments, then its functional de-

pendence changes, and the left-hand side of the subsidiary condition undergoes the infinitesimal change

$$\delta' \mathrm{H} = (\Gamma, \mathrm{H}). \tag{2.9}$$

We find that the whole formalism is invariant with respect to infinitesimal transformations which are generated by constants of the motion, i.e., dynamical variables (which may depend on t explicitly) whose value does not change along a trajectory. Incidentally, the Poisson bracket symbol (Γ, H) is to be understood in terms of the expanded phase space,

$$(\mathrm{A}, \mathrm{B}) \equiv \sum_{s=1}^{f+1} \left(\frac{\partial \mathrm{A}}{\partial q_s} \frac{\partial \mathrm{B}}{\partial p_s} - \frac{\partial \mathrm{A}}{\partial p_s} \frac{\partial \mathrm{B}}{\partial q_s} \right). \tag{2.10}$$

In Sec. III, we shall construct ensembles in the expanded phase space. Let it be noted that only trajectories satisfying the subsidiary condition may be incorporated in any ensemble that is to be meaningful. On the other hand, any trajectory satisfying the subsidiary condition at one point satisfies the condition everywhere. The subsidiary condition is itself a constant of the motion.

B. Quantum Mechanics

In quantum mechanics, one might think first of parametrizing by starting out from the wave-mechanical picture, introducing the time t as an additional dimension of configuration space. While this procedure is perfectly feasible and leads to the desired results, it suffers from the aesthetic disadvantage that the results obtained are not obviously independent of the representation chosen. That is why we shall adopt a different approach. Without changing the usual definitions of norm, Hermitian operator, etc., we shall introduce, in addition to the usual operators in Hilbert space, the operations of multiplication by, and differentiation with respect to, time, applied in the Schrödinger representation. Considered at first merely as linear operators in the linear vector space of time-dependent Hilbert vectors (i.e., Hilbert vectors as functions of t), these new operators obviously commute with the operators p_k, q_k, and with each other they satisfy the commutation relation

$$[\bar{E}, t] = h/i, \quad \bar{E} \overset{S}{=} (h/i)\partial/\partial t. \tag{2.11}$$

It is not possible to extend the definition of the usual Hilbert space so that these new operations become Hilbert operators. That is because the operation $(H+\bar{E})$ also is conjugate to t (satisfies a relation like (2.11)), and therefore as a Hilbert operator cannot have any normalized eigenfunctions. On the other hand, every solution of the Schrödinger equation is a null vector of the operator $(H+\bar{E})$. Hence, $\bar{E}$ and t cannot both become Hilbert operators.

On the other hand, it is quite possible to construct new operations from the set q_k, p_k, t, $\bar{E}$ which as linear operations satisfy the standard commutation relations. It is appropriate to call the transition to a new set of $(2f+2)$ such operations an expanded canonical transformation. The question arises how among all these linear operations one can characterize the Hilbert operators, which alone can have the mathematical properties that enable them to represent measurable physical quantities.

To this end, we shall consider, among all the conceivable time-dependent Hilbert vectors, the subset of those satisfying the condition

$$(H+\bar{E})\psi = 0, \tag{2.12}$$

i.e., the Schrödinger equation. This equation has a meaning independent of the Schrödinger representation, because the operations t and $\bar{E}$, while defined originally only in the Schrödinger representation, can be generalized by the proviso that in any other representation they are to be realized by the corresponding transformed operations. We can bring the subset of time-dependent Hilbert vectors consistent with Eq. (2.12) into one-to-one correspondence with the set of ordinary Hilbert vectors, by identifying each ordinary Hilbert vector with the one in the time-dependent subset which is identical with it at the fixed time t_0. Moreover, on the strength of this identification the concepts of norm and of scalar bracket can be transferred to the subset of time-dependent Hilbert vectors in a unique manner which is independent of the choice of representation. Briefly, the subset forms again a Hilbert space, with all its ordinary properties. An "operation" will be an "operator" in that Hilbert space if it maps members of the subset into the subset again. The operation t, for instance, clearly does not possess this properly. It is not an operator in the new Hilbert space.

The new Hilbert space consists of solutions of the Schrödinger equation. An operator in our new sense must be an operation that applied to a solution of the Schrödinger equation produces another solution of the Schrödinger equation. Operations having this property are ordinarily called constants of the motion. In a Heisenberg representation, they are the operators that are constant in time.

The characteristic of a constant of the motion is that it commutes with the operation $(H+\bar{E})$, which henceforth we shall designate by $\bar{H}$. Since $\bar{H}$ certainly commutes with itself, it is an operator, albeit a trivial one: all quantum-mechanical states are eigenstates belonging to the eigenvalue 0. Ordinary operators, such as "the value of q_1 at the time t_1" can be converted into constants of the motion by a simple expedient: at all other times we identify with the operator $q_1(t_1)$ that operator $Q(t)$ which has the same bracket (Dirac bracket) value with any two states at the time t that $q_1(t_1)$ has at the time t_1. The operation t cannot be so extended except in a trivial manner. "The time t at the time t_1" is simply the c-number t_1.

These new characterizations of the ordinary tools of

quantum mechanics have the advantage that only invariant formations occur and that they are invariant with respect to the expanded canonical transformations in which the time t is handled symmetrically with other canonical variables. Even without the explicit introduction of the parameter θ, which we used in the classical part of this section, it is clear that t no longer plays a special role.

III. ENSEMBLE DENSITY

In the ordinary construction of a Gibbs ensemble in classical statistical mechanics, the density of the representative points in phase space is described by a variable μ, a function of the canonical variables q_k, p_k and the time t, which satisfies Liouville's theorem

$$\partial\mu/\partial t+(\mu, H)=0, \quad \int \mu dX=1. \tag{3.1}$$

The ensemble average of an observable A is given by the integral $\int \mu A dX$. In the quantum-mechanical formulation a similar role is played by a Hermitian operator μ, constructed in such a manner that the ensemble-average expectation value of any observable A is given by the trace $\mathrm{tr}\{\mu A\}$, with $\mathrm{tr}\{\mu\}=1$.

In the expanded phase space, the individual systems are described not by representative points, but by representative trajectories. Moreover, these trajectories cannot form a field of curves throughout the expanded phase space, but only on the hypersurface given by Eq. (2.2). Our problem is then to introduce in some fashion a quantity describing the density of trajectories on this hypersurface. We shall find again that this density will be a scalar with respect to (expanded) canonical transformations.

To describe the situation, we shall, in addition to the $(2f+2)$ canonical coordinates q_k, p_k, introduce $(2f+2)$ new coordinates, call them "parameters" for purposes of distinction, $\xi^1, \cdots, \xi^{2f}, \theta$, H. The parameters are not necessarily assumed to be canonical, but the Jacobian of the equations leading from the coordinates to the parameters is assumed to be finite and different from zero, H has the meaning given in Eq. (2.7), and θ satisfies Eq. (2.3). A $2f$-dimensional hypersurface S, $\theta=\text{const.}$, $H=0$, will intersect all mechanical trajectories. The desired ensemble density m will have such a significance that an integral extended over part of the hypersurface just introduced,

$$I=\int_{H=0,\ \theta=\theta_1} m d\xi^1 \cdots d\xi^{2f}, \tag{3.2}$$

will equal the fraction of trajectories within the ensemble that are intersected by the chosen domain of integration. If extended over the whole hypersurface, its value should be 1. Once having obtained such a density, we shall also want to be able to carry out similar integrals in terms of the original canonical coordinates.

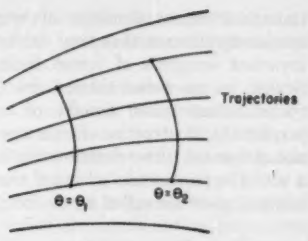

FIG. 1. Domain of integration, Eq. (3.2).

Clearly, the integral I, denoting as it does the ratio between two integers (both of which may be finite or infinite) must be an invariant. Moreover, its value must be independent of the location of the hypersurface S cutting across the $(2f+1)$-dimensional hypersurface $H=0$, providing the bounding $(2f-1)$-dimensional edge intersects the same trajectories. Figure 1 represents this requirement.

It is well known that in the $(2f+1)$ dimensional "reduced space" $H=0$ all these requirements are equivalent to the one that the integrand m be the θ-component of a contravariant vector density $\mathbf{C}$ whose divergence is zero,

$$\partial C^i/\partial \xi^i=0, \quad i=1, \cdots, 2f+1; \quad \xi^{2f+1}\equiv\theta. \tag{3.3}$$

and which is everywhere parallel to the trajectories. The direction of the trajectories is given in the expanded phase space by the equations of motion. In the reduced space these directions can be represented adequately through projection operations and come out as

$$D^i=\frac{\partial \xi^i}{\partial q_a}\frac{\partial H}{\partial p_a}-\frac{\partial \xi^i}{\partial p_a}\frac{\partial H}{\partial q_a}=(\xi^i, H). \tag{3.4}$$

In the absence of a metric, a direction is given only modulo an arbitrary factor. Let it be noted in passing that the expressions (3.4) transform as the components of a contravarient vector with respect to parameter transformations in the reduced space, i.e., with respect to parameter transformations not involving H.

We may conclude that the vector density $\mathbf{C}$ must be parallel to the vector $\mathbf{D}$, and that the constant of proportionality must be a scalar density. The principal shortcoming in this preliminary result is that $\mathbf{D}$ also changes when we transform H, even though this transformation has no geometric meaning in the reduced space. The most obvious approach, to construct a vector density in the expanded space and project it into the reduced space, is actually geometrically not feasible. Specifically, although projection leads from a vector or tensor in the higher-dimensional space to a vector or tensor in the lower-dimensional space, the same is not true of densities.

A different approach, seemingly more elaborate, is geometrically sound and leads to the desired vector density in the reduced space. In a space without a Riemannian metric, the completely antisymmetric con-

travarient tensor densities of weight one have the special significance that they can be used to construct invariant integrals of lower dimensionality. In particular, in an n-dimensional space a skewsymmetric contravariant tensor density of rank $(n-m)$, $m \leqslant n$, permits the construction of an integral over an m-dimensional domain. If we describe this domain by means of a set of m parameters u^i and if the coordinates in the original space are called x^i, the integral

$$I=\frac{1}{(n-m)!}\int \delta_{\alpha_1\cdots\alpha_{n-m}\beta_1\cdots\beta_m}s^{\alpha_1\cdots\alpha_{n-m}}\prod_{i=1}^{m}\left(\frac{\partial x^{\beta_i}}{\partial u^i}du^i\right), \qquad \delta_{1\cdots n}=1,\quad \delta_{\alpha_1\alpha_2\cdots}+\delta_{\alpha_2\alpha_1\cdots}=0,\quad \text{etc.}, \tag{3.5}$$

is invariant. Now suppose we construct a space of n' dimensions, imbedded in the original n-dimensional space, with $m \leqslant n' < n$. Then a tensor density can be constructed in the n'-dimensional subspace, such that it leads to exactly the same integral I of Eq. (3.5). If we call the parameters of the n'-dimensional subspace v^r, we have

$$s^{\gamma_1\cdots\gamma_{n'-m}}=\frac{1}{m!(n-m)!}\delta^{\gamma_1\cdots\gamma_{n'-m}\beta_1\cdots\beta_m}_{\alpha_1\cdots\alpha_{n-m}\beta_1\cdots\beta_m}\times\prod_{i=1}^{m}\left(\frac{\partial x^{\beta_i}}{\partial v^{\gamma_i}}\right)s^{\alpha_1\cdots\alpha_{n-m}}. \tag{3.6}$$

The rank of the new tensor density in the n'-dimensional subspace is lower than the rank of the original density in the expanded space by $(n-n')$. The operation characterized by Eq. (3.6) is, in a certain sense, also a projection in that the new density has fewer components than the original density, and the original density cannot be reconstructed uniquely from the new one. The partial equivalence between the new and the original density is expressed mathematically by the identity

$$\frac{1}{(n-m)!}\int_u \delta_{\alpha_1\cdots\alpha_{n-m}\beta_1\cdots\beta_m}s^{\alpha_1\cdots\alpha_{n-m}}\prod_{i=1}^{m}\left(\frac{\partial x^{\beta_i}}{\partial u^i}du^i\right)\equiv\frac{1}{(n'-m)!}\int_u \delta_{\gamma_1\cdots\gamma_{n'-m}\cdots\beta_m}s^{\gamma_1\cdots\gamma_{n'-m}}\prod_{i=1}^{m}\left(\frac{\partial v^{\gamma_i}}{\partial u^i}du^i\right). \tag{3.7}$$

Without going into a lower dimensional subspace, we can also gain densities of lower rank by processes of differentiation. The "curl"

$$s^{\alpha_1\cdots\alpha_{n-m+1},\alpha_{n-m+1}}=f^{\alpha_1\cdots\alpha_{n-m}} \tag{3.8}$$

satisfies the theorem (a generalization of Gauss' and Stokes' theorems) that if the $(m-1)$ parameters w^k describe the edge (closed surface) of the m-dimensional domain (u^i), then

$$\frac{1}{(n-m)!}\int_u \delta_{\alpha_1\cdots\alpha_{n-m}\beta_1\cdots\beta_m}s^{\alpha_1\cdots\alpha_{n-m+1},\alpha_{n-m+1}}\prod_{i=1}^{m}\left(\frac{\partial x^{\beta_i}}{\partial u^i}du^i\right) \equiv\frac{1}{(n-m+1)!}\oint_w \delta_{\alpha_1\cdots\alpha_{n-m+1}\beta_1\cdots\beta_{m-1}}s^{\alpha_1\cdots\alpha_{n-m+1}}\prod_{k=1}^{m-1}\left(\frac{\partial x^{\beta_k}}{\partial w^k}dw^k\right). \tag{3.9}$$

Our problem is now to find a vector density in the reduced space which is parallel to a given field of directions and whose divergence vanishes. In the expanded space, we should have to find a contravariant tensor density of rank 2 whose surface integral vanishes for any $2f$-dimensional closed surface lying wholly in the reduced space. Or, we may require (and this requirement is equivalent) that the divergence of the tensor density, while not zero, vanishes when integrated over a $(2f+1)$-dimensional surface forming a part of the reduced space.

Let us call the $(2n+2)$ parameters ξ^α, $\alpha=1, \cdots, 2f+2$. We shall first show that the contravariant tensor density

$$S^{\alpha\beta}=\mu'(\xi^\alpha,\xi^\beta), \tag{3.10}$$

where μ' is a scalar density, projects into a vector density in the reduced space whose components are proportional to the Poisson brackets (3.4). The proof is almost trivial because we are using the same parameters (except for $\xi^{2f+2}\equiv$H) in both the reduced and the expanded space. In that case, Eq. (3.6) reduces to a rule which requires that we strike out rows and columns in which not at least one index is H.

Next, we shall form the divergence of $S^{\alpha\beta}$, $S^{\alpha\beta}{}_{,\beta}$, but in a canonical coordinate system, In a canonical coordinate system the tensor density $S^{\alpha\beta}$ assumes the values

$$S^{\alpha\beta}=\begin{pmatrix}0 & \mu\delta^{\kappa\lambda}\\ -\mu\delta^{\kappa\lambda} & 0\end{pmatrix},\qquad \kappa,\lambda=1,\cdots,f+1. \tag{3.11}$$

Its divergence, therefore, is

$$S^{\alpha\beta}{}_{,\beta}=\left(\frac{\partial\mu}{\partial p_\kappa},-\frac{\partial\mu}{\partial q_\kappa}\right). \tag{3.12}$$

In terms of general parameters, this vector density in the expanded space has the components

$$S^{\alpha\beta}{}_{,\beta}=(\xi^\alpha,\mu)J,\quad J=\det\left|\frac{\partial(q_\kappa,p_\kappa)}{\partial(\xi^i,\theta,\mathrm{H})}\right|,\quad \mu'=J\mu, \tag{3.13}$$

where J is the Jacobian of the transformation leading from any canonical coordinate system to a parameter system (the Jacobian of a canonical transformation is always 1). The variable μ (without prime) is a scalar. The vector density (3.13) will have vanishing integrals if its H-component is zero, if, in other words,

$$(\mathrm{H}, \mu)=0. \tag{3.14}$$

This last equation is the invariant formulation of Liouville's theorem in the expanded phase space. It is not a condition satisfied merely by stationary distributions, but a perfectly general condition obeyed by the scalar μ.

With the help of the expression (3.10), where we now replace the density μ' by the expression μJ, we can form the vector density $\mathbf{C}$ in the reduced space that leads to the formation of ensemble densities. We have

$$C^{\alpha}=(\xi^{\alpha}, \mathrm{H})\mu J. \tag{3.15}$$

The integral (3.2) turns into

$$I=\int(\theta, \mathrm{H})\mu J d\xi^{1}\cdots d\xi^{2f}. \tag{3.16}$$

With this expression, it is now possible to describe arbitrary Gibbs ensembles in terms of the expanded canonical formalism. If the function H is chosen so that it serves as the Hamiltonian, with θ the argument appearing in the canonical equations of motion, then the Poisson bracket in Eq. (3.16) equals 1.

The introduction of the ensemble density operator μ in quantum mechanics is much more conventional and requires no differential-geometrical derivation. Assuming that to each possible Hilbert vector we assign an ensemble probability P_k (where k is a parameter which may either take discrete or continuous values), so that the sum or integral $\sum_k P_k$ equals 1, then, in Dirac's bracket notation, μ is

$$\mu=\sum_k P_k |k\rangle\langle k|. \tag{3.17}$$

The average expectation value of any observable A is given by the expression

$$\langle A\rangle_{\mathrm{av}}=\mathrm{tr}\{\mu A\}, \tag{3.18}$$

and this expression corresponds to the classical integral $\int \mu A dX$.

IV. CANONICAL ENSEMBLES

With an invariant ensemble density, we can now proceed to duplicate the procedures of classical statistical mechanics. The chief difference is that we cannot single out the total energy of the system from among all the other variables of state to construct canonical ensembles. We shall, therefore, generalize the concept of canonical ensemble and call an ensemble canonical whenever it has the same distribution in phase space (or in Hilbert space) that it would assume if its systems were not isolated, but components of much larger systems (with infinitely many degrees of freedom, in the asymptotic limit) which in turn form a microcanonical ensemble in their phase space.

This generalized definition is based on the physical notion of statistical equilibrium in interaction with a very large constant-temperature bath. Ordinarily, we motivate the assumption of canonicity by saying that a system will assume canonical distribution if it is in interaction with a very large temperature bath and if nothing is known about the combined system except that the total energy lies within a specified narrow interval (E_1, E_2). In that portion of phase space (for the combined system) that is bounded by the energy surfaces E_1 and E_2 the ensemble density is, therefore, assumed to be constant. The canonical distribution is not sensitive to a transition to an energy interval of zero width. To generalize this approach, we must extend it to other variables, and to combinations of other variables. We must assume that it is possible to provide the type of interaction with a large system (bath) in which not only the energy, but also other constants of the motion (for the isolated system) are exchanged, and we must then determine the distribution of the system in which we are interested on the assumption that for the combined system certain variables (e.g., total energy, total linear momentum) are limited to narrow domains, but that within that domain the ensemble density is constant.

This approach will be physically interesting only if the result is insensitive to the detailed structure of the large temperature bath and to the precise nature of the coupling bath and thermodynamic system. That will be the case only if the variables we are interested in are "additive," i.e., if we can naturally construct constants of the motion for the combined system which are sums of two terms, one depending only on the state of the system, the other only on the state of the bath. If that is the case, then all that matters is that the coupling parameter may be permitted to go to zero, and the size of the bath to go to infinity, without destroying the physical meaning of the whole setup. Most of the variables ordinarily of interest will have this property of "additivity." Aside from the standard integrals of the motion, total energy, linear momentum, and angular momentum, the density at a particular location, all sorts of occupation numbers, intensity of radiation in a particular part of the spectrum (all the latter taken at a particular time), and so forth, are additive variables in the sense explained here.

With these assumptions, the system under scrutiny will always assume a distribution in phase space which has the general form

$$\mu=Z^{-1}\exp(-\textstyle\sum_i \beta_i A_i), \tag{4.1}$$

with

$$Z=\int(\theta, \mathrm{H})J\exp(-\textstyle\sum_i \beta_i A_i)d\xi^{1}\cdots d\xi^{2f}. \tag{4.2}$$

The variables A_i are those additive constants of the motion for which we have specified the microcanonical distribution in the combined system (or the mean values in the isolated system), Z is the partition function of the ensemble under these conditions, and the β_i are a set of parameters whose values are determined by the required values of the ensemble averages $\langle A_i\rangle_{Av}$. It is, of course, assumed that the quantities A_i are all independent of each other; that none of them may be expressed as a function of the others nor as a function of the other A's plus the Hamiltonian constraint H.

It is clear that the expression (4.1) is invariant with respect to a transformation that leads from the set A_i to a set A_k' consisting of linear combinations of the A_i. Therefore, an ensemble distribution is relativistically covariant automatically if with any component of a vector or similar covariant among the A_i the other components are included, too.

Equation (4.1) is the natural definition for canonical distributions in the generalized theory. It is interesting to note that with this definition an ensemble may be canonical if its average energy and linear momentum are specified, but also if only its average energy is specified. These two ensembles are by no means identical, but there appears no valid reason for accepting one of them as physically interesting and rejecting the other. It is, of course, true that if we choose as the A_i the four components of the energy-momentum vector, then this choice is relativistically invariant. If in one system we choose just the energy, then in another frame the corresponding choice is a particular linear combination of energy and linear momentum.

V. ENTROPY

All canonical ensembles can be obtained by means of a variational problem with subsidiary conditions. If we define the entropy of an ensemble by means of the integral

$$S=k\int(\theta, \mathrm{H})\mu J\ln(\mu_0/\mu)d\xi^1\cdots d\xi^{2f} \qquad (5.1)$$

(k being the Boltzmann constant and μ_0 an arbitrary constant), then the canonical ensembles are those in which the entropy is maximized under the subsidiary conditions that a set of ensemble averages $\langle A_i\rangle_{Av}$ assumes specified values. The larger the number of these subsidiary conditions, the smaller the value of the entropy. Naturally, we always have the one subsidiary condition (3.1), that $\langle 1\rangle_{Av}$ equals 1.

The value of the entropy for a canonical ensemble is

$$S=k(\ln\mu_0+\ln Z+\textstyle\sum_i \beta_i\langle A_i\rangle_{Av}). \qquad (5.2)$$

With the help of this expression, the partition function itself may be represented as a function of purely "thermodynamic" (i.e., macroscopic) variables:

$$Z=\exp\left[\frac{1}{k}(S-\textstyle\sum_i \beta_i\langle A_i\rangle_{Av}-\ln\mu_0)\right]. \qquad (5.3)$$

We shall call the entropy defined by Eq. (5.1) the "ensemble entropy." Because of Liouville's theorem, it is an integral of the motion. In order to find another variable, the "system entropy," which will change its value in the course of the motion, we may proceed as follows. Regardless of whether we have a single system or a canonical or noncanonical ensemble, we define the system entropy S^* by means of Eq. (5.2), where the partition function Z and the multipliers β_i are all determined by the average values $\langle A_i\rangle_{Av}$ on the fictitious assumption of a canonical ensemble. System entropy and ensemble entropy have the same value for a canonical ensemble, for all other cases the system entropy is the larger of the two. That is because for given values of the $\langle A_i\rangle_{Av}$, the canonical distribution is the one that maximizes the ensemble entropy, and the system entropy equals the ensemble entropy of this "corresponding" canonical ensemble. In contrast to the ensemble entropy, the system entropy is not a constant of the motion.

Now consider a set of dynamical variables A_i which are constants of the motion and which depend explicitly on the parameter θ. Naturally, if we construct an ensemble that is canonical with respect to this set of variables, it will remain so, and thus its system entropy as well as its ensemble entropy will have the same value for all values of the parameter θ. But now we can introduce a new set of variables, B_i, by means of the defining equations

$$B_i(\xi^1, \cdots, \xi^{2f}, \theta_1)=A_i(\xi^1, \cdots, \xi^{2f}, \theta_0) \qquad (5.4)$$

and the further requirement that the B_i also be constants of the motion. This requirement is particularly suggested if we should have chosen a set of parameters in which the Hamiltonian constraint H is independent of the parameter θ. Such a choice produces formally a conservative system, and in this case Eq. (5.4) together with the requirement that both the A_i and the B_i be constants of the motion leads automatically to the stronger relationship

$$B_i(\xi^1, \cdots, \xi^{2f}, \theta)=A_i(\xi^1, \cdots, \xi^{2f}, \theta+\theta_0-\theta_1). \qquad (5.5)$$

In other words, the two sets of variables are quite similar in nature and differ only by a rigid translation of the "time" scale. We shall now consider both the ensemble entropy and the system entropy of an ensemble that is canonical with respect to the A_i, but not with respect to the B_i. Because the ensemble is in general not canonical with respect to the B_i, the system entropy with respect to the B_i will exceed the ensemble entropy. The ensemble entropy, on the other hand, is an intrinsic property of the ensemble and does not depend on whether we consider the A_i or the B_i. It can therefore be asserted that the system entropy with respect to the B_i for our ensemble exceeds the system entropy with respect to the A_i.

Intuitively, the difference between the set of A_i and the set of B_i is that B_i represents the "same" set of

variables, but observed a "time" $(\theta_1-\theta_0)$ "later"—"earlier" if $(\theta_1-\theta_0)$ is chosen negative. With respect to the "fixed" observable A_i^0, i.e., those θ-independent observables which permanently equal $A_i(\theta_0)$, our ensemble is canonical only at the "time" θ_0. Therefore, at all other "times" the ensemble entropy S is a lower bound for the system entropy S^*, determined with the help of the averages of the A_i^0.

Let it be noted in passing that this version of the H-theorem holds for the "past" as well as for the "future"—in our theory, all results must be symmetric with respect to the time because nowhere have we introduced into the foundations any element of asymmetry. However, we may introduce this element of asymmetry by focusing our attention on the present and the future only, assuming that any observation requires interaction with our large and bulky measuring devices in such a manner that as a result of this interaction our state of knowledge about the system under observation immediately following the measurement(s) is adequately represented by a canonical ensemble. Repetition of the "same" measurements, i.e., determination of the "fixed" A_i^0, at some subsequent time will then show an increase of the system entropy. Whether this method of introducing thermodynamic concepts (the Second Law) is completely satisfactory shall not be examined in this paper. At any rate, this approach is the natural analog of that usually taken and, at least, requires no assumptions concerning equilibrium or quasistatic processes.

VI. HEAT FLUX

In order to formulate ordinary thermodynamics, it is necessary to introduce into statistical mechanics the concepts of performance of work and of transfer of heat; these concepts are required to formulate both the first and the second law of thermodynamics. The most satisfactory manner of defining these two quantities in statistical mechanics is first to define the mechanical work and then describe the heat transfer as the difference between the change in energy and the work done on the system. The heat transfer obtained in this manner then leads to an exact differential (the change in entropy) when divided through by the absolute temperature.

In our generalized theory, very similar results may be obtained, but with one significant difference. Instead of the single inexact differential "work," we have such a differential for each of the constants of the motion A_i, describing the adiabatic change of its ensemble average. Starting with a canonical ensemble, we obtain the change in (system) entropy by multiplying the "heat transfer" of each separate variable A_i by its appropriate β_i and adding them all together. We first define, for a canonical ensemble, the adiabatic change in $\langle A_i\rangle_{\text{Av}}$ as the expression

$$\delta_{\text{ad}}\langle A_i\rangle_{\text{Av}}=\int \mu\delta A_i dX,$$

$$\mu=\frac{1}{Z}e^{-\sum_k \beta_k A_k},\quad dX=(\theta,\mathrm{H})d\xi^1\ldots d\xi^{2f}, \tag{6.1}$$

which is the analog of the definition given by Schrödinger.[6] Our parameter system should be chosen so that $\delta[(\theta,\mathrm{H})\mu]$ vanishes. If the total change in $\langle A_i\rangle_{\text{Av}}$ is denoted by $\delta\langle A_i\rangle_{\text{Av}}$, we find then for the change due to random interaction with the surroundings the expression

$$\delta_Q\langle A_i\rangle_{\text{Av}}=\delta\langle A_i\rangle_{\text{Av}}-\delta_{\text{ad}}\langle A_i\rangle_{\text{Av}}$$

$$=\int A_i\delta\mu dX. \tag{6.2}$$

These expressions are the analogs of the heat transfer. Finally, if we multiply each of these expressions by its β_i and add, we get

$$\sum_i \beta_i\delta_Q\langle A_i\rangle_{\text{Av}}=\sum_i\int \beta_i A_i\delta\mu dX$$

$$=\delta\int(\textstyle\sum_i \beta_i A_i)\mu dX-\int\mu\delta(\sum_i \beta_i A_i)dX$$

$$=\delta(\textstyle\sum_i \beta_i\langle A_i\rangle_{\text{Av}})+\delta\ln Z=k^{-1}\delta S^*. \tag{6.3}$$

This result shows that in a relativistic thermodynamics it is natural to retain the concept of a scalar entropy; but work must be replaced by a set of quantities having similar transformation properties as the chosen A_i, and the same holds for the heat transfer. Thus, if we formulate thermodynamics for a system having a distribution in space (e.g., a finite volume element within a fluid), the heat transfer across its bounding surface should not be a vector, but a tensor or tensor-like formation, which respresents not only a flux of energy, but also of linear momentum.

VII. CONCLUSION

In this paper, we have confirmed the intuitive assumption that entropy should be retained as a scalar; but it turns out that the energy, work, and heat concepts must be adjusted in each case to the physical situation encountered and to each other. It is planned to develop the general framework further and to attempt its application to interesting situations far removed from the conventional quasistatic process.

The writer should like to acknowledge with gratitude the stimulation he has received from R. Wildt in many discussions involving the thermodynamics of stellar atmospheres.

[6] E. Schrödinger, *Statistical Thermodynamics* (Cambridge University Press, Cambridge, 1946), p. 11ff.

Response of Some Scintillation Crystals to Charged Particles*†

C. J. TAYLOR,‡ W. K. JENTSCHKE, M. E. REMLEY, F. S. EBY, AND P. G. KRUGER
Department of Physics, University of Illinois, Urbana, Illinois
(Received June 11, 1951)

The dependence of the response of anthracene, stilbene, and sodium iodide crystals in a scintillation detector on the type and energy of charged particles incident on the crystal has been investigated. Electrons with energies from 500 ev to 624 kev, deuterons and molecular hydrogen ions with energies of 1 to 11 Mev, protons of 1 to 5 Mev, and alpha-particles of 4 to 21 Mev were employed. With the exception of protons and deuterons in sodium iodide, which gave a linear response over the entire energy region investigated, plots of pulse height *vs* energy for heavy particles gave a nonlinear relation for low energies tending toward linearity with increasing particle energy. Electrons in anthracene and stilbene show a nonlinear response below 100 kev, while the sodium iodide curve is linear above 1000 ev. The response of anthracene, whose behavior may be typical of organic crystals, has been compared for different ionizing radiations by considering the variation of the specific energy loss. Both electrons and heavy particles seem to show regions of linear response which start at quite different values of dE/dx. As the specific energy loss increases the response becomes nonlinear, with the ultimate saturation of the specific fluorescence for large values of dE/dx.

I. INTRODUCTION

THE fluorescence of certain crystals under bombardment by energetic particles has been known for some time. The combination of such a crystal and a photomultiplier tube results in a device suitable for electronic counting of individual particles entering the crystal.[1] A recent survey of the important properties of these crystals has been given by Hofstadter.[2] The greater part of the work done so far has been concerned with the response of various crystals to gamma-rays and high energy beta-particles, and Pringle[3] has given an excellent summary of the developments in this field. A relatively small amount of information has been reported concerning the response of scintillation crystals to heavy particles,[4–11] but knowledge of this kind is essential to the successful employment of the scintillation counter technique in the field of quantitative energy measurements of heavy particles. The response of organic crystals to fast protons is particularly interesting due to the possibility of using such crystals for fast neutron energy measurements.

Protons of 1 to 5 Mev, deuterons and molecular hydrogen ions of 1 to 11 Mev, alpha-particles of 4 to 21 Mev from the University of Illinois cyclotron, and polonium alpha-particles were used in the measurements with heavy particles. The response of anthracene, stilbene, and thallium activated sodium iodide to these particles has been studied.

The investigation was then extended to a study of the fluorescence of these crystals with incident monoenergetic electrons. This extension was particularly directed toward an investigation of the fluorescence

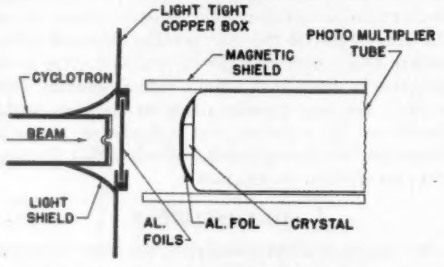

FIG. 1. Experimental arrangement for the measurement of the fluorescence of crystals to heavy particles. Note that the distance from the Nylon foil to absorber and from absorber to crystal are not to scale.

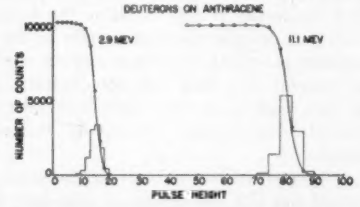

FIG. 2. Typical integral and differential pulse-height distribution curves for deuterons incident on anthracene.

* Assisted by the joint program of the ONR and AEC.
† Parts of this work were presented by one of us (C.J.T.) in partial fulfillment of the requirements for the Ph.D. at the University of Illinois.
‡ Now at North American Aviation, Inc., Downey, California.
[1] H. Kallman, Natur und Technik (July 1947), M. Deutsch, Massachusetts Institute of Technology Technical Report No. 3 (December 1947); Marshall, Coltman, and Bennett, Rev. Sci. Instr. **19**, 744 (1948); R. J. Moon, Phys. Rev. **73**, 1210 (1948); P. R. Bell, Phys. Rev. **73**, 1405 (1948); R. Hofstadter, Phys. Rev. **74**, 100 (1948); H. Kallmann, Phys. Rev. **75**, 623 (1949). W. Hanle, Naturwiss. **38**, 176 (1951).
[2] R. Hofstadter, Nucleonics **6**, No. 5, 70 (1950).
[3] R. W. Pringle, Nature **166**, 11 (1950).
[4] Harding, Flowers, and Eppstein, Nature **163**, 990 (1949).
[5] E. G. Michaelis, Helv. Phys. Acta **23**, Sup. 3, 155 (1950).
[6] J. B. Birks, Proc. Phys. Soc. **A63**, 1294 (1950) and private communication.
[7] Franzen, Peele, and Sherr, Phys. Rev. **79**, 742 (1950) and private communication.
[8] Frey, Grim, Preston, and Gray, Phys. Rev. **82**, 372 (1951).
[9] J. Broser and H. Kallmann, Ann. Physik **3**, 317 (1948).
[10] B. Collinge, E. J. Rolbins, Nature **166**, 1109 (1950).
[11] S. A. E. Johansson, Ark. Fys. **2**, 171 (1950).

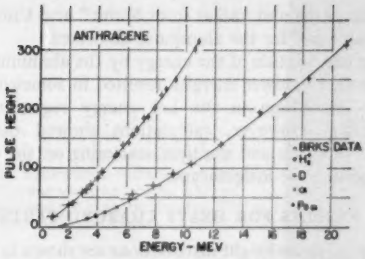

FIG. 3. Pulse heights resulting from the fluorescence radiation of anthracene when excited by heavy particles of different energies.

efficiency of crystals to electrons and heavy particles with the same specific energy loss. It was further desirable to obtain additional data to that already available on the response of various scintillation counters to electrons.[12–14] This would be necessary for the use of these detectors as beta- and gamma-ray spectrometers. With this intent, data were obtained on the response of the crystals to electrons in the low energy region (500 ev to 5000 ev) using a specially fabricated pulsed electron gun, while for a higher energy region (27 kev to 624 kev), the electrons were supplied by internal conversions and x-rays from radioactive sources.

II. EXPERIMENTAL PROCEDURE FOR HEAVY CHARGED PARTICLES

The magnetically analyzed beam of the cyclotron was collimated by a set of brass slits 2 mm in diameter and brought out into air through a thin Nylon window (1 cm air equivalent) and allowed to strike the scintillation crystal under investigation. The crystal was mounted in optical contact with the photosensitive surface of an RCA 5819 photomultiplier tube and covered with a 0.16 mg/cm² reflecting aluminum foil as shown in Fig. 1.

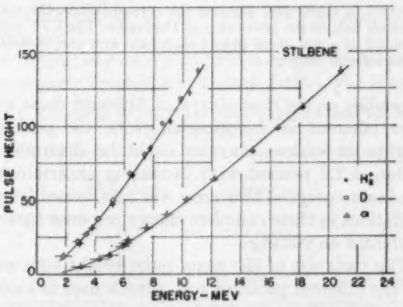

FIG. 4. Pulse heights resulting from the fluorescence radiation of stilbene when excited by heavy particles of different energies.

[12] J. I. Hopkins, Rev. Sci. Instr. **22**, 29 (1951).
[13] West, Meyerhof, and Hofstadter, Phys. Rev. **81**, 141 (1951).
[14] P. R. Bell, Science **112**, 7 (1950).

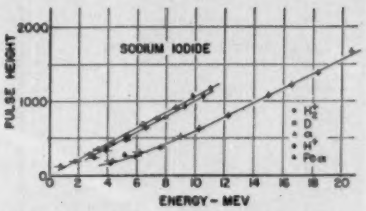

FIG. 5. Pulse heights resulting from the fluorescence radiation of thallium activated sodium iodide when excited by heavy particles of different energies.

An anthracene crystal 2.5×2.5×0.3 cm, a stilbene crystal 1×1×0.15 cm, and freshly cleaved sodium iodide crystals approximately 1.5×1×0.3 cm were used in obtaining the data to be described. The sodium iodide crystals were cleaved in a dry box, and the atmosphere inside the light-tight container was kept dry with calcium chloride. Frequent checks were made to guard against surface deterioration. Aluminum absorbers were interposed in the beam to vary the energy of the particles striking the crystal. The photomultiplier tube was magnetically shielded by four concentric cylinders of annealed mu-metal insulated from each other. An integrating time constant of 0.3 microsecond was used at the output of the photomultiplier tube for pulses from anthracene and stilbene, which have decay times of approximately 0.03 and 0.006 microsecond respectively,[15] while a time constant of 2.5 microseconds was used for pulses from sodium iodide, which has a decay time of approximately 0.25 microsecond.[2] These pulses were then applied to a cathode follower and a Los Alamos type model 100 linear pulse amplifier[16] and, after being shaped to flat-topped pulses

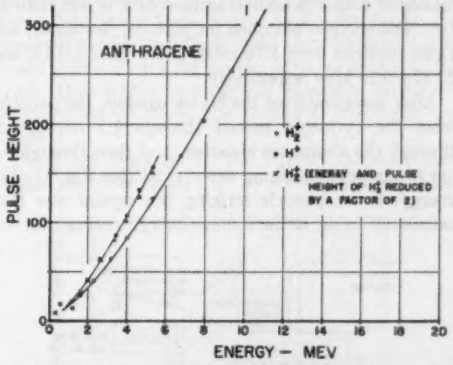

FIG. 6. Pulse heights resulting from the fluorescence radiation of anthracene when excited with molecular hydrogen ions and protons. A comparison is shown between the proton points and the H_2^+ points with the energies and pulse heights of the latter reduced by a factor of two.

[15] A. Lundby, Phys. Rev. **80**, 477 (1950).
[16] W. C. Elmore and M. Sands, *Electronics* (McGraw-Hill Book Company, Inc., New York, 1949).

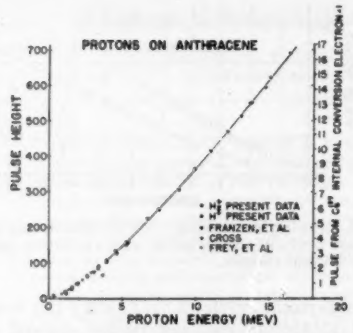

FIG. 7. Fluorescence radiation as a function of proton energy for an anthracene scintillation counter. The arbitrary ordinate scale on the left is the same as in Figs. 3–6, while the scale on the right is given in units of pulse height of the Cs^{137} conversion electrons.

7 microseconds wide, were analyzed with a twelve channel pulse amplitude analyzer using Atomic Instrument Company discriminators and scalers.

The cyclotron was operated with a very low beam to give approximately 100 counts per second from the scintillation counter. A total of 10,000 counts was taken at each energy.

The energy of the incident particles was determined under the same cyclotron conditions by measuring their ranges in air. This was done by passing the beam through a monitor consisting of a double-end-window proportional counter, whose stopping power was known, and then into a thin zinc sulfide screen placed on the end of a movable 5819 photomultiplier tube. This second detector had a threshold detection energy as measured with a polonium alpha-source of less than 30 kev. The energies obtained for protons, deuterons, and alpha-particles were 5.76 ± 0.06 Mev, 11.51 ± 0.12, and 22.87 ± 0.23 Mev respectively.

After emerging from the Nylon window, the particles from the cyclotron passed through 1.5 cm of air, through the aluminum absorber, and then through 3.5 cm of air before striking the crystal (see Fig. 1). The energy of the particle striking the crystal was then calculated using Bethe's range-energy curves[17] for the two air paths and values from Smith[18] and University of California[19] for the aluminum absorbers.

The degradation of the energy by the aluminum foils to obtain the lower energies resulted in somewhat less energy resolution in the low energy region due to straggling. However, calculations showed that the effects of single and multiple scattering on the energy resolution were insignificant.

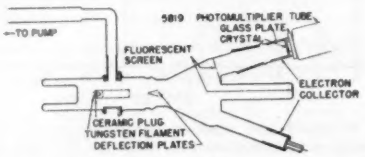

FIG. 8. Vacuum tube showing electron gun, crystal position, and electron collectors as used for the electron beam experiments.

[17] H. A. Bethe and L. M. Brown, private communication; H. A. Bethe, Revs. Modern Phys. 22, 213 (1950).

III. RESULTS FOR HEAVY CHARGED PARTICLES

Typical pulse-height distributions are shown in Fig. 2. The differential histograms obtained essentially fit gaussian distributions with full widths at half-maxima of six to eight percent for the higher energy particles depending on the type of crystal. Although these widths were inherent in the gaussian plots, the peak pulse heights at various energies could be determined to within ±2.0 percent with increasing uncertainties at the lower energies. This error was ascertained from the deviations in three complete energy response curves for deuterons on stilbene.

The variation of the mean pulse height with energy for the different particles and crystals used is shown in Figs. 3–5. The pulse-height scale is common to the three figures. The vertical lines indicate estimates of

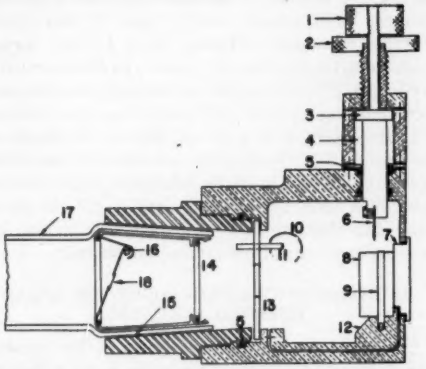

FIG. 9. Chamber used to cleave the sodium iodide crystals in the vacuum. 1,2-knurled knobs, 3-key, 4-keyway, 5-"O" ring, 6-razor edge, 7-Lucite window, 8-NaI crystal, 9-aluminum strap, 10-aluminum shield, 11-polonium alpha-source, 12-removable cradle, 13-aluminum plate, 14-piano wire spring, 15-34/45 standard taper for a greased joint. 16-mu metal tip. 17-Pyrex arm of vacuum tube. 18-Cs^{137} source. Optical contact is made between the crystal and the Lucite window by means of a thin layer of silicone high vacuum grease. Rotating knurled knob 2 forces the piston down and presses the razor edge 6 against the upper face of the crystal. A penetration of a few millimeters is sufficient to cleave and separate the crystal halves, the rear half of which falls to the lower step of the cradle. The Cs^{137} source is mounted on a mu metal tipped aluminum arm and is positioned by an exterior magnet.

[18] J. H. Smith, Phys. Rev. 71, 32 (1947).

[19] University of California Radiation Laboratory Report 121, Revised November 1948.

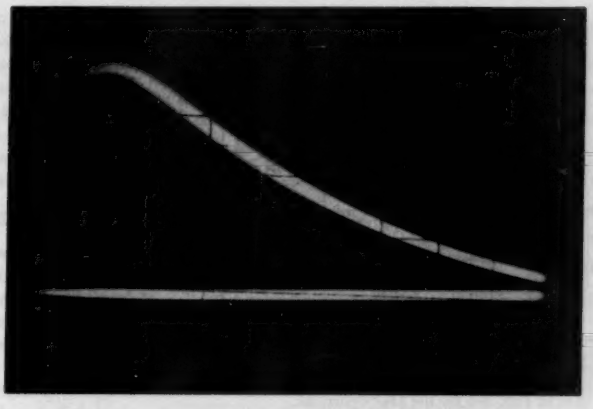

FIG. 10. Pulses resulting from the fluorescence radiation of anthracene when excited by 5000 ev electrons with approximately 300 electrons in each pulse.

the pulse-height errors. The major error in the energy is introduced by the initial uncertainty of one percent in the energy. As the energy of the particles is reduced by the introduction of absorbers, the initial one percent error produces progressively larger uncertainties for the lower energy particles. The horizontal lines attached to the points show the total variation in energy at a given energy corresponding to a variation of one percent in the initial energy. These are not to be interpreted as errors in the determination of the energies, but rather as the amount by which the entire curve would be translated in energy for a one percent change in the initial energy. Errors introduced in the determination of an energy corresponding to a given aluminum absorber are certainly less than 0.1 Mev.

Although two curves were drawn for the deuteron and molecular hydrogen ion points for all three crystals in a preliminary report of these data,[20] further investigation has shown that the points for the organic crystals should all essentially lie on one curve for each type crystal, as in Figs. 3 and 4. The apparent small difference in the fluorescence radiation from sodium iodide when excited by deuterons and H_2^+ ions is not understood.

The figures show a distinct difference in the behavior of the organic crystals and sodium iodide. The organic crystals have a nonlinear response of pulse height to energy in the entire region investigated. In sodium iodide protons and deuterons give linear response, while alpha-particles have a nonlinear relation over a low energy region with a linear response above an energy of about 10 Mev. The possibility of a deterioration of the crystal surface (due to the hygroscopic properties of sodium iodide) during a run which could contribute to this nonlinearity of response has been checked by experiments with crystals freshly cleaved in a vacuum. Results obtained in this way agreed with earlier ones, as indicated by the polonium alpha-point at 5.3 Mev in Fig. 5.

Figure 6 shows the response of anthracene to both protons and molecular hydrogen ions. It should be noted here that the H_2^+ ions were actually detected as two protons entering the crystal simultaneously since the ions were dissociated when they passed through the Nylon foil. Hence if one divides both pulse height and energy of the H_2^+ points by two, these reduced points should coincide with the proton curve as shown in the figure. Thus proton pulse height *vs* energy curves are readily obtained from the molecular hydrogen ion curves.

Using the response of the 624-kev internal conversion electrons[21] from Cs^{137} as a normalization value,

TABLE I. Sources of internal conversion electrons used for single electron pulses.

Source	Energy of *K*-electron kev	Energy of *L*-electron kev	*K* : *L* ratio
Nb^{91} [a]	86.9	103.0	2.5:1
In^{114} [b]	164.1	187.7	1:1
Hg^{203} [b]	196	264	3:1
Cs^{130} [c]	623.9	655	5:1[b]

[a] J. Ovadia, University of Illinois Ph.D. thesis, 1951.
[b] Nuclear Data, National Bureau of Standards Circular 499 (1950).
[c] L. M. Langer and R. D. Moffat, Phys. Rev. 78, 74 (1950).

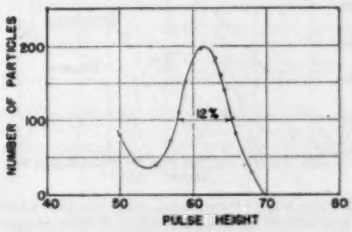

FIG. 11. Pulse-height distribution of the fluorescence radiation from Cs^{137} conversion electrons incident on anthracene.

[20] Taylor, Remley, Jentschke, and Kruger, Phys. Rev. 83, 169 (1951). Jentschke, Eby, Taylor, Remley, and Kruger, Phys. Rev. 83, 170 (1951).

[21] L. M. Langer and R. D. Moffat, Phys. Rev. 78, 74 (1950).

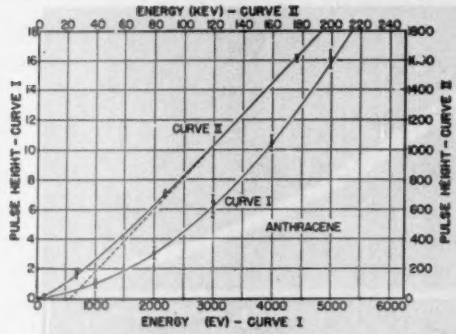

FIG. 12. Pulse heights from the fluorescence radiation of anthracene as a function of electron energy. The arbitrary ordinate scale must be multiplied by the factor 0.00673 to obtain the same scale used in Figs. 3–6 for the heavy particles.

the proton data for anthracene by Franzen, *et al.*,[7] the data of Frey, *et al.*,[8] some recent data by Cross,[22] and the above data have been plotted to the same scale giving the results shown in Fig. 7. The agreement of these sets of data is very satisfactory with the exception of the point of 3.7 Mev by Franzen, *et al.*,[7] the exact energy of which might be questionzed as they indicate.

The ratio of the stilbene pulse height to the anthracene pulse height is closely the same for all three particles over the energy range investigated. This ratio is about 0.40 for H_2^+ ions between 3 and 11 Mev, 0.40 for deuterons between 2 and 11 Mev, and 0.44 for alpha-particles between 5 and 21 Mev. Harding, *et al.*[4] have reported 0.5 for this ratio using 8.76-Mev alpha-particles.

Michaelis[5] gives pulse heights obtained for alpha-particles with energies of 3.1, 3.75, and 4.45 Mev incident on sodium iodide. Unfortunately, the amount of overlap with the results of this investigation is small. However, the results of Michaelis fit reasonably well on the low energy end of the observed sodium iodide curve when normalized at 4.45 Mev. The response of anthracene to alpha-particles in the energy range from 0.7 to 5.3 Mev as given by Birks[6] agrees well with the results obtained in this investigation as shown in Fig. 3. The results reported here for protons on sodium iodide show the same characteristic linearity as those of Franzen, *et al.*,[7] and appear to intersect very nearly at the origin.

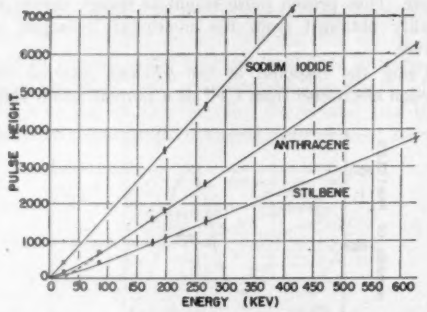

FIG. 13. Pulse heights from fluorescence radiation of anthracene, stilbene, and sodium iodide as a function of electron energy. The ordinate scale is the same as in Fig. 12.

[22] W. G. Cross, Chalk River Laboratory, private communication.

IV. PROCEDURE FOR THE ELECTRON EXPERIMENTS

Since electrons with energies of 500 to 5000 ev produce ionization densities comparable to those produced by protons of two to fifteen Mev, the fluorescence of crystals when excited by electrons in this energy range was investigated. As it is practically impossible to measure the pulse heights of single electrons in this low energy region with any accuracy using organic crystals,[23] a pulsed monoenergetic electron beam was produced by a special cathode-ray gun for the examination of scintillations produced by electrons of these energies. This apparatus, shown in Fig. 8, produced an electron beam which impinged on the crystals after being deviated by the deflecting plates of the electron gun. This was done to effectively shield the crystal and photomultiplier tube from light produced by the filament of the gun. The magnetically shielded RCA 5819 tube was placed with the photocathode in contact with the glass plate on which the crystal was mounted at the end of the vacuum tube. Crystals 1 cm×1 cm×0.25 cm were mounted in the apparatus, as indicated in Fig. 8. A vibrating reed electrometer,[24] with which the average beam current was measured, was connected to the electron collector.

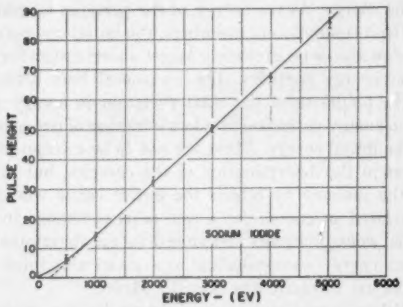

FIG. 14. Pulse heights from the fluorescence radiation of sodium iodide as a function of electron energy. The ordinate scale is the same as in Figs. 12 and 13.

The electron beam was pulsed at a rate of ten thousand per second with pulse durations of 0.5 and 2.0 microseconds. Identical results were obtained with

[23] W. J. Ramler and M. S. Freedman, Rev. Sci. Instr. **21**, 784 (1950).

[24] Palevsky, Swank, and Grenchik, Rev. Sci. Instr. **18**, 298 (1947).

both types of pulses indicating that no long-lived fluorescence of appreciable intensity could have been present. The average electron beam current was maintained at less than 5×10^{-13} ampere, so that no more than 300 electrons were incident on the crystal during any one pulse. Since the electron beam was defocused over an area of four mm² on the crystal, the particle density was small enough that the mechanism for producing fluorescence was assumed to be the same as that for single electrons, and hence a pulse height *vs* energy relation for single electrons could be obtained.

The secondary emission coefficients of the crystals used are greater than one for the electron energies investigated, so that no significant charge collection should occur on these insulating crystals. As a check the

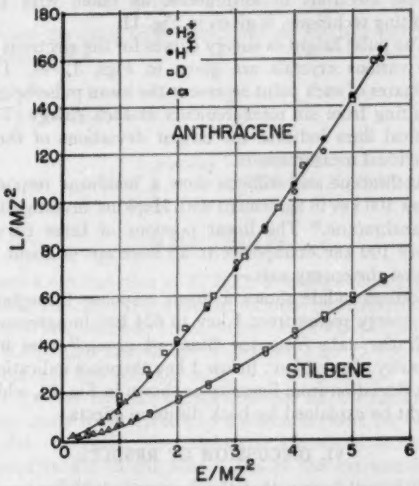

FIG. 15. Fluorescence radiation of anthracene and stilbene when excited by heavy particles of different energies with ordinates and abscissas reduced by the factor $1/MZ^2$; M and Z are mass and charge of the incident particle respectively.

current could also be measured with a similar charge collector made completely of tungsten, and shown in the lower arm of the vacuum tube in Fig. 8. No difference in the current measurements could be detected if a sufficiently large potential (25 volts) was applied to this second collector to prevent the escape of an appreciable number of secondary electrons.

The proper performance of the apparatus could be checked by a variation of the beam intensity. Varying the electron current by a factor of ten produced a proportionate change in the output pulses of the photomultiplier.

The effect of the back diffusion[25] of the electrons striking the crystal restricts the accuracy of the results achieved with the electron gun. Extrapolating the

[25] W. Bothe, Handbuch der Physik **22**, Part 2, 23 (1933).

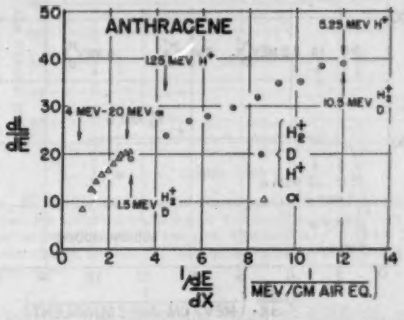

FIG. 16. The differential efficiency of fluorescence, dL/dE, for anthacene as a function of the reciprocal of the specific energy loss, dE/dx, of the incident heavy particles of different energies. dL/dE is found from the curves in Fig. 3 and is expressed in arbitrary units per Mev, where the arbitrary units are the same as the ordinate scale in Fig. 3.

results of Schonland[26] to the low energy region and to elements of low atomic number, the ratio of the number of electrons which escape by back diffusion to the number incident should be less than 10 percent for the organic crystals, but the ratio could be as large as 30 percent for sodium iodide.

In order to normalize the data taken with the electron gun to other data, a small source of Cs^{137} on a 3.2 mg/cm² aluminum foil was mounted in such a manner that the conversion electrons were incident on the crystals at the same spot as the electron beam. During the electron beam runs, the radioactive source was moved out of the beam path with a magnet.

Since sodium iodide is quite hygroscopic, a special chamber was constructed for the experiments with these crystals. This chamber, shown in Fig. 9, permitted

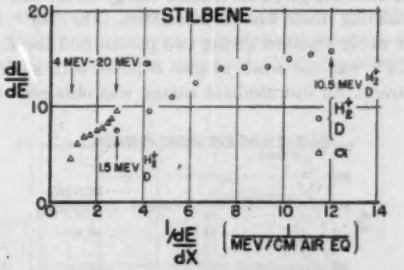

FIG. 17. The differential efficiency of fluorescence, dL/dE, for stilbene as a function of the reciprocal of the specific energy loss, dE/dx, of the incident heavy particles of different energies. dL/dE is found from the curves in Fig. 4. The ordinate scale is the same as Fig. 16.

[26] B. F. J. Schonland, Proc. Roy. Soc. (London) **A104**, 235 (1923); **108**, 187 (1925). He has shown that for a parallel beam of electrons normally incident on the surface, the ratio of back scattered to incident electrons is practically energy independent within the investigated region of 10 to 70 kev. Hence our extrapolation to lower energies seems to be justified.

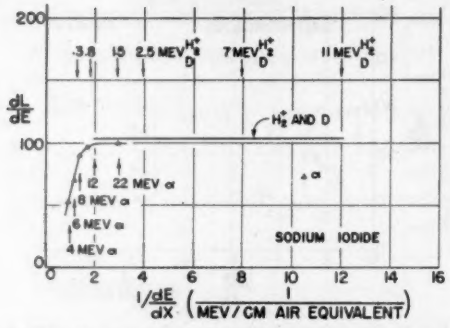

FIG. 18. The differential efficiency of fluorescence, dL/dE, for sodium iodide as a function of the reciprocal of the specific energy loss, dE/dx, of the incident heavy particles of different energies. dL/dE is found from the curves in Fig. 5. The ordinate scale is the same as Figs. 16 and 17.

the installation of a crystal in the vacuum associated with the gun. The crystal could then be cleaved in the vacuum just prior to taking data, and no deterioration of the crystal surface could occur.

Positive pulses were taken from the photomultiplier tube, amplified by a linear amplifier, and photographed on a Tektronix high speed oscilloscope.

In order to extend the data for these low energy electrons to higher energies, internal conversion electrons from radioactive sources were used. These artificial sources are summarized in Table I. Since there were "Auger electrons" present in the radiation striking the crystal, the distance from the source to the crystal was kept at greater than one cm to minimize the simultaneous detection of a conversion electron with an Auger electron. The K and L conversion lines could not be resolved for the Nb^{91} and In^{114} sources, so the points from these are given for a mean energy of the two lines considering their known intensities. The Hg^{203} lines were easily resolved giving two points, and the L line of Cs^{137} was too weak to give a point with sufficient accuracy. An intermediate energy was obtained using

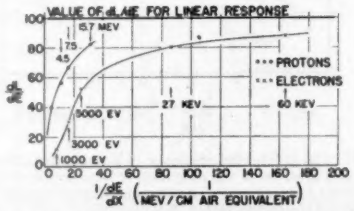

FIG. 19. The differential efficiency of fluorescence, dL/dE, for anthracene as a function of the reciprocal of dE/dx of the incident protons and electrons of different energies. The arbitrary ordinate scale has been chosen so that 100 is the value of dL/dE resulting from electrons of sufficiently high energy (above 100 kev) to give linear response. The efficiency for conversion of incident particle energy into light energy attains its maximum value here and amounts to about 2 or 3 percent.

the 27-kev x-rays from L to K electron transitions in Te^{127}. Using the same type optical arrangement as for the heavy particles, the pulses from these single electrons were amplified and analyzed with the twelve channel pulse amplitude analyzer. In these measurements with the higher energy single electrons back diffusion of the electrons, though present, did not affect the data since the histograms of the pulse-height distributions of the conversion electrons appeared to be symmetrical about the maximum.

V. RESULTS OF THE ELECTRON EXPERIMENTS

A typical photograph of the pulse height resulting from 5000-ev electrons incident on anthracene is shown in Fig. 10. The pulse-height distribution from the cesium electrons in anthracene, as taken with the counting technique, is given in Fig. 11.

The pulse height *vs* energy curves for the electrons in the various crystals are given in Figs. 12–14. The ordinates of each point represent the mean pulse height resulting from six measurements at each energy. The vertical lines indicate the largest deviations of these individual measurements.

Anthracene and stilbene show a nonlinear response below 100 kev in agreement with Hopkins' investigation of anthracene.[12] The linear portions of these curves above 100 kev extrapolate to an intercept of about 22 kev on the energy axis.

Sodium iodide shows a linear response throughout the energy region from 1 kev to 624 kev in agreement with the data from the Stanford group,[13] who find linearity above 2 kev. Below 1 kev there are indications of a deviation from linearity as shown in Fig. 14, which might be explained by back diffusion effects.

VI. DISCUSSION OF RESULTS

It is well known that the fluorescence efficiency of a crystal is dependent on the current density of the incident particles. It has also been suggested, probably first by Kallmann,[27] that the fluorescence efficiency of a crystal for single particles is dependent on the density of ionization along the path of the particle in the crystal. We are indebted to Professor F. Seitz for the following formal approach to a possible explanation of the difference in response of a single organic crystal to different heavy particles. If one assumes that the differential fluorescence efficiency, dL/dE, for producing fluorescent radiation depends on the specific energy loss of the particles, dE/dx, then one can write:

$$dL/dE = e = f(dE/dx) \tag{1}$$

or

$$dL/dx = e(dE/dx) = (dE/dx)f(dE/dx). \tag{2}$$

The expression for the specific energy loss as given by

[27] H. Kallmann, Z. Naturforsch. **3a**, 6 (1948); H. Kallmann, Conference on Scintillation Counters, Oak Ridge, Tennessee, June, 1949.

Livingston and Bethe[18] can be written as:

$$-(dE/dx)=(2\pi Z^2z e^4NM/mE)\ln(4mE/MI) \quad (3)$$

where Ze, M, and E are the charge, mass, and energy of the incident particle and Nz, m, and I are the number of electrons per cm³ of the stopping material, the mass of the electron, and the average excitation potential of the atom of stopping substance. For a given crystal N, z, m, and e are constant and the logarithm term is practically constant—varying between 3.3 and 5.1—for the particles and energies used. Therefore to a good approximation, Eq. (3) can be written as:

$$dE/dx=(MZ^2/E)B \quad (4)$$

where B is essentially constant. Then we can express:

$$dL/dE=g(E/MZ^2) \quad (5)$$

whence the total light output for an incident particle of energy E is:

$$L=\int_0^E g(E'/MZ^2)dE'$$

$$=MZ^2\int_0^{E/MZ^2} g(E'/MZ^2)d(E'/MZ^2) \quad (6)$$

or

$$L/MZ^2=h(E/MZ^2), \quad (7)$$

where h is a function of E/MZ^2. Therefore for a given crystal, the curves for different incident particles should reduce to a common curve when L/MZ^2 is plotted *vs* E/MZ^2. Such curves are shown in Fig. 15 for the anthracene and stilbene data.

It appears that the curves obtained for the different heavy particles do reduce to a common curve for each crystal. However, the alpha-particle curve is compressed to the extent that it lies at the extreme low energy end of the proton and deuteron curves, so that much higher energy alpha-particles would be required for a more thorough check. The data are somewhat insensitive to this approach, but they do support the assumption that, for heavy particles, the fluorescence efficiency is dependent on the specific energy loss in the crystal, which is proportional to the ionization density.

A more sensitive dependence to the rate of energy loss, dE/dx, can be presented by plotting the fluorescence efficiency, dL/dE, obtained by taking the slopes of the curves in Figs. 3–5, as a function of dE/dx. The resulting curves for the heavy particles are shown in Figs. 16–18, where the fluorescence efficiency is plotted *vs* the reciprocal of dE/dx. The specific energy loss has been calculated for these curves from the range-energy data of Bethe.[17] If the response of the crystals were proportional to the energy of the particles, the efficiency would be a constant, independent of the energy. For the organic crystals dL/dE increases

[18] M. S. Livingston and H. A. Bethe, Revs. Modern Phys. 9, 263 (1937).

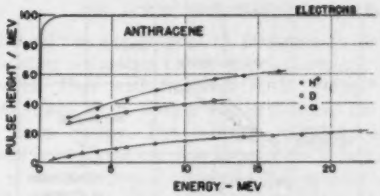

FIG. 20. Ratios of the total fluorescence radiation from anthracene for different particles to the energies of the particles plotted as functions of the energies. The arbitrary ordinate scale has been chosen so that the maximum value for electrons is 100 units per Mev.

continuously with increasing values of $1/dE/dx$, with the proton and deuteron values lying closely together, while the points from the alpha-particle data appear to be consistent with a continuation of the proton and deuteron points. However it is possible that the alpha points lie slightly above the continuation. If this is true, it could be a result of the different energy spectrum of the secondary electrons from alpha-particles as compared to the secondary electrons from protons and deuterons of the same specific energy loss. Since the secondaries from the alpha-particles have greater energies, the ionization density along the paths of the particles will be less, and this will result in a larger value of dL/dE for a given value of dE/dx.

For sodium iodide the fluorescence efficiency for protons and deuterons is constant, as would be indicated by the linear response to those particles. The deviations from linearity for the alpha-particles—the variable portion of the curve in Fig. 18—occur at values of dE/dx corresponding to H_2^+ and deuteron energies of about 0.4 Mev, which are too small for any region of nonlinear response to be detected.

The fluorescence efficiency *vs* the reciprocal of the specific energy loss for electrons and protons in anthracene is compared in Fig. 19. The values of dL/dE for the higher proton energies were obtained from the data of Franzen, *et al.*[7] The values of dE/dx for electrons

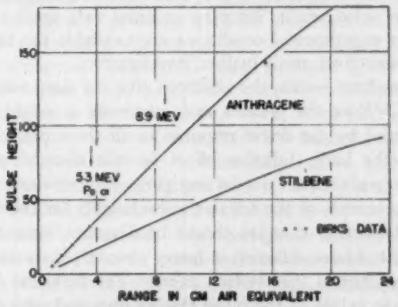

FIG. 21. Pulse heights resulting from the fluorescence radiation of anthracene and stilbene when excited by alpha-particles plotted as a function of the range of the particles in air. The ordinate scale is the same as in Figs. 3–6.

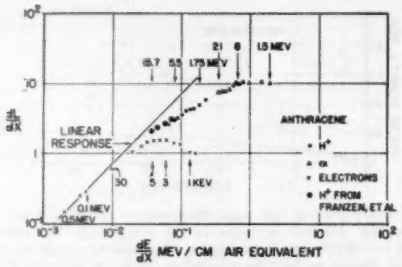

FIG. 22. Variation of the specific fluorescence, dL/dx (expressed in arbitrary units per cm of air equivalent), of anthracene with the specific energy loss, dE/dx, of the incident alpha-particles, protons, and electrons of different energies. The straight line indicates linear response of the crystal.

were calculated for anthracene from Bethe's theoretical formula[29] using a calculated value of 1200 as a mean value for the stopping power of anthracene relative to air. Since the energy loss per ion is about the same for both protons and electrons, one might expect that the two curves would roughly coincide if the fluorescence efficiency is dependent only on the ionization density. As is shown in Fig. 19, the curves certainly are not coincident, but the values of dL/dE for the higher proton energies appear to be approaching about the same constant value attained by dL/dE for electrons of energies sufficiently high enough to give linear response; i.e., above 100 kev. It should be noted, however, that the constant value of dL/dE for protons is perhaps reached at a considerably different value of dE/dx than for the electrons. If one considers the loss of pulse height due to the back diffusion of the electrons in the electron gun experiment, the actual difference between the two curves in the low energy region should be smaller than the measured difference. However if the estimated numbers of back scattered electrons (as given in Sec. IV) are correct, the difference in the curves cannot be explained by this effect alone, particularly since the electrons lost by back diffusion lose some energy in the crystal and thus make a small contribution to the pulse height. Since no accurate data applicable to our experimental conditions are available the back diffusion effect needs further investigation.

In sodium iodide, the electrons give the same values of dL/dE as the protons and deuterons as might be indicated by the linear response to all three particles. Here the back diffusion effect for the electron gun experiments should not be negligible. Nevertheless, the measurements of the relative pulse heights for the different electron energies should be accurate, since the amount of back diffusion in heavy elements is certainly independent of the electron energy. The fact that the absolute values of the pulse heights obtained with the electron gun measurements do compare so favorably with the measurements taken with the single electrons is not understood.

A useful presentation of the data for anthracene is shown in Fig. 20, where the ratio of total pulse height at a given energy divided by that energy is plotted as a function of the energy for the particles investigated. The arbitrary ordinate scale has been chosen so that the maximum value for electrons is 100, this being attained in the region of linear response for the electrons. Thus the heavy particle curves give the response in percentage of the maximum light output per Mev.

For specific energy losses of heavy particles greater than 0.63 Mev/cm air equivalent, as in our case for alpha-particles below nine Mev, the specific fluorescence (the light output per cm air equivalent) attains a constant value in the organic crystals and is then independent of the specific energy loss. This is indicated in Fig. 21, in which plots of pulse height *vs* range in air of alpha-particles incident on anthracene and stilbene are shown. The curves are essentially linear up to a range of nine cm, and thus dL/dx is constant over this range, where dE/dx is greater than the above mentioned value.

This effect in anthracene was first noted by Birks[6] and has been studied by Cross[30] using alpha-particles from ThC′, ThC, Cm, Am, Pu, and from nuclear reactions. Reynolds, Harrison, and Hill[31] have found a similar saturation effect using liquid scintillation substances. It is interesting to note that in all the results mentioned here the linear portion of the line does not extrapolate through the origin.

Similarly, if the same types of curves are plotted for electrons on anthracene and stilbene the same results seem to be indicated, namely, a region where the curve is linear and hence dL/dx is constant, but the saturation of dL/dx is attained at a much smaller value of dE/dx than in the case of heavy particles. However due to the uncertainty of the correction for the back diffusion no definite conclusion can be made.

A survey of the response of the anthracene crystal to the different ionizing radiations is presented in Fig. 22, where the variation of the specific fluorescence is given as a function of the specific energy loss in a log-log plot. This curve seems to show the following trends. Both the heavy particles and electrons apparently give regions of linear response (the specific fluorescence increasing linearly with energy) but these probably starting at quite different values of dE/dx. An extrapolation is required to reach this linear region for the heavy particles. At larger values of dE/dx, but different for the heavy particles and electrons, the response becomes nonlinear for both types of particles, and at even larger values of the specific energy loss, the specific fluorescence for

[29] H. A. Bethe, Handbuch der Physik **24**, Part 1, 521 (1933).

[30] W. G. Cross, Chalk River Laboratory, private communication.

[31] Reynolds, Harrison, and Hill, Phys. Rev. **82**, 317 (1951), and private communication.

heavy particles saturates. The same effect is indicated for electrons, but due to the uncertainty of the magnitude of the back diffusion effect in this case no quantitative statement can be made. However, we do not believe that the different results for electrons and heavy particles could be a result of surface effects and back diffusion alone, since the experiments with the 27-kev x-rays, which produced electrons inside the crystal, gave data in agreement with the above results.§

§ *Note added in proof*:—J. B. Birks, Phys. Rev. 84, 364 (1951), has recently used the exciton theory to explain the general features of these results.

VII. ACKNOWLEDGMENTS

The authors are grateful to Professor F. Seitz for stimulating discussions concerning the interpretation of the data. They wish to thank A. L. Atkins, R. O. Kerman, and W. E. Kreger who determined the cyclotron beam energy. The valuable assistance of Mr. Chester Lob and the use of facilities of the Tube Laboratory of the Electrical Engineering Department in performing the electron experiments are deeply appreciated. The authors also would like to thank W. G. Cross of Chalk River Laboratory who kindly sent them his data prior to publication.

PHYSICAL REVIEW VOLUME 84, NUMBER 5 DECEMBER 1, 1951

Investigation of the Gliding Process in Ionic Crystals by Prismatic Punching

ALEXANDER SMAKULA* AND MYRON W. KLEIN
Engineer Research and Development Laboratories, Fort Belvoir, Virginia

(Received June 28, 1951)

The prismatic punching method applies a unidirectional stress on a very small surface (approximately 0.001 square centimeter) of a crystal lying on a support which is softer than the crystal itself. The method is very convenient for low and high temperature and for small samples. The glide system of thallium bromoiodide crystals determined by the prismatic punching method contains dodecahedron planes {110} as glide planes and cubic planes [001] as glide directions. The width of the glide bands ranges from 1 to 5 microns. The stress-strain curve shows a linear relation between the shear angle δ and the applied stress σ ($\delta=a'\sigma+b$). The creep takes place according to the exponential law ($\delta=at^m$). The glide bands have to be displaced a distance of about 100 ions at room temperature and about 15 ions at -190°C before rupture takes place (plastic limit). Prismatic punching on sodium chloride crystals produces gliding along dodecahedron planes (110) in $[1\bar{1}0]$ direction. Apparent cleavage of sodium chloride crystals along dodecahedron planes and normal cleavage along cubic planes are explained as ruptures between neighboring glide planes.

I. INTRODUCTION

GLIDING is the basic process in the plastic deformation of crystals. Although numerous investigations have been made in this field, many problems are still unsolved. There exists a great need for new experiments which may contribute to their solution. Great progress has been achieved in the study of the gliding process, mainly by investigations of single metal crystals.[1] Nonconducting crystals as compared with metals have some advantages. Since most of them are transparent, they permit study of the gliding process in their interior by observation between crossed polarizers.[2] On the other hand, nonconducting crystals have the disadvantage of a very narrow plastic range; therefore, the method for studying the gliding process must be very sensitive. However, there exist a few ionic crystals which possess plastic properties resembling metals. Those crystals are the silver and thallium halides which can be easily grown in large sizes. As pure silver and thallium halides are very soft, they require special care when specimens are being prepared. Mixed crystals of thallium halides are almost ideal for gliding studies as their hardness is considerably greater than that of their pure components. Thallium bromoiodide crystals of the composition 41.7 percent TlBr+58.3 percent TlI by weight have been used in this investigation.

The methods generally used for investigation of the gliding process are based on the study of shear stress-strain curves. The simplest conditions exist when pure shear stress is applied. Under tension or volumetric compression, however, no pure shear stress is present. The same is true of torsion method. The Bausch method,[3] which claims to give a unidirectional stress, gives no uniform shear stress, as has been shown by Read.[4] In addition, all these methods require large crystal specimens which are seldom obtainable; other disadvantages which should also be mentioned are the variable influence of the specimen surface on the stress-strain and the multiple gliding along different glide planes.

* Now at Laboratory for Insulation Research, Massachusetts Institute of Technology, Cambridge 39, Massachusetts.

[1] For general summary and references see: *A Symposium on the Plastic Deformation of Crystalline Solids*, Mellon Institute, Pittsburgh 19, 20 May 1950.

[2] E. Schmidt and W. Boas, *Kristallplastizität* (Verlag-Springer, Berlin, 1935).

[3] K. Bausch, Z. Physik. 93, 479 (1935).

[4] W. T. Read, see reference 1, p. 111.

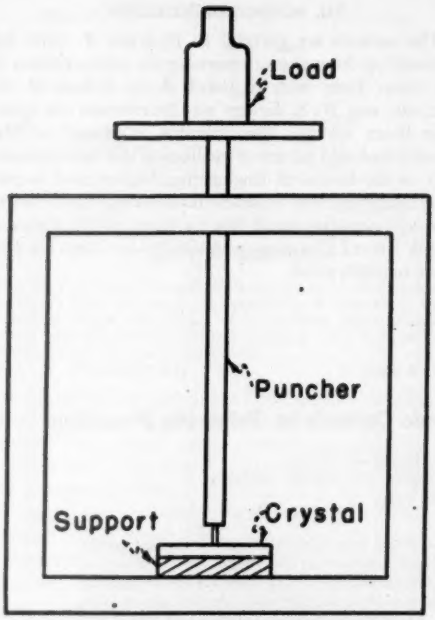

FIG. 1. Schematic diagram of punching apparatus.

II. EXPERIMENTAL METHOD

Some disadvantages mentioned in the preceding paragraph can be eliminated by using the prismatic punching method which already has been used for the determination of crystal orientation.[5] The method involves the application of a force on a prismatic puncher with a square or circular cross section which compresses a small part of a thin crystal specimen lying on a support which is softer than the crystal itself. The method is actually static and, therefore, the word "punching" is somewhat misleading but already accepted in the literature. The puncher is merely pressed into the surface as the load is slowly applied. The compressed part of the crystal under the puncher glides through the crystal in the glid direction along the glide planes. On the side opposite the punch point one or more elevated mounds appear. With increase of stress, the height and the lateral dimensions of the mound increase. The gliding parts of the crystal carry along their adjacent layers, thus forming glide bands. From the dimensions and the structure of the mounds one can obtain information about the gliding process.

The prismatic punching method essentially resembles the hardness test of Vickers. It differs, however, in two points. Whereas the indenter of the hardness tester of Vickers has the shape of a four-sided pyramid, the prismatic punching method uses a cylindrical indenter to provide a constant stress cross stress section regardless of the depth. (For qualitative investigation a conical indenter may also be used.) The other point concerns the method of observation. In hardness measurements only the dimensions of the indentation are determined, whereas in gliding measurements by the prismatic punching method, the elevated mound on the opposite side of the indentation is measured.

The cross section of the puncher is not important. However, for practical reasons it is convenient to use small cross sections, so that the load and the crystal specimen may be small. The punchers used here had cross sections of about 0.03 cm×0.03 cm. The optimum thickness of the crystal specimens is a few tenths of a centimeter. It is important that the dimensions of the sample surface be at least two times greater than the thickness; otherwise, the gliding may take place in the direction of the shortest distance. This effect has already been observed in single aluminum crystals by Wu and Smoluchowski.[6] The crystal specimens used had surfaces of a few square centimeters, so that many punch points could be obtained on the same sample. The thickness was between 0.1 and 0.2 cm. The samples were cut with proper orientation, then ground and polished as described in a previous paper.[7] The apparatus used is shown in Fig. 1.

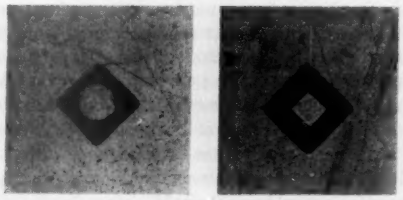

(a) (b)

FIG. 2. Punch patterns on a cube face [100], puncher cross section 4.2×10^{-4} cm², load 1.27 kg, crystal thickness 0.118 cm; (a) punched surface; (b) opposite surface; magnification 50×.

III. RESULTS

(A) Glide Planes and Glide Directions

The glide planes and glide directions of thallium bromoiodide have already been determined.[8] The glide directions are perpendicular to the cubic faces [100] and the glide planes are dodecahedron faces (110). In Fig. 2(a) is shown the pattern on the top surface obtained by punching the cubic face [100] with a circular puncher. The bright circle in the middle of the pattern indicates the cross section of the puncher. The dark square surrounding the bright circle is the indented portion outside of the actual punched area. This surface,

[5] A. Smakula and M. W. Klein, J. Opt. Soc. Am. 30, 445 (1949).

[6] T. L. Wu and R. Smoluchowski, Phys. Rev. 78, 468 (1950).

[7] A. Smakula and M. W. Klein, J. Opt. Soc. Am. 40, 748 (1950).

[8] See Smakula and Klein, reference 5.

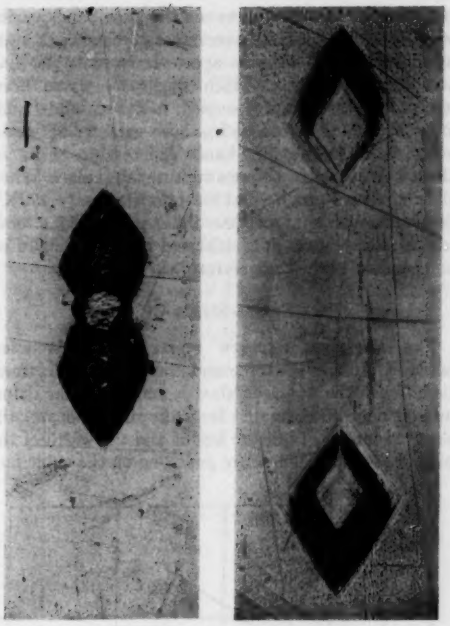

(a) (b)

FIG. 3. Punch patterns on a dodecahedron face [110], puncher cross section 4.2×10^{-4} cm², load 2.53 kg, crystal thickness 0.136 cm; (a) punched surface; (b) opposite surface; magnification 50×.

in the figure shown, is 2.5 times larger than the cross section of the puncher. The indented area does not depend on the shape of the puncher cross section. It is always limited by four straight sides. On the surface opposite the punch point a truncated pyramid appears [see Fig. 2(b)]. The sides of the pyramid are not planes but slightly curved surfaces. The base of the pyramid is larger than the indented area on the opposite side. The top of the pyramid is smaller than the actual punched area on the opposite surface. The relation between the applied stress and the dimensions of the pyramid is treated later.

Punching on a dodecahedron face [110] produces an indentation on the top surface under the puncher and, in addition, an elevation in the form of two wings, as shown in Fig. 3(a). The wings are formed by the gliding of plastic deformed crystal parts in [100] directions along (110) glide planes. On the opposite side two rhombic truncated pyramids appear displaced 45° from the punch direction and pointing toward [100] directions [see Fig. 3(b)]. Their linear distance depends on the thickness of the sample.

Punching on an octahedron face [111] produces around the punched surface three wings directed toward [100] planes [see Fig. 4(a)]. On the opposite side three pyramids appear which are rotated 60° with respect to the wings on the top surface [see Fig. 4(b)]. The pyramids may be considered as projected patterns from cubic faces onto octahedron faces.

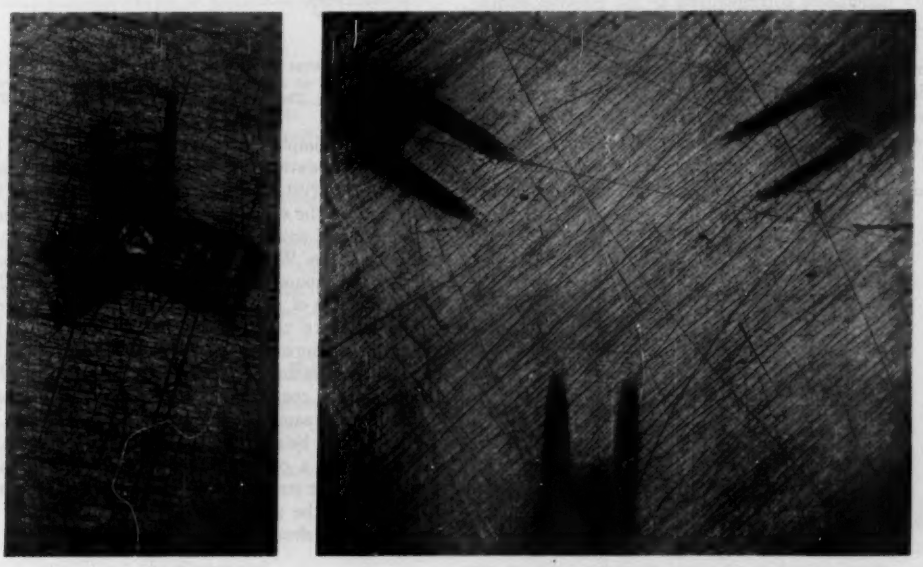

(a) (b)

FIG. 4. Punch patterns on an octahedron face [111], puncher cross section 4.2×10^{-4} cm², load 3.83 kg, crystal thickness 0.125 cm. (a) Punched surface. (b) Opposite surface. Magnification 50×.

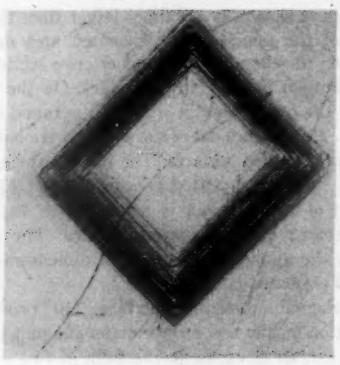

FIG. 5. Glide bands on a cubic face, magnification 100×.

(B) Glide Bands

The sides of the elevated pyramids shown in Figs. 2 through 4 are not smooth, but have a steplike structure, called glide bands. Such glide bands are shown in Fig. 5. The formation of the glide bands takes place quite uniformly. If the puncher has a square shape and its edges coincide with the directions of the glide planes, that is, cubic faces, the first bands appear directly under the edges of the puncher. If the cross section of the puncher is circular, or if the edges of a square puncher do not coincide with the directions of the glide planes, the elevated mound will still have a square shape with dimensions corresponding to the puncher dimensions in the direction perpendicular to the glide planes. If a circular puncher is used, the square mound circumscribes the puncher circle. This result indicates that the gliding is transmitted outside of the stress area until two perpendicular glide bands meet each other. If the stress increases, new glide bands develop on both sides of the bands already present. As a consequence, the base of the pyramid increases, and the top surface decreases. The distance between the glide bands varies from 1 to 5 microns. An average of 25 bands has been found to be 3.36 microns apart. It is probable that narrower bands exist which might not have been resolved by the microscope used. A Bausch and Lomb metallographic microscope has been used for all strain measurements. The glide bands can reach a height of about 1 to 2 microns before a rupture takes place. When glide bands are produced at low temperature (−190°C) they are much sharper than those produced at room temperature, but their widths and heights seem to be independent of the temperature.

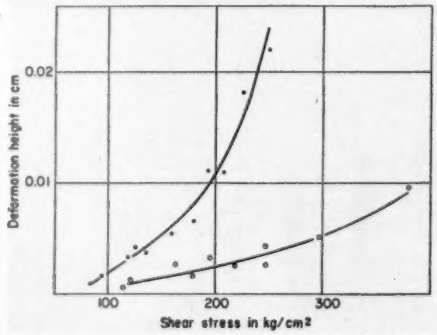

FIG. 6. Strain-stress curve in terms of the height of the elevated pyramid on a cube face. The dots represent room temperature values. The open circles represent values at −190°C.

(C) Stress-Strain Curve

The stress-strain curve represents the relation between the applied force and the resulting deformation. When the punch method is employed, the deformation may be estimated from the dimensions of the elevated mound. Both the height and the width of the mound are measured. Since punching on the cubic face produces the simplest conditions, it has been used for the quantitative study. Application of different amounts of stress on a crystal by the punch method changes the dimensions of the elevated mound. In Fig. 6 the height of the pyramid *versus* stress is shown. The curve has a parabolic shape. With an increase of stress the lateral sides of the mound change, as shown in Fig. 7. The lateral increase of the mound is linear with the stress.

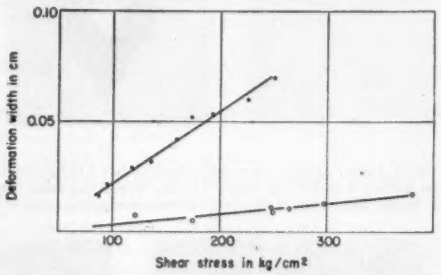

FIG. 7. Strain-stress curve in terms of the strained width of the elevated pyramid on a cube face. The dots represent values at room temperature. The open circles represent values at −190°C.

The influence of stress on the dimensions of the mound at a temperature of −190°C is similar to that at room temperature. The only difference is that at low temperature a considerably higher stress is necessary to produce the same sized mound.

Neither the height nor the width of the elevated pyramid gives a complete relationship between shear stress and shear strain. If the direction of applied stress is parallel to the glide planes, the strain may be expressed by the shear angle δ. It can be expressed

$$\delta = \text{arc tg}(h/w),$$

where h = the height of the elevated pyramid and w = the

width of the strained pyramid sides. In the elastic range, δ is directly proportional to the applied stress σ. We have a linear relation in the plastic range too, as can be seen in Fig. 8 where the shear angle δ is plotted *versus* applied stress σ. The relatively wide scattering of experimental points might be caused partly by not uniformly applying the stress and partly by the inaccuracy of microscopic readings. The remarkable result is that the points obtained at low temperature (−190°C) coincide with those at room temperature. This indicates that the ratio of the height of the pyramid to the strained width does not depend on temperature.

The strain-stress curve of Fig. 8 may be represented by

$$\delta = a'\sigma + b,$$

where a' and b are constants. The linear relation has

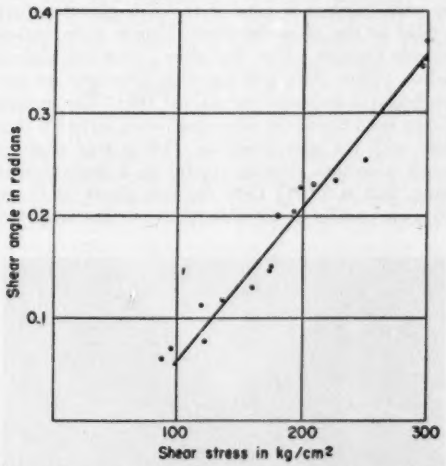

FIG. 8. Strain-stress curve in terms of the shear angle of the elevated pyramid on a cube face. The dots represent room temperature values. The open circles represent values at −190°C.

already been found for other body-centered cubic and hexagonal crystals and the parabolic relation for face-centered cubic crystals.[9] In the transition region between the elastic and plastic range we may expect in thallium bromoiodide a parabolic relation too.

(D) Strain-Time Curve (Creep, Plastic Flow)

There are two kinds of creep: transient creep which occurs at the moment when the stress is applied and quasi-viscous creep which continues to extend under constant stress. The transient creep obeys the law

$$\delta = at^m,$$

and the quasi-viscous creep

$$\delta = kt,$$

[9] G. I. Taylor, Proc. Roy. Soc. (London) **145**, 362 (1934).

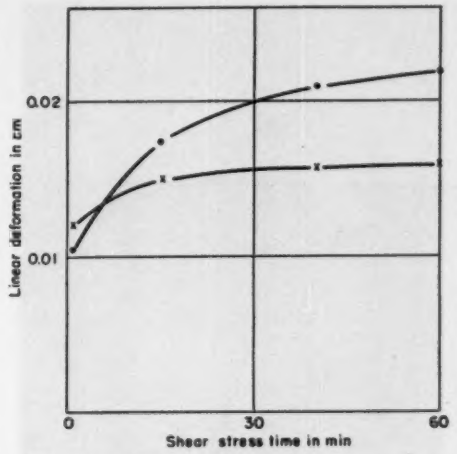

FIG. 9. Plastic flow of the elevated pyramid on the cube face. The dots represent height, and the crosses represent the strained width.

where t is time, a and k are coefficients of flow and m is creep exponent.[10,11]

All our results so far have been obtained by applying the stress for 5 seconds. Figure 9 shows the change of the width w and the height h of the elevated pyramid extending the stress time up to one hour. Both increase with time at a decreasing rate. The height is influenced by time more than the width. In Fig. 10 is plotted $\log\delta$ *versus* $\log t$. The straight line indicates that the exponential law of transient creep is valid for thallium

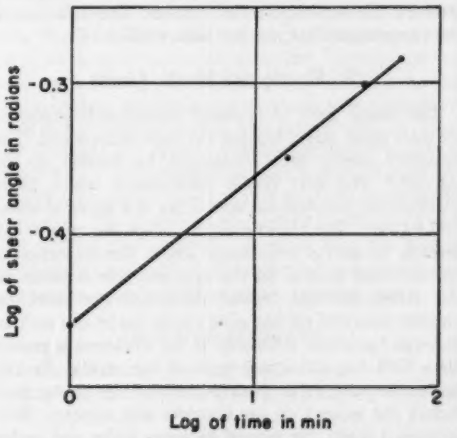

FIG. 10. Plastic flow of the elevated pyramid on the cube face in terms of shear angle.

[10] E. N. Andrade, Proc. Roy. Soc. (London) **A84**, 1 (1910); and **A90**, 392 (1914).
[11] E. P. T. Tyndall, see reference 1, p. 49.

FIG. 11. Punch pattern on a dodecahedron face [110] of NaCl, surface opposite to the puncher, puncher cross section 8.1×10^{-3} cm², crystal thickness 0.2 cm, magnification 50×.

bromoiodide crystals. If t is given in minutes, $a=0.44$ min^{-1} and $m=0.095$ for a stress of 200 kg/cm² and room temperature. The coefficient a depends on the applied stress, while m seems to be constant. The influence of the temperature has not yet been studied.

(E) Elastic and Plastic Limits

The elastic limit of thallium bromoiodide produced by pure shear stress has not yet been determined. The apparent elastic limit estimated by torsion is 163 kg/cm².[12] The first visible deformation which takes place on the punched surface occurs at a stress of about 100 kg/cm². The glide bands inside of the crystal can already be seen at even lower stress. The formation of the elevated mound on the opposite side depends on the stress and the crystal thickness. For thickness smaller than 0.05 cm the glide bands can be transmitted through the whole thickness. If the thickness is greater than 0.05 cm, the upper part of the crystal directly under the puncher is distorted beyond the plastic limit before the mound on the opposite side appears. With increased stress the mound becomes wider and higher (see Figs. 6 and 7), until finally it breaks. The maximum height which the mound may obtain at room temperature is about 0.02 cm and the width 0.07 cm. At a temperature of −190°C the maximum height obtained is 0.003 cm and the width 0.01 cm. The corresponding total shear stress of the plastic limit is about 250 kg/cm². The maximum shear angle (the slope of the sides of the mound) is about 20°. If we consider that the nearest glide bands are about 1 micron apart, we obtain a maximum glide of one band $=3\times10^{-6}$ cm. This indicates that a lattice plane must be shifted about 100 atoms until the binding force is broken.

(F) Gliding in Sodium Chloride Crystals

The glide system (glide planes and directions) in thallium bromoiodide are of the highest possible symmetry; there are four glide planes parallel to one glide direction. The punched part, therefore can be pushed through the crystal as a prism. It is quite interesting to see what happens if some of the glide planes are not parallel to the glide directions. This is so in sodium chloride crystals where the glide planes are dodecahedron planes (110) and the glide directions are perpendicular to dodecahedron planes $[1\bar{1}0]$.[13] The simplest gliding conditions exist when the punch direction coincides with the glide direction. This is true when we punch a sodium chloride crystal on a dodecahedron plane, that is, [110]. Only the two planes $(01\bar{1})$ and $(0\bar{1}1)$ are parallel to the glide direction. The other four

FIG. 12. Glide bands in NaCl as seen between crossed polarizers produced by punching on a cube face at 350°C, magnification 100×.

[12] Combes, Ballard, and McCarthy, J. Opt. Soc. Am. **41**, 215 (1951).

[13] Under certain conditions sodium chloride may glide also along (100) planes. See: M. J. Buerger, Am. Mineral. **15**, 174 (1930).

are at 45° angles. Sodium chloride crystals are too brittle for punching at room temperature. Therefore, the experiments have been carried out at a temperature of 350°C. The result of punching on the [110] plane is shown in Fig. 11. The elevated mound is limited only on two sides by glide bands. The other two sides of the mound show a diffuse transition between the mound and the undeformed crystal surface. From this result we may conclude that if the glide planes are not parallel to the glide direction, no glide bands are formed.

Punching on a cube face [001] of sodium chloride produces gliding along four adjacent dodecahedron planes (101), (011), ($\bar{1}$01), and (0$\bar{1}$1). We should expect four mounds similar to the one shown in Fig. 11. The glide bands formed inside the crystal by punching on a cubic face are shown in Fig. 12. Since a conical puncher has been used in this experiment the two bands do not split into two components. On the punched cubic surface of sodium chloride four cracks appear along dodecahedron planes (Fig. 13). This effect is already known and is called an "apparent cleavage" in contrast to the normal along the cubic planes. Both cleavages have actually the same cause. If a stress is applied on a point or small surface of the cubic plane, the material glides in four different directions and the cracks appear along the boundaries of the glide planes. To cleave a crystal along a cube face, a stress must be applied on a line parallel to a cube face. The crystal is forced to glide along two dodecahedron planes only, and the crack appears along the boundary between those two glide planes. Hence, the cleavage in sodium chloride can be explained as a simple separation of glide planes.

IV. DISCUSSION

A mechanism of plastic deformation produced by punching has been described by Seitz.[14] According to Seitz, spirals or rings of dislocation are generated along the periphery of the contact area between the indenter and crystal surface in the manner of Frank-Read mechanism.[15] These dislocation rings or spirals can move along the glide planes in glide direction through the crystal sample. It is generally assumed that the shearing stress, determined by stress-strain measurements, corresponds to the production or liberation of the dislocations from some stable array and not to their movement in the crystal. This conclusion has been drawn indirectly from the smallness of the shearing stress and from the strong influence of impurities. We can give a direct proof from our experiments for this mechanism. As it has been shown under III-A there

[14] F. Seitz, Phys. Rev. **79**, 723 (1950).
[15] F. C. Frank and W. T. Read, Phys. Rev. **79**, 722 (1950).

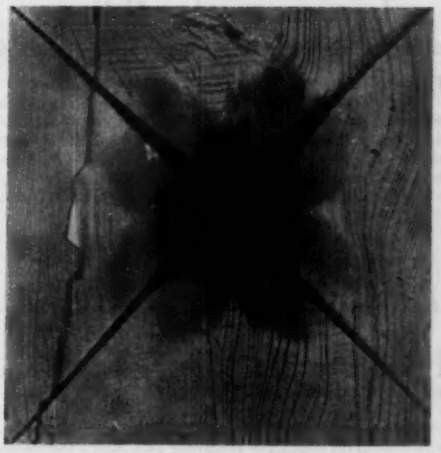

FIG. 13. Apparent cleavage of NaCl produced by punching on a cube face at room temperature, magnification 100×.

can be produced one, two, or three mounds depending on the crystal orientation. It is very surprising that the necessary stress is the same whether we produce one, two, or three mounds of the same size. This experimental fact can be explained only by the assumption that the shearing stress is used only to start the deformation.

V. CONCLUSIONS

One can see from the results of the experiments presented in this paper that prismatic punching is a very convenient method for study of plastic deformation. The linear dimensions of the crystal specimen may be as small as 0.1 cm or even smaller. The high or low temperature study is very simple since the punching only is made at desired temperatures and the subsequent microscopic measurements are carried out at room temperature. The surface influence of the specimen is eliminated in the prismatic punching method since the crystal is forced to deform in that area where the stress is applied. The formation of glide bands in space and time can be studied easily. Crystals with low plastic properties such as sodium chloride can be studied easily by the punching method at higher temperatures.

ACKNOWLEDGMENT

The authors are indebted to Professor F. Seitz for reading the manuscript and for his valuable comments.

Letters to the Editor

PUBLICATION of brief reports of important discoveries in physics may be secured by addressing them to this department. The closing date for this department is five weeks prior to the date of issue. No proof will be sent to the authors. The Board of Editors does not hold itself responsible for the opinions expressed by the correspondents. Communications should not exceed 600 words in length.

A Sensitive and Reproducible Thermometer in the Range 2° to 20°K*

A. BROWN, M. W. ZEMANSKY,† and H. A. BOORSE‡
Pupin Physics Laboratories, Columbia University, New York, New York
(Received October 15, 1951)

IN connection with our measurements of the heat capacity of niobium in the normal and superconducting state, it was desirable to find a secondary thermometer for use in the range 2° to 20°K with the following requirements: reproducibility after cycling to room temperature, high sensitivity, negligible change of calibration in the presence of a magnetic field. Such a thermometer has been the subject of a wide search by investigators in low temperature physics for many years. The most commonly used secondary thermometer, leaded phosphor-bronze, is reproducible but has sensitivity only below 7.2°K owing to the superconductivity of the lead. However, in addition to being insensitive above 7.2°K, it is also insensitive below 7.2°K in the presence of a magnetic field.

The fact that carbon possesses desirable resistance-temperature properties in the liquid helium temperature range is well known, and considerable use has been made of carbon thermometers in various forms, such as india ink, Aqua Dag, etc. None of these carbon thermometers showed reproducibility from day to day, and in some cases the sensitivity was not sufficient. At the Low Temperature Symposium held at the National Bureau of Standards in March, 1951, J. R. Clement of the Naval Research Laboratory pointed out that a very convenient and sensitive carbon thermometer was available commercially in the form of carbon radio resistors, and that those rated at one watt manufactured by the Allen-Bradley Company showed high sensitivity in the helium range.

Because a one-watt resistor was larger than desirable for mounting in our specimen of niobium, we chose a half-watt resistor at random from the stock on hand at Columbia University. The outer plastic covering was ground away so as to expose the carbon. The resistor was then covered with a 0.001-inch layer of clear glyptal lacquer and baked. It was then cemented into a cylindrical hole bored in the niobium. The total weight of the resistor and leads was then less than 0.2 gram. During the period April through August, 1951, the specimen and thermometer were cooled from room temperature to about 2°K seven times. Using a constant measuring current of 10 microamperes and a Wenner potentiometer, a careful resistance-temperature calibration was made each time using the vapor pressure of liquid helium. In this temperature range about 50 different calibration points were obtained. These points were found to lie on a smooth curve with over 90 percent of the points differing from the curve by less than 0.002 degrees.

TABLE I. Typical thermometer calibration and sensitivity.

T, °K	R, ohms	dR/dT, ohms/deg K
Room temperature	55	...
20.37	134.4	4.595
14.00	179.6	11.16
4.20	1061.8	583.4
2.40	5108	7012

The semiconductor equation[1] written in the form

$$\log R = A + BT^{-1} - \tfrac{1}{2}\log T$$

was found to agree fairly well with the measured resistance at room temperature, 77°K, and in the liquid helium range. In view of the remarkable reproducibility of this thermometer, it occurred to us that by means of a calibration in both the helium and hydrogen ranges intermediate temperatures from 4.2°K to 14°K could be determined with great accuracy and ease. Accordingly, the necessary additional calibration data were taken in the liquid hydrogen range (14°K to 20°K). It was then found that all the data from 2.4° to 20°K could be represented with high accuracy by a modification of the semiconductor equation, as follows

$$\log R = A + BT^{-1} + CT^{-2} - KT^{2},$$

where, for our particular resistor, $A=1.90554$, $B=5.22291$, $C=-2.14932$, and $K=0.000068$. A few selected values are given in Table I.

In making measurements of the heat capacity of niobium it was found that: (1) a magnetic field of 6000 gauss did not affect the calibration; (2) the molar heat capacity in the normal state was found to be a smooth curve agreeing with the accepted equation

$$C_v = \gamma T + 464.4(T/\theta)^3$$

in the range 2.5°K to 14°K. This lends support to the view that no anomalies in the resistance-temperature relation exist for this particular carbon resistor in the uncalibrated range from 4.2°K to 14°K.

Most of the above results were reported by us in a paper on the specific heat of niobium at the Conference on Low Temperature Physics held at Oxford University, August 22–27, 1951. A much more extensive investigation of these carbon resistors was reported by J. R. Clement and E. H. Quinnell at this conference. The results of both investigations are in good agreement.

* Assisted by the ONR and Linde Air Products Company.
† Permanent address: The City College of New York, New York, New York.
‡ Permanent address: Barnard College, Columbia University, New York.
[1] Seitz, *Modern Theory of Solids* (McGraw-Hill Book Company, Inc., New York, 1940), p. 191.

An Explanation of Differences in Counting Properties among Diamond Specimens

G. P. FREEMAN AND H. A. VAN DER VELDEN
Physical Laboratory, University of Utrecht, Utrecht, The Netherlands
(Received October 15, 1951)

WHILE investigating the counting properties of diamond counters several authors[1] have found large variations in their characteristics. To understand this fact and also to select counters among a large number of diamonds, it would be valuable to know other diamond properties which are correlated to the counting one. The first property probably answering this requirement was found by Friedman, Birks, and Gauvin[2] to be a spectral transmission in the region from 3000 to 2250A. Selecting 36 flat diamonds by means of this criterion, the present authors found only 13 of these diamonds (of type II) to count α-particles. From this result, the criterion can be judged fair but not excellent. The efficiency varied among the 13 counters from 4 to 94 percent, and was different in each specimen, dependent on the flat side which was irradiated. That is to say, the α-particles always entered the crystals at the cathode, but the efficiency was measured for one side chosen as cathode, as well as for the other. The largest charge pulses given by polonium α-particles, measured under identical circumstances, displayed variations similar to that of the efficiencies.

On previously obtained evidence,[3] it was considered reasonable to search the crystals for the presence of laminations, e.g., at right angles with the surface of a counter. This was performed

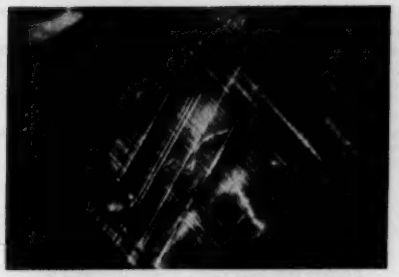

FIG. 1. Birefringence pattern of a noncounting diamond.

with the aid of a petrographic microscope with a Federov rotation stage, in an investigation largely resembling that of Ramachandran. This disclosed a mosaic structure of most of the noncounting diamonds, instead of the laminated structure found by Raman and Ramachandran.[4] The counting diamonds displayed a very poor pattern of birefringence, contrary to the noncounting specimens. This is illustrated by Figs. 1 and 2. The first photograph gives a birefringence pattern of a noncounting specimen. This photograph was taken with the polarizer and analyzer of the microscope set in the directions of the bisectors of the angle of 70° between the streaks of birefringence. The second picture shows a few streaks of birefringence in a counting diamond. Using this experience to eliminate noncounting diamonds from the collection (already selected as stated by transmission in the ultraviolet) it is found that 75 percent of the remaining crystals are counters.

From this investigation the following conclusions can be drawn:

(1) The counting property is a property of the crystal itself and not a consequence of the imperfection of the crystal, as was suggested by Lonsdale.[5] This is proved by the high counting efficiency of some of the diamonds and by the (relative) perfection of the counters.

(2) The laminations observed by Raman, Rendall, and Ramachandran[4] are in fact a well-ordered mosaic superstructure of small octahedrons. This view is supported by another experiment with two diamonds in which the variation of birefringence was observed along the four directions normal to the octahedron surfaces.

(3) The selection of counters is improved from about 30 percent to about 75 percent if the absence of streaks of birefringence is used as a criterion together with the ultraviolet transparency. This improvement is obtained with a Federov rotation stage to obtain the correct inclination of the crystal and a petrographic microscope.

The investigation was completed with the comparison of luminescence of the 36 diamonds. A large variety of intensity and of color (blue in most cases) was observed. In general this result supported the view taken by Pringsheim[6] that luminescence in diamonds will be a consequence of impurities. However, this is contrary to the experience of Raman and co-workers who found absence of luminescence in this kind of diamond (of type II) and presence of blue luminescence only in ultraviolet nontransparent specimens (of type I).[4] Moreover, the suggestion of Frerichs[7] on the correlation between counting and luminescence obtained with irradiation at 2250A was not confirmed.

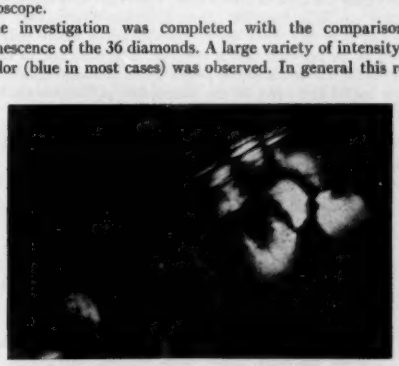

FIG. 2. Birefringence pattern of a counting diamond (with a few laminations).

A detailed report of this investigation will be published elsewhere[8] in the near future. The authors are indebted to Professor Milatz for his highly valued and stimulating interest in this investigation.

[1] G. Stetter, Verhandl. deut. phys. Ges. **22**, 13 (1941); W. Jentschke, Phys. Rev. **73**, 77 (1948); D. E. Wooldridge, *et al.*, Phys. Rev. **71**, 913 (1947); L. F. Curtiss and B. Brown, Phys. Rev. **72**, 643 (1947); A. J. Ahearn, Phys. Rev. **73**, 1113 (1948); D. R. Corson and R. R. Wilson, Rev. Sci. Instr. **19**, 1467 (1948); H. Ess and J. Rossel, Helv. Phys. Acta **23**, 484 (1950); and **24**, 247 (1951).
[2] Friedman, Birks, and Gauvin, Phys. Rev. **73**, 186 (1948).
[3] G. P. Freeman and H. A. van der Velden, Physica **17**, 565 (1951).
[4] C. V. Raman, *et al.*, Proc. Indian Acad. Sci., Symposium on the Properties of Diamond (I) **19A** (1944); Symposium II, **24A** (1946).
[5] K. Lonsdale, Phys. Rev. **73**, 1467 (1948).
[6] P. Pringsheim, *Fluorescence and Phosphorescence* (Interscience Publishers, Inc., New York, 1949), p. 648.
[7] R. Frerichs, J. Opt. Soc. Am. **40**, 219 (1950).
[8] G. P. Freeman and H. A. van der Velden, Physica, in preparation.

Angular Distribution of γ-Radiation from Polarized Nuclei

N. R. STEENBERG
Clarendon Laboratory, Parks Road, Oxford, England
(Received October 15, 1951)

THE intensity of γ-emission from polarized nuclei is expected to show a dependence on the angle between the direction of emission and the axis of polarization. Spiers[1] has given the dependence for a single emission for arbitrary degree of polarization, and considerably simpler formulas valid for low degrees of polarization. These latter have been extended by the present author to apply to a cascade of γ-rays from an oriented γ-emitting nucleus and to a cascade of γ-rays following a β-emission from an oriented γ-emitting nucleus. It is assumed that (a) the half lives of the intermediate states are sufficiently short, (b) only "pure" radiations are involved, i.e., no mixture of electric and magnetic radiation in the case of γ-emission, or, in the case of β-emission, no mixtures of j-values, where j is the total angular momentum of the β-neutrino system,[2] (c) the multipole order of any γ-transition $L=|J_i-J_f|$, where J_i = initial spin and J_f = final spin. A number of methods for polarizing nuclei are discussed by Bleaney.[3]

Let $w(M_0)$ be the mean population of states of the initial nucleus, of spin J_0 and z-component $\pm M_0$. For low degrees of polarization it can be expanded in powers of M_0.[2] Taking only the term in M_0^2, $w(M_0)$ is in all cases of the form

$$w(M_0)=\{1+\tfrac{1}{2}f[3M_0^2-J_0(J_0+1)]\}/(2J_0+1).$$

If the polarization is accomplished by a magnetic field, H, acting on the nuclear magnetic moment, μ,

$$f=\tfrac{1}{3}\{H\mu/kTJ\}^2$$

where k is Boltzmann's constant and T is the absolute temperature. If it is accomplished by a crystalline field, E, acting on the quadrupole moment,[4]

$$f=3eQ\ \mathrm{grad}E/[kT2J_0(J_0-1)],$$

in the notation of reference 4.

By using this approximation the following simple expressions for angular distribution can be obtained, applying equally to either electric or magnetic radiation. Investigation shows that they should be valid for $|f|\leqq 1/2J_0(J_0+1)$.

Case 1, a single 2^L-pole γ-emission, spin change $J_0\to J_1$:
The angular distribution, $I(\theta)$, is

$$I(\theta)=1-\tfrac{1}{2}f\alpha(L)h(J_0,J_1)(1-3\cos^2\theta),$$

where

$$h(J_0, J_1) = J_0(2J_0-1) \quad \text{if } J_0<J_1,$$
$$h(J_0, J_1) = (J_0+1)(2J_0+3) \quad \text{if } J_0>J_1,$$
$$\alpha(L) = [3-L(L+1)]/[(L+1)(2L+3)].$$

The asymmetry factor to this order of approximation is

$$\epsilon = [I(0)-I(\pi/2)]/I(\pi/2) = \tfrac{1}{2}f\alpha(L)h(J_0, J_1).$$

Note that for $L=1$ (dipole), $\alpha=1/10$, for $L=2$ (quadrupole), $\alpha=-1/7$, and for all higher multipoles $\alpha(L)<0$, so that in the case of magnetic polarization ($H\mu$) all emissions have an excess in the equatorial plane with the exception of dipole emission. In the case of polarization by an electric field this effect will depend on the sign of the quadrupole moment.

Case 2, two γ-rays in cascade, 2^{L_1}, 2^{L_2}-pole, $J_0 \xrightarrow{\gamma_1} J_1 \xrightarrow{\gamma_2} J_2$:

The angular distribution of γ_1 is calculated as for single emission. The angular distribution of γ_2 is

$$I^{(2)}(\theta) = 1-\tfrac{1}{2}fg(J_0, J_1)\alpha(L_2)h(J_1, J_2)(1-3\cos^2\theta),$$

where

$$g(J_0, J_1) = [J_0(2J_0-1)/J_1(2J_1-1)] \quad \text{if } J_0<J_1,$$
$$g(J_0, J_1) = [(J_0+1)(2J_0+3)/(J_1+1)(2J_1+3) \quad \text{if } J_0>J_1.$$

The observed angular distribution of both γ-rays will be $I(\theta) = \delta_1 I^{(1)}(\theta) + \delta_2 I^{(2)}(\theta)$, where δ_1 and δ_2 are the relative efficiencies of the detecting device for the two γ-rays. The observed asymmetry for both γ-rays is

$$\epsilon = \tfrac{1}{2}f[\{\delta_1/(\delta_1+\delta_2)\}\alpha(L_1)h(J_0, J_1) + \{\delta_2/(\delta_1+\delta_2)\}\alpha(L_2)g(J_0, J_1)h(J_1, J_2)].$$

Case 3, three γ-rays in cascade, 2^{L_1}, 2^{L_2}, 2^{L_3}-pole,

$J_0 \xrightarrow{\gamma_1} J_1 \xrightarrow{\gamma_2} J_2 \xrightarrow{\gamma_3} J_3$:

These formulas readily extend to three or more emissions. $I^{(1)}(\theta)$ and $I^{(2)}(\theta)$ are calculated without regard to γ_3 and

$$I^{(3)}(\theta) = 1-\tfrac{1}{2}fg(J_0, J_1)g(J_1, J_2)\alpha(L_3)h(J_2, J_3)(1-3\cos^2\theta).$$

Case 4, a single 2^L-pole γ-ray following a β-particle, spin change, $J_0 \xrightarrow{\beta} J_1 \xrightarrow{\gamma} J_2$:

The angular distribution of the γ-ray is

$$I(\theta) = 1-\tfrac{1}{2}fk(J_0, J_1)\alpha(L)h(J_1, J_2)(1-3\cos^2\theta)$$

where $k(J_0, J_1) = g(J_0, J_1)$ if $j = |J_0-J_1|$, j being the total angular momentum of the β-neutrino system, and

$$k(J_0, J_1) = \frac{(2J_0-1)}{(2J_1-1)}\left[\frac{(J_1+1)^2-j(J_1+4)}{J_1(J_1+1)}\right] \text{ if } j=J_1-J_0+1.$$

$$k(J_0, J_1) = \frac{(2J_0+3)}{(2J_1+3)}\left[\frac{J_1^2+j(J_1-3)}{J_1(J_1+1)}\right] \text{ if } j=J_0-J_1+1.$$

The asymmetry factor is $\epsilon = \tfrac{1}{2}fk(J_0, J_1)\alpha(L)h(J_1, J_2)$. Note that the only effect of the β-emission on the asymmetry is to modify it by the factor k.

Case 5, two γ-rays following a β-particle, 2^{L_1}, 2^{L_2}-pole, spin change $J_0 \xrightarrow{\beta} J_1 \xrightarrow{\gamma_1} J_2 \xrightarrow{\gamma_2} J_3$:

The angular distribution of γ_1, $I^{(1)}(\theta)$, is calculated without regard to γ_2, and the angular distribution of γ_2 is

$$I^{(2)}(\theta) = 1-\tfrac{1}{2}fk(J_0, J_1)g(J_1, J_2)\alpha(L_2)h(J_2, J_3)(1-3\cos^2\theta).$$

The asymmetry for the two observed γ-rays is

$$\epsilon = \tfrac{1}{2}fk(J_0, J_1)[(\delta_1/\delta_1+\delta_2)\alpha(L_1)h(J_1, J_2) + (\delta_1/\delta_1+\delta_2)\alpha(L_2)g(J_1, J_2)h(J_2, J_3)].$$

It should be noted that in all cases if $J_0=\frac{1}{2}$ or 0, all emissions have spherical symmetry; and if $J_1=\frac{1}{2}$ or 0, the second, third, and all subsequent emissions have spherical symmetry, and so forth.

It will be seen from the behavior of $\alpha(L)$ that high multipole orders favor large asymmetries and that asymmetries for transitions in which the spin decreases are larger than for those in which the spin increases.

The author is indebted to Dr. J. A. Spiers for advice on this problem.

[1] J. A. Spiers, National Research Council of Canada publication No. 1925.
[2] R. J. Blin-Stoyle and J. A. Spiers, Phys. Rev. **82**, 969 (1951).
[3] B. Bleaney, Proc. Phys. Soc. (London) **A64**, 315 (1951).
* The derivation is straightforward when M_S is a "good" quantum number. It can be shown that an expansion of this form is also valid in the more complex cases that can arise in paramagnetic salts.
[4] R. V. Pound, Phys. Rev. **79**, 685 (1950).

Remarks Concerning the Existence of the Foldy-Wouthuysen Transformation*

HARTLAND S. SNYDER
Brookhaven National Laboratory, Upton, Long Island, New York
(Received October 5, 1951)

FOLDY and Wouthuysen[1] have shown for a free Dirac particle that there exists a unitary transformation which removes all odd operators[2] from the Hamiltonian. In the case where there is an electromagnetic field present such a transformation was not found explicitly, and a power series expansion in inverse powers of the particle mass was given for the unitary transformation and for the transformed Hamiltonian. These authors raised questions concerning the convergence of these series but did not answer them.

It is the purpose of this note to show that a complete transformation of the Foldy-Wouthuysen type does not in general exist, and thus, in some circumstances these power series cannot converge. This is done by showing that the existence of the Foldy-Wouthuysen transformation is incompatible with known properties of the solution of Dirac's equation in the presence of external electromagnetic fields. To do this we consider the case where the electromagnetic field is present only in a finite portion of space-time. If we consider any solution of the Dirac equation which has only positive (negative) frequency parts at times before there was any electromagnetic field present, then at times after the electromagnetic field has disappeared the solution will have both positive and negative frequency parts. If the Foldy-Wouthuysen transformation exists, the original Dirac equation is decomposed into two sets of uncoupled two-component equations. For times earlier or later than the region in which the electromagnetic field is present, this transformation insures that one of these two sets of equations corresponds to positive, the other to negative frequency solutions of Dirac's equation. Since these two sets of equations are uncoupled, a solution of Dirac's equation which contains only positive (negative) frequency components before the time of interaction would contain only positive (negative) frequency components after the time of interaction. This is not true and one may therefore conclude that the complete Foldy-Wouthuysen transformation does not exist under circumstances where pair production by an external field is possible. This does not, of course, mean that a few terms of the power series of Foldy-Wouthuysen are not useful and valid for the description of the nonrelativistic aspects of the Dirac equation.

* Research carried out under contract with the AEC.
[1] L. L. Foldy and S. A. Wouthuysen, Phys. Rev. **78**, 29 (1950).
[2] For definition of odd and even operators see reference 1.

Penetrating Showers in Copper

P. C. BHATTACHARYA*
Division of Physics, National Research Council of Canada, Ottawa, Canada
(Received October 5, 1951)

THE penetrating showers produced by cosmic radiation in various materials have been studied extensively with Geiger-Müller counters. Since little or no work on showers produced in copper has been reported, measurements were taken

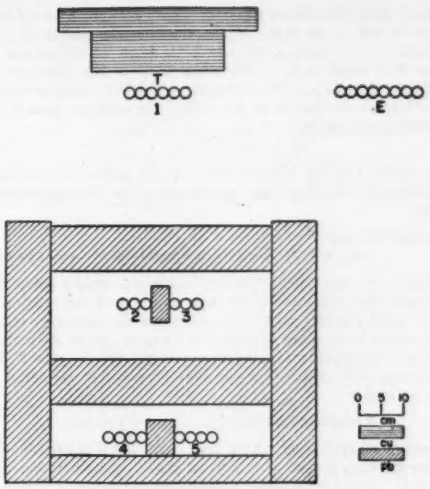

FIG. 1. Arrangement for observing penetrating showers.

with copper over a prolonged period, and the results are presented here.

The apparatus was set up at Ottawa (about 300 ft above sea level) and consisted of a fivefold coincidence set P containing five trays of counters as shown in Fig. 1. Trays 2 and 3 had 4-cm lead between them, and trays 4 and 5, 6-cm lead between them. Ten cm of lead was placed above each of these pairs of trays as shown, and these two groups of trays were surrounded on all sides by lead walls 10 cm thick. Thus the coincidence set P recorded showers of at least two particles of range greater than 20-cm lead. In addition to the set P, an unshielded tray of eight counters (E) was placed at a distance of 50 cm from tray 1 for detecting the presence of air showers and thus separating them from the showers generated in copper.

Besides observing the fivefold coincidences P, records were taken of the coincidences P accompanied by a discharge in any of the counters of the air shower tray E. Such coincidences are called (P, E). The anticoincidences $(P, -E)$, i.e., fivefold coincidences P which were not associated with a discharge of the air shower tray E, are classified as local penetrating showers or simply "local showers," while the coincidences (P, E) are classified as extensive penetrating showers or simply "extensive showers." This is in conformity with the nomenclature already established by previous workers.[1]

The counters were one inch in diameter and have an active length of 16 inches. Each counter group was connected to Neher-Harper type quenching devices. The resolving time of the circuits was of the order of 10^{-4} sec. The individual counter groups were tested once a week during the course of experiment.

TABLE I. Dependence of penetrating showers on the thickness of copper at sea level (Ottawa $\lambda = 56.8°$; $h \sim 300$ ft).

Thickness Inch	Thickness g/cm²	Time t (hr)	Local showers $(P, -E)$ n	Local showers $(P, -E)$ $\frac{n}{t} \pm \frac{\sqrt{n}}{t}$	Extensive showers (P, E) n	Extensive showers (P, E) $\frac{n}{t} \pm \frac{\sqrt{n}}{t}$
0	0	475	98	0.206 ±0.02	93	0.196 ±0.02
1	22.6	476	143	0.30 ±0.025	111	0.233 ±0.02
2½	56.5	475	172	0.362 ±0.03	124	0.261 ±0.02
5	113	505	194	0.384 ±0.03	119	0.235 ±0.02
7½	170	423	150	0.354 ±0.03	91	0.215 ±0.02
10	226	458	149	0.325 ±0.027	95	0.207 ±0.02
12½	282	408	102	0.25 ±0.025	76	0.186 ±0.02

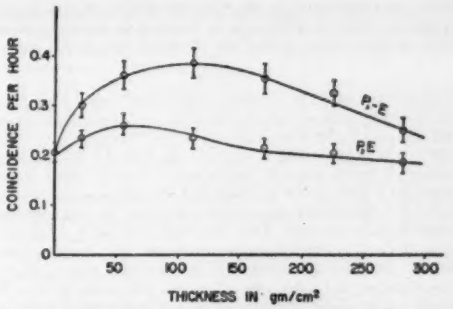

FIG. 2. Transition curves in copper for (a) local penetrating showers (curve $P, -E$), (b) extensive penetrating showers (curve P, E).

The copper absorbers were in the form of plates 6 in.×24 in. ×½ in. and were placed at T close above the top tray 1. Absorbers were placed in a "cyclic manner," changing to a different thickness of copper after every two or three days so as to avoid any instrumental selectivity.

The results of about five month's continuous observation are given in Table I and these are plotted in Fig. 2.

The transition curve for extensive showers (curve P, E) gives an indication of a cascade type maximum showing that in air showers electrons are present along with groups of penetrating particles and that these electrons are responsible for the slight increase in shower intensity. The position of this maximum is near 6- to 7-cm copper corresponding to 4 cascade units in agreement with the result obtained by George and Jason[1] in the case of lead.

The curve for local showers (curve $P, -E$) shows a marked transition effect with signs of a saturation in the vicinity of 80 to 120 g/cm² of copper. The primary radiation producing such showers appears to have a collision length of this order, which corresponds approximately to the geometrical cross section of copper nuclei.

In regard to the number of primary particles responsible for local showers it was found further that there was about one such primary for every 6000 mesons crossing the absorber within the cone formed by the extreme counters, *viz.*, by tray 1 and trays 4 and 5 put together.

The probabilities of knock-on showers were determined by the method adopted by Janossy[2] and found to be 0.008 per hour, a very small contribution compared to the observed shower rate.

In conclusion, the author expresses his sincere thanks to Dr. D. C. Rose for the interest he has taken in this work.

* On leave from the University of Calcutta, India. Holder of a National Research Council postdoctorate fellowship.

[1] E. P. George and A. C. Jason, Proc. Phys. Soc. (London) **A63**, 1081 (1950).

[2] L. Janossy, Proc. Roy. Soc. (London) **A179**, 361 (1942).

High Energy Nucleon-Nucleon Scattering*

G. BREIT
Yale University, New Haven, Connecticut
(Received October 15, 1951)

ATTEMPTS[1] to account for high energy nucleon-nucleon scattering by means of a symmetric hamiltonian have met with difficulty. In the Case-Pais work the sign of the spin-orbit term is opposite to that convenient for the shell model. In Jastrow's calculations[1] the connection between the mass of the π-meson and the apparent range of force is hard to maintain. Without a hard core, low energy proton-proton scattering favors a meson mass of $\sim 330\ m$. With a hard core the agreement with the measured mass of the π-meson is even worse. Approximate mag-

nitudes can be estimated by observing that if the scattering length approaches infinity conditions of equivalence for scattering cross section at zero energy and for rate of change with energy give

$$r_0=r_0'+r_1',$$

where r_0 is the radius of the square well without core, while r_1' is the core radius and r_0' is the outer radius of the modified square well. If $r_0=2.7\times10^{-13}$ cm and $r_1'=1\times10^{-13}$ cm, then $r_0'=1.7\times10^{-13}$ cm. A shortening of range in the ratio 1.7/2.7 gives an increase of meson mass by the factors ~2.7/1.7, which corresponds to a mass ~500 m. Unpublished calculations of M. H. Hull and A. Herschman support the conclusion that the apparent meson mass is too high. They also find that the p-p and p-n interactions are in slightly poorer agreement with the core than without. An exact agreement with the measured mass is hardly to be expected, and reasons for differences of the order of 10 or 20 percent can be given.[2] The connection with meson theory becomes forced, however, if the disagreement is by a factor of about 2.

The approximate independence of the p-p scattering cross section on the scattering angle is usually made to appear as a result of the superposition of angle dependent effects. For a few Mev bombarding energy it is very probable that one deals with pure S-scattering. No definite effects have been observed which would indicate the setting in of p or d waves between 0.2 Mev and 30 Mev. There is an uninvestigated gap of energies between 30 Mev and 75 Mev. From here on[3] the scattering is again spherically symmetric. The standard reason for assuming that at the higher energies superposition of angle dependent effects takes place is that the cross section is too large for pure S-scattering.

There appears to be no compelling reason for supposing that at energies comparable with the rest mass energy of the π-meson the collision process does not change the nature of the protons. If, after collision, the protons are not identical, they can exist in ^3S as well as ^1S states. A statistical factor 4 is gained and the explanation of angular independence can again be reduced to dominance of S-scattering. The changed state of the proton need not be one of different mass. Any change, even that of an otherwise unobservable internal coordinate, would be satisfactory. It would be of interest to see whether scattered protons are identical with other protons in all respects. Effects depending on symmetry properties of the wave-function would be most decisive. In principle there is the possibility of rescattering. Polarization effects would have to be separated from effects sought for in such tests.

If collisions produce isomeric states it would be natural to suppose that the formation occurs through an intermediate state of the two-nucleon system, requiring for its formation a relative kinetic energy of the order of the meson mass energy. The observed flatness of the cross-section energy curve for p-p scattering would be the result of compensation of the decrease in scattering of identical protons and an increase in scattering of nonidentical ones. The view discussed above has been presented in part at the Chicago International Conference on Nuclear Physics and Fundamental Particles.

* Assisted by the joint program of the ONR and AEC.
[1] Chamberlain, Segrè, and Wiegand, Phys. Rev. **83**, 923 (1951). This paper contains a discussion of theoretical work and references to articles quoted in present note.
[2] G. Breit and M. C. Yovits, Phys. Rev. **81**, 416 (1951).
[3] Birge, Kruse, and Ramsey, Phys. Rev. **83**, 274 (1951).

Limitations on Mass Changes of Scattered Nucleons*

G. Breit and H. M. Jones
Yale University, New Haven, Connecticut
(Received October 15, 1951)

In connection with the preceding note[1] it is of interest to determine the degree to which scattering experiments performed by the coincidence method exclude changes in mass of protons on scattering. The collision of two particles of equal mass M is considered. After the collision the mass of one of the particles is taken to be M and of the other M_1. In the reference system of zero momentum (rest system) the scattering angle for the particle of mass M is taken to be θ. The angle between the directions of motion of the two particles when observed in the reference system in which one of them is at rest before the collision (laboratory system) is denoted by

$$\chi=(\pi/2)-\delta.$$

For small values of $\Delta M/M=(M_1-M)/M$ and small velocities, conservation of energy and momentum gives the approximate value

$$\tan\delta=(\beta^2/2)\sin\theta+\cdots$$
$$+(\Delta M/2M)(1-\beta^2)^{\frac{1}{2}}[(\beta^{-2}/\sin\theta)+\cot\theta-\tfrac{1}{2}\sin\theta]+\cdots,$$

where $\beta=v/c$ and v is the velocity in the rest system before the collision. The first term is an approximation to the relativistic effect which makes χ differ from $\pi/2$ even if the masses are equal. The second term shows the effect of changing one of the masses. The incident energy in the laboratory is $2Mc^2\beta^2/(1-\beta^2)=T$. Introducing $\epsilon=T/(2Mc^2)$, one has $\beta^2=\epsilon/(1+\epsilon)$ and the effect of ΔM on $\tan\delta$ is

$$\delta'=[\Delta M/(2M\epsilon\sin\theta)]\{1+\epsilon[\cos\theta+\tfrac{1}{2}\cos^3\theta]\}.$$

Terms of relative order ϵ have been kept. For $T=300$ Mev the factor in braces is close to 1, and one has the approximation

$$\delta'=c^2\Delta M/(T\sin\theta).$$

If δ' is allowed to be 1°, then at 100-Mev bombarding energy one may suppose $c^2\Delta M=0.87$ Mev; while at 300-Mev, bombarding energy $c^2\Delta M=\pm2.6$ Mev would not be excluded for $\theta=30°$. This scattering angle corresponds to $\Theta=15°$. It is not clear from the publications on high energy scattering whether the relativistic angle relation is obeyed to better than 1°. The more significant tests are those having to do with small scattering angles. Presumably these are the least favorable for good geometry. Tests at $\Theta\cong45°$, $\theta=90°$ to 1° would limit the mass within $\sim\pm1.7$ Mev for 100-Mev incident energy. In either case the change in mass is not so small as to discourage tests.

* Assisted by the joint program of the ONR and AEC.
[1] G. Breit, Phys. Rev. **84**, 1053 (1951).

Thermal Expansion and Specific Heat of Tungsten Oxide at High Temperatures

Shozo Sawada, Rinjiro Ando, and Shoichiro Nomura
Institute of Science and Technology, University of Tokyo, Tokyo, Japan
(Received October 8, 1951)

We have previously reported[1] that tungsten oxide has ferroelectric properties and that its Curie point seems to be situated at about 710°C; these results followed from our observations of many of its properties, i.e., domain structure, hysteresis loop, permitivity, thermal expansion, specific heat, etc. Afterwards it was ascertained, by x-ray analysis,[2] that the crystal structure changes from orthorhombic to tetragonal ($a=b$) at 700~750°C. In addition to our previous investigations, we shall now report briefly the quantitative results of our observations of thermal expansion and specific heat above room temperature.

The thermal expansion was measured by a dilatometer of the rotating-rod type with a sensibility of $\Delta l/l=4\times10^{-6}$. Figure 1 shows the linear thermal expansion coefficient, measured by heating at a rate of about 2°C/min. A rather gradual expansion is observed at 330°C and a remarkable contraction at 755°C, the latter amounting to about $\Delta l/l=1.2\times10^{-2}$. On cooling, a temperature hysteresis exists for one anomaly but not for the other; that is, the anomalies of the thermal expansion coefficient in the cooling process are observed at 725°C and 330°C, respectively. We measured the specific heat by a vacuum calorimeter of the same type as the ones used by Bantle[3] for KH_2PO_4

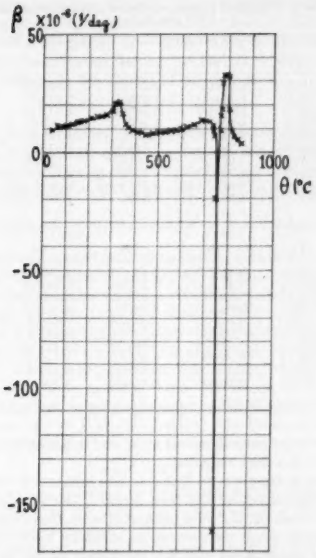

FIG. 1. Linear thermal expansion coefficient *vs* temperature.

and by Blattner *et al.*[4] for $BaTiO_3$. The specific heat was found to be normal near 330°C, and its behavior near 740°C, measured by heating at a rate of about 1°C/min, is shown in Fig. 2. The amount of anomalous heat capacity near 740°C is about 450 cal/mol, the corresponding entropy change being about 0.2 R, and the peak value is observed at 728°C. This temperature is lower than the one at which the thermal expansion coefficient shows a negative peak. Although a part of this discrepancy will be eliminated by the $c_p - c_v$ correction, the residual part may be caused by defects of our apparatus. Previously the anomalies were observed at a lower temperature, i.e., at 710°C, probably owing to the impurity of our previous sample.

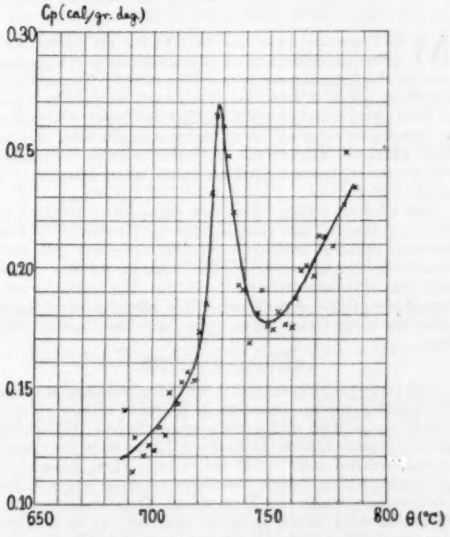

FIG. 2. Isobaric specific heat *vs* temperature.

Although the apparent behavior of the 740°C transition of tungsten oxide thus resembles closely that of the 120°C transition of barium titanate, its essential nature will be revealed only by further thorough investigations. Our observation of an anomaly in the thermal expansion near 330°C, on the other hand, agrees with an anomaly in the dc resistance observed by Nagasawa and Fukui,[5] but it seems yet to be doubtful whether this temperature is a transition point which is closely related to the ferroelectricity of the substance.

The authors wish to thank Professor T. Muto for his kind criticism and advice.

[1] Sawada, Ando, and Nomura, Phys. Rev. **82**, 952 (1951); S. Sawada and R. Ando, Rep. Inst. Sci. and Tech. Univ. Tokyo **4**, 228 (1950).
[2] R. Ueda and T. Ichinokawa, Phys. Rev. **82**, 563 (1951).
[3] W. Bantle, Helv. Phys. Acta **15**, 382 (1942).
[4] Blattner, Kaenzig, and Merz, Helv. Phys. Acta **22**, 35 (1949).
[5] S. Nagasawa and S. Fukui, Busseiron-kenkyu No. **31**, 90 (1950).

Isotope Shifts in Erbium

L. WILETS* AND L. C. BRADLEY, III
Palmer Physical Laboratory, Princeton University, Princeton, New Jersey
(Received October 8, 1951)

AN investigation of the isotope shifts in erbium ($Z=68$) is being conducted in this laboratory using a Fabry-Perot interferometer for the necessary resolving power. The oxide is excited in a hollow cathode discharge cooled with liquid nitrogen, similar to the type described by Arroe and Mack.[1]

Three components of the isotope shift are clearly resolved in more than fifty lines in the region between 4250A and 6000A. The three components can be unambiguously attributed to the isotopes Er^{166}, Er^{168}, and Er^{170} on the basis of the intensity of the components compared with the relative abundances of the isotopes. Natural erbium contains six isotopes: Er^{162} (0.136 percent), Er^{164} (1.56 percent), Er^{166} (33.4 percent), Er^{167} (22.9 percent), Er^{168} (27.1 percent), and Er^{170} (14.9 percent). The odd isotope, Er^{167}, is reported[2] to have a nuclear spin of 7/2. Despite its relatively large abundance, the components caused by the odd isotope are not resolved, and this may be attributed to the large number of components into which the 167 component is split as a result of its magnetic hyperfine structure. In only a few lines do the intensities deviate from the expected values sufficiently to be attributed to the presence of the odd isotope.

In a few overexposed lines a fourth component has been detected; on the basis of intensity and position it could be attributed to Er^{164}, although it is also possible that it is the result of Er^{167}. Measurements have not yet been completed on this component. Table I shows the results of measurements on 11 lines using four different spacer sizes. The individual measurements are probably accurate to within ± 0.0015 cm^{-1}, and the mean is accurate to within ± 0.0010 cm^{-1}. These limits do not include the possibility of disturbing effects as a result of the odd isotope. The ratio $(\nu_{168}-\nu_{170})/(\nu_{166}-\nu_{168})$ is in most cases quite close to unity, and as far as the measurements have proceeded, there is no evidence that the ratio is other than unity.

The shifts have been taken as positive where the heaviest isotope has the smallest wave number, and negative where the converse is true. To the best of our knowledge, the occurrence of both positive and negative shifts in rare earth spectra has not been reported before. According to the nuclear volume picture of isotope shifts,[3] s-electrons are more tightly bound in light isotopes than in heavy isotopes. Since electrons with greater orbital angular momentum (except $p_{\frac{1}{2}}$) are not affected appreciably by the nuclear charge distribution, observable isotope shifts appear only in transitions between levels which have different numbers of

TABLE I. Isotope splittings in erbium, in wave-number units. $\Delta\nu_{mean}$ are the mean values of measurements using four different spacer sizes. The upper numbers are $\nu_{168}-\nu_{170}$ and the lower numbers are $\nu_{168}-\nu_{166}$. R gives the ratio of the splittings.

λ, A	$\Delta\nu_{mean}$	R	λ, A	$\Delta\nu_{mean}$	R
4729	0.046$_2$	1.00	4496	0.044$_2$	0.96
	0.046$_2$			0.046$_2$	
4722	−0.050$_6$	0.99	4426	−0.047$_2$	0.94
	−0.051$_2$			−0.050$_6$	
4673	−0.049$_3$	1.06	4424	−0.043$_2$	1.08
	−0.046$_9$			−0.040$_4$	
4606	−0.045$_8$	1.00	4409	−0.045$_1$	0.98
	−0.045$_8$			−0.046$_7$	
4552	0.045$_9$	0.96	4331	−0.053$_3$	1.02
	0.047$_8$			−0.052$_8$	
4531	0.047$_5$	1.07			
	0.044$_4$				

TABLE I. Threshold values of internal conversion coefficients for the K-shell.

Z	α_1	α_2	α_3	α_4	α_5
10	7.329(3)	8.184(5)	4.281(7)	1.340(9)	2.867(10)
20	4.510(2)	1.251(4)	1.596(3)	1.232(6)	6.459(6)
30	8.720(1)	1.030(3)	6.060(3)	1.922(4)	4.338(4)
40	2.603(1)	1.606(2)	5.600(2)	9.300(2)	1.123(3)
50	1.085(1)	3.741(1)	8.317(1)	8.112(1)	5.926(1)
60	5.190(0)	1.081(1)	1.623(1)	1.035(1)	4.834(0)
70	2.713(0)	3.604(0)	3.721(0)	1.598(0)	5.479(−1)
80	1.636(0)	1.334(0)	9.516(−1)	3.152(−1)	8.995(−2)
88	9.989(−1)	6.622(−1)	3.551(−1)	1.094(−1)	2.977(−2)
96	6.691(−1)	3.661(−1)	1.848(−1)	4.991(−2)	8.452(−3)

Z	β_1	β_2	β_3	β_4	β_5
10	4.222(2)	2.219(8)	3.472(7)	2.587(9)	1.124(11)
20	1.087(2)	1.415(4)	5.471(5)	9.874(6)	1.084(8)
30	5.075(1)	2.893(3)	4.867(4)	3.919(5)	1.841(6)
40	3.072(1)	8.942(2)	8.830(3)	3.892(4)	1.003(5)
50	2.123(1)	3.881(2)	2.374(3)	6.466(3)	1.032(4)
60	1.737(1)	2.033(2)	8.215(2)	1.484(3)	1.626(3)
70	1.548(1)	1.225(2)	3.393(2)	4.257(2)	3.158(2)
80	1.528(1)	8.304(1)	1.605(2)	1.436(2)	7.637(1)
88	1.764(1)	6.582(1)	9.549(1)	6.576(1)	2.714(1)
96	2.313(1)	5.608(1)	6.060(1)	3.394(1)	1.034(1)

s-electrons. For instance, the usual change of a p-electron to an s-electron would give a positive shift. No analysis is available for erbium, but the isotope structure may give useful clues. The hollow cathode source usually enhances the ionized spectra, and since the shifts are of the magnitude to be expected from the second spectrum, it is presumed that the lines showing the shifts are caused by Er II. The positive isotope shifts probably arise from the electronic transitions $4f^{12}6p$ to $4f^{12}6s$ and $4f^{11}6s6p$ to $4f^{11}6s^2$, and the negative shifts probably arise from the two-electron transition $4f^{11}6s6p$ to $4f^{11}5d^2$. The configurations $4f^{12}6s$ and $4f^{11}6s6p$ should give similar splittings; the configuration $4f^{11}6s^2$ would give splittings twice as great if it were not that the mutual screening of the $6s$-electrons tends to reduce the effect.

The work is being continued, lines are being measured in other regions of the spectrum, and the complete results will be reported later.

The authors wish to express their gratitude to Professor A. G. Shenstone for many helpful discussions and for his constant encouragement, to Professor H. N. Russell for a stimulating discussion of the rare earth spectra, and to Professor K. Murakawa for suggesting the problem.

* AEC Predoctoral Fellow.
[1] O. H. Arroe and J. A. Mack, J. Opt. Soc. Am. **40**, 6 (1950).
[2] B. Bleaney and H. E. D. Scovil, Proc. Phys. Soc. (London) **A64**, 204 (1951).
[3] J. E. Rosenthal and G. Breit, Phys. Rev. **51**, 459 (1932); G. Breit, Phys. Rev. **42**, 348 (1932).

Threshold Values of Internal Conversion Coefficients for the K-Shell

B. I. SPINRAD AND L. B. KELLER
Argonne National Laboratory, Chicago, Illinois
(Received October 18, 1951)

RECENT computations of the internal conversion coefficients for the K-shell have been reported for various Z and for k (γ-ray energy) greater than 0.3–0.5 electron masses.[1] The extrapolation of these results to lower energies is uncertain for two reasons: first, the mathematical formulation of the problem is of such complexity that no simple extrapolation rule can be used; second, the numbers are computed for unscreened wave functions.

In an attempt to resolve the mathematical difficulties, computations have been made on the threshold values of the conversion coefficients. These computations were performed by taking the limiting values of the formulas of reference 1, as p, the electron momentum, approaches zero positively. Under these conditions many simplifications arise, and it is possible to compute the results on a desk machine.

The results are given in Table I. The notation is that of reference 1. Since screening has been ignored, the threshold energies for which these results were computed were those obtained from the relativistic single-electron model, given by $k=1-(1-[\alpha Z]^2)^{\frac{1}{2}}$. Figures in parentheses indicate the power of 10 by which the number must be multiplied.

[1] Rose, Goertzel, Spinrad, Harr, and Strong, Phys. Rev. **83**, 79 (1951).

Primary Specific Ionization of Cosmic Rays in Hydrogen*

M. H. SHAMOS, *Washington Square College, New York University, New York, New York*
AND
I. HUDES, *Brooklyn College, Brooklyn, New York*
(Received October 17, 1951)

MANY attempts have been made to test the dependence of primary specific ionization upon momentum for high energy particles. Such measurements have been made by Kunze,[1] Corson and Brode,[2] J. G. Wilson,[3] Sen Gupta,[4] and Hazen[5,6] by the use of cloud chamber techniques. Except for Sen Gupta, who reported an increase for electrons but not for mesons, the other observers were unable to support the relativistic increase in ionization beyond the minimum as predicted in the theory of collision loss given by Bethe.[7]

Low efficiency counters have been employed by Danforth and Ramsey,[8] Cosyns,[9] and most recently by Hereford.[10] Of these, Hereford obtained results in substantial agreement with theory upon comparing the primary specific ionization of 1-Mev electrons with that of the sea-level cosmic radiation. This technique makes use of the unique dependence of the efficiency of a counter, operating in the Geiger region, upon the primary specific ionization,

$$\text{efficiency}=1-\epsilon^{-JLP/78}.$$

The present experiment makes use of this technique to compare the primary specific ionization in hydrogen of two groups of cosmic-ray particles of different average momenta. The efficiency of a low pressure (2.0 cm Hg) hydrogen-filled counter was measured at sea level and under ~140 feet of rock. These measurements were made with a fourfold coincidence telescope which included the hydrogen counter and 20 cm of lead. The average momentum of the sea-level cosmic radiation (presumed to be principally μ-mesons because of the Pb filter), computed on the basis of the

combined data of Wilson, Blackett, and Jones,[11] is ~3500 Mev/c, while the average momentum under 140 feet of rock (effective thickness ~13,800 g/cm²) is ~48,000 Mev/c. The ratio of the primary specific ionization underground (J_{140}) to that at sea level (J_0), computed from the measured efficiencies, is

$$(J_{140}/J_0)_{\text{exp}}=1.17\pm0.03,$$

where the error indicated is the standard statistical error. The use of the ratio of the specific ionizations avoids the need for determining the average path length (L) through the counter.

The theoretical values of J were determined from the expression,

$$\langle J\rangle=\int_{p_{\min}}^{\infty} J(p)\cdot S(p)dp \Big/ \int_{p_{\min}}^{\infty} S(p)dp,$$

where $J(p)$ is obtained from Bethe's theory, $S(p)$ is the momentum distribution of the mesons, and $\langle J\rangle$ is consequently the expected average ionization. The sea-level momentum distribution $S_0(p)$ was obtained directly from the data of Wilson, Blackett, and Jones,[11] while the underground spectrum $S_{140}(p)$ was computed from the sea-level data by taking into account the absorption in the rock. The integrations were performed numerically, and $p_{\min}$ represents the cutoff resulting from the 20 cm of Pb in the telescope. This was selected to be at ~400 Mev/c, which is at the minimum of the $J(p)$ distribution. The theoretical value of the ratio so obtained is

$$(J_{140}/J_0)_{\text{th}}=1.20$$

if the underground spectrum is determined on the basis of Bethe-Bloch absorption in the rock, and becomes 1.18 if the Halpern-Hall[12] correction is applied.

The agreement with theory obtained here is in direct contrast with the results obtained by Hazen,[5] who measured the primary ionization at sea level and under 100 feet of rock with the aid of a cloud chamber. It is our feeling that the cloud chamber technique has inherent limitations which prevent the accurate measurement of the primary ionization produced by extremely high energy particles.

A more detailed account of this experiment is in preparation and will be submitted for publication shortly.

We are greatly indebted to the New York City Board of Transportation for permission to conduct the underground measurements in one of the subway stations, and for the facilities provided us while working there.

The assistance of the Research Corporation in the form of a grant is gratefully acknowledged.

* Based in part on work done under contract with the ONR.
[1] P. Kunze, Z. Physik **83**, 1 (1933).
[2] D. R. Corson and R. B. Brode, Phys. Rev. **53**, 773 (1938).
[3] J. G. Wilson, Proc. Roy. Soc. (London) **A172**, 517 (1939).
[4] R. L. Sen Gupta, Nature **146**, 65 (1940).
[5] W. E. Hazen, Phys. Rev. **65**, 259 (1944).
[6] W. E. Hazen, Phys. Rev. **67**, 269 (1945).
[7] H. A. Bethe, Handbuch der Physik (Verlag. J. Springer, Berlin) **24**, 522 (1933).
[8] W. E. Danforth and W. E. Ramsey, Phys. Rev. **49**, 854 (1936).
[9] M. G. E. Cosyns, Nature **139**, 802 (1937).
[10] F. L. Hereford, Phys. Rev. **72**, 982 (1947).
[11] J. G. Wilson, Nature **158**, 414 (1946).
[12] O. Halpern and H. Hall, Phys. Rev. **73**, 477 (1948).

High Energy Elastic Proton-Deuteron Scattering

GEOFFREY F. CHEW
Department of Physics, University of Illinois, Urbana, California
(Received October 17, 1951)

EXPERIMENTAL results on elastic p-d scattering[1,2] at high energies have recently been reported. Since data on n-p and p-p scattering at corresponding energies are also available, the impulse approximation[3,4] may be applied to the analysis of the three-body experiments.

The impulse approximation is most conveniently expressed in terms of the distribution of momentum transfers, κ:

$$d\sigma_{pd}{}^{el}/d\kappa^3=\tfrac{1}{4}\left|\,|r_{np}{}^0+r_{pp}{}^0|^2+\tfrac{3}{4}\,|r_{np}{}'+r_{pp}{}'|^2\right|S(\kappa). \quad (1)$$

$S(\kappa)$ is the "sticking" factor defined and evaluated in reference 4. The quantities, r, are the amplitudes for scattering the proton without spin flip ($r_{np}{}^0$ and $r_{pp}{}^0$) and with spin flip ($r_{np}{}'$ and $r_{pp}{}'$) of the target particle. The normalization of these amplitudes is chosen so that the two-body scattering cross sections are

$$d\sigma_{np}/d\kappa^3=|r_{np}{}^0|^2+|r_{np}{}'|^2, \quad d\sigma_{pp}/d\kappa^3=|r_{pp}{}^0|^2+|r_{pp}{}'|^2. \quad (2)$$

Note that the relation between κ and the center-of-mass angle in the two-body problem is $\kappa=k_0\sin(\theta_2/2)$ if k_0 is the momentum of the incident proton when the target particle is at rest. In the three-body scattering, the connection between κ and the center-of-mass angle is $\kappa=(4/3)k_0\sin(\theta_3/2)$. Thus $d\cos\theta_3/d\cos\theta_2=16/9$.

Formula (1) is general enough to include any kind of nuclear forces. In the special case of no coupling between spin and orbital angular momentum, the quantities r^0 and r' are connected to the familiar singlet and triplet amplitudes, r^s and r^t, according to

$$r^0=\tfrac{1}{4}(3r^t+r^s), \quad r'=\tfrac{1}{4}(r^t-r^s)\sigma_p,$$

where σ_p is the spin of the incident proton.

As discussed in reference 4, a knowledge of the two-body cross sections [Eq. (2)] is insufficient to evaluate formula (1) because the relative phases of the n-p and p-p amplitudes are needed, as well as the relative magnitudes of spin flip and nonspin flip amplitudes. These quantities depend on the detailed nature of the forces, which is still unknown. For purposes of illustration, however, we shall here evaluate (1) by making a very crude assumption. We assume S scattering only and no spin dependence except that forced by the Pauli principle in the p-p system. Even though the true picture is much more complicated than this, we may expect to find the right order of magnitude so long as the experimental n-p and p-p cross sections are used to fix the normalization. Also the angular distribution ought not to be far from the truth, since the most rapidly varying function in (1) is $S(\kappa)$, which is independent of the force assumption.

The preceding postulate leads to the following formula for the angular distribution in the center-of-mass system:

$$d\sigma_{pd}{}^{el}/d\omega_3=(16/9)\{d\sigma_{np}/d\omega_1+\tfrac{1}{2}d\sigma_{pp}/d\omega_2 +[(d\sigma_{np}/d\omega_1)(d\sigma_{pp}/d\omega_2)]^{\frac{1}{2}}\cos\Delta\}S(\theta_3), \quad (3)$$

where $d\omega_3=2\pi d\cos\theta_3$, $d\omega_2=2\pi d\cos\theta_2$, and Δ is the difference between n-p and p-p phase shifts. Since only S scattering has been assumed, we must take $d\sigma_{np}/d\omega_2$ and $d\sigma_{pp}/d\omega_2$ to be constants at the energy in question. This may seem unreasonable for n-p scattering, but actually the steepest part of the experimental n-p angular distribution is concentrated in a small solid angle near $\theta_2=180°$. For such large momentum transfers formula (1) is not valid in any case because the "pick-up" mechanism[5] becomes important.

Formula (3) has been evaluated for proton energies of 95 and 240 Mev, corresponding to the Berkeley[2] and Rochester[1] experiments, respectively. Table I gives the values of $d\sigma_{np}/d\omega_2$ and $d\sigma_{pp}/d\omega_2$ which were employed. These numbers are rough averages based on Berkeley measurements.[6] We have taken $\Delta=0$, although strictly speaking, this condition would imply $d\sigma_{np}/d\omega_2=d\sigma_{pp}/d\omega_2$, which is not quite consistent with Table I.

In Fig. 1 our results are compared with experiment. The agreement is about as good as expected. The fact that our theory is consistently too high except at very small angles no doubt means that the phase difference between n-p and p-p amplitudes is not negligible. (The small angle ($<20°$) theoretical prediction would be larger if we allowed $d\sigma_{np}/d\omega_2$ to increase there, as it actually does experimentally,[6] to twice the average value.) With a more realistic assumption for the fundamental two-particle

TABLE I. Differential n-p and p-p scattering cross sections.

Proton energy (Mev)	$d\sigma_{np}/d\omega_2$(mb/ster)	$d\sigma_{pp}/d\omega_2$(mb/ster)
95	5	4
240	3	4

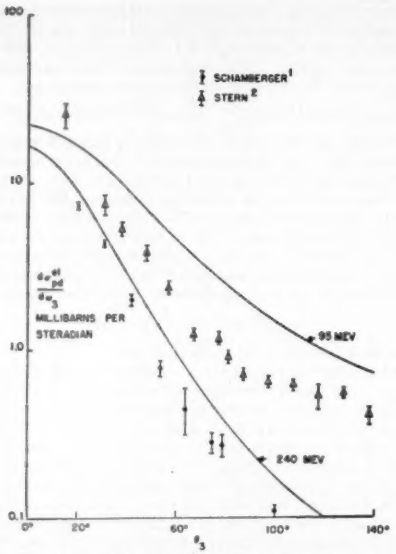

FIG. 1. Comparison of theory with experiment. The solid curve represents formula (3), with the values of $d\sigma_{np}/d\omega_3$ and $d\sigma_{pp}/d\omega_3$ listed in Table I.

interactions, it should be possible to improve the theoretical calculation, at least for angles less than about 100°. A theory of the large angle scattering ("pick-up"), however, will require the solution of a real three-body problem, since these collisions have no analog in two-body processes. (The "pick-up" theory presented in reference 5 is quantitatively inadequate.)

[1] R. D. Schamberger, Phys. Rev. **83**, 1276 (1951).
[2] Martin O. Stern, University of California Radiation Laboratory Report No. 1440 (1951) (to be published).
[3] G. F. Chew, Phys. Rev. **80**, 196 (1950).
[4] G. F. Chew, Phys. Rev. **84**, 710 (1951).
[5] G. F. Chew and M. L. Goldberger, Phys. Rev. **77**, 470 (1950).
[6] Kelly, Leith, Segrè, and Wiegand, Phys. Rev. **79**, 96 (1950); Chamberlain, Segrè, and Wiegand, Phys. Rev. **83**, 923 (1951).

Scattering of Fast Neutrons from O^{16}

E. BALDINGER, P. HUBER, AND W. G. PROCTOR*
Physikalische Anstalt der Universität Basel, Basel, Switzerland
(Received September 24, 1951)

MEASUREMENTS of the total neutron cross section σ_T of O^{16} between 2.0 and 4.0 Mev[1–4] have shown a "negative" resonance[5] near 2.35 Mev, and a broad rise at 3.5 Mev. Zünti and Ricamo[3] have suggested that the former is to be associated with an $S_{\frac{1}{2}}$ level of the compound state because the potential scattering could be expected to be about $-90°$ at this energy, and Freier, Fulk, Lampi, and Williams[1] have suggested that the latter may be caused by two broad overlapping resonances. We have measured the differential cross section in this energy region and have found, by trial and error, a scattered wave phase behavior, illustrated in Fig. 1, which satisfactorily predicts the total and differential cross sections at each energy and substantiates the proposals of Zünti and Ricamo[3] and Freier *et al.*[1]

The differential cross sections were measured using an ionization chamber containing oxygen gas. The spectrum of energy of the collision-recoil oxygen nuclei can be easily shown[6,7] to be linearly related to the distribution in θ of the scattered neutrons, i.e., the differential cross section $\sigma(\theta)$. This method has been used for the study of $\sigma(\theta)$ in a number of light gases.[6,8,9] Monochromatic D, d neutrons from a thin heavy ice target were used, and the data were recorded by a 19-channel automatic pulse spectrum analyzer.[10]

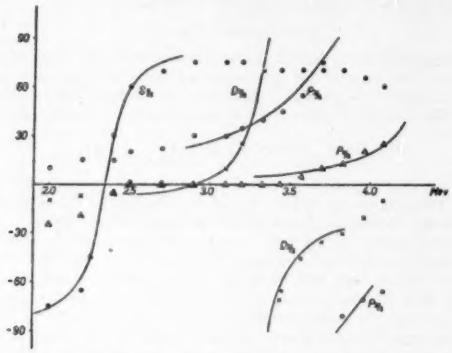

FIG. 1. Phase behavior which describes the scattering between 2 and 4 Mev.

The data were analyzed using the expressions for scattering from potentials having a spin-orbit coupling term.[11,12] The phases $\eta_{l,J}$ of the scattered waves described in the conventional notation by the quantum numbers l and J may be written[5]

$$\eta_{l,J}=\tan^{-1}\frac{\Gamma_{l,J}/2}{E_{l,J}-E}+\phi_{l,J} \qquad (1)$$

in the close neighborhood of $E_{l,J}$, where $\Gamma_{l,J}$ and $\phi_{l,J}$ may be taken as constant. The curves drawn through the points in Fig. 1 are the fits of this equation, and the parameters, as defined by Eq. (1), are given in Table I.

TABLE I. Level identification for O^{17} in the laboratory system.

Level	E in Mev	Γ in kev	Potential phase, ϕ
$P_{\frac{1}{2}}$	1.9	...	...
$S_{\frac{1}{2}}$	2.35	180	$-90°$
$D_{\frac{3}{2}}$	3.33	220	$-15°$
$P_{\frac{3}{2}}$	3.80	800	0°
$P_{\frac{1}{2}}$	4.40	280	0°

The observed variation with energy of the so-called anisotropy, that is, the ratio of 180°- to 90°-scattering, described in an earlier report upon this work,[8] as well as other features of the differential and total cross section, are well predicted by the phase behavior shown. From examination of Fig. 1 and σ_T, it is clear that resonances in the cross section near 1.9 and 4.4 Mev, although outside the region studied, are both caused by $P_{\frac{1}{2}}$ levels.

Details of this work will be reported in the *Helvetica Physica Acta*. The authors are grateful to Dr. R. K. Adair and Dr. W. Zünti and Dr. R. Ricamo for sending them their results on σ_T in advance of publication.

* Now at Stanford University, Stanford, California.
[1] Freier, Fulk, Lampi, and Williams, Phys. Rev. **78**, 508 (1950).
[2] Ricamo, Zünti, Baldinger, and Huber, Helv. Phys. Acta **XXIII**, 508 (1950).
[3] W. Zünti and R. Ricamo (private communication).
[4] R. K. Adair (private communication).
[5] Feshbach, Peaslee, and Weisskopf, Phys. Rev. **71**, 145 (1947).
[6] H. H. Barshall and M. H. Kanner, Phys. Rev. **58**, 590 (1940).
[7] B. Rossi and H. Staub, *Ionisation Chambers and Counters: Experimental Techniques* (McGraw-Hill Book Company, Inc., New York, 1949), p. 135.
[8] J. H. Coon and H. H. Barshall, Phys. Rev. **70**, 592 (1946).
[9] Baldinger, Huber, Ricamo, and Zünti, Helv. Phys. Acta **XXIII**, 503 (1950).
[10] E. Baldinger and R. Casale, Helv. Phys. Acta **XXI**, 173 (1948).
[11] F. Bloch, Phys. Rev. **58**, 829 (1940).
[12] C. L. Critchfield and D. C. Dodder, Phys. Rev. **76**, 602 (1949).

Forbidden Beta-Spectra of Sb^{124} and I^{124} *

LAWRENCE M. LANGER
Department of Physics, Indiana University, Bloomington, Indiana
(Received October 19, 1951)

IN a recent letter,[1] an attempt was made to fit the 2.291-Mev beta-spectrum of Sb^{124} with a linear combination of twice-forbidden factors instead of the once-forbidden p^2+q^2 factor previously proposed.[2] This suggestion arises, in part, from the apparently high comparative half-life ($\log ft=10.1$) for the transition.

It is interesting to note that in the decay[3] of I^{124}, the 2.2-Mev positron transition appears to be in the same excited state of Te^{124}. Taking account of the alternative modes of decay, including those by K-capture,[4] one finds that the comparative half-life for this transition corresponds to $\log ft=8.1$, with $\log(W_0^2-1)ft=9.5$. These values are quite in line with those found for other once-forbidden transitions involving a spin-change of 2. The spectrum of I^{124} is also fitted by the C_1T, p^2+q^2 factor.

According to the nuclear shell model, the state in Sb^{124} is best described as $I=3$, $+$, arising from the combination of a $g_{7/2}$ proton and an $s_{1/2}$ neutron. The state of I^{124} is also expected to be $I=3$, $+$, arising from a $d_{5/2}$ proton and an $s_{1/2}$ neutron. The resultant "L" state would then be 4 for the Sb^{124} and 2 for the I^{124}.

Although there seems to be some tendency[5] for the first excited state of an even-even nucleus to be $I=2$, $+$, this rule is not without exceptions. It is therefore not unreasonable, in view of the spectrum shapes, to assign $I=1$, $-$, to the 0.60-Mev level in Te^{124}.

The somewhat high comparative half-life for the Sb^{124} transition apparently results then from its being "ΔL-forbidden" in addition to its involving a parity change and a total angular momentum change of 2 units.

* This work was assisted by a grant from the Frederick Gardner Cottrell Fund of the Research Corporation and by the joint program of the ONR and AEC.
[1] Nakamura, Umezawa, and Takebe, Phys. Rev. **83**, 1273 (1951).
[2] Langer, Moffat, and Price, Phys. Rev. **79**, 808 (1950).
[3] Mitchell, Mei, Maienschein, and Peacock, Phys. Rev. **76**, 1450 (1950).
[4] L. Marquez and I. Perlman, Phys. Rev. **78**, 189 (1950).
[5] M. Goldhaber and A. W. Sunyar, Phys. Rev. **83**, 906 (1951).

The Decay of Bi^{207}

M. A. GRACE AND J. R. PRESCOTT*
Clarendon Laboratory, Oxford, England
(Received October 16, 1951)

BISMUTH 207 has been prepared by bombarding lead foil with 25-Mev protons in the Harwell cyclotron and extracting the bismuth chemically as bismuth oxychloride. The decay of the bismuth isotopes was followed for 300 days and the Bi^{207} identified by its long half-life and the presence of lead K-radiation resulting from the K-capture decay.

Measurements using a NaI(Tl) scintillation detector show prominent γ-ray lines at 0.56 ± 0.03 Mev and 1.1 ± 0.05 Mev. These can probably be identified with the 0.565- and 1.063-Mev lines reported by Neumann and Perlman.[1] Although the resolution of the scintillation spectrometer is less than that of the β-ray spectrograph, the former has the advantage that the measured magnitude of the peaks is simply related to the γ-ray intensities provided that the γ-rays are only weakly converted. We conclude that the two lines are of equal intensity within the experimental error. This suggests that the two γ-rays are emitted in cascade, and coincidences between them were detected using two scintillation counters. A pulse-height analyzer operating on one counter was gated by pulses from the other, and the results show that at least half of the 0.56- and 1.1-Mev γ-rays are emitted in cascade.

Taken with the β-ray spectrograph measurements of Neumann and Perlman[1] these results give the ratio of K internal conversion coefficients. This is consistent with the level assignment given by Goldhaber and Sunyar[2] in which the 1.1-Mev γ-ray is $M4$ and precedes the 0.56-Mev γ-ray which is $E2$ (electric quadrupole). These γ-rays are presumably to be identified with those found by Campbell and Goodrich[3] in the 0.9-sec isomeric state of Pb^{207}.

We are indebted to the Director of A.E.R.E., Harwell, for the cyclotron irradiation, to Mr. C. H. Collie for drawing our attention to this problem, and to Dr. P. F. D. Shaw for assistance with the chemistry.

* Australian National University Scholar.
[1] H. M. Neumann and I. Perlman, Phys. Rev. **81**, 958 (1951).
[2] M. Goldhaber and A. W. Sunyar, Phys. Rev. **83**, 906 (1951).
[3] E. C. Campbell and M. Goodrich, Phys. Rev. **78**, 640(A) (1950).

A Search for Gamma-Rays from the 4.8-Mev Level in Li^7 *

H. E. GOVE
Department of Physics and Laboratory for Nuclear Science and Engineering, Massachusetts Institute of Technology, Cambridge, Massachusetts
(Received October 11, 1951)

IN order to make a preliminary determination as to whether Li^7 in the 4.8-Mev excited state[1] decays by gamma-emission, a comparison was made between the gamma-spectrum from the reaction

$$C^{13}(p,p')C^{13*}\rightarrow C^{13}+\gamma+4.5\text{ Mev}$$

and that from $Li^7(p,p')Li^{7*}$, $Q=-4.8$ Mev, using the 8-Mev protons from the MIT cyclotron. The gamma-spectrum was measured alternately from thin, unbacked carbon and lithium targets using a NaI-Tl scintillation counter located at 90° to the beam. The carbon gamma-spectrum showed a pronounced peak corresponding to the 4.5-Mev gamma-ray, whereas in the case of the lithium target there was no evidence of a gamma-peak in the 4.8-Mev region above a low background of very high energy gammas. The inelastic proton groups from the two targets were roughly equal in intensity, as measured in a double proportional counter. It appears that the preferred mode of decay for the 4.8-Mev level in Li^7 is not by gamma-emission but by particle emission —probably breaking up into He^4 and H^3.

* This work has been supported in part by the Joint program of the ONR and AEC.
[1] H. E. Gove and J. A. Harvey, Phys. Rev. **82**, 658 (1951).

Positron Spectra of Certain Mirror Nuclei*

F. I. BOLEY† AND D. J. ZAFFARANO
Iowa State College and Institute for Atomic Research, Ames, Iowa
(Received October 15, 1951)

THE positron energy end points and half-lives of the "mirror" nuclei Mg^{23}, Si^{27}, S^{31}, Cl^{33}, K^{37}, and Ca^{39} have been investigated with a scintillation spectrometer and pulse recording equipment. These nuclei were produced by (γ,n) and $(\gamma,2n)$ reactions induced by 70-Mev x-ray irradiation.

Most of these activities have been studied previously by cloud chamber and absorption techniques.[1–4] The present work provides confirmation of some earlier values, and yields the additional end points of K^{37} and Ca^{39}.

Except in the case of Mg^{23} where magnesium foil was used, sources were prepared from finely-powdered compounds, chosen so as to yield no short-lived high energy activities which might interfere with those of the isotopes being investigated. Each powdered compound was mixed with a small amount of Zapon lacquer, which acted as a binder, and was formed into a thin wafer. This was supported by 0.00025-inch-thick paper covering a $\frac{1}{4}$-inch opening in a source holder made of 0.005-inch thick nickel. The surface densities of the samples were 20–30 mg/cm^2. Background activity due to the source holder was always less than 2 percent of the activity being studied. Samples were irradiated at maximum beam energy for approximately one half-life of the desired activity.

TABLE I. Observed radiations.

Activity	Compound irradiated	Half-life (sec)	End point (Mev)	ft (sec)
Mg^{27}	Mg	12.3±0.4	2.99±0.09	4670±720
Si^{31}	SiO_2	5.4±0.4	3.48±0.10	3740±630
S^{35}	S	3.2±0.3	4.06±0.12	4320±770
Cl^{38}	NH_4Cl	1.8±0.1	4.43±0.13	3440±550
K^{42}	KI	1.2±0.2	4.57±0.13	2700±610
Ca^{45}	CaF	1.1±0.2	5.13±0.15	3990±940

By use of a pneumatic tube the irradiated samples were transferred from the x-ray beam to an anthracene scintillation spectrometer in about 0.1 second. Each disintegration detected was displayed in the form of a dot on an oscilloscope screen which was photographed on a rapidly moving film.[6] The height of the dot above the base line was proportional to the amplitude of the light pulse produced by the scintillation crystal. An amplitude analysis of these dots provided an energy spectrum and a time analysis yielded a decay curve. The amplitude analysis was calibrated by comparison with the β-end points of Y^{90} at 2.25±0.03 Mev[7] and Cl^{34} at 4.45±0.11 Mev.[8] Resolution corrections involving the first and second derivatives of the number of counts *vs* amplitude curve were applied to the data.[9]

Table I gives the compounds irradiated, half-lives, end points, and ft values for the activities. End points were obtained with the aid of Fermi plots. The values for half-life were obtained by observing approximately three half-lives of each activity. Values of ft were obtained by use of the graphs by Feenberg and Trigg.[10]

Reasonable agreement with positron energies calculated from available coulomb repulsion energy[11] is obtained. Increased accuracy may be expected with this technique when more preise magnetic spectrometer measurements of high energy beta-spectra become available for calibration use.

A value of $r_0=(1.40\pm0.07)\times10^{-13}$ cm for the nuclear radius is indicated from this work.

It is a pleasure to acknowledge the support given to one of us (F.I.B.) in the form of a Socony-Vacuum Research Fellowship.

* Contribution No. 158 from the Institute for Atomic Research and Department of Physics, Iowa State College, Ames, Iowa. Work was performed in part in the Ames Laboratory of the AEC.
† Now at Wesleyan University, Middletown, Connecticut.
[1] White, Delsasso, Fox, and Creutz, Phys. Rev. **56**, 512 (1939).
[2] White, Creutz, Delsasso, and Wilson, Phys. Rev. **59**, 63 (1941).
[3] D. Elliott and L. King, Phys. Rev. **60**, 489 (1941).
[4] Barkas, Creutz, Delsasso, Sutton, and White, Phys. Rev. **58**, 383 (1940).
[5] McCreary, Kuerti, and Van Voorhis, Phys. Rev. **57**, 351 (1940).
[6] The detailed experimental equipment and procedure will be described in AEC report ISC-154.
[7] E. Jensen and L. Laslett, Phys. Rev. **75**, 1949 (1949).
[8] L. Ruby and R. Richardson, Phys. Rev. **81**, 659 (1951).
[9] J. Palmer, unpublished thesis, Iowa State College (1950).
[10] E. Feenberg and G. Trigg, Revs. Modern Phys. **22**, 399 (1950).
[11] E. Wigner, Phys. Rev. **51**, 947 (1937).

An Anomalous Effect in the Ultrasonic Absorption of Electrolytic Solution*

ROBERT E. BARRETT AND ROBERT T. BEYER
Department of Physics, Brown University, Providence, Rhode Island
(Received October 8, 1951)

IN both theoretical and experimental studies of ultrasonic absorption in electrolytic solutions, it has been the custom to treat the absorption coefficient as the sum of the coefficient due to the solvent alone and that due to the solute.[1-3] These two contributions have then been treated independently, under the assumption that they are additive.

It has recently been suggested† that these quantities may not be additive. The following experimental results, obtained in the course of a general study of ultrasonic absorption in electrolytes, support this hypothesis.

The amplitude absorption coefficient α has been measured in aqueous solutions of sodium acetate, by means of the radiation pressure method, in the frequency range 9 to 45 megacycles. The results are shown in Fig. 1, in which the value of α/ν^2 (ν=sound frequency) is plotted against log ν. Measurements have been made at 20°C in 0.1 and 0.2 molal solutions, and at 5°C and 10°C in 0.2 molal solutions.

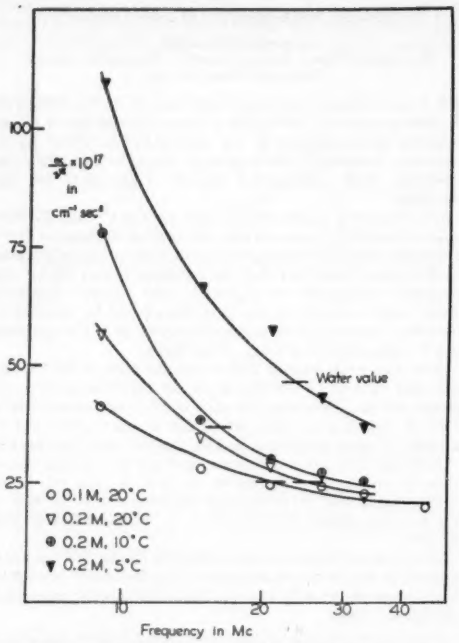

FIG. 1. Ultrasonic absorption in aqueous solutions of sodium acetate.

The average value of α/ν^2 for water at each temperature has been computed from published measurements.[4-6] These values are indicated in the figure by a horizontal bar through each curve at the appropriate point. (It should be recalled that α/ν^2 is independent of frequency for water at all frequencies so far studied.)

The results indicate that the absorption coefficient for these solutions varies from a value considerably above that of water at the low frequencies, to a value which is lower than the corresponding value of the absorption coefficient in water at the higher frequencies. At the highest frequency measured, (45 Mc), α for the solution was about 20–30 percent below α for pure water. The relative decrease in the absorption coefficient appears to be greater at the lower temperatures.

The measurements thus far are insufficient to indicate the concentration effect of the phenomenon. A few measurements made in 0.05 molar solution indicate that the effect is very small at such a concentration.

It is apparent from these results that some sort of extra absorption process due to the presence of the solute exists at the lower frequencies. The explanation of the high frequency effect would appear to lie in a disruption of the simple two-state process hypothesized by Hall[7] in order to explain the observed absorption coefficient for water.

In the Hall theory, water is considered as a mixture of molecules in an ice-like arrangement and molecules which are closely packed. The passage of the sound wave upsets the equilibrium between the two states and the resultant structural relaxation produces the sound absorption. The presence of the solute contributes an additional absorption, due presumably to some sort of

disturbance of the dissociation equilibrium. At high frequencies, however, such a term should become negligible.

It would appear then that the presence of the solute produces an additional effect, which is observable only at high frequencies. In this case, the solute hinders the transition from the ice-like state to the closely packed state. Such a hindrance, in terms of the Hall formulation, would decrease the contribution of structural relaxation to the absorption.

Further measurements are in progress to determine the concentration and temperature dependence of this effect.

* This work was supported in part by the ONR.
[1] M. Leontovich, J. Exptl. Theor. Phys. U.S.S.R. **8**, 40 (1938).
[2] P. Bazulin, J. Exptl. Theor. Phys. U.S.S.R. **9**, 1147 (1939).
[3] I. Liebermann, Phys. Rev. **76**, 1520 (1949).
† This suggestion was made to one of the authors by Dr. Ernest Yeager of Western Reserve University.
[4] F. E. Fox and G. D. Rock, Phys. Rev. **70**, 68 (1946).
[5] J. M. M. Pinkerton, Nature **160**, 128 (1947).
[6] M. C. Smith and R. T. Beyer, J. Acoust. Soc. Am. **20**, 608 (1948).
[7] Leonard Hall, Phys. Rev. **73**, 775 (1948).

Radiative Capture of Thermal Neutrons by Li^7

R. G. THOMAS
Kellogg Radiation Laboratory, California Institute of Technology, Pasadena, California
(Received October 8, 1951)

HUGHES, Hall, Eggler, and Goldfarb[1] found the cross section for production of radioactive Li^8 from the capture of thermal neutrons by Li^7 to be 33 ± 5 millibarns, and noted that this value is from ten- to fifty-times larger than the maximum cross section expected for electric dipole emission as given by the usual estimates in which the contribution to the matrix element of the electric dipole transition moment arises from the internal region of the nuclear system. This large cross section can, however, be understood if one takes into account the contribution of the extra-nuclear parts of the wave functions, which can be shown in this particular case to have a predominant effect, the reason being essentially that Li^7 has negative neutron scattering lengths and that Li^8, in the ground state, may have a moderately large wave function in the Li^7+n channel of the external region. In the development which follows, the magnitude of the extra-nuclear contribution will be estimated from data obtained in Li^7-neutron scattering experiments. Here we use the theory and terminology of Wigner and Eisenbud[2,3] to describe the nuclear configuration space. For this problem the external region is the alternative Li^7+n with a channel radius r_c and the internal region is the rest of the nuclear configuration space, extending out to infinity in all the other (energetically-forbidden) channels.

Li^7 has spin $\frac{3}{2}$ and presumably odd parity so that in the interaction with s-wave neutrons there are triplet and quintet channel spin states i with which are associated two scattering lengths a_i, designated a_1 and a_3, and two statistical factors, $g_1=\frac{1}{4}$ and $g_3=\frac{3}{4}$, respectively. The ground state of Li^8 is considered to be $^3P_2$ with even parity;[4] hence, the radiative capture of thermal neutrons is expected to be the result of electric dipole emission. Neglecting exchange or interaction effects and a possible contribution from the internal region, the electric dipole capture cross section for either channel state i is given by[4]

$$\sigma_\gamma(i\to f)=64\pi^4(h\nu)^3e^2A^2g_i{g_i}'\left|\int_{r_c}^{\infty}ru_iu_f\,dr\right|^2\Big/3h^4c^2, \qquad (1)$$

where the u's are the radial parts of the wave function, multiplied by r, representing the system Li^7+n in the initial and ground states, $h\nu=2.04$ Mev is the transition energy, $A=\frac{7}{8}$ is the reduced charge number, ${g_i}'$ is the angle-spin integration factor. For values of r for which there is a significant contribution to the integral of (1) (neglecting radiative damping) we can approximate

$$u_i=(4\pi/v)^{\frac{1}{2}}(r-a_i), \quad r>r_c. \qquad (2)$$

In the external region the ground-state wave function for Li^7+n is assumed to have unit orbital angular momentum, so that

$$u_f(r)=(N/r_c)^{\frac{1}{2}}w(r)/w(r_c), \quad w(r)=(1+x^{-1})e^{-x}; \quad x=\beta r, \quad \beta=(2Mh\nu/\hbar^2)^{\frac{1}{2}}, \qquad (3)$$

where M is the reduced mass. The normalization constant N is proportional to the probability that the external channel is occupied, and can be expressed in the terms of the reduced width γ^2 of Wigner and Eisenbud[2] by the relation

$$\gamma_f{}^2=(\hbar^2/2M)u_f{}^2(r_c)\Big/\Big(1-\int_{r_c}^{\infty}u_f{}^2(r)dr\Big); \qquad (4)$$

the integral in the denominator is included because the wave function associated with u_f in Eq. (1) must be normalized to unity over the entire nuclear volume, internal plus external, whereas $\gamma_f{}^2$ is defined in terms of a wave function which is normalized to unity in the internal region. Using Eqs. (2), (3), and (4) the radial integral is found to be

$$\left|\int_{r_c}^{\infty}ru_iu_f\,dr\right|^2=4\pi r_c{}^2Q_i{}^2N/v,$$

with

$$Q_i=[(x_c{}^2+3x_c+3)-a_i\beta(x_c+2)]/x_c{}^2(1+x_c),$$
$$N=\theta_f{}^2[1+\theta_f{}^2(x_c+2)/2(x_c+1)^2]^{-1}, \qquad (5)$$
$$x_c=\beta r_c, \quad \theta_f{}^2=\gamma_f{}^2(2Mr_c/\hbar^2).$$

We note the similarity of this treatment using dispersion theory, wherein the reduced width serves to normalize the ground-state wave function, to the treatment of the photoelectric disintegration of the deuteron using the effective-range theory, in which the effective range enters in the same normalization.[6]

In order to evaluate Eq. (5) it is necessary to know the zero-range scattering lengths, the ground-state reduced width, and the factors ${g_i}'$. The coherent thermal neutron scattering cross section of Li^7, as measured by Shull and Wollan,[7] is $4\pi(8/7)^2a^2=0.8$ barn, and the coherent scattering amplitude $a=g_1a_1+g_3a_2$ is negative according to Fermi and Marshall.[8] Adair has measured the Li^7 total cross section for 0.2- to 1.4-Mev neutrons.[9] Extrapolating his curve to zero energy gives a value 1.1 barn for $4\pi(g_1a_1{}^2+g_3a_2{}^2)$. Using these data we solve for the scattering lengths obtaining two possible solutions: (I) $a_1=0.2$, $a_3=-3.7$; (II) $a_1=-4.6$, $a_2=-0.7$, in units of 10^{-13} cm. The above scattering lengths are such as to give a large value for the quantities $Q_i{}^2$ of Eq. (5). Furthermore, since they are less than the nuclear radius of Li^7, the s-wave scattering should show resonances; indeed, Adair has found a broad s-wave resonance at about 1.4 Mev with a width of about 2.4 Mev.

The reduced width of the ground state of Li^8 required in Eq. (5) is not known. However, Adair reports a p-wave Li^7+n resonance at 270 kev with a width of 45 kev; taking into account the variation of the level shift with respect to energy,[10] this resonance has a reduced width $\theta^2=0.30$ if the channel radius is taken to be 4.0×10^{-13} cm. Since the ground-state decomposition in which we are interested is also a p-orbital, it seems reasonable to assume this value for $\theta_f{}^2$ in Eq. (5). Using a radius 4.0×10^{-13} cm (the computation is not sensitive to this) we obtain for

$$^3s_{\frac{1}{2}}\to{}^3p_{\frac{3}{2}}({g_1}'=5/9), \quad \sigma_I=10 \text{ and } \sigma_{II}=25 \text{ mb};$$

and for

$$^5s_{\frac{1}{2}}\to{}^5p_{\frac{3}{2}}({g_3}'=1/3), \quad \sigma_I=22 \text{ and } \sigma_{II}=15 \text{ mb},$$

the ls notation being used to refer to the relative orbital angular momentum in the external channel and to the channel spin. Mixtures of the aforementioned transition types may, of course, occur. Thus, considering the uncertainty of the $\theta_f{}^2$, we can only conclude that the large capture cross section is qualitatively explainable as the result of a large extra-nuclear contribution to the matrix element of the dipole moment.

The one-level nuclear dispersion formula for radiative capture is derived on the assumption that the radiation arises from the moments of the internal region. Consequently, if there is an appreciable contribution to the moments from the external wave functions, which might be the case if the level involved is broad,

then one may expect a deviation from the energy dependence of the cross section as given by the usual one-level formula. For example, in the capture of s-wave neutrons and protons by C^{12}, deviations from this energy dependence of more than a factor of two are found which can be attributed to the extra-nuclear contribution to the electric dipole moment, as in the case of the capture of thermal neutrons by Li^7. This problem will be considered in detail in a paper which is in preparation.

The writer is grateful for discussions with Professor R. F. Christy and Professor T. Lauritsen. This investigation was made during tenure of an AEC predoctoral fellowship.

[1] Hughes, Hall, Eggler, and Goldfarb, Phys. Rev. **72**, 648 (1947).
[2] E. P. Wigner and L. Eisenbud, Phys. Rev. **72**, 29 (1947).
[3] E. P. Wigner, Phys. Rev. **70**, 15 (1946) and **73**, 1002 (1948).
[4] M. E. Rose and H. A. Bethe, Phys. Rev. **51**, 205 (1937).
[5] G. Breit and F. L. Yost, Phys. Rev. **48**, 203 (1935).
[6] H. A. Bethe and C. Longmire, Phys. Rev. **77**, 647 (1950).
[7] C. G. Shull and E. O. Wollan, Phys. Rev. **81**, 527 (1951).
[8] E. Fermi and L. Marshall, Phys. Rev. **71**, 666 (1947).
[9] R. K. Adair, Phys. Rev. **79**, 1018 (1950).
[10] R. G. Thomas, Phys. Rev. **81**, 148 (1951).

Search for Production of V^0 Particles by a 310-Mev Bremsstrahlung Beam

G. Cocconi and A. Silverman
Cornell University, Ithaca, New York
(Received October 16, 1951)

A SEARCH has been made for the production of V^0-particles by 310-Mev bremsstrahlung radiation incident on carbon and lead. If, as the most recent evidence[1] seems to indicate, the products of the disintegration of the V^0-particles are three or more heavy particles (mesons or nucleons), production of V^0's by 310-Mev γ-rays is energetically impossible. If however the V^0-particles disintegrate according to the scheme: $V^0 \rightarrow$proton $+\pi^-$-meson$+Q$ (with $Q \cong 30$ Mev), as indicated by earlier experiments,[2] V^0-particles may be produced by 300-Mev γ-rays, the threshold for the process being at $\sim$190 Mev, in carbon.[3]

Assuming the two-particle disintegration with $Q=30$ Mev, one find that the energy of a V^0 produced in carbon by 300-Mev γ-rays at 90° to the beam direction lies between 65 and 110 Mev, depending on whether momentum is conserved via recoil of one nucleon or of the entire nucleus. Assume that a 65-Mev V^0 ($\beta=0.3$) is produced at 90° to the beam direction; in the laboratory system its path length before disintegration is $\simeq 1$ cm ($\tau \simeq 10^{-10}$ sec).[4] The angle that the decay proton makes with the direction of the V^0-particle never exceeds 15°, and its energy lies between 30 Mev and 90 Mev. The meson, however, can be emitted in any direction with respect to the direction of the V^0, with energy from 5 Mev to 66 Mev. The most probable angle between the two decay products is approximately 60° and the corresponding energies are $E_p=58$ Mev and $E_\pi=37$ Mev.

The detection of the two disintegration products has been attempted with the arrangement sketched in Fig. 1 (a and b). A V^0-particle emitted at 90° to the γ-ray beam and disintegrating in the region Σ of Fig. 1(b) would give rise to a proton detected by the scintillating counter P, and a meson detected by the crystal counters a and b. The ½-in. Pb-shield separating the carbon target from the counters served the purpose of absorbing most of the ionizing particles emitted by the target, thus lowering the background substantially, without affecting the V^0-particles very much. A particle produced in the target had to traverse an average path in lead of approximately 4 cm in order to reach counters a and b. The proton counter (NaI, 7.5 g cm^{-2} thick) was biased to detect protons of energies greater than 15 Mev. Counters a and b were biased to detect mesons of energies between 18 and 70 Mev. The coincidences $(P+b)$ were recorded with a resolving time of 2×10^{-8} sec and the threefold coincidences $[(P+b)+a]$ with a resolving time of 5×10^{-7} sec. Most of the chance coincidences were caused by events involving a real coincidence between a and b. With a beam of approximately 2×10^9 "Q"/min ("Q" effective quanta), as measured with an integrating ion chamber, the expected rate of chance coincidence $[(P+b)+a]$ was approximately 1/hr. Several runs have been made in which the angle between proton detector and meson detector was varied from 65° to 115°.

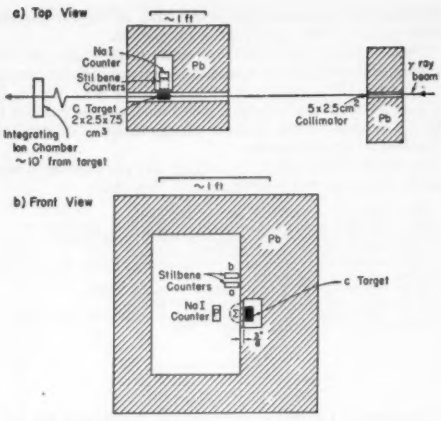

FIG. 1.

With an integrated beam of 9×10^{11} "Q", 9 coincidences were observed. The expected number of chance coincidences was 10. Assuming that all the observed coincidences are decay products of V^0-particles, and that the life-time is 10^{-10} sec one can establish that the upper limit of the differential cross section per carbon nucleus for production of V^0-particles is 5×10^{-32} cm²/sterad "Q". This is approximately 0.3 percent of the cross section for production of charged mesons in carbon.

The same experiment has been performed with lead as the target material, as well as with geometry appropriate to detect disintegration products of V^0-particles emitted at approximately 30° with respect to the γ-ray beam. The events recorded never exceeded the rate of chance coincidences. These negative results may be an additional evidence that the two-particle decay hypothesis is not correct.

We would like to express our thanks to Professor R. R. Wilson for many valuable discussions during the course of this work.

[1] R. B. Leighton *et al.*, Phys. Rev. **83**, 843 (1951).
[2] R. Armenteros *et al.*, Nature **167**, 501 (1951).
[3] If the light particle is a μ-meson, the threshold is correspondingly decreased.
[4] W. B. Fretter (private communication).

Scintillations in Thallium-Activated CaI_2 and CsI*

W. Van Sciver and R. Hofstadter
Department of Physics and Microwave Laboratory, Stanford University, Stanford, California
(Received October 18, 1951)

SEVERAL samples of polycrystalline thallium-activated CaI_2 have been prepared in this laboratory by adding 1 percent of TlI to the melt of CaI_2 in a helium atmosphere. It has been found that this material scintillates with a high luminous efficiency.

Measurements of pulse size and decay constant have been made on polycrystals and small crystal fragments as follows. Individual CaI_2(Tl) scintillations due to Co^{60} gamma-rays have been photographed on an oscilloscope screen and subsequently plotted and measured. An integrating RC load of time-constant 22 microseconds was used in all the measurements. This value of time

constant is long enough to allow the $CaI_2(Tl)$ pulses to approach saturation. Under these conditions the decay constant $(1/e)$ for $CaI_2(Tl)$ has been measured as 1.1 ± 0.1 microsecond. A small correction has been included for the superimposed decay of the load circuit.[1] Under the same conditions the pulse heights of $CaI_2(Tl)$ and NaI(Tl) have been compared and are equal within the experimental error (~3 percent). Applying again the small corrections caused by the load circuit, the integrated light output for $CaI_2(Tl)$ is 10 percent larger than that of NaI(Tl). [Possibly a larger result might be obtained with a single crystal of $CaI_2(Tl)$.] This result has been obtained with both 5819 photomultiplier and with the ultraviolet sensitive (C7140) counterpart of this tube. A large fraction of the emitted light lies in the blue-green so that the output should be nearly the same in both tubes, as found. The large pulse size of $CaI_2(Tl)$ may possibly make this crystal useful in measurements of energies of gamma-rays.

With the same apparatus, Harshaw-supplied crystals of CsI(Tl)[2] have been examined. The integrated light output for CsI(Tl) is about 0.28 ± 0.03 that of NaI(Tl) as measured with a 5819 tube and 22-microsecond load circuit. The decay constant $(1/e)$ for CsI(Tl) is also 1.1 ± 0.1 microsecond. This value agrees with an earlier determination made by one of the authors and Mr. E. C. Booth at Princeton University.

We wish to thank the Harshaw Chemical Company for kindly supplying us with the CsI(Tl) sample.

* This work was aided by the joint program of the ONR and AEC.

[1] Specifically we take the voltage curve to be $V=I_0R[\tau/(\tau_0-\tau)]\times(\exp(-t/\tau_0)-\exp(-t/\tau))$, where the scintillator light output is proportional to $I=I_0\exp(-t/\tau)$ and τ_0 = time constant of load circuit $=RC$.

[2] R. Hofstadter, Research Revs. (ONR) 1, 4 (September, 1949); Nucleonics 6, 70 (1950).

The Interaction of π-Mesons with Carbon Nuclei*

ANATOLE M. SHAPIRO†
Cornell University, Ithaca, New York
(Received October 15, 1951)

IN an earlier experiment[1] an investigation of the interaction of positive and negative π-mesons with carbon and aluminum nuclei was begun. The work with carbon has now been considerably extended. The experimental arrangement used is very similar to that of the earlier experiment (see Fig. 1 of reference 1). π-mesons, produced in targets placed in the 310-Mev bremsstrahlung beam of the synchrotron, are focused by a double magnet system into a 12-inch cloud chamber containing 9 thin carbon plates. The mesons incident on the cloud chamber have an initial energy of 65 ± 5 Mev; their energy in the chamber is primarily between 35 and 60 Mev, averaging 48 Mev.

The pictures have been analyzed stereoscopically and only events and traversals occurring within a prescribed region have been counted. Deflections in a plate with no perceptible change of ionization (<10–15-Mev energy loss) have been classified as elastic scatterings. All other events—inelastic scatterings and 0-, 1-, 2-, and 3-prong stars—have been classified as nuclear interactions. The data are presented in Table I.

The elastic scatterings with angles <20° include a large number of undetected π-μ decays occurring in or near the plates. Twelve of the 17 events in this group are expected to be π-μ decays or coulomb scatterings. The remaining five events agree well with the number of scatterings expected from the calculated diffraction pattern, assuming that all elastic scatterings are diffraction scatterings.

TABLE I. The number of nuclear interactions, scatterings, and traversals observed.

	Nuclear interactions (stars and inel. scat.)	Elastic scatterings 10°–20°	20°–75°	>75°	No. of traversals of 0.520 g/cm² C plates
π^+	33	10	11	2	6133
π^-	20	7	8	0	3310
Total	53	17	19	2	9443

TABLE II. The corrected mean-free-paths and corresponding cross sections for nuclear interactions and elastic scatterings.

	Nuclear interactions (stars and inel. scat.) λ_{ni}, g/cm²	σ_{ni}, mb	Elastic scatterings (>20°) λ_{el}, g/cm²	σ_{el}, mb	Total diffraction scat. (>0°) λ_t, g/cm²	σ_t, mb
π^+	93 ± 16	214 ± 37	255 ± 75	78 ± 23	....	....
π^-	83 ± 19	240 ± 54	210 ± 75	96 ± 34	....	....
Total	89 ± 13	223 ± 32	237 ± 55	84 ± 19	175 ± 35	115 ± 25

One of the π^+ scatterings with angle >20° can be expected to be an undetected π-μ decay. The number of traversals must also be corrected for a 3 percent contamination[1] of the beam by μ-mesons and electrons. After making these corrections, the cross sections listed in Table II have been calculated. From the diffraction angular distribution, about 75 percent of the total number of diffraction scatterings are expected to occur with angles >20° and outside of the solid angle obscured by the carbon plate containing the event. Thus, the total diffraction cross section has been calculated on the basis of $(21-1)/0.75$ or 27 scatterings. The errors indicated are the statistical standard deviations.

These results agree with those of the previous experiment.[1] As we observed earlier,[2] the cross sections for π^+- and π^--mesons are equal within the present statistics. Contrary to the measurement of Steinberger and collaborators[3] with 85-Mev π^--mesons, we find the carbon nucleus considerably transparent (Table III). The difference may be a result of the energy dependence of the interactions.

From the opacity $(=\sigma_{ni}/\pi R^2)$ one can calculate the mean-free-path λ of π-mesons in nuclear matter and the corresponding cross section σ_i for interaction of a meson and a nucleon in the nucleus. This has been done for several values of the nuclear radius R (Table III) to indicate the variation of the various quantities with this uncertain parameter. The unusually large value of r_0 in column 4 has been included to indicate the possible effect of the meson's finite wavelength. From the transparent nucleus theory[4] as extended by Bethe and Wilson,[5] one can calculate the average potential in the nucleus V_0 and from this the total scattering cross section σ_s of a meson by a nucleon: $\sigma_s=0.735r_0^2V_0^2\mu b$, where r_0 is measured in units of 10^{-13} cm and V_0 in Mev. This calculation[6] assumes that the amplitudes for scattering a meson by a proton, a_P, and a neutron, a_N, are isotropic and equal in magnitude and sign.

For pseudoscalar mesons, the amplitudes would have the same sign for pseudoscalar coupling, and opposite signs for pseudovector coupling.[6] Anderson[7] has measured the total scattering cross section of 50-Mev mesons by protons: 11 ± 5 mb for π^- and 37 ± 8 mb for π^+-mesons. If a_P and a_N have the same sign, one would expect in carbon $\sigma_s\approx|\frac{1}{2}(37^{\frac{1}{2}}+11^{\frac{1}{2}})|^2=22\pm5$ mb, which disagrees considerably with our calculated σ_s. If they have opposite signs, $\sigma_s\approx|\frac{1}{2}(37^{\frac{1}{2}}-11^{\frac{1}{2}})|^2=1.9\pm1.4$ mb, which agrees very well. This indicates that a_P and a_N have opposite signs and that the coupling is probably pseudovector.

TABLE III. Nuclear and interaction parameters calculated from the observed σ_{ni} and σ_t.

$r_0=RA^{-\frac{1}{3}}$, $\times10^{13}$, cm	1.37	1.47	1.70
Opacity $=\sigma_{ni}/\pi R^2$	0.72 ± 0.10	0.63 ± 0.09	0.47 ± 0.07
λ, mean free path of meson in nuclear matter, $\times10^{13}$, cm	3.0 ± 1.0	4.3 ± 1.1	7.8 ± 1.6
σ_i, cross section for interaction of meson and nucleon in the nucleus, mb	36 ± 12	31 ± 8	27 ± 6
V_0, Mev	15 ± 15	15 ± 9	12 ± 5
σ_s, total scattering cross section of meson by nucleon, mb	$1.1^{+3.3}_{-1.1}$	$1.7^{+2.6}_{-1.5}$	$2.5^{+2.5}_{-1.6}$

The author wishes to thank Professor R. R. Wilson, Professor D. R. Corson, and other members of the earlier experiment for their aid and many valuable discussions.

* Supported in part by the ONR.
† Now at the Brookhaven National Laboratory, Upton, New York.
[1] Camac, Corson, Littauer, Shapiro, Silverman, Wilson, and Woodward, Phys. Rev. **82**, 745 (1951).
[2] A. M. Shapiro, Phys. Rev. **83**, 874 (1951).
[3] Chedester, Isaacs, Sachs, and Steinberger, Phys. Rev. **82**, 958 (1951).
[4] Fernbach, Serber, and Taylor, Phys. Rev. **75**, 1352 (1949).
[5] H. A. Bethe and R. R. Wilson, Phys. Rev. **83**, 690 (1951).
[6] H. A. Bethe, private communication.
[7] H. L. Anderson, Chicago International Conference, September 17–22, 1951.

Photoproton and Photoneutron Relative Yields

R. K. SHELINE*
Institute for Nuclear Studies, University of Chicago, Chicago, Illinois
(Received September 20, 1951)

MARQUEZ[1] has suggested a model for photonuclear reactions for the lighter elements in which the gamma-ray is absorbed by a single nucleon in a process similar to the photoelectric effect. There are many indications[1] that neither a statistical model in which nucleons evaporate from a compound nucleus nor a resonance model can fully explain photonuclear reactions in the light elements. If there is single particle interaction, as in the model of Marquez, one would expect the ratio $\sigma_{(\gamma,p)}/\sigma_{(\gamma,p)}$ to equal unity for different isotopes of the same light elements. This may be expected to be a more stringent test than the requirement that the ratio $\sigma_{(\gamma,p)}/\sigma_{(\gamma,n)}\cong 1$.

The betatron spectrum of 0- to 48-Mev gamma-rays were used to induce (γ,n) and $(\gamma,\dot{p})$ reactions in magnesium and silicon. In order to measure $(\gamma,\dot{p})$ to (γ,n) yield ratios in two different sets of magnesium isotopes a bar of spectroscopically pure magnesium metal was mounted directly in the beam and counted in place immediately after the beam was turned off. Changing the energy of the beam from 35 to 48 Mev or changing the shape and size of the sample produced no effect greater than the intrinsic errors of the experiment. This produced no effect greater than the intrinsic errors of the experiment. This was to have been expected since Perlman and Friedlander[2] have shown that relative yields are not affected by changing the beam maximum energy from 50 to 100 Mev. In all cases the relative yields reported here were determined by measuring the activity of the product nuclei. Two-particle reactions such as (γ,d), (γ,pn), and $(\gamma,2n)$ which produce the product nuclei have been neglected in computing relative yields. The results of the $(\gamma,\dot{p})$ to (γ,n) yield ratios for two different sets of magnesium isotopes and the $(\gamma,\dot{p})$ to $(\gamma,\dot{p})$ yield ratio for a single set of magnesium isotopes are given in Table I.

In the case of elemental silicon the great difference of positron and electron energies in the (γ,n) and $(\gamma,\dot{p})$ products makes an accurate yield ratio of $(\gamma,\dot{p})$ to (γ,n) impossible with the set up used to determine this yield ratio in magnesium. However, it was possible using the traditional set up of bombarding and removing a thin sample to a shielded counter to obtain a yield ratio of $(\gamma,\dot{p})$ to $(\gamma,\dot{p})$ for silicon. The silicon used had no spectroscopic observable impurities greater than 0.003 of a percent and was bombarded in the form of a fine powder. Mountings were such as to reduce backscattering and absorption to a minimum. Except for the (γ,n) yield on magnesium in which the size of the sample was specifically studied, all yields were corrected for absorption using the curves of Perlman and Friedlander.[2]

The $(\gamma,\dot{p})$ irradiations on silicon were monitored by measuring the C^{11} activity induced in a weighed amount of spectrographically pure powered graphite. The monitors presented to the beam the same area cross section as did the targets and were always mounted in tandem. Only a single radioactive species was observed in the monitor over a period of six half-lives.

The relative yields of $(\gamma,\dot{p})$ to $(\gamma,\dot{p})$ for two silicon isotopes are shown in Table I. With the use of the monitor it is possible to compare the $(\gamma,\dot{p})$ on Si^{30} to that obtained by Perlman and Friedlander.[2] The agreement is shown in Table I and is within experimental error.

Although it is not easily possible to make quantitative calculations because of the complexity of the betatron gamma-ray spectrum, it is immediately apparent that these are further data not easy to reconcile with the idea of evaporation from a compound nucleus. The energetics of proton or neutron emission in a compound nucleus determine the competition between the (γ,n) and the $(\gamma,\dot{p})$ cross section. If the probability of creating the compound nucleus is assumed to be approximately the same for different isotopes of the same element, then from the energetics one would expect in general the Γ_p/Γ_n to be very different for different isotopes of the same element. Specifically, one expects for any model involving a compound nucleus the $(\gamma,\dot{p})$ to $(\gamma,\dot{p})$ yield ratios to be very different from one for the different isotopes of both Mg and Si. In the case of silicon the ratio $\sigma_{(\gamma,p)}/\sigma_{(\gamma,p)}$ equals unity within the experimental error for the isotopes Si^{29} and Si^{30}. In the case of magnesium, the ratio is 1.82 ± 0.25 for the isotope ratio Mg^{25}/Mg^{26}. This relatively high yield of Na^{24} may have arisen from its production by the process $Mg^{25}(\gamma,pn)Na^{24}$. It would appear from these limited data that there is a considerable contribution to photonuclear reactions for light elements of the type proposed by Marquez.[1]

TABLE I. Ratios of yields of (γ,n) and $(\gamma,\dot{p})$ reactions.[a]

Parent isotope	Reaction	Product half-life	Product betas and energy (Mev)	Ratio of yields (this research)	Ratio of yields (Perlman and Friedlander)[b]
Si^{29}	$(\gamma,\dot{p})$	2.30 min	3.01	1.12 ± 0.16	...
Si^{30}	$(\gamma,\dot{p})$	6.56 min	2.5 (70 percent) 1.4 (30 percent)	2.67 ± 0.31	2.87
C^{10}	(γ,n)	20.35 min	0.970		
Mg^{25}	$(\gamma,\dot{p})$	14.9 hr	1.390	1.82 ± 0.25	...
Mg^{26}	$(\gamma,\dot{p})$	62.5 sec	3.7 (55 percent) 2.7 (45 percent)	$3.6\ \pm0.5$	...
Mg^{24}	(γ,n)	11.9 sec	2.82		

[a] Note that the yield is given in between the columns of the parent isotopes and reactions which determine the yields. Thus the value 1.12, in between the Si^{29} and Si^{30} columns refers to the $(\gamma,\dot{p})$ yield on $Si^{29}/(\gamma,\dot{p})$ yield on Si^{30}.
[b] See reference 2.

* Now at Oak Ridge Institute of Nuclear Studies as a research participant from Florida State University.
[1] L. Marquez, Phys. Rev. **81**, 897 (1951).
[2] M. L. Perlman and G. Friedlander, Phys. Rev. **74**, 442 (1948).

An Asymmetric Nuclear Model

S. GALLONE AND C. SALVETTI
Istituto di Fisica dell'Università e Laboratori CISE, Milan, Italy
(Received October 15, 1951)

WE want to discuss here some features of an asymmetric nuclear shell model proposed by Rainwater.[1] This model may be fitted to predict nuclear quadrupole moments of the right order of magnitude.

We consider a core formed by the nucleons grouped in saturated orbits; this core is treated as a liquid drop whose surface acts on the remaining nucleons (which we shall call extranucleons) as an impenetrable barrier. It is also assumed that there is a strong spin-orbit coupling of the type:

$$\text{const. } \mathbf{l}\cdot\mathbf{s}. \tag{1}$$

The shape of the core may be described by:

$$R(\mu)=R_0[1+\Sigma_n \alpha_n P_n(\mu)], \tag{2}$$

R_0 being the radius of the undistorted core.

If deviations from the spherical shape are small, a perturbation method already described[2] may be applied to the calculation of

the energy shift of the extranucleons' energy levels (the unperturbed levels being those of the spherical core case). Owing to the strong spin-orbit coupling (1) the zero-approximation eigenfunctions are given by the well-known formulas:

$$\psi_{n,l,l-\frac{1}{2},m}=[\rho_{n,l}(r)/(2l+1)^{\frac{1}{2}}]\{(l+\tfrac{1}{2}-m)^{\frac{1}{2}}Y_{l,m-\frac{1}{2}}(\vartheta,\varphi)\alpha(\sigma) -(l+\tfrac{1}{2}+m)^{\frac{1}{2}}Y_{l,m+\frac{1}{2}}(\vartheta,\varphi)\beta(\sigma)\},$$
$$\psi_{n,l,l+\frac{1}{2},m}=[\rho_{n,l}(r)/(2l+1)^{\frac{1}{2}}]\{(l+\tfrac{1}{2}+m)^{\frac{1}{2}}Y_{l,m-\frac{1}{2}}(\vartheta,\varphi)\alpha(\sigma) +(l+\tfrac{1}{2}-m)^{\frac{1}{2}}Y_{l,m+\frac{1}{2}}(\vartheta,\varphi)\beta(\sigma)\}; \quad (3)$$

where $\rho_{n,l}(r)$ is the radial part of the wave function.

The perturbation calculation yields for the energy shift relative to the unperturbed energy level $E_{n,l,j,m}$:

$$\Delta E_{n,l,j,m}=-\frac{\hbar^2 x_{n,l}^2}{MR_0^2}\left\{\alpha_2\frac{j(j+1)-3m^2}{4j(j+1)} +\alpha_4\frac{3}{64}\frac{3m^4-5m^2[6j(j+1)-5]+3j(j^2-1)(j+2)}{j(j^2-1)(j+2)}\right\}, \quad (4)$$

where $x_{n,l}$ is the nth zero of the Bessel function of order $l+\frac{1}{2}$, M the mass of the extranucleon, and only the first two nonvanishing coefficients of the α's have been retained.

This result, together with the Bohr-Wheeler formula giving the electrostatic and surface energies of the core, allows a calculation of the equilibrium shape of the nucleus and of the corresponding total energy variation.

The nuclei we consider are supposed to be heavy enough so that both assumptions, of adiabatic rotation of the core with respect to the extranucleons' motion and of applicability of the liquid drop model, are permissible.

For $N+P$ extranucleons the equilibrium shape is defined by the following values of the deformation parameters:

$$\tilde{\alpha}_2=\frac{\hbar^2}{4\pi R_0^4\tau M}\sum_{k=1}^{N+P} x_{n_k,l_k}^2 I_{j_k,m_k,2}/[4(1-x)/5];$$
$$I_{j_k,m_k,2}=j_k(j_k+1)-3m_k^2/4j_k(j_k+1),$$
$$\tilde{\alpha}_4=\frac{\hbar^2}{4\pi R_0^4\tau M}\sum_{k=1}^{N+P} x_{n_k,l_k}^2 I_{j_k,m_k,4}/[2(1-10/27x)];$$
$$I_{j_k,m_k,4}=\frac{3}{64}\frac{35m_k^4-5m_k^2[6j_k(j_k+1)-5]+3j_k(j_k^2-1)(j_k+2)}{j_k(j_k^2-1)(j_k+2)}, \quad (5)$$
$$x=\frac{Z^2}{(4\pi/3)(R_0^3/e^2)10\tau}$$

where τ is the surface tension and Z the "atomic number" of the core.

The total energy gain corresponding to the equilibrium values $\tilde{\alpha}_2$, $\tilde{\alpha}_4$ is:

$$\Delta E_{tot}=-\frac{\hbar^4}{16\pi R_0^4\tau M^2}\left\{\frac{5}{2}\left(\sum_{k=1}^{N+P} x_{n_k,l_k}^2 I_{j_k,m_k,2}\right)^2\Big/(1-x) +\left(\sum_{k=1}^{N+P} x_{n_k,l_k}^2 I_{j_k,m_k,4}\right)^2\Big/(1-10x/27)\right\}. \quad (6)$$

The sums in (5) and (6) include all states occupied by extranucleons. These states are to be filled in accordance with the exclusion principle; furthermore, for the ground state of nuclei this filling must be made in such a way that the unperturbed energy of the extranucleons plus the energy gain [Eq. (6)] should be a minimum.

It might be observed that when the extranucleons are grouped in saturated orbits the energy gain (6) vanishes and spherical symmetry is restored. This is consistent with the initial assumption of a core formed by nucleons clustered in saturated orbits.

For medium weight nuclei and for a single extranucleon, $\tilde{\alpha}_4$ may be of the order of one-tenth of $\tilde{\alpha}_2$, giving thus a very small contribution to the total energy gain (6).

An interesting consequence of the asymmetry of the model is the partial removal of m degeneracy, so that the sublevels belonging to the same l and j are filled with pairs of protons (neutrons) with antiparallel total angular momenta. This reproduces one of the fundamental features of the j-j coupling shell model with no need of a special hypothesis.

As for spin and magnetic moments, the present model leads to a coupling of A. Bohr's B_{I}-type.[3] In even-odd nuclei the spin would thus be equal or smaller than the odd nucleon total angular momentum j, and, in the case of a single extranucleon, the magnetic moments would fall on the B_2 curves of Bohr's paper.

A paper on these subjects is in press and will appear in the *Nuovo Cimento*.

[1] J. Rainwater, Phys. Rev. **79**, 432 (1950).
[2] S. Gallone and C. Salvetti, Phys. Rev. **82**, 551 (1951).
[3] A. Bohr, Phys. Rev. **81**, 134 (1951).

The Beta-Spectrum of La^{141}*

ROBERT B. DUFFIELD, *University of Illinois, Urbana, Illinois*
AND
LAWRENCE M. LANGER, *Indiana University, Bloomington, Indiana*
(Received October 5, 1951)

THE beta-spectrum of La^{141} has been investigated using a lens spectrometer. This 3.7-hour activity was discovered by Joliot-Curie and Savitch[1] but was not recognized as an isotope of lanthanum until the experiments of Hahn and Strassmann.[2] From an aluminum absorption curve on the radiation, Katcoff[3] reported the beta end point to be 2.8 Mev and concluded that there was little or no gamma-radiation.

The La^{141} used in these experiments was made by slow neutron fission of uranium. One gram of U^{235} was irradiated for 30 minutes in the thermal column of the Los Alamos fast reactor. The 18-minute Ba^{141} was isolated and purified by precipitation as barium chloride. In the early experiments some difficulty was caused by small amounts of strontium activities carried along with the barium, so for the spectrometer samples the barium was reprecipitated ten times to get the necessary purity. The Ba^{141} so isolated was allowed to decay for 60 minutes, and the La^{141} which had grown in was precipitated as lanthanum hydroxide. This material was then mounted on a dural foil of thickness 0.7 mg/cm^2 to form the spectrometer sources. The active material had a thickness of 50 micrograms/cm^2, and autoradiographs showed the activity to be uniformly spread to within a factor of two over the entire area of the sources.

The Fermi plot of the data obtained is shown in Fig. 1. There is a high energy group with an end point at 2.43±0.03 Mev and a lower energy group with an end point at approximately 0.91 Mev. The relative intensity of the lower energy group is only about 5 percent. Its intensity remained unchanged during additional purification of the material so it appears unlikely that it was caused

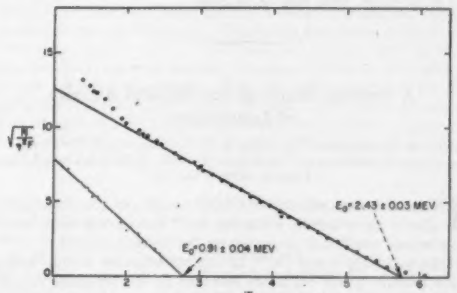

FIG. 1. Fermi plot of La^{141}.

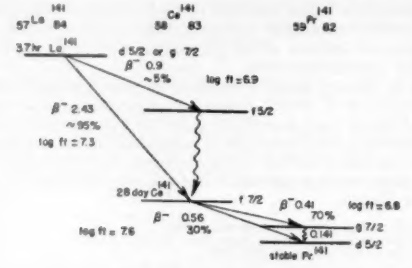

FIG. 2. Decay scheme of La^{141}.

by an impurity. The gamma-radiation from the source was examined with a sodium iodide crystal scintillation counter and pulse height selector. There appeared to be a gamma-ray of low intensity which decayed with a 3.7-hour half-life at approximately 1.3 to 1.6 Mev, but accurate measurements were not possible in the presence of the numerous gamma-rays from the small amounts of La^{140} and La^{142} unavoidably present in the sample. Beta-gamma coincidences, subject to the same difficulties, were observed at a rate which, compared to Sc^{46}, was consistent with a beta-branch of 5 percent in La^{141}. The only coincidences observed were with betas of energy less than 1.5 Mev.

After the decay of the La^{141}, the gamma-rays from the Ce^{141} formed in one of the spectrometer sources were examined with the scintillation counter. The 0.14-Mev gamma-ray was found, but no others were observed between 0.3 and 0.6 Mev.[4] If present, such gamma-rays could not have had intensities greater than 0.5 percent of that of the 0.14-Mev gamma-ray. Prompt beta-gamma coincidences were found, indicating that the 0.14-Mev gamma-ray follows a beta-branch.

These data are consistent with the decay scheme shown in Fig. 2. The levels shown for Ce^{141} are taken from the summary of previous work in the National Bureau of Standards Circular 499. The spin of the stable Pr^{141} has been experimentally determined[5] and the other spins have been chosen to agree with the beta-decay data and the nuclear shell model of M. G. Mayer.[6]

We are indebted to many members of the Los Alamos Laboratory for help with these experiments, particularly to Dr. B. E. Watt and Dr. B. C. Diven.

* This document is based on work performed under the auspices of the AEC at the Los Alamos Scientific Laboratory, Los Alamos, New Mexico.

[1] I. Joliot-Curie and P. Savitch, J. phys. et radium **9** (7), 355 (1938).

[2] O. Hahn and F. Strassmann, Naturwiss. **27**, 11 (1939); **30**, 324 (1942).

[3] S. Katcoff, *Radiochemical Studies: The Fission Products* (McGraw-Hill Book Company, Inc., New York, 1951), Paper No. 172, National Nuclear Energy Series, Plutonium Project Record, Vol. 9.

[4] For a summary of previous work on Ce^{141}, see *Nuclear Data* (National Bureau of Standards, Washington, D. C., 1951), Circular No. 499. A gamma-ray of 0.315 Mev has been seen by some investigators but not by others.

[5] H. E. White, Phys. Rev. **34**, 1397 (1929).

[6] M. G. Mayer, Phys. Rev. **78**, 16 (1950).

A Further Study of the Natural Activity of Lanthanum

R. W. PRINGLE, S. STANDIL, H. W. TAYLOR, AND G. FRYER
Physics Department, University of Manitoba, Winnipeg, Canada
(Received October 18, 1951)

IN an earlier communication[1] it was announced that an activity due to the naturally occurring La^{138} isotope had been found in a search which was prompted by the isobaric relation of La^{138} to the nuclei Ba^{138} and Ce^{138}. In this investigation a scintillation spectrometer of low resolution was used to test the possibility of a gamma-radiation associated with such an activity, and it was estimated that ordinary lanthanum gave rise to 0.7 quanta/sec-g

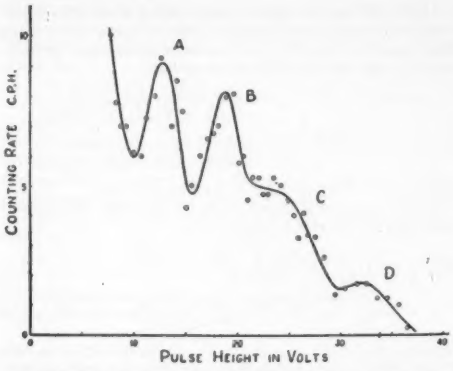

FIG. 1. Scintillation spectrometer pulse height distribution for the gamma-radiation of lanthanum, obtained with a five-channel kicksorter.

of energy 1.05 Mev although it was recognized that softer components might also be present. No search was made for the x-radiation which would be associated with a K capture process, but the absence of electrons or positrons suggested that the gamma-ray was to be associated with a K capture process to Ba^{138}.

A further study of this activity has recently been made with a scintillation spectrometer of improved resolution to determine whether the initial activity could have been due to some unsuspected short-lived contaminant, and also to investigate the possible complexity of the gamma-ray spectrum. The same highly purified 39 g La_2O_3 source was used, and surrounded a $\frac{3}{4}$-inch cube NaI-Tl crystal mounted on an E.M.I. 5311 photomultiplier. The spectrometer was enclosed in a 3-in. lead castle. The resulting pulse height distribution (Fig. 1), obtained with a Harwell Type 1074A five-channel kicksorter, gives three lines A, B, and D, attributed to gamma-rays of energy 535±15 kev, 807±15 kev, and 1390±30 kev in terms of the known gamma-radiation of I^{131} and Co^{60}, used for calibration. The feature at C corresponds to the 1390-kev gamma-ray Compton edge at approximately 1100 kev, and in the earlier low resolution experiment[1] had appeared to give the gamma-

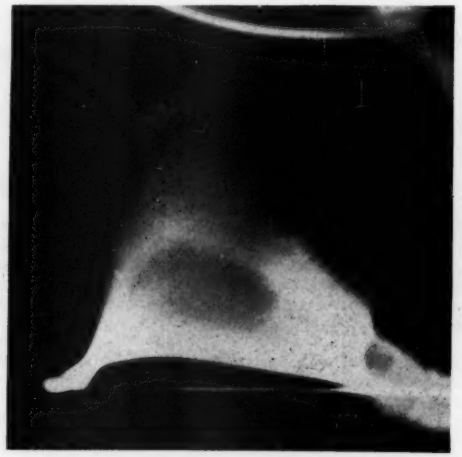

FIG. 2. Oscillogram of the scintillation spectrometer pulse height distribution for the gamma-radiation of lanthanum.

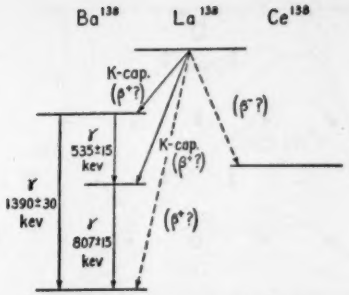

FIG. 3. Suggested disintegration scheme for La¹³⁸ (half-life 2.0×10^{11} years).

ray spectrum end point. The distribution of Fig. 1 has been confirmed by photography of the spectrometer pulse height distribution displayed on the screen of a Tektronix 511A oscilloscope. Figure 2 corresponds to a 40 hour exposure at f:4.5 with fast ortho film. The top line in this spectrum is due to the 1390-kev gamma-ray, and below we have a broad band corresponding to the Compton distribution marked C in Fig. 1, and two sharper lines at 807 kev and 535 kev. A halo is observed on the film due to light coming from the oscilloscope filament.

Use was made of the known variation of instrumental detection sensitivity with gamma-ray energy to estimate the relative intensities of the gamma-rays at 1390 kev, 807 kev, and 535 kev as 1:0.65:0.3, respectively. If we recognize that, within the limits of error for the measurement of the gamma-ray energy, the 1390-kev gamma-ray appears to correspond to a crossover transition, we are then led to a decay scheme of the form given in Fig. 3, in which the gamma-rays have been associated with a K capture process to Ba^{138}. A search for electrons or positrons with a thin window Geiger counter indicated that the number of these particles with energy greater than 100 kev is less than 0.2/sec-g of ordinary lanthanum. On the basis of the proposed gamma-ray transitions of Fig. 3 and their estimated relative intensities, the activity of La^{138} has been estimated at approximately 0.45 disintegrations/sec-g of ordinary lanthanum, corresponding to 0.6 gamma quanta/sec-g of all energies. In obtaining this latter figure a comparison of the observed gamma-activity was made to the gamma-activity of a known mass of potassium salt (giving rise to 3.3 gamma-quanta/sec-g.[2]

It remained to find evidence for the proposed decay scheme of Fig. 3 in the Ba x-rays which should accompany the K capture process. Figure 4 gives the result of a search for this radiation in which the height distribution of the scintillation spectrometer pulses was examined in the region of 30 kev. For calibration and comparison the 29-kev x-ray following the decay of I^{131} is also given in Fig. 4. We are led to the conclusion that an x-radiation of energy 32 ± 1 kev is associated with the decay of La^{138}, a value which corresponds better to the Ba x-ray line at 31.4 kev than to the 33.7 kev x-ray line of Ce which might arise if La^{138} decayed by beta-emission to Ce^{138}. In order to estimate the number of x-rays emitted, a much smaller sample (½ g) was used, and a value of approximately 0.4 x-rays/sec-g of ordinary lanthanum was found, in good agreement with the number to be expected on the basis of the proposed decay scheme. We conclude that the half life of La^{138} is approximately 2.0×10^{11} years.

Our thanks are due to the National Research Council of Canada for the support of this work.

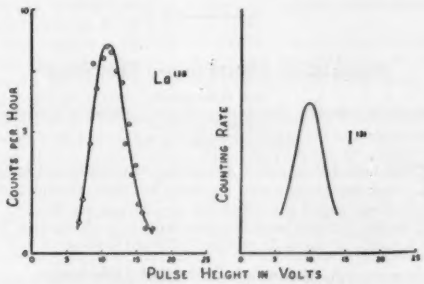

FIG. 4. Scintillation spectrometer pulse height distributions in the x-ray region, showing (left) the 32-kev radiation associated with the natural activity of lanthanum, and (right) the x-radiation associated with the decay of I^{131} for calibration.

[1] Pringle, Standil, and Roulston, Phys. Rev. **78**, 303 (1950).
[2] G. A. Sawyer and M. L. Wiedenbeck, Phys. Rev. **79**, 490 (1950).

Coincidence Studies in the Decay of La^{140}*

BEROL L. ROBINSON† AND LEON MADANSKY
Johns Hopkins University, Baltimore, Maryland
(Received October 5, 1951)

PREVIOUS work on the decay of La^{140} has been confined largely to energy determinations.[1–3] The coincidence experiments that have been reported were absorption measurements[4] performed with Geiger counters. Two different decay schemes have been proposed.[1,2] Therefore it might be of interest to investigate the decay of this isotope using the new techniques based on the proportional properties of scintillation detectors.[5]

A sample of La^{140} was obtained by neutron irradiation of lanthanum oxide in the Oak Ridge pile. Using a thick source (~0.1 g/cm²) a beta-gamma coincidence experiment was performed. The beta-ray detector has been described elsewhere.[6] The gamma-rays were detected in a 3-cm cube of NaI(Tl). This experiment indicated that the 1.60-Mev gamma-ray is in coincidence with the most energetic beta-rays. Gamma-gamma coincidence experiments showed that the 1.60-Mev and 0.82-Mev gamma-rays are coincident.

The angular correlation[6–8] between these two gamma-rays was also investigated. Again the 1.60-Mev quantum was detected in a 3-cm cube of NaI(Tl). One discriminator was set to accept those pulses in the unresolved "Compton plus photoelectric" peak of the pulse-height spectrum. The 0.82-Mev quantum was detected in a cleaved piece of NaI(Tl) having dimensions ½ in.×½ in.×½ in. The pulse-height spectrum from the thin crystal showed a strong photoelectric peak for the 0.82-Mev gamma. A second discriminator was set to accept this (0.82-Mev) photoelectric peak. The outputs of the discriminators were fed to a coincidence circuit. Parallel channels of fast amplifiers and a fast coincidence circuit served to reduce the accidental coincidence rate by requiring a fourfold coincidence. Some 2-3000 fourfold coincidences were counted at each of four angles. The results are shown in Table I.

We may begin to build a decay scheme by observing that the most energetic beta-ray branch of energy 2.26 Mev,[1] is followed by the 1.60-Mev gamma-ray; probably to the ground state of Ce^{140}. The softer beta-ray branches[1] must lead to the 1.60-Mev level through the emission of the 0.82-Mev gamma-ray, and to other levels of Ce^{140} through the emission of the other gamma-rays which have been observed.[1–3] We assume a partial decay scheme

TABLE I. Angular correlation of La^{140} gamma-rays.

	$W(90°)$	$W(120°)$	$W(150°)$	$W(180°)$
Experiment	1	1.016±0.027	1.146±0.031	1.147±0.033
Theory (see text for assumptions)	1	1.033	1.112	1.157

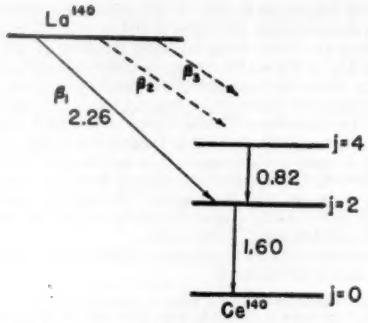

FIG. 1. Partial decay scheme of La^{140} with spins assigned on the basis of angular correlation experiments.

which is shown in Fig. 1. This scheme is similar to the decay schemes[8] of other odd-odd beta-emitters such as Co^{60}, Na^{24}, Cs^{134}, Sc^{46}, Y^{88}. On this assumption, the results of the angular correlation experiment may be used to assign spins to the 1.60-Mev and 2.42-Mev excited states of Ce^{140}. Table I shows the correlation function W to be expected with finite geometry for the assignment of spins 4, 2, 0 and quadrupole radiation.[7,8] This would be in accordance with the rule[9] for the spin of the first excited state of even-even nuclei.

There is some uncertainty[10] in the assignment of the 0.093-Mev gamma-ray in the decay scheme proposed by Beach *et al.*[1] If this gamma-ray does indeed occur between the 0.82- and 1.60-Mev gamma-rays, then the interpretation of the angular correlation experiment must be made on the basis of the triple correlation theory.[11] Further investigation of this isotope by means of precision coincidence spectrometry is necessary in order to determine the decay scheme unambiguously.

The authors are indebted to Professor George E. Owen of this university for helpful discussions of this problem.

* Work supported by the AEC.
† AEC Predoctoral Fellow, 1950–1952.
[1] Beach, Peacock, and Wilkinson, Phys. Rev. **76**, 1624 (1949).
[8] J. M. Cork *et al.*, Phys. Rev. **83**, 856 (1951).
[9] A. Wattenberg, Phys. Rev. **71**, 497 (1947); Bishop, Wilson, and Halban, Phys. Rev. **77**, 416 (1950).
[4] C. E. Mandeville and M. V. Scherb, Phys. Rev. **73**, 1434 (1948); R. K. Osborne and W. C. Peacock, Phys. Rev. **69**, 679 (1946).
[5] R. Hofstadter and J. A. McIntyre, Phys. Rev. **80**, 631 (1950).
[6] B. L. Robinson and L. Madansky, Phys. Rev. **84**, 604 (1951).
[7] D. R. Hamilton, Phys. Rev. **58**, 122 (1940).
[8] E. L. Brady and M. Deutsch, Phys. Rev. **78**, 558 (1950).
[9] M. Goldhaber and A. W. Sunyar, Phys. Rev. **83**, 906 (1951).
[10] Charles L. Peacock (private communication).
[11] Biedenharn, Arfken, and Rose, Phys. Rev. **83**, 586 (1951); M. E. Rose (private communication).

The Symmetry of Graphite

JOSEPH S. LUKESH
Knolls Atomic Power Laboratory, General Electric Company, Schenectady, New York*

(Received October 11, 1951)

THE writer has discussed the symmetry of graphite in an earlier communication.[1] At that time there was suggested a fundamental twofoldness of the c-axis. Evidence for this was presented in the form of a c-axis precession-type photograph of the zero-level of the reciprocal lattice. Because of the small size of the unit cell of graphite and the wavelength employed (Cu K_α), only the six reflections of the $10\bar{1}0$ group appeared on the film. Four of these were accompanied by satellite reflections which were symmetrically related among themselves by the operation of two perpendicular mirror planes rather than by rotation about the

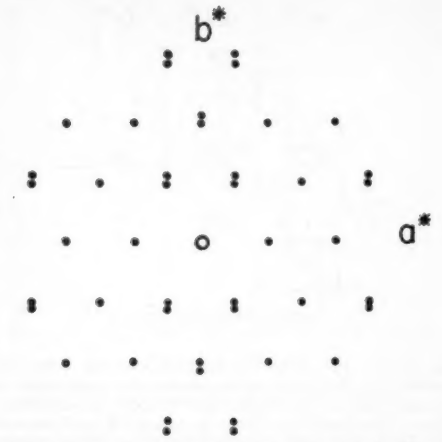

FIG. 1. Schematic representation of the c-axis, zero-level of the reciprocal lattice of graphite showing array of satellite reflections.

c-axis. The satellites were separated from the parent reflections by a distance one-fifteenth of the reciprocal a-axis.

Since there were insufficient data to permit interpretation of the satellite reflections when copper radiation was used, experiments are being conducted with Mo K_α radiation monochromatized with rocksalt. Although these experiments are incomplete, it is believed that the accompanying illustration, Fig. 1, of the c-axis, zero-level of the reciprocal lattice, drawn schematically, is of considerable interest, since it extends and confirms the earlier results.

The inner ring of Fig. 1 represents that part of the reciprocal lattice illustrated in Fig. 3(b) of the earlier communication.[1] As mentioned before, the satellites are separated from their parent reflections by one-fifteenth of the reciprocal a-axis (conventional hexagonal graphite cell). This separation is maintained as one proceeds out the reciprocal a-axis of the orthorhombic supercell. The separation doubles and then triples in the direction of the reciprocal b-axis. The intensities of the satellites are of the order of one-fiftieth that of the parents.

Work on the n levels is continuing. Preliminary results indicate that satellites associated with reflections on the first level lie on the opposite side of the parent reflection from those on the zero-level.

* The Knolls Atomic Power Laboratory is operated by the General Electric Company for the AEC.
[1] J. S. Lukesh, Phys. Rev. **80**, 226 (1950).

Polarization Effects in n-p Scattering*

DON R. SWANSON
Radiation Laboratory, Department of Physics, University of California, Berkeley, California

(Received October 15, 1951)

THE expected azimuthal asymmetry in a double scattering of high energy neutrons by protons has been calculated using the "half-exchange" n-p interaction of Christian and Hart.[1]

If the first incident beam and both targets are unpolarized, then the intensity of the twice-scattered neutrons is given by

$$J(\theta_1, \theta_2, \phi_2) = I_1(\theta_1) I_2(\theta_2) + Q_1(\theta_1) Q_2(\theta_2) \cos\phi_2.$$

$P_y(\theta_1, \phi_1 = 0) = [Q_1(\theta_1)/I_1(\theta_1)]$ is the component of polarization normal to the plane of the first scattering of the once scattered neutron beam. $Q_2 \cos\phi_2$ is the I_P defined by Wolfenstein.[2]

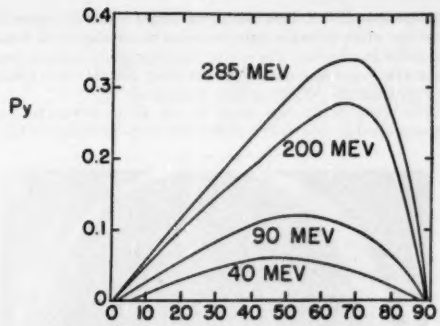

FIG. 1. The polarization $P_y(\theta, \phi=0) = [Q(\theta)/I(\theta)]$ as a function of scattering angle θ (c.m. system) for a single n-p collision at laboratory energies of 40, 90, 200, 285 Mev.

$(\theta_1, \phi_1=0)$ are the coordinates of the second target with the first target as origin and the incident beam as z-axis. (θ_2, ϕ_2) are the coordinates of the twice-scattered neutrons with the second target as origin and a z-axis defined by the two targets; ϕ_2 is measured from the plane of the first scattering. $I_1(\theta_1)$, $I_2(\theta_2)$ are the differential cross sections with polarization terms omitted.

Although polarization effects vanish in the Born approximation, the higher angular momentum states in a partial wave analysis can profitably be so calculated since interference terms with states of lower angular momentum (computed exactly) do not vanish. Accordingly, the calculations were carried out using the phase shifts of Christian and Hart in the $^3S_1$, $^3D_1$, $^3D_2$, and $^3D_3$ states, with all higher states included in the Born approximation.

Q_1 and Q_2 are equal (at the same angle and energy), provided that, in a partial wave analysis, all Wronskian conditions on the phase shifts of the coupled equations are satisfied. In Fig. 1, values of $Q(\theta)/I(\theta)$ are plotted as a function of center-of-mass angle for any single n-p scattering. One can see from the equations of Wolfenstein[3] that $Q(\theta)$ is antisymmetric about $\pi/2$ for odd or even parity states alone (hence zero at $\pi/2$), but symmetric for odd-even interference terms. Detection of azimuthal asymmetry at $\pi/2$ would therefore indicate the presence of both odd and even terms, and so disprove the "even" exchange hypothesis. In the case of p-p scattering, the $\pi/2$ point should of course give no polarization regardless of the assumed interaction since the even triplet states are not present.

It is of interest to note that almost the entire energy dependence of the polarization $Q(\theta)/I(\theta)$ lies in the differential cross section $I(\theta)$. This behavior is not entirely surprising since $Q(\theta)$ is determined principally by the $^1S-^3D$ interference terms; the S phase shifts decrease and the D increase with increasing energy apparently in such a way as to leave $Q(\theta)$ almost independent of energy between 90 Mev and 285 Mev.

With energies of 220 Mev and 160 Mev for the two scatterings, respectively, the ratio $J(\phi_2=0)/J(\phi_2=\pi)$ is 1.12 ± 0.03 at $\theta_1=65°$, $\theta_2=60°$. The ±0.03 is based on an estimate of the accuracy to which the phase shifts are known.

Although the problem has been formulated for two scatterings of a neutron beam, the first scattered beam could just as well have arisen from a (p,n) reaction. This follows from the equality of polarization of the two scattered particles and from the invariance of the scattering amplitude under the substitution $\theta \to \pi-\theta$ and $\phi \to \phi+\pi$ because of the exchange dependence assumed. A similar argument for the second scattering shows that the scattered intensity of the protons at any angle is the same as that of the neutrons. In an accompanying letter, Wouters[4] reports an experiment in which a beam of polarized neutrons was produced by a (p,n) reaction in LiD and detected by means of an n-p scattering. The resulting asymmetry agrees in sign and order of magnitude with the foregoing calculations. The experiment was also carried out with LiH as first target; for this case no significant asymmetry was detected.

A more refined interpretation of the results could be obtained by calculating the polarization from the $D(p,n)$ reaction, here assumed equivalent to a scattering of protons by free neutrons. The failure to detect asymmetry with the LiH target does not seem particularly disturbing since scattering from neutron bounds in Li^7 might reasonably be expected to yield less polarization than would scattering from free neutrons, sufficiently less to escape detection in Wouters' experiment.

The experimental results, although consistent with the "even" theory, are not of sufficient precision to allow one on this basis to rule out interaction in the odd triplet states. This point is under further investigation in the hope that a quantitative argument can be made.

The author wishes to thank Professor R. Serber, Dr. R. S. Christian, and Dr. J. V. Lepore for helpful discussions and suggestions.

* This work was performed under the auspices of the AEC.
[3] R. S. Christian and E. W. Hart, Phys. Rev. **77**, 441 (1950).
[3] L. Wolfenstein, Phys. Rev. **76**, 541 (1949).
[3] L. Wolfenstein, Phys. Rev. **75**, 1664 (1949).
[4] L. Wouters, Phys. Rev. **84**, 1069 (1951).

Detection of the Azimuthal Polarization of the n-p Interaction at 150 Mev

L. F. WOUTERS
Radiation Laboratory, Department of Physics, University of California, Berkeley, California
(Received October 15, 1951)

A DOUBLE-SCATTERING experiment for the purpose of measuring the polarization due to the noncentral n-p interaction at high energy is in progress at this laboratory. The azimuthal effect appears notably as a change in the right/left ratio of second scattered flux intensity as the scattering angles are altered; the concurrent paper[1] presents the theoretical predictions concerning the magnitude of the effect in an ideal experiment.

The principal problem encountered in a double-scattering experiment in the 150-Mev region is the large accidental background in the azimuthal counter array caused by single scattered particles. In order to circumvent this, the first scattering (p,n) is performed inside the 184-inch cyclotron vacuum tank, utilizing the excellent neutron collimating features of the concrete shielding. The "neutron" target is a cast LiD block, which can be moved along the center line of the emergent neutron beam by means of a sliding probe. It thus intercepts the circulating proton beam at various radii corresponding to a range of first scattering angles of 0° to 45°. This geometrical arrangement has the advantage that the emergent neutron beam has almost the same energy at any angle; it also makes possible normalizing the system to 0°, where clearly no polarization is to be expected. LiH has also been used to show that the predominent contribution to the polarization effect is indeed a result of the relatively "free" deuteron neutron.

The second scattering (n,p) is performed by the orthodox carbon-paraffin difference method; the proton detectors consist of coincidence scintillation counter telescopes subtending a wide aperture (~8°). Four such telescopes detect the second scattered particles at the azimuthal angles 0° (right), 90° (up), 180° (left), and 270° (down). The scattering angle for all four is fixed at 30°, the theoretically optimum angle, throughout the experiment. Thus, the external second scattering apparatus operates under essentially constant conditions, and the independent variable is the first scattering angle.

The theory of the concurrent paper predicts no polarization at 45° lab angle, with a maximum asymmetry at 30°; quantitatively, this is expressed as a right/left second-scattered flux ratio of 1.12 or, as is more convenient, 12 percent polarization. Experimentally,

account must be taken of the masking caused by Li neutrons; a rough yield measurement indicates that a multiplying factor of two to three should be applied to the measured numbers.

The results exhibit a reasonably unique pattern of behavior; various "false" polarization mechanisms have been hypothesized, but none can entirely match this pattern:

(1) The azimuthal flux distribution is consistently sensitive to changes in first scattering angle and scatterer material.

(2) No consistent changes appear in up/down ratios outside probable error for any scatterer.

(3) The carbon (second-scatterer) data show no angular dependence in right/left ratio for either LiD or LiH; thus there exists an experimental situation in which no polarization is observed by the adopted rules of procedure and analysis.

(4) The LiD first-scatterer, paraffin second-scatterer data exhibit a consistent increase in right/left ratio from 0° to 30°, and a decrease from 30° to 45°. Calculated from the change in the paraffin-carbon difference, the former amounts to an observed polarization of 6.5 percent (±2.4 percent) and the latter change corresponds to 7.5 percent (±4.5 percent).

(5) The LiH data show no comparable changes in left/right ratios, indicating that at least the major part of the effect must be attributed to the *D* neutrons.

These results thus correspond to an "ideal" polarization of 15 percent to 20 percent; they are interpretable as showing the existence of noncentral forces in the high energy n-p interaction. Considering the probable errors, they do not disagree with the theoretically calculated magnitude.

Extensive improvement of the method is underway with the intent of more closely tracing the polarization curves in greater detail.

The author wishes to thank Professors E. O. Lawrence and R. L. Thornton for their suggestions and continued interest. This research was performed under the auspices of the AEC.

[1] Don R. Swanson, Phys. Rev. **84**, 1068 (1951).

Neutron Stars in Krypton*

J. K. Bøggild† and F. H. Tenney
University of Rochester, Rochester, New York
(Received October 11, 1951)

CONTINUING the preliminary survey of neutron stars in various gases,[1] approximately 200 neutron stars have been observed in an 8-inch Wilson cloud chamber filled with krypton to about one atmosphere of pressure. The neutrons were produced in the forward direction by 240-Mev protons bombarding Cu or Be targets in the Rochester cyclotron. The cloud chamber was placed about 25 feet from the target behind 9 feet of copper collimation which passed a neutron beam of circular cross section 2¼ inches in diameter. The energy spectrum of the neutron beam from a Be target had its maximum at about 190 Mev with a width of approximately 70 Mev at half maximum.[2]

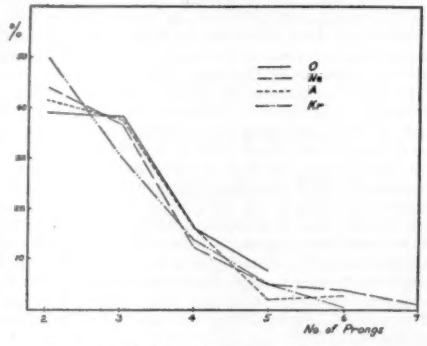

FIG. 1. Percent of stars observed *vs* number of prongs.

The prong distribution found for the Kr stars together with those previously reported for O, Ne, and A[1] are presented in Fig. 1,

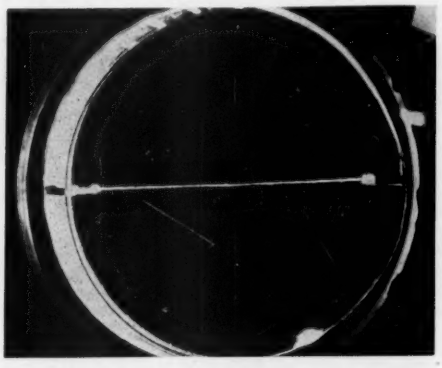

FIG. 2. 4-prong neutron star in krypton.

according to which the distribution for the three lighter gases is rather similar, whereas the relative number of stars with two prongs is found to be considerably higher in Kr.

An attempt to obtain a classification of the ejected charged particles has been made by a combined judgment of the track width and density and the number of delta-rays. Light or medium ionizing tracks with few ($\lesssim$2) delta-rays per inch were called protons, charge$=|e|$. Light or medium ionizing tracks with many ($\gtrsim$4) delta-rays per inch and heavily ionizing tracks were called alphas, charge$=2|e|$. Recoiling residual nuclei were not counted as either protons or alphas. For example, the 4-prong Kr star in Fig. 2 would be treated as 2 protons, 1 alpha, and a recoil. On this basis the alpha to proton ratios found for Kr and, for comparison, those previously found for O, Ne, and A are as follows:

	2-prong stars	3-prong stars	4-prong stars
O	2.68	1.57	2.82
Ne	2.14	1.35	1.30
A	0.88	0.98	0.84
Kr	0.11	0.29	0.21

The Kr ratios bear out the downward trend with increasing atomic number suggested by the corresponding ratios found for O, Ne, and A.

The alpha to proton ratio for star particles ejected in reactions produced by slow negative π-mesons is reported by Menon, Muirhead, and Rochat,[3] who for the heavy nuclei in photographic emulsions found a value of 0.3 and for the light group of nuclei 1.55 (or 1.0 by a more indirect method). The tendency in our table is in fair agreement with these results; however, the 2-prong stars show rather high values in the light gases and a low value in Kr. A reasonable explanation would be that one must expect that the low energy tail of the neutron distribution will induce more (n,α) than (n,p) reactions in light elements, whereas the yield of (n,α) reactions by low energy neutrons will be small in heavy elements due to the high potential barrier. For 3- and 4-prong stars the contribution of low energy neutrons is likely to be smaller, and here the agreement with the emulsion values is quite good. The relatively high ratio for 4-prong O stars can be understood on the basis of an alpha-particle structure for the O nucleus.

On the basis of all stars analyzed we find the following alpha to proton ratios: O—2.1, Ne—1.4, A—0.9, Kr—0.21.

* This work was supported by the AEC.
† Now at the Institute for Theoretical Physics, Copenhagen, Denmark.
[1] J. K. Bøggild and F. H. Tenney, Phys. Rev. **82**, 307 (1951).
[2] Guernsey, Mott, and Nelson (private communication of preliminary data).
[3] Menon, Muirhead, and Rochat, Phil. Mag. **41**, 583 (1950).

Beta-Gamma Angular Correlation in the Decay of I^{126} and K^{42}

DONALD T. STEVENSON AND MARTIN DEUTSCH
Department of Physics and Laboratory for Nuclear Science and Engineering, Massachusetts Institute of Technology, Cambridge, Massachusetts
(Received October 19, 1951)

WE have measured the beta-gamma angular correlation in the decay of I^{126} and of K^{42}. The apparatus used and the treatment of the data have been described in a previous paper.[1]

I^{126} was prepared in the MIT cyclotron by a $(d,2n)$ reaction on enriched Te^{126}.[2] The iodine was separated from the tellurium by distillation from nitric acid. Any short-lived iodine isotopes were allowed to decay before the beginning of the experiments. It was assumed that the 8-day I^{131} present was negligible since the target material contained only very small amounts of Te^{130}. Thin sources were prepared by drying a drop of radioactive NaI solution in an atmosphere of nitrogen. The average thickness of the sources used was less than $\frac{1}{2}$ mg/cm^2. Some loss of source activity was noted during the experiment which presumably resulted from oxidation of iodide to free iodine. Sources were changed and the spectrometer decontaminated frequently to reduce errors introduced by this phenomenon. Figure 1 shows the observed anisotropy of the beta-gamma coincidence rate, $E(180°)$, as a function of beta-ray energy. E is the excess of the coincidence rate at 180° over that at 90°, corrected for the finite resolution of the apparatus as described in reference 1.

K^{42} was obtained by neutron irradiation of potassium in the Brookhaven reactor.[2] Sources were prepared by evaporation of active KCl in vacuum, and were less than 2 mg/cm^2 thick. The anisotropy found for beta-rays of 1.23 Mev was $E=-0.055 \pm 0.024$, and at 1.55 Mev $E=-0.065 \pm 0.023$. These results are not incompatible with that of Beyster and Wiedenbeck[3] who reported an integral anisotropy of about -0.07.

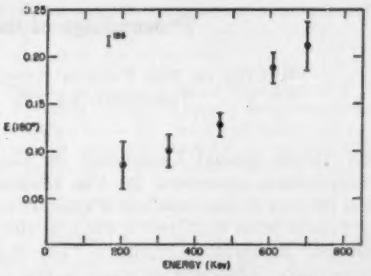

FIG. 1. Beta-gamma angular correlation of I^{126} as a function of beta-ray energy.

The decay schemes of Rb^{86}, I^{126}, and K^{42} are very similar.[4] The shapes of the high energy spectra all indicate $\Delta J=2$, yes, with the single matrix element B_{ij} of the tensor or the axial vector interaction. Since the even-even ground states are probably $J=0$, even, the beta-active states must be $J=2$, odd. The low energy beta-spectra of Rb^{86} and I^{126} which give rise to the observed coincidences have very nearly allowed shapes.[5,6] Fuchs[7] has been able to fit both the spectrum shape and our results[1] on the angular correlation of Rb^{86} by assuming $J=2$, even, for the excited state of Sr^{86} and a combination of tensor interaction matrix elements B_{ij} and $\int \beta\alpha$ for the low energy spectrum. The great similarity of the angular correlation in I^{126} (Fig. 1) to that of Rb^{86} makes it appear probable that the same terms will explain both decays. The shape of the low energy spectrum of K^{42} is not known. In view of the lower atomic number and higher beta-energy the observed angular correlation may be consistent with a transition of the same type as Rb^{86} and I^{126}.

* This work has been supported in part by the joint program of the ONR and AEC.
[1] D. T. Stevenson and M. Deutsch, Phys. Rev. **83**, 1202 (1951).
[2] Obtained from the Isotopes Division, AEC.
[3] J. R. Beyster and M. L. Wiedenbeck, Phys. Rev. **79**, 728 (1950).
[4] K. Way *et al.*, *Nuclear Data* (National Bureau of Standards Circular 499, 1950); M. L. Perlman and G. Friedlander, Phys. Rev. **82**, 449 (1951); Mitchell, Mei, Malenschen, and Peacock, Phys. Rev. **76**, 1450 (1950).
[5] H. R. Muether and S. L. Ridgeway, Phys. Rev. **80**, 750 (1950).
[6] C. S. Wu (private communication).
[7] Morton Fuchs, thesis, University of Michigan (1951).

Proceedings of the American Physical Society

Minutes of the Fourth Annual Conference on Gaseous Electronics, Sponsored by the Division of Electron Physics

THE fourth annual Conference on Gaseous Electronics, sponsored by the Division of Electron Physics of the American Physical Society, was held on October 4, 5, and 6, 1951, at the General Electric Research Laboratory "The Knolls" at Schenectady. Abstracts of some of the papers there presented are printed hereunder. The first of these abstracts belongs, however, to the 1950 Conference, from the Minutes of which (Physical Review 82, 566 (1951)) it was inadvertently omitted.

R. L. Sproull, *Secretary*
Division of Electron Physics
Cornell University
Ithaca, New York

E6. The Use of an Arc-Cathode as a Source of Emission for High Power Tubes.*† P. H. Kafitz, D. H. Goodman, and D. H. Sloan, *University of California, Berkeley.*—The metal vapor arc has been investigated as an electron source for high power, high frequency vacuum tubes. In the arc-cathode tube, a trigger spark near the cathode provides copper vapor for the main high frequency discharge that is created and maintained by the rf fields in the grid-cathode region. When the grid is positive, many of the electrons accelerated toward the grid pass on through to the anode, thus traversing a region that is at high vacuum. Condensation of the neutral metal vapor and a high degree of ionization in the arc plasma help to preserve the high vacuum condition for a considerable time. One tube, pump-operated as a self-excited oscillator, developed 100 kilowatts at 100 megacycles on pulsed operation. The peak current drawn from the discharge plasma was 3 amp/cm² of grid area. Direct current tests indicate that the maximum emission may exceed this by a factor of 10 to 100. Pulse lengths up to 40 microseconds have been obtained.

* Part of a thesis to be submitted by the first of the authors to the University of California in partial fulfillment of the requirements for the degree of Doctor of Philosophy. This work was supported by the Air Materiel Command, U. S. Air Force.
† Presented at the 1950 Conference on Gaseous Electronics.

A2. Attachment of Thermal Electrons in Oxygen. Manfred A. Biondi, *Westinghouse Research Laboratories.*—Microwave techniques[1] are used to measure the removal of electrons in oxygen. At sufficiently high gas pressures and low electron densities, attachment of electrons to oxygen molecules becomes the dominant removal process. The cross section for attachment of thermal electrons (0.04 ev average energy) is found to be $Q_a = 1.2 \times 10^{-22}$ cm², independent of pressure over the range 8–25 mm Hg. This value agrees with the calculated cross section for radiative capture of electrons. On the other hand, it disagrees with the Bloch-Bradbury theory of electron capture by excitation of molecular vibration[2] which predicts a cross section of 10^{-19} cm² for thermal electrons in O_2. It is hoped that future studies of the attachment in O_2 as a function of electron energy will resolve this discrepancy.

[1] M. Biondi, Rev. Sci. Instr. 22, 500 (1951).
[2] F. Bloch and N. Bradbury, Phys. Rev. 48, 689 (1935).

A3. Ionization and Attachment in Oxygen. Melvin A. Harrison and Ronald Geballe, *University of Washington.*—Ionization currents have been measured in oxygen using plane-parallel electrodes separated as far as four centimeters. The curves thus obtained cannot be fitted by assuming that ionization alone takes place. If the effects of attachment are also considered, good fits are possible. Values for the coefficients of both of these processes have been determined for E/p in the range from 30 to 75 volts/cm/mm. The first Townsend coefficient behaves normally and does not exhibit the sudden dropping-off found by K. Masch[1] for $E/p < 40$, which probably was due to the increasing importance of attachment. Furthermore, an appreciable attachment probability persists to considerably larger E/p (>60) than indicated by previous results,[2,3] which may have been obscured by ionization. An explanation of the process now becomes possible in terms of atomic rather than molecular ions.

[1] K. Masch, Arch. f. Elektrotechnik 26, 587 (1932).
[2] N. Bradbury, Phys. Rev. 44, 883 (1933).
[3] R. H. Healey and J. W. Reed, *The Behavior of Slow Electrons in Gases* (Amalgamated Wireless, Limited, Sydney, 1941).

A4. Probability of the Formation of He_2^+, Ne_2^+, and A_2^+ from Excited Atoms. J. A. Hornbeck, *Bell Telephone Laboratories.*—Rough measurements of the probability of forming molecular ions in the noble gases have been obtained from studies[1] of the pulsed Townsend discharge in which the pressure is varied at constant E/p_0, the ratio of electric field to gas pressure. Equations based on the established formation process[2] when fitted to the data give values of two parameters; first, the ratio η_{exc}/η_i, where η_{exc} and η_i are first Townsend coefficients, i.e., the number of excitations (of the proper kind) and ionizations/volt/electron, and second, the product $\tau\sigma$, where τ is a mean lifetime before decay by radiation of the several excited atomic states involved and σ is a mean cross section for the process. The results are: $\tau\sigma \times 10^{22}$ cm² sec = 0.5 in helium, 0.5 in neon, and 0.9 in argon; the order of magnitude of η_{exc}/η_i is 0.2 in helium at $E/p_0 = 14$ volts/cm × mm Hg, 0.2 in neon at $E/p_0 = 15$, and 1 in argon at $E/p_0 = 30$. These results indicate that molecular ions should cause observable deviations from the Paschen breakdown (similitude) law; also dc measurements of η as usually defined should show a pressure dependence at low E/p_0.

[1] J. A. Hornbeck, Phys. Rev. 83, 374 (1951).
[2] J. A. Hornbeck and J. P. Molnar, Phys. Rev. (to be published).

A5. Positive Ions in the Afterglow of a Low Pressure Helium Discharge.* Arthur V. Phelps,† *Massachusetts Institute of Technology.*—The positive ions responsible for the ambipolar diffusion coefficient for helium reported by Biondi and Brown[1] have been identified as He^+ ions. The positive ions which diffuse to the walls were studied with a mass spectrometer. The average electron density was determined from the shift in the resonant frequency of the microwave cavity. As the pressure of the helium was increased, the dominant ion in the afterglow was found to change from He^+ to He_2^+. The rate of conversion of He^+ ions to He_2^+ ions was estimated from the electron density decay data to be about one-third the value predicted by Bates.[2] These experiments show that there is good agreement between the theoretical predictions and recent experimental determinations of the mobility of the He^+ ion in helium. The dominance of the He_2^+ ion at the higher pressures lends support to the proposal[2] that

the He_2^+ ion is responsible for the large electron-positive ion recombination coefficients observed by Biondi and Brown.

* This work has been supported in part by the Signal Corps, the Air Materiel Command, and ONR.
† Now at Westinghouse Research Laboratories, East Pittsburgh, Pennsylvania.
[1] M. A. Biondi and S. C. Brown, Phys. Rev. 75, 1700 (1949).
[2] D. R. Bates, Phys. Rev. 77, 718 (1950).

A6. The Formation and Decay of Metastable Mercruy Molecules. A. O. McCoubrey, *Westinghouse Research Laboratories.*—The program on the persistent band fluorescence of mercury vapor[1] has now achieved the point where the observations can be classified in a physically interpretable manner. The following results have been obtained: (a) The ratio of intensity of the visible band (4850A) to that of the ultraviolet band (3350A) is essentially proportional to the square of the vapor density N. (b) Both bands decay according to a curve which is characterized by two time constants. The longer of these has been studied quite extensively; it is found to obey a relationship of the type $1/\tau = A/N + B + CN^2$. (c) By the use of two different enclosure geometries the diffusion contribution has been separately evaluated; the collision radius obtained therefrom is 7A. These results may be interpreted according to the following picture. Incident 2537A radiation creates $^3P_1$ atoms which upon collision are converted to the $^3P_0$ metastable state. The metastable atoms then combine chemically with normal mercury atoms to form the $^3O_u^-$ state of Hg_2. This state decays both spontaneously by the emission of the ultraviolet band and by collision-induced radiation of the visible band.

[1] Phys. Rev. 82, 567 (1951); 76, 1259 (1949).

B1. Preliminaries on Photoionization in N_2 and O_2 in the Vacuum Ultraviolet.* G. L. Weissler and Nathan Wainfan, *The University of Southern California.*—Using a normal incidence vacuum spectrograph as a monochromator, radiation from a constant intensity light source is passed through an exit slit into a chamber which contains at low pressures either N_2 or O_2. Photoionization produced in these gases is measured as a function of wavelength with a low voltage ionization chamber. Energy measurements of the radiation passing through the exit slit are made with a sensitive thermocouple, and the number of photons per second entering the ionization chamber is determined. From this and the ions collected the photoionization cross sections can be obtained. A detailed description of the apparatus will be given together with preliminary results.

* The aid of the ONR is gratefully acknowledged.

B2. Dissociative Attachment of Electrons to Diatomic Molecules. T. Holstein, *Westinghouse Research Laboratories.*—According to the Franck-Condon principle, the reaction $XY + e \rightarrow X + Y^-$ proceeds in two stages. The electron is first captured by the neutral molecule without alteration of the positions and velocities of the nuclei; the resultant XY^- complex then dissociates into the final products. Now, in the region where the potential curve of XY^- lies above that of XY, the molecular ion is unstable towards autodetachment. Hence, the cross section Q for the reaction is equal to the cross section Q_e for the formation of XY^-, multiplied by the probability e^{-T_S/τ_A} that XY^- dissociate without autodetachment. (Here, τ_A is the autodetachment lifetime and T_s the "stabilization" time required for the nuclei to reach the crossing point of the XY and XY^- potential curves.) Q_e itself is readily obtained in terms of τ_A from the "one-level dispersion" formula often employed in the theory of nuclear reactions. The final expression for Q contains τ_A which, for the present, we treat as a phenomenological constant. Values of τ_A required to effect agreement with experiment, e.g., for the case of O_2, are $\sim 10^{-13}$ sec, which, though somewhat smaller, is still of the order of magnitude of auto-ionization times computed for light atoms.[1]

[1] Ta-You Wu, Phys. Rev. 66, 291 (1944).

B4. Cleanup of Helium in an Arc Discharge. M. J. Reddan and G. F. Rouse, *National Bureau of Standards.*—The results of an investigation of the cleanup of helium gas in an arc discharge by a negatively charged tantalum wire probe were reported earlier. More recent studies have been made with a tube in which the probe is a nickel cylinder. A particularly important feature of the tube design is that the amount of gas recoverable from the probe can be clearly distinguished from that which is recoverable from parts of the tube near the probe. The following statements apply to a nickel probe: 1. Severe sputtering of nickel onto the glass wall of the tube occurs at probe potentials as low as 100 volts. 2. Over-all recovery of gas has averaged about 85 percent. 3. Heating the sputtered layer to 325°C for three hours drives off gas to about 70 percent of the total recovered. 4. Heating the probe to 825°C for 1.5 hours yields gas to about 30 percent of the total recovered. 5. Using the number of atoms recovered from the probe as a measure of the number trapped in the probe, one finds that the rate of cleanup increases with probe voltage in a manner quite like that reported previously for tantalum. At a probe potential of about 100 volts, three out of every ten thousand ions which strike will stick in the probe.

B5. Tritium Tracer Experiment for Investigating Gas Cleanup in Hydrogen Thyratrons. Sol Schneider, *Signal Corps Engineering Laboratories.*—As a means of studying the cleanup of hydrogen in pulse-operated thyratrons, standard hydrogen thyratrons are filled with a 1 percent tritium (H_2^3), 99 percent hydrogen (H_2^1) mixture to normal pressure (600 microns). These tubes are then operated in a line-type pulse modulator circuit. At various stages during the life of the tube, from initial filling to destruction, the tubes are disassembled and the parts are checked for activity using an "inside" beta-counter and autoradiographs. The "inside" beta-counter is calibrated against standard beta-sources, and the activity can be interpreted in terms of quantities of tritium. The activity on the surfaces of the parts of the tube as indicated by the "inside" beta-counter neglects the variations in distribution of the tritium over the surface of the parts. The autoradiographs, however, give detailed pictures of the distribution of tritium on any surface. Examination of autoradiographs has indicated considerable tritium on those surfaces which are covered with evaporated materials, subjected to heavy ion bombardment, or are in a strained state. Examination of the distribution of tritium with respect to depth for both the glass and metal parts are now being made.

C1. Ambipolar Diffusion of Electrons and Ions into a Cylinder. Joseph Slepian and L. S. Frost, *Westinghouse Research Laboratories.*—Previously reported experiments in ambipolar diffusion done under the direction of the senior author gave results at variance with the behavior expected from Schottky's theory of ambipolar diffusion. This paper extends the study and shows how experimental data and theoretical predictions are brought into agreement in the absence of a magnetic field and under suitable experimental conditions. The causes of the previous disagreement are shown to be (1) operation of the arc at a voltage above normal, resulting in reduced rates of decay of ion density; (2) the presence of probe currents due to electron emission from the probe; (3) insufficient ion current densities in the early experiments to assure equal ion and electron densities, as required by the theory; and (4) an extension to the theory necessary because of the appreciable size of the ionic mean free path relative to the tube radius. New experimental data is pre-

sented illustrating all these considerations, and equations are derived governing causes (3) and (4).

C2. Energies of Positive Ions in a Cold-Cathode Discharge in a Magnetic Field.* JOHN BACKUS AND NORMAN E. HUSTON, *The University of Southern California.*—Studies are being made of the energy distribution of positive ions in a cold-cathode discharge in a strong magnetic field. The discharge is of the Philips ionization gauge type previously described[1] operating at about 0.3 amp at 800 volts in a magnetic field of 2000 gauss, using copper cathodes in argon gas at about 1–3 microns pressure. The discharge is shut off periodically for approximately 50 microseconds by means of a pulsing unit to be described, and the ion current to the cathode during the off period is observed on an oscilloscope. Analysis of this current shows that the ions flowing to the cathode after the discharge is extinguished have an approximately Maxwellian distribution with a temperature equivalent of 0.8 to 1.3 volts, depending on the discharge current.

* Supported by the Research Corporation and ONR.
[1] A. Guthrie and R. K. Wakerling, *Electrical Discharges in Magnetic Fields* (McGraw-Hill Book Company, Inc., New York, 1949), Chapter 11.

C3. On the Discharge Mechanism in Hot-Cathode Rare-Gas Diodes, Especially with Negative Arc Drop. G. MEDICUS AND G. WEHNER, *WCESD, Wright Field.*—By decreasing the work function of the anode (evaporation of Ba) and at the same time increasing the work function of the cathode (indirectly heated Ta cathode), the voltage-current characteristic is shifted so that regions of negative dc voltage drop appear. Emf's of 0.8 volt at amperages in the order of 0.5 amp were obtained in Xe of about 200μ Hg pressure. In this case about 0.3 percent of the cathode heating power was directly transformed into electrical energy. The effect is brought about by the electrostatic field existing between the high work function cathode and the low work function anode short circuited outside, which is superimposed to the space charge field of the discharge. The electrons emitted from the cathode have a potential energy with respect to the anode that is roughly equal to the work-function difference between cathode and anode. Otherwise such a emf discharge in essence behaves like a normal low voltage arc discharge with the characteristic potential maximum between the electrodes.

C5. Reliability of Probe Measurements in Hot-Cathode Gas Diodes. GOTTFRIED WEHNER AND GUSTAV MEDICUS, *Wright Field.*—Probe measurements in gas discharges can give quite erroneous results owing to changes in the work function ϕ of the probe that may be in the same order of magnitude as the plasma electron velocities or as the plasma potentials to be measured. The different influences which determine the ϕ-change (oxidation, contamination with barium compounds, sputtering and evaporation from the probe) were separated by studying several diodes with different kinds of cathodes. The probe characteristics were recorded by an *X-Y* plotter which reduced the recording time to some seconds per run. In oxide or barium cathode tubes the work function of a tungsten probe near the cathode decreases so fast that reliable results can only be obtained if the time between measuring and cleaning procedure is less than some seconds. In the anode region the influence of oxygen released from an oxide cathode predominates (ϕ-increase) because most of the barium compounds return to the cathode after becoming ionized. With the proper probe cleaning procedure no deviation from the Maxwellian velocity distribution of the plasma electrons could be found, even in oxide cathode tubes (pressure 150μ) with the probe only ten mm away from the cathode and over a range of four powers of ten in probe current.

C7. Magneto-Ionic Resonance in Microwave Cavities. BENJAMIN LAX, *Air Force Cambridge Research Center.*—The complex resonant frequency ω of a cavity containing a non-uniform plasma in a magnetic field can be calculated exactly from

$$\omega^2-\omega_\mu{}^2=j\frac{\omega}{\epsilon_0}\frac{\int \mathbf{J}\cdot\mathbf{E}_\mu{}^*dv}{\int \mathbf{E}\cdot\mathbf{E}_\mu{}^*dv}$$

if **E**, the perturbed electric field, and **J**, the current density in the magneto-ionic gas given by the product of the conductivity matrix and **E**, are known. The subscript μ indicates unperturbed quantities. For the first-order effect of the plasma take $\mathbf{E}\approx\mathbf{E}_\mu$. Applying this to a cylindrical cavity in an axial magnetic field gives for the TE_{111} mode a split resonance. The frequency shifts $\Delta\omega_0\sim 1/(\omega_\mu+\omega_b)$ and $\Delta\omega_e\sim 1/(\omega_\mu-\omega_b)$ are respectively those of the ordinary and extraordinary modes of the cavity, each with the same proportionality factor, for a given plasma density and gyromagnetic frequency ω_b. Experimental verification of the theoretical results will be presented.

D2. High Frequency Discharge at Low Pressures Characterized by Secondary Electron Resonance.* ALBERT J. HATCH AND H. BARTEL WILLIAMS, *New Mexico College of A. and M. A.*—Gas discharge characteristics have been studied at frequencies from 30 to 90 mc/sec using flat electrodes of aluminum, copper, and silver-plated copper at separations of one to four cm inside a bell jar. Pressures have been held at one micron Hg or less. For each spacing a cut-off frequency is observed below which it is impossible to obtain breakdown with field strengths of several hundred volts/cm. Double values of breakdown field strength are observed above cutoff, with lower values of 15 to 20 volts/cm being observed in certain cases. The cutoff and double breakdown values define a breakdown region not previously reported. This type of breakdown observed first by Gutton[1] in 1924 appears to be initiated by multiplication of secondary electrons at the electrode surfaces, these electrons oscillating between the electrodes in approximate resonance with the applied high frequency potential. Theories reported by Alfven and Cohn-Peters[2] and Gill and von Engel[3] to describe this type of discharge have not been very successful. A new approach to the theory has been developed which gives promising correlation with observations.

* Supported by the Navy Bureau of Ordnance.
[1] C. Gutton, Compt. rend. **178**, 467–470 (1924).
[2] H. Alfven and H. J. Cohn-Peters, Arkiv f. Mat., Astron. Fysik **31**, 1 (1944).
[3] E. W. B. Gill and A. von Engel, Proc. Roy. Soc. (London) **A192**, 446–463 (1948).

D4. Electron Distribution Functions in Combined DC Space Charge and AC Fields. IRA B. BERNSTEIN AND T. HOLSTEIN, *Westinghouse Research Laboratories.*—Most previous treatments of this problem have assumed the effect of dc space-charge fields, such as ambipolar fields, to be small. Here it is considered dominant. This implies that the electron can be considered as moving with constant energy w (equal to the kinetic energy u plus the electrostatic potential energy φ) in the space-charge well. The effects of collisions and the ac field are regarded as perturbations. In particular it is assumed that on the average the electron executes many oscillations in the well before suffering appreciable energy change due to collisions and the ac field. This indicates the desirability of introducing the variable w into the Boltzmann equation instead of u. The mathematical elaboration of these ideas leads to a difference-differential potential equation which can be solved under certain simplifying assumptions regarding the cross sections. The distribution function and specific ionization rate thus derived are compared with the corresponding quantities for the case of no space-charge field.

D5. Further Results of Studies of Microwave Oscillations in Gaseous Discharges. ROGER P. WELLINGER, JOSEPH A.

SALOOM, AND JAMES E. ETTER, *University of Illinois.*—In the process of investigating the causes of microwave oscillations in gaseous discharges, a new series of measurements has been made on the Wehner oscillator, using improved microwave circuitry and a more stable discharge. It was found that under certain conditions the band width of the oscillator spectrum was as broad as seven percent, but by proper adjustment of the discharge parameters the band width could be made to be as narrow as approximately 0.3 percent. Measurements have shown that the broad band width was associated with the presence of several simultaneous oscillations at different frequencies. Only when the oscillator operated in one dominant mode was it possible to obtain accurate quantitative measurements on the wavelength characteristics of the oscillations. The rf power distribution in the discharge was measured using biased probes, which indicated the presence of bunched electrons in the discharge. By using small rf probes, the phase difference between rf signals present at any two points in the discharge was measured. By changing various elements of the Wehner oscillator a correspondence between this oscillator and the gas discharge diode oscillators investigated by previous workers is shown. The envelope of the diode oscillator is equivalent to one of the elements of the Wehner structure.

D6. Retrograde Arc Motion of Supersonic Speed. CHARLES G. SMITH, *Raytheon Manufacturing Company.*—A mercury arc in a vertical magnetic field was raced around a carboloy cylinder projecting about three mm above the mercury. Arc current and field were parallel except at the carboloy anchor. Revolutions per second were observed by probe methods. The motion was retrograde (contrary to amperes law) for all fields. The speed curve rose rapidly between 1000 and 3000 oersteds and leveled off at 120 meters per sec (approximately sonic speed in the Hg vapor). At about 9000 oersteds the curve rose rapidly to about twice the plateau value and continued a less rate of rise to the highest field, 16,500 oersteds. Studies could be made of an arc running around in a shallow groove cut in the carboloy near its top. This arc was above the junction of liquid and carboloy. Its speed curve showed a short plateau but with speeds about three times those noted above. Ultimate speeds about six times sonic were found. These and other observations seem to leave us without a satisfactory theory of the retrograde motion.

D7. The Tungsten Arc in Mixtures of Argon and Helium.* T. B. JONES AND MERRILL SKOLNIK, *Johns Hopkins University.*—An experimental study was made of the properties of the electric arc with one-fourth-inch diameter tungsten-rod electrodes in mixtures of argon and helium pressure. The current range was from 10 to 100 amperes. Measurements were obtained of the plasma gradients and of the variations of the arc voltage as a function of the composition of the mixture for constant current. The change in arc appearance with the mixture was also observed. It was found that the properties of the arc in mixtures were a cross between the properties observed in the pure gases. With mixtures ranging from pure argon to argon containing 85 percent helium, the properties of the argon arc were more dominant, while the influence of the helium was more pronounced for concentrations of helium greater than this amount. When the properties of the argon arc were more dominant, the chief effect of the helium was observed at the cathode region. In general, small amounts of argon in helium have greater effect on the arc characteristics than small amounts of helium in argon. However, the dependence of the arc properties on the presence of the lower ionization potential gas is considerably less than that observed in glow discharges.

* This work was supported by the ONR

D8. Electrical Phenomena in the Hissing Arc.* T. B. JONES AND B. H. LIST, *Johns Hopkins University.*—When the carbon arc begins to hiss in air, several phenomena occur simultaneously: (1) there is an abrupt drop in arc voltage of about ten volts; (2) the anode spot begins to move in a rapid random manner; (3) audiofrequency and radiofrequency oscillations are produced by the arc; and (4) there is a darkening of the anode, indicating a lower anode temperature. A study of the hissing arc at atmospheric pressure in air, nitrogen, oxygen, argon, helium, and carbon dioxide showed that these characteristic changes occurred only in air, nitrogen, and oxygen. The abrupt drop in voltage was shown to be related to the mechanism of supplying positive ions in the vicinity of the anode. The magnitude of the voltage drop is believed to be dependent upon the ionization potential of the chemical products formed in the arc. Both types of oscillations were independent of circuit parameters. The low frequency random oscillations of voltage, current, and sound were produced by the rapid motion of the anode spot. The radiofrequency oscillations occurred in narrow bands at 1, 2, 4, 8, 16, 32, and 64 megacycles per second. It was shown that these oscillations might be caused by motions of positive ions in the arc plasma.

* This work was sponsored by the ONR.

E2. Band Spectra in Pulsed Nitrogen Discharges.* C. F. HENDEE,† *Northwestern University.*—When the high voltage trigger pulse is applied to the external electrode of a condenser discharge flash tube, a short duration light flash is emitted that precedes the main light flash associated with the discharge of the condenser. This light flash has been studied oscillographically and has a duration generally between 10^{-6} sec and 10^{-7} sec. Using this technique to produce a discharge in nitrogen, the light pusle shapes of the first and second positive bands have been studied. The first positive band pulse has a decay time about ten times that of the second positive band, and decreases with increasing pressure. The decay time *vs* pressure curve is of the form expected when a metastable level is involved. This may be due to a slight metastability in the upper $B^3\pi g$ level of the first positive band system or to metastability of the $a^1\pi$ level[1] from which the $B^3\pi g$ level may be populated by the process suggested by Nicholls.[2]

* This work has been supported by the Bureau of Ships under contract NObs-28373, Dr. W. S. Huxford, Director.
† Now at Philips Laboratories, Inc., Irvington-on-Hudson, New York.
[1] G. Herzberg, Phys. Rev. 69, 362 (1946).
[2] R. W. Nicholls, Nature 162, 231 (1948).

E4. Positive Point-to-Plane Corona Studies in Air.* M. MENES AND L. H. FISHER, *New York University.*—Measurements were made of formative time lags of the positive point-to-plane corona in dry air, using points of radii 0.07, 0.2, and 0.3 mm, gaps of 5, 10, and 15 mm, and steady ultraviolet illumination. Pressures ranged from 700 to 30 mm Hg. Pre-onset current-voltage measurements with illumination were made for these geometries. The formative time lags at a given pressure and gap geometry increase with decreasing overvoltage, showing a limiting upper value at onset. These threshold lags range from less than 0.1 μsec near atmospheric pressure to 1 μsec at 30 mm Hg and show a slight but not marked dependence on point radius, gap length, or illumination level. The steady-state current curves are continuous and reversible up to onset, and unless breakdown occurs, remain so through and beyond onset. Space-charge effects are noticeable below onset. The steady-state corona manifests itself as a burst pulse glow in all but one point-gap combination where pre-onset streamers occur. Moisture was found to favor streamer formation. The short threshold lags together

with their slight dependence on geometry indicate that the positive corona onset in air is gas dependent.

* Supported by the ONR and the Research Corporation.

E6. Hollow Cathodes for *VR*-Tubes with Extended Current Range. F. C. TODD AND J. E. DRENNAN, *Battelle Memorial Institute.*—Penning and his associates at Philips have shown that very stable voltage-regulator tubes are obtained when the noble gases contain less than one part per million of impurities and when the internal surface of the glass envelope is covered with sputtered metal. To further improve *VR*-tubes, the origin and elimination of hysteresis in tubes with these very pure noble gases was presented to this conference last year. As another improvement, the current range of *VR*-tubes can be extended to 600 milliamperes, or more, by the use of hollow cathodes. Satisfactory tubes show spectral lines of the cathode metal in the hollow-cathode glow. The voltage response to superimposed pulses of current through these tubes indicates a variation in the relative importance of the different *V*-processes for different cathode metals. Although the metal is important, the mechanism of the hollow-cathode glow depends on the kinetic theory properties of the gas, which have been discussed in the literature.[1] This is demonstrated for molybdenum plates in argon and neon by the smooth curves that are obtained for plots of the regulation of the tube in volts against the product of the gas pressure on the tube by the separation of the plates of the hollow cathode.

[1] L. B. Loeb, *Fundamental Processes of Electrical Discharge in Gases*, p. 601.

MINUTES OF THE 1951 AUTUMN MEETING OF THE NEW YORK STATE SECTION AT ROCHESTER

THE fall meeting of the New York State Section of the American Physical Society was held in Rochester, New York, on Friday and Saturday, October 5 and 6, 1951. Some 175 physicists attended the two-day session. Meetings on Friday afternoon were held in Strong Memorial Auditorium on the River Campus of the University of Rochester; Saturday sessions convened in the Recreation Building of the Eastman Kodak Company in Kodak Park.

The local committee, under the chairmanship of Donald Morey, was responsible not only for an excellent program, but also for two minor breaks with tradition which appear to have found favor with the members. Security regulations make it increasingly difficult to arrange for plant tours, the traditional item on the Friday agenda; the committee therefore scheduled a session of invited papers, some of them accompanied by demonstrations, for Friday afternoon. The second break with tradition involved replacing the usual Friday evening dinner by a "mixer" with a somewhat (nay, considerably) more informal atmosphere. Refreshments (liquid and solid), music, and other entertainment—some of it contributed unknowingly by participants in a U of R football rally— all helped to make the mixer a distinct success, despite the abnormally (according to the Rochester contingent) warm weather. Highlight of the evening was a most interesting talk on violins and violin-making by Louis Condax, a member of the Kodak Research Laboratories.

Two concurrent sessions on Saturday morning were devoted to contributed papers; Saturday afternoon was given over to a Symposium on the Physics of the Photographic Latent Image. Titles of the invited papers, and abstracts of the contributed papers, appear below.

L. W. PHILLIPS, *Secretary*
New York State Section,
American Physical Society,
University of Buffalo,
Buffalo 14, New York

Invited Papers

Principles of Automatic Mechanical Regulation. W. I. CALDWELL, *Taylor Instrument Company.*

The Response to Radiation of Alkali Halides. S. M. MACNEILLE, *Development Department, Eastman Kodak Company.*

The Response to Radiation of Certain Glasses. N. J. KREIDL, *Chemical Research Laboratory, Eastman Kodak Company.*

Counters and Circuits Used in High Energy Nuclear Research. J. B. PLATT, *University of Rochester.*

Crystallizing the Objectives of the National Science Foundation in Regard to College Teaching. C. L. HENSHAW, *Colgate University.*

Symposium on the Physics of the Photographic Latent Image. H. Hoerlin, Ansco Research Laboratory, *Moderator.*

The Present Status of Latent Image Theory. J. H. WEBB, *Eastman Kodak Company.*

Electron and Hole Conduction in Silver Chloride Crystals. L. P. SMITH, *Cornell University.*

Photographic Sensitivity and Related Properties of Ionic Lattices. F. D. URBACH, *Eastman Kodak Company.*

Contributed Papers

Analog Computers for Coordinate Transformation. N. L. FRITZ, *Kodak Research Laboratories.*—One method of ana-

lytical density measurement of color film images makes use of three transformation equations of the form, analytical density $=a_1D_R+a_2D_G+a_3D_B+K$, where the a's are constants and D_R, D_G, and D_B are densities to red, green, and blue light. The three equations must be solved once for every film area tested, or 20 times to obtain a single set of characteristic curves of a sample of a product. Analog computers have been developed to do this rapidly and accurately. Voltage addition and current addition types have been constructed. Either can be ac or dc operated. The analytical density indicator can be either a meter or a servo-driven dial. The accuracy of computation is dependent both on the quality of certain of the components, and on the design—primarily on the loading effect. The systematic errors of computation as functions of design have been computed and optimum design selected. Instruments now in use solve the 3 equations and present the 3 answers simultaneously and practically instantaneously, with maximum error of elss than 0.2 percent of maximum density.

A Direct Current Analog Computer for Color Analysis. MONROE H. SWEET, *Ansco Research Laboratories.*—Stimulated primarily by the necessity to determine the I.C.I. trichromatic coefficients of large numbers of color film patches, a direct current analog "curve computer" was improvised. It serves similar purposes as curve computers designed by Middleton[1] and Davidson[2] but has several additional features of interest. The functions to be analyzed are graphed and the graphs wrapped around synchronously dirven drums. The abscissa, usually representing the common independent variable for the two functions, is oriented circumferentially, and for each drum a pointer photoelectrically "follows" the curve as the drum rotates. The pointer is connected to a potentiometer. The fraction of the voltage applied to the potentiometer, which is delivered from the variable tap, is proportional to the ordinate of the function at that abscissa value. Although operations of the type

$$\int_a^b E_\lambda \cdot T_\lambda \cdot d\lambda$$

(where E_λ and T_λ are continuous functions of a common independent variable, λ) have been the most frequently used, circuits have also been developed and used which perform the multiplication, division, addition, subtraction, logarithmic, and antiloragithrim operations.

[1] W. E. K. Middleton, Can. J. Research **F28**, 324–332 (1950).
[2] H. R. Davidson and L. W. Imm, J. Opt. Soc. Am. **39**, 633 (1949).

On the Statistics of Geiger Counter Response. L. G. PARRATT AND H. EHRENREICH, *Cornell University.**—The resolving time T of a Geiger counter is usually assumed to be constant (independent of counting rate N_c) in the correction $N=N_c/(1-N_cT)$ for "lost counts." This assumption, since it is wrong, often leads to a false sense of security at rates greater than about 1000 cps (for reasons other than that of spurious counts[1]). At a very low rate, we safely assume that no more than one positive ion sheath exists at any time in the counter tube. At about 1000 cps the probability is significant that two sheaths exist simultaneously. The new sheath is not full-sized if an older shielding sheath is also present. T is then reduced, being the time for the new *small* sheath to move out the reduced distance to allow critical recovery of the anode field, i.e., recovery sufficient to support another countable discharge. At still higher rates, the probability becomes significant that the new sheath is formed before the field has critically recovered; in this case the pulse is not counted but the effective T is appreciably extended. Analytical treatment of the multiple-sheath cases is discussed.

* Supported in part by the ONR.
[1] L. G. Parratt and C. F. Hempstead, J. Appl. Phys. (to be published).

Sensitization of Xerographic Plates by Corona Discharge. H. E. CLARK AND R. G. VYVERBERG, *The Haloid Company.*—The photoconductive layer which constitutes the photosensitive element of xerographic plates[1] must be prepared for exposure to a photographic image by depositing upon it a uniform electrostatic charge. Fine wires at high potential have been used for a corona source to produce this charge. By introducing between the corona-emitting electrode and the xerographic plate an additional electrode held at a fixed potential, L. E. Walkup[2] of Battelle Memorial Institute has succeeded in obtaining significantly more uniform charging. Some first-order theory of the operation of the simple and improved devices has been developed and gives good agreement with experimental results.

[1] R. M. Schaffert and C. D. Oughton, J. Opt. Soc. Am. **38**, 991 (1948).
[2] Private communication.

The Diffraction Pattern of Electromagnetic Waves Near Apertures (with Demonstrations). C. L. ANDREWS, *New York State College for Teachers at Albany.*—By using microwaves of 12-cm wavelengths, one may demonstrate diffraction of apertures that are but a few wavelengths in diameter. The Fresnel zones are the same size as the circles that the teacher draws on the blackboard. It is observed that Kirchoff's refinement of Fresnel zone theory yields the correct values of the intensity on the axis of the ciruclar aperture all the way up to the aperture. It comes as a surprise, however, that the sharpest part of the diffraction pattern is in the plane of the aperture itself. Thomas Young's theory, that the diffraction pattern is the resultant of the direct wave through the aperture and re-radiated wavelets from the edges, yields quantitatively the intensity distribution in the plane of the aperture for the cases calculated. A brief review is made of current problems in diffraction and methods of measurement employed by other laboratories

Soft X-Ray Absorption of Selenium.* M. PARKER GIVENS AND WALTER P. SIEGMUND, *University of Rochester.*—The absorption for a thin layer of solid selenium was determined for the wavelength region between 180 and 240A. Two foils differing in thickness by about 1900A were prepared by evaporating selenium onto thin celluloid films *in vacuo*. The difference in absorption for these two foils was measured using a form of photographic photometry similar to that used by Skinner and Johnston[1] in their studies. The source used was a vacuum spark between copper electrodes which gave many strong lines in the region under investigation. The results indicate a strong absorption edge at 225A which is the result of raising electrons from the M_{IV} and M_V levels to the conduction band. The edge is seen as double, corresponding to the separation between the M_{IV} and M_V levels. There is a sharp drop in absorption toward shorter wavelengths which probably corresponds to a decrease in the density of states $Np(E)$.

* This research was supported by ONR under contract N6onr-24109.
[1] Skinner and Johnston, Proc. Roy. Soc. (London) **A161**, 420 (1937).

Side-Band Suppression in Multilayer Interference Filters. G. J. KOCH AND D. S. BRINSMAID, *Eastman Kodak Company.*—More than 12 years ago Cartwright and Turner proposed the use of multilayer interference films for optical beam splitters.[1] Alternate layers of high and low refractive index materials, usually zinc sulfide and magnesium fluoride, are deposited on glass by the high vacuum vaporization process. The resulting multilayer film reflects broad bands of radiation at wavelengths corresponding to an optical film thickness of an odd number of quarter wavelengths, and transmits the remaining radiation. The techniques for the calculation and deposition of satisfactory layers has been steadily, if slowly, improving, largely in the laboratories of industrial optical firms. Two of the basic problems in the design of multilayer film combinations are: (1) the attainment of a sharp cut in the reflection *vs* wavelength curve, and (2) suppression of the unwanted light in the

side bands adjacent to the principal reflection bands. Two new combinations of layers which largely overcome these problems will be discussed.

[1] C. H. Cartwright and A. F. Turner, Phys. Rev. 55, 1128 (1939).

The Photoconductive Negative Effect in Silver Bromide. W. WEST, *Kodak Research Laboratories.*—In contrast to the normal increase in electrical conductivity caused by exposure to light in annealed crystals of silver bromide, unannealed films exhibit a decrease in conductivity upon exposure at room temperature. The experimental conditions are such that a photochange in conductivity is measured against a balanced-out electrolytic background. The spectral sensitivity of this negative effect is similar to that of the normal internal photoelectric effect in silver bromide and, like the latter, the negative effect shows optical sensitization by dyes. Annealed films can be induced to exhibit the negative effect by immersion in silver nitrate solution, followed by drying; treatment with potassium bromide diminishes the negative effect. Low temperature, the presence of divalent ions in the lattice, and adsorbed gelatine layers also cause the disappearance of the effect. The effect appears associated with a surface condition of the film, and the observations are consistent with the hypothesis that unannealed crystals contain surface positive carriers of relatively high mobility, contributing to the dark conductivity of the sample, which on exposure to light are immobilized by capturing photoelectrons with a consequent reduction in the dark conductivity. The mobile positive carrieres could be adsorbed silver ions or, possibly, if Schottky defects are present, missing bromide ion sites near the surface.

Temperature Dependence of the Spectral Sensitivity of Photographic Emulsions. M. BILTZ, *Kodak Research Laboratories.*—A study of the spectral sensitivity of pure silver bromide emulsions, containing no optical sensitizer, at room and liquid nitrogen temperatures, was used to obtain information on the nature of chemical sensitization. Results on the following four emulsions are given: (a) a primitive (not chemically sensitized) emusilon, (b) a reduction-sensitized emulsion, (c) a sulfur sensitized emulsion, and (d) a primitive emulsion treated with silver nitrate solution. The ratio of their sensitivities at −190°C and 25°C decreases rapidly from 400 mμ toward longer wavelengths. While this decrease continues for (a), the sensitivity ratio of the other emulsions reaches a minimum between 460 and 490 mμ. Beyond the minimum, the sensitivity ratio of (b) rises continuously toward longer wavelengths; the ratio of (c) rises to a maximum and decreases again; and the ratio of (d) rises somewhat and then remains nearly constant. Assuming that these behaviors are connected with the optical absorption of the substances formed by chemical sensitization, the substances are considered to be finely dispersed metallic silver in emulsion (b) and silver sulfide in (c). In emulsion (d) a deformation of the lattice near the surface might have taken place. It seems that in all three cases, the chemical sensitization causes the formation of bromide ion vacancies which could facilitate the formation of the latent image by temporarily capturing electrons liberated during exposure.

Electron Microscopical Studies of Latent Image Distribution. F. A. HAMM, *General Aniline and Film Corporation,* AND H. HOERLIN, *Ansco Research Laboratories.*—The photographic latent image of a negative emulsion cannot be resolved directly by known electron micriscopical techniques. The initial stages of the printed-out image can be demonstrated in elctron micrographs of replicas of emulsion grains. However, this procedure fails to show the initial surface distribution of the latent image. A new technique was therefore developed which permits enlarging the latent image while maintaining the distribution pattern. The technique consists in slow physicial development of the exposed grains in a solution of gold ions[1] and subsequent removal of the gelatin matrix by enzyme treatment, followed by fixation of the grains on the specimen secreen. The presence of a silver-gelatinate envelope tightly surrounding each grain was observed. This relatively insoluble complex retains the physically developed latent image centers. The procedure was used to learn the distribution of the latent image obtained by exposures to alpha-particles, 65-kv x-rays, to light of optimum intensity (1/100 sec) and of very low intensity (40-hr exposure time). The electron micrographs show distinctly different distribution patterns which are in line with expectations based on current photographic theory.

[1] Described by T. H. James, J. Coll. Sci. 3, 447 (1948).

A Novel Aspect and Application of Electromagnetic Induction. DON CORNISH, *Kodak Research Laboratories.*—Simple experiments prove that a transformer with novel core structure and exactly similar primary and secondary coils can have an output voltage (or current) exceeding the input voltage (or current). The core structure departs from present practices in two essential respects, namely: (1) the core is threaded two or more times through one of the coils, and (2) magnetic flux "leakage" between separate turns of the core is minimized by deliberate use of nonferromagnetic materials (e.g., air) between the core turns. Mathematically, winding a magnetic core (or magnetic circuit) around an electric circuit and the converse are electromagnetic equivalents because they are topologically identical. The usual induction equations remain valid, with one exception, e.g., the number of turns parameter, N, must be redefined to mean the product of the number of coil turns by the number of core turns. Potential applications include various induction devices utilizing magnetic circuits with complex permeabilities of absolute magnitudes significantly greater than unity, e.g., transformers, antennas, transductors, generators, etc.